Between order and disorder

Ultracold atoms in a quasicrystalline optical lattice

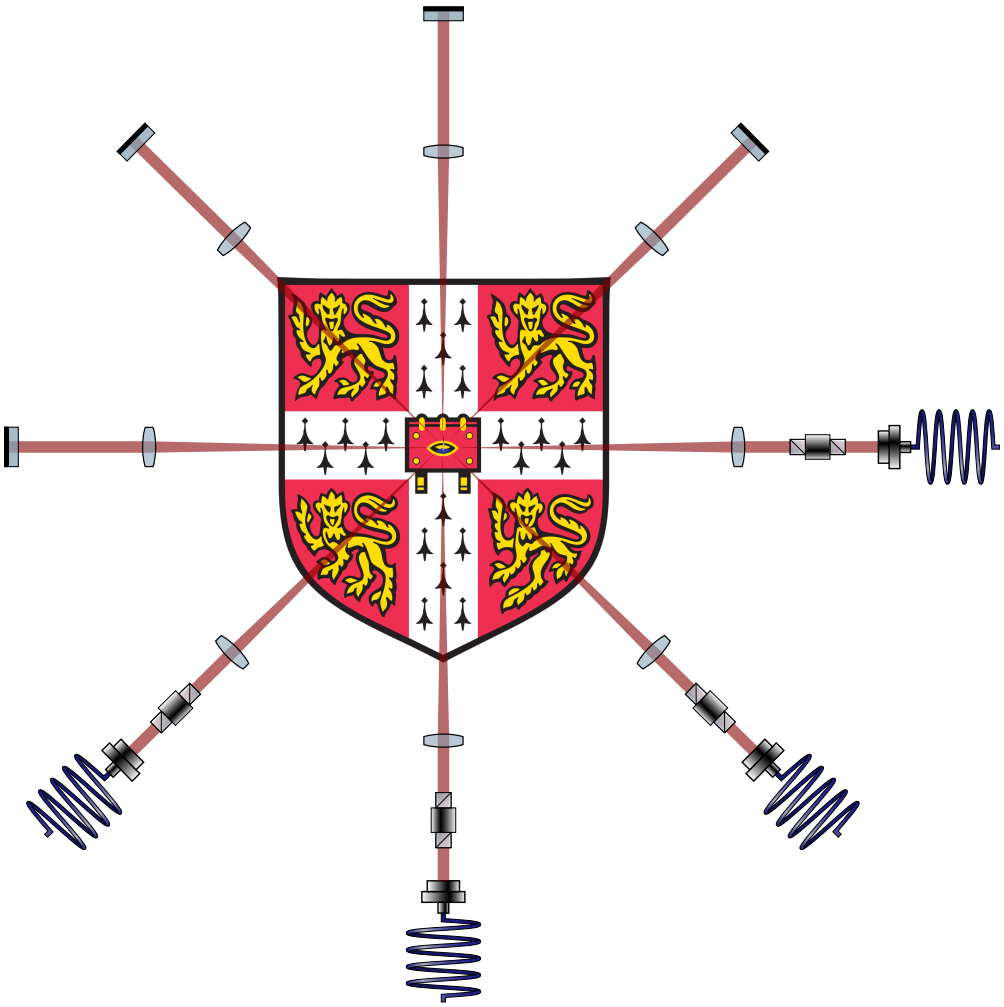

Matteo Stefano Sbroscia

This dissertation is submitted for
the degree of Doctor of Philosophy

University of Cambridge
Churchill College
August 2019

“Twixt order and disorder lies but a silver mean” was the originally intended title. But I did not want it to appear on my CV for the rest of my life.

To my grandparents Guido Paletti and Ursula Seweron,
and to my great-aunt Rita Paletti.

Declaration

This dissertation is the result of my own work and includes nothing which is the outcome of work done in collaboration except as specified in the text.

It is not substantially the same as any work that I have submitted, or, is being concurrently submitted for a degree or diploma or other qualification at the University of Cambridge or any other University.

I further state that no substantial part of my dissertation has already been submitted, or, is being concurrently submitted for any such degree, diploma or other qualification at the University of Cambridge or any other University.

This thesis does not exceed the word limit of 60,000 words, including abstract, tables, footnotes and appendices, imposed by the Faculty of Physics and Chemistry.

Abstract

Between order and disorder:
ultracold atoms in a quasicrystalline optical lattice
by Matteo Stefano Sbroscia

Quasicrystals are long-range ordered and yet non-periodic. This interplay results in a wealth of intriguing physical phenomena, such as self-similarity, the inheritance of topological properties from higher dimensions, and the presence of non-trivial structure on all lengthscales.

However, quasicrystalline materials are notoriously hard to synthesise, as defects and impurities may greatly alter their final microscopic composition. The field of quantum simulation with ultracold atoms offers a solution to this problem, namely the use of optical lattices – standing waves of light. Optical lattices are free of impurities and therefore ideally suited to study quasicrystals, enabling unprecedented access to observables that are unattainable in condensed matter systems.

This study presents the first experimental realisation of a two-dimensional quasicrystalline potential for ultracold atoms, based on an eightfold symmetric optical lattice. Features pertaining to both ordered and disordered phases are observed, from sharp diffraction peaks in the matter-wave interference pattern, to a disorder-induced localised phase emerging at a critical lattice depth $V_{\mathrm{loc}} \approx 1.78\, E_{\mathrm{rec}}$. The localised phase seems to be resilient against moderate interactions, which would make this the first experimental realisation of a 2D Bose glass.

Contents

The noblest pleasure is the joy of understanding.

Leonardo da Vinci

Introduction

Past, present and future research in the field

The work presented in this thesis belongs to the field of quantum simulation with ultracold atoms in optical lattices. This is contained in the macrocanonical ensemble that spans (ultra)cold atoms, quantum gases and optical lattices, and has seen both experimental and theoretical breakthroughs with the former leading the latter on several fronts.

The experiments described in this thesis employ Rb and K, two of the most widely used species in cold atoms. Rb and Na were the first to be Bose-condensed in 1995 [1, 2] which led to the 2001 Physics Nobel prize. Potassium, on the other hand, exhibits experimentally accessible Feshbach resonances which allow investigation of strongly interacting physics, though still contact and short-range. Other established atomic species to date are H, He, Cs, Li, Na, Yb, Sr, Er, Dy, Ca and Cr, which have all been Bose-condensed (in some cases multiple isotopes) along with more elements soon to join the list, such as Fe and Ti [3]. Novel, different and alternative cooling and trapping schemes are also being investigated, and are culminating in technical milestones such as an all-laser-cooled Bose-Einstein condensate of Rb [4].

A field of great interest is strongly interacting gases, as interactions and correlations lead to the emergence of new and distinct many-body phenomena ("more is different"[5]). These range from the creation of quantum droplets [6, 7] to the unitarity and universality regimes in Fermi gases [8] and (recently emerging) Bose gases [9, 10].

After the generation of the first degenerate Fermi gas [11], tuneable interactions enabled observation of the BCS-BEC crossover [12] and creation and subsequent condensation of molecules [13, 14]. These not only grant access to the field of ultracold quantum chemistry, but also to long-range interactions, where they join the ranks of Rydberg and two-electron atoms.

The controllable and tuneable environment provided by cold atoms enabled the experimental investigation of the BKT phase [15] and theoretical proposals to realise the FFLO phase [16], as well as empirical studies of out-of-equiliubrium phenomena from turbulence [17] to the Kibble-Zurek mechanism [18]. Cold atoms are also being used to reproduce effects pertaining to high-energy physics and cosmology, such as Sakharov waves [19], the dynamical Casimir effect [20], Hawking radiation [21], and the Unruh effect [22].

These last applications fall under the umbrella of *quantum simulation*, Feynman's original idea [23, 24] to circumvent the numerical intractability of large Hilbert spaces by performing the investigation directly on a quantum platform. A system of 300 spins would require 10^{300} bits of storage on a classical transistor-based computer, more than the number of protons in the Universe; simulating a macroscopic quantum device with an Avogadro's number of particles would therefore be impossible.

Key protagonists of quantum simulation are *optical lattices*, generated from interfering a variable number of laser beams, enhancing interactions and providing a flexible platform to study cold atoms in systems exhibiting different symmetries and dimensionalities. These have allowed direct observation of quantum phase transitions [25] and generation of novel phases of matter such as supersolids [26, 27], Bose glasses [28, 29], Anderson localised [30] and many-body localised [31, 32] states. They have also been combined with the single-site resolution enabled by quantum gas microscopes [33, 34].
Optical lattices also offer insight into topological phases of matter, where many-body effects may emerge even in the absence of interactions. These range from the experimental implementations of the Haldane [35] and Harper [36] models, to artifical gauge fields and synthetic dimensions [37, 38], also encompassing Floquet and Hamiltonian engineering in the time domain, leading to new dynamics [39] and phase transitions [40]. Finally, optical lattices can be used as clocks [41], where they join the metrology and ultra-high precision measurements brigade along with long-lived Rydberg and two-electron atoms.

Quantum simulation is also perfomed on other platforms, from trapped ions (though hard to produce in large numbers, the current record is 200 [42]) and Bose-condensed photons [43], where thermo-optic phase imprinting [44] provides an analogue to optical lattices, to photonic crystals, waveguides and solid-state systems probed by scanning electron microscopy.

From talks and grant proposals, the goal of cold atoms research seems to be providing a platform for quantum computation, and indeed trapped ions and Rydberg atoms are being used for quantum information processing owing to their long lifetimes and individual addressability. This is also driving the miniaturisation and commercialisation of quantum technologies.

Realistically, however, no quantum computer is likely to be made of cold atoms, at least not anytime soon. Rather, these platforms hold the high ground because of their ability to perform *analogue* quantum computation, i.e. quantum simulation. This renders them ideal to implement, test and disprove theories from all fields of physics, from the latest measurements of the electric dipole moment [45], to proposals to couple cold matter to dynamical gauge fields [46], investigate AdS/CFT correspondance [47, 48] and detect gravitational waves [49]. These might soon question the need for expensive and bulky experiments such as particle accelerators.

Our work

We have implemented a novel geometry of optical lattices in order to study 1D and 2D quasicrystalline phases of matter, which lack translational invariance and periodicity but still possess long-range order.

The fractal and self-similar nature of quasicrystals results in non-trivial structure on all lengthscales which adds complexity to the otherwise *too* simple and *too* clean optical lattices.

Novel phases of matter are expected to emerge, from Anderson to many-body localised states in both fermions and bosons (Bose glasses). Our system also allows investigation of 4D physics, access to synthetic dimensions, and excitations of new quasiparticles such as phasons.

The lack of a unit cell, the invalidity of Bloch's theorem, and the non-separability of

the 2D potentials discussed in this thesis make the study of quasicrystals a numerically intractable problem. A quantum simulator is hence an ideal platform to investigate the properties of this class of materials.

This thesis

This is one of the first theses produced by our group, and it is meant to be a manual for all our future recruits. I tried to write the thesis that I would have wanted to read when I started my own PhD, having transitioned from a different field and lacking the necessary theoretical foundations and experimental knowledge.

The manuscript is divided into the following sections:

- Part I: This introduces statistical physics and the Bose-Einstein condensed phase (chapter 1), and discusses cooling and trapping schemes for cold atom experiments (chapter 2). A review of the current physical and mathematical understanding of quasicrystals is presented in chapter 3.
- Part II: The experimental apparatus, including its hardware and software components, is detailed in chapters 4 and 5. Chapter 6 summarises the imaging and characterisation methods of atomic samples.
- Part III: Matter-wave diffraction experiments yielding sharp diffraction peaks and establishing long-range order are presented in chapter 7, while chapter 8 discusses the numerical and experimental investigation of an extended-to-localised phase transition. Finally, other miscellaneous findings are presented in chapter 9.

Contributions

The experimental apparatus described in chapters 4 and 5 was jointly designed, assembled, and characterised by (Dr.) Konrad Viebahn and myself, as we were the first PhD students in the group. Major contributions were made by Dr. Stephen Topliss (group electronic engineer), Hendrik von Raven, Oliver Brix, Edward Carter, Max Melchner, Michael Höse, and Jr-Chiun Yu.

Part I

Theoretical foundations

Modern Physics

Aristotle said a bunch of stuff that was wrong.
Galileo and Newton fixed things up. Then Einstein broke everything again.
Now, we've basically got it all worked out, except for small stuff, big stuff, hot stuff, cold stuff, fast stuff, heavy stuff, dark stuff, turbulence, and the concept of time.

Zach Weinersmith [50]

Do you guys just put the word quantum *in front of everything?*
Scott Lang, from *Ant-Man and the Wasp* [51]

1 Quantum, interacting gases

This chapter discusses the thermodynamic equilibrium distributions and the phase transition to a Bose-Einstein condensate, introducing equations and notions used later in the thesis such as phase space density and collisional dynamics.

1.1 Statistics

1.1.1 Indistinguishability

The Pauli exclusion principle

A wavefunction Ψ depending on two sets of variables $\{1, 2\}$, e.g. the positions of the two electrons in a Helium atom, can be constructed in the absence of interactions from the single-particle eigenstates ψ and φ:

$$\Psi(1, 2) = \psi(1)\,\varphi(2). \tag{1.1}$$

The exchange operator Ex is defined to swap the labels $1 \leftrightarrow 2$:

$$\mathrm{Ex}\,[\Psi(1, 2)] = e\,\Psi(2, 1), \tag{1.2}$$

and upon its double action one would expect to return to the initial configuration:

$$\mathrm{Ex}^2\,[\Psi(1, 2)] = e^2\,\Psi(2, 1) \stackrel{!}{=} \Psi(1, 2). \tag{1.3}$$

The eigenvalues of Ex must therefore satisfy $e^2 = 1$, and hence $e = \pm 1$: upon label exchange, the wavefunction may either acquire an overall minus sign (*antisymmetric* wavefunction) or remain exactly the same (*symmetric* wavefunction).

Quantum particles are identical and hence indistinguishable, a fact that needs to be encoded in the wavefunction itself, as shown in eq. 1.4, to ensure the invariance of physics

upon particle relabelling, for it was us the observers who had (arbitrarily) labelled them in the first place:

$$\Psi_{\text{ind}}(1,2) = \frac{1}{\sqrt{2}}\left[\,\psi(1)\varphi(2) \pm \psi(2)\varphi(1)\,\right]. \tag{1.4}$$

As a consequence of eq. 1.4, an antisymmetric wavefunction with the same set of labels (or *quantum numbers*) is equal to zero. Two identical particles can therefore not co-exist at the same position, an effect known as the *Pauli exclusion principle* and observed by *fermions*. A symmetric wavefunction, on the other hand, is displayed by *bosons*. The particles' positions can thus be affected in the absence of any external force, as illustrated in fig. 1.1. This dramatically impacts the physical and chemical properties of macroscopic materials, such as ^{3}He and ^{4}He which show distinct superconductivity mechanisms and transition temperatures despite possessing the same electronic structure.

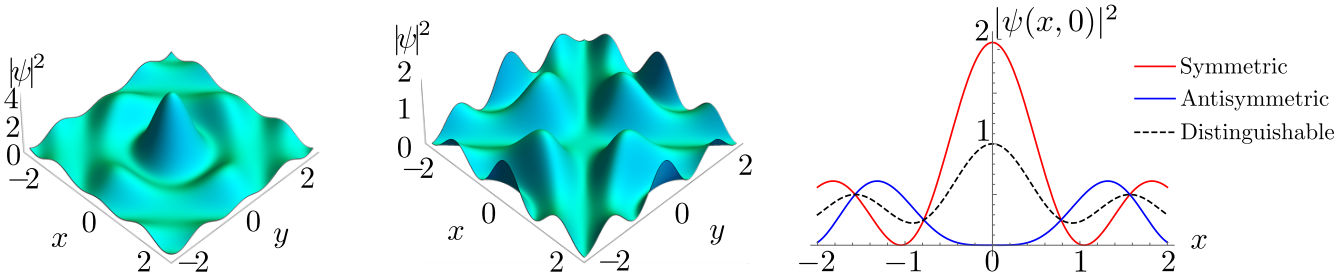

(a) symmetric: $|\cos(x)\cos(2y) + \cos(y)\cos(2x)|^2$

(b) antisymmetric: $|\cos(x)\cos(2y) - \cos(y)\cos(2x)|^2$

(c) cut along $y = 0$

Figure 1.1 : Visualisation of the Pauli exclusion principle exhibited by two electrons in the ground and first excited states of a square well. In (a), the symmetric combination enables coexistence at $x = y = 0$ while in (b), the probability density $\forall x = y$ is exactly zero. The indistinguishability of quantum particles leads to bunching and anti-bunching effects (c).

Topological argument

The following section is quite mathematical and is provided as a more rigorous proof for the Pauli exclusion principle in all dimensions, in order to dot the i's and cross the $\hbar$'s. It is not relevant for the rest of the thesis so it can be regretlessly skipped.

The argument presented in the section above is short, simple, and quite common in the literature. It is however a bit *too* simple: why should $\text{Ex}^2\left[\Psi(1,2)\right]$ in eq. 1.3 be exactly equal to $\Psi(1,2)$ and not just proportional to it? Quantum mechanics is defined over a projective Hilbert space, so any phase factor would not affect the physical observables either way.

Permutation of the particles' labels is a *continuous* operation over a parameter space, as illustrated in fig. 1.2, and it cannot reliably be characterised by the action of the instantaneous operator Ex. The system will acquire a phase factor depending on the specific loop that was traced out in this space, akin to the geometric and Berry phases gained during parallel transport in general relativity and quantum mechanics [52].

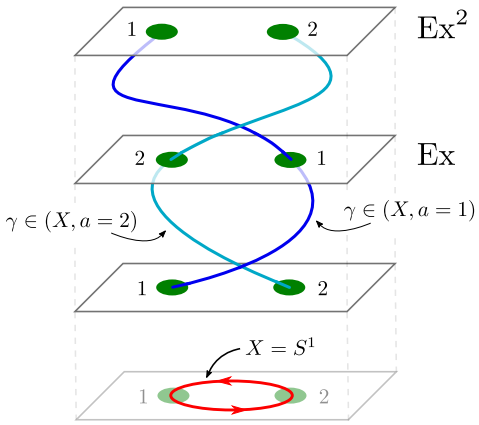

Figure 1.2 : The double action of the exchange operator Ex^2 in eq. 1.3 is a continuous transformation corresponding to a loop γ traced out by particles 1 and 2 in a pointed topological space (X, a).

The description of loops and spaces requires basic topology. A topological space X is a mathematical structure whose details are not needed here, while a *pointed* topological space (X, a) is the same as X but with a specified point $a \in X$ enabling definitions of closed loops γ about a. The n^{th} homotopy group consists of the *topologically distinct* n-dimensional spheres S^n, i.e. that cannot be deformed into one another. In order to classify the symmetries of the one-dimensional loops, we employ the first homotopy (or fundamental) group π_1:

$$\pi_1(X, a) = \{[\gamma] \,|\, \gamma : [0, 1] \to X, \quad \gamma(0) = \gamma(1) = a\}. \tag{1.5}$$

The smooth and continuous label exchange operation defined in eq. 1.3 and shown in fig. 1.2 is a proper rotation in d dimensions, represented by the the Special Orthogonal group $SO(d)$:

$$SO(d) = \{R \text{ being a } d \times d \text{ matrix} : R^T = R^{-1}, \det R = 1\}. \tag{1.6}$$

$SO(d)$ is a Lie group, hence a differentiable manifold and a type of topological space: its fundamental groups are listed in table 1.1.

dimension d	group $SO(d)$	fundamental group π_1	comments
1	SO(1)	identity	trivial, just one element
2	SO(2)	$\mathbb{Z}$	winding number, countably infinite
$\geqslant 3$	SO($d \geqslant 3$)	$\mathbb{Z}_2$	only two topologically distinct elements

Table 1.1 : Fundamental groups of $SO(d)$.

In $d = 2$, it is impossible to avoid a crossing and hence there are countably infinite topologically distinct ways of looping from a back to itself, each distinguished by the winding number w as illustrated in fig. 1.3.

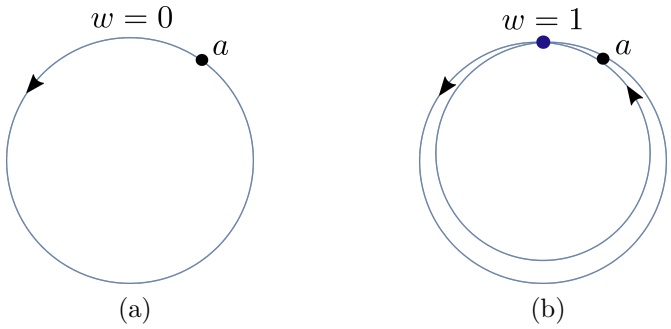

Figure 1.3 : In $d = 2$, rotations are represented by $SO(2)$ and visualised as a circle S^1. Closed loops about a are topologically distinguished by the winding number w.

However, in $d \geqslant 3$, there exist only two topologically distinct permutations, as illustrated in fig. 1.4. This is a consequence of the 2-sphere S^2 being mapped onto $SU(2)$, which is the *double cover* of the rotation group $SO(3)$: $SO(3) \cong SU(2)/\mathbb{Z}_2$. The space of proper rotations $SO(3)$ is then confined to a *hemisphere* with opposite ends identified. This redundancy is justified by noting that a rotation of θ about $\mathbf{n}$ is identical to one of $\pi - \theta$ about $-\mathbf{n}$.

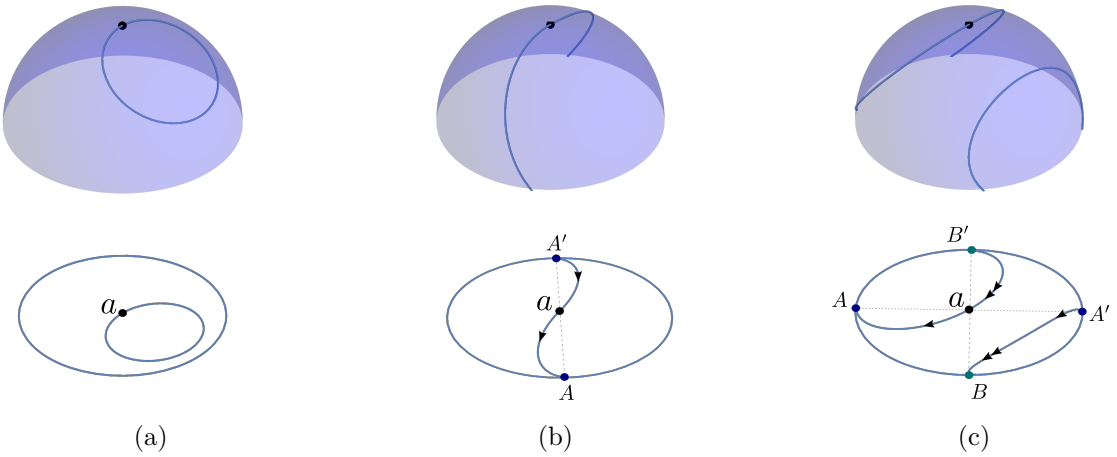

Figure 1.4 : The paths on the $SO(3)$ hemisphere shown in (a) and (b) are topologically distinct, as the former is contractible to a point while in the latter A and A' are fixed on the boundary. The path in (c) is topologically equivalent to (a), since deformation of B and B' allows bringing the loops above the boundary and hence shrinking them to a point. In $d = 3$, therefore, there exist only two distinct loops.

The results in table 1.1 result from the existence of a double cover for any $d \geqslant 3$, which guarantees only two topologically distinct loops.

Particle exchange can only amount to an overall phase factor θ in the wavefunction:

$$\mathrm{Ex}[\Psi(2,1)] = \mathrm{e}^{\mathrm{i}\theta}\Psi(1,2), \tag{1.7}$$

which can be acquired in π_1 distinct ways: $2\pi/\mathbb{Z}_2$ in $d \geqslant 3$ and $2\pi/\mathbb{Z}$ for $d = 2$. In 3D space, the eigenvalues of the exchange operator are ± 1 and correspond to bosons and fermions, but in 2D they may be any rational divisor of 2π, and are referred to as *anyons*.

As shown in fig. 1.1, the symmetry of the overall wavefunction determines whether particles can exist in the same quantum state. Hence, bosons and fermions are distinguished by the commutator (anti-commutator) of their creation and annihilation operators a and $a^\dagger$:

$$\begin{aligned} \text{for bosons:} \quad & \left[a, a^\dagger\right] = 0, \\ \text{for fermions:} \quad & \left\{a, a^\dagger\right\} = 0. \end{aligned} \tag{1.8}$$

Technical note

While quantum field theory is needed to relate particle statistics to spin, it is not required here. The foundation of the proof lies in the existence of a double cover for $SO(d \geqslant 3)$, which is satisfied by both the Poincaré $\mathcal{P} = SO(1,3) \ltimes \mathbb{R}^{1,3}$ and the Galilean group $\mathcal{G} = (SO(3) \ltimes \mathbb{R}^3) \times (\mathbb{R}^1 \times \mathbb{R}^3)$ because $SO(1,3) \xleftarrow{2:1} SL(2,\mathcal{C})$ and $SO(3) \xleftarrow{2:1} SU(2)$.

1.1.2 Classical, ideal gases

Classical and *ideal* are opposed to *quantum* and *interacting*[1].
An atom in a classical gas follows a defined trajectory in real space ($\mathbf{r}$) and in momentum space ($\mathbf{p}$), which together characterise its state $s(\mathbf{r}, \mathbf{p})$ in *phase space*.
The Hamiltonian for non-interacting particles in an external potential $V(\mathbf{r})$ is given by:

$$H_0(\mathbf{r}, \mathbf{p}) = \frac{\mathbf{p}^2}{2m} + V(\mathbf{r}). \tag{1.9}$$

In the grand canonical ensemble, the system is in thermal and chemical equilibrium with a large reservoir at temperature T and chemical potential μ. The occupation probability of a state at energy E is given by:

$$P = \frac{1}{Z} \mathrm{e}^{-\beta(E-\mu N)} \quad \text{with} \quad Z = \sum_j \mathrm{e}^{-\beta E - \mu N}, \tag{1.10}$$

where Z is the grand partition function and $\beta = 1/k_\mathrm{B}T$. P describes a *Boltzmann distribution*.

In the continuum, assuming the classical regime of dilute occupation of each state such that $E \gg \mu$, one can write:

$$P(\mathbf{r}, \mathbf{p}) = \frac{1}{Z} \mathrm{e}^{-H_0(\mathbf{r},\mathbf{p})/k_\mathrm{B}T} \quad \text{with} \quad Z = \int \mathrm{d}^3\mathbf{p}\, \mathrm{d}^3\mathbf{r}\, \mathrm{e}^{-H_0(\mathbf{r},\mathbf{p})/k_\mathrm{B}T}, \tag{1.11}$$

where P is now the probability *density* of finding a particle at position $\mathbf{r}$ and momentum $\mathbf{p}$. We then introduce the *phase space density* as the number of singly occupied points per unit phase space volume, $\rho(\mathbf{r}, \mathbf{p}) = N \cdot P(\mathbf{r}, \mathbf{p})$.

- The probability density of finding a particle at position $\mathbf{r}$ is $n(\mathbf{r})$:

$$\begin{aligned} n(\mathbf{r}) = \int \mathrm{d}^3\mathbf{p}\, \rho(\mathbf{r}, \mathbf{p}) = N \int P(\mathbf{r}, \mathbf{p})\, \mathbf{r} = \\ \rho(0,0)\, \mathrm{e}^{-\frac{V(\mathbf{r})}{k_\mathrm{B}T}} \int_0^\infty \mathrm{e}^{-\frac{p^2}{2mk_\mathrm{B}T}}\, 4\pi p^2 \mathrm{d}p \\ \Rightarrow n(\mathbf{r}) = n_0\, \mathrm{e}^{-\frac{V(\mathbf{r})}{k_\mathrm{B}T}}, \end{aligned} \tag{1.12}$$

[1] However, even an ideal gas is weakly interacting, in order to be able to reach thermal equilibrium.

where $\rho(0,0)$ and n_0 are the central densities[2] in phase space and in real space, related by:

$$\rho(0,0) = \frac{N}{Z} = \frac{n_0}{(2\pi m k_\mathrm{B} T)^{3/2}} = \frac{n_0 \lambda_\mathrm{th}^3}{(2\pi\hbar)^3} = \frac{D}{(2\pi\hbar)^3}. \tag{1.13}$$

$\lambda_\mathrm{th} \equiv \sqrt{2\pi\hbar^2/mk_\mathrm{B}T}$ is the thermal de Broglie wavelength and $D = n_0\lambda_\mathrm{th}^3 \propto N/Z$ the *degeneracy parameter*. The regime where $D \sim 1$ corresponds to one particle per Planck volume, where the (classical) treatment of low state occupation is no longer applicable thus signifying the onset of quantum degeneracy.

The number of particles N_tot can be expressed as:

$$N_\mathrm{tot} = \int n(\mathbf{r}) \mathrm{d}^3\mathbf{r} = n_0 \int \mathrm{e}^{-\frac{V(\mathbf{r})}{k_\mathrm{B}T}} \mathrm{d}^3\mathbf{r}. \tag{1.14}$$

The potentials $V(\mathbf{r})$ usually employed to trap cold atom are power-laws of the form:

$$V(\mathbf{r}) = V_0 r^{3/\gamma}, \tag{1.15}$$

where $\gamma \to 0$ results in a spherical square well (the free system limit), $\gamma \geqslant 3$ in dimple traps, and $\gamma = 3/2$ corresponds to the *harmonic* trap $V_0 = {}^1\!/_2\, m\bar{\omega}^2 r^2$ used in our experiments.
For future use, it is useful to quote the following integral:

$$\int \mathrm{e}^{-\frac{V_0 r^{3/\gamma}}{k_\mathrm{B}T}} \mathrm{d}^3\mathbf{r} \propto \left(\frac{k_\mathrm{B}T}{V_0}\right)^\gamma. \tag{1.16}$$

- The probability density of finding a particle at momentum $\mathbf{p}$ is $n(\mathbf{p})$:

$$\begin{aligned} n(\mathbf{p}) &= \int \mathrm{d}^3\mathbf{r}\, \rho(\mathbf{r},\mathbf{p}) = N_\mathrm{tot} \int P(\mathbf{r},\mathbf{p})\, \mathbf{r} = \\ &\rho(0,0)\, \mathrm{e}^{-p^2/2mk_\mathrm{B}T} \int \mathrm{e}^{-\frac{V(\mathbf{r})}{k_\mathrm{B}T}}, \\ \Rightarrow n(\mathbf{p}) &= N \underbrace{\left(\frac{1}{2\pi m k_\mathrm{B} T}\right)^{3/2} \mathrm{e}^{-\frac{\mathbf{p}^2}{2mk_\mathrm{B}T}}}_{f_\mathrm{M}(\mathbf{p})}, \end{aligned} \tag{1.17}$$

  where the space integral was replaced by eq. 1.14.
  $f_\mathrm{M}(\mathbf{p})$ is the *Maxwell-Boltzmann* distribution, also expressed for the magnitude $p = |\mathbf{p}|$ as:

$$f_\mathrm{M}(p) = 4\pi p^2 f_\mathrm{M}(\mathbf{p}). \tag{1.18}$$

The de Broglie wavelength $\lambda_\mathrm{th} = h/p$ controls the size of a wavepacket with momentum p. Quantum degenerate effects become important when the wavepackets start overlapping so that the wave nature of matter cannot be neglected, in the same way as geometric optics is not applicable when the wavelength λ is comparable to the object size d.
This is equivalent to the regime where there is one particle per volume λ_th^3:

$$1 \sim \frac{N_\mathrm{tot}}{V}\lambda_\mathrm{th}^3 = n_0\lambda_\mathrm{th}^3 = D, \tag{1.19}$$

[2] and usually also the *peak* densities, since most confining potentials used for trapping atoms have a minimum at their centre.

where N_{tot} is the number of particles, V is the volume, and D the degeneracy parameter. Typical values of D are shown in table 1.2.

System	T [K]	D	regime
Air	300	$\sim 10^{-10}$	Classical
Superfluid ^{4}He	4	~ 1.5	Quantum
Valence electrons in Cu	300	$\sim 2,000$	Very quantum

Table 1.2 : The degeneracy parameter D determines when the wave nature of matter is dominant hence requiring a quantum treatment.

1.1.3 Quantisation

Quantum distributions

When $D \sim 1$ the assumption of sparse population of states breaks down and one needs to account for particles in the same (quantum) state, which will be subject to the consequences of indistinguishability discussed in section 1.1.1.

The Hamiltonian is replaced by a quantum operator with eigenstates $|\Psi_i\rangle$ and eigenvalues E_i. In thermal equilibrium, a multitude of many-body energy eigenstates are occupied in order to maximise the entropy, resulting in a thermal density matrix of the form:

$$\mathrm{e}^{-\beta(H-\mu N)} = \sum_i \mathrm{e}^{-\beta(E_i-\mu N_i)} \, |\Psi_i\rangle\langle\Psi_i|. \tag{1.20}$$

Every many-body state is then "Boltzmann" distributed as in eq. 1.10.

For non-interacting particles, the energy eigenstates are the single-particle states $|n_j\rangle$, yielding n_j particles at energy E_j. The average number of particles per state, the *occupancy* f, is defined as:

$$f = \bar{n} = \frac{1}{Z} \sum_j \langle n_j | \, \mathrm{e}^{-(H-\mu N)/k_{\mathrm{B}}T} n | n_j \rangle = \frac{\sum_j n_j \, \mathrm{e}^{-n_j(E_j-\mu)/k_{\mathrm{B}}T}}{\sum_j \mathrm{e}^{-n_j(E_j-\mu)/k_{\mathrm{B}}T}}. \tag{1.21}$$

Expressing the mean as $\bar{n} = \sum_j n_j P(n_j)$, we identify the probability density of finding n particles in the same state of energy E to be:

$$P(n) = \frac{1}{Z} \, \mathrm{e}^{-n(E-\mu)/k_{\mathrm{B}}T} \quad \text{with} \quad Z = \sum_n \mathrm{e}^{-n(E-\mu)/k_{\mathrm{B}}T} = \sum_n \left(\mathrm{e}^{-r}\right)^n. \tag{1.22}$$

For bosons, the commutation relation in eq. 1.8 imposes no restriction on the number of particles in the same state. Hence $Z = \sum_{n=0}^{\infty} r^n = (1-r)^{-1}$ and:

$$\begin{aligned} \bar{n} = \sum_{n=0}^{\infty} n \, P(n) = \frac{1}{Z} \sum_{n=0}^{\infty} n \, \mathrm{e}^{-n(E-\mu)/k_{\mathrm{B}}T} = \frac{1}{Z} \sum_{n=0}^{\infty} n \, r_s^n \\ \Rightarrow \bar{n} = f_{\mathrm{BE}}(E) = \frac{1}{\mathrm{e}^{(E-\mu)/k_{\mathrm{B}}T} - 1}, \end{aligned} \tag{1.23}$$

For fermions, on the other hand, only two particles of opposite spin can be accommodated in each state. This restricts the sum $Z = \sum_{n=0}^{1} r^n = 1 + r$ and results in:

$$\begin{aligned} \bar{n} = \sum_{n=0}^{1} n\, P(n) = \frac{1}{Z}\, \mathrm{e}^{-(E-\mu)/k_{\mathrm{B}}T} = \frac{r}{1+r} \\ \Rightarrow \bar{n} = f_{\mathrm{FD}} = \frac{1}{\mathrm{e}^{(E-\mu)/k_{\mathrm{B}}T} + 1}. \end{aligned} \tag{1.24}$$

In the above, $f_{\mathrm{BE}}(E)$ and $f_{\mathrm{FD}}(E)$ are the Bose-Einstein and Fermi-Dirac equilibrium distributions obeyed by quantum degenerate particles. Both of these taper off into the classical, Boltzmann limit for $E \gg \mu$ and high temperatures T, as shown in fig. 1.5.

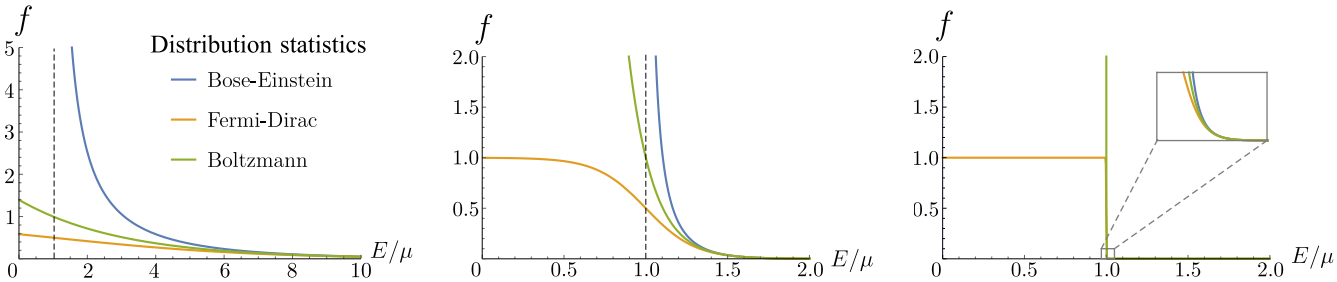

(a) T_1 (b) T_2 (c) T_3

Figure 1.5 : The occupancy $f(E)$ determined by the three equilibrium distributions. While they converge at large E, their behaviour is dramatically different for low temperatures $T_3 < T_2 < T_1$.

Relation to spin

Section 1.1.1 required indistinguishability of quantum particles based on them being *identical*. In the true sense of the word, *identical* particles transform in the same irreducible representation of the Poincaré group, uniquely identified by their mass and spin. Proper treatment of spin requires quantum field theory, since quantum mechanics is incompatible with special relativity as it does not obey causality.

For a theory to be causal, the time ordering of physical events affecting the system's evolution cannot be reversed. This is especially problematic for space-like separations where a Lorentz boost may reverse the chronological order $t_{\mathrm{final}} - t_{\mathrm{initial}} < 0$. For causality to hold, any two space-like separated operators are required to commute:

$$[\mathcal{O}_1(x), \mathcal{O}_2(y)] = 0 \quad \text{if} \quad (x-y)^2 < 0, \quad g_{\mu\nu} = (+,-,-,-), \tag{1.25}$$

to ensure their time ordering is irrelevant and not resulting in any physical consequence.

The relativistic counterparts of the commutation relations in eq. 1.8 are:

$$\begin{aligned} \text{bosons:} \qquad & [a(\mathbf{p},s), a^\dagger(\mathbf{p}',s')] = 2E_{\mathbf{p}}(2\pi)^3\delta^{(3)}(\mathbf{p}-\mathbf{p}')\delta_{s,s'}, \\ \text{fermions:} \qquad & \{a(\mathbf{p},s), a^\dagger(\mathbf{p}',s')\} = 2E_{\mathbf{p}}(2\pi)^3\delta^{(3)}(\mathbf{p}-\mathbf{p}')\delta_{s,s'}. \end{aligned} \tag{1.26}$$

A general field operator ϕ for non-interacting particles A and B is given by:

$$\phi_{A,B}(x) = \int \frac{\mathrm{d}^3\mathbf{p}}{(2\pi)^3}\frac{1}{2E_{\mathbf{p}}} \sum_s \left[\mathrm{e}^{-\mathrm{i}px} f_{A,B}(\mathbf{p},s)a(\mathbf{p},s) + \mathrm{e}^{\mathrm{i}px} h_{A,B}(\mathbf{p},s)a^\dagger(\mathbf{p},s)\right]_{p^0=E_{\mathbf{p}}}. \tag{1.27}$$

Because operators $\mathcal{O}(x)$ are usually just a product of $\prod_i \phi_i(x)$, requiring $[\mathcal{O}_1(x), \mathcal{O}_2(y)] = 0$ is the same as requiring $[\phi_A(x), \phi_B(y)] = 0$.
This results in:

$$\begin{aligned} \text{for bosons:} \quad & [\phi_A(x), \phi_B(y)] \propto 1 - (-1)^{2j}, \\ \text{for fermions:} \quad & [\phi_A(x), \phi_B(y)] \propto 1 + (-1)^{2j}, \end{aligned} \tag{1.28}$$

where j, in the absence of orbital angular momentum, is the particle's spin. The proof of these relations is provided in [53], and is outlined in appendix D.1.

The ladder operators used in angular momentum algebra result in a quantised spectrum bounded by j and $-j$, so that $-j + n = j$ with $n \in \mathbb{N}$. This requires $j = n/2$, i.e. either an integer or a half integer.

Hence, in conclusion:

$$\begin{aligned} \text{bosons} &\Leftrightarrow \left[a, a^\dagger\right] = 0 \Leftrightarrow \text{integer spin}, \\ \text{fermions} &\Leftrightarrow \left\{a, a^\dagger\right\} = 0 \Leftrightarrow \text{half-integer spin}. \end{aligned} \tag{1.29}$$

1.2 Bose-Einstein condensation

The theory presented here is thoroughly and rigorously discussed in [54] and [55].

1.2.1 A distinct phase of matter

There is a profound consequence of the Bose-Einstein distribution given in eq. 1.23. Not only is the occupancy $f(E)$ allowed to be larger than 1, meaning multiple bosons can exist in the same quantum state, but it has to always be *positive*, requiring $(E_j - \mu)/k_\text{B}T > 0 \; \forall j$. The ground state energy, chosen to be $E_0 = 0$, sets an upper bound for the chemical potential $\mu \leqslant 0$. The occupancy of *any* state $j \neq 0$ is therefore capped at:

$$\max\{f_j(E_j)\} = \frac{1}{\mathrm{e}^{E_j/k_\text{B}T} - 1}. \tag{1.30}$$

While still large for high temperatures, this starts becoming worryingly small as $T \to 0$, where the only state retaining infinite occupancy is the ground state with $E_0 = 0$.

Decreasing the temperature T at constant particle number N, increasing N at constant T, or a mixture of the two, eventually causes the excited states to reach their maximal occupancies making only the ground state statistically accessible. Reaching the critical number N_c or temperature T_c thus triggers a macroscopic occupation of the ground state in a process known as *Bose-Einstein condensation* (BEC), as shown in fig. 1.6a.

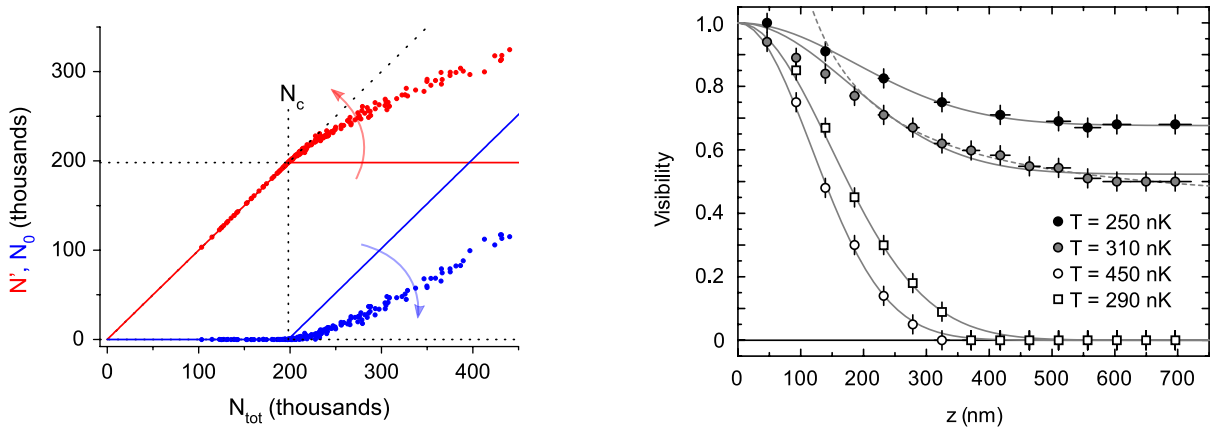

(a) Figure taken from [56]

(b) Figure taken from [57]

Figure 1.6 : a) Bose-Einstein condensation can be interpreted as a saturation effect. The solid lines show that at constant temperature, a cloud of non-interacting N_{tot} atoms amass in the condensed fraction (N_0) as opposed to the excited states N' when increased above a critical value N_{c}. The presence of interactions (experimental data), changes the critical point and the saturation behaviour. b) The visibility of the fringes in a matter-wave interference pattern as a function of the spatial extent of the atomic cloud. For a thermal state, this decays to zero within the thermal de Broglie wavelength λ_{th}, whereas for a BEC it stays constant owing to the presence of off-diagonal long-range order.

The total number of particles N_{tot} can be written as:

$$N_{\mathrm{tot}} = N_0 + \underbrace{\int_0^\infty f(E)g(E)\,\mathrm{d}E}_{N_{\mathrm{ex}}}, \tag{1.31}$$

where the population of the ground (Bose-condensed) state N_0 is separated because its energy $E_0 = 0$ is not taken into account by the integral of the occupancy $f(E)$ and density of states $g(E)$, which therefore only results in the excited state population N_{ex}.

The density of states $g(E)$ is usually given by

$$g(E) \propto E^{\alpha-1} \quad \text{with} \quad \begin{cases} \alpha = d/2 \text{ for free particles in } d \text{ dimensions} \\ \alpha = d \text{ for particles in a } d-\text{dimensional harmonic trap} \end{cases}$$

The critical transition temperature T_{c} is reached when the total number of particles can be *just* accommodated in the excited states:

$$\begin{aligned} N_{\mathrm{tot}} = N_{\mathrm{ex}} = \int_0^\infty \mathrm{d}E\, f(E)\, g(E) = c(\alpha)\cdot(kT_{\mathrm{c}})^\alpha \\ \Rightarrow \quad kT_{\mathrm{c}} = \frac{N_{\mathrm{tot}}^{1/\alpha}}{c(\alpha)}. \end{aligned} \tag{1.32}$$

A BEC transition occurs if T_{c} exists and is non-zero, which is only allowed for $\alpha > 1$ by the convergence of the integrals in the constant $c(\alpha)$. Hence, a BEC can only be produced in $d \geqslant 3$ dimensions, or in $d \geqslant 2$ if in the presence of a confining $d \geqslant 2$ harmonic potential. The functional dependence of the density of states $g(E) \propto E^{\alpha-1}$ controls the value of T_{c} as it determines whether or not particles can still be accommodated in the exicted states as $T \to 0$. This is also explained by the Mermin-Wagner theorem [58–60].

The condensed and excited (thermal) populations N_0 and N_{ex} can then be expressed as:

$$N_{\text{ex}} = N_{\text{tot}} \left(\frac{T}{T_{\text{c}}}\right)^{\alpha}, \quad N_0 = N_{\text{tot}} \left(1 - \frac{T}{T_{\text{c}}}\right)^{\alpha}. \tag{1.33}$$

A BEC is described by a macroscopically occupied wavefunction, characterised by a single, physical and non-gaugeable phase which results from breaking the $U(1)$ symmetry corresponding to particle number conservatio [61]. The BEC is a coherent state $|\alpha\rangle$ with zero entropy, whereas a generic thermal ground state consists of the statistical mixture of single-particle states that maximises entropy. Reaching a BEC therefore not only requires loss of energy via cooling, but also, more importantly, the removal of entropy, as further discussed in section 2.3.1.

The mechanism that guarantees stabilisation of the single phase in the BEC is constructive interference. In the absence of interactions, the Hamiltonian commutes with the particle number operator, resulting in the time evolution for single-particle eigenstates ψ_n of the form $\psi_n(x,t) = \mathrm{e}^{-\mathrm{i}E_n t/\hbar}\psi_n(x)$.

A coherent state is defined as:

$$\langle\alpha|x\rangle = \phi_\alpha(x) = \mathrm{e}^{-\frac{1}{2}|\alpha|^2} \sum_{n=0}^{\infty} \frac{\alpha^n}{\sqrt{n!}} \psi_n(x), \tag{1.34}$$

and its time evolution is given by:

$$\phi_\alpha(x,t) = \mathrm{e}^{-\frac{1}{2}|\alpha|^2} \sum_{n=0}^{\infty} \frac{\alpha^n}{\sqrt{n!}} \psi_n(x,t) = \mathrm{e}^{-\frac{1}{2}|\alpha|^2} \sum_{n=0}^{\infty} \frac{\alpha^n}{\sqrt{n!}} \psi_n(x,0)\mathrm{e}^{-\mathrm{i}\frac{E_n t}{\hbar}}. \tag{1.35}$$

In the absence of interactions, $E_n = \mu + \eta_n n$, where $\mu = E_0$ is the ground state energy and η_n is the energy of every particle in a level n, which then results in:

$$\phi_\alpha(x,t) = \mathrm{e}^{-\mathrm{i}\frac{\mu t}{\hbar}} \phi_\alpha(x,0). \tag{1.36}$$

The time evolution of a pure coherent state is solely controlled by the chemical potential, which therefore guarantees its phase stability. In a thermal state with multiple occupied single-particle eigenstates, the presence of a single phase is precluded by the destructive interference between the different E_n phase factors.

The emergence of a single phase is confirmed by the asymptotic behaviour of the off-diagonal one-body density matrix[3]. In the first quantisation formalism, this is defined as:

$$\begin{aligned} n^{(1)}(\mathbf{r},\mathbf{r}') &= \sum_i n_i\, \psi_i^*(\mathbf{r})\psi_i(\mathbf{r}') \\ &= n_0\, \phi_0(\mathbf{r})^*\phi_0(\mathbf{r}') + \sum_{i\neq 0} n_i\, \psi_i(\mathbf{r})^*\psi_i(\mathbf{r}) \\ &= n_0\, \phi_0(\mathbf{r})^*\phi_0(\mathbf{r}') + \sum_{i\neq 0} n_i\, \mathrm{e}^{-\frac{\mathrm{i}}{\hbar}\mathbf{p}\cdot(\mathbf{r}-\mathbf{r}')}, \end{aligned} \tag{1.37}$$

where in the last term a special case of free particles was assumed, to express them as plane waves. At increasing separation, this tends to a constant value because the contributions of $\mathbf{p} \neq 0$ average out:

$$\lim_{|\mathbf{r}-\mathbf{r}'|\to\infty} n^{(1)}(\mathbf{r},\mathbf{r}') \to n_0 \neq 0. \tag{1.38}$$

Experimental confirmation is provided in fig. 1.6b, where the BEC exhibits phase coherence across its entire spatial extent.

[3] This is used in the Penrose-Onsager criterion [62] as a rigorous definition for a BEC.

1.2.2 Useful formulae

For a confining potential $V(\mathbf{r})$, the density of particles in the excited states can be expressed as:

$$n_{\mathrm{ex}}(\mathbf{r}) = \frac{N_{\mathrm{ex}}}{\text{volume}} = \frac{g_{3/2}\left(\mathrm{e}^{-V(\mathbf{r})/k_{\mathrm{B}}T}\right)}{\lambda_{\mathrm{th}}^3}, \tag{1.39}$$

where N_{ex} is the same as in eq. 1.31, and the polylogarithmic g_γ and Riemann zeta ζ functions are defined as:

$$g_\gamma(z) = \sum_{n=1}^{\infty} \frac{z^n}{n^\gamma}, \quad g_\gamma(1) = \zeta(\gamma). \tag{1.40}$$

Most confining potentials in our experiments are three-dimensional harmonic traps of the form:

$$V(\mathbf{r}) = \frac{1}{2}m(\omega_x^2 x^2 + \omega_y^2 y^2 + \omega_z^2 z^2) = \frac{1}{2}m\bar{\omega}^2 r^2, \tag{1.41}$$

where $\bar{\omega}$ is the geometric mean of the trapping frequencies ω_i, and m the mass of the atom.

The critical temperature and atom number from eqs. 1.32 and 1.33 with $\alpha = 3$ are:

$$T_{\mathrm{c}} = \frac{\hbar\bar{\omega}}{k_{\mathrm{B}}}\left(\frac{N}{\zeta(3)}\right)^{1/3} = 0.94\frac{\hbar\bar{\omega}}{k_{\mathrm{B}}}N^{1/3}, \tag{1.42}$$

$$\frac{N_0}{N_{\mathrm{tot}}} = 1 - \left(\frac{T}{T_{\mathrm{c}}}\right)^3. \tag{1.43}$$

Defining the *Thomas-Fermi* radii R_i and their average $\bar{R}$ as:

$$R_i^2 = \frac{2k_{\mathrm{B}}T}{m\omega_i^2}, \quad \bar{R}^2 = \frac{2k_{\mathrm{B}}T}{m\bar{\omega}^2}, \tag{1.44}$$

the total number of particles N_{tot} in the absence of interactions is found using 1.14:

$$\begin{aligned} N_{\mathrm{tot}} = n_0 \int \mathrm{d}^3\mathbf{r}\, \mathrm{e}^{-\frac{V(\mathbf{r})}{k_{\mathrm{B}}T}} = n_0 \int \mathrm{d}^3\mathbf{r}\, \mathrm{e}^{-\frac{r^2}{\bar{R}^2}} = n_0\pi^{3/2}\bar{R}^{-3} \\ \Rightarrow n_0 = N\left(\frac{m\bar{\omega}^2}{2\pi k_{\mathrm{B}}T}\right)^{3/2}. \end{aligned} \tag{1.45}$$

The peak density in real space n_0 allows expressing the degeneracy parameter D (eq. 1.19) in a 3D harmonic trap as:

$$D = n_0\lambda_{\mathrm{th}}^3 = N_{\mathrm{tot}}\left(\frac{\hbar\bar{\omega}}{k_{\mathrm{B}}T}\right)^3. \tag{1.46}$$

In the presence of weak interactions the BEC can be described by the non-linear *Gross-Pitaevskii equation* (GPE):

$$\left(-\frac{\hbar^2}{2m}\nabla^2 + V(\mathbf{r}) + g|\psi|^2\right)\psi = \mu\psi \quad \text{with} \quad g = \frac{4\pi\hbar^2 a}{m}, \tag{1.47}$$

where a is the scattering length quantifying the inter-particle interaction strength and is discussed in section 1.3. The GPE is a mean-field approximation because each particle (ψ) is made to experience the averaged interaction from the others ($|\psi|^2$).
An approximate solution for the density $n(\mathbf{r})$ of the many-body ground state is obtained using the *Thomas-Fermi* approximation, where the cloud is assumed to be cold enough to neglect the kinetic energy:

$$\begin{aligned} \left(V(\mathbf{r}) + g|\psi|^2\right)\psi &= \mu\psi \\ \Rightarrow n(\mathbf{r}) = |\psi(\mathbf{r})|^2 &= \frac{\mu - V(\mathbf{r})}{g}. \end{aligned} \tag{1.48}$$

The chemical potential $\mu = k_{\text{B}}T$ controls the spatial extent of the cloud, from eq. 1.44:

$$R_i^2 = \frac{2\mu}{m\omega_i^2}. \tag{1.49}$$

In a harmonic trapping potential, the density of the condensed fraction is therefore described by the inverted paraboloid:

$$n(\mathbf{r}) = n_0 \left(1 - \frac{x^2}{R_x^2} - \frac{y^2}{R_y^2} - \frac{z^2}{R_z^2}\right). \tag{1.50}$$

Bose-Einstein Condensate vs Superfluid

Unlike many familiar phase transitions, the BEC is not driven by the interactions between particles but is a natural consequence of their quantum statistics. The BEC is an equilibrium phase of matter, in which *one* quantum state is macroscopically occupied[4].

Superfluidity relates to the transport properties of the ultracold gas, introducing an interaction-dependent *critical velocity* v_{c} below which atoms do not experience viscosity. In this context, a non-interacting BEC has $v_{\text{c}} = 0$ whilst a weakly interacting BEC has $v_{\text{c}} \neq 0$ and may thus be referred to as a superfluid (the presence of interactions also shifts the transition point [63]).

The two phase are, however, quite distinct.
Superfluidity, for example, does not necessarily interest only one quantum state (the condensed fraction in liquid ^{4}He is predicted to be $\sim 10\%$ even at $T = 0$) and may arise in systems where Bose-Einstein condensation is forbidden (such as in BKT transitions), as further discussed in the introduction of [64].

Irregardless of these differences, the term "superfluid" is sometimes (inappropriately) extended to also include the non-interacting BEC, especially in the context of the localised phases of matter discussed in chapter 8.

1.3 Interactions

1.3.1 Collisions and Feshbach resonances

Collisions

The interaction between two atoms $V_{\text{int}}(\mathbf{r})$ with separation $\mathbf{r}$ is usually modelled by the Lennard-Jones potential shown in fig. 1.7a, which phenomenologically describes the Van

[4] Unless it is a *fragmented* BEC, see [62].

der Waals interaction. The repulsion of the electronic clouds at short separation and the attraction driven by the mutually induced electric dipoles give rise to an attractive well of size $r_0 \sim 10^{-9} - 10^{-10}$ m [65].

In cold and dilute gases, the inter-particle separation and the thermal de Broglie wavelength are both much larger than r_0. The atoms will hence not be able to resolve the details of the interaction potential, which justifies its replacement with a spherically symmetric *pseudopotential* resulting in the same behaviour at large distances.
One then expects an asymptotic scattering solution of the form:

$$\psi_{\mathbf{k}}(\mathbf{r}) \sim \mathrm{e}^{\mathrm{i}kz} + f(k,\theta)\frac{\mathrm{e}^{\mathrm{i}kr}}{r}, \tag{1.51}$$

where an incoming plane wave along the z axis is scattered into a spherical wave along r, of amplitude f determined by the initial momentum k and the deflection angle θ.

The spherical symmetry allows use of the spherical Bessel functions $j_\ell(kr)$ and spherical harmonics $Y_\ell^m(\theta,\phi) = P_\ell(\cos\theta)$, where the m dependence has been dropped owing to the axial symmetry of the system. In this basis, the incident plane wave can be written:

$$\mathrm{e}^{\mathrm{i}kz} = \sum_{\ell=0}^{\infty}(2\ell+1)i^\ell j_\ell(kr)P_\ell(\cos\theta) \quad \text{with} \quad j_\ell(kr) = \frac{1}{2\mathrm{i}kr}\left[(-1)^{\ell+1}\mathrm{e}^{-\mathrm{i}kr} + \mathrm{e}^{\mathrm{i}kr}\right]. \tag{1.52}$$

The general solution ψ_k in eq. 1.51 can also be expressed in the spherical basis, identifying $\mathrm{e}^{-\mathrm{i}kr}$ as the incoming waves and $\mathrm{e}^{\mathrm{i}kr}$ as the outgoing waves. Since we expect the scattered wave to retain the same functional form, the potential only amounts to a multiplicative factor for the outgoing waves S:

$$\psi_{\mathbf{k}} = \frac{1}{2\mathrm{i}kr}\sum_\ell(2\ell+1)\mathrm{i}^\ell P_\ell(\cos\theta)\left[(-1)^{\ell+1}\mathrm{e}^{-\mathrm{i}kr} + S\mathrm{e}^{\mathrm{i}kr}\right]. \tag{1.53}$$

Upon comparing eq. 1.53 with eqs. 1.51 and 1.52, the scattering amplitude f is found to be:

$$f = \sum_{\ell=0}^{\infty}\frac{1}{2\mathrm{i}k}(S-1)(2\ell+1)\mathrm{i}^\ell P_\ell\cos\theta = \sum_{\ell=0}^{\infty}(2\ell+1)\mathrm{i}^\ell P_\ell\cos\theta f_\ell. \tag{1.54}$$

If the flux is conserved, $|S|=1$ and is hence a pure phase factor $S = \mathrm{e}^{2\mathrm{i}\delta_\ell}$:

$$f_\ell = \frac{1}{2\mathrm{i}k}\left(\mathrm{e}^{2\mathrm{i}\delta_\ell} - 1\right) = \frac{1}{k\cot\delta_\ell - \mathrm{i}k}. \tag{1.55}$$

In [54] it is given that $\delta_\ell \propto k^{2\ell+1}$, which results in $f_\ell \to 0 \quad \forall \ell \neq 0$. Physically, this corresponds to atoms not possessing non-zero angular momenta because the kinetic energy ($\propto k^2$) at low temperatures is lower than the centrifugal potential barrier. The only non-zero contributions to the scattering amplitude at low temperatures are from s-waves:

$$\lim_{k\to 0} f = \lim_{k\to 0} f_s = -\frac{1}{\frac{1}{a} + \mathrm{i}k + \mathcal{O}(k^2)} = a, \tag{1.56}$$

where a is the scattering length. The scattering cross section is given by $\sigma = \int|f|^2\mathrm{d}\Omega = 4\pi a^2$, which is the interaction term in eq. 1.47.

For bosons, low-temperature moderate interactions are fully determined by the s-wave scattering length a which justifies treating them as *contact* interactions. For fermions,

however, the anti-symmetry of the wavefunction precludes s-wave scattering and dramatically reduces interactions at low temperatures.

Finally, a negative scattering length a may result in s-wave scattering also being absent, which occurs at some $k \neq 0$ for which $f_s = 0$ and is known as a Ramsauer-Townsend minimum.

Feshbach resonances

For large separations, the energy associated with the internal atomic structure dominates over the inter-atomic attractive potential. This gives rise to different potentials experienced by distinct hyperfine states, and distinguishes the scattering channels between *open* (energetically accessible) or *closed*, as shown in fig. 1.7a.

An external magnetic field $\mathbf{B}$ interacts with the spins of free atoms and may bring their energy into resonance with a molecular bound state. This causes a drastic variation of the scattering length with $|\mathbf{B}| = B$ [66]:

$$a(B) = a_{\text{bg}} \left(1 - \frac{\Delta}{B - B_{\text{res}}}\right), \tag{1.57}$$

where a_{bg} is the background scattering length in the absence of a magnetic field, and Δ is the width of the *Feshbach resonance* about B_{res}.
Table 1.3 lists the resonances employed in our experiment to tune interactions and study both many-body and non-interacting effects.
The strongly interacting regime where $a \to \infty$ is known as *unitarity*, where both two- and three-body contact interactions are necessary to describe the ensuing phenomena [9].

A negative (positive) scattering length corresponds to attractive (repulsive) interactions, as illustrated in fig. 1.7b where a square well was used as a pseudopotential.

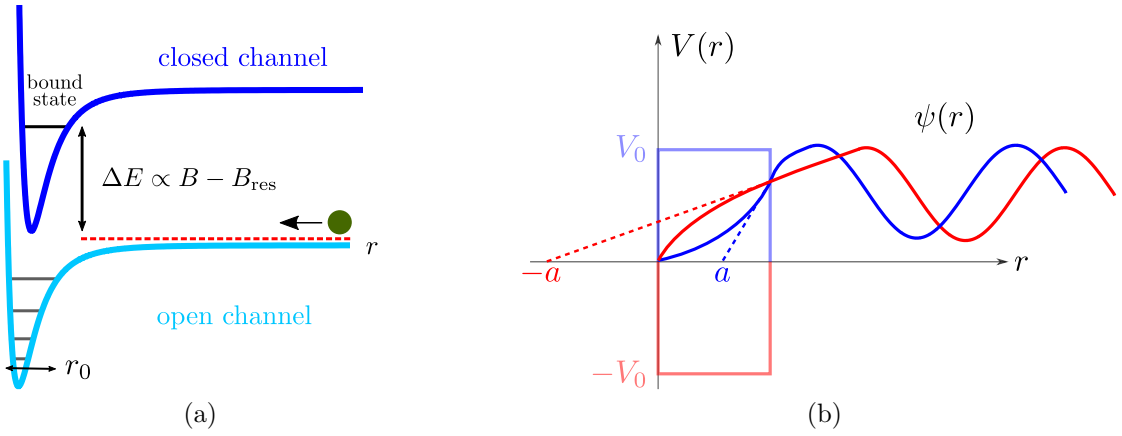

Figure 1.7 : a) Different hyperfine states experience different inter-particle potentials. Free atoms with negligible kinetic energy may be brought into resonance with a molecular bound state by tuning the external magnetic field. b) The scattering length a corresponds to the shift of the scattered wave with respect to a free solution.

nomenclature	species	resonant field	width	background scattering length	zero-crossing field
		B_{res}/G	Δ/G	a_{bg}/a_0	B_0
inter-species	^{87}Rb-^{39}K	317.9	7.6	34	325.6
intra-species	^{39}K-^{39}K	402.70	−52	−29	350.5

Table 1.3 : The Feshbach resonances used in our experiments, for the scattering channels $|F = 1, m_F = 1\rangle$. Values taken from [9, 66].

1.3.2 Two- vs three-body losses

Elastic collisions result in energy redistribution and are essential for the success of the evaporative cooling scheme discussed in section 2.3.3. Inelastic collisions, on the other hand, may lead to particle loss as the released energy is usually larger than the trap depth.

For two atoms in their absolute ground state, there are no available final states after the collision which prevents any interaction between them. Energy and momentum may still be conserved, however, in three-body recombination events, where two of the atoms form a molecule and release the associated binding energy. These phenomena are allowed because the BEC is only a metastable state of matter, the true ground state being a solid, and occur at a rate $\Gamma_{\text{loss}} \propto L_3 n^2$ where $L_3 \propto a^4$ [67] and n is the atomic density.

To quantify the interplay between particle loss and strong interactions, the diluteness parameter is defined as na^3, such that:

$$\frac{E_{\text{kin}}}{E_{\text{int}}} \propto \frac{1}{(na^3)^{1/3}}, \quad \frac{\hbar\Gamma_{\text{loss}}}{E_{\text{int}}} \propto na^3, \tag{1.58}$$

where

$$E_{\text{kin}} \sim \frac{\hbar^2 n^{2/3}}{2m}, \quad E_{\text{int}} \sim \frac{4\pi\hbar^2 an}{m}. \tag{1.59}$$

In dilute and weakly interacting gases where $na^3 \ll 1$, three-body recombinations are low enough to guarantee a long lifetime of the BEC. The quantity $\sqrt{na^3}$ also quantifies the effects of quantum depletion [63]. Two-body losses may still arise due to the long-range nature of the Lennard-Jones potentials. In the ground state, the inter-atomic separation is much larger than the extent of the short-range ($\propto 1/r^6$) interaction, hence not enough kinetic energy is provided to escape the trap. However, if there are photons present, one of the atoms may be promoted to the excited state which results in a long-range interaction ($\propto 1/r^3$) owing to the larger electric dipole. Two atoms can therefore participate in *light assisted collisions*, shown in fig. 1.8, where the atoms may acquire enough kinetic energy to escape the trap and result in a particle loss quantified by the two-body loss rate β [68].

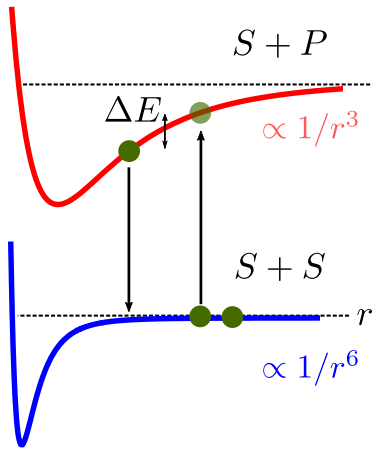

Figure 1.8 : In the presence of light, an atom in the ground state S may be promoted to the excited state P, resulting in a long-range interaction capable of providing enough kinetic energy ΔE to escape the trap. These *light assisted collisions* enable a two-atom loss channel otherwise prevented by kinematic conservation laws.

By convention sweet is sweet, bitter is bitter, hot is hot, cold is cold, colour is colour; but in truth there are only atoms and the void.

Democritus [69]

2 Cold atoms

This chapter reviews the scattering and confining effects arising from matter-wave interactions, that are employed for cooling and trapping cold atoms. The importance of removing both energy and entropy is emphasised, enabling the increase of phase space density to reach quantum degeneracy. Optical lattices are also introduced as a versatile and flexible platform to perform quantum simulation of condensed matter systems.

2.1 Atom-light interactions

2.1.1 Semi-classical treatment

The atom will be treated as a quantum object with discrete energy levels, while the electromagnetic (EM) field is assumed to contain a sufficiently large number of photons not to require quantisation. This is a semi-classical approximation, and it does not apply to spontaneous emission or to few-photon phenomena.

In the presence of an external EM potential $A^\mu = (\phi/c, \mathbf{A})$, the Hamiltonian for the atomic electron is:

$$H = \frac{(\mathbf{p} + q\mathbf{A})^2}{2m} - q\phi + V(\mathbf{r}), \tag{2.1}$$

where $V(\mathbf{r})$ is the Coulomb interaction with the nucleus. Choosing the Coulomb gauge $\nabla \cdot \mathbf{A} = 0$ such that $[\mathbf{p}, \mathbf{A}] = 0$, this can be expanded:

$$H = \underbrace{\frac{\mathbf{p}^2}{2m} + V(\mathbf{r})}_{H_0} + \underbrace{\frac{q\mathbf{A}\cdot\mathbf{p}}{m} - q\phi + \frac{q^2\mathbf{A}^2}{2m}}_{H_1}, \tag{2.2}$$

where H_1 can be treated as a perturbation on the bare electronic Hamiltonian H_0 provided $H_0 \gg H_1$.

For an external static magnetic field $\mathbf{B} = \nabla \times \mathbf{A}$, the $\mathbf{A} \cdot \mathbf{p}$ and $\mathbf{A}^2$ terms are the *linear* and *quadratic* Zeeman effects, discussed in section 4.3.1 and appendix A.
Here, a monochromatic plane wave is considered, with $\phi = 0$, $\mathbf{A} = 2A_0 \sin(\mathbf{k} \cdot \mathbf{r} - \omega t)\, \hat{\mathbf{e}}$, and a small enough amplitude to neglect the $\mathbf{A}^2$ term. H_1 can then be written:

$$H_1 = -\mathrm{i}\frac{qA_0}{m}\left(\mathrm{e}^{\mathrm{i}(\mathbf{k}\cdot\mathbf{r}-\omega t)} - \mathrm{e}^{-\mathrm{i}(\mathbf{k}\cdot\mathbf{r}-\omega t)}\right)\hat{\mathbf{e}} \cdot \mathbf{p}, \tag{2.3}$$

which is an example of a harmonic perturbation [70]. Acting on the stationary eigenstates of H_0 with phase factors $\mathrm{e}^{\mathrm{i}\omega_0 t} = \mathrm{e}^{\mathrm{i}E_0 t/\hbar}$, the terms in eq. 2.3 change the energy to $E_0 \to E_0 \pm \hbar\omega$ and can thus be interpreted as *absorption* and *stimulated emission*.

The probability amplitude of a transition between an initial $|i\rangle$ and final $|f\rangle$ atomic state is given by the matrix element $\langle f|H_1|i\rangle$, where only the spatial dependence of H_1 needs to be considered. Detailed balance guarantees equal rates of the two processes, hence only one needs to be analysed.

Redefining H_1 as:

$$H_1 = qA_0\omega\, \mathrm{e}^{\mathrm{i}\mathbf{k}\cdot\mathbf{r}}\, \hat{\mathbf{e}} \cdot \mathbf{d}, \tag{2.4}$$

allows introducing the operator $\mathbf{d}$:

$$\mathbf{d} = \frac{-\mathrm{i}}{m\omega}\langle f|\mathrm{e}^{\mathrm{i}\mathbf{k}\cdot\mathbf{r}}\mathbf{p}|i\rangle. \tag{2.5}$$

A power expansion of the incident plane wave:

$$\mathrm{e}^{\mathrm{i}\mathbf{k}\cdot\mathbf{r}} = 1 + \mathrm{i}\mathbf{k} \cdot \mathbf{r} + \ldots \tag{2.6}$$

then enables a perturbative expansion of H_1 (derived in appendix D.2):

$$\begin{aligned} H_1 &= qA_0\omega\, \hat{\mathbf{e}} \cdot \mathbf{d} \quad = \\ &= qA_0\omega \left(\underbrace{\langle f|\hat{\mathbf{e}} \cdot \mathbf{r}|i\rangle}_{\text{electric dipole}} + \underbrace{\frac{1}{2mc}(\hat{\mathbf{k}} \times \hat{\mathbf{e}}) \cdot \langle f|\mathbf{L} + 2\mathbf{S}|i\rangle}_{\text{magnetic dipole}} + \underbrace{\frac{\mathrm{i}\omega}{2c}\hat{\mathbf{e}} \cdot \mathbf{Q} \cdot \hat{\mathbf{k}}}_{\text{electric quadrupole}} \ldots \right). \end{aligned} \tag{2.7}$$

The names assigned to the first two terms stem from recognising $q\mathbf{r}$ as the electric dipole moment, and $1/c\,(\hat{\mathbf{k}} \times \hat{\mathbf{e}})$ as the magnetic component of the plane wave.

For $|i\rangle \neq |f\rangle$, non-vanishing matrix elements result in the *selection rules* determining the allowed transitions, discussed in the next section. On the other hand, the diagonal matrix elements $|i\rangle = |f\rangle$ cause energy shifts[1] of the bare atomic states. For neutral atoms with no permanent electric dipole moment and hence with an inversion symmetry $\mathbf{r} \to -\mathbf{r}$, energy corrections caused by the electric dipole term vanish and no first-order Stark shift ($\propto \mathbf{E}$) is expected. However, $\mathbf{L} + 2\mathbf{S}$ is an axial vector and thus unchanged by a parity transformation, resulting in a non-zero first-order Zeeman shift ($\propto \mathbf{B}$).

[1] While transitions $|i\rangle \neq |f\rangle$ are represented by Feynman diagrams with one vertex only, diagonal energy shifts $|i\rangle = |f\rangle$ are visualised by Feynman diagrams with two or more vertices, and the same incoming and outgoing states. This is further discussed in section 7.1.3.

Selection rules

An atom can accommodate electrons in its discrete energy levels labelled by the principal quantum number n and the orbital angular momentum ℓ, defining electronic shells and sub-shells. In the absence of an external magnetic field, the ℓ sub-shells are degenerate in their $2\ell+1$ states labelled by m_ℓ. This is known as the gross structure of the atom.

An electron possesses spin $s = 1/2$, which can be combined with ℓ to define the total electronic angular momentum $j = |\ell - s|, |\ell - s|{+}1, \ldots, \ell + s - 1, \ell + s$. When multiple electrons occupy the same sub-shell, the same reasoning can still be applied by combining the angular momenta of all shell occupants into L, S and J. J is only a good quantum number within the LS coupling scheme, not valid in the presence of a strong interaction with an external magnetic field, as discussed in appendix A. For the same n and L, different J split the energy levels in the *fine structure* of the atom.

The electronic angular momentum also interacts with the nuclear angular momentum I. Within the IJ coupling scheme, the total atomic angular momentum $F = |J - I|, |J - I|{+}1, \ldots, J + I - 1, J + I$ is defined, leading to a further splitting of energy levels which form the *hyperfine structure*. Each F is $2F+1$ degenerate in its m_F sub-levels.

The lowest order transitions and their associated selection rules are listed in table 2.1. When incident along the magnetic field, linearly polarised light (π) drives $\Delta m_F = 0$ transitions, while circularly polarised light ($\sigma^\pm$) drives $\Delta m_F = \pm 1$ transitions. The spontaneous decay rate was estimated from analytical expressions for hydrogenic atoms. The electric quadrupole transition is quoted for reference, but it does not affect electrons in the s shell because of their isotropic charge distribution.

Order	type	symbol	parity	spontaneous decay rate	selection rule	forbidden transitions
Dipole	electric magnetic	E1 M1	odd even	1 α^{-8}	$\Delta F, \Delta m_F$ $= 0, \pm 1$	$F : 0 \not\leftrightarrow 0$
Quadrupole	electric	E2	even	α^{-2}	$\Delta F, \Delta m_F$ $= 0, \pm 1, \pm 2$	$F : 0 \not\leftrightarrow 0, 1$ $1/2 \not\leftrightarrow 1/2$

Table 2.1 : Lowest order transitions and associated selection rules. The same rules are valid beyond IJ coupling just by replacing $F \to J$ and $m_F \to m_J$. The spontaneous decay rate is normalised to $1 = \alpha^5(m_e c^2/\hbar)$ as derived in appendix D.3.

2.1.2 AC Stark shift

Within the *dipole approximation*, only the lowest term in eq. 2.7 is retained, resulting in the interaction Hamiltonian $\langle f|H_I|i\rangle = q\langle f|\hat{\mathbf{e}}\cdot\mathbf{r}|i\rangle E_0\cos(\omega t)$. Defining the *Rabi frequency* as $\Omega = {}^{qE_0}/_{\hbar}\,\langle f|\hat{\mathbf{e}}\cdot\mathbf{r}|i\rangle$ allows writing:

$$H_I = \hbar\Omega|e\rangle\langle g|\cos(\omega t) + \text{c.c.}, \tag{2.8}$$

which only includes off-diagonal elements because of the inversion symmetry discussed earlier.

A two-level atom is considered for simplicity, consisting of a ground state $|g\rangle$ with energy $E_g = 0$ and an excited state $|e\rangle$ with energy $E_e = \hbar\omega_0$, detuned from the EM wave frequency by $\Delta = \omega - \omega_0$.

The evolution of the electronic wavefunction is encoded in the time dependence of its bare, unperturbed stationary states:

$$|\psi\rangle_t = c_g(t)|g\rangle + c_e(t)|e\rangle \mathrm{e}^{-\mathrm{i}\omega_0 t}. \tag{2.9}$$

Solving the Schrödinger equation $\mathrm{i}\hbar\partial_t|\psi\rangle = H_\mathrm{I}|\psi\rangle$ and neglecting the oscillatory terms $\omega + \omega_0$ as per the *rotating wave approximation*, results in:

$$\begin{aligned} \mathrm{i}\hbar \begin{pmatrix} \dot{c}_g \\ \dot{c}_e \end{pmatrix} &= \frac{\hbar}{2} \underbrace{\begin{pmatrix} 0 & \mathrm{e}^{\mathrm{i}\Delta t}\,\Omega \\ \mathrm{e}^{-\mathrm{i}\Delta t}\,\Omega & 0 \end{pmatrix}}_{H(t)} \begin{pmatrix} c_g \\ c_e \end{pmatrix}, \\ \Rightarrow \quad |c_e(t)|^2 &= \frac{\Omega^2}{\sqrt{\Omega^2+\Delta^2}} \sin^2\left(\frac{\sqrt{\Omega^2+\Delta^2}}{2} t\right), \end{aligned} \tag{2.10}$$

where the population in the excited state $|e\rangle$ performs a *Rabi oscillation*.

It is beneficial to seek a solution where the Hamiltonian is not time-dependent as in eq. 2.10, hence we redefine the coefficient of the excited state in eq. 2.9 to $c'_e = c_e \mathrm{e}^{\mathrm{i}\Delta t}$:

$$\begin{gathered} |\psi\rangle_t = c_g(t)|g\rangle + c'_e(t)\mathrm{e}^{-\mathrm{i}\omega t}|e\rangle, \\ \text{change of basis} : |g\rangle \to |g,\hbar\omega\rangle, \quad \mathrm{e}^{-\mathrm{i}\omega t}|e\rangle \to |e,0\rangle, \\ \Rightarrow |\psi\rangle_t = c_g(t)|g,\hbar\omega\rangle + c'_e(t)|e,0\rangle. \end{gathered} \tag{2.11}$$

The new *dressed* basis combines the bare electronic states with the external photon of frequency ω, though the ground state energy is the same in both formalisms. The Schrödinger equation now results in the time-independent Hamiltonian:

$$H = \frac{\hbar}{2} \begin{pmatrix} 0 & \Omega \\ \Omega & -2\Delta \end{pmatrix}. \tag{2.12}$$

Diagonalisation of H yields the ground state energy E_g:

$$E_g = \frac{\hbar}{2}\left(-\Delta + \sqrt{\Omega^2+\Delta^2}\right) \underbrace{\approx}_{\Delta \gg \Omega} \pm\frac{\hbar\Omega^2}{4\Delta}, \tag{2.13}$$

which is shifted from $E_g = 0$ depending on the detuning of the incident radiation, as shown in the $|\Delta| \gg \Omega$ regions of fig. 2.1. This shift is known as the *AC Stark shift* and results in a repulsive interaction for blue detuned light ($\Delta > 0$), and in an attractive (confining) interaction for red detuned light ($\Delta < 0$).

The functional form of the leading correction to E_g in eq. 2.13 is reminiscent of second-order perturbation theory. This is in fact due to $H(t)$ in eq. 2.10 only containing off-diagonal elements:

$$H = \begin{pmatrix} E_g & a \\ a^* & E_e \end{pmatrix} = \underbrace{\begin{pmatrix} E_g & 0 \\ 0 & E_g \end{pmatrix}}_{H_0} + \underbrace{\begin{pmatrix} 0 & a \\ a^* & 0 \end{pmatrix}}_{V}, \tag{2.14}$$

where H_0 is the bare atomic Hamiltonian and V the perturbation which, because $\langle k|V|k\rangle = 0$, results in no first-order corrections. In this context, the AC Stark shift can be interpreted as a virtual two-photon transition, quantitatively discussed in section 7.1.3.

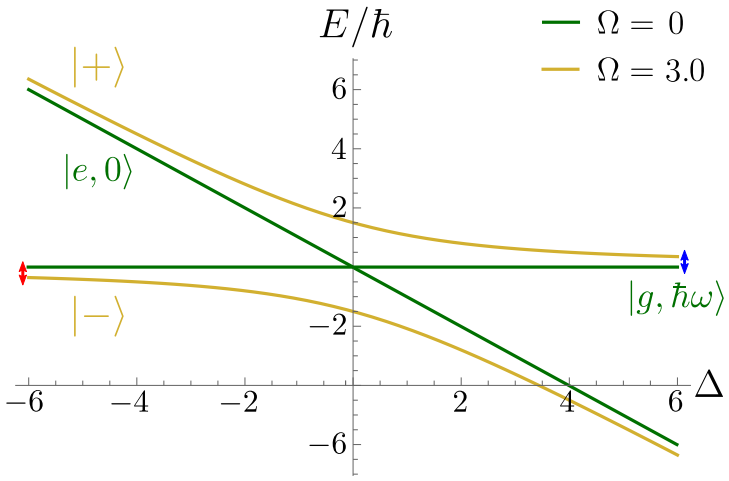

Figure 2.1 : In the limit $|\Delta| \gg \Omega$, the perturbative effect of the external EM field results in a shift of the bare ground state energy. Red detuned $\Delta < 0$ light (blue detuned $\Delta > 0$) causes an effective attractive (repulsive) potential for the atom. In the region $|\Delta| < \Omega$, the presence of a coupling Ω opens a gap between the two diabatic states, enabling a Landau-Zener transition between them.

Fig. 2.1 is also an example, in the $|\Delta| < \Omega$ region, of a minimal coupling Ω lifting the degeneracy at $\Delta = 0$ and leading to *level repulsion* or an *avoided crossing* between the new eigenstates $\{|-\rangle, |+\rangle\}$. In the experiment (section 5.3.3), this is employed to perform a state transfer between two diabatic states $|m_F = -1\rangle$ and $|m_F = 1\rangle$ ($|g, \hbar\omega\rangle$ and $|e, 0\rangle$ in fig. 2.1) known as a *Landau-Zener* transition [71]. A coupling Ω between the two states is introduced, and the detuning Δ is ramped from $-\infty$, where $|-\rangle = |m_F = -1\rangle$, to $+\infty$, where $|-\rangle = |m_F = 1\rangle$. The probability of tunnelling through the gap is proportional to $e^{-1/\dot{\Delta}}$, hence in the limit $\dot{\Delta} \to 0$ the population is adiabatically transferred between the two states.

2.1.3 Steady state forces

The unitary time evolution enforced by quantum mechanics prevents the introduction of a loss term such as spontaneous emission. Hence, we extend the Hamiltonian H formalism to the Liouville equation, which accommodates dissipation:

$$\frac{\mathrm{d}\rho}{\mathrm{d}t} = \frac{\mathrm{i}}{\hbar}[\rho, H] - \begin{pmatrix} -\Gamma\rho_{ee} & \frac{\Gamma}{2}\rho_{ge} \\ \frac{\Gamma}{2}\rho_{ge} & \Gamma\rho_{ee} \end{pmatrix}, \tag{2.15}$$

where H is from eq. 2.12, Γ is the spontaneous decay rate (assumed to be purely radiative), and ρ the density matrix:

$$\rho = \begin{pmatrix} \rho_{ee} & \rho_{ge} \\ \rho_{ge} & \rho_{ee} \end{pmatrix} \qquad \text{with} \qquad \rho_{ij} = \langle i|\rho|j\rangle = c_i\, c_j^*. \tag{2.16}$$

The above equation is valid under the rotating wave approximation and the constraints $\rho_{ee} + \rho_{gg} = 1$, $\rho_{ge} = \rho_{eg}^*$, and is usually cast as the *Optical Bloch equations*:

$$\frac{\mathrm{d}}{\mathrm{d}t}\begin{pmatrix} u \\ v \\ w \end{pmatrix} = \begin{pmatrix} u \\ v \\ w \end{pmatrix} \times \begin{pmatrix} \Omega \\ 0 \\ \Delta \end{pmatrix} - \begin{pmatrix} \Gamma/2 \\ \Gamma/2 \\ \Gamma \end{pmatrix} \quad \text{with} \quad \begin{cases} u = {}^1\!/_2\,(\rho_{ge} + \rho_{eg}), \\ v = {}^1\!/_{2\mathrm{i}}\,(\rho_{ge} - \rho_{eg}), \\ w = {}^1\!/_2\,(\rho_{gg} - \rho_{ee}). \end{cases}$$

The state of the two-level atom is described by the Bloch vector (u, v, w) precessing about $(\Omega, 0, \Delta)$ but decreasing in magnitude because of the damping terms Γ.

The steady-state solution is obtained by setting the time derivatives to 0, which results in the following expression for ρ_{eg}:

$$\rho_{eg} = \mathrm{i}\frac{I/I_\mathrm{S}}{2\Omega}\frac{\Gamma^2}{2(\Gamma/2 - \mathrm{i}\Delta)(1+s)}, \quad \text{with} \quad s = \frac{I/I_\mathrm{S}}{1 + (2\Delta/\Gamma)^2}, \tag{2.17}$$

where I is the intensity and I_S the *saturation intensity*, defined from:

$$I = \frac{1}{2}\epsilon_0 c E_0^2, \quad I_\mathrm{S} = \frac{\pi h c \Gamma}{3\lambda^3}, \quad |\langle e|q\mathbf{r}|g\rangle|^2 = \frac{3\pi\epsilon_0\hbar c^3\Gamma}{\omega^3}. \tag{2.18}$$

The last term is needed to relate the electric field amplitude E_0, the Rabi frequency $\Omega = {}^{E_0}\!/_\hbar \langle e|e\mathbf{r}|g\rangle$ and the excited state lifetime Γ^{-1}, and is obtained from the Wigner-Weisskopf theory of spontaneous decay.

The force experienced from a two-level atom in the presence of an external potential U is $\mathbf{F} = -\nabla U$. Within the dipole approximation, the potential is due to the interaction of the electron's dipole moment $q\mathbf{r}$ with the external electric field $\mathbf{E} = E_0\,\mathrm{e}^{\mathrm{i}(\mathbf{k}\cdot\mathbf{r}+\omega t)}\hat{\mathbf{e}}$. Hence:

$$\mathbf{F} = q\nabla\left(\mathbf{r}\cdot\hat{\mathbf{e}}\,E_0\,\mathrm{e}^{\mathrm{i}\mathbf{k}\cdot\mathbf{r}}\right)\mathrm{e}^{\mathrm{i}\omega t} \propto \nabla(E_0) + \mathbf{k}E_0, \tag{2.19}$$

where the constant of proportionality is calculated from expressing r in density matrix formalism:

$$\mathbf{r} = \langle e|\mathbf{r}|g\rangle\rho_{eg} + \langle g|\mathbf{r}|e\rangle\rho_{eg}^*. \tag{2.20}$$

Using the steady-state value for ρ_{eg} in eq. 2.17, the force acting on the atom is given by:

$$\mathbf{F} = \underbrace{-\frac{\hbar\Delta}{2}\frac{\nabla(\frac{I}{I_\mathrm{S}})}{1 + \frac{I}{I_\mathrm{S}} + \left(\frac{2\Delta}{\Gamma}\right)^2}}_{\mathbf{F}_\mathrm{dip}} + \underbrace{\hbar\mathbf{k}\cdot\overbrace{\frac{\Gamma}{2}\frac{\frac{I}{I_\mathrm{S}}}{1 + \frac{I}{I_\mathrm{S}} + (\frac{2\Delta}{\Gamma})^2}}^{R_\mathrm{scat}}}_{\mathbf{F}_\mathrm{scat}}. \tag{2.21}$$

The first term ($\mathbf{F}_\mathrm{dip}$) is the *dipole force* resulting from the spatially varying intensity of the incoming electric field. For a large detuning $\Delta \gg \Gamma$, $\mathbf{F}_\mathrm{dip} \propto \nabla(U_\mathrm{dip}) = \nabla(\hbar\Omega^2/\Delta)$ where the *dipole potential* U_dip is the generalisation of the AC Stark shift of eq. 2.13. The second term ($\mathbf{F}_\mathrm{scat}$) is the *scattering force* arising from the momentum imparted on the atom by the absorbed (or emitted) photon.

We then identify two regimes of matter-wave interaction distinguished by the detuning Δ. For large detuning, the scattering contribution $\mathbf{F}_\mathrm{scat} \propto I/\Delta^2$ is negligible while the dipole potential $U_\mathrm{dip} \propto I/\Delta$ is dominant: this is the regime used for the optical trapping techniques discussed in section 2.2.2. For small detuning, scattering dominates, which underlies the cooling schemes presented in section 2.3.

2.2 Trapping

2.2.1 Magnetic trapping

The *Zeeman effect* governs the interaction between an external magnetic field $\mathbf{B}$ and an atom with magnetic moment $\boldsymbol{\mu}$, resulting in a potential $U = -\boldsymbol{\mu} \cdot \mathbf{B}$. A trap can therefore be engineered by a particular choice of a spatially varying magnetic landscape.

Earnshaw's theorem

A static and source-less solution to Maxwell's equations require $\nabla \times \mathbf{B} = \mu_0 \mathbf{J} + \mu_0 \epsilon_0 \frac{\partial \mathbf{E}}{\partial t} = 0$, where $\mathbf{J}$ is the current density and $\mathbf{E}$ the electric field. This results in:

$$\cancel{\nabla \times (\nabla \times \mathbf{B})} = \nabla(\cancel{\nabla \cdot \mathbf{B}}) - \nabla^2 \mathbf{B} = 0 \quad \Rightarrow \quad \nabla^2 B_x = \nabla^2 B_y = \nabla^2 B_z = 0. \tag{2.22}$$

Extrema in the magnetic field occur when $\nabla |\mathbf{B}| = \nabla^2 B^2 = 0$, where the equality holds as $|\mathbf{B}| = \sqrt{B^2}$ is a monotonic function in B^2. Combined with eq. 2.22, this implies:

$$\begin{gathered} \nabla^2 B^2 = 2(\nabla B_x)^2 + 2B_x \cancel{\nabla^2 B_x} + 2(\nabla B_y)^2 + 2B_y \cancel{\nabla^2 B_y} + 2(\nabla B_z)^2 + 2B_z \cancel{\nabla^2 B_z}, \\ \Rightarrow \nabla^2 B^2 \geqslant 0. \end{gathered} \tag{2.23}$$

The second derivative of B always being positive, a static magnetic field in vacuo never exhibits maxima, which is known as *Earnshaw's theorem*. Only the minima of the magnetic field can thus be used to devise a trap.

The first-order energy shift of an atom in the presence of a magnetic field is given by the *Zeeman effect*:

$$\Delta E = \langle m_F | -\boldsymbol{\mu} \cdot \mathbf{B} | m_F \rangle = g_F m_F \mu_\mathrm{B} B, \tag{2.24}$$

where the field was chosen to lie along the z axis in order to use the angular momentum basis $|F, m_F\rangle$. g_F is the Landé factor and μ_B the Bohr magneton.

States for which $g_F m_F > 0$ are termed *low-field seekers* as they increase their energy in the presence of a magnetic field, and are suitable for a magnetic trap as they are energetically localised near the field minimum. The states with $g_F m_F < 0$ are known as *high-field seekers* as they lower their energy in the presence of a magnetic field. While this prevents them from being trapped magnetically, in the optical traps discussed in section 2.2.2 these states have a lower energy and atoms transition into them via spin-relaxation processes, releasing energy and leading to particle loss.

Quadrupole field

A common magnetic field configuration is the *quadrupole field*, which is shown in fig. 2.2 and, near its centre, is given by:

$$\mathbf{B} = b \begin{pmatrix} x \\ y \\ -2z \end{pmatrix} \quad \Rightarrow \quad |\mathbf{B}| = \sqrt{x^2 + y^2 + 4z^2}\,. \tag{2.25}$$

The full expression depends on the geometry of the (electro)magnets generating it, and is given in appendix B.2 for rectangular and circular coils.

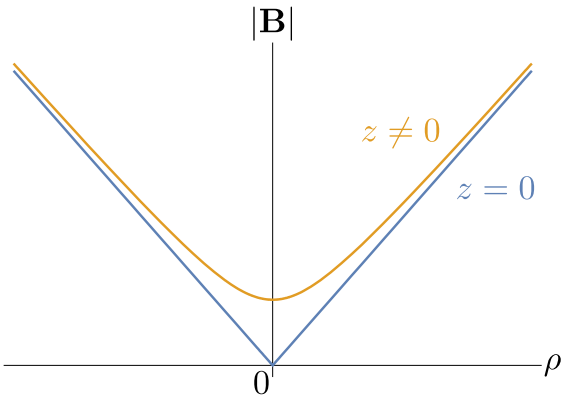

Figure 2.2 : The spatial configuration of the quadrupole magnetic field given in eq. 2.25. At its centre, the field is exactly zero.

In order for atoms to remain trapped while moving through this spatially inhomogeneous field, they need to adiabatically follow its changes and stay in the same m_F state with respect to the local field orientation. From dimensional analysis, this is only guaranteed if:

$$\frac{\mathbf{v} \cdot \nabla \mathbf{B}}{|\mathbf{B}|} \ll \omega_L, \tag{2.26}$$

where $\mathbf{v}$ is the velocity of the atom and ω_L the Larmor frequency. In a region of space where the field is too small or too rapidly varying, the adiabaticity condition is not satisfied and atoms may flip to an untrapped m_F state and hence be lost. These losses become significant for cold clouds with an increasing population at the centre of the field, and are known as *Majorana spin flips* [72]. They can be avoided by using different magnetic field geometries (Ioffe-Pritchard [73] or QUIC [74] traps) or by superimposing an optical repulsive potential ("plug") at the trap minimum.

Optical pumping

In order to maximise the number of atoms captured by the magnetic trap, the sample is spin-polarised into a low-field seeking m_F state. Ideally, this is a state at the edge of the manifold with the largest magnetic moment and the strongest interaction with the magnetic field. This also suppresses spin-changing collisions by conservation of angular momentum:

$$2 \times |F, m_F\rangle \rightarrow |F, m_F - 1\rangle + |F, m_F + 1\rangle, \tag{2.27}$$

where for a state with maximal m_F there is no available $m_F + 1$ state, hence reducing particle loss.

Spin-polarisation may be achieved via *optical pumping*, where σ polarised light induces successive transitions between neighbouring m_F states, in order for the atoms to accumulate into a dark state, as shown in fig. 2.3.

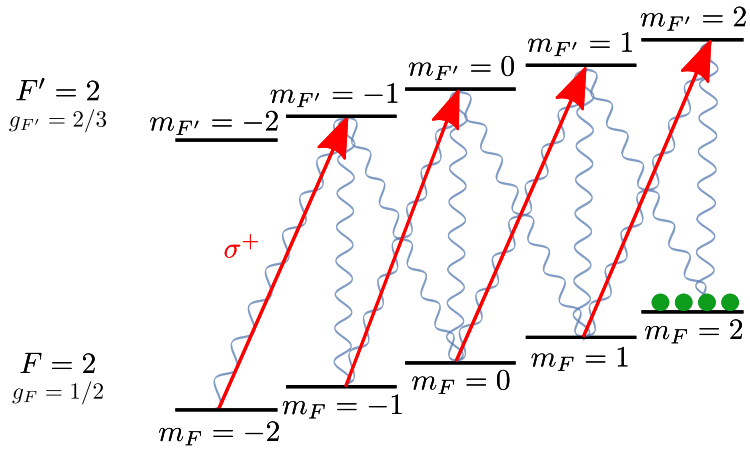

Figure 2.3 : Optical pumping of atoms into the $|F = 2, m_F = 2\rangle$ state. σ^+ radiation causes $\Delta m_F = 1$ transitions to the excited manifold F', from which the atoms spontaneously decay back into F. Successive transitions eventually lead to the accumulation of the atoms into the dark state, which does not couple to the due to the absence of an $m_{F'} = 3$ state.

2.2.2 Optical trapping

Polarisability

Optical trapping is enabled by the dipole potential U_{dip} in eq. 2.21, which for large detuning is equivalent to the AC Stark shift.

The full second-order perturbative treatment [75] results in an atomic energy shift ΔE:

$$\Delta E(\mathbf{r}) = \frac{3\pi c^2}{2\omega_0^3}\Gamma\left(\frac{1}{\omega - \omega_0} + \frac{1}{\omega + \omega_0}\right) I(\mathbf{r}), \tag{2.28}$$

where ω_0 is the transition frequency of the two-level atom, Γ the natural linewidth of the excited state, ω the frequency of the incident radiation and $I(\mathbf{r})$ its intensity distribution. The rotating wave approximation was not used in order for this expression to be applicable to arbitrarily large detuning, where the scattering force is suppressed.

The intensity profile of the incident radiation can be engineered to result in a spatially varying potential enabling to trap the atoms. The dipole potential $U_{\text{dip}}(\mathbf{r})$ is usually expressed as:

$$U_{\text{dip}}(\mathbf{r}) = \alpha(\omega) I(\mathbf{r}), \tag{2.29}$$

where α is the *polarisability* of the atom.

The species considered in this thesis, ^{87}Rb and ^{39}K, are both multilevel atoms with two distinct transitions from the ground state, the D1 and the D2 lines discussed in section 4.3.1. Both need to be taken into account, with a relative strength determined by the internal structure of the excited states [76]:

$$U(\mathbf{r}) = \frac{\pi c^2}{2}\left(\frac{\Gamma_{\text{D2}}}{\omega_{\text{D2}}^3}\frac{2}{\Delta_{\text{D2}}} + \frac{\Gamma_{\text{D1}}}{\omega_{\text{D1}}^3}\frac{1}{\Delta_{\text{D1}}}\right) I(\mathbf{r}), \quad \text{with} \quad \frac{1}{\Delta_{\text{D}}} = \frac{1}{\omega - \omega_{\text{D}}} + \frac{1}{\omega + \omega_{\text{D}}}, \tag{2.30}$$

where the pre-factor to the intensity $I(\mathbf{r})$ is the scalar polarisability. Vector and tensor contributions to the polarisability [77] depend on the internal states m and m^2, and can be ignored for far detuned light which cannot resolve them.

For red detuned radiation, $\Delta < 0$ and hence $U(\mathbf{r}) < 0$, resulting in an attractive potential.

Crossed-beam dipole trap

A common geometry for laser radiation is a Gaussian beam, the fundamental TEM_{00} mode for the vacuum in the paraxial approximation. Its intensity profile $I(\mathbf{r})$ when propagating along y is given by:

$$I(\mathbf{r}) = \frac{2P}{\pi w_x(y)\, w_z(y)} \mathrm{e}^{-\frac{2x^2}{w_x^2(y)} - \frac{2z^2}{w_z^2(y)}}, \quad w_i(y) = w_{0,i}\sqrt{1 + \left(\frac{y}{y_\mathrm{R}}\right)^2}, \tag{2.31}$$

where w_i are the waists (w_0 at $y = 0$), y_R the Rayleigh range and P the optical power. The optical potential resulting from a single red detuned Gaussian beam is shown in fig. 2.4a, and only allows for confinement in the transverse (x, z) directions. Hence, a crossed-beam configuration comprising two orthogonal beams may be employed, shown in fig. 2.4b.

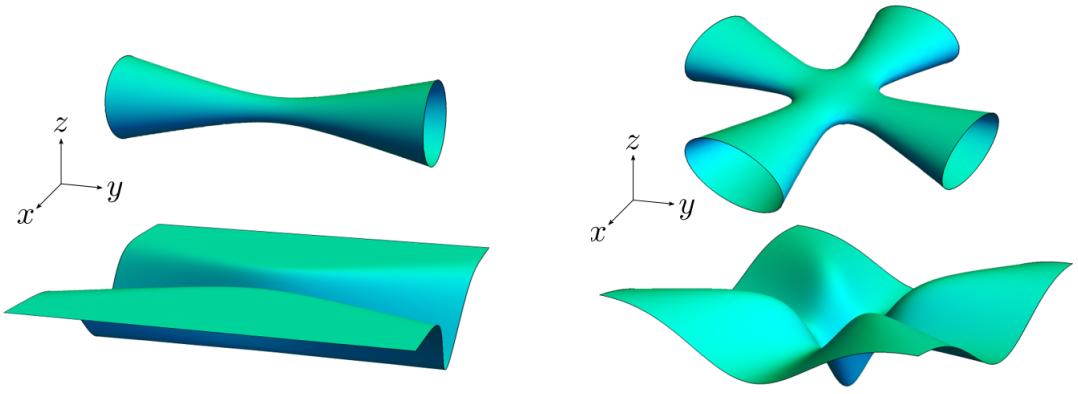

(a) single beam (b) crossed-beam

Figure 2.4 : Red detuned beams can be used to optically trap atoms.

At the centre of the trap, the intensity may be approximated as:

$$I(\mathbf{r}) = \frac{2P}{\pi w_\mathrm{h}\, w_\mathrm{v}} \left(1 - \frac{2x^2 + 2y^2}{w_\mathrm{h}^2} - \frac{4z^2}{w_\mathrm{v}^2} - \dots\right), \tag{2.32}$$

where $w_\mathrm{h} = w_{x,0} = w_{y,0}$ and $w_\mathrm{h} = w_{z,0}$ are the horizontal and vertical waists. The optical potential is then given by:

$$U(\mathbf{r}) = \alpha I(\mathbf{r}) = \underbrace{\alpha \frac{2P}{\pi w_\mathrm{h}\, w_\mathrm{v}}}_{U_0} \left(1 - \frac{2x^2 + 2y^2}{w_\mathrm{h}^2} - \frac{4z^2}{w_\mathrm{v}^2} + \dots\right), \tag{2.33}$$

where U_0 is the peak trap depth. This can be further simplified by approximating the central region as a harmonic trap with trapping frequencies ω_ρ and ω_z:

$$\begin{aligned} \frac{1}{2} m\omega_\rho^2 \rho^2 = U_0 \frac{2\rho^2}{w_\mathrm{h}^2} \quad &\Rightarrow \quad \omega_\rho = \sqrt{\frac{4U_0}{m w_\mathrm{h}^2}}, \\ \frac{1}{2} m\omega_z^2 z^2 = U_0 \frac{4z^2}{w_\mathrm{v}^2} \quad &\Rightarrow \quad \omega_z = \sqrt{\frac{8U_0}{m w_\mathrm{v}^2}}. \end{aligned} \tag{2.34}$$

2.3 Cooling

2.3.1 Phase space density increase

As discussed in section 1.1.2, the onset of quantum degeneracy is enabled by the increase of phase space density. In the following, we show that this can only be performed by dissipative processes causing entropy loss.

Dissipative processes

Given the phase space density $\rho(\mathbf{r}, \mathbf{p}, t)$ introduced in section 1.1.2, the total probability of finding a particle is given by:

$$P = \int \mathrm{d}^3\mathbf{r}\, \mathrm{d}^3\mathbf{p}\, \rho(\mathbf{r}, \mathbf{p}, t). \tag{2.35}$$

Conservation of probability requires:

$$\begin{aligned} \frac{\mathrm{d}P}{\mathrm{d}t} = \frac{\partial}{\partial t} \int \mathrm{d}^3\mathbf{r}\, \mathrm{d}^3\mathbf{p}\, \rho(\mathbf{r}, \mathbf{p}, t) = -\oint_S (\dot{\mathbf{r}} \cdot \mathrm{d}^2\mathbf{r} + \dot{\mathbf{p}} \cdot \mathrm{d}^2\mathbf{p}) \rho(\mathbf{r}, \mathbf{p}, t) = \\ -\int \mathrm{d}^3\mathbf{r}\, \mathrm{d}^3\mathbf{p}\, \{\nabla_{\mathbf{r}} \cdot [\rho(\mathbf{r}, \mathbf{p}, t)\dot{\mathbf{r}}] + \nabla_{\mathbf{p}} \cdot [\rho(\mathbf{r}, \mathbf{p}, t)\dot{\mathbf{p}}]\} = 0, \end{aligned} \tag{2.36}$$

where Gauss' theorem was used. Equating the integrands, as the integration can be performed on an any arbitrarily chosen volume, yields the continuity equation:

$$\frac{\partial \rho(\mathbf{r}, \mathbf{p}, t)}{\partial t} + \nabla_{\mathbf{r}} \cdot (\rho(\mathbf{r}, \mathbf{p}, t)\dot{\mathbf{r}}) + \nabla_{\mathbf{p}} \cdot (\rho(\mathbf{r}, \mathbf{p}, t)\dot{\mathbf{p}}) = 0. \tag{2.37}$$

Using $\nabla_{\mathbf{q}}(\rho\mathbf{q}) = \dot{\mathbf{q}} + \nabla(\rho) + \rho\nabla \cdot \dot{\mathbf{q}}$ and employing Hamilton's equations of motion, we obtain:

$$\begin{aligned} \nabla_{\mathbf{r}} \cdot \dot{\mathbf{r}} &= \frac{\partial}{\partial \mathbf{r}} \left(\frac{\partial \mathbf{r}}{\partial t} \right) = \frac{\partial}{\partial \mathbf{r}} \left(\frac{\partial H}{\partial \mathbf{r}} \right), \\ \nabla_{\mathbf{p}} \cdot \dot{\mathbf{p}} &= \frac{\partial}{\partial \mathbf{p}} \left(\frac{\partial \mathbf{p}}{\partial t} \right) = -\frac{\partial}{\partial \mathbf{p}} \left(\frac{\partial H}{\partial \mathbf{p}} \right), \\ \Rightarrow \dot{\mathbf{r}} \cdot \nabla_{\mathbf{r}}[\rho(\mathbf{r}, \mathbf{p}, t)] + \dot{\mathbf{p}} \cdot \nabla_{\mathbf{p}}[\rho(\mathbf{r}, \mathbf{p}, t)] &= 0, \end{aligned} \tag{2.38}$$

which reduces eq. 2.37 to:

$$\frac{\partial \rho(\mathbf{q}, t)}{\partial t} + \dot{\mathbf{q}} \cdot \nabla_{\mathbf{q}}(\rho[\mathbf{q}, t)] = \frac{\mathrm{d}\rho(\mathbf{q}, t)}{\mathrm{d}t} = 0, \tag{2.39}$$

where $\mathbf{q} = (\mathbf{r}, \mathbf{p})$.

The phase space density of a system obeying Hamiltonian mechanics is constant, as guaranteed by *Liouville theorem*. The Hamiltonian formalism rests upon the conservation of energy, enforced by position-dependent forces and *conservative* potentials. In order to cause a change in phase space density, dissipative forces depending on velocity are required, such as friction.

Entropy

Section 1.1.2 presented a thermodynamic reasoning to relate the phase space density to the degeneracy parameter D. Here we show how this depends on the entropy of the system S.

Thermodynamics and statistical physics are related by the following expression involving the Helmholtz free energy $F = E - TS$ and the partition function Z:

$$F = -Nk_{\mathrm{B}}T\ln(Z) \quad \Rightarrow \quad Z = N\mathrm{e}^{-\frac{F}{k_{\mathrm{B}}T}} = N\exp\left(-\frac{E}{Nk_{\mathrm{B}}T} + \frac{S}{Nk_{\mathrm{B}}}\right), \tag{2.40}$$

where N, E, T and S are the particle number, energy, temperature and entropy of the thermodynamic system.

The degeneracy parameter introduced in eq. 1.13, $D = n_0\lambda_{\mathrm{th}}^3 \propto NZ^{-1}$, is therefore given by:

$$D \propto \exp\left(\frac{E}{Nk_{\mathrm{B}}T} - \frac{S}{Nk_{\mathrm{B}}}\right). \tag{2.41}$$

The energy can be extracted from Z as:

$$E = Nk_{\mathrm{B}}T^2\frac{\partial \ln Z}{\partial T}, \tag{2.42}$$

where

$$Z \propto \underbrace{\int \mathrm{d}^3\mathbf{p}\,\mathrm{e}^{-\frac{p^2}{2mk_{\mathrm{B}}T}}}_{\propto T^{3/2} \text{ from eq. 1.12}} \cdot \underbrace{\int \mathrm{d}^3\mathbf{r}\,\mathrm{e}^{-\frac{V(\mathbf{r})}{k_{\mathrm{B}}T}}}_{\propto T^{\gamma} \text{ from eq. 1.16}}, \tag{2.43}$$

which after some manipulation results in:

$$E \propto \left(\frac{3}{2} + \gamma\right) Nk_{\mathrm{B}}T. \tag{2.44}$$

The degeneracy parameter D can therefore be expressed as:

$$D = n_0\lambda_{\mathrm{th}}^3 \quad \propto \quad \exp\left(\gamma - \frac{S}{Nk_{\mathrm{B}}}\right), \tag{2.45}$$

where γ is the power law of the confining trapping potential.

An increase in the phase space density and therefore in D results from varying the trap geometry, or from reducing the entropy S of the system. Hence, the laser and evaporative cooling schemes presented in sections 2.3.2 and 2.3.3 make use of dissipative and loss mechanisms in order to extract entropy from the atomic cloud and reach quantum degeneracy.

2.3.2 Laser Cooling

Optical Molasses

Laser cooling relies on the momentum transfer between atoms and radiation enabled by the scattering force $\mathbf{F}_{\mathrm{scat}}$ in eq. 2.21. This depends on the ratio I/I_{S}, I_{S} being the saturation intensity, above which the force saturates. For a high intensity resonant beam, $I \gg I_{\mathrm{S}}$ and $\Delta = 0$, the maximum scattering force $F_{\max}$ and acceleration $a_{\max}$ exerted on the atom are:

$$F_{\max} = \hbar k\frac{\Gamma}{2}, \quad a_{\max} = \frac{\hbar k}{M}\frac{\Gamma}{2}. \tag{2.46}$$

When absorbing an incoming photon, an atom moving at speed v recoils in order to conserve momentum, resulting in a decrease of its speed as it continues to propagate along x:

$$\frac{\mathrm{d}v}{\mathrm{d}t} = v\frac{\mathrm{d}v}{\mathrm{d}x} = -a_{\max} \qquad \Rightarrow \qquad v^2 = v_0^2 - 2a_{\max}x. \tag{2.47}$$

The atom returns to its ground state by spontaneously emitting a photon, but the recoil associated with this event averages to zero because of the random direction of the scattered radiation.

Photons absorbed from the coherent laser radiation have less entropy than the incoherent spontaneously emitted photons, which results in the atomic cloud losing entropy.

Atoms in a thermal gas, however, require addressing velocities in arbitrary directions. This is implemented by shining a pair of counter-propagating red detuned beams of frequency $\omega < \omega_0$ along each orthogonal direction. A stationary atom that has already been cooled is not resonant with either beam, as shown in fig. 2.5a, so further light scattering is avoided. However, atoms with a finite speed v experience Doppler-shifted laser frequencies $\omega' = \omega \pm kv$ which may be closer (farther) to (from) resonance, as shown in fig. 2.5b. For a right-moving atom, the left-propagating beam is *closer* to resonance, increasing its absorption rate and hence providing a net decrease of the atom speed, whereas the right-moving beam is farther from resonance and results in fewer transitions.

The net force experienced by the atoms, F_{molasses}, is shown in fig. 2.5c and is given by:

$$\begin{aligned} F_{\text{molasses}} &= F_{\text{scat}}[(\omega - kv) - \omega_0] - F_{\text{scat}}[(\omega + kv) - \omega_0] \simeq -2\frac{\partial F_{\text{scat}}}{\partial \omega} kv, \\ \Rightarrow F_{\text{molasses}} &= -\alpha v, \qquad \text{with} \qquad \alpha = 2k\frac{\partial F}{\partial \omega} = 4\hbar k^2 \frac{I}{I_{\text{S}}} \frac{-2\Delta/\Gamma}{1 + \left(\frac{2\Delta}{\Gamma}\right)^2}. \end{aligned} \tag{2.48}$$

Red detuned light with $\Delta < 0$ ensures $\alpha > 0$ and results in the force $F_{\text{molasses}} \propto -v$ being dissipative, so as to reduce the kinetic energy of the atoms:

$$\frac{\mathrm{d}E}{\mathrm{d}t} = \frac{\mathrm{d}}{\mathrm{d}t}\left(\frac{1}{2}mv_i^2\right) = v_i F_{\text{molasses}} = -\alpha v_i^2 = -\frac{2\alpha}{m}E. \tag{2.49}$$

MOT

Optical molasses only decelerates the atomic sample but provides no confinement about a point, preventing the increase of its spatial density. A Magneto-Optical Trap (MOT) combines the velocity-dependent dissipative mechanism with a spatially-dependent restoring force arising from a magnetic field modulating the scattering rate.

A pair of current-carrying coils in the anti-Helmholtz configuration generates the quadrupole field $\mathbf{B}$ which lifts the degeneracy among the m_F states and shifts their energies according to the *Zeeman effect*:

$$\Delta E_{\text{Zeeman}} = g_F \, m_F \, \mu_{\text{B}} \, B_z(z), \tag{2.50}$$

where z is chosen as the direction of the local magnetic field defining the (local) quantisation axis, and the other symbols are the same as in eq. 2.24

The field is rather weak and does not provide confining by generating a magnetic trap, but by spatially modulating the absorption rate of the incident radiation, as illustrated in fig. 2.6. The counter-propagating beams are still red detuned but now also σ^- polarised (with respect to the *local* magnetic field) in order to drive $\Delta m_F = -1$ transitions: atoms farther away from the trap centre will be closer to resonance with the incoming beam and therefore scatter more photons.

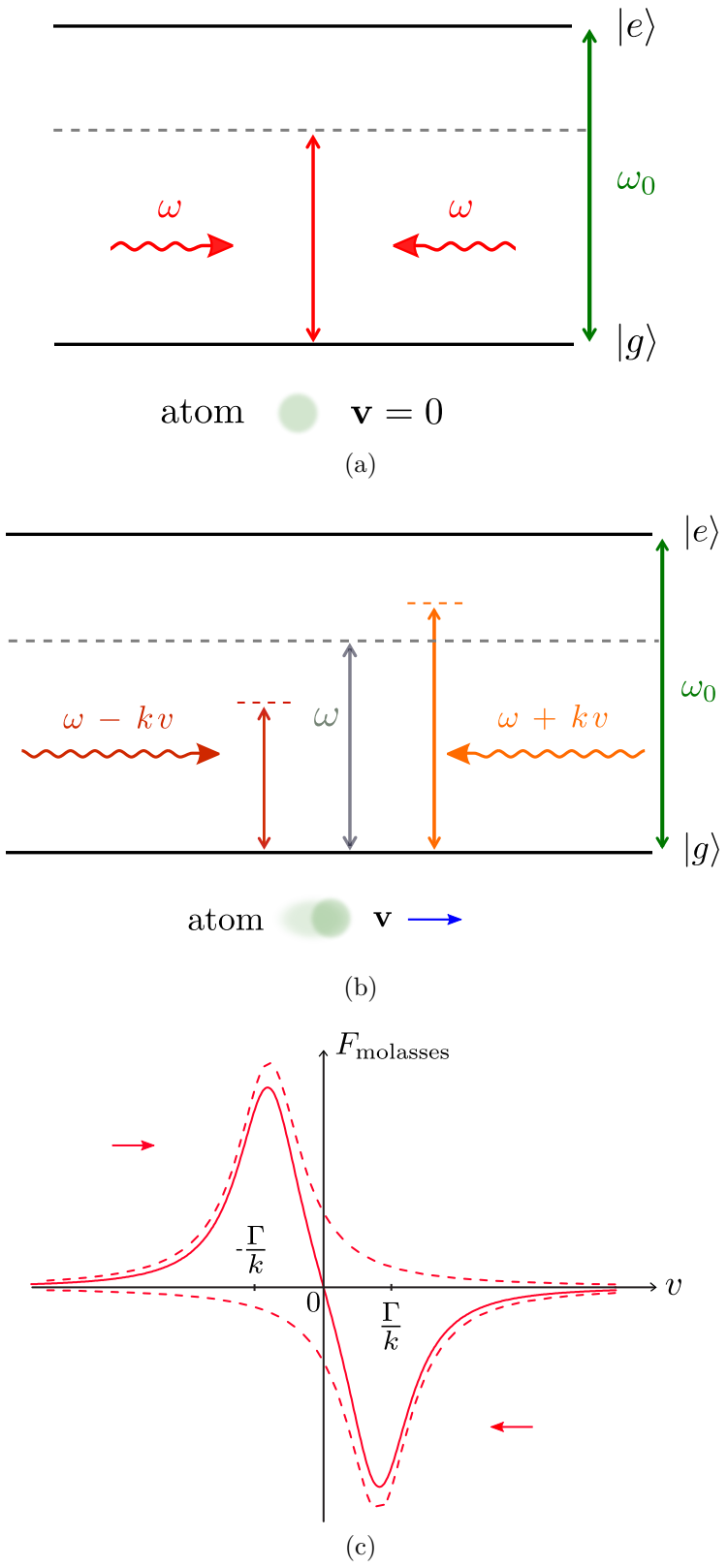

Figure 2.5 : Optical molasses consists of two red detuned counter-propagating beams. While neither is resonant with stationary atoms (a), they induce a preferential absorption of photons depending on the atom's speed (b). This results in the atoms experiencing a frictional force that slows them down (c).

The total force on the atoms F_{MOT} is given by:

$$F_{\mathrm{MOT}} = F^{\rightarrow}_{\mathrm{scat}}[\overbrace{(\omega - kv)}^{\text{Doppler}} - \overbrace{(\omega_0 + \beta z))}^{\text{Zeeman}}] - F^{\leftarrow}_{\mathrm{scat}}[(\omega + kv) - (\omega_0 - \beta z)], \tag{2.51}$$

where

$$\beta = \frac{g_F m_F \mu_{\mathrm{B}}}{\hbar} \frac{\mathrm{d}B_z}{\mathrm{d}z} z. \tag{2.52}$$

This can be approximated as:

$$F_{\mathrm{MOT}} \simeq -2\frac{\partial F}{\partial \omega} kv + 2\frac{\partial F}{\partial \omega_0}\beta z = -\alpha v - \frac{\alpha\beta}{k} z, \tag{2.53}$$

which not only contains a frictional term ($\propto -v$) as in eq. 2.48, but also a restoring force ($\propto -z$) providing confinement about the centre of the quadrupole field.

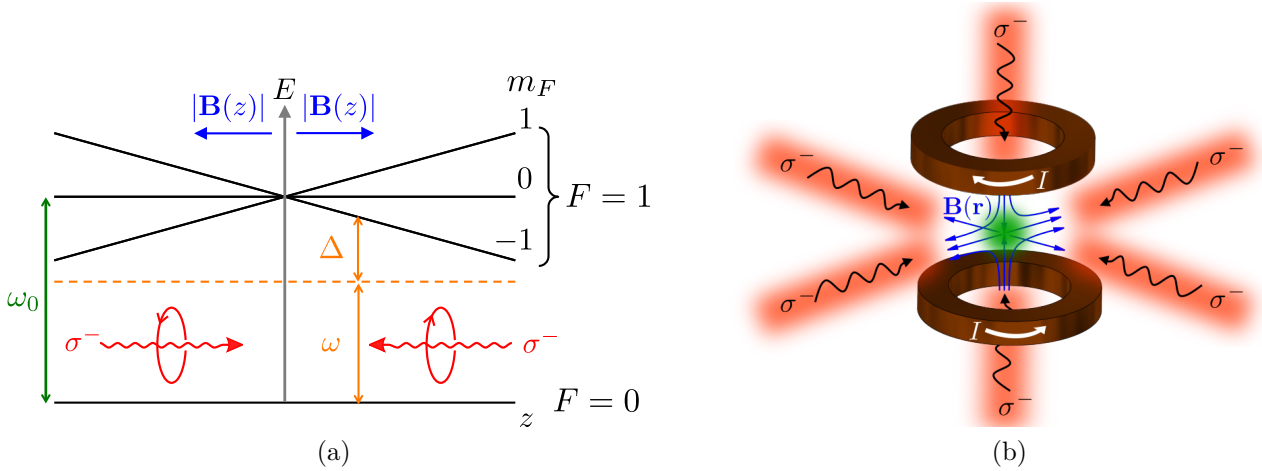

Figure 2.6 : A Magneto-Optical trap provides both a dissipative force to slow down the atoms, and a restoring force to confine them near the centre of the trap (a). The quadrupole magnetic field is produced by a pair of coils in the anti-Helmholtz configuration (b).

Optical molasses and MOTs rely on the atoms differentiating between the two incoming beams by their Doppler shifted frequencies. When the frequency difference between the two beams becomes comparable to the natural linewidth Γ of the atoms, cooling becomes less efficient and eventually stops. The theoretical lower limit is the *Doppler temperature* T_{D}:

$$T_{\mathrm{D}} = \frac{\hbar\Gamma}{2k_{\mathrm{B}}}, \tag{2.54}$$

rigorously derived in [78], which is 146 µK for both ^{39}K and ^{87}Rb.

Polarisation gradient cooling

Sub-Doppler cooling schemes can further reduce the temperature by making use of the multiplicity of the sub-levels in the atomic ground state. One such technique is polarisation gradient cooling, which combines the conservative potential resulting from the AC Stark shift with the spontaneous emission needed to lose entropy.

A common example is *Sisyphus cooling* [79], where two counter-propagating beams of equal amplitude E_0 but orthogonal linear polarisations ("lin $\perp$ lin" configuration) interfere to form a standing wave with a spatially varying polarisation:

$$\mathbf{E} = E_0 \left[(\hat{\mathbf{x}} + \hat{\mathbf{y}}) \cos(\omega t) \cos(kz) + (\hat{\mathbf{x}} - \hat{\mathbf{y}}) \sin(\omega t) \sin(kz)\right]. \tag{2.55}$$

This results in a spatially varying AC Stark shift which distinguishes the internal states m_J by their vector polarisability (section 2.2.2), as shown in fig. 2.7. If no coupling to the excited state were present, the atoms would lose kinetic energy climbing the hill, to be re-gained upon descending it, resulting in no energy loss. The spatial dependence of the polarisation, however, allows atoms in one of the m_J sub-levels at the top of the hill to transition to the excited states, from which it may spontaneously decay into the *other* m_J sub-level. The short lifetime of the excited state ($\sim 10\,\mathrm{ns}$) guarantees the transitions occur at the same position, and the atom decays to the bottom of the hill, thereby losing a net amount of energy.

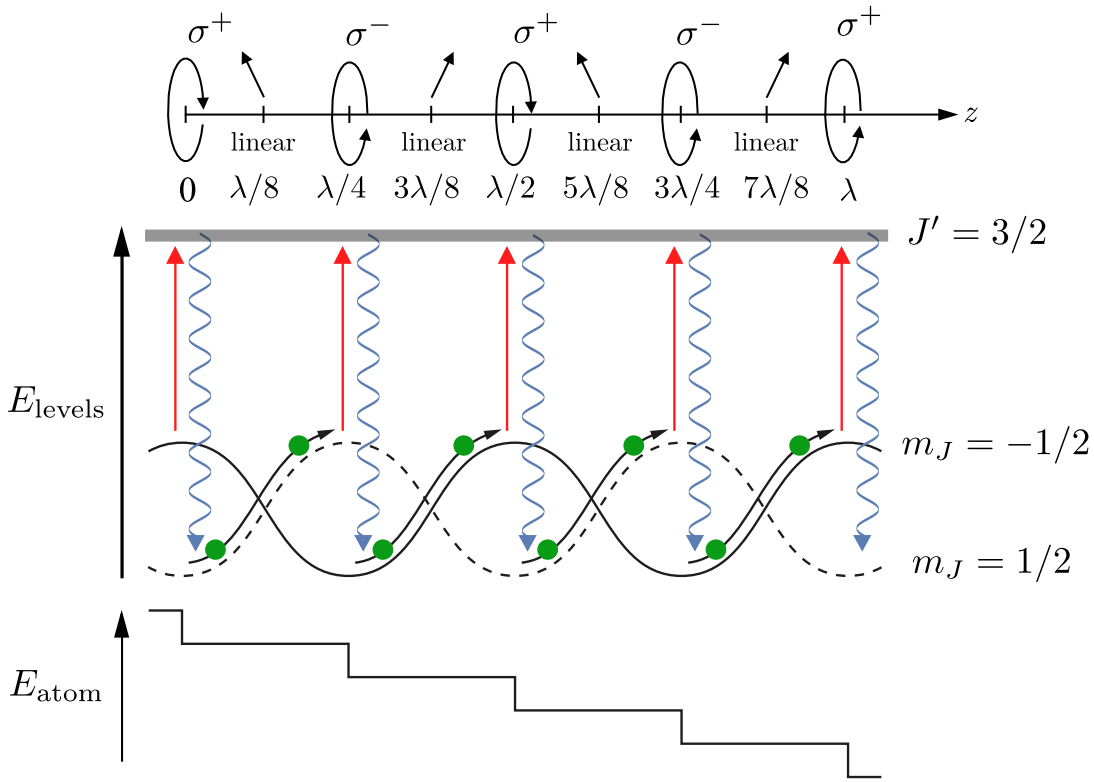

Figure 2.7 : In Sisyphus cooling, an atom in the $|m_J = 1/2\rangle$ state climbs the hill in the spatially varying potential resulting from the AC Stark shift. At the top of the hill, σ^- polarised light enables a transition into an excited state which may then decay into the $|m_J = -1/2\rangle$ state, at the bottom of the hill. This allows the atom to lose energy as it propagates in space.

In our experiment, the same beams that are used in the MOT are also used to perform polarisation gradient cooling. These are σ polarised but still allow sub-Doppler cooling, though in the $\sigma^+ - \sigma^-$ configuration which only results in a spatially rotating linear polarisation:

$$\mathbf{E} = 2E_0 \cos(\omega t)[\hat{\mathbf{x}} \cos(kz) + \hat{\mathbf{y}} \sin(kz)]. \tag{2.56}$$

As discussed in [80], this causes an imbalance of the radiation pressure exerted by the two beams, because of the spatial dependence of the polarisation and hence of the transition rate to the excited state.

The ultimate limit of cooling schemes based on scattering of light is the recoil temperature T_{rec}:

$$T_{\mathrm{rec}} = \frac{\hbar^2 k^2}{2m k_{\mathrm{B}}}, \tag{2.57}$$

where m is the mass of the atom, and corresponds to the energy acquired upon a single spontaneous emission event. Polarisation gradient cooling is likely to become ineffective even before this limit, as colder atoms increase their de Broglie wavelength λ_{th} and lose the ability to resolve the details of the potential landscape.

The recoil temperatures for ^{87}Rb and ^{39}K are $T_{\mathrm{rec}} \sim 360\,\mathrm{nK}$ and $\sim 420\,\mathrm{nK}$. Further cooling is allowed by sub-recoil techniques such as evaporative cooling.

2.3.3 Evaporative cooling

The temperature of an atomic cloud can be reduced by adiabatically relaxing the trap confining it, which however also decreases the spatial density and therefore prevents the increase of phase space density. For example, in a harmonic trap of depth U_0, the temperature $T \propto \hbar\omega/k_{\mathrm{B}}$ and the number of particles N scale as:

$$\underbrace{T \propto U_0^{1/2}}_{\text{from eq. 2.34}}, \quad \underbrace{N \propto U_0^{3/2}}_{\text{from eq. 1.14}} \quad \Rightarrow \quad D = n_0 \lambda_{\mathrm{th}}^3 \quad \propto \quad U_0^{-3/2} U_0^{3/2} \quad \sim \quad 1, \tag{2.58}$$

leaving the degeneracy parameter constant. This is classically explained in the context of *adiabatic invariants* [81].

Once again, a dissipative process is needed in order to increase phase space density, such as the particle loss used in evaporative cooling. This was first introduced in [82] and is illustrated in fig. 2.8. The trap is gradually lowered to new depths U_0 so as to lose all atoms with energies $E > U_0$ and allow the remaining cloud to thermalise to a lower temperature.

In order for the evaporation to be successful, the elastic collision rate γ_{el} needs to be larger than the inelastic collision rate, so that thermalisation of the remaining particles in the trap occurs faster than particle loss mechanisms. The desired regime to operate in is then the *run-away regime*, where γ_{el} increases with decreasing number of particles and allows for a fast evaporative stage in order to minimise losses. A theoretical model for evaporative cooling is presented in [55], and makes use of the truncation parameter $\eta = U_0/(k_{\mathrm{B}}T)$ to identify a suitable evaporation process, ensuring both a run-away regime and phase space density increase.

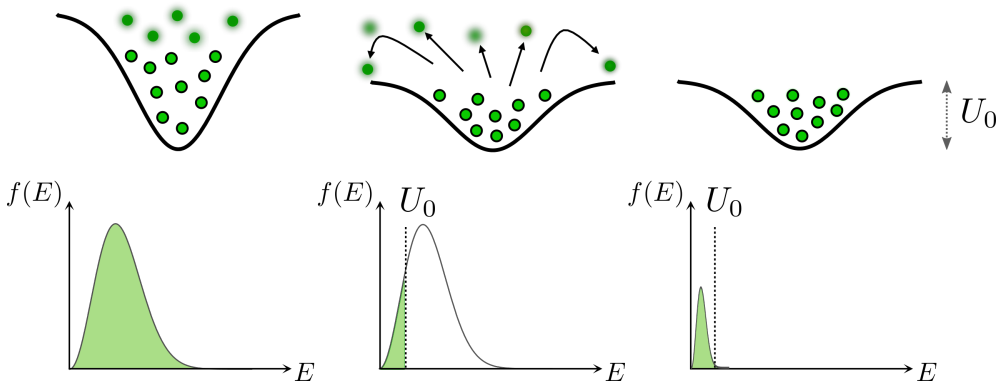

Figure 2.8 : Illustration of the working principle of evaporative cooling. The atoms in the trap are in thermal equilibrium (a) and their energy distribution is given by eq. 1.18. The trap depth is then lowered (b) to release highly energetic atoms, corresponding to a truncation in the energy distribution. The remaining atoms thermalise (c) to a lower temperature.

Evaporative cooling reaches its ultimate limit when the elastic and inelastic collision rates become comparable, as they may be governed by different functional dependences at low temperatures [79]. In experiments, however, a Bose-Einstein condensate usually emerges before any of the assumptions break down.

2.4 Optical lattices

2.4.1 Quantum simulators

Optical lattices are generated from the interference of counter-propagating beams, which gives rise to a standing wave pattern of intensity maxima and minima of variable geometry and dimensionality, as shown in fig. 2.9.

In 1D (fig. 2.9a), the resulting intensity is:

$$I = \langle [E_0 \cos(kz - \omega t) + E_0 \cos(-kz + \omega t)]^2 \rangle \propto \cos^2(kz), \tag{2.59}$$

with a separation between extrema of $d = \lambda/2$.

Because of the AC Stark shift (eq. 2.13), the atoms experience an attractive force towards the intensity minima (maxima) of a blue (red) detuned optical lattice. Hence, they are distributed according to the same geometry as the interference pattern generated from the beams. The optical lattice determines the spatial arrangement of the atoms, analogous to the role played by the ionic lattice for electrons in condensed matter. Because of the qualitative similarity between the two systems, cold atoms in optical lattices are used as *quantum simulators* for solid-state physics, as illustrated in fig. 2.10.

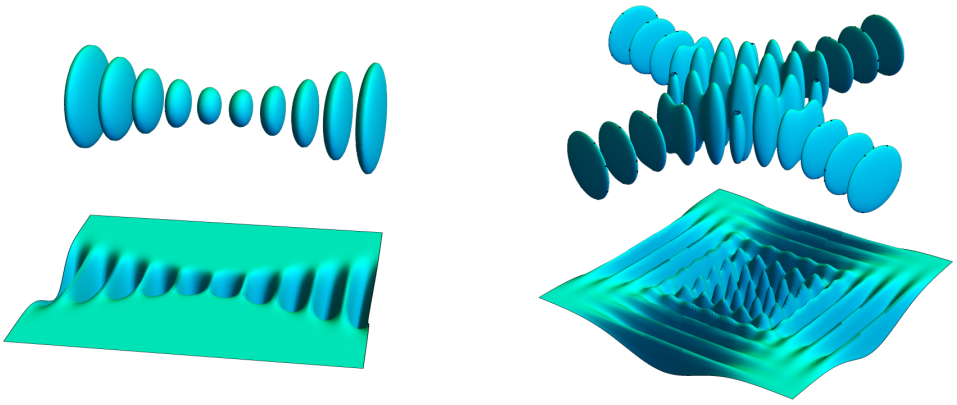

(a) (b)

Figure 2.9 : A pair of counter-propagating beams gives rise to a 1D optical lattice (a) in which each disc ("pancake") is a 2D system. Interference of four beams at orthogonal angles results in a 2D optical lattice with square geometry (b), where each tube is a 1D system.

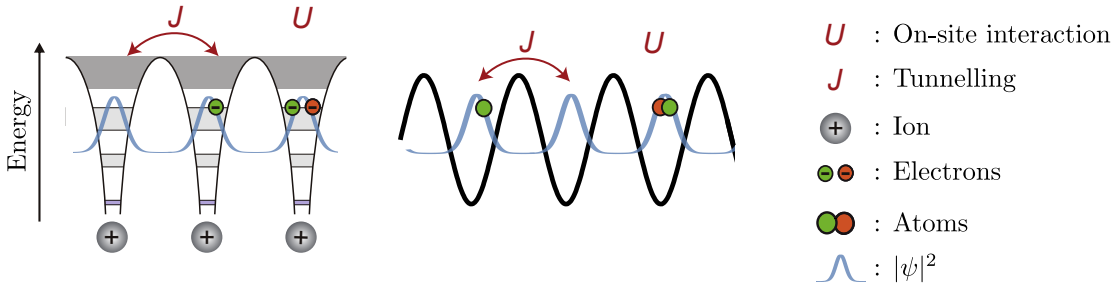

Figure 2.10 : Electrons in ionic potentials in condensed matter systems are qualitatively equivalent to neutral atoms in optical lattices, making the latter a platform to perform quantum simulation of the former.

Quantum simulation was first introduced by Feynman [23] as a way to circumvent the numerical intractability of large quantum systems by performing the investigation on a different but analogous quantum system. For instance, electron transport in a real crystalline solid cannot be reliably simulated on a classical computer given the exponential growth of the Hilbert space governing the dynamics. However, an analogous system can be engineered with cold atoms in an optical lattice in order to experimentally record the atomic spatial distribution as a function of time.

An advantage of optical lattices over condensed matter systems is their much slower dynamics, which enables easier and better experimental investigations. A simple dimensional analysis treatment of the Schrödinger equation results in the following relation between the timescale T and lengthscale L of a system:

$$\mathrm{i}\left[\frac{\partial}{\partial t}\right][\Psi] = -\frac{\hbar^2}{2m}\left[\nabla^2\right][\Psi] \quad \Rightarrow \quad \mathrm{i}\frac{1}{T} \sim -\frac{\hbar^2}{2m}\frac{1}{L^2}. \tag{2.60}$$

The ratio of the timescales for electrons in solids and atoms in optical lattices is then:

$$\frac{T_{\text{atom}}}{T_e} \sim \frac{L_{\text{atom}}^2}{L_e^2}\frac{m_{\text{atom}}}{m_e} \sim \left(\frac{10^{-7}}{10^{-11}}\right)^2 \left(\frac{10^{11}}{10^3}\right) \sim 10^{15}, \tag{2.61}$$

where $m_e \sim 1\,\text{keV}/c^2$, $m_{\text{atom}} \sim 100\,\text{GeV}/c^2$, $L_e \sim 0.1\,\text{Å}$ as for the hydrogen atom, and $L_{\text{atom}} \sim 0.1\,\mu\text{m}$ given by the minima spacing $\lambda/2$ with typical $\lambda \sim 1\,\mu\text{m}$.
While electronic interactions and chemical bonds formations occur on the attosecond timescale [83], dynamical processes in optical lattices range from microseconds to milliseconds. This allows long exposure to incident radiation and thus high-resolution imaging by a camera. Further differences between condensed matter systems and optical lattices are summarised in table 2.2.

Interest in optical lattices sparked when the d-wave superconductivity exhibited in several high-temperature superconductors was reproduced in the phase diagram of the Fermi-Hubbard model [84]:

$$H = -J\sum_{\langle i,j\rangle}\left(c_{i,\sigma}^\dagger c_{j,\sigma} + \text{h.c.}\right) + U\sum_i n_{i,\uparrow}n_{i,\downarrow}, \tag{2.62}$$

where U is the on-site interaction, J the tunnelling between nearest neighbours, and $c^\dagger, c$ and n the creation, annihilation and number operators on lattice site i for a spin state $\sigma \in \{\uparrow,\downarrow\}$. This model is easily implemented by cold fermionic atoms in a square optical lattice, which so far have allowed probing the anti-ferromagnetic area of the phase diagram [85, 86] preceding the d-wave superconducting region.

Optical lattices cannot capture the full complexity of the materials displaying high-temperature superconductivity, but they offer a platform to implement the toy model that reproduces their key features. While real systems include defects and impurities that undermine accurate investigation of the material, optical lattice solely rely on the interference of light resulting in (essentially) perfect patterns, as displayed in fig. 2.11.

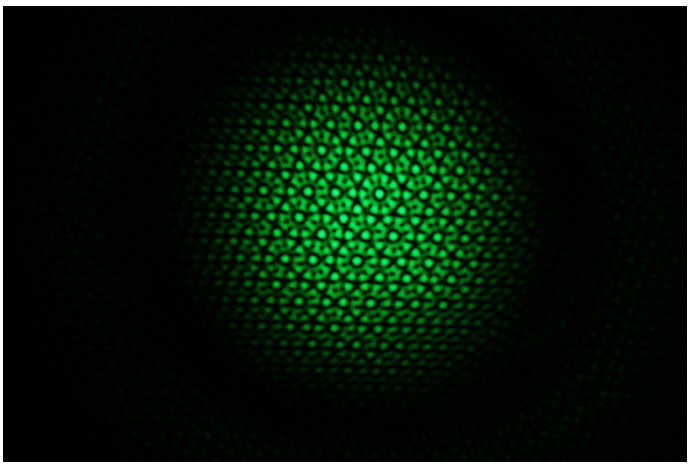

Figure 2.11 : The measured intensity pattern resulting from the interference of five slits placed on the vertices of a pentagon. Optical lattices rely on interference to generate the potentials for the atoms, and are therefore not subject to defects and impurities as in real solids. Picture courtesy of Prof. Theodor Hänsch.

	Cold atoms	Condensed matter
Temperature	$10^{-9} - 10^{-6}$ K	$10^{-6} - 10^{2}$ K
Confinement	Optical/magnetic potentials	positively charged ionic lattice
Density	$10^{13} - 10^{15}$ cm^{-3}	$\sim 10^{22}$ cm^{-3}
number of components	Variable	two (spin 1/2)
Particle statistics	bosons or fermions	fermions (electrons)
Geometry & dimensionality	highly tuneable	depends on chemical composition, pressure ...
Interactions	tuneable, also non-interacting	Coulomb attraction
Disorder	none but can be engineered	unavoidable: defects, impurities

Table 2.2 : Comparison between cold atoms and condensed matter systems, based on [87].

Why ultracold?

In a solid, the lattice spacing d is of order ~ 1 Å while in an optical lattice it is controlled by the wavelength of commercially available lasers, $d = \lambda/2 \sim 1$ µm. In order to reproduce the quantum regime, where the wave nature of matter is dominant, the temperature of the atoms needs to be reduced so as to increase their de Broglie wavelength:

$$\frac{\lambda_{\text{th}}}{d} \gg 1, \quad \lambda_{\text{th}} \propto T^{-1/2}. \tag{2.63}$$

2.4.2 Band structure

The potential experienced by atoms in the 1D standing wave of eq. 2.59 is given by

$$V = V_0 \cos^2(kz) = \frac{V_0}{2}[1 + \cos(2kz)], \tag{2.64}$$

where V_0 is the lattice depth, often quoted in units of the recoil energy $E_{\text{rec}} = \hbar^2 k^2/2m$.

The periodicity of the potential guarantees a periodic wavefunction as a solution, thanks to Bloch's theorem. An electron in a band n with quasimomentum[2] q is therefore described by the Bloch wave:

$$\phi_{n,q}(x) = \mathrm{e}^{\mathrm{i}qx} u_{n,q}(x), \tag{2.65}$$

where the functions u have the same periodicity as the lattice, and are extended over all space as shown in fig. 2.12a. Owing to their periodicity, the functions u can be expressed as a discrete Fourier series:

$$\phi_{n,q}(x) = \mathrm{e}^{\mathrm{i}qx} \sum_{\ell} c_{n,q}\, \mathrm{e}^{\mathrm{i}2\ell kx}. \tag{2.66}$$

[2]Technically $\hbar q$ is the quasimomentum, though the term is often used for q itself.

A Bloch wave is then composed of plane waves with wavectors $q + 2\ell k$, and in the limit of a free particle this reduces to a single plane wave with momentum $p = \hbar q$.

The Bloch wave can however also be constructed from a basis localised on each lattice site x_i. These are the Wannier functions $w_n(x - x_i)$, the eigenstates of the band projected position operator, and allow the following, equivalent expression:

$$\phi_{n,q}(x) = \frac{1}{\sqrt{N}} \sum_i \mathrm{e}^{\mathrm{i}qx_i} w_n(x - x_i), \tag{2.67}$$

where N is the number of sites, needed for normalisation. The functional form of $w_n(x-x_i)$ is shown in fig. 2.12b, which illustrates how the confinement of the Wannier function to a single site grows with lattice strength V_0.

For deep lattices, the lattice sites that experience a significant contribution from the i^{th} Wannier state are only x_i and its nearest neighbours. This is the *tight-binding* regime, where the Hamiltonian only includes an on-site interaction energy U and a nearest-neighbour tunnelling element J, as shown in fig. 2.10. For very deep lattices, the wavefunction is fully confined to a single potential minimum and transport is completely eliminated. This then justifies treating each lattice site as an independent system, approximated by a harmonic oscillator as shown in fig. 2.12c.

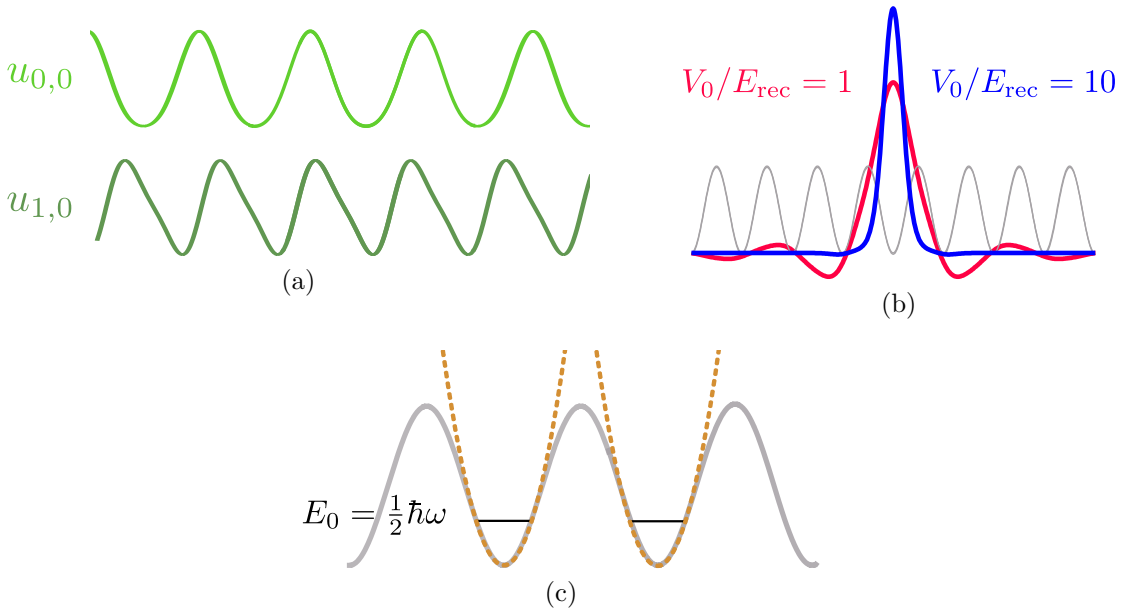

Figure 2.12 : The Bloch wave $\phi_{n,q}$ can be expanded in the periodic and extended basis $u_{n,q}$ (a) as in eq. 2.65, or in the Wannier functions $w_n(x - x_i)$, each confined to a lattice site x_i (b). Deep lattices cause the wavefunction to tightly localise on a single site, which allows approximating it as an independent harmonic oscillator (c). 1D lattices were used for these figures (shown in grey).

The strength of the lattice V_0 determines the energies that the particles are allowed to possess, which are clustered in *bands*. The band structure for a 1D and 2D simple cubic lattice is shown in figs. 2.13 and 2.14, and was computed from diagonalising the Hamiltonian constructed in the plane wave basis as described in section 7.1.4.

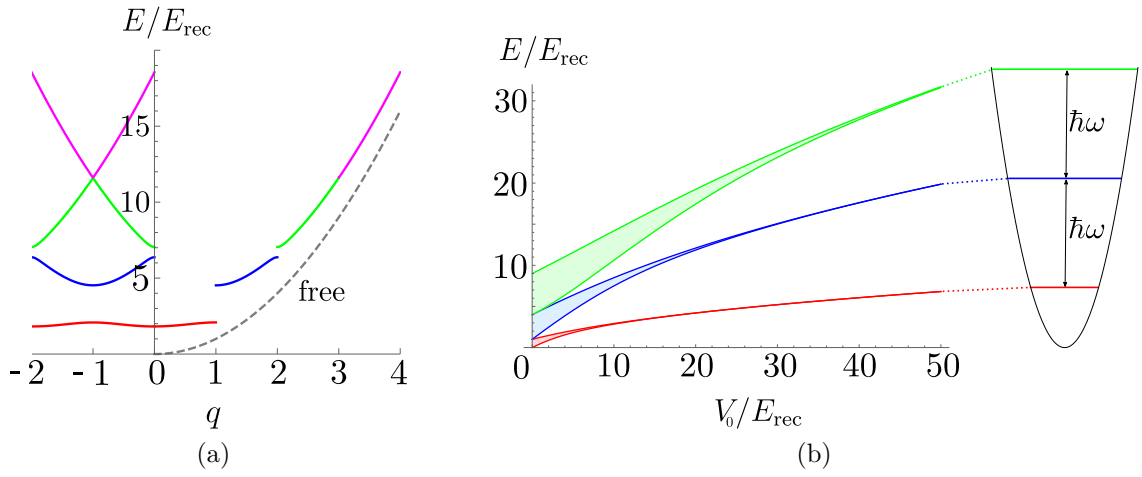

Figure 2.13 : Band structure for a 1D lattice. a) A free particle exhibits a parabolic dispersion relationship (dashed line), which the presence of the lattice separates into finite bands and gaps. The reduced band scheme is shown on the left. b) The width of the bands depends on the lattice strength V_0 and tends to a point in the deep lattice limit, where a single harmonic oscillator can describe each potential minimum. Only the first three bands are shown.

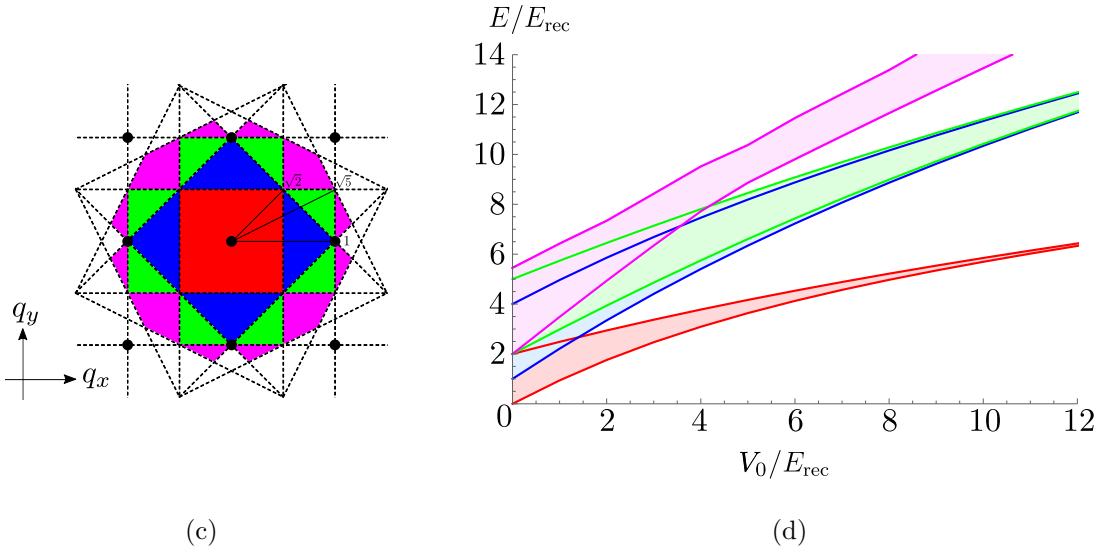

Figure 2.14 : Band structure for a 2D square lattice. The bands are defined over a vector quasimomentum $\mathbf{q} = (q_x, q_y)$ (a). Similarly to the 1D lattice in fig. 2.13, the widths of the bands decrease with increasing lattice strength (b) but in this case the gaps only appear at a finite depth V_0. Only the first four bands are shown. In the deep lattice limit, the p_x (blue) and p_y (green) bands become degenerate.

I wanted to persuade myself that these were only apparent flaws, that they were all part of a much vaster regular structure, in which every asymmetry we thought we observed really corresponded to a network of symmetries so complicated we couldn't comprehend it...

Italo Calvino [88]

3 Quasicrystals

This chapter summarises the currently accepted description of regular crystals and aperiodic structures, providing a historical introduction and establishing the mathematical formalism necessary to appreciate the results in chapters 7 and 8. Quasicrystals display non-trivial structure on all lengthscales, and usual investigation techniques such as spectral decompositions are not sufficient to unequivocally discern order from disorder, placing aperiodic structures in an interesting middle ground.

3.1 From periodic to quasiperiodic

The following review is largely based on [89–91].
This chapter is at times heavily theoretical and abstract, which is unavoidable given the much vaster literature on aperiodic structures available in the field of mathematics. Although I tried my best to provide consistent and rigorous definitions and proofs, this chapter is not essential to the understanding of the rest of the thesis.

3.1.1 Regular crystals

Crystallographic restriction theorem

The elegant simplicity of symmetrical structures has always been a source of fascination and inspiration for mankind. Ancient cultures used it for decorations, architectural plans, ornative motifs, mosaics and painting proportions because of the apparent pleasing aesthetic of regular shapes. A quantitative investigation was performed by Johannes Kepler in *On the six-corner snowflake* [92] where he explained the symmetrical pattern of snowflakes by means of close packing of spheres. This was the first inkling of the macroscopic consequences of microscopic symmetries. In 1801 René Haüy published his four-volume *Traité de minéralogie* [93], winning him the title of "father of modern crystallography"

and a name on the Eiffel tower. He specifically states that no fivefold symmetry is allowed in crystals, which was the first connection between the ability to "pack spheres", or *tile* n-dimensional space via translations of the same microscopic constituent, and the rotational symmetry of the resulting macroscopic structure. With the discovery of X-rays and Bragg scattering at the beginning of the 20^{th} century, the empirically-driven and generally accepted consensus was that the ground state of matter always consisted of a periodic arrangement of atoms and molecules, mathematically described by a *space group* (230 in three dimensions) or a *plane group* (17 in two dimensions). It was however already known that, at finite temperatures, defects and impurities would spoil the otherwise perfect symmetry. The rest of the discussion will focus on two dimensions (2D).

The plane group symmetry determines the microscopic arrangement of the constituents, and its macroscopic consequence is the crystal's morphology. The group symmetry implies that the crystal is invariant under a certain combination of rigid (distance-preserving, *Euclidean*) transformations:

$$\mathbf{r} \to R\mathbf{r} + \mathbf{t}, \tag{3.1}$$

where rotations R and translations $\mathbf{t}$ constitute a *plane group* if the latter are generated by a finite set of d vectors $\{\mathbf{a}_i\}$:

$$\mathbf{r} = \sum_{j=1}^{d} n_j \, \mathbf{a}_j, \quad \text{with} \quad n \in \mathbb{N}. \tag{3.2}$$

These vectors span the lattice structure, and underpin the translational invariance of the crystal. Hence, the treatment of the solid can be simplified by only considering the *unit cell*, the finite space from which every other point in the lattice is reached by translations. The contents of the unit cell determine the structure of whole crystal.

The lattice is also invariant under rotations about a fixed point, i.e. *point groups*:

$$R\mathbf{a}_i = \sum_j M(R)_{ji} \, \mathbf{a}_j, \tag{3.3}$$

where, having chosen the lattice vectors $\{\mathbf{a}_i\}$ as the basis, M is an integer matrix. In a different basis, e.g. orthogonal Cartesian (x, y) coordinates, M is the usual rotation matrix:

$$M'(R) = \pm \begin{pmatrix} \cos\phi & -\sin\phi \\ \sin\phi & \cos\phi \end{pmatrix}, \tag{3.4}$$

where the minus denotes an improper rotation, i.e. a reflection.
Because M and M' are related by a similarity transformation $M' = SMS^{-1}$, the trace is invariant:

$$2\cos\phi = n \in \mathbb{N} \qquad \textbf{crystallographic restriction theorem}. \tag{3.5}$$

The above equation is only satisfied for $\phi = 0, \pi, \pi/2, \pi/3, 2\pi/3$, which restrict the rotational symmetries of 2D lattices to the five 2D *Bravais lattices* exhibiting rectangular, square, rhombic, oblique or hexagonal unit cells. A more detailed discussion is presented in appendix D.5.

Tiling of the whole 2D plane is achieved by successive translations of the unit cell, with the constraint imposed by eq. 3.5 that only allows a few *rotational* symmetries, establishing a (one-way) relation between rotation and translation. A mathematical discussion of tilings is provided in section 3.2.2.

Reciprocal space

The symmetry of the atomic density $\rho(\mathbf{r})$ also affects its Fourier transform $\hat{\rho}(\mathbf{k})$:

$$\rho(\mathbf{r}) = \rho(R\mathbf{r} + \mathbf{t}) \quad \Leftrightarrow \quad \hat{\rho}(\mathbf{k}) = \mathrm{e}^{\mathrm{i}(R\mathbf{k}\cdot\mathbf{t})}\,\hat{\rho}(R\mathbf{k}), \tag{3.6}$$

where R and $\mathbf{t}$ are elements of the plane group defined in eq. 3.1, and it is proved in appendix D.4. This aids in structure determination as it provides *extinction rules* to identify glide reflections, e.g. when $\mathbf{k} = R\mathbf{k}$, the above relation implies either $\hat{\rho}(\mathbf{k}) = 0$ or $\mathbf{k}\cdot\mathbf{t} = 0 \mod 1$. The space defined by $\mathbf{k}$ is termed *momentum* or *reciprocal* space.

Experimentally, one may probe the Fourier transform by bombarding a sample with X-rays or neutrons, since the matrix element for scattering off a potential $V(\mathbf{r})$ is given by:

$$\langle \mathbf{k}_{\text{out}}|V(\mathbf{r})|\mathbf{k}_{\text{in}}\rangle \propto \int \rho(\mathbf{r})\,\mathrm{e}^{-\mathrm{i}\mathbf{k}\cdot\mathbf{r}}\mathrm{d}^3\mathbf{r} \equiv \hat{\rho}(\mathbf{k}), \tag{3.7}$$

where $\mathbf{k} = \mathbf{k}_{\text{out}} - \mathbf{k}_{\text{in}}$ is the change of momentum between incident and detected particles.

In crystallography, $\hat{\rho}(\mathbf{k})$ is also referred to as the *static structure factor*, $F(\mathbf{k})$:

$$F(\mathbf{k}) = \int \rho(\mathbf{r})\,\mathrm{e}^{-\mathrm{i}\mathbf{k}\cdot\mathbf{r}}\,\mathrm{d}^3\mathbf{r} = \sum_{n=1}^{N} f_n \mathrm{e}^{-\mathrm{i}\mathbf{k}\cdot\mathbf{r}}, \tag{3.8}$$

where the expression was further simplified by noting that the density distribution of a regular crystal is discrete. f_n is the atomic scattering factor of the n^{th} particle, and N is the total number of constituents.

In real space, the position vector $\mathbf{r}$ can be expressed as an integer combination of lattice vectors $\mathbf{a}_i$ (eq. 3.2), and an analogous indexing scheme exists in reciprocal space:

$$\mathbf{K} = \sum_i h_i \mathbf{b}_i, \tag{3.9}$$

where $h_i \in \mathbb{N}$ are known as *Miller indeces*. The unit cell in reciprocal space is the Brillouin zone.

The measured scattering intensity, ignoring diffuse and multiple scattering events, is defined as:

$$I(\mathbf{k}) \propto |F(\mathbf{k})|^2, \tag{3.10}$$

from which it is evident that the presence of sharp peaks crucially depends on the constructive interference of the scattered radiation, enabled by the long-range order of the structure. Diffraction experiments, such as the ones discussed in chapter 7, rely on eq. 3.8 and hence probe long-range order, whilst local ordering may be investigated with microscopes and in-situ techniques. Real systems, however, include impurities and defects: this disorder increases the peaks' size, reduces their heights by the *Debye-Waller* factor, and adds a continuous diffuse background.

Fig. 3.1 shows examples of scattering intensities from a regular crystal (a), an amorphous solid such as a glass (b), and a 1D quasicrystal. For regular crystals, the $n > s$ part of the sum in 3.8 is redundant, s being the number of particles in the unit cell, hence $I(\mathbf{k})$ consists of a repetitive pattern. The lack of translational order in a quasicrystal results in the lack of a unit cell, hence the sum in eq. 3.8 extends to $N \to \infty$, uncovering non-trivial structure on all lengthscales.

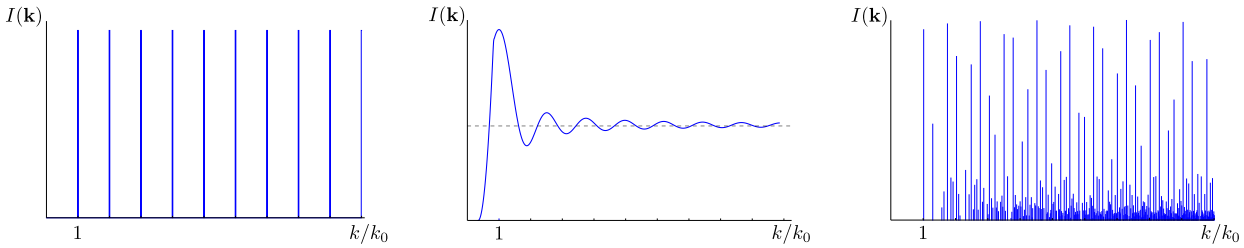

(a) Regular crystal (b) Amorphous solid (glass) (c) 1D Quasicrystal

Figure 3.1 : The unit cell uniquely determines the structure of a regular crystal, hence the repeated, redundant pattern in its scattering intensity (a). The lack of a unit cell, on the other hand, may have two distinct effects. In an amorphous solid (e.g. glass), with particles at uncorrelated positions, $F(\mathbf{k}) = F(k)$ reduces to an average constant (b), where residual short-range interactions may still give rise to limited non-trivial stucture. A quasicrystal, however, provides an interesting middle ground between order and disorder, as it exhibits a dense set of sharp peaks (c) and hence non-trivial structure at all lengthscales. The particular pattern shown in (c) is produced by a 1D Fibonacci chain, rigorously discussed in [94].

The scattering intensity in eq. 3.10 depends on the absolute value of the structure factor, which causes the loss of phase information. The structure is therefore not uniquely determined by its diffraction pattern, and the symmetry of $I(\mathbf{k})$ is larger than the one of $F(\mathbf{k})$, resulting in the existence of centrosymmetric points $(\mathbf{k}, -\mathbf{k})$ of equal intensity termed *Friedel's pairs*.

3.1.2 Aperiodic crystals

Paradigm shift

The conviction that the ground state of matter is always an ideal periodic crystal started to weaken in the 1960s. It was already known that real crystals had defects and impurities, and that these caused not only broadening of existing Bragg peaks, but also an additional diffuse background. Furthermore, periodic variations such as spurious crystal growth and twinning[1] caused additional peaks to appear in the diffraction spectra, called *lattice ghosts* or *Gittergeister*. All of the above had been modelled as mere perturbations on regular crystal structures, though with increasing difficulty. For instance in [95] a material was found where the magnetic properties occurred at a different period than the crystal structure, though this was exquisitely solved by modelling it as a long-range modulation with an incommesurate wavelength, the first instance of aperiodicity in condensed matter[2]. This *modulated structure* approach, consisting of a periodic lattice with spacing a and an incommensurate modulation λ such that $a/\lambda \notin \mathbb{Q}$, quickly spread in popularity as it also helped understanding previous results from alloys, such as [96], and provided a simpler, more elegant framework.

From eq. 3.9, a modulation λ along an existing direction requires an additional Miller index:

$$\mathbf{K} = h\mathbf{b}_1 + \ell\mathbf{b}_2 = h\mathbf{b}_1 + (\ell' + \lambda)\mathbf{b}_2\,, \tag{3.11}$$

[1] The intergrowth of two separate crystals that share some of the same lattice points.

[2] Two commensurate periods a and b will be periodic every $a \cdot b$, but if one of them is an irrational number, perfect recurrence will never happen.

where $\mathbf{b}_1$ and $\mathbf{b}_2$ would be enough to span the 2D plane, but the structure requires the use of $n > 2$ integers.

In 1972, a new description of the modulated phase method was proposed [97] that finally managed to bring symmetry back in the picture: a 3D aperiodic structure can be thought as a projection from a 4D regular lattice, where group symmetries reign supreme[3]. The higher dimensional method is used to generate and simulate the results for the optical quasicrystals presented in chapters 7 and 8, and is rigorously discussed in section 3.2.4.

Finally, in 1982, Dan Shechtman [99] found that electron diffraction from a particular alloy of Al and Mn displayed sharp peaks, hinting at a high degree of coherence and long-range order in the material, but arranged in the tenfold symmetric pattern of fig. 3.2. This was in direct disagreement with the crystallographic restriction theorem, and hence paved the way for the field of quasiperiodic crystals, or *quasicrystals*, which eventually won him the 2011 Nobel prize in Chemistry. In the publication they explicitly rule out the possibility that the unexpected symmetry may be due to artefacts such as twinning. Unbeknownst to Shechtman, another group had been working on the theory of *crystalloids* for years, especially on the icosahedral phase shown in fig. 3.2, and published their results in [100].

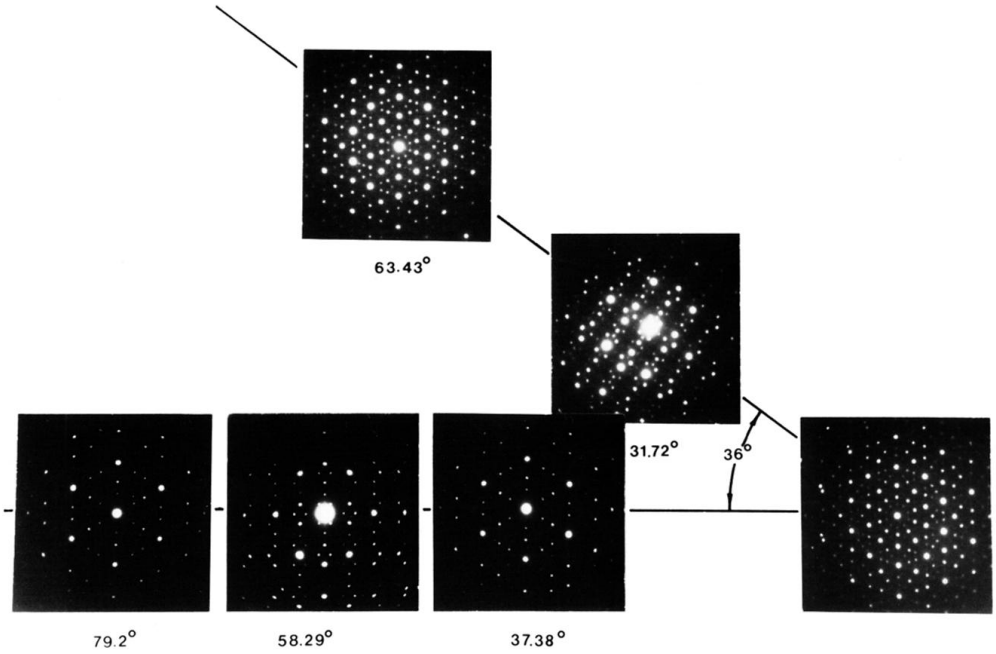

Figure 3.2 : Selected-area electron diffraction patterns from an alloy of Al and Mn, consistent with stereographic projections of an icosahedral phase ($A_5 \times \mathbb{Z}_2$). The tenfold symmetry displayed by sharp Bragg peaks established the existence of quasicrystals, a new form of matter between crystals and amorphous solids. Figure taken from [99].

Having established the existence of quasicrystals, a number of fundamental questions arose:

1. What are the conditions needed for a material to solidify into a quasicrystalline phase?
2. Can a real material display (or be made to display) a stable quasicrystalline phase?

[3]This idea stemmed from 4D space-time groups studied in the context of electro-magnetism [98].

3. What are the transport properties of quasicrystals?

4. Can crystals, quasicrystals and (structural[4]) glasses be unified under the same theoretical framework?

These are discussed in the remainder of the section.

Definitions

Aperiodic order has been drawing an increasing amount of attention and is now a topic of study of pure mathematics, theoretical and experimental physics, material science and metallurgy. Definitions are therefore not unique and not consistent, and I will here present my favourite ones, taken verbatim from [90].

1: Translationally ordered structure

> A translationally ordered structure is a structure whose scattering amplitude is given by a discrete sum of Bragg peaks.

2: Basis

> A translationally ordered structure [...] with Bragg peaks centred at the discrete set of reciprocal vectors $\{\mathbf{k}_i\}$, is said to have a basis if there exists a finite set of vectors $\{\mathbf{b}_j\}$, such that each $\mathbf{k}_i$ can be expressed as an integer linear combination of [them].

3: Rank

> A minimal set of vectors necessary to span a reciprocal lattice is a *basis set* of reciprocal vectors, [...] the number of elements in this basis is the *rank* of the reciprocal lattice.

4: Crystal

> A crystal in d dimensions is a translationally ordered structure with a basis whose rank n is equal to d.

5: Quasiperiodic structure

> A quasiperiodic structure in d dimensions is a translationally ordered structure with a **finite** basis whose rank n exceeds d.

The term "quasiperiodic" is used not only in contrast to "regular", but also "chaotic" and "disordered". The generalisation of the reciprocal lattice $\mathbf{K}$ to aperiodic structures is known as a *Fourier module* $\mathbf{H}$ of rank n.
Quasiperiodic structures can be further divided into two categories.

[4]Intended here as an amorphous solid with no long-range diagonal order, to be distinguished from the *Bose glass* phase discussed in chapter 8, whose name refers to the lack of off-diagonal long range order (phase coherence) and not necessarily to its microscopic structure.

6: Incommensurate crystal

> An incommensurate crystal is a quasiperiodic structure with a crystallographically allowed orientational symmetry.

7: Quasicrystal

> A quasicrystal is a quasiperiodic structure with a crystallographically **disallowed** orientational symmetry.

Crystals possess long-range *translational* order that restricts the rotational symmetry of the unit cell, known as *orientational symmetry*, which leads to five 2D Bravais lattices as per eq. 3.5. Translational order therefore implies orientational order, but the reverse is not true, as shown by the Penrose and Ammann-Beenker tilings in fig. 3.5. Glasses and amorphous solids possess neither long-range translational nor orientational order (apart from the trivial isotropy)[5].

Quasicrystals are a new and distinct state of matter as they display both long-range translational order, and long-range orientational order with a crystallographically forbidden symmetry, distinguishing them from glasses, and from regular crystals. The incommensurate ratios present in the quasicrystal phases are different from the ones in the *modulated* phases, as they are constrained by geometry (discussed in section 3.2.4) and are hence insensitive to temperature and pressure. Modulated phases structures, on the other hand, are observed to change the modulation period as a function of external parameters, suggesting a distinct physical interpretation than in quasicrystals.

2D quasicrystals can still exist in 3D, but the aperiodicity is only noticeable in planes: the rank of a stacked pentagonal quasicrystal is $4 > 3$ but the redundancy in the linear dependence is only among 2D vectors that span the same plane, which makes it an *axial* quasicrystal [101], whereas the icosahedral structure in fig. 3.2 is a truly 3D quasicrystal.

All of the above only really apply in $d \geqslant 2$, since they rely on the presence of rotational symmetries. It is therefore useful to quote the definition provided by the International Union of Crystallography (IUCr) [102]:

8: IUCr definition

> The term quasicrystal stems from the property of quasiperiodicity observed for the first alloys found with forbidden symmetries. Therefore, an alternative definition is: a quasicrystal is an aperiodic crystal with diffraction peaks that may be indexed by n integral indeces, where n is a finite number, larger than the dimension of the space (in general).

Not only does this, along with the above, establish the collapse of the old paradigm order $\Leftrightarrow$ periodicity, but it requires quasiperiodic structures to (only) display sharp diffraction peaks as a sign of long-range order, a criterion easily applicable to 1D structures as well.

[5] Technically, between glasses and crystals there are also *paracrystals*, defined to lack crystal-like long-range order in at least one direction.

3.1.3 Physical properties and current research

The first question on this quasicrystalline phase of matter concerns its stability and occurrence. A huge variety of quasicrystals have been so far created in alloys and other composite mixtures, though the only stable ones seem to be decagonal, dodecagonal and icosahderal. A *natural* quasicrystal (the "second kind of impossible" [103]) was eventually also discovered [104] in a meteorite fragment in Kamchatka[6]. The discovery faced fierce scepticism because of the abnormal concentration of natural aluminium and the absence of rust, which could only be the result of industrial treatment, at least on Earth. Indeed, extreme conditions are needed for the formation of quasicrystals, such as those experienced by a meteorite. The alloys discussed in the previous section are made by rapidly cooling (quenching) the material, thereby preventing it from crystallising and freezing its metastable quasiperiodic structure as in a glass. As a matter of fact, Shechtman in [99] specifies how mean-field theory calculations had predicted the metastable phase, since the diffusion velocity was slower than the crystallisation velocity but yet high enough to allow for atomic rearrangements – essentially slow enough to allow its formation but rapid enough to prevent it form crystallising into the true, regular ground state. The presence of aperiodicity may be the result of structural deformations resulting in a lower energy, of competition between mechanisms that favour different periodicities, or simply of the structure stabilisation by the introduction of a distinct species. In fact, so far quasicrystalline order has always been observed in composite materials, and the existence of "pure" stable quasicrystals remains an open question.

It is still undecided whether the formation of the phase is driven by energy or entropy minimisation. The latter is favoured since aperiodic structures possess quasiparticle excitations known as *phasons* (or *simpletons*), which may result in a rearrangement of the atomic positions thereby increasing the entropy S and minimising the overall free energy[7] $F = U - TS$. Phasons have been investigated in [105], observed in [106], and are further discussed in section 3.2.4.

There is also active research in the spontaneous occurrence of quasicrystalline order. For example, simulations in soft matter and colloids [107] showed that "a judicious design of an isotropic pair potential" results in the spontaneous formation of clusters with forbidden geometries. Self-emerging quasicrystalline order has also been proposed for cold atoms in dipolar gases [108], in optical lattices [109], and in the time domain [110].

Quasicrystals possess promising properties for technological applications [111]: hardness, low surface-energy, low friction, oxidisation resistance, hydrogen storage capacity and a transition from brittle to ductile behaviour at high temperatures. Electrical, magnetic and thermal transport mechanisms are anisotropic [112, 113]: crystallographically non-equivalent directions exhibit ballistic, diffusive, and insulating behaviours, along with thermoelectric power and Hall coefficients of opposite signs. Superconductivity in quasicrystals has also been observed [114], though at a very low transition temperature $T_c \approx 0.05\,\mathrm{K}$.

The quenching processes utilised to create the alloys result in non-ideal quasicrystals, with vacancies, dislocations, finite domains, chemical inhomogeneities, strains, and additional disorder. Hence, a number of alternative, more controllable and cleaner experimental platforms have been employed to reproduce and investigate quasicrystals. In material

[6] which I had only otherwise heard of from the boardgame Risk©.

[7] The importance of minimising the free energy is discussed in appendix D.6.

science and condensed matter, these include layered semiconductors [115], liquid crystals [116], polymers [117], colloids [118, 119], nanoparticles [120], and twisted bilayer graphene [121]. Photonic structures have also been used [122], as well as optical diffraction patterns [123, 124].
Experiments in cold atoms have so far only probed the dissipative regime [125, 126], but there is a multitude of theoretical proposals – from transport properties [127], to magnetism [128] and phason-stabilised order [129].

Our experiment is the first to probe degenerate quantum gases in a quasicrystalline potential. As discussed in the next section, this results in non-trivial structure on all length-scales and opens avenues to synthetic dimensions, so far only achieved via internal states [37, 38].
The presence of non-trivial structure is of interest within computer science in the context of search algorithms [130, 131], and has also been used in the proof of the undecidability of the spectral gap theorem [132].

3.2 Mathematical treatment

The key to periodicity is the repetition of constituents at a fixed frequency. In order to break this, various elements need to occur at incommensurate frequencies, easily achieved by introducing an irrational number.
Quasicrystals may be generated by substitutional sequences, matching rules, and projections from higher dimensional spaces, as discussed in the remainder of this section.

3.2.1 1D: sequences

Fibonacci

The substitutional rule for the Fibonacci sequence is $\sigma_F : L \to LS, S \to L$, or:

$$\sigma_F : \begin{pmatrix} L \\ S \end{pmatrix} \to \underbrace{\begin{pmatrix} 1 & 1 \\ 1 & 0 \end{pmatrix}}_{=\mathcal{S}} \begin{pmatrix} L \\ S \end{pmatrix} = \begin{pmatrix} LS \\ L \end{pmatrix}. \tag{3.12}$$

$\mathcal{S}$, the substitution matrix, has eigenvalues $\epsilon_1 = \varphi$ and $\epsilon_2 = 1 - \varphi = -1/\varphi$, with φ being the golden ratio, related to the Fibonacci numbers F_n:

$$\lim_{n\to\infty} \frac{F_n}{F_{n-1}} = \varphi = \frac{1+\sqrt{5}}{2} \approx 1.618. \tag{3.13}$$

One of the eigenvectors is $(\varphi, 1)$, from which it is evident that a chain with $L = \varphi, S = 1$ is self-similar and invariant under inflations (deflations) by φ^n, such as the one shown in fig. 3.10b. The eigenvalues of the substitution matrix therefore determine the self-similarity of the structure.
Periodic lattices scale with integer factors, and so do the eigenvalues of their substitution matrices $\mathcal{S}$. In quasiperiodic lattices the eigenvalues of $\mathcal{S}$ are *algebraic numbers*[8] or *Pisot numbers*, which satisfy the *Pisot-Vijayaraghavan* (PV) property:

$$\epsilon_1 > 1, \quad |\epsilon_i| < 1 \quad \forall i > 1. \tag{3.14}$$

[8] Actually *integer* algebraic numbers, that is they are solutions to polynomials with integer coefficients.

Octonacci

The substitutional rule for the Octonacci (or Pell) sequence is $\sigma_O : L \to LLS, S \to L$, or:

$$\sigma_O : \begin{pmatrix} L \\ S \end{pmatrix} \to \underbrace{\begin{pmatrix} 2 & 1 \\ 1 & 0 \end{pmatrix}}_{=\mathcal{S}} \begin{pmatrix} L \\ S \end{pmatrix} = \begin{pmatrix} LLS \\ L \end{pmatrix}. \tag{3.15}$$

The eigenvalues of $\mathcal{S}$ are $\epsilon_1 = \lambda$ and $\epsilon_2 = -1/\lambda$, where λ is the silver mean, related to the Pell numbers P_n:

$$\lim_{n\to\infty} \frac{P_n}{P_{n-1}} = \lambda = 1 + \sqrt{2} \approx 2.414. \tag{3.16}$$

These eigenvalues also satisfy the PV condition, and the eigenvector $(\lambda, 1)$ requires the mapping $L = 1+\sqrt{2}$ and $S = 1$ in order for the structure to be self-similar upon inflations (deflations) by λ^n.

However, it is useful for later considerations to find a basis of ratio $L : S = 1 : \sqrt{2}$, such as the sides of ◹ and ▱. The n^{th} inflation and deflation factor can be written in the closed form:

$$(1+\sqrt{2})^n = H_n + P_n\sqrt{2}, \quad \text{and} \quad (1-\sqrt{2})^n = H_n - P_n\sqrt{2}, \tag{3.17}$$

where the Pell number P_n and its half-companion H_n satisfy the following recursion relation:

$$\begin{pmatrix} P_n \\ H_n \end{pmatrix} = \underbrace{\begin{pmatrix} 1 & 1 \\ 2 & 1 \end{pmatrix}^n}_{\mathcal{S}'} \begin{pmatrix} 0 \\ 1 \end{pmatrix}. \tag{3.18}$$

The eigenvalues of $\mathcal{S}'$ are still λ and $-1/\lambda$, but the eigenvectors may be now mapped onto $L \to 1/\sqrt{2}$ and $S \to 1$.

Prime numbers

Substitution rules result in self-similarity and inflation rules, but are only a subset of the deterministic recipe to construct a sequence based on the roots of a polynomial.
A famous polynomial is the Riemann zeta function $\zeta(s)$, whose non-trivial roots are given by:

$$\zeta(s) = \sum_{n=1}^{\infty} \frac{1}{n^s}, \qquad \zeta(s_j) = 0 \quad \text{at} \quad s_j = \frac{1}{2} + \mathrm{i}k_j, \tag{3.19}$$

where the Riemann hypothesis was assumed. The 1D structure constructed from $\mathrm{Im}[s_j]$ is depicted in fig. 3.3, and its diffraction pattern is given by:

$$f(x) = \left| \sum_{k=1}^{\infty} \mathrm{e}^{\mathrm{i}k_j x} \right|^2, \tag{3.20}$$

which yields sharp peaks centred at prime numbers p and at integer powers of prime numbers p^n $(n \in \mathbb{N})$ as shown in fig. 3.4.

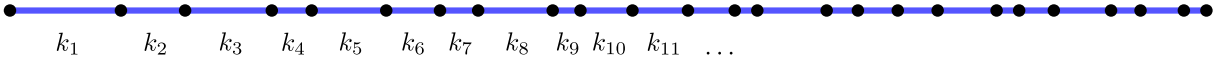

Figure 3.3 : 1D structure made from the "matching rule" of knowing the zeros of the Riemann zeta function.

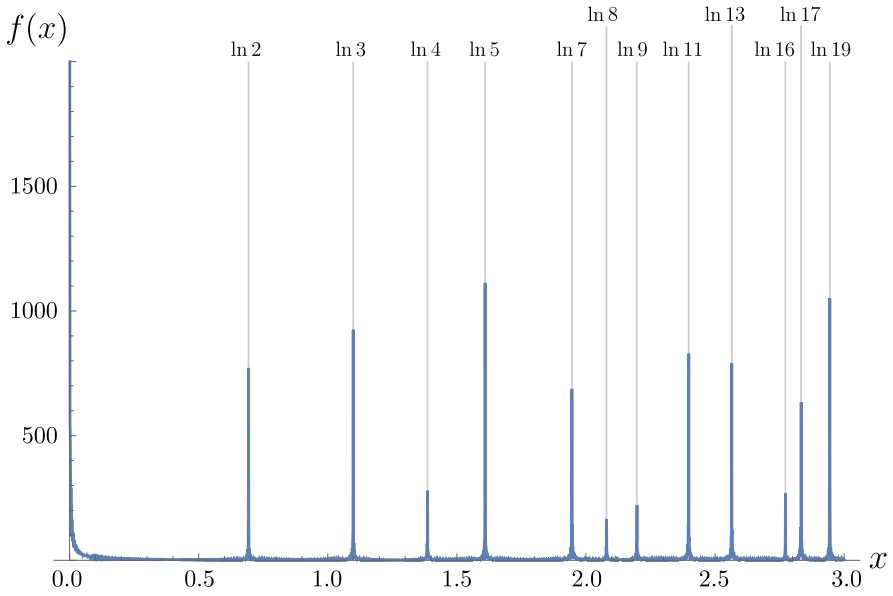

Figure 3.4 : The imaginary part of the zeroes of the Riemann zeta function, combined in a 1D structure, yield a pure point diffraction spectrum centred at prime numbers p and prime-powers p^n, $n \in \mathbb{N}$. As more roots are included, the peaks become infinitely sharp.

Despite my initial excitement and intrigue in the finding, this is actually a known result, which pertains to the hypothesis that every 1D quasicrystal is uniquely identified by a distinct algebraic number fulfilling the PV condition. Classifying 1D quasicrystals would therefore also prove the Riemann hypothesis [133].

3.2.2 2D: tilings

Not just decorations

Euclidean or Achimedean tilings are coverings of the 2D plane by convex regular polygons, and have been used since ancient times for art and decoration, such as in the mosaic of fig. 3.5a. While the Romans and Greeks made all of their tilings periodic, the Arabic and Persian civilisations experimented with crystallographically forbidden rotational symmetries, as shown in fig. 3.5b and 3.5c.

Tilings were formally classified by Johannes Kepler in his *Harmonices Mundi* [134], the same book where he introduces the third law of planetary motion which he is, potentially, better known for. Kepler did not only focus on periodic tilings, fig. 3.6a, but discovered by trial and error that gapless tilings with various rotational symmetries could be created by the careful use of distinct regular polygons, fig. 3.6b. It was not until Roger Penrose published the celebrated *Penrose tilings* [135, 136] in 1974 that such coverings of the 2D plane could be generated by just *two* distinct tiles, using Penrose's *matching rules*, establishing the order encoded in aperiodic structures. Penrose (fig. 3.6c) and Ammann-Beenker (fig. 3.6d) tilings both display crystallographically forbidden rotational symmetries, fivefold and eightfold respectively.

(a)

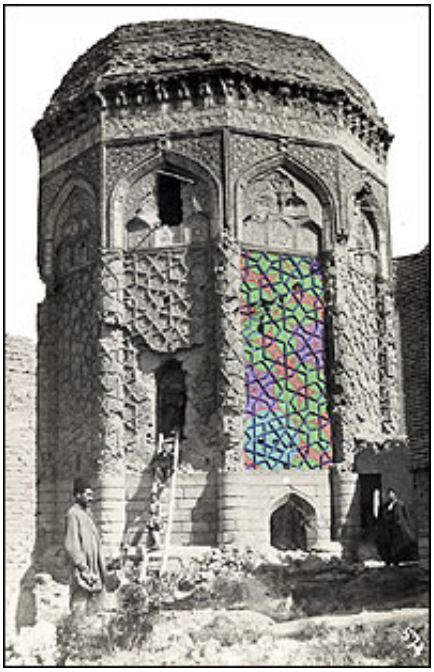

(b)

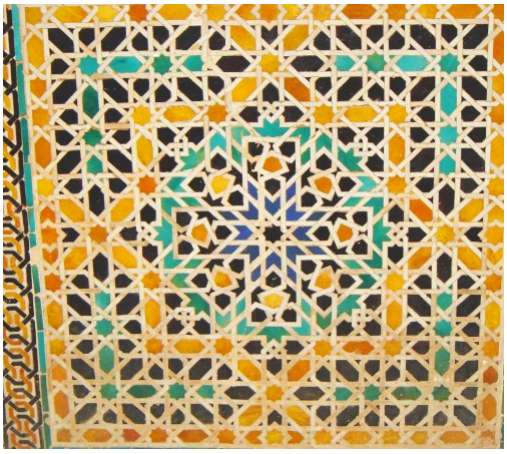

(c)

(d)

Figure 3.5 : Examples of tessellation. a) Roman mosaic (IV century CE). b) Gunbad-i Kabud tomb tower in Maragha (1197 CE), Iran (Harvard College Library). c) Alhambra, Granada (XIII century CE). d) *Circle Limit III*, woodcut made in 1959 by Maurits Escher showing tessellation in a non-Euclidean geometry, specifically an alternated octagonal tiling of the hyperbolic plane.

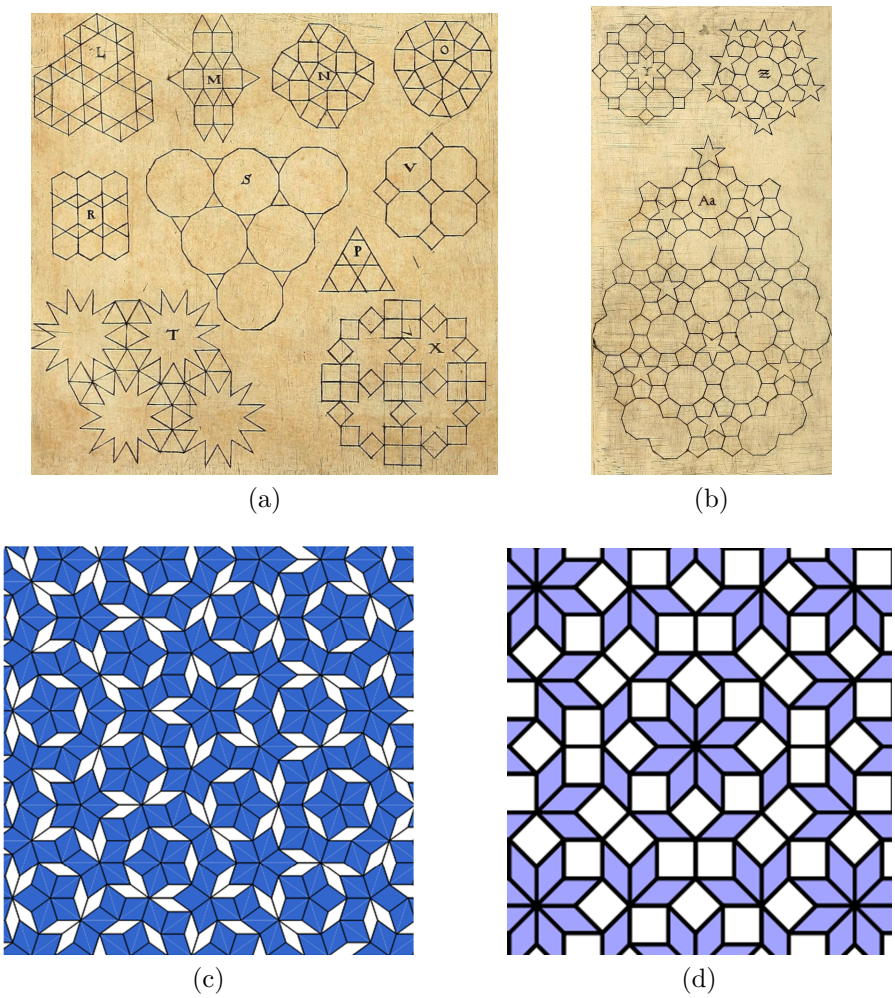

(a) (b)

(c) (d)

Figure 3.6 : a) and b): periodic and non-periodic tilings classified by Kepler in *Harmonices Mundi* (1619) from [134]. c) and d): Penrose and Ammann-Beenker tilings, showcasing crystallographically forbidden fivefold and eightfold rotational symmetries.

Ammann-Beenker tiling

Akin to the 1D substitution rules presented earlier, 2D tilings can be generated by the inflation (deflation) rules of their elementary ingredients, the *prototiles*. Choosing these to be ◺ and ▱, with sides ratio $1 : \sqrt{2}$, the inflation of the tiling (area) follows from the inflation of the side, given by Octonacci rule in eq. 3.18:

$$\Sigma = \mathcal{S}'^2 = \begin{pmatrix} 1 & 1 \\ 2 & 1 \end{pmatrix}^2 = \begin{pmatrix} 3 & 2 \\ 4 & 3 \end{pmatrix}, \tag{3.21}$$

where the matrix acts on the basis (◺, ▱) as illustrated in fig. 3.7.

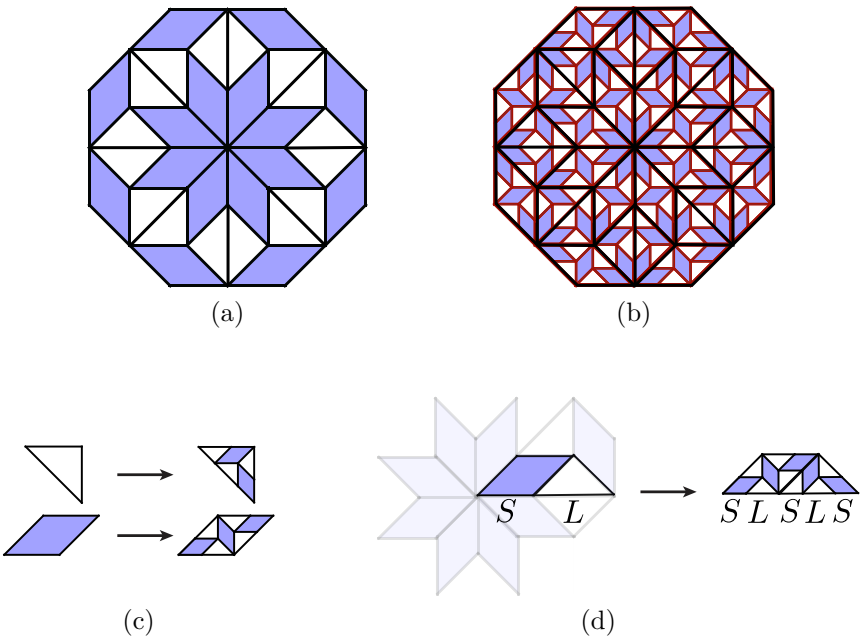

Figure 3.7 : The Ammann-Beenker tiling, with eightfold symmetry, can be generated by the inflation rule (c) which, acting on (a), generates (b). The side of the tiling scales with λ, the silver mean, according to the Octonacci sequence (eq. 3.18), while the area scales with λ^2.

3.2.3 Quasicrystals as the path to complexity

More advanced treatment of aperiodic order and the place of sequences is presented in [137, 138].

Non-trivial structure at all lengthscales

The eigenvalues of a substitution or inflation matrix $\epsilon_1 > \epsilon_2$ are:

$$\text{Eigs}\left[\begin{pmatrix} a & b \\ c & d \end{pmatrix}\right] \quad \Rightarrow \quad \begin{aligned} \epsilon_1 &= \frac{a+d+\sqrt{(a-d)^2+4bc}}{2}, \\ \epsilon_2 &= \frac{a+d-\sqrt{(a-d)^2-4bc}}{2}. \end{aligned} \tag{3.22}$$

If the tiles are assumed to be indivisible, the entries of the matrix are $\in \mathbb{Z}$, and the characteristic polynomial is a monic (unit leading coefficient) polynomial with integer coefficients, whose roots are known to be either irrational, or $\in \mathbb{Z}$.
Additionally, it is trivial to show that:

1. $\epsilon_1 \in \mathbb{Z} \Rightarrow \epsilon_2 \in \mathbb{Z}$,
2. $\epsilon_1 \cdot \epsilon_2 = \Delta = ad - cd$.

Condition 1 implies that both eigenvalues belong in the same set of numbers, while condition 2 sets the relation between the two. For $\mathbb{Z}$ solutions, *rational* numbers only appear as eigenvalues of the *inverse* matrix, since $\text{Eigs}[A] = \epsilon \Rightarrow \text{Eigs}[A^{-1}] = \epsilon^{-1}$, and so only when performing a deflation operation on a previously inflated structure. On the other hand,

substitution matrices obeying the PV condition have $|\epsilon_2|< 1$, which allows for non-trivial deflation[9].

When $\Delta = 0$, one of the eigenvalues is also 0: what does it mean to be self-similar when scaled by 0, or even by 1/0? Maybe this the reason behind the peculiar diffraction spectra of the Thue-Morse and Rudin-Shapiro sequences, discussed later.

Finally, if $(a + d) = (a - d)^2$ and $bc = 1$, the eigenvalues can be expanded as a continued fraction with the *same leading coefficient*. For the Fibonacci and Octonacci sequences, for instance, the golden and silver means can be written as:

$$\begin{aligned} \varphi &= \frac{1+\sqrt{5}}{2} = [1,1,1,1,\cdots] = 1 + \cfrac{1}{1+\cfrac{1}{1+\cdots}}, \\ \lambda &= 1+\sqrt{2} = [2,2,2,2,\cdots] = 2 + \cfrac{1}{2+\cfrac{1}{2+\cdots}}, \end{aligned} \tag{3.23}$$

and $\varphi^{-1} = [0,-1,-1,-1,-1,\cdots]$, $\lambda^{-1} = [0,-2,-2,-2,-2,\cdots]$. This causes very slow convergence and would hence require very large rational approximants to reliably describe the ensuing pattern.

The non-trivial structure encoded in aperiodic tilings was already known to Erwin Schrödinger when he proposed them as an explanation for how a fragile ensemble such as the DNA could retain so much information while still obeying the second law of thermodynamics [140, 141].

Spectra

The scattering intensity I in eq. 3.10, used to probe and classify the ordering of the structure, is usually divided into a discrete, or *pure point* I^{pp}, and a continuous component. The latter can be further divided into an *absolutely continuous* I^{ac} and a *singularly continuous* I^{sc} contribution, for a grand total of:

$$I(\mathbf{H})_{\text{total}} = I^{\text{pp}}(\mathbf{H}) + I^{\text{sc}}(\mathbf{H}) + I^{\text{ac}}(\mathbf{H}). \tag{3.24}$$

The character of the distinct spectral components is identified from the following definitions [142]:

- A function $f : [a,b] \to D$ is *continuous* at a point $x_0 \in [a,b]$ if $\forall \epsilon > 0 \quad \exists \delta > 0$ such that $\forall x \in [a,b]$: $|x - x_0|< \epsilon \Rightarrow |f(x) - f(x_0)|< \delta$. Essentially, this means that the function exhibits no discontinuous jumps of any size, which would otherwise result in a lower bound for δ.
  Continuity, however, only describes the behaviour of a function at a single point x_0. Analysis of its first derivative f' characterises the trend of the function in the neighbourhood of x_0 and allows to further classify it into *absolutely* and *singularly* continuous.

  ▪ A function $f : [a,b] \to D$ is absolutely continuous if its derivative f', wherever it exists, satisfies:

$$f(x) = f(x_0) + \int_{x_0}^{x} f'(t)\mathrm{d}t \quad \forall x \in [a,b]. \tag{3.25}$$

[9] At least when $|\Delta|= 1$, in accordance with the Pisot conjecture [139].

▪ A function $f : [a, b] \to D$ is singularly continuous if its derivative f', wherever it exists, does not satisfy:

$$f(x) = f(x_0) + \int_{x_0}^{x} f'(t)\mathrm{d}t \quad \forall x \in [a, b]. \tag{3.26}$$

This means that $f'(t)$ is zero, i.e. the function f is composed of *steps*.

- A *discrete* function $f : [a, b] \to D$ does not satisfy continuity because there is a lower bound on δ such that $|x - x_0| < \epsilon \not\Rightarrow |f(x) - f(x_0)| < \delta_{\min}$.

The pure point contribution to the diffraction spectrum usually consists of the Bragg peaks of a translationally invariant crystal, while the absolutely continuous component is normally the diffuse background caused by points defects, impurities, dynamic excitations, and structural disorder. However, [143] showed that even a deterministic structure may exhibit only a continuous spectrum without any sharp peaks, suggesting that the presence of disorder cannot be established solely from the absence a pure point spectral component.

An example of a singularly continuous function is the Cantor function, or "Devils's staircase", shown in fig. 3.8. This is defined as $c : [0, 1] \to [0, 1]$, where $c(x)$ is determined by the following iterative procedure:

- Given a domain $\sigma_n^{(i)}$, starting from $\sigma_0 = [0, 1]$,
- divide σ_n into three equal segments $\sigma_{n+1}^{(1)}, \sigma_{n+1}^{(2)}$ and $\sigma_{n+1}^{(3)}$,
- assign the value $0.5 \cdot n$ to the middle segment $\sigma^{(2)}$,
- and iterate for n.

This function satisfies the condition for continuity, since $\exists n$ such that $|c(x) - c(x_0)| < \delta \quad \forall x, x_0 \in [0, 1]$, but it is not absolutely continuous because its derivative is zero wherever it exists. The Cantor function is therefore singularly continuous, and it is of physical relevance as it describes the *energy* spectrum of some 1D quasiperiodic Hamiltonians, such as the ones described by the Aubry-André model [144].

Other 1D quasiperiodic models are also known to exhibit singularly continuous *energy* spectra, such as the Fibonacci, the Thue-Morse and the Rudin-Shapiro chains [145–148]. However, the *diffraction* spectra of these structures are found to be pure point, singularly continuous and absolutely continuous respectively, establishing that the diffraction spectrum is not sufficient to determine the ordering of the structure [143].
An example of a pure point diffraction spectrum from a quasiperiodic model is the Riemann-based sequence presented in fig. 3.4, where the addition of more segments only results in sharper peaks at pre-existing $\mathbf{k}$ points.

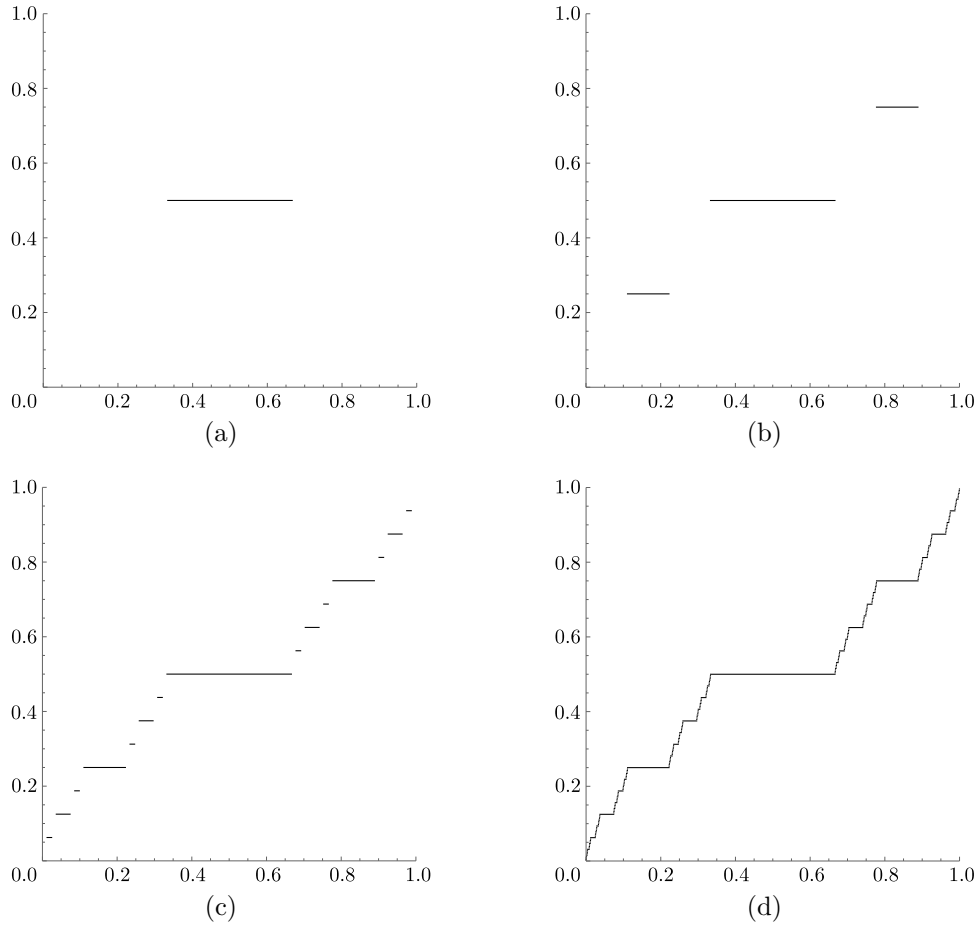

Figure 3.8 : The Cantor function c defined in the text is a singularly continuous function. Iterations $n = 1, 2, 4$ and 8 are shown in (a)-(d). Its fractal dimension is $d_\mathrm{f} = 0.61 \notin \mathbb{N}$.

Fractals

Self-similarity and non-trivial structure on all lengthscales are properties characteristically found in *fractals*. A fractal is a region of d-dimensional space whose filling capacity scales with a fractal dimension $d_\mathrm{f} \neq d$ which may not be an integer. They are also generated by a rule, substitutional (such as the Sierpinski gasket in fig. 3.9) or polynomial (the Mandelbrot[10] set). The Sierpinski gasket of fig. 3.9 is defined by subdividing an equilateral triangle of side L into four equal equilateral triangles of side $L/2$, and removing the central one. The ensuing structure is therefore self-similar only upon certain integer divisors of L, and its area is known to scale as L^{d_f} where $d_\mathrm{f} = 1.585 \notin \mathbb{N}$. The discrete nature of self-similarity is richer than scale invariance as it is non-trivial and leads to an increased complexity.

Fractality is nature's way to seek optimal area to volume ratio, enabling efficient capture of sunlight by leaves or optimal exchange of oxygen in lungs. Applications of fractal structures include antennae [149], biosensors and search and compression algorithms [150]. Synthetic fractal structures have been investigated experimentally so far only in solid-state system [151] – our 2D quasiperiodic optical lattice provides a chance to implement this kind of complexity to quantum simulation with ultracold atoms.

[10]The B in Benoît B. Mandelbrot stands for Benoît B. Mandelbrot.

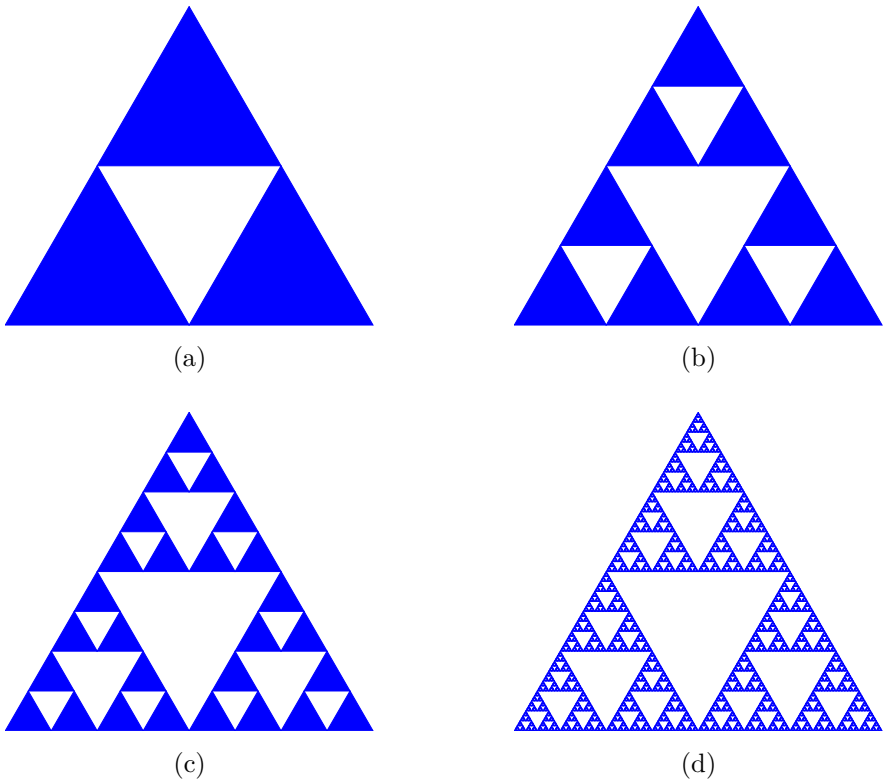

Figure 3.9 : The Sierpinski gasket is generated from diving an equilateral triangle of side L into four of side $L/2$ and removing the central one. Iterations $1, 2, 3$ and 6 are shown in (a)-(d). The ensuing structure is self-similar only for certain $L/n (n \in \mathbb{N})$, and the blue area possesses a fractal dimension of $d_\mathrm{f} = 1.585 \notin \mathbb{N}$.

3.2.4 Higher dimensions

Method

An alternative, and probably more satisfying, procedure for generating aperiodic patterns is the higher dimensional method, also known as *cut and project* or *strip projection* method. The quasiperiodic sequence or tiling of interest is defined on an n-dimensional *physical* space, be in 1D, 2D or 3D, which becomes the *parallel space* component $V^{\parallel}$ of a regular and periodic m-dimensional hyperspace V:

$$V = V^{\parallel} \oplus V^{\perp}, \tag{3.27}$$

where $V^{\perp}$ are the *perpendicular* or *augmented* dimensions. The m vectors defining the Fourier module $\mathbf{H}$ (the generalised reciprocal lattice) are projections from the m-dimensional regular lattice $\mathbf{\Sigma}$:

$$\mathbf{H} = \mathcal{P}^{\parallel}(\mathbf{\Sigma}) \qquad \text{and} \qquad \mathbf{b}_i = \mathcal{P}^{\parallel}(\mathbf{d}_i), \tag{3.28}$$

where $\mathbf{b}_i$ span the reciprocal lattice of the quasicrystal according to eq. 3.11, and $\{\mathbf{d}_i\}$ is the rationally independent basis of $\mathbf{\Sigma}$. Crystallographic symmetries, theorems and techniques can be applied in the higher dimensional space owing to its periodicity.

For example, the Fibonacci sequence of eq. 3.12 comprises *two* distinct and incommensurate segments L and S, despite being a 1D structure. As shown in fig. 3.10, it can

be generated by an irrational projection the 2D square lattice points that fall within a specified projection window.

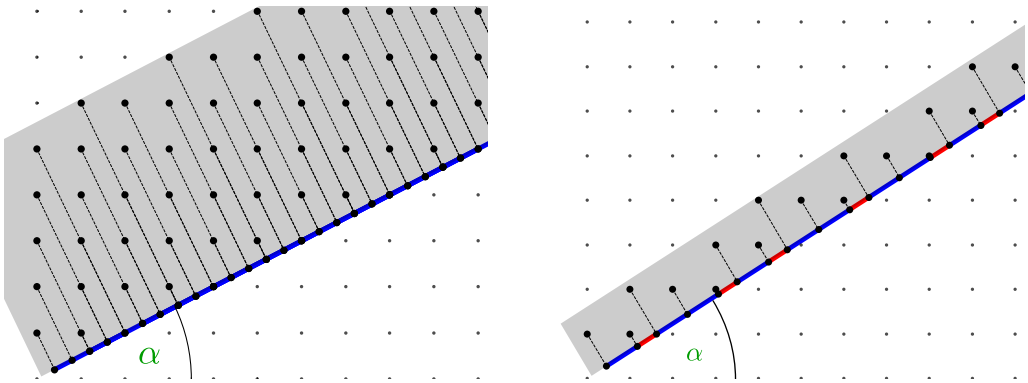

(a) $\tan\alpha \in \mathbb{Q}$ (b) $\tan\alpha \notin \mathbb{Q}$

Figure 3.10 : The 2D square lattice points that are contained within a projection window (grey) are projected onto a 1D line inclined at an angle α. This results in a periodic pattern if the $\tan\alpha$ is rational (a), and in a quasiperiodic structure if $\tan\alpha$ is irrational (b). In (b), $\tan\alpha = \varphi$ (the golden ratio) generates the 1D Fibonacci chain specified by eq. 3.12.

The higher dimensional method is a technique common to other areas of physics, where an internal state of the system is used to augment its physical space. For instance, protons p and neutrons n are both composed of u and d quarks, which thus justify extending the physical space by means of the isospin $I_3 = {}^1\!/_2\,(n_u - n_d)$, where n_i is the number of quarks of flavour i. This results in:

$$p = \begin{pmatrix} 1 \\ 0 \end{pmatrix}, \quad n = \begin{pmatrix} 0 \\ 1 \end{pmatrix} \quad \Rightarrow \quad \begin{pmatrix} p \\ n \end{pmatrix} \xrightarrow{SU(2)} \exp\left(-\frac{\mathrm{i}}{2}\theta_a\sigma_a\right)\begin{pmatrix} p \\ n \end{pmatrix}, \tag{3.29}$$

where σ are the Pauli matrices and θ are arbitrary parameters. In this higher dimensional space, the nucleons are symmetric by forming an (approximate[11]) $SU(2)$ doublet.

The 2D Ammann-Beenker tiling of fig. 3.6d can be projected from a 4D simple cubic lattice. Due to the difficulty of printing 4D cubes on A4 paper, this procedure is divided into projection from the 3D simple cubic lattice shown in fig. 3.11, stacking the resulting 2D patterns in the third dimension, and then projecting again resulting in fig. 3.12. The projected structures bear a striking resemblance to the diffraction patterns produced by real eightfold symmetric quasicrystals shown in fig. 7.15, and to the matter-wave diffraction spectra from the 2D quasiperiodic optical lattice of fig. 7.14.

The (minimum) required dimension of the hyperspace is determined by the minimum number of rationally linearly independent vectors required to span the Fourier module **H**. In 2D, the basis vectors needed to span the diffraction pattern of a n-fold periodic structure are the n^{th} roots of unity; the number of rationally independent n^{th} roots of unity is equal to the Euler totient function $\phi(n)$ [152], which counts the number of integers less than n that are relatively prime to n. The dimension m of the regular lattices is related to the n-fold rotational symmetry [153] as reported in table 3.1.
Not all quasicrystals can be obtained from higher dimensions, such as the pinwheel pattern, and the projections are unlikely to be unique: for instance, fivefold symmetry can be explained in 4D but also, more intuitively, in 5D.

[11] exact in the limit of equal masses $m_u = m_d$.

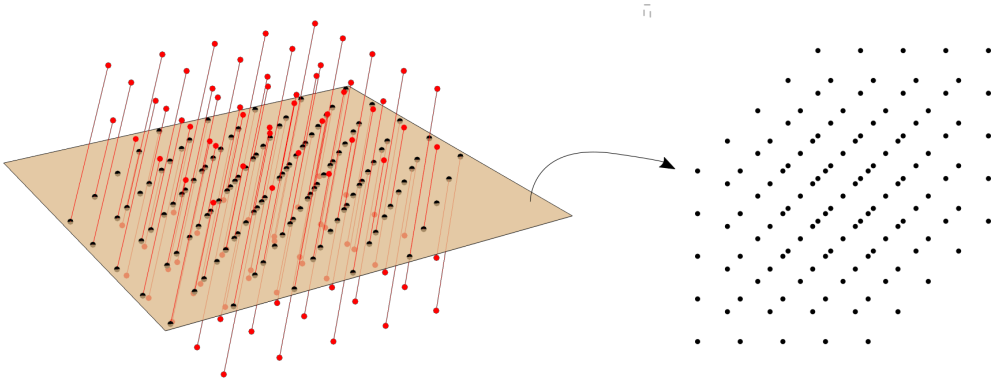

Figure 3.11 : A 3D simple cubic lattice, projected by $\pi/4$, results in a structure with periodicity along one direction and quasiperiodicity along the other.

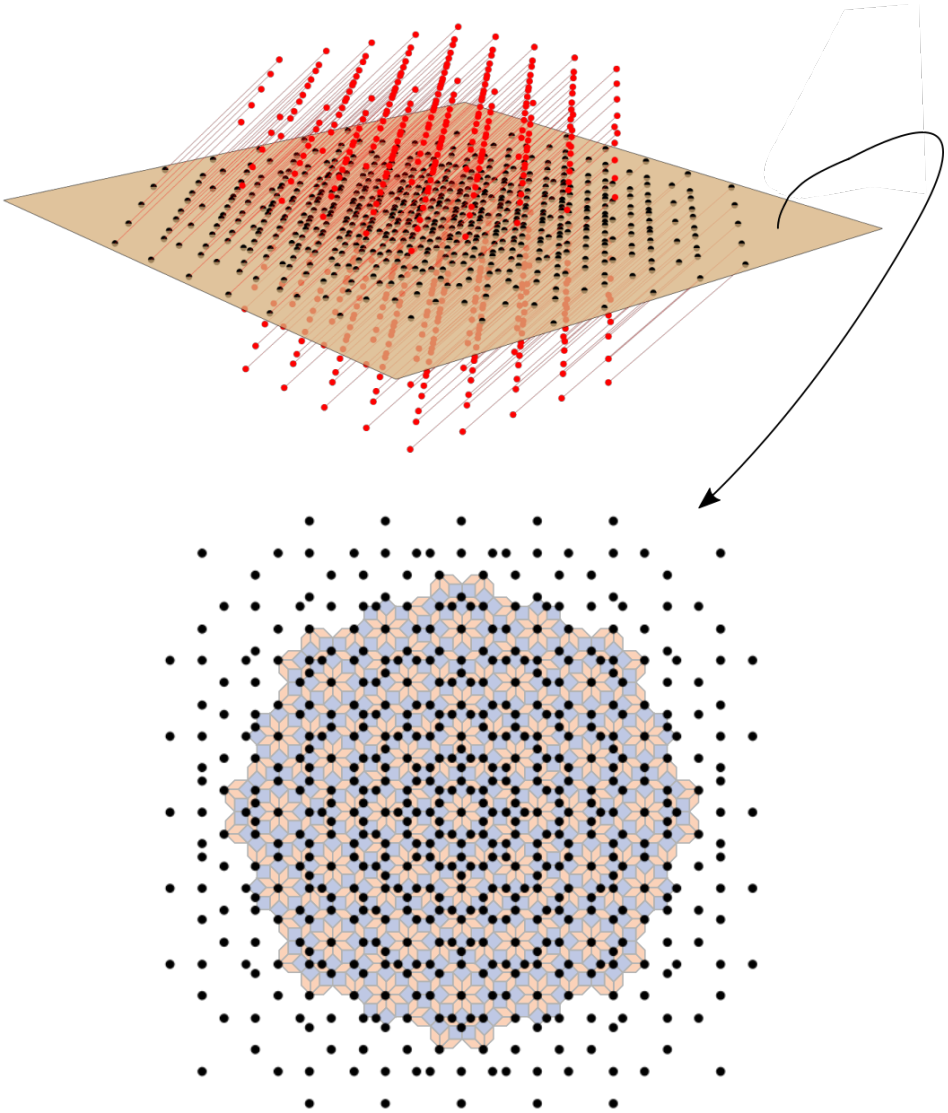

Figure 3.12 : The planes obtained in fig. 3.11 are stacked in z to mimic a 4D simple cubic lattice, and then projected again by $\pi/4$ to result in an eightfold symmetric pattern which can be mapped onto the Ammann-Beenker tiling of fig. 3.6d.

m-dimensional hyperspace m	n-fold symmetry in 2D n
0	1
1	2
2	3, 4, 6
4	5, 8, 10, 12
6	7, 9, 14, 15, 18, 20, 24, 30
8	16, 21, 28, 36, 40, 42, 60
10	11, 22, 35, 45, 48, 56, 70, 72, 84, 90, 120
12	13, 26, 33, 44, 63, 66, 80, 105, 126, 140, 168, 180, 210
14	39, 52, 55, 78, 88, 110, 112, 132, 144, 240, 252, 280, 360, 420
16	17, 32, 34, 65, 77, 99, 104, 130, 154, 156, 198, 220, 264, 315, 336, 504, 630, 840
18	19, 27, 38, 51, 54, 68, 91, 96, 102, 117, 176, 182, 195, 231, 234, 260, 312, 390, 396, 440, 462, 560, 660, 720, 1260
20	25, 50, 57, 76, 85, 108, 114, 136, 160, 170, 204, 273, 364, 385, 468, 495, 520, 528, 546, 616, 770, 780, 792, 924, 990, 1008, 1320, 1680, 2520
22	23, 46, 75, 95, 100, 119, 135, 143, 150, 152, 153, 190, 216, 224, 228, 238, 270, 286, 288, 306, 340, 408, 455, 480, 585, 624, 693, 728, 880, 910, 936, 1092, 1155, 1170, 1386, 1540, 1560, 1848, 1980, 2310

Table 3.1 : The m-dimensional regular hyperspace compatible with n-fold rotational symmetry in 2D. The 120-fold symmetry in the $m = 10$ line is the icosahedral symmetry ($A_5 \times \mathbb{Z}_2$) displayed by the quasicrystal in fig. 3.2. Table taken from [153].

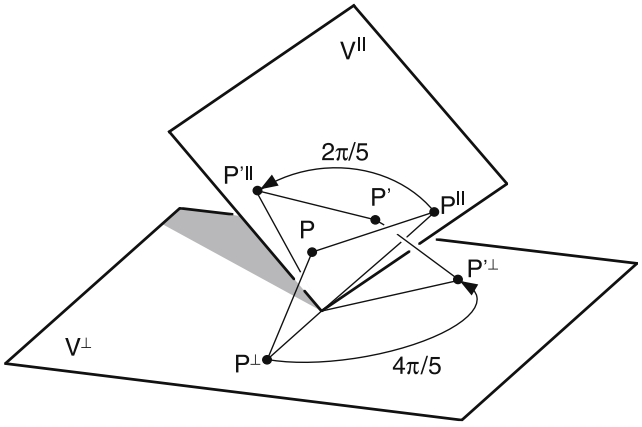

Figure 3.13 : A $2\pi/5$ rotation in the physical 2D (parallel) space is equivalent to a $4\pi/5$ rotation in the augmented (perpendicular) dimension. Figure taken from [91].

Phasons

A fivefold symmetric pattern in 2D represented by (x, y) vectors on V can, as per table 3.1, be represented by a 4D basis on D: $|1\rangle = (1, 0, 0, 0)$, $|2\rangle = (0, 1, 0, 0)$, $|3\rangle = (0, 0, 1, 0)$, $|4\rangle = (0, 0, 0, 1)$, and $|5\rangle = (-1, -1, -1, -1)$.
Rotation by $2\pi/5$ in V corresponds to a cyclic permutation of the vertices, and can therefore be written in D as:

$$\mathcal{R} = \begin{pmatrix} 0 & 0 & 0 & -1 \\ 1 & 0 & 0 & -1 \\ 0 & 1 & 0 & -1 \\ 0 & 0 & 1 & -1 \end{pmatrix}_D , \tag{3.30}$$

which can be block diagonalised[12] to:

$$\begin{pmatrix} \cos 2\pi/5 & -\sin 2\pi/5 & 0 & 0 \\ \sin 2\pi/5 & \cos 2\pi/5 & 0 & 0 \\ 0 & 0 & \cos 4\pi/5 & -\sin 4\pi/5 \\ 0 & 0 & \sin 4\pi/5 & \cos 4\pi/5 \end{pmatrix}_V = \begin{pmatrix} \mathcal{R}^{\parallel} & \mathbf{0} \\ \mathbf{0} & \mathcal{R}^{\perp} \end{pmatrix}. \tag{3.31}$$

We identify this matrix to be constructed from a basis (x, y, x', y') corresponding to the Cartesian coordinates of the parallel (physical) and perpendicular (augmented) spaces. The rotation is depicted in fig. 3.13, which shows that the augmented dimension may possess its own distinct symmetries. These may therefore result in new and distinct excitations – *phasons*.

An excitation along the parallel space is a phonon, and one along the perpendicular space is a phason. As discussed in [105], phononic $\mathbf{u}$ and phasonic $\mathbf{w}$ strains cause a phase ϕ:

$$\phi = \mathbf{k}_{\parallel} \cdot \mathbf{u} + \mathbf{k}_{\perp} \cdot \mathbf{w}. \tag{3.32}$$

The phason can be visualised as originating from the modulation of the projection window, as shown in fig. 3.14: for strong enough strain, more or fewer hyperspace points fall within

[12] Compute the complex eigenvalues of $\mathcal{R}$, $\alpha_j \pm \mathrm{i}\beta_j$, and its eigenvectors $\mathbf{v}_j \pm \mathrm{i}\mathbf{w}_j$, with $j = 1, 2$ and $\alpha_i, \beta_i, \mathbf{v}_i, \mathbf{w}_i \in \mathbb{R}$. Construct a *real* basis by noting that $\mathcal{R}\mathbf{v}_i = \alpha_i \mathbf{v}_i - \beta_i \mathbf{w}_i$ and $\mathcal{R}\mathbf{w}_i = \beta_i \mathbf{v}_i + \alpha_i \mathbf{w}_i$, such that $\mathcal{R} \begin{pmatrix} \mathbf{v}_j \\ \mathbf{w}_j \end{pmatrix} = \begin{pmatrix} \alpha_j & -\beta_j \\ \beta_j & \alpha_j \end{pmatrix} \begin{pmatrix} \mathbf{v}_j \\ \mathbf{w}_j \end{pmatrix}$, i.e. the usual rotation matrix in Cartesian coordinates.

the window and are therefore projected onto the physical space. As observed in [106], this may lead to a non-local rearrangements of the atomic density.

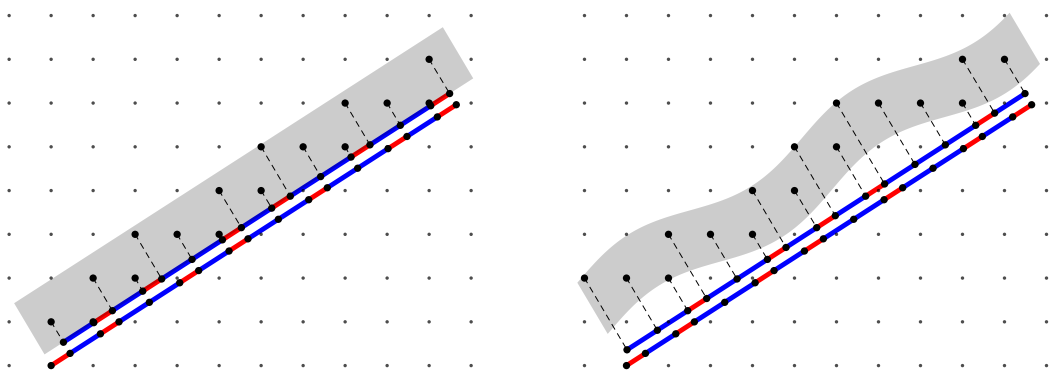

(a) $\mathbf{k}_\perp = 0$ (b) $\mathbf{k}_\perp \neq 0$

Figure 3.14 : Phasonic strain is driven by modulating the projection window. In the infinite wavelength limit, this just corresponds to a translation in the augmented dimension (a), but it is generally more complex (b).

It is known that there are as many phononic modes as the dimension d of the regular crystal, though the transition from an amorphous to a crystalline solid actually breaks the whole Euclidean group $\mathbb{E}^d = SO(d) \ltimes \mathbb{R}^d$, that is both rotations and translations. These are continuous groups with $d(d-1)/2$ and d generators respectively, hence the Goldstone theorem would predict the presence of $d(d+1)/2$ massless modes.

To justify the absence of the expected additional modes, let us consider the following.

1. Invariance by a translation $\mathbf{u}$:
   $\mathbf{r} \to \mathbf{r} + \mathbf{u} \quad \Rightarrow \quad \psi(\mathbf{r}) \to T(\mathbf{u})\psi(\mathbf{r}) = \mathrm{e}^{-\mathrm{i}\frac{\mathbf{u}\cdot\mathbf{p}}{\hbar}}\psi(\mathbf{r})$.
2. Invariance by a global, rigid rotation $\delta\phi$ about $\mathbf{n}$:
   $\mathbf{r} \to \mathbf{r} + (\mathbf{n} \times \mathbf{r})\delta\phi \quad \Rightarrow \quad \psi(\mathbf{r}) \to R(\delta\phi)\psi(\mathbf{r}) = \mathrm{e}^{-\mathrm{i}\delta\phi\frac{\mathbf{n}\cdot\mathbf{L}}{\hbar}}\psi(\mathbf{r})$.

If the structure is a regular lattice with translational and rotational symmetries, then the two must coincide for some $\mathbf{u}$ and $\mathbf{n}$:

$$\mathrm{e}^{-\mathrm{i}\frac{\mathbf{u}\cdot\mathbf{p}}{\hbar}} = \mathrm{e}^{-\mathrm{i}\delta\phi\frac{\mathbf{n}\cdot\mathbf{L}}{\hbar}} \quad \Rightarrow \quad \mathbf{u}\cdot\mathbf{p} = (\mathbf{n}\times\mathbf{r}\delta\phi)\cdot\mathbf{p}, \tag{3.33}$$

i.e. breaking translational invariance automatically breaks rotational invariance as well. Additionally, $\delta\phi \sim \partial_\mathbf{r}\mathbf{u}$, $\mathbf{u} \sim 1/\mathbf{k}$ and $\partial_\mathbf{r} \sim \mathbf{k}$, so even as $k \to 0$, one finds that $\langle|\delta\phi(\mathbf{k})|^2\rangle \neq 0$: the rotational modes are gapped, and can therefore not be the results of a broken *continuous* symmetry as required by Goldstone's theorem.

Finally, the Mermin-Wagner theorem invoked in section 1.2 also applies to diagonal (density-density) long-range order in crystalline structures. True long-range order in $d \leqslant 2$ at $T \neq 0$ is therefore forbidden and 2D crystals cannot strictly speaking exist. However, the five 2D Bravais lattice can still be found in nearly 2D systems or in planar cuts of 3D structures.

Part II

Experimental details

Physics and Engineering

Conceive of a sinner who is Catholic and devout. What complexity in his feeling for the Church, what pities of observance live between his sins. He has to make such intricate shows of concealments to his damned habits. Yet how simple is the Church's relation to him. Extreme Unction will deliver his soul from a journey through hell.

So it is with physics and engineering. Physics is the Church, and engineering the most devout sinner. Physics is the domain of beauty, law, order, awe, and mystery of the pursue sort; engineering is partial observance of the laws, and puttering with machines which never work quite as they should work: engineering, like acts of sin, is the process of proceeding boldly into complex and often forbidden matters about which one does not know enough - the law remain to be elucidated - but the experience of the past and hunger for the taste of the new experience attract one forward. So bridges were built long before men could perform the mathematics of the bending moment.

Norman Mailer [154]

If it [engineering] was easy, everyone would do it.

Nigel Palfrey, Head of the Student Workshop until 2017

4

Design, assembly and control

This chapter provides an overview of the necessary equipment that enables trapping and cooling of cold atoms, namely the vacuum, laser and software infrastructure.

4.1 Design

4.1.1 Setup overview

The experimental apparatus is shown in figs. 4.1 and 4.2.
The atomic sources are heated to achieve a high vapour pressure in the 2D MOT, where they are pre-cooled in large numbers. Both species are simultaneously loaded, cooled and trapped in the 3D MOT and subsequently magnetically transported to the science cell. Here, evaporative cooling is performed first in a magnetic trap and then in a crossed-beam dipole trap, resulting in the creation of a Bose-Einstein condensate (BEC). The BEC is then illuminated with the optical lattice to perform experiments.

Differential pumping sections between the various chambers guarantee a low pressure in the science cell to ensure a long lifetime of the BEC, and are discussed in section 4.2.

The stages of the experimental sequence employed to produce a BEC are summarised in table 4.1. A detailed explanation of each experimental stage is provided in chapter 5.

4.1.2 Starting a lab from an empty room

A good architecture allows postponing decision-making as long as possible.
In every design decision we made while setting up the lab from scratch, we tried to abide by this rule and avoid accumulation of "technical debt"[1]. We strived to guarantee flexibility and versatility of all aspects of the system to ease future upgrades and experiments, as

[1] Dr. Ulrich Schneider©.

well as including plenty of diagnostics for the day-to-day maintenance and operation of the machine.

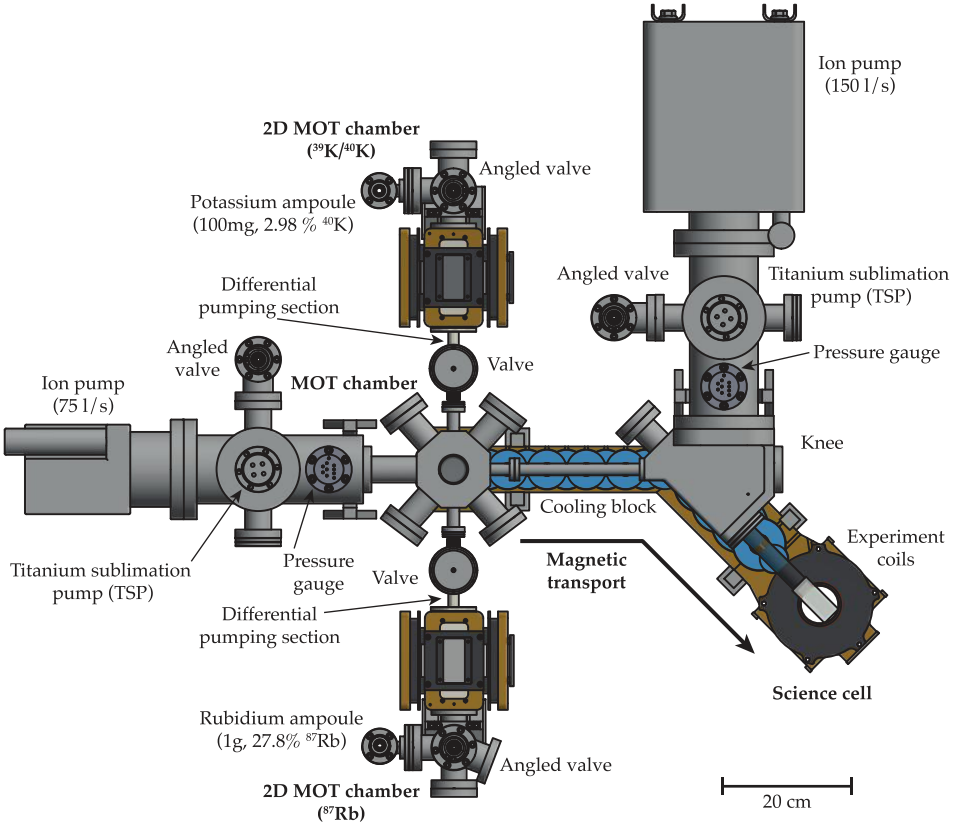

Figure 4.1 : Schematic diagram of the experimental apparatus. Figure adapted from [94].

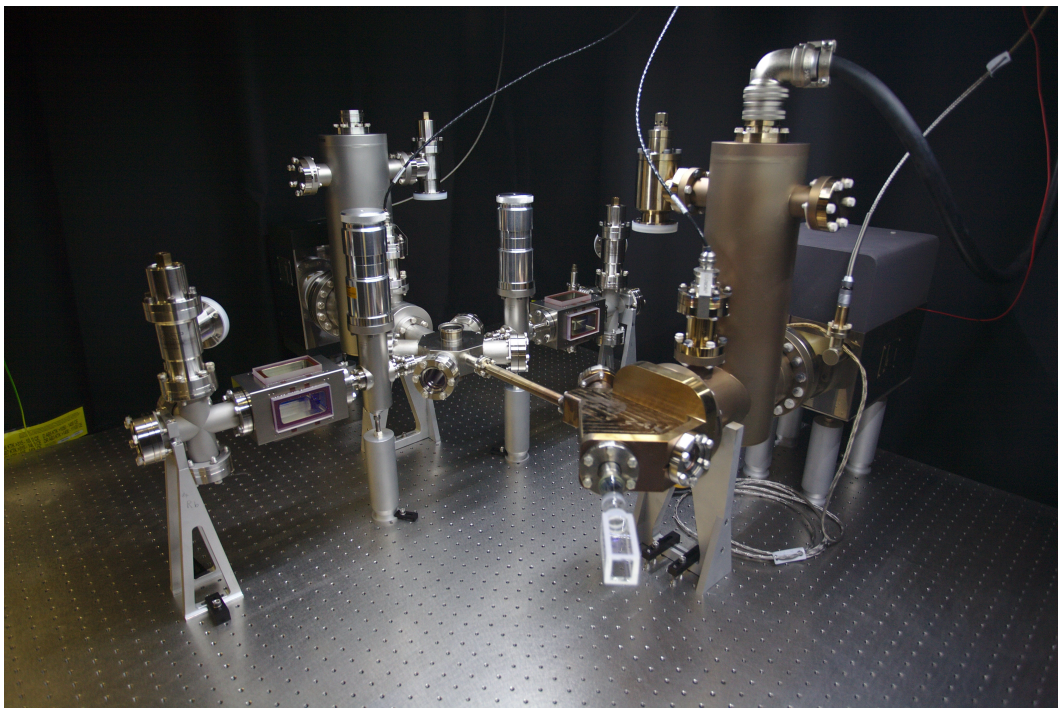

Figure 4.2 : Assembled vacuum system, July 4$^{\text{th}}$ 2016.

stage	duration	section
2D & 3D MOT	2.5 s	5.1
"temporal dark-spot" MOT	10 ms	
polarisation gradient	4.5 ms	
optical pumping	0.7 ms	
magnetic transport	5 s	5.2
evaporation in magnetic trap	7.5 s	5.3.2
state transfer	20 ms	5.3.3
evaporation in optical trap	3 s	
total	$\sim$ 23 s	

Table 4.1 : Overview of the experimental sequence.

The theme for our experiment had been established to be quantum simulation in a quasicrystalline optical lattice, given the surprisingly little experimental research on quasiperiodic potentials with degenerate quantum gases.

Choice of atomic species

^{87}Rb and $^{39,\,40}$K atomic species were chosen because their cooling, trapping and manipulation techniques had been thoroughly investigated and were thus well established. This enabled performance of novel experiments just by applying the optical lattice tool-kit to our new geometry.

The bosonic ($A = 39$) and fermionic ($A = 40$) isotopes of potassium possess experimentally accessible Feshbach resonances, being at relatively low fields (< 600 G) and reasonably broad ($\sim$ 10s of G) to be stable against ambient magnetic field noise. These allow tuning the inter-species scattering length thereby enabling investigation of single-particle (non-interacting) and strongly interacting physics, and it is the main reason as to why K was utilised despite the difficulties it presents compared to Rb.

The challenges and the solutions to producing large quantum degenerate samples of potassium are listed as follows:

- Smaller concentrations. The fermionic isotope ^{40}K has a low natural abundance of 0.012%. Our potassium source was enriched to increase the ^{40}K concentration to 2.98%, and the pre-cooling stage in the 2D MOT enhances the number of atoms loaded into the 3D MOT. Both isotopes, in addition, have low background vapour pressures, which is compensated by constantly heating the samples to increase their evaporation rate.
- A narrow hyperfine structure. The hyperfine splitting of the excited states of potassium is of the same order as their natural linewidths ($\sim$ 10 MHz), preventing

individual addressability and hence hindering the efficiency of usual laser cooling schemes. This results in the atoms reaching a higher final temperature at the end of the laser cooling stage.

- A higher two-body loss parameter β (discussed in section 1.3.2) which limits the size of the potassium MOT. For comparison, β for ^{39}K is $\sim 2 \cdot 10^{-10}\,\mathrm{cm^3\,s^{-1}}$ [155], 10 times larger than for ^{87}Rb, for which it is $\sim 2 \cdot 10^{-11}\,\mathrm{cm^3\,s^{-1}}$ [156].
  This, combined with the higher final temperature of K atoms resulting from the less efficient laser cooling, would require a larger particle loss during evaporation. Hence, K is directly evaporated only in the final stage of the process, while relying on sympathetic cooling with ^{87}Rb for the most part.
- The negative background scattering length in ^{39}K renders the BEC unstable and leads to its collapse. This is avoided by an appropriate choice of scattering length, by tuning the Feshbach resonance, to guarantee repulsive interactions.
- The negative scattering length in ^{39}K also causes a Ramsauer-Townsend minimum for the inter-species s-wave cross section at $\sim 400\,\mu\mathrm{K}$ [157], where other partial waves' contributions are negligible. This is circumvented by using a positive inter-species scattering length, and also by using ^{87}Rb as a sympathetic coolant for most of the evaporation process. The use of ^{87}Rb will also aid in the cooling of fermionic ^{40}K, hindered by the lack of s-wave scattering channels.

All-optical cooling of ^{39}K has been achieved [158] and would render the presence of ^{87}Rb redundant, were it not for the possibility of future experiments involving Bose-Bose and Bose-Fermi mixtures.
At the time of writing this thesis, only a MOT of ^{40}K has been obtained since we decided to perform the first experiments with degenerate bosons.

Design guidelines and Munich model

The priorities in the design process were optimising the sequence duration and maximising the optical access around the science cell. The former to aid in optimising, diagnosing and obtaining results, and the latter to allow inclusion of future upgrades with minimal disruption. Hence, all the laser light is prepared on different optical tables and routed to the experiment chambers via optical fibres, which however cause power loss and increased phase noise.

In addition, to guarantee stability and to preserve optical alignment, no moving parts are present on the main experiment table, along with unnecessary sources of heat. Temperature, humidity and airflow of the tables are all actively stabilised.

Our design was based on an existing experiment at the Ludwig-Maximiliens Universität in Munich, code named Fermi-II and described in the following theses, heavily used at the beginning of my PhD: [159–163].

A number of upgrades were made on the Munich design:

- Rb and K were each given their own 2D MOT, so as to allow for independent optimisation of parameters, from the magnetic field gradient to the vapour pressure.
- A longer differential pumping section between the 3D MOT and the science cell was used, to allow for more space and hence more complex optical beam paths to be

implemented. The increase in length was accompanied by an increase in diameter to maintain the same conductance ($\propto$ diamter^3/length).

- Our science cell is rectangular with parallel sides, which allows for closer experiment coils and stronger magnetic fields, but results in back-reflection for normally incident beams.
- The magnetic transport was re-designed to be more compact and to minimise heating of the atomic cloud.

4.2 Vacuum

Why a vacuum?

Collisions between trapped cold atoms ($\sim 100\,\mathrm{nK}$) and the room-temperature background gas ($\sim 300\,\mathrm{K}$) would transfer enough energy to eject them from the trap, thereby causing a significant loss. These are reduced at low pressures. Hence, while a high pressure region is required at the location of the sources for efficient loading, low pressures are needed in the science cell to ensure a long lifetime of the trapped atoms. This is achieved by *differential pumping*.

Differential pumping

Steady-state pressure gradients are guaranteed by the *differential pumping* of the various components, akin to voltage drops in electrical circuits. This analogy can be made quantitative in a regime where molecular flow dominates over viscous flow, i.e. where the mean free path of the background particles λ_{mfp} is larger than the lengthscale of the system $D \sim 1\,\mathrm{m}$. The pressures in our experiment ($10^{-7} - 10^{-11}$ mbar) satisfy this condition as the Knudsen number $\mathrm{Kn} = \lambda_{\mathrm{mfp}}/D \gg 1$, and λ_{mfp} is in the $\sim$ km range. The vacuum system can be treated as an electronic circuit (fig. 4.3) with the following equivalences:

$$P \Leftrightarrow V, \qquad C \Leftrightarrow \frac{1}{R}, \qquad Q \Leftrightarrow I, \qquad \text{so} \qquad V = IR \;\Leftrightarrow\; P = \frac{Q}{C}, \tag{4.1}$$

where P is the pressure (V the voltage), C is the conductance (R the resistance) and $Q = \mathrm{d}(PV)/\mathrm{d}t$ is the throughput (I the current).

The calculation is detailed in appendix B.1 and results in the following design pressure gradients:

$$\frac{P_1}{P_0} \approx 10^{-4}, \qquad \frac{P_2}{P_1} \approx 10^{-2}. \tag{4.2}$$

The atomic vapour pressure P_0 for both species is kept at $\sim 10^{-7}\,\mathrm{mbar}$, hence the 3D MOT pressure was expected to be $P_1 \sim 10^{-11}\,\mathrm{mbar}$ and the science cell pressure $P_2 = P_3 \sim 10^{-13}\,\mathrm{mbar}$.
Experimentally, the 3D MOT pressure is found to be $\sim 7 \times 10^{-11}\,\mathrm{mbar}$ and the science cell $\sim 1.2 \times 10^{-11}\,\mathrm{mbar}$, the latter being higher than the target value but comparable to other experiments, suggesting it is limited by the degassing rate of the inner surfaces.

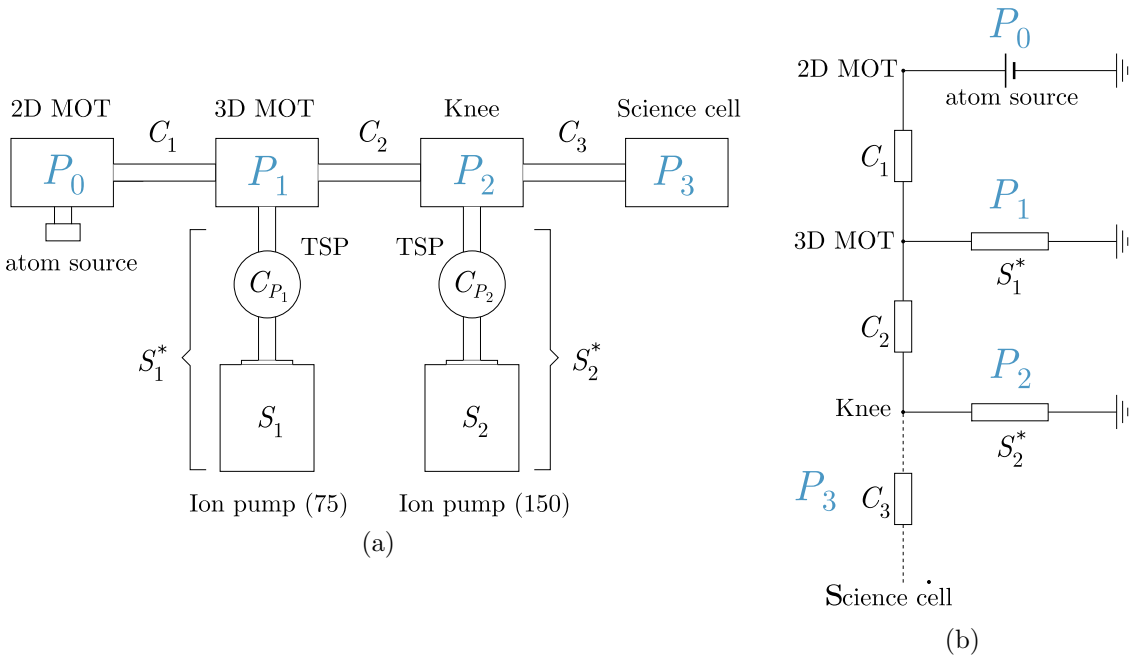

Figure 4.3 : Schematic diagrams of the vacuum system (a) and its electronic analogue (b). The atomic sources act like batteries providing a constant evaporation rate, while apertures and pipes hinder the flow. Pumps are modelled as having no pressure (grounded), and with conductance equal to their effective pumping speed S^*.

Pumps and gauges

There are three types of vacuum pumps, distinguished by the underlying physical mechanisms and attainable pressures.

A *positive displacement pump* comprises a cavity and a seal: a crankshaft expands the cavity and lets fluid in, then seals it gradually guiding it to the exhaust. The cycle repeats until the pump reaches its ultimate pressure, governed by the tightness of the seal and the performance of the mechanical components. We used a *scroll* pump, in which two interleaving spiral scrolls, with low-degassing grease as a seal, rotate inside each other. This allowed reaching $5 \times 10^{-2} - 1.2 \times 10^{-1}$ mbar base pressures.

A vacuum lower than 10 mbar was needed in order to operate the *turbomolecular* pump. This is a type of *momentum transfer* pump, which relies on molecules impinging on rotating propellers that direct them towards the exhaust. This stage occurs at the boundary between viscous and molecular flow, hence the pump's operation is not just suction, but akin to a "black hole". The best pressures achieved were in the low 10^{-9} mbar.

The scroll and turbomolecular pumps were only temporarily connected to the system, via vacuum hoses and corner valves, in order to reach a sufficiently low pressure to enable the use of *entrapment pumps*, which are constantly operational. These are sealed containers with a large surface area, covered in a *getter* material that background gas particles chemically bond with. Our system comprises two *Ion getter* pumps and two *Titanium Sublimation Pumps* (TSP). The former include a hot cathode and a strong magnet (800 – 2000 G) in order to emit electrons and allowing them to spiral in the vacuum system, ionising gas particles which are then attracted towards the pump inlet. Ion pumps are needed as well as the other getter pumps, as noble gases would not be pumped unless

first ionised.

These pumps enable maintaining pressures of $\sim 10^{-11}$ mbar in the 3D MOT and in the science cell which are measured with Bayard-Alpert gauges[2].

Sources and materials

The base pressure inside the vacuum chambers is determined by the equilibrium between the pumping speed of the entrapment pumps and the degassing rate of the inner surfaces, due to evaporation, de-absorption or diffusion from within the material. Low degassing materials such as specialised alloys, glues and glasses were hence selected, and thoroughly cleaned following the procedure detailed in appendix B.1. The system was also heated to high temperatures ("baked") in order to accelerate the degassing and diffusion rates and achieve lower pressures faster. The presence of alkali metals aids in attaining low pressures, as their chemistry allows them to act like getters once they coat the chamber walls. Their aggressive chemistry may unfortunately also result in the degradation and eventual failure of non-alkali compatible materials, such as certain makes of viewports[3].

The ^{87}Rb and ^{39}K, ^{40}K atoms were contained in two hermetically sealed ampoules ~ 7 cm long (fig. 4.4) and have the following specifications:

- 200.0 mg of potassium: $Z = 19$, ^{39}K at natural abundance (93%) and ^{40}K enriched to 2.98%. Chemical Form: potassium chloride.
- 1 g of rubidium: $Z = 37$, ^{87}Rb at natural abundance (29%). Chemical form: rubidium nitrate.

The ampoules were inserted in two bellows valved to the vacuum system prior to the start of the pumps, and then broken when high vacuum was achieved. The bellows are wrapped in aluminium foil and heating wire in order for the vapour pressure to be kept at $\sim 10^{-6} - 10^{-7}$ mbar, as summarised in table 4.2.

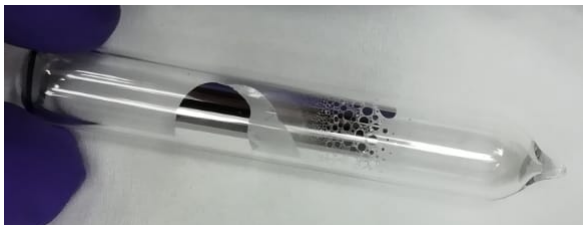

Figure 4.4 : The sealed ampoule filled with argon, containing 200 mg of potassium, with an enriched fermionic isotope concentration.

[2]Ionisation gauges use a hot cathode to create electrons and an anode to accelerete them. These create positive ions in the gas, which are later collected by another cathode and whose current measurement provides an estimate for the gas density. However, some electrons impinge on the anode and lead to X-ray production, which generates an additional photocurrent in the collecting electrode thereby undermining its accuracy [164]. The gauge next to the science cell includes enhanced features to force the *X-ray barrier* below 5×10^{-12} mbar, as opposed to 3×10^{-11} mbar of the gauge next to the 3D MOT.

[3]Which we found out the hard way.

species	melting point	pressure at 295 K	pressure at 333 K
Rb	313 K	3.8×10^{-7} mbar	-
K	337 K	1.7×10^{-8} mbar	9×10^{-7} mbar

Table 4.2 : Vapour pressures for our Rb and K sources [165], the former kept at room temperature and the latter heated to $\sim 60\,^{\circ}$C.

4.3 Lasers and magnets

4.3.1 Transitions

Spectral structure

As discussed in section 2.3.2, increasing phase space density requires the absorption and subsequent incoherent scattering of many photons so as to lose entropy. An effective implementation would see cooling happening on a *closed* or *cyclic* transition, where selection rules permit the light to only couple two atomic states. The presence of other states, however, results in transitions to *dark states* which do not participate in the cooling process. While this is beneficial in the last stages of laser cooling, where further scattering only increases temperature, these atoms generally need to be *repumped* back into a state affected by the cycling transition.

Rubidium and potassium have the following electronic structures:

Rb $1s^2\ 2s^2\ 2p^6\ 3s^2\ 3p^6\ 4s^2\ 4p^6\ 5s$,
K $1s^2\ 2s^2\ 2p^6\ 3s^2\ 3p^6\ 4s$.

They both have only one electron in the outermost shell, which for both possesses orbital angular momentum $L = 0$. All other shells are full, hence only the outermost electron contributes to the angular momentum. The electron spin being $s = 1/2$, the ground state of the manifold is then $^2S_{1/2}$. The first excited state corresponds to the electron being in the p shell with $L = 1$, leading to a fine structure splitting between $J = 1/2$ and $J = 3/2$, written as $^2P_{1/2}$ and $^2P_{3/2}$. Transitions between the ground and the first excited states in alkalis are called D1 and D2 lines.

The nuclear angular momentum is $I = 3/2$ for both ^{87}Rb and ^{39}K ($I = 4$ for ^{40}K), which results in the hyperfine structure splitting among different F states, calculated in appendix A and shown in figs. 4.6 and 4.7. Each F state has $2F + 1$ sub-states, labelled by the magnetic quantum number m_F, whose degeneracy is lifted by an external magnetic field[4], discussed in section 4.3.1.

Only the D2 lines are used in our cooling schemes, hence F and F' will denote the ground ($S_{1/2}$) and the excited ($P_{1/2}$) states.
Laser cooling requires the following beams to illuminate the atoms:

- *Cooling*
  The MOT cycling transition for ^{87}Rb and ^{39}K is $|F = 2, m_F = -2\rangle \rightarrow |F' = 3, m'_F = -3\rangle$, driven by σ^- polarised light.

[4]Interestingly, only an external magnetic field fully lifts m_F degeneracy, as it violates time reversal symmetry. The linear Stark shift, for instance, causes an energy splitting depending on $|m_F|$.

- *Repump*
  The cooling beam may also cause the transition $|F = 2, m_F = -2\rangle \rightarrow |F' = 2, m'_F = -2\rangle$[5], from which atoms may decay to $|F = 1, m_F = -1\rangle$. This is dark with respect to the cycling transition, hence a repump beam is tuned to the $|F = 1\rangle \rightarrow |F' = 2\rangle$ transition in order to provide the atoms with another chance to decay into $|F = 2, m_F = -2\rangle$. Because of the larger separation of the F' states in ^{87}Rb than in ^{39}K, fewer atoms populate the dark state and hence lower repump optical powers are required.

- *Optical pumping*
  Atoms are spin-polarised by being pumped into the same $m_F = 2$ or $m_F = -2$, as described in section 2.2.1. This is achieved by a $\sigma^{+\text{or}-}$ polarised beam tuned to the $|F = 2\rangle \rightarrow |F' = 2\rangle$ transition.

- *Push*
  In the 2D MOT, discussed in section 5.1.1, a repulsive blue detuned beam is used to drive the atoms towards the 3D MOT, by causing a momentum kick in the opposite direction to that received upon absorption of red detuned light.

- *Imaging*
  Atoms are detected by recording their spatial position, as detailed in chapter 6. This relies on them interacting strongly with the incident light, in order to maximise the signal. Hence, the imaging beam addresses the cycling transition $|F = 2, m_F = 2\rangle \rightarrow |F' = 3, m'_F = 3\rangle$ and it is on resonance.

The lifetime of the excited states F' is $\sim 10\,\text{ns}$ for both ^{87}Rb and ^{39}K, which corresponds to a natural linewidth of $\Gamma \sim 2\pi \cdot 6\,\text{MHz}$. In ^{39}K, the energy separation between the F' states are on the order of Γ, which prevents individual addressability of the transitions and therefore limits the effectiveness of laser cooling by reaching a higher final temperature than in ^{87}Rb.

High fields

In the presence of an external magnetic field, the relevant contributions to the Hamiltonian (appendix A) are:

$$H = H_{\text{hyp}} + H_{\text{Zeeman}}, \tag{4.3}$$

where the hyperfine structure H_{hyp} is modified by the interaction H_{Zeeman} coupling the atomic magnetic moment $\boldsymbol{\mu}$ and the external magnetic field $\mathbf{B}$, chosen to lie along the z axis. Its first order energy shift ΔE_{Zeeman} is given by:

$$\Delta E_{\text{Zeeman}} = -\langle \boldsymbol{\mu} \cdot \mathbf{B} \rangle = \begin{cases} g_F m_F \mu_{\text{B}} B & \text{for weak } \mathbf{B}, \\ g_J m_J \mu_{\text{B}} \text{B} & \text{for strong } \mathbf{B}. \end{cases} \tag{4.4}$$

For weak fields, $H_{\text{hyp}} \gg H_{\text{Zeeman}}$ and the energy shift is a perturbation on the total angular momentum states $|F, m_F\rangle$. For strong fields, $H_{\text{Zeeman}} \gg H_{\text{hyp}}$ which causes $\mathbf{J}$ and $\mathbf{I}$ to decouple and precess about the z axis, the hyperfine structure amounting to a perturbation on the $|m_J, m_I\rangle$ basis.

For intermediate field strengths, the energy shifts are found by exact diagonalisation of the Hamiltonian, and are shown in figs. 4.8-4.12. The low-field states $|F, m_F\rangle$ are divided into

[5] The magnetic field being inhomogeneous, the quantisation axis of the atoms vary with their positions in the trap.

high-field seekers (grey) and low-field seekers (blue), and are adiabatically connected to the states $|m_J, m_I\rangle$. As discussed in chapter 6, at any finite field strength, the $|m_J, m_I\rangle$ states are not pure and prevent a fully closed transition at high fields. Imaging was nonetheless performed on the transition $|m_J = -1/2, m_I = 3/2\rangle \rightarrow |m_{J'} = -3/2, m_{I'} = 3/2\rangle$, whose predicted shift was found to agree with the experimental measurement shown in fig. 4.5.

Useful quantum numbers and parameters are provided in tables 4.3 and 4.4.

Parameter	$S_{1/2}$	$P_{3/2}$
g_F	$-1/2$ for $F = 1$ $1/2$ for $F = 2$	2/3
g_J	2.000	4/3

Table 4.3 : Landé factors for ^{39}K and ^{87}Rb. Values from [166, 167].

	Dominant	good as $\mathbf{B} \rightarrow 0$	good as $\mathbf{B} \rightarrow \infty$	not good†	always good
Weak $\mathbf{B}$	H_{hyp}	$\mathbf{I} \cdot \mathbf{J}$, $\mathbf{F}^2$		J_z, I_z	$\mathbf{J}^2$, $\mathbf{I}^2$, $\mathbf{F}_z$
Strong $\mathbf{B}$	H_{Zeeman}		J_z, I_z	$\mathbf{I} \cdot \mathbf{J}$, $\mathbf{F}^2$	

Table 4.4 : Relevant quantum numbers for strong and weak magnetic fields, valid until IJ coupling fails. †: but still apply for stretched states.

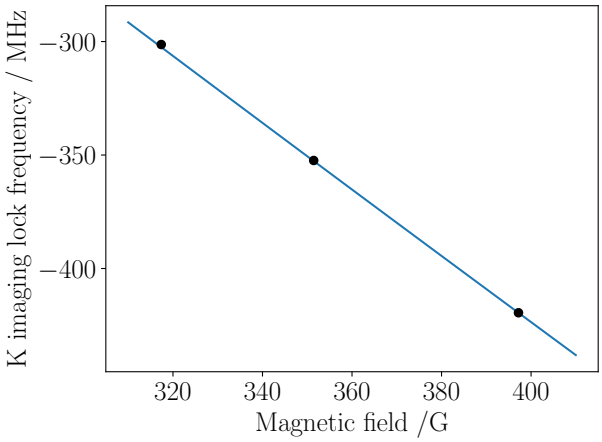

Figure 4.5 : The potassium imaging frequency for high magnetic fields was varied until resonant with the atoms. A scan was performed to determine the frequency of maximum signal, which corresponds to the black points. The solid line is the expected shift of the $|m_J = -1/2, m_I = 3/2\rangle \rightarrow |m_{J'} = -3/2, m_{I'} = 3/2\rangle$ transition from exact diagonalisation of the Hamiltonian.

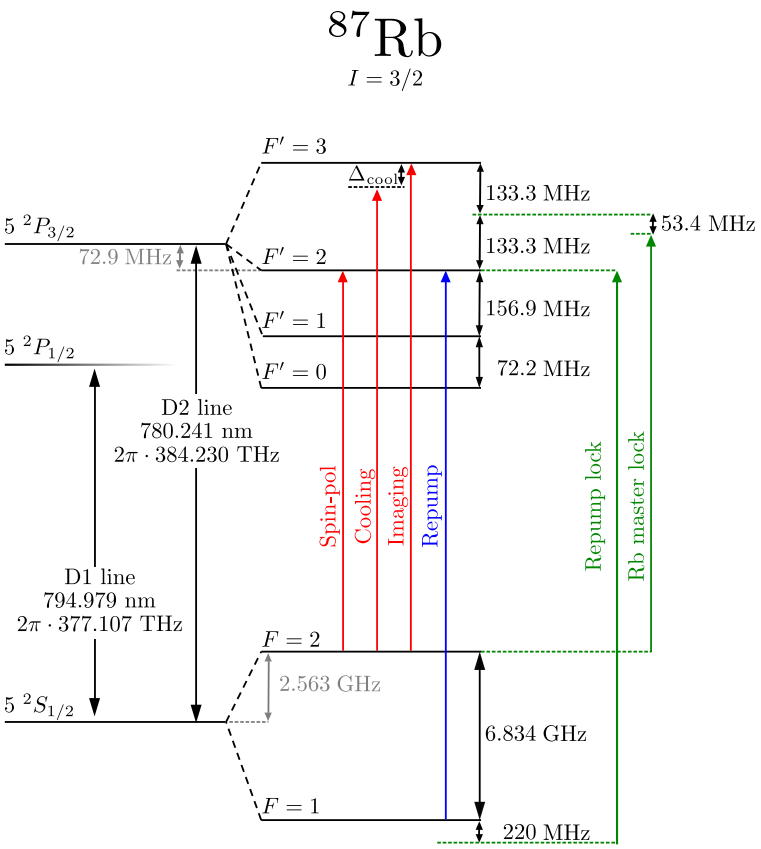

Figure 4.6 : Hyperfine structure of ^{87}Rb.

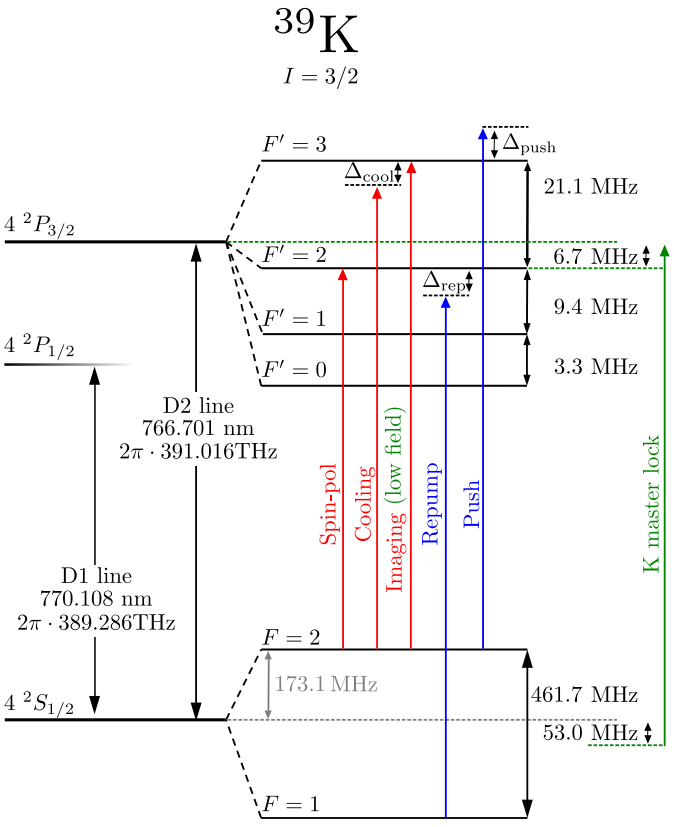

Figure 4.7 : Hyperfine structure of ^{39}K.

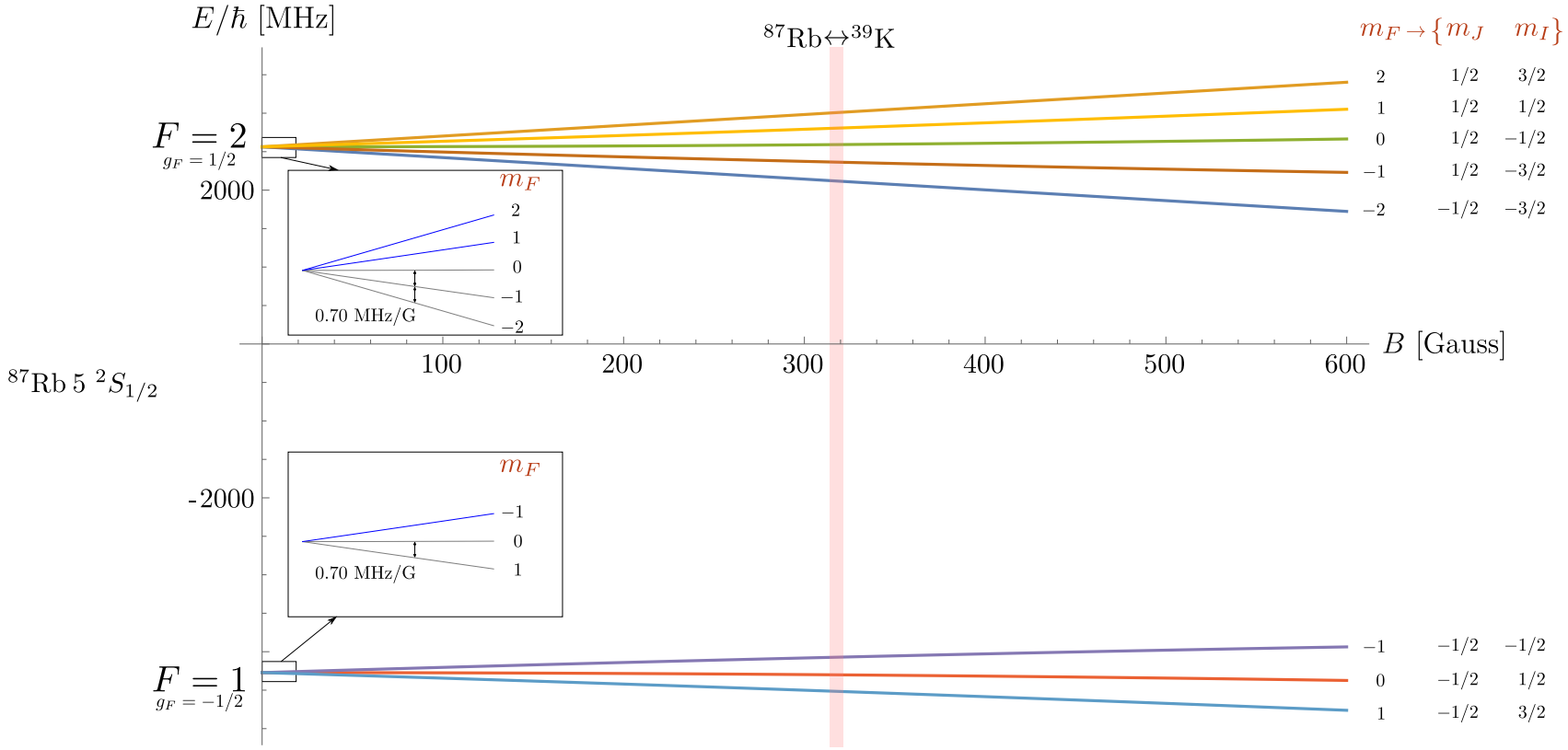

Figure 4.8 : Energy levels shifts caused by an external magnetic field in ^{87}Rb $S_{1/2}$. Feshbach resonances shown as red dashed rectangle.

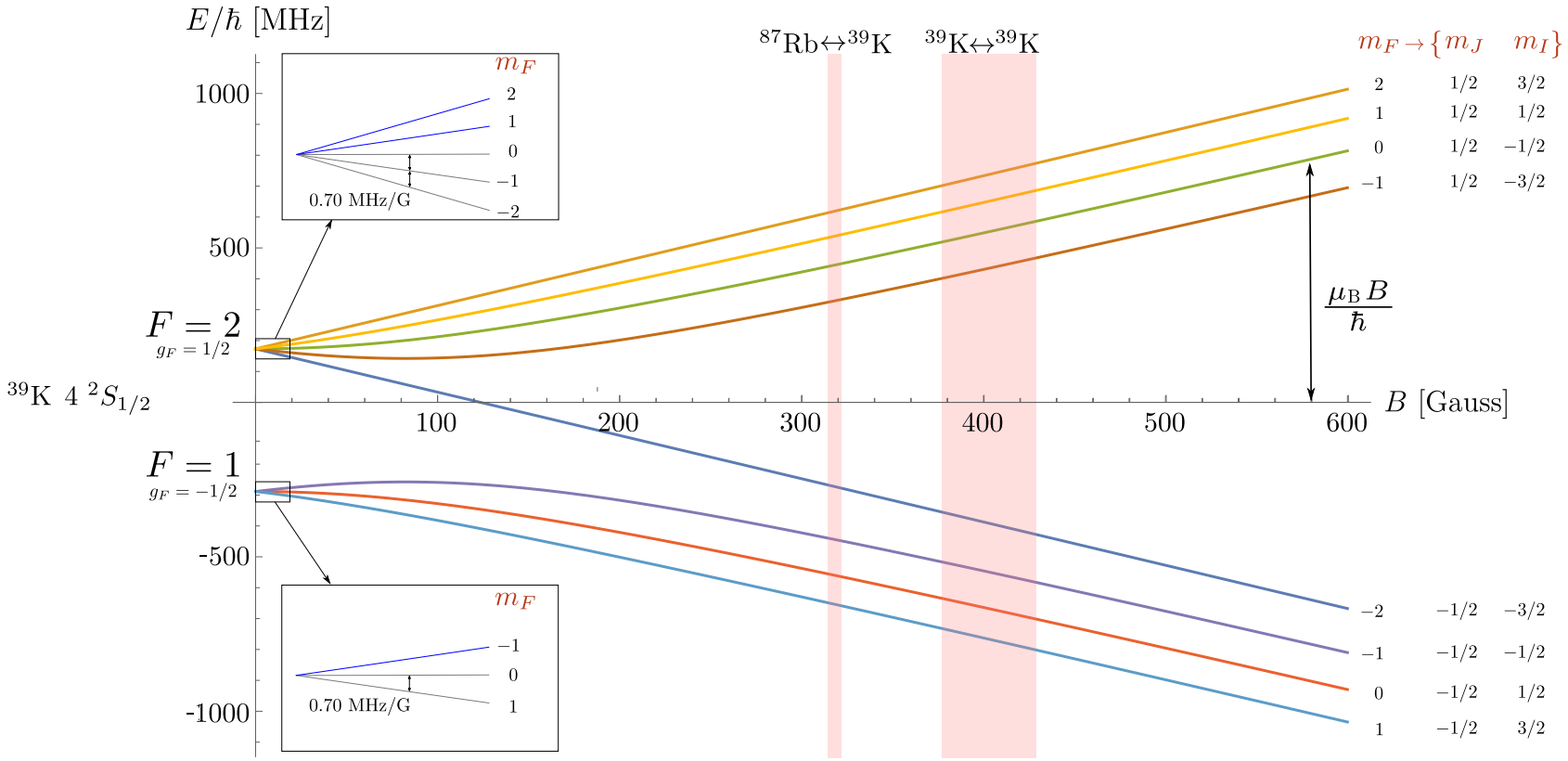

Figure 4.9 : Energy levels shifts caused by an external magnetic field in ^{39}K $S_{1/2}$. Feshbach resonances shown as red dashed rectangle.

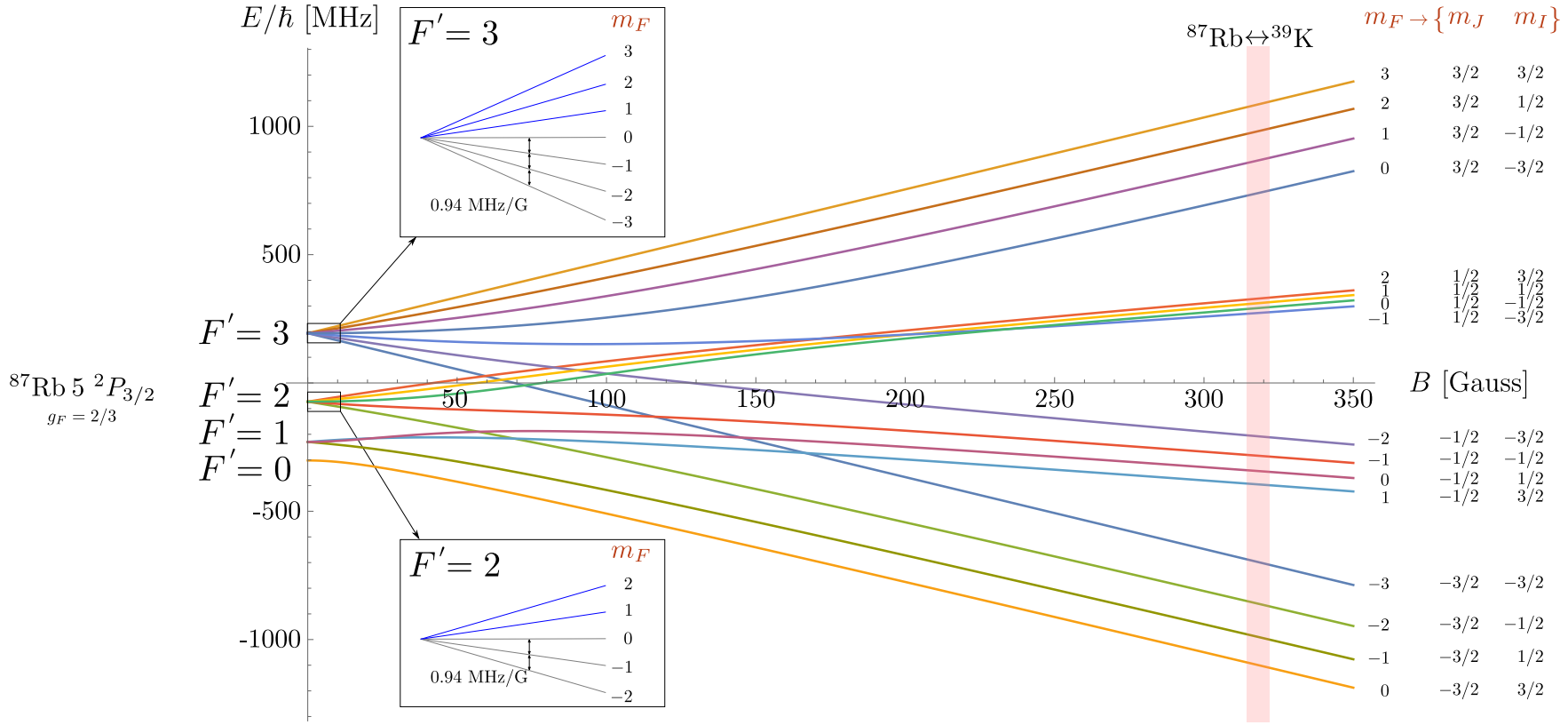

Figure 4.10 : Energy levels shifts caused by an external magnetic field in ^{87}Rb $P_{3/2}$. Feshbach resonances shown as red dashed rectangle.

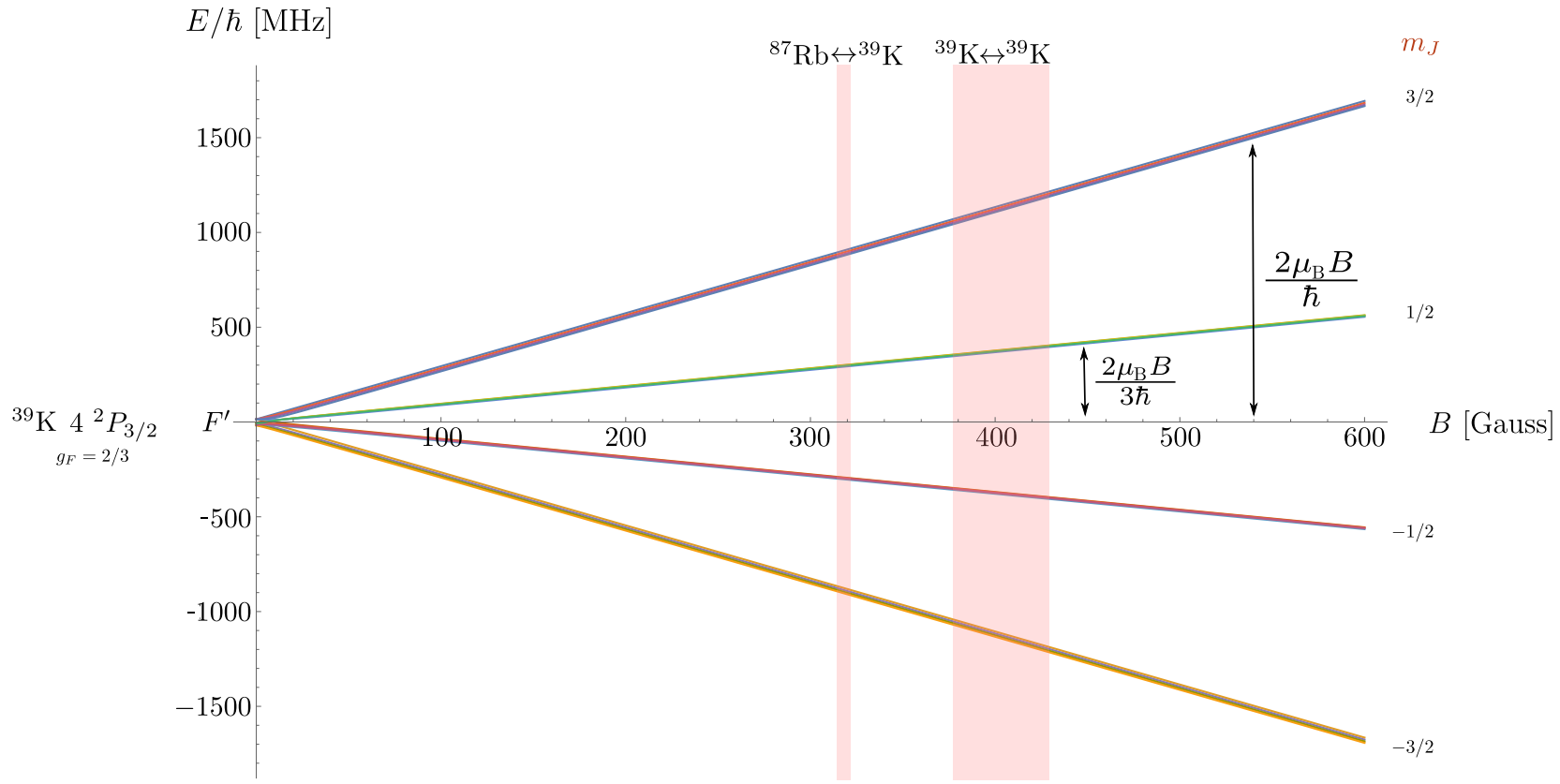

Figure 4.11 : Energy levels shifts caused by an external magnetic field in ^{39}K $P_{3/2}$. Feshbach resonances shown as red dashed rectangle.

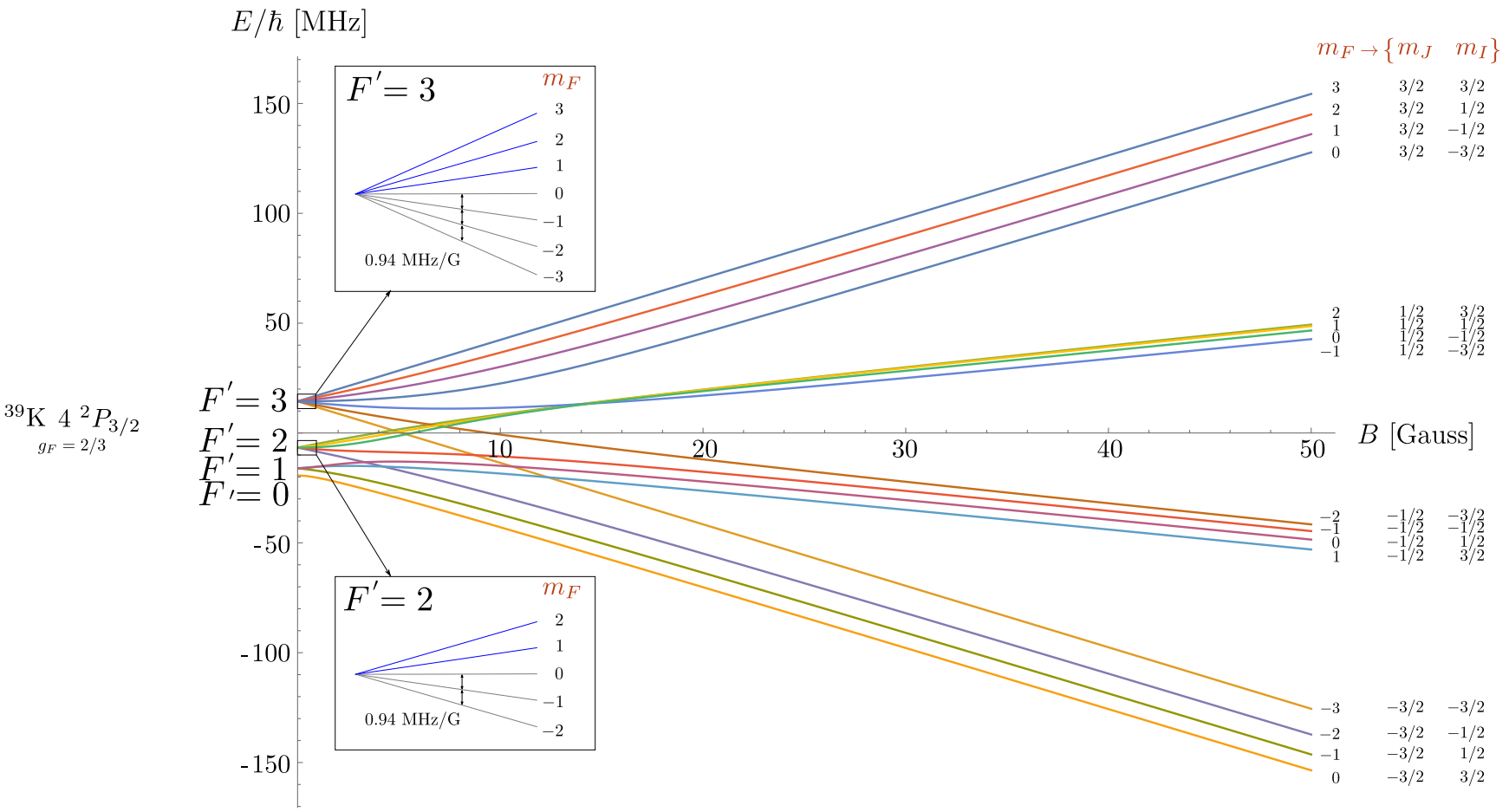

Figure 4.12 : Energy levels shifts caused by an external magnetic field in ^{39}K $P_{3/2}$, here plotted for low field strengths.

4.3.2 Frequency Locking

Doppler free saturation spectroscopy

Laser cooling relies on the individual addressability of atomic transitions, which requires the laser frequency to be stable to less than the natural atomic linewidth $\Gamma \sim 2\pi \cdot 6\,\mathrm{MHz}$.

The frequency stability of a laser is undermined by thermal drifts and ambient noise, and hence needs to be actively corrected ("locked"). To guarantee stability within Γ, a PID loop responds to an error signal generated by the absorption lines of ^{87}Rb and ^{39}K sources in a separate vapour cell using Doppler-free saturation spectroscopy [168, 169]. As illustrated in fig. 4.13, a portion of the laser radiation is split between a powerful *pump* beam and a weak *probe* beam, both directed onto the vapour cell. The probe beam is incident onto a photodiode measuring its transmission through the atomic cloud. As the frequency of the laser is varied ("scanned") a Doppler-broadened signal ($\sim 1\,\mathrm{GHz}$ wide) is recorded by the photodiode as none of the atoms are generally resonant with either beam. A special case, however, are atoms at rest, for which both beams will become resonant with the same transition: the pump beam will then saturate the transition, resulting in reduced absorption of the probe beam and hence an increased transmission. Another special case concerns atoms with a velocity such that the Doppler shifted beams are resonant with distinct transitions, resulting in *crossover peaks* situated at the average frequency of each pair of transitions. In ^{87}Rb , the excited states $|F'\rangle$ are well separated and resolved, so each ground state $|F = 1, 2\rangle$ is coupled to them individually. At the crossover, the pump beam will have already depleted the ground state, hence the probe will again experience a reduced attenuation. In ^{39}K, on the other hand, the $|F'\rangle$ states are too close to be individually resolved. At the crossover frequency, the pump and probe beams then create a Λ system with the two ground states $|F = 1, 2\rangle$, pumping atoms from one to the other, which results in an *enhanced* absorption of the probe beam. These mechanisms are schematically shown in figs. 4.14 and 4.15, along with the experimental signatures shown in figs. 4.16, 4.17, and 4.18.

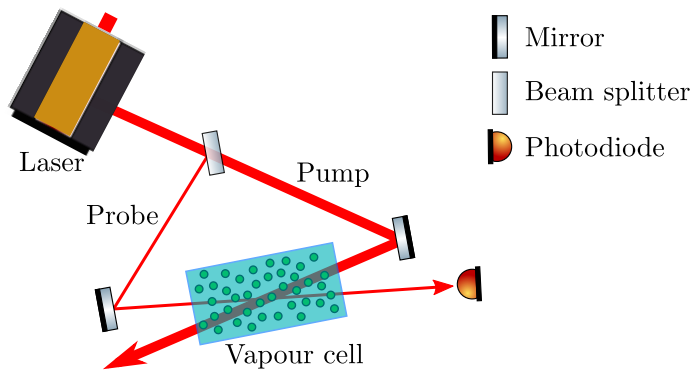

Figure 4.13 : The Doppler-free saturation spectroscopy apparatus. The pump beam ensures the ground state is depleted so as to induce a higher transmission of the probe beam, measured by a photodiode.

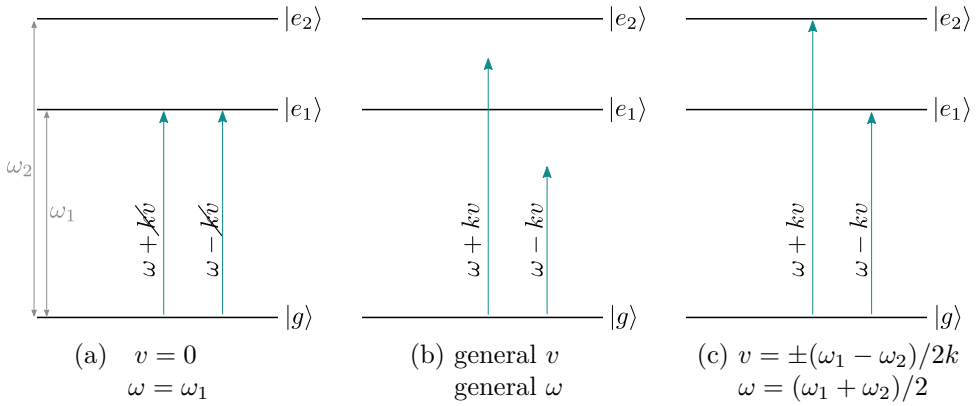

Figure 4.14 : In general, atoms at rest will be resonant with the both beams (a) while the others experience a Doppler-broadened absorption (b). In ^{87}Rb , the degeneracy in the distinctly resolved excited states causes a reduced absorption of the probe beam at the crossover peaks (c).

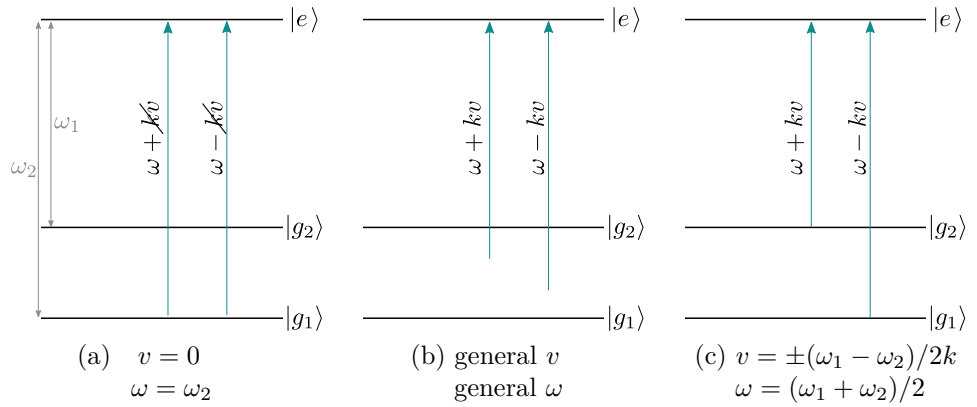

Figure 4.15 : In ^{39}K, the degeneracy is in the ground states, which at the crossover frequency form a Λ system causing an increased absorption of the probe beam (c).

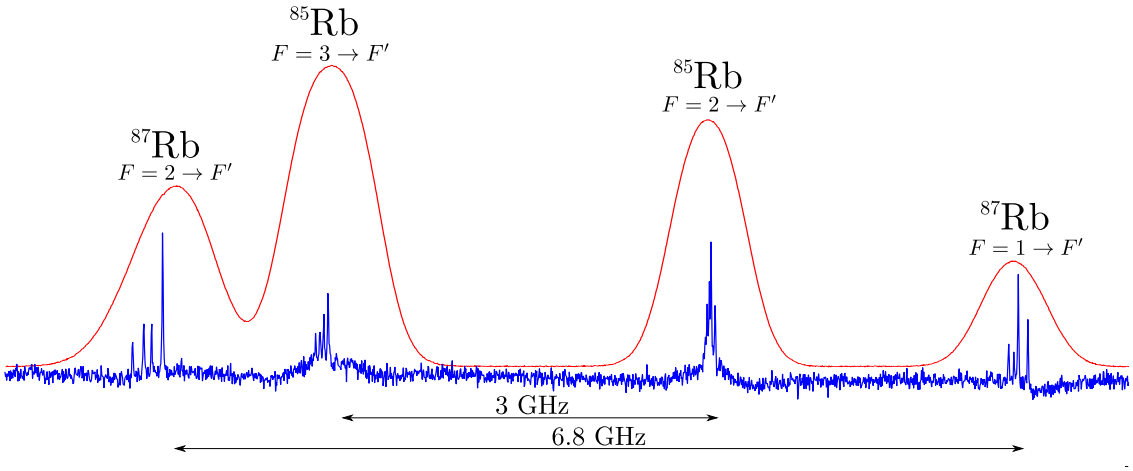

Figure 4.16 : Doppler-broadened (red) and Doppler-free (blue) transmission signals of the probe beam, for both isotopes of ^{85}Rb and ^{87}Rb present in the vapour cell.

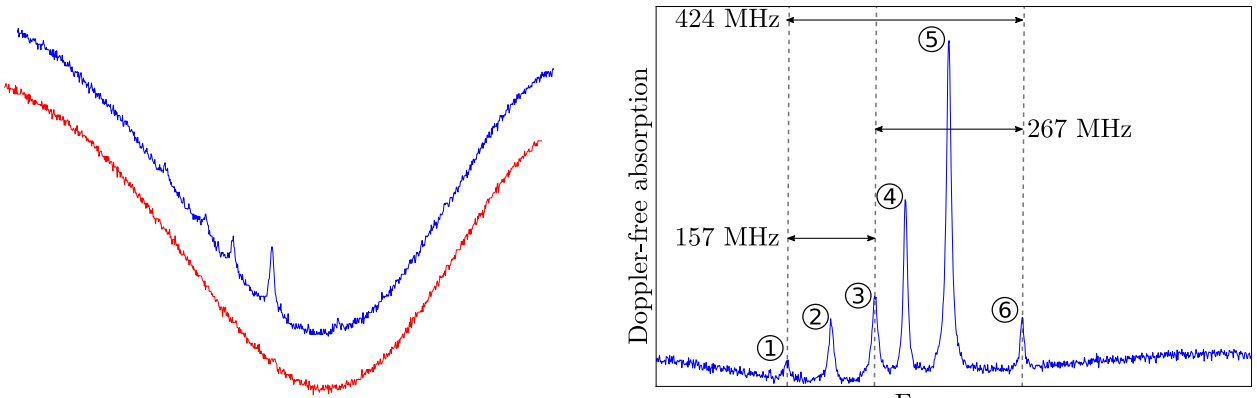

(a) Doppler broadened

(b) Doppler free

Figure 4.17 : Doppler-broadened (a) and Doppler-free (b) transmission signals of the probe beam for the $|F = 2\rangle \rightarrow F'$ transitions in ^{87}Rb. Peaks 1, 3 and 6 correspond to the transitions $|F = 2\rangle \rightarrow |F' = 1, 2, 3\rangle$, while 2, 4 and 5 are the crossover peaks. We lock on peak 5.

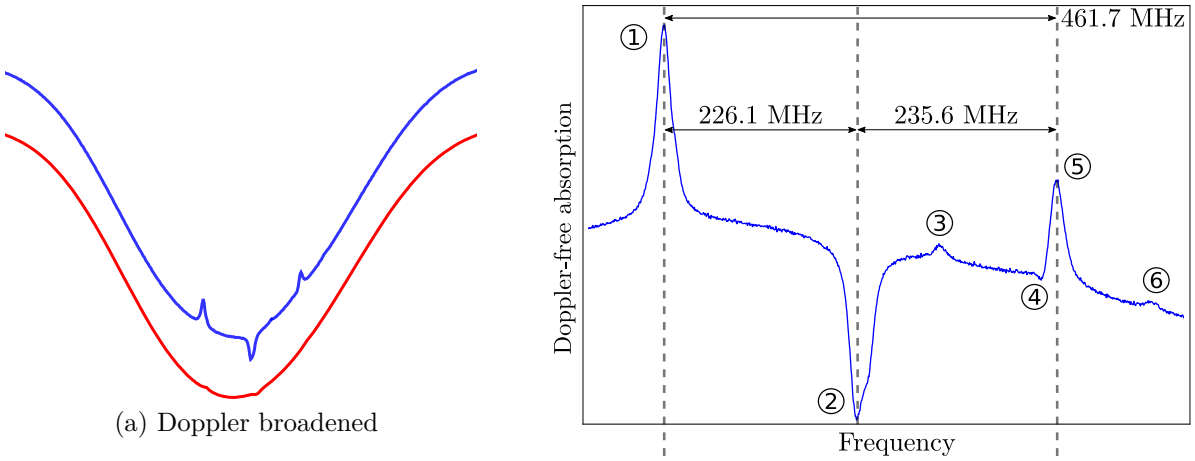

(a) Doppler broadened

(b) Doppler free

Figure 4.18 : Doppler-broadened (a) and Doppler-free (b) transmission signals of the probe beam for the $|F = 1\rangle \rightarrow F'$ (peak 1) and $|F = 2\rangle \rightarrow F'$ (peak 5) transitions in ^{39}K. Peak 2 is the crossover peak[6] (which we lock to), and peaks 3, 4 and 6 are the transitions and crossover peak for ^{41}K, also present in the vapour cell.

PDH locking

A PID stabilisation circuit requires an antisymmetric signal in order to provide feedback. The frequency may be locked to one of the slopes of the absorption peaks, *side of fringe locking*, but this causes it to be highly sensitive to intensity fluctuations. *Top of fringe locking* is therefore preferred as the peak's position is fixed irregardless of the intensity of the probe beam. Its symmetrical profile is circumvented by utilising its derivative as the

[6] Or, better, the resultant of the many crossover peaks caused by transitions among the internal $|F\rangle$ and $|F'\rangle$ states, as discussed in [94].

error signal to feed into the PID electronics. The technique is known as *Pound-Drever-Hall* (PDH) locking [170, 171] and it consists in modulating the laser carrier frequency ω with a small frequency Ω in order to add sidebands at $\omega \pm \Omega$:

$$\mathbf{E} = \mathbf{E}_0 \left(1 + \sin \Omega t\right) \mathrm{e}^{-\mathrm{i}\omega t} \propto \mathrm{e}^{-\mathrm{i}\omega t} + \mathrm{e}^{-\mathrm{i}(\omega-\Omega)t} + \mathrm{e}^{-\mathrm{i}(\omega+\Omega)t}, \tag{4.5}$$

where amplitude modulation was used above, but phase modulation is also common. The optical power P of the light can then be Taylor expanded to extract its derivative:

$$P(\omega \pm \Omega) \approx P(\omega) \pm \frac{\mathrm{d}P}{\mathrm{d}\omega}\Omega + \ldots. \tag{4.6}$$

The modulation frequency Ω needs to be large enough for its higher harmonics to be effectively filtered out, but also small enough not to interfere with the atomic transitions, and was chosen to be between $20 - 30\,\mathrm{kHz}$.

In order to obtain the steepest slope and hence the best error signal, we locked on the highest absorption peaks, i.e. the crossover lines in figs. 4.17 and 4.18. The linewidth of the lasers is $\sim 100 - 200\,\mathrm{kHz}$, and the emitted frequency of ^{87}Rb was shifted by 53 MHz to aid in later manipulation.

Delay-line locking

With one master laser ω_M locked to an atomic transition, the frequency of other diodes ω_D can be referenced to ω_M by means of *offset* or *delay-line* locking. All other atomic transitions are addressed using *acousto-optical modulators* (AOMs), where a laser beam propagating through an RF-driven crystal absorbs a phonon and experiences a deflection and a frequency shift. The optical power of this light may be later amplified by *Tapered Amplifiers* (TAs), which owe their name to the tapered shape in order to avoid an increase of the optical intensity which would lead to damage.

As illustrated in fig. 4.19, the two beams $\mathbf{E}_1$ and $\mathbf{E}_2$ are shone onto a photodiode, and eventually split into two paths of unequal length (the delay-line) so as to acquire a net phase difference $\phi(\omega_\mathrm{D} - \omega_\mathrm{M} = \Delta\omega)$, which yields the error signal:

$$V(t_\mathrm{scan}) = A(\Delta\omega)\, \mathbf{E}_1 \cdot \mathbf{E}_2 \cos\left(\frac{\omega_0 - \Delta\omega}{c}\Delta x \cdot t_\mathrm{scan}\right), \tag{4.7}$$

where A is the frequency dependence of the circuit, and ω_0 is a local oscillator mixed with the beat-note $\Delta\omega$. This allows remote change of the lock point (e.g. to vary the imaging frequency for ^{39}K in high magnetic fields) and results in a lower operational frequency, reducing loss and attenuation. A typical error signal is shown in fig. 4.20.

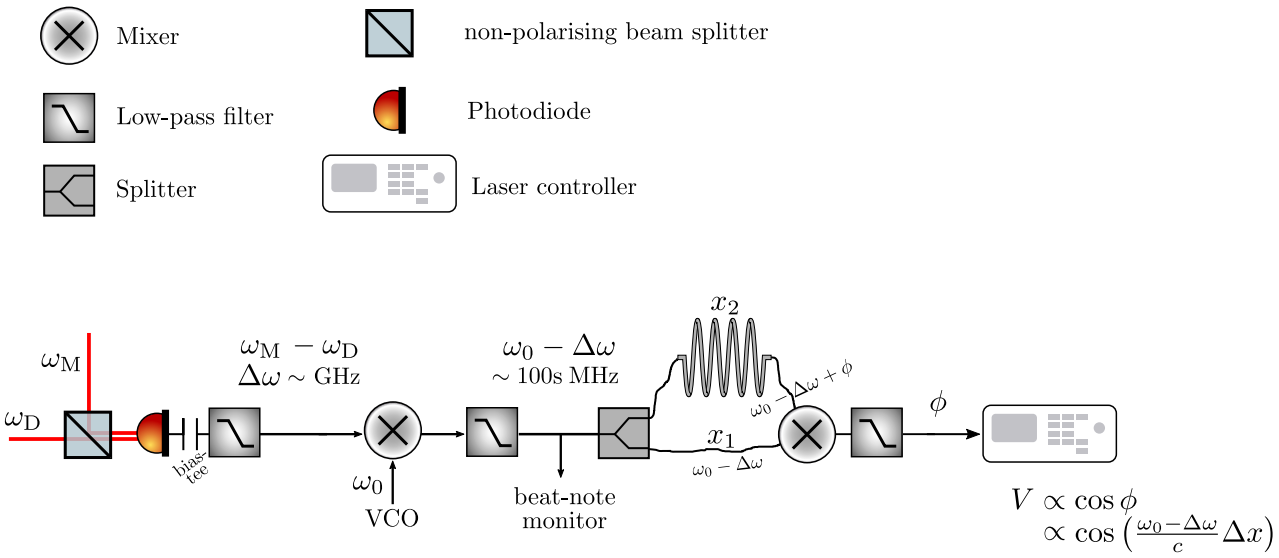

Figure 4.19 : Schematic diagram of a delay-line lock.

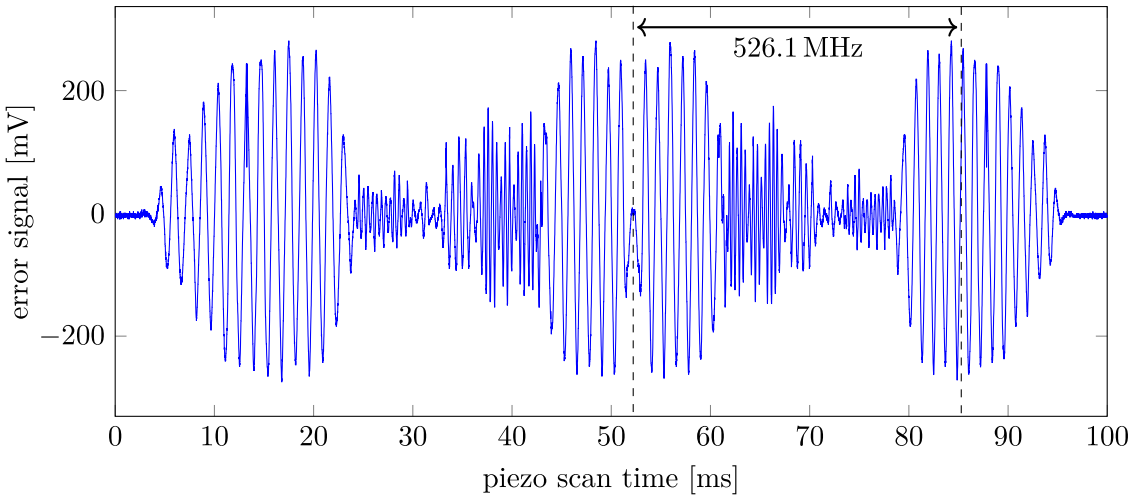

Figure 4.20 : The error signal for the Rb repump laser, locked at the marked position. Note the symmetry about the point where $\Delta\omega = 0$. Figure adapted from [172].

Isotope switch

Appendix B.2 details the optical beam paths of all laser radiation.
The experiment was designed to address the energy manifolds of both isotopes ^{39}K and ^{40}K, which only differ by the *isotope shift* [78]. To implement this "isotope switch", the laser apparatus consists of double-pass AOMs that guarantee a fixed direction of the outgoing beam irregardless of the drive frequency, so that it can inject the same fibre and reach the experiment chamber. This is shown in fig. 4.21.

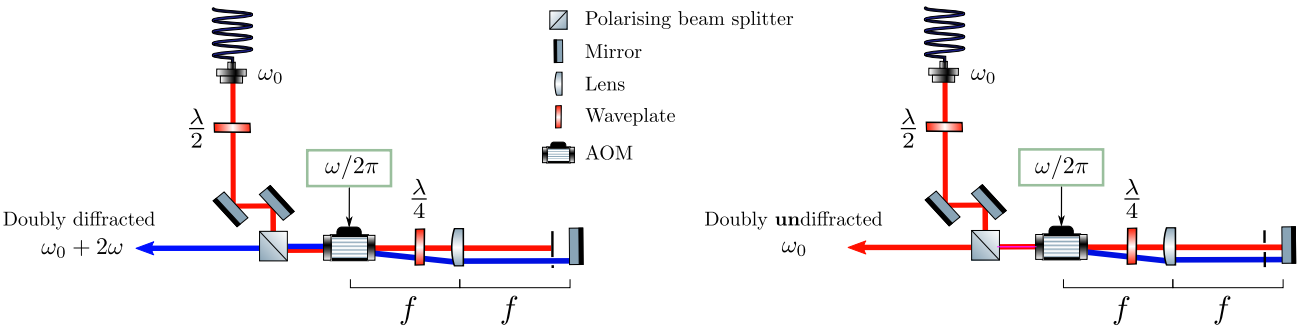

Figure 4.21 : The optical switch used to address either ^{39}K or ^{40}K. The lens in the double-pass AOM ensures that both the diffracted and undiffracted beams emerge along the same direction.

4.4 Control

Probing of the BEC occurs at the end of the cooling sequence. In order to investigate its evolution and its dependence on variable parameters, many identical sequences need to be performed. These rely on the reproducibility and reliability of the programmed time intervals, and is allowed by a centralised unit responsible for setting the absolute timing which all hardware devices are synchronised to.

This unit needs to be independent from the operating system, which is designed to always respond to tasks with higher priorities, from keyboard strokes to incoming network packages. Hence, the time keeping duties are delegated to external timing cards, that provide independent reference clocks and counters along with programmable digital and analogue output channels, schematically illustrated in fig. 4.23.

The software used for sequence programming and equipment control was written in `python` and developed by reserach groups at LMU and MPQ in Munich. It was installed for us by Hendrik von Raven. Having an open-source platform allowed developing and including more functionalities, such as a genetic algorithm to aid in optomisation [173] and a large number of devices such as cameras, the DDS[7] and the signal generators creating arbitrary optical lattice ramps. A short documentation for the signal generators programming is provided in appendix D.9.

Software and hardware communicate over a private network (`LAB network`) in order to reduce traffic and delays, and only require the building's network (`AMOP network`) to access the group's shared drive and save the data. Network communication is handled by `Pyro`, a python library consisting of a *name server*, listing the (logical) names of different objects on the network, and an *event server*, publishing and subscribing to information on the network.

Whilst the external cards ensure the timings of all controls are fixed relative to a master clock, the *mains synchroniser* guarantees the sequence starts at the same time relative to the 50 Hz mains frequency. Since mains noise cannot be completely eliminated, this synchronisation guarantees that the effect is the same on each experimental run. Its principle of operation is depicted in fig. 4.22, and its effect can be quantified by the recovery of Rabi oscillations (eq. 2.10) shown in fig. 4.23.

[7]Direct Direct Synthesis, a programmable frequency generator developed by Hendrik von Raven [172].

The machine also includes an alarm system, known as the *Schutzschaltung* thanks to (or because of) the intrinsic German heritage of the group, and an independent monitoring system that logs diagnostics online. `CARBON` is an open-source software that received data over the network and stores it in order to be subsequently manipulated by various web interfaces for monitoring, diagnostics, alarm raising etc. with API such as `Icinga2`, `Graphite` and `Grafana`.

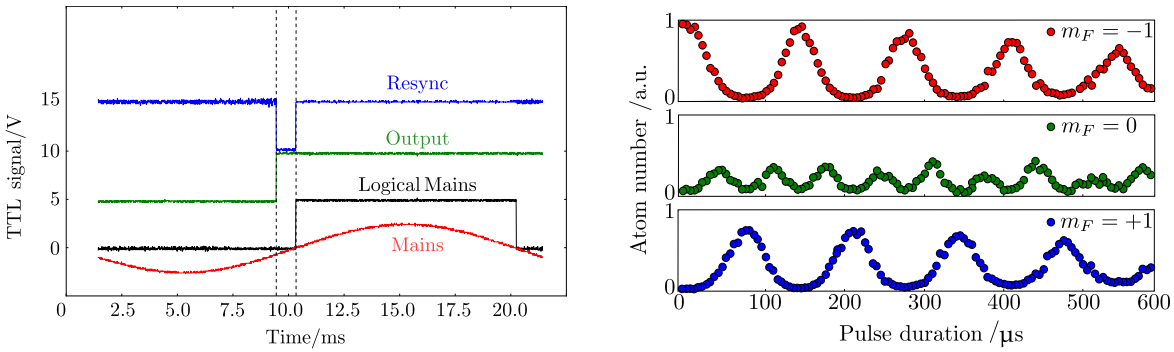

(a) Mains sync signals

(b) Rabi oscillations

Figure 4.22 : a) The main synchroniser allows the sequence to start (Resync) only when the previous sequence has finished (Output) and the mains frequency hits a rising edge. b) A small magnetic field lifts the m_F degeneracy in the ^{87}Rb $|F = 1\rangle$ ground state. An applied RF pulse of variable duration is expected to induce Rabi oscillations between these states, but the ambient field noise does not allow a discernible signal to be identified unless the mains synchroniser is operational.

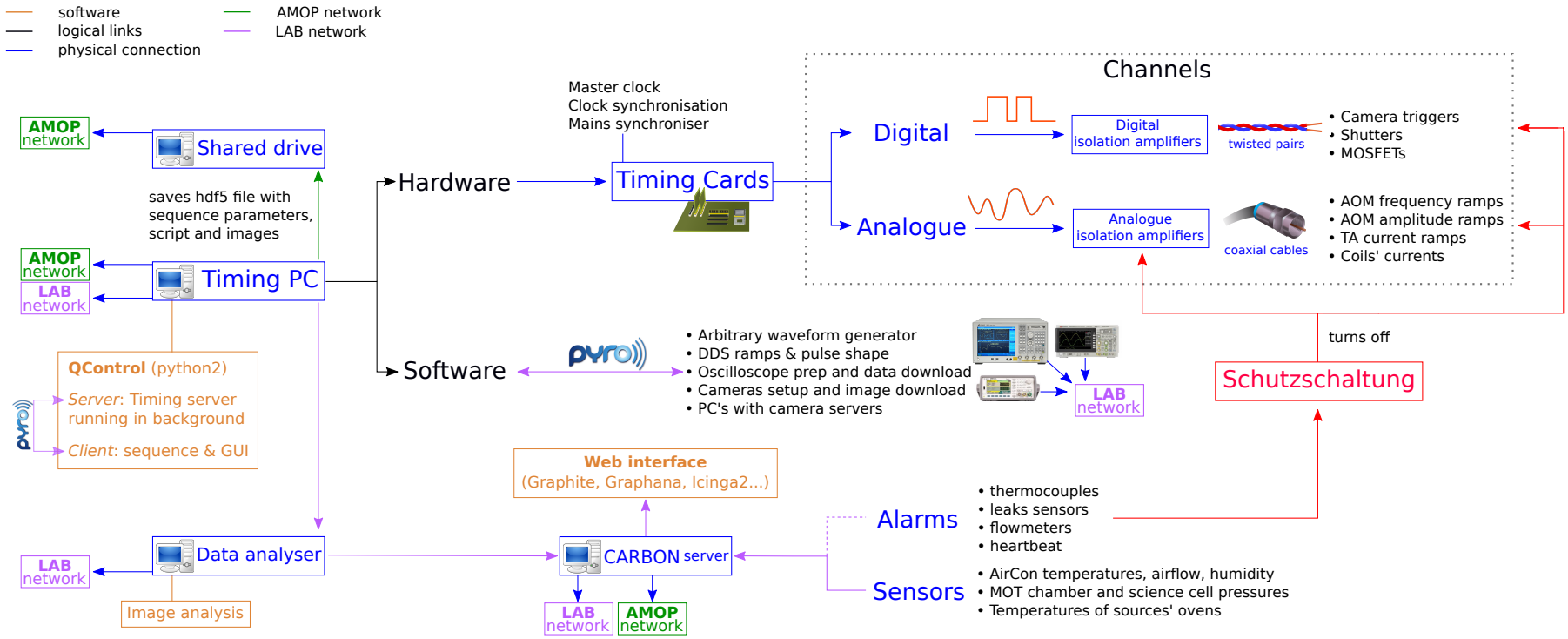

Figure 4.23 : Schematic diagram of the software and hardware control of the experiment. Dashed lines are yet to be implemented.

You can't go back and change the beginning but
you can start where you are and change the ending.

C.S. Lewis

5

Reaching quantum degeneracy

This chapter details the components taking part in the cooling stages, providing quantitative information about their assembly, operation and performance.

5.1 MOT chambers

The left section of the apparatus shown in fig. 4.1 performs laser cooling using the optical molasses, MOT and polarisation gradient techniques outlined in section 2.3.2.

5.1.1 2D MOT

The pressure in the 3D MOT is $\sim 10^{-11}$ mbar and it would take > 10 s to capture a large amount of atoms from the background vapour. Hence, each atomic source is placed next to a 2D MOT, filled with high-pressure atomic vapour ($\sim 10^{-7}$ mbar) whose purpose is to provide a stream of pre-cooled atoms to enable fast loading of the 3D MOT.

The 2D MOT is illustrated schematically in fig. 5.1, and shown in the experiment in fig. 5.4. This stage consists of the following simultaneous processes:

- a MOT along the two *transverse* directions x and y, giving it its name "2D" MOT;
- optical molasses along z provided by a linearly polarised *axial cooling beam*, whose reflected intensity is attenuated by an absorptive filter;
- continuous loading of cold atoms along the central axis $x = y = 0$ into the 3D MOT by a blue detuned, repulsive *push beam* propagating through the $\phi = 1.5$ mm differential pumping section.

The magnetic field is generated by two pairs of rectangular coils, arranged in the anti-Helmholtz configuration, to result in a quadrupole field in the transverse xy plane which is invariant along z, as shown in fig. 5.2. Table 5.1 summarises the magnetic field para-

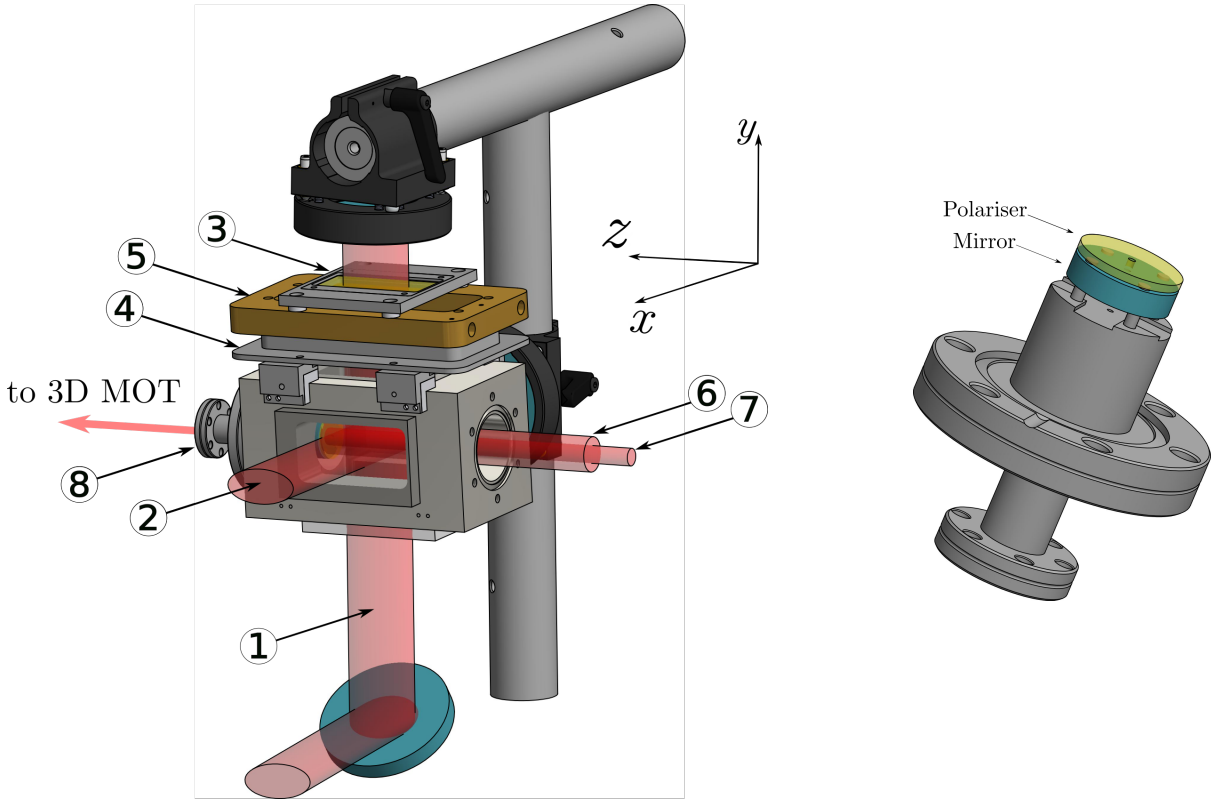

(a) 2D MOT (b) Differential pumping section

Figure 5.1 : Diagrams of the 2D MOT (a) and the differential pumping section (b). Two σ polarised elliptical beams (1, 2) are shone from the sides and retro-reflected through large $\lambda/4$ waveplates (3) to ensure maintenance of σ polarisation. A quadrupole magnetic field is generated by coils wound around a holder (4) and water-cooled by a brass heat sink (5). Optical molasses is performed along the z direction by the *axial cooling* beam (6), retro-reflected by a mirror on the differential pumping section (8) and through a polariser to tune its intensity. A blue detuned, repulsive *push* beam (7) continuously loads the cold atoms on the central axis of the 2D MOT into the 3D MOT.

meters, computed from the analytical solutions for rectangular coils quoted in appendix B.2.

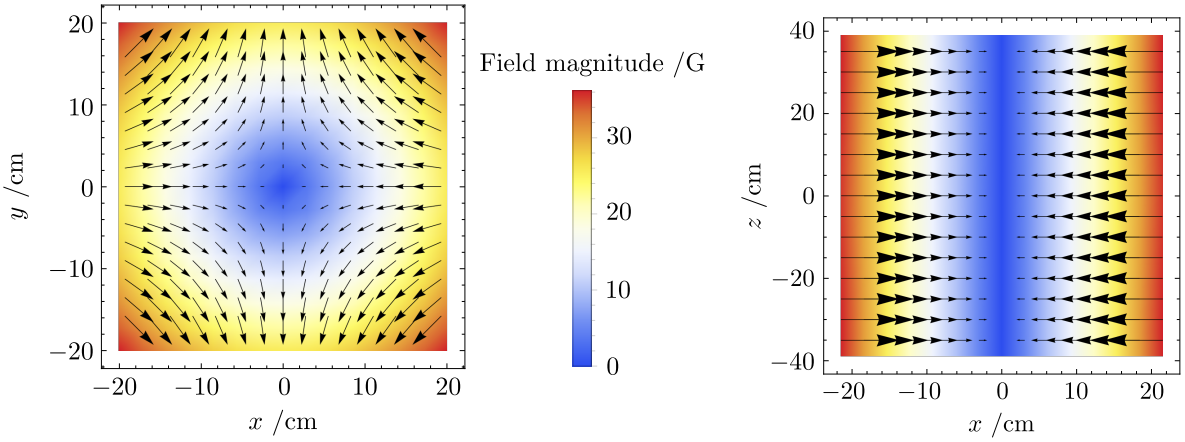

(a) Cross section (b) From above

Figure 5.2 : The magnetic field generated by the 2D MOT rectangular coils is a quadrupole field in xy (a) invariant along z (b).

	parameter	^{87}Rb	^{39}K
quadrupole field	gradient @ 1 A (per pair)	2.4 G/cm	
	windings per coil	63	
	current per coil	8.5 A	9.0 A
	field gradient	21 G/cm	22 G/cm
bias field	field @ 1 A (per pair)	1 G	
	windings per coil	8	
	current in x pair	0 A	2.5 A
	current in y pair	2.5 A	0.6 A

Table 5.1 : Magnetic field parameters for the 2D MOTs of each atomic species. On top of the quadrupole field coils connected in the anti-Helmholtz configuration, offset coils in the Helmholtz configuration were also wound in order to cancel the strong fields caused by the ion pumps and optical isolators.

The optical apparatus for the 2D MOT laser beams is shown in fig. 5.3 and summarised in table 5.2.
The transverse beams are elliptical in order to address a larger volume of the vapour, and their centres are shifted closer to the start of the differential pumping section as this resulted in enhanced loading. While the push beam was essential in the ^{39}K 2D MOT, it was not used on the ^{87}Rb side, where a power imbalance 60 : 40 between the incident and reflected axial cooling beams was found to be sufficient.
Alignment of the axial and push beams were crucial for a successful, efficient and quick loading of the 3D MOT.

	parameter	^{87}Rb	^{39}K
duration		2.5 s	1.0 s
cooling	detuning	−19 MHz	−28 MHz
	power	x : 230 mW, y : 320 mW	x : 190 mW, y : 260 mW
	single-waist	20 mm × 10 mm	
repump	detuning	0 MHz	−15 MHz
	power	x : 48 mW, y : 39 mW	x : 230 mW, y : 170 mW
	single-waist	20 mm × 10 mm	
axial cooling	detuning	−19 MHz	−28 MHz
	power	8.5 mW	1 mW
	single-waist	2 mm	
push	detuning		42 MHz
	power		2 mW
	single-waist		0.8 mm

Table 5.2 : The parameters for the lasers employed in the 2D MOT cooling stage.

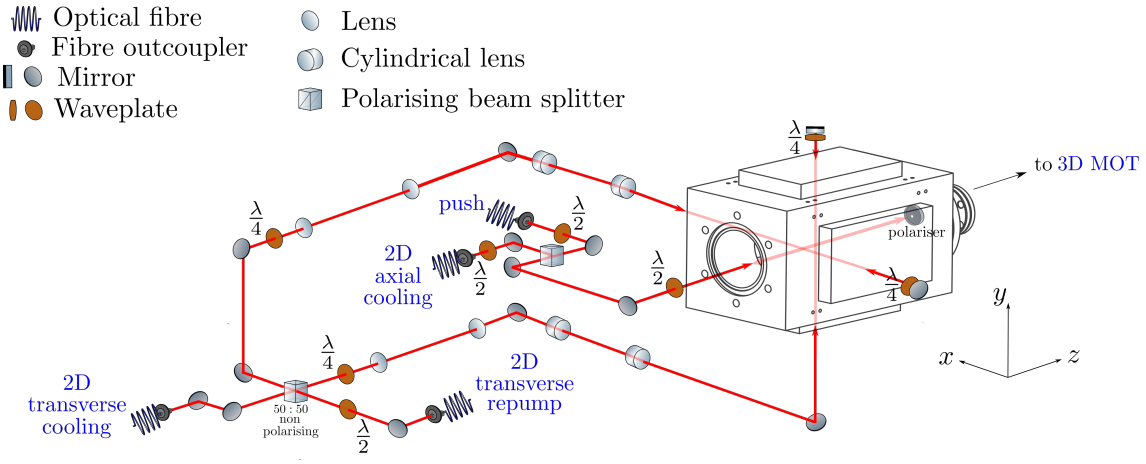

Figure 5.3 : The optical setup that delivers light to the 2D MOT.

Assembly

The 2D MOTs were assembled in-house, selecting vacuum-compatible materials with similar thermal expansion coefficients in order to allow baking.

A titanium (grade 2[1]) frame and bespoke windows were ordered for the chamber to be assembled in-situ. The components utilised in the assembly are listed in Table 3. These all have similar thermal expansion coefficients, to avoid thermal shocks and cracks while baking. The mirror, polariser and differential pumping sections are separated by titanium spacers, which minimised the glued area and thus the potentially trapped air that could undermine the integrity of the vacuum; this glue is thermally conductive to allow baking of the components.

[1]The grade indicates which alloy and what concentrations are present. They differ in strength, ductility and corrosion resistance, but should not be important for vacuum applications.

Component	Material	Thermal expansion $10^{-6}\,\mathrm{K}^{-1}$	Thermal conductivity $10^{-3}\,\mathrm{W/(m \cdot K)}$
Frame	Titanium, grade 2	9.2	20,800
Differential pumping section	Titanium, grade 2	9.2	20,800
Windows	BK7 glass	7.1	6.5
Mirror	BK7 glass	7.1	6.5
Polariser	N-BK7 glass	8.3	N/A
Spacers	Titanium, unknown grade	N/A	N/A
Glue (windows $\mapsto$ frame)	EPO-TEK® 353ND	54	N/A
Glue (mirror & polariser $\mapsto$ spacers)	EPO-TEK® 920	24	970

Table 5.3 : Components used in the assembly of the 2D MOT.

In order to guarantee vacuum compatibility, the glue was degassed with a desiccator pumped by the Scroll pump, reaching low 10^{-1} mbar.
A thin layer of Kapton film was added between the frame and the windows, so as for the windows not to expel all the glue.

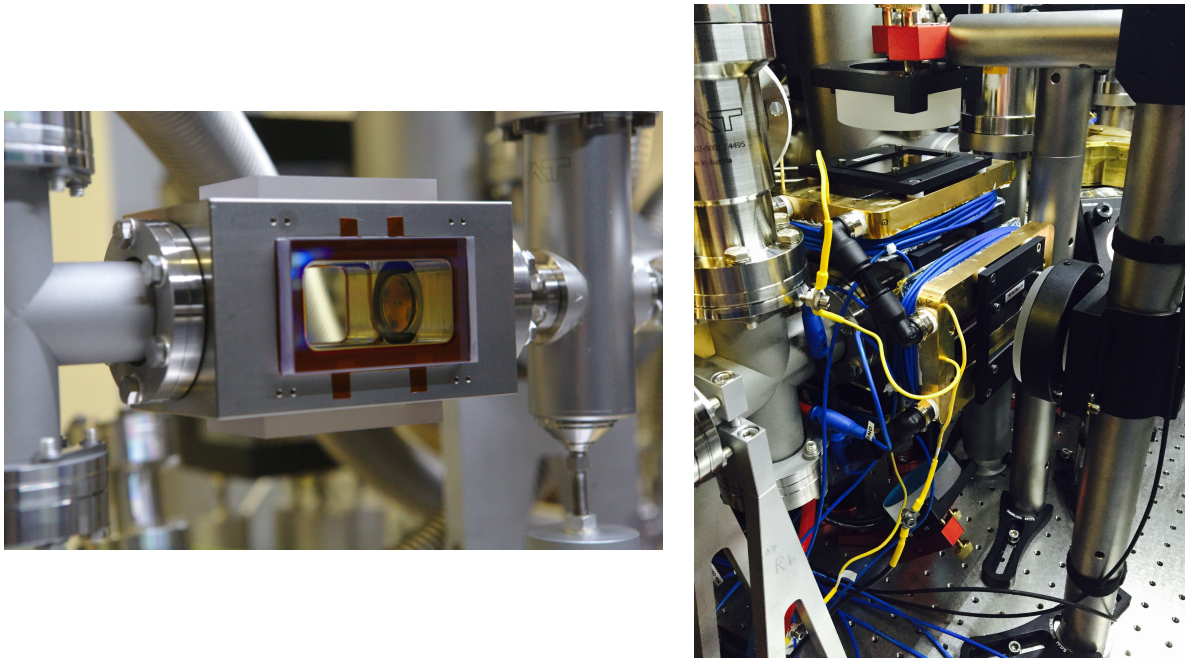

(a) (b)

Figure 5.4 : The assembled 2D MOT just after integration in the vacuum system (a) and during the operation of the experiment. Once cured, the glue attaching the windows turned orange. The yellow and blue wires are the quadrupole and the offset coils respectively.

5.1.2 3D MOT

Simultaneous to the incoming flux of pre-cooled atoms from the 2D MOTs, another MOT stage takes place for the combined species in the 3D MOT. This is exactly as outlined in

section 2.3.2, with a pair of circular coils providing a quadrupole field and three pairs of counter-propagating beams along each orthogonal direction.

The 3D MOT is shown in fig. 5.7 and its operating parameters are summarised in table 5.4. Cooling and repump light for both species are overlapped and distributed among the 6 fibres delivering them to the chamber by a commercial $2 \mapsto 6$ fibre cluster.

The density and temperature of the atomic cloud is eventually limited by the re-scattering of incoming photons, which results in additional effective forces preventing further increase of phase space density. In the last 10 ms of the MOT stage, the ^{39}K repump power was lowered to 2% of its previous value, in order to perform a "temporal dark-spot MOT" where the atoms in the $F = 1$ state would no longer participate in cycling transitions and hence experience a reduced scattering rate.

The MOT is followed by a polarisation gradient cooling stage, performed by the same laser beams and hence in the $\sigma^+ - \sigma^-$ configuration outlined in section 2.3.2, whose parameters are summarised in table 5.5. This is very short because the magnetic field is turned off and hence no restoring force counteracts the cloud's expansion.

The laser cooling stage lasts 2.5 s resulting in $\sim 3 \times 10^9$ ^{87}Rb atoms at $\sim 30\,\mu$K and $\sim 2 \times 10^8$ ^{39}K atoms at $\sim 470\,\mu$K, while the temperatures before polarisation gradient were $\sim 580\,\mu$K and ~ 1.1 mK respectively. Both laser cooling stages are better performing for ^{87}Rb owing to its resolved excited state manifold. ^{39}K is only loaded in the last 1 s of the MOT stage, which was found to result in the maximum number of atoms for both species.

A ^{87}Rb MOT is shown in fig. 5.7, and the fluorescence curves recorded during the loading stage are shown in fig. 5.6.
The size of the MOT is eventually limited by its high spatial density, which increases collisions with the background gas and enhance light assisted collisions. High densities also cause re-scattering of photons, which result in an equilibrium between a repulsive (from atoms absorbing re-scattered photons) and an attractive (from the beams' attenuation) force [174, 175].

5.1.3 Optical pumping

The atoms need to be spin-polarised into a low-field seeking m_F state in order to maximise the capture efficiency of the magnetic trap, as described in section 2.2.1 and shown in fig. 2.3. The experimental parameters used are summarised in table 5.6.

A ~ 10 G homogeneous field is present during this stage in order to provide a quantisation axis and to lift the degeneracy among the m_F sub-levels. For ^{87}Rb, σ^- light is used, and repump is only active for the first half of the procedure, in order to accumulate atoms in the $|F = 1, m_F = -1\rangle$ state. For ^{39}K, we did not manage to efficiently perform optical pumping, hence no radiation addressing this species is used. The success of the evaporative cooling stage established enough ^{39}K was being transported to the science cell, hence further investigations into the failure of optical pumping were not performed.

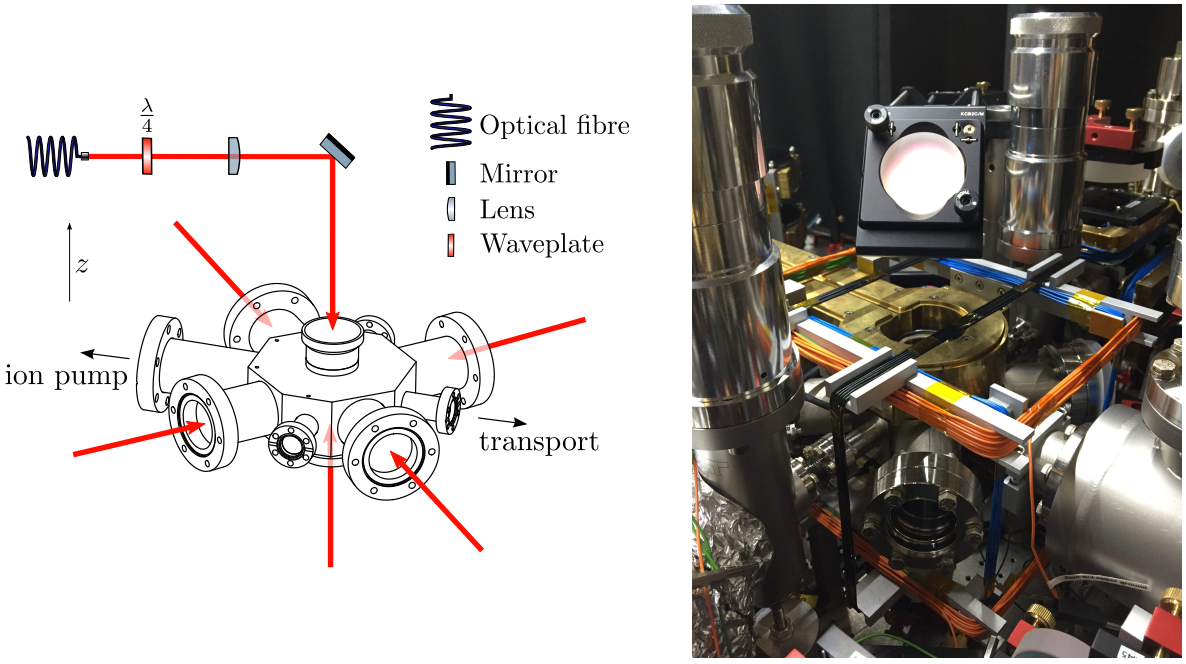

(a) (b)

Figure 5.5 : The optical apparatus to shine laser light into the 3D MOT is schematically shown in (a) and looks like (b) in real life. The brass circular structure houses the coils generating the quadrupole magnetic field.

	parameter	^{87}Rb	^{39}K
duration		2.5 s	1.0 s
cooling	detuning	−23 MHz	−52 MHz
	power	95 − 130 mW	40 − 46 mW
	single-waist	13 mm	
repump	detuning	0 MHz	−25 MHz
	power	0.7 − 1.0 mW	60 − 87 mW
	single-waist	13 mm	
quadrupole field	z gradient @ 1 A	1.78 G/cm	
	current per coil	11 A	
	field gradient	20 G/cm	
bias field	field @ 0.4 A (per pair)	1 G	
	windings per coil	6	
	current in x pair	1.5 A	
	current in y pair	1.5 A	
	current in z pair	0.3 A	

Table 5.4 : Parameters for the dual-species 3D MOT stage.

	parameter	^{87}Rb	^{39}K
duration		4.5 ms	
cooling	detuning	−63 MHz	−4 MHz
	power	26 − 35 mW	16 − 18 mW
repump	detuning	0 MHz	−45 MHz
	power	0.7 − 1.0 mW	1.9 − 2.8 mW

Table 5.5 : Parameters for the polarisation gradient cooling stage that follows the 3D MOT stage.

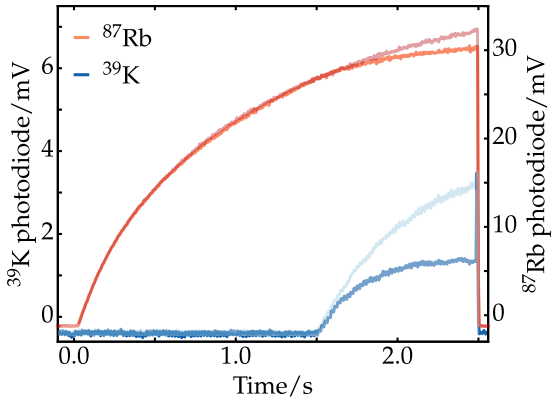

Figure 5.6 : Fluorescence curves measured by the appratus shown in fig. 6.1, when the two species are loaded alone (opaque) or together (solid). These provide a measurement for the loading time and final atom number of both species. Figure taken from [94].

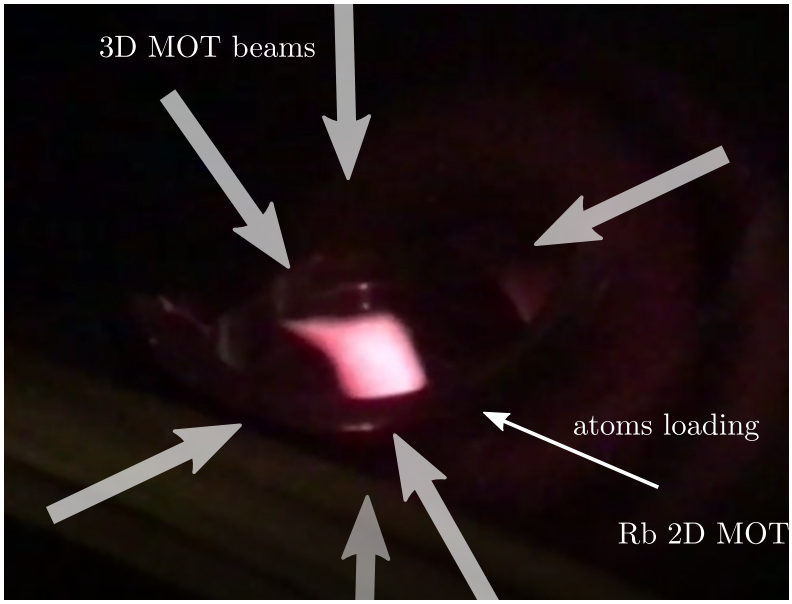

Figure 5.7 : Picture of ^{87}Rb in the 3D MOT chamber, without any ^{39}K present. The incoming flux of atoms from the 2D MOT pierces the cloud and results in the tail appearing in the top-left corner.

	parameter	^{87}Rb
pumping	duration	100 µs
	detuning	−3 MHz
	power	1.5 mW
	single-waist	3 mm
repump	duration	45 µs
	detuning	0 MHz
	power	0.4 mW
	single-waist	3 mm
guide field	field @ 1 A (pair)	1 G/cm
	windings per coil	15
	field	10 G

Table 5.6 : Parameters for the optical pumping stage of ^{87}Rb. No optical pumping was performed for ^{39}K.

5.2 Magnetic transport

After optical pumping, a quadrupole magnetic field in the 3D MOT chamber is ramped to $\sim 100\,\mathrm{G/cm}$ to magnetically trap the atomic cloud. This is then transported to the science cell via the series of overlapping coil pairs shown in fig. 5.8, each connected in the anti-Helmholtz configuration and varying its current to allow the smooth transition of the field minimum illustrated in fig. 5.9.

The atoms cover a total distance of $\sim 65\,\mathrm{cm}$ in 5 s. The magnetic field ramps were designed to maintain the atomic cloud aspect ratio and minimise heating. Including a smooth acceleration at the beginning and end of each current ramp proved to be crucial to the success of magnetic transport. Non-magnetic materials were employed both in the vacuum system and in the water-cooled coils holder in order to guarantee minimal disruption to the simulated magnetic field configuration. Eddy currents were also reduced by including slots in the metallic components, where possible.

The transport efficiencies for the two species are summarised in fig. 5.10. A ^{87}Rb cloud at $\sim 50\,\mu\mathrm{K}$ at the start of the transport stage was found to have increased its temperature to $\sim 200\,\mu\mathrm{K}$ when reaching the science cell.

Only 3 pairs of coils are active at any given moment during magnetic transport, enabling the use of a limited number of current sources. These are switched between the coil pairs via MOSFETs[2], as shown in fig. 5.11a. The final coil pair, the "experiment coils", was manufactured in-house and is connected to an H-bridge (fig. 5.11b) to allow operation both in the Helmholtz and anti-Helmholtz configuration, thus switching from the trapping quadrupole field to a homogeneous Feshbach field. The technical details and magnetic field parameters of the experiment coils are summarised in tables 5.7 and 5.8.

[2]The electronics for the magnetic transport was designed and manufactured by Dr. Stephen Topliss. Field effect transistors (MOSFETs) are used instead of bipolar transistors (BJTs). In BJTs, the collector-emitter current is related to the base-emitter *current* by the h_{FE} parameter, such that a $\sim 100\,\mathrm{A}$ current in the coils would require $\sim 100\,\mathrm{mA}$ to open the channel, large enough to require its own specialised current source. In MOSFETs, on the other hand, the drain-source current is controlled by the gate-source *voltage*.

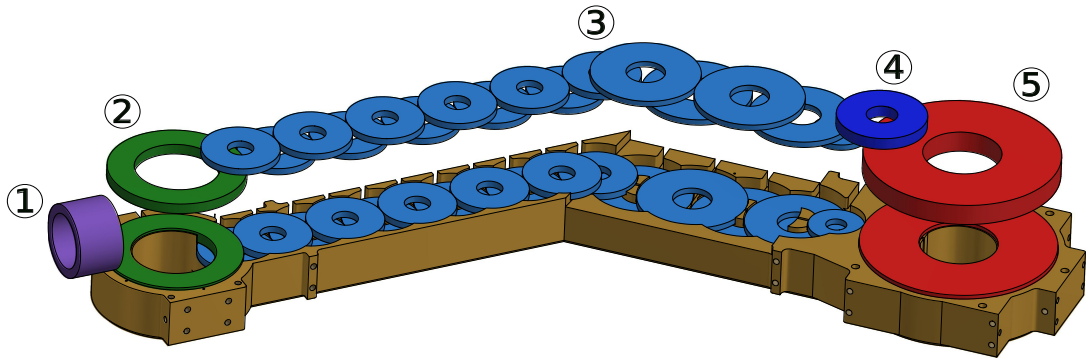

Figure 5.8 : Magnetic transport is performed by a series of coils connected in the anti-Helmholtz configuration, as shown in fig. 5.9. These include a "push" coil (1) which aids in initiating the transfer, the coils used in the MOT stage (2), other transport coils (4, 5) and finally the experiment coils, which also provide the Feshbach field. The coils are placed in a water-cooled brass "cooling block" which guarantees stability and reproducibility of the fields.

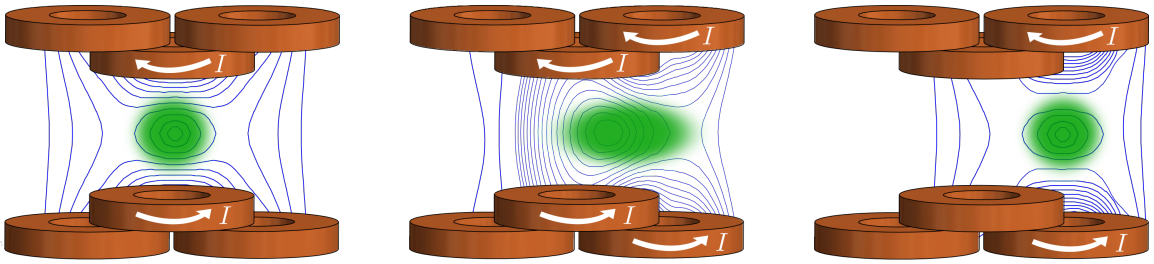

Figure 5.9 : In order to transfer the atomic cloud (green), the current in the next coil pair is gradually increased while the one in the previous pair is reduced, resulting in a smooth translation of the magnetic field minimum.

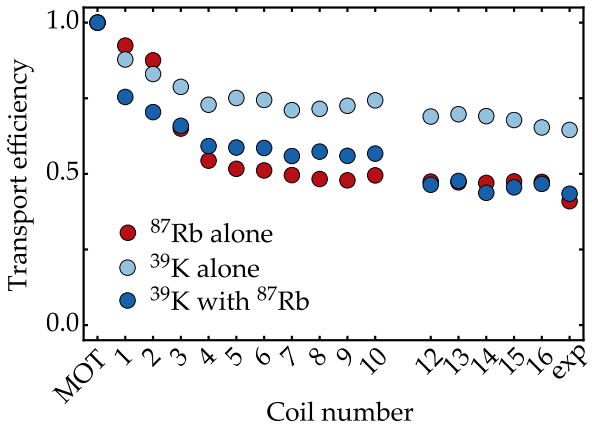

Species	Efficiency
^{87}Rb alone	64%
^{39}K alone	80%
^{39}K with ^{87}Rb	66%

Figure 5.10 : The magnetic transport efficiency is measured by the cloud's fluorescence in the 3D MOT chamber. The return (left) and single-journey (right) efficiencies are shown here. Figure adapted from [94].

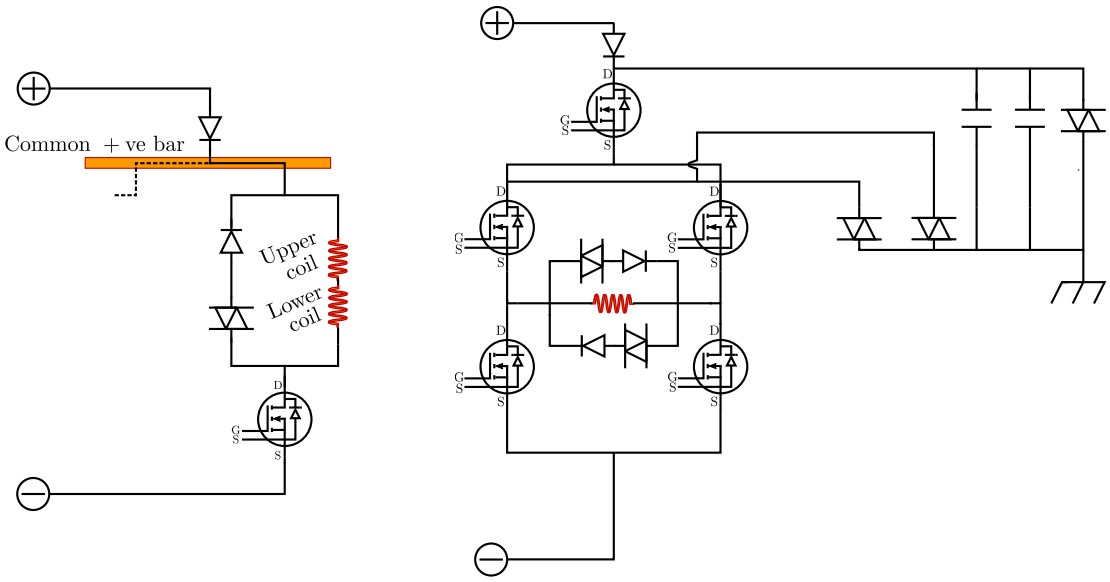

(a) (b)

Figure 5.11 : a) Each power supply is connected to multiple MOSFETs, each enabling current to reach a particular coil pair, in order to drive the 19 pairs of coils with only 3 current sources. The circuitry also includes a return path for the current (with a diode and a varistor) when the MOSFET is open, in order to reduce the back-emf spike and avoid damage. b) The upper coil in the final pair is connected to an H-bridge, which allows the current direction to be reversed. This enables the "experiment coils" to generate either a quadrupole or a homogeneous field.

thickness	inner diameter	outer diameter	windings	electrical resistance
h	ϕ_{in}	ϕ_{out}		R
$16.9 - 17.1\,\text{mm}$	$62 - 63\,\text{mm}$	$148\,\text{mm}$	75	$45,55\,\text{m}\Omega$

Table 5.7 : The experiment coils were machined in-house, their parameters are reported here.

configuration	field @ 1 A
anti-Helmholtz	3.44 G/cm
Helmholtz	11 G

Table 5.8 : The H-bridge of fig. 5.11 allows the experiment coils to produce either a quadrupole or a homogeneous magnetic field, when connected in the anti-Helmholtz or in the Helmholtz configurations.

5.3 Evaporative cooling

5.3.1 Science cell

Layout

The magnetic transport allows transferring the atoms to the science cell, shown in fig. 5.12, where the evaporative cooling stage and all subsequent lattice experiments are performed. Additional coils were wound around the science cell to cancel any ambient magnetic field caused by the ion pumps or by the optical isolators, whose parameters are summarised in table 5.9. In particular, the pair providing the vertical homogeneous field is driven by a programmable current source, in order to shift the magnetic trap minimum to efficiently load the optical trap.

Two breadboards are placed around the science cell, as shown in fig. 5.13 and schematically illustrated in fig. 5.14. These provide the optical beam paths for imaging light, the crossed-beam dipole trap and the optical lattices. The length of the beam paths was minimised in order to increase stability and maximise optical access.

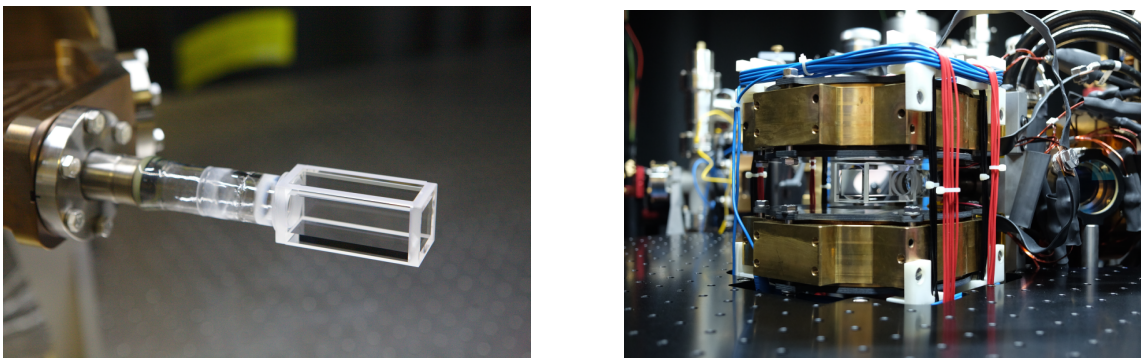

(a) (b)

Figure 5.12 : The science cell just after its inclusion in the vacuum system (a) and in the operational experiment (b).

axis	field @ 1 A (pair)	windings	current (pair)
D	0.6 G	6	4.5 A
T	0.6 G	6	1.5 A
Z	0.6 G	12	0.2 A

Table 5.9 : Three pairs of coils in the Helmholtz configuration are wound around the science cell as shown in fig. 5.12b to cancel background magnetic fields.

5.3.2 Evaporation in a magnetic trap

The magnetic transport stage ends with the atomic cloud in the $|F = 1, m_F = -1\rangle$ state, magnetically trapped in the science cell in a quadrupole trap of gradient 100 G/cm. This has a large acceptance region and can therefore accommodate a larger number of highly energetic ("hotter") atoms, the majority of which would otherwise be lost if the crossed-dipole optical were loaded directly.

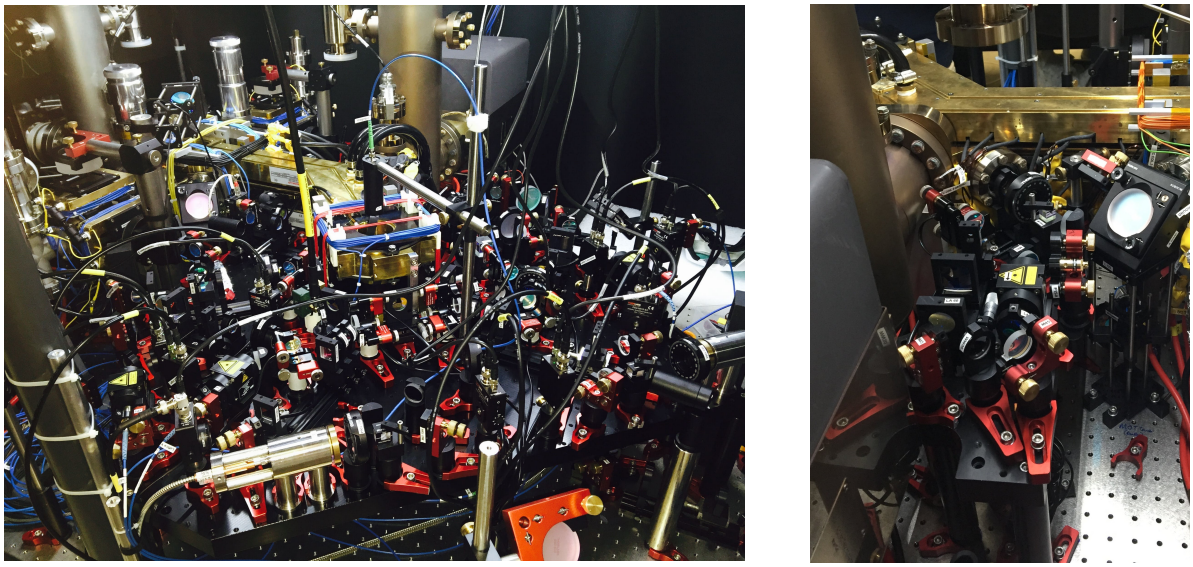

(a) Science breadboard (b) Knee breadboard

Figure 5.13 : A Hamiltonian in real life. The optical beams paths to probe and trap the atoms are assembled on two breadboards, code-named "science" (a) and "knee" (b).

A first evaporative cooling stage is then performed in the magnetic trap. When compared to the atomic cloud size, the extent of the magnetic trap is essentially infinite for any field strength. Hence, the reduction of the trap depth explained in section 2.3.3 cannot be performed by decreasing the magnetic field. Instead, a microwave (MW) radiation generated by a waveguide is shone onto the atoms in order to cause a transition to the magnetically untrapped state $|F = 2, m_F = -2\rangle$, resulting in particle loss and enabling thermalisation of the remaining atoms to a lower temperature. This is then referred to as *forced evaporation*. The gradient of the magnetic trap is ramped to 300 G/cm to increase the spatial density and enhance the elastic scattering and thermalisation rates.

Because of the smaller ^{39}K cloud produced in the 3D MOT chamber, further loss of ^{39}K atoms in this stage is avoided by only evaporating ^{87}Rb. The cold ^{87}Rb cloud then sympathetically cools ^{39}K, whose temperature decreases while maintaining the same number of atoms. The frequency of the MW radiation (often called a "knife") is ramped from low frequencies to high frequencies in order to first address the most energetic atoms, situated far from the centre of the trap, as shown in fig. 5.15.

The stage consists of three linear ramps, each lasting 2.5 s, with edge values of 176 MHz, 190 MHz, 279 MHz and 327 MHz, which were mixed with a 6.8 GHz VCO in order to address the ^{87}Rb ground state hyperfine splitting. The precise values of the frequencies were optimised by a genetic algorithm [173] programmed to maximise the phase space density of the cloud loaded in the crossed-dipole trap, given by eq. 1.46.

H]

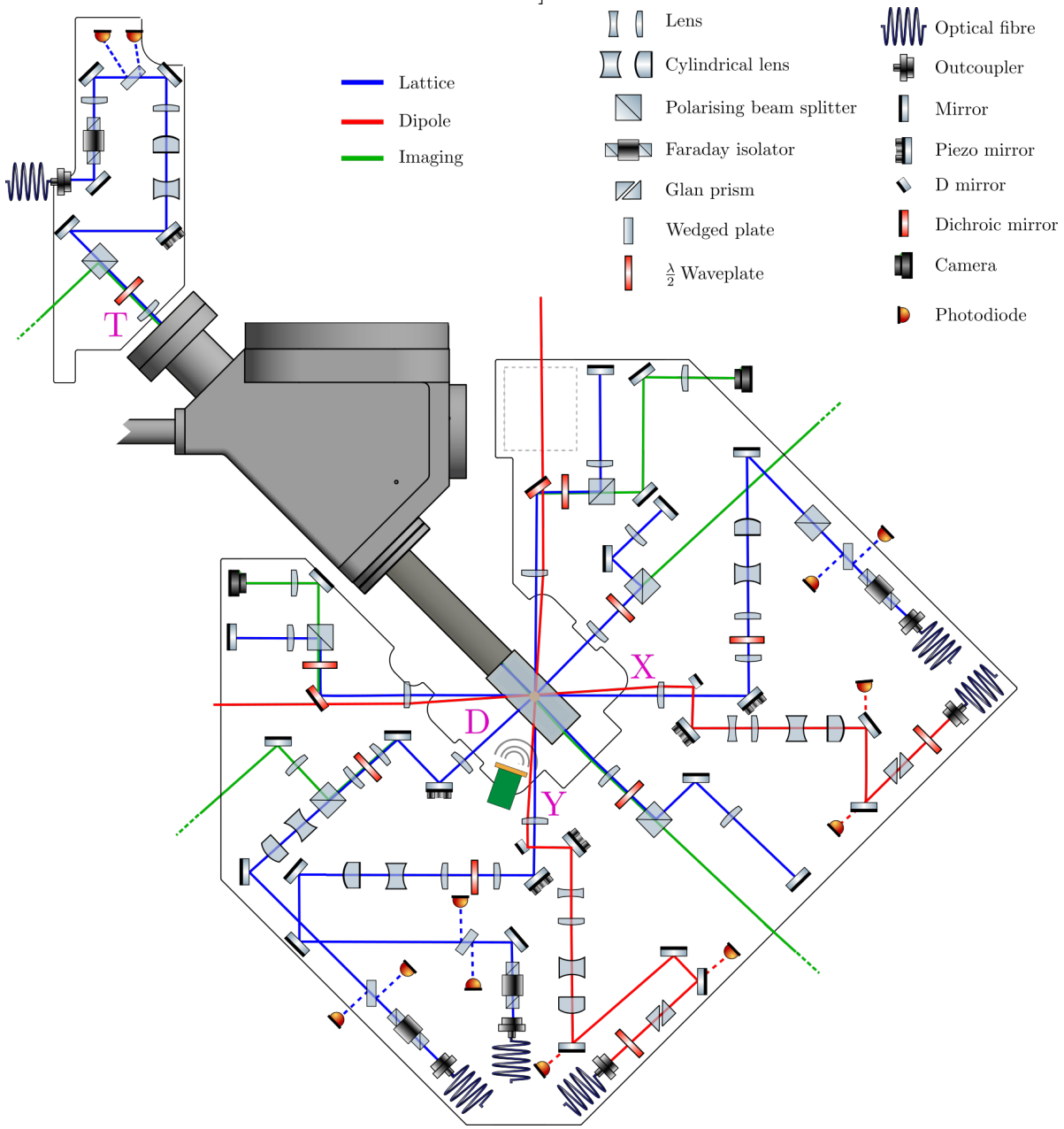

Figure 5.14 : A schematic illustration of the laser beams illuminating the atoms in the science cell. All radiation is collected in one of four axes X, Y, D (diagonal), and T (transport). The dashed rectangle next to the knee is the fluorescence imaging setup illustrated in fig. 6.1.

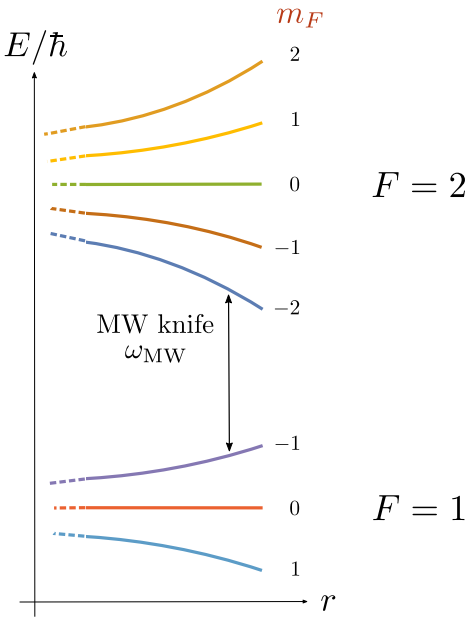

Figure 5.15 : The microwave radiation ω_{MW} results in atoms transitioning to the untrapped $|F = 2, m_F = -2\rangle$ state and hence escape from the trap. The frequency is increased in order to address less energetic atoms situated nearer the magnetic trap minimum.

This evaporation stage results in $\sim 3 \times 10^7$ ^{87}Rb atoms at $\sim 10\,\mu$K and in $\sim 2 \times 10^6$ ^{39}K atoms at $\sim 7\,\mu$K. These temperatures were found to be sufficiently low to efficiently load the crossed-beam dipole trap, which enables the use of a homogeneous magnetic field to induce repulsive interactions in ^{39}K, whose negative background scattering length would otherwise lead to a collapse preventing the onset of a stable Bose-Einstein condensate.

Further cooling is hindered by the Majorana losses discussed in section 2.2.1, which become more severe as the cloud increases its density near the centre of the trap. An optical plug was originally superimposed with the magnetic trap minimum, which allowed the evaporation to be performed for longer, reaching $2 - 3\,\mu$K (quantitatively investigated in [94]). However, the $\sim 10\,\mu$K clouds were found to already be efficiently loaded in the dipole trap. Furthermore, the plug had a $\sim 20\,\mu$m single beam waist and was hence very sensitive to misalignment. Its elimination from the apparatus thus caused more joy than sorrow.

5.3.3 Evaporation in an optical trap

State transfer

The transfer from the magnetic trap to the crossed-dipole optical trap is illustrated in fig. 5.16. After the optical trap is ramped to its highest power, 7 W, the quadrupole field is ramped to zero. A guide field of $\sim 2.8\,$G is produced by the z offset coils of the science to provide a quantisation axis for the atoms not to lose their spin-polarisation.

A radio frequency (RF) wave generated by an antenna (whose design is detailed in [94]) above the science cell is shone onto the atoms for 20 ms, its frequency ramped between $1.95\,\mathrm{MHz} \pm 20\,\mathrm{kHz}$ in order to perform a Landau-Zener transition from the $|m_F = -1\rangle$ to the $|m_F = 1\rangle$ state in both ^{87}Rb and ^{39}K, as explained in section 2.1.2. This state transfer

allows the atomic cloud to now be in the absolute ground state of the energy manifold, where the reduced loss channels guarantee a longer lifetime.

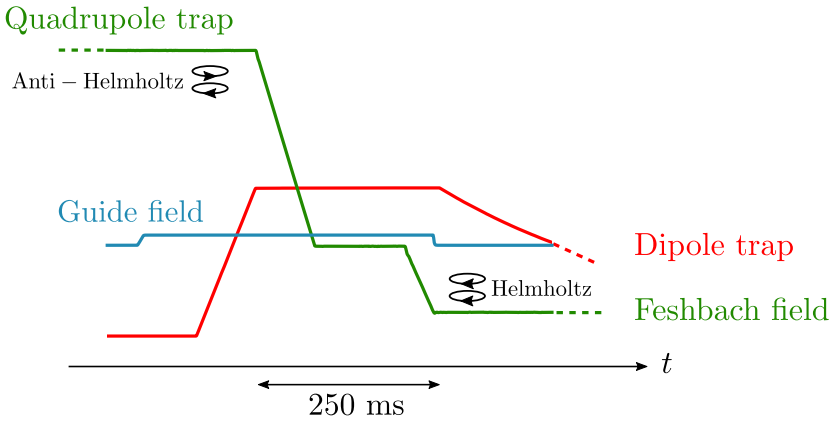

Figure 5.16 : The atoms are transferred from a magnetic to an optical dipole trap. A guide field provides a quantisation axis in order for an RF wave (light red solid rectangle) to perform a Landau-Zener transition from $|m_F = -1\rangle$ to $|m_F = 1\rangle$, the absolute ground state. At the start of the second evaporative cooling stage, the experiment coils produce a homogeneous magnetic field to access the Feshbach resonance.

axis	w_h /µm	w_v /µm
X	284	64
Y	280	47

Table 5.10 : Horizontal (h) and vertical (v) waists of the beams generating the dipole trap.

Magnetic field calibration

The efficiency of the state transfer is also used to calibrate the magnetic field strength at the atomic position. A Stern-Gerlach coil provides a magnetic field gradient in the vertical (z) direction during the first 3 ms of time-of-flight. The interaction with the inhomogeneous field results in an m_F dependent force which allows recording the population of the individual m_F sub-levels when imaging from an orthogonal direction (D), as shown in fig. 5.17. It is important for the Stern-Gerlach field to be in the same direction as the bias field of the science cell in that direction: if not, at some time the two field will cancel, resulting in no guide field for the atoms, which leads to a complete admixture of all m_F sub-levels.

The centre frequency of the RF sweep is varied until a complete state transfer is achieved. The frequency at which this occurs provides a measurement for the magnetic field, using the plots in section 4.3.1. The width of the sweep is reduced until it has no effect on the measured linewidth of fig. 5.18a. This was found to be ~ 20 kHz, and is due the ambient magnetic field noise.

The magnetic field calibration is then used to locate the Feshbach resonance, as shown in fig. 5.18b. Atoms are held in the dipole trap in the presence of a homogeneous magnetic field which, as discussed in section 1.3.1, affects their scattering length a and increases

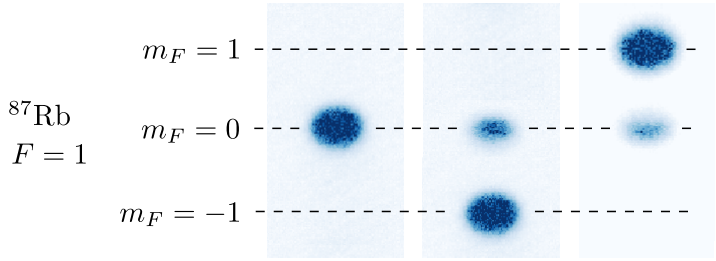

Figure 5.17 : Imaging the cloud after time-of-flight yields no information on its m_F states (left), as they fall equally under gravity. A Stern-Gerlach coil produces a magnetic field gradient and hence an m_F dependent force. Without state transfer, the cloud is in $|m_F = -1\rangle$ (middle), while a successful state transfer results in the cloud being in $|m_F = 1\rangle$ (right). The spurious $|m_F = 0\rangle$ are probably created by the Stern-Gerlach pulse.

the three-body recombination losses ($\propto a^4$). The Feshbach resonance B_{res} of eq. 1.57 is then identified as the magnetic field resulting in the greatest loss.

Evaporation

The evaporative cooling stage in the crossed-beam dipole trap occurs exactly as described in section 2.3.3. The intensity of the red detuned beams is decreased in order to reduce the trap depth, inducing particle loss and thermalisation of the remaining atoms to a lower temperature.

However, the dipole potential U_{dip} is not the only interaction affecting the atoms. A gravitational gradient mgz is also present and shifts the location of the trap minimum z_0:

$$z_0 \quad \Leftrightarrow \quad \frac{\mathrm{d}}{\mathrm{d}z}\left(U_{\text{dip}} + mgz\right) = 0, \tag{5.1}$$

as shown in fig. 5.19. This results in a minimum value of the laser intensity below which atoms cannot be trapped, referred to as "dipole bottom", found to be $\sim 200\,\text{mW}$ for ^{39}K and $\sim 400\,\text{mW}$ for ^{87}Rb. Because the gravitational sag depends on the atomic mass, it causes a spatial separation between the two species, reducing the efficiency of sympathetic cooling. Eventually, ^{87}Rb is completely lost from the trap, leaving a pure ^{39}K cloud.

In order to enhance the thermalisation efficiency, a homogeneous magnetic field is used to tune the interaction strength of the atoms. As summarised in table 5.11, this is first tuned near the inter-species ^{87}Rb-^{39}K Feshbach resonance, and, when ^{87}Rb atoms are lost, near the intra-species resonance in ^{39}K to ensure a repulsive interaction and prevent collapse. The trap depth is reduced until the onset of the Bose-Einstein condensate, as shown in fig. 5.20.

The trapping frequencies of the crossed-dipole are measured by ramping the optical power P to $P+\epsilon$ and then instantaneously decreasing it to P. Because of the imperfect alignment of the beams, this is sufficient to provide the atoms with a transverse velocity, resulting in a simple harmonic motion in the trap. The trapping frequencies are shown in fig. 5.21, and they exhibit the square root behaviour expected from eq. 2.34, but deviate from it because of the presence of gravity.

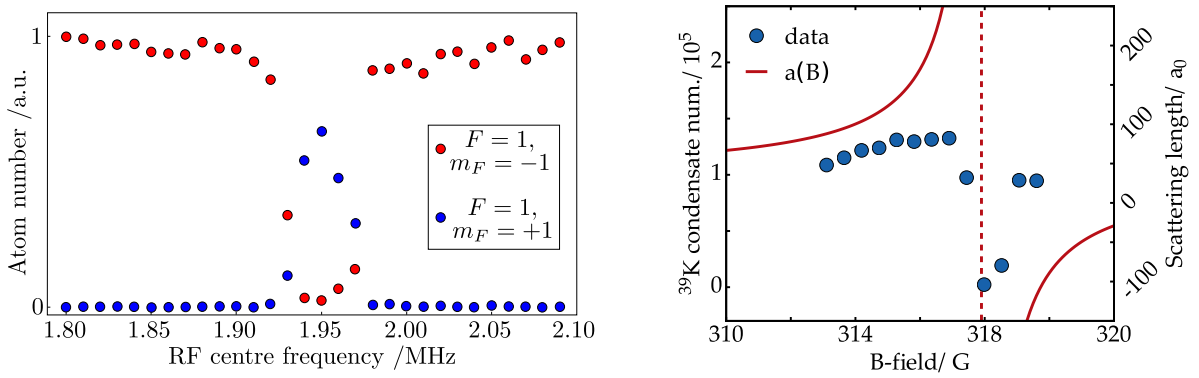

(a) (b)

Figure 5.18 : a) Magnetic field calibration via RF spectroscopy. The frequency of an RF signal is varied until resonant with the Zeeman shift, enabling maximal state transfer and hence providing a measurement of the field. b) The atoms are held in the dipole trap at different homogeneous magnetic field strengths. Three-body recombinations increase with scattering length ($\propto a^4$) and hence cause maximal loss at the Feshbach resonance, shown here for the inter-species interaction ^{87}Rb-^{39}K.

		duration	magnetic field B	scattering length a/a_0
inter-species	^{87}Rb-^{39}K	1.7 s	315.5 G	141
intra-species	^{39}K-^{39}K	1.3 s	397.8 G	280

Table 5.11 : During the evaporation in the dipole trap, a homogeneous magnetic field is used to access the Feshbach resonances for the $|F = 1, m_F = -1\rangle$ scattering channels given in table 1.3.

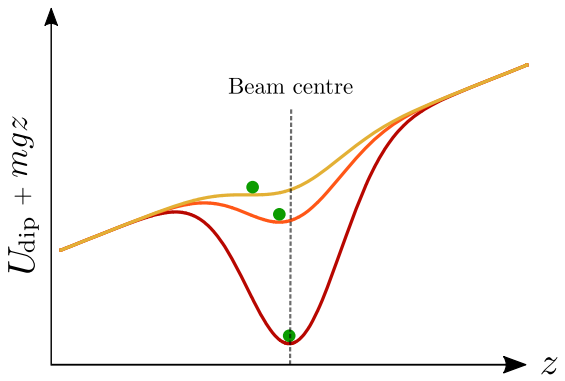

Figure 5.19 : Gravity introduces a gradient in the crossed-dipole trap potential and shifts its minimum. This establishes a minimum of the intensity ("dipole bottom") for which the potential is confining, below which atoms are lost.

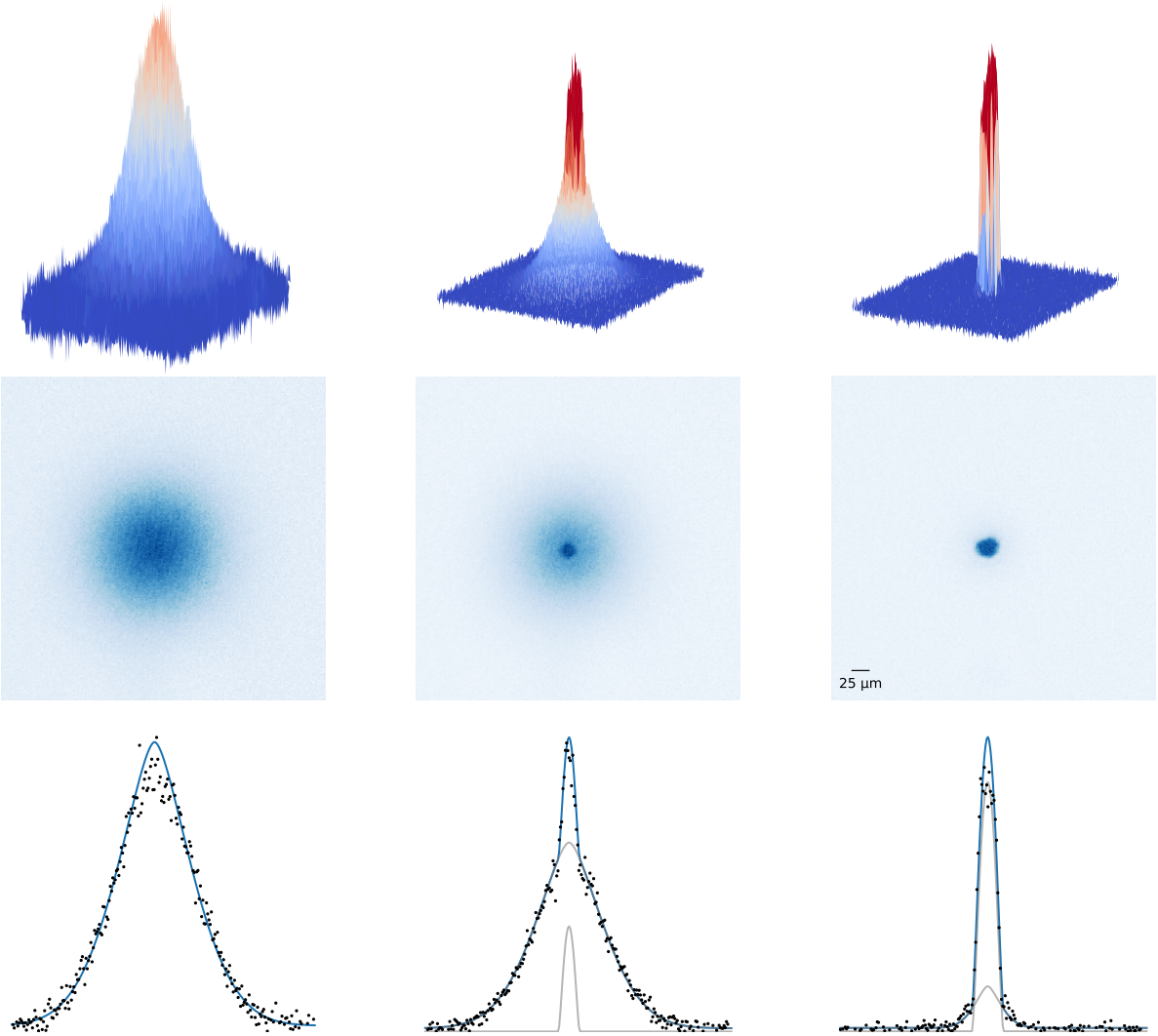

(a) $T > T_c$ (b) $T < T_c$ (c) $T \ll T_c$

Figure 5.20 : The atomic cloud measured in the direction perpendicular to the crossed-beam dipole trap, at three different trap depths and hence temperatures. The decrease of the temperature T below the critical value T_c triggers the macroscopic occupation of the ground state associated with Bose-Einstein condensation. The thermal and condensed fractions (grey solid lines) are individually fitted by the functions listed in section 6.2.

5.3.4 Quantum degeneracy

As explained in section 2.3.1, the removal of energy from the atomic cloud and the concomitant decrease in temperature are not sufficient to reach quantum degeneracy. The spatial extent of the wavefunction also needs to increase, in order for the de Broglie wavelength λ_{th} to become comparable to the inter-particle separation and ensure a dominant wave-nature of matter. This requires an increase in the phase space density, quantified by the degeneracy parameter $D = n_0 \lambda_{\mathrm{th}}^3$, where n_0 is the central spatial density.

A summary of the temperatures and atom numbers is provided in table 5.12, and the associated increase in phase space density is shown in fig. 5.22.

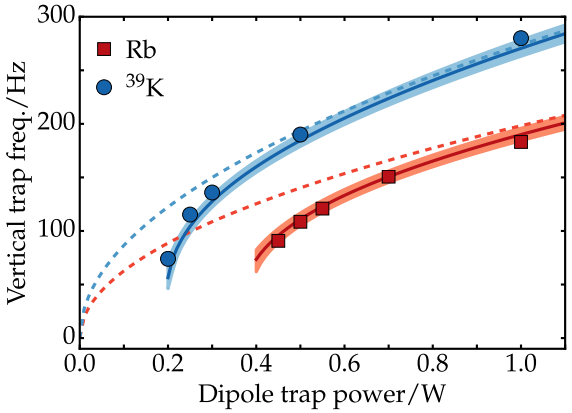

(a) Vertical

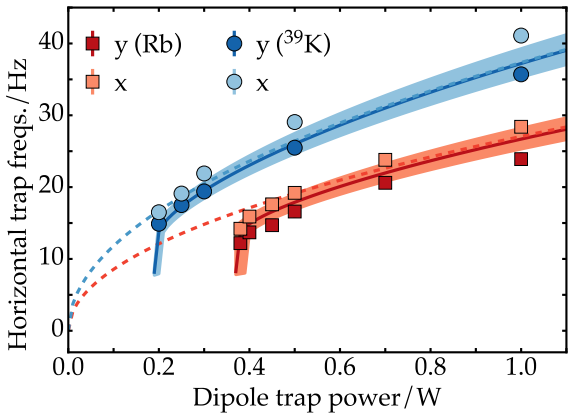

(b) Horizontal

Figure 5.21 : The vertical (a) and horizontal (b) trapping frequencies of the crossed-beam dipole trap. The dashed lines are the expectations from eq. 2.34, whereas the solid lines are the numerical solution accounting for the presence of gravity, with error bars from the uncertainty on the waists reported in table 5.10. Figure taken from [94].

	stage	Atom number ^{87}Rb	Atom number ^{39}K	Temperature ^{87}Rb	Temperature ^{39}K
1	Background vapour pressure			295 K	333 K
2	MOT	3×10^9	5×10^8	580 µK	1.1 mK
3	Polarisation gradient			30 µK	470 µK
4	Microwave evaporation	3×10^7	2×10^6	10 µK	7 µK
5	Mid-dipole evaporation	2×10^7	1.2×10^6	2 µK	2.6 µK
6	BEC		$\sim 3 \times 10^5$		~ 50 nK

Table 5.12 : Summary of the atoms numbers and temperatures after each cooling stage. These not only result in the atomic cloud to be colder, but also to exhibit a macroscopic de Broglie wavelength, quantified by the degeneracy parameter $D \sim 1$ shown in fig. 5.22.

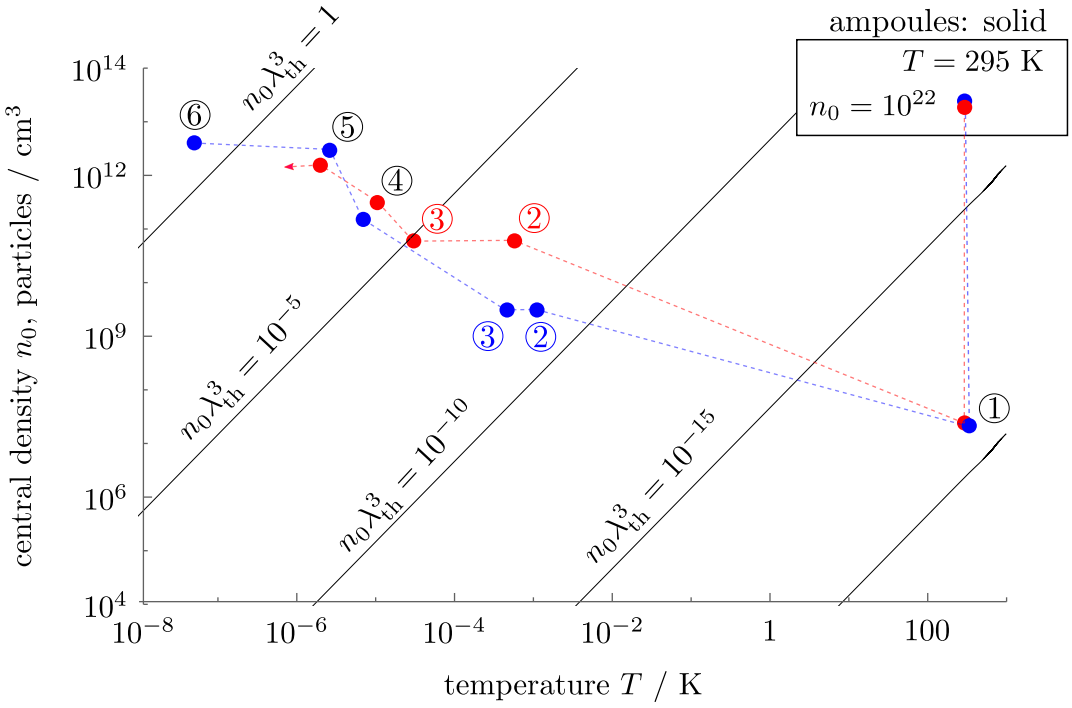

Figure 5.22 : The cooling stages of table 5.12 ultimately lead to a Bose-Einstein condensate of ^{39}K (blue) when the degeneracy parameter $D = n_0\lambda_{th}^3$ is of the order ~ 1. ^{87}Rb, shown in red, is completely lost during the optical evaporation stage.

On the walls of the cave, only the shadows are the truth.
Plato, from "The Allegory of the Cave" [176]

6 Probing and characterisation

This chapter details the methods employed to image and characterise the atomic cloud, and derives the functions used to extract the atom number and the temperature.

6.1 Imaging

6.1.1 Fluorescence

In fluorescence imaging, the atomic cloud is illuminated with near resonant light which is then scattered according to the second term in eq. 2.21. The number of photons collected by a camera is related to the total scattering rate R_{scat} and hence to the atom number N_{atoms}. In our experiment, this method was used to estimate the number of atoms in the 3D MOT chamber, as shown in fig. 6.1.

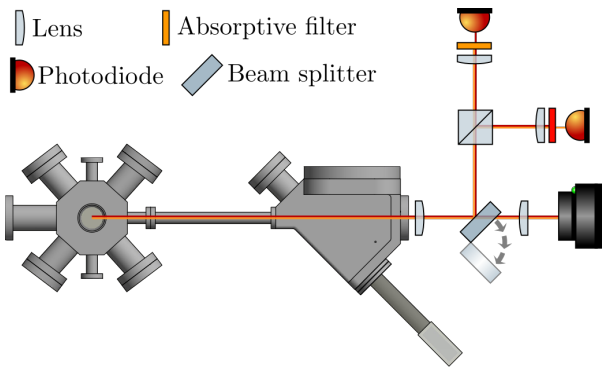

Figure 6.1 : The optical apparatus to perform fluorescence imaging comprised both a camera and two photodiodes, whose trace is shown in fig. 5.6. These provided an estimate for the atom number loaded into the 3D MOT.

The atom number N_{atoms} is calculated as:

$$N_{\text{atoms}} = \frac{N_\gamma}{\eta\tau \sum_j W_j R_j}, \tag{6.1}$$

and is derived in [177]. N_γ is the number of photons collected by a camera during an exposure time τ and with a detection efficiency η, and R is the scattering rate of every transition j driven by the incoming radiation, each weighted by the relevant Clebsch-Gordan coefficients W_j. Accounting for multiple simultaneous transitions is especially important for ^{39}K whose F' states are not well resolved.

Scattered light was also collected by two photodiodes, each with an absorptive filter so as to only record one species, providing a real-time diagnostic of the 3D MOT loading, as shown in fig. 5.6. The number of atoms N_{atoms} was extracted from the phenomenological equation describing MOT loading [178]:

$$\frac{\mathrm{d}N_{\text{atoms}}}{\mathrm{d}t} = L - \frac{N_{\text{atoms}}}{\xi} - \beta\frac{N_{\text{atoms}}^2}{V}, \tag{6.2}$$

where L is the loading rate, ξ the lifetime of the atoms due to background gas collisions, V the volume of the cloud and β the two-body loss parameter for light assisted collisions, discussed in section 1.3.2. An analytical solution is allowed when assuming low densities and hence eliminating the term with β, resulting in $N_{\text{atoms}}(t) = N_0\left(1 - \mathrm{e}^{-t/\tau}\right)$ which was used to fit the fluorescence traces of fig. 5.6. The use of this equation is also justified for $\beta \neq 0$, since the functional form of the solution is qualitatively similar, as shown in fig. 6.2.

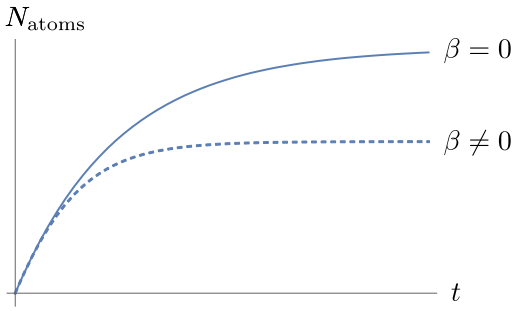

Figure 6.2 : Analytical ($\beta = 0$) and numerical ($\beta \neq 0$) solutions of eq. 6.2 describing the number of atoms N_{atoms} loaded in a 3D MOT. The two functions being qualitatively similar, the use of the analytical solution also for $\beta \neq 0$ is justified.

This method only provided a lower estimate for the atom number in the MOT, limited by re-scattering events when high densities are reached: an atom may scatter a photon which, before being collected by the camera, may be absorbed and re-scattered by other atoms.

6.1.2 Absorption

Formulae

The method employed to image the spatial distribution of the atoms in the science cell was absorption imaging, which measures the transmission of a beam through the cloud.

A laser beam with intensity I propagating along z through an atomic cloud of density n is attenuated according to the Beer-Lambert law:

$$\frac{\mathrm{d}I}{\mathrm{d}z} = -\sigma n I. \tag{6.3}$$

σ is the absorption cross section defined from:

$$\sigma I = \hbar\omega R_{\mathrm{scatt}} = \frac{3\lambda^2}{2\pi} \frac{1}{1 + \frac{I}{I_{\mathrm{S}}} + \left(\frac{2\Delta}{\Gamma}\right)^2}, \tag{6.4}$$

where R_{scatt} is the scattering rate from eq. 2.21, and ω, λ and Δ the frequency, wavelength and detuning of the incident radiation, Γ the atomic natural linewidth and I_{S} the saturation intensity. For ^{87}Rb and ^{39}K, $I_{\mathrm{S}} \sim 2\,\mathrm{mW/cm^2}$.

Imaging was performed on resonance to maximise the signal, and with low intensities $I \ll I_{\mathrm{S}}$ so as not to saturate the transition, which would cause an underestimation of the atom number. For simplicity, in eq. 6.4 we assumed $I = 0$, since careful calibration of I_{S} was not performed, but is known to only result in a correction by a factor of $1.5 - 2$ [179].

A beam with initial intensity $I_0(x, y)$ is incident on the camera with an attenuated intensity $I(x, y)$ given by:

$$I(x, y) = I_0(x, y) \exp\left(-\sigma \int n(x, y, z)\,\mathrm{d}z\right) = I_0(x, y)\,\mathrm{e}^{-\mathrm{OD}(x,y)}. \tag{6.5}$$

The optical density OD is defined as:

$$\mathrm{OD}(x, y) = \sigma \underbrace{\int n(x, y, z)\,\mathrm{d}z}_{\text{column density n(x,y)}} = -\ln\left(\frac{I(x, y) - I_{\mathrm{dark}}(x, y)}{I_0(x, y) - I_{\mathrm{dark}}(x, y)}\right), \tag{6.6}$$

where I_{dark} is the background intensity illuminating the camera even in the absence of imaging light and/or atoms.

Three images are taken in a typical experimental run: an *absorption* image in the presence of atoms to record $I(x, y)$, a *reference* image in the absence of atoms to record $I_0(x, y)$, and a *dark* image to measure $I_{\mathrm{dark}}(x, y)$. These images are taken with the least possible temporal separations in order to avoid intensity fluctuations of the light due to ambient thermal drifts.

The number of atoms N is then calculated as:

$$N = \int n(x, y, z)\,\mathrm{d}^3\mathbf{r} = \frac{1}{\sigma} \int \mathrm{OD}(x, y)\,\mathrm{d}^2\mathbf{r}. \tag{6.7}$$

For ^{87}Rb and ^{39}K, the imaging transition was chosen to be the cycling transition $|F = 2, m_F = 2\rangle \rightarrow |F' = 3, m_{F'} = 3\rangle$. The correct polarisation, σ^+, needs to be ensured in order for atoms not to accumulate in dark states and avoid detection. For atomic clouds in the absolute ground state $|F = 1, m_F = 1\rangle$, σ^+ repump light was also shone in order to induce the transition $|F = 1, m_F = 1\rangle \rightarrow |F' = 2, m_{F'} = 2\rangle$ from which atoms spontaneously decay into $|F = 2, m_F = 2\rangle$ and couple to the cycling transition. This repump beam is referred to as "repump flash".

Camera

The choice of a suitable camera is motivated primarily by its cost and by our requirements. In an ideal camera, each photon scattered by an atom excites an electron in the pixel, which is converted into a signal and hence recorded. In reality, this is limited by quantum efficiency (the number of electrons excited by incident photons), dark counts (electrons excited in the absence of incident photons) and electrical read-out noise. Cooling the chip reduces the extent of the latter two effects, and buying an expensive camera may take care of the former. While low quantum efficiencies are detrimental to single-photon measurements, they can easily be coped with in usual cold atom experiments.

We use a scientific CMOS (s-CMOS) camera, which has a lower quantum efficiency than its CCD counterpart but a much faster read-out because the electrical charge on each pixel is collected individually and at the same time. This allows to take the three images (absorption, reference and dark) at $\sim 50\,\mathrm{ms}$ from each other.

Time-of-flight

Images are either taken *in-situ*, with the atoms sitting in the magnetic/optical traps, on in *time-of-flight*.
This technique involves releasing the atomic cloud from any trapping potentials, and allowing it to fall under gravity for a time t_{tof}. To motion of each atom is then classically described by:

$$\mathbf{r}(t_{\mathrm{tof}}) = \mathbf{r}_0 + \mathbf{v}_0 t_{\mathrm{tof}} - \frac{1}{2}\mathbf{g}t_{\mathrm{tof}}^2. \tag{6.8}$$

The initial velocity $\mathbf{v}_0$ is related to the initial momentum $\mathbf{p}_0$. Hence, a time-of-flight image allows measuring the initial momentum distribution of the atomic cloud, as the different velocities cause the atoms to spatially separate before being recorded.

For thermal clouds, the initial momentum distribution is determined by the temperature T, hence measurement of the width of cloud σ also provides a measurement of its temperature:

$$\sigma \propto \sqrt{\frac{\langle \mathbf{p}_0^2 \rangle t_{\mathrm{tof}}^2}{m^2}}, \tag{6.9}$$

where m is the mass of the atom.

An example of time-of-flight imaging is shown in fig. 6.5.

Magnification

The optical apparatus between the atoms and the camera may include additional lenses to increase (or decrease) the *magnification* of the image, as shown in fig. 6.3. This introduces a factor M between the imaged and the real spatial distributions:

$$\text{Image} = M \times \text{Real}, \tag{6.10}$$

which, theoretically, is equal to the ratio of the eyepiece to the objective focal lengths f_2/f_1.

For imaging along axes perpendicular to gravity (D,X,Y and T in fig. 5.14), M is easily extracted from time-of-flight imaging of the central position of the cloud:

$$\mathbf{r}_{\mathrm{image}}(t_{\mathrm{tof}}) = M \cdot \left(\mathbf{r}_0 + \mathbf{v}_0 t_{\mathrm{tof}} - \frac{1}{2} g t_{\mathrm{tof}}^2 \right). \tag{6.11}$$

For axes along gravity (Z), the magnification was calibrated by measuring distances of known numerical value. These included cloud sizes previously measured by other, orthogonal imaging axes, or the $2\hbar k$ separation of the Kapitza-Dirac diffraction peaks of fig. 7.9. The imaging axes parameters for our experiment are summarised in table 6.1.

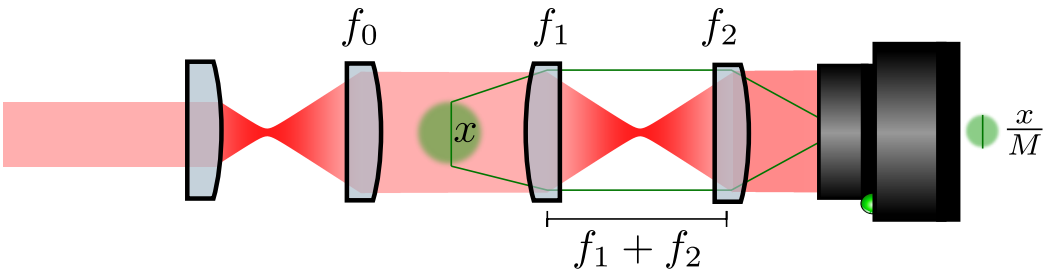

Figure 6.3 : The last lens f_0 produces a collimated imaging beam that is shone onto the atoms (green blob). The imaging beam is then made to propagate through a $4f$ setup until incident onto the camera. The actual image x (green solid line) starts focussed at the atomic position, and is focussed again onto the camera, albeit reduced/increased by M, the magnification of the imaging system. Ideally, $M = f_2/f_1$.

Axis	Angle from $\downarrow z$	measured M	expected $M = f_2/f_1$	pixel side / µm	Camera type
X	0.7°	0.802	0.8	4.5	BeamCam
Y	−0.5°	0.816	0.8	4.5	BeamCam
D	1.3°	3.07	3	5.86	Manta
T	−1.12°	2.45	2.5	4.5	BeamCam
Z	N/A	0.996	1	6.5	Andor Zyla

Table 6.1 : A list of the parameters pertaining to our imaging systems.

The lenses f_0 and f_1 in fig. 6.3 are also used by the dipole trap and optical lattice beams (fig. 5.14) in order to be focussed onto the atomic position. The atoms, therefore, need to be *exactly* at a distance f_0 from the first lens, and at a distance f_1 from the second. The procedure to select the optimal position of the lenses is detailed as follows:

1. With the atoms in the magnetic trap, the position of the lens f_1 is varied so as to result in the smallest cloud size recorded on the camera. This corresponds to the f_1 lens being exactly a distance f_1 from the magnetic trap minimum;

2. Once the atoms are loaded into the optical crossed-beam dipole trap, the position of the lens f_0 is varied so as to result in the smallest cloud size with maximum signal recorded on the camera. This corresponds to the dipole beam being focussed onto the atoms and coinciding with the magnetic trap position.

Once the positions of the lenses are fixed, any other beam which is collimated when incident on f_0 is automatically focussed onto the atoms.

High field imaging

For ^{39}K, a repulsive interaction strength is needed in order to prevent its collapse when reaching quantum degeneracy. This is guaranteed by a strong homogeneous magnetic field, enabling access to its Feshbach resonance. The imaging of the cloud, therefore, also needs to occur at high magnetic fields, for ramping them down to zero would cause the BEC to implode into a bosenova.

As shown in fig. 6.4, in the presence of a (strong) magnetic field, the polarisation of the imaging light is of crucial importance.

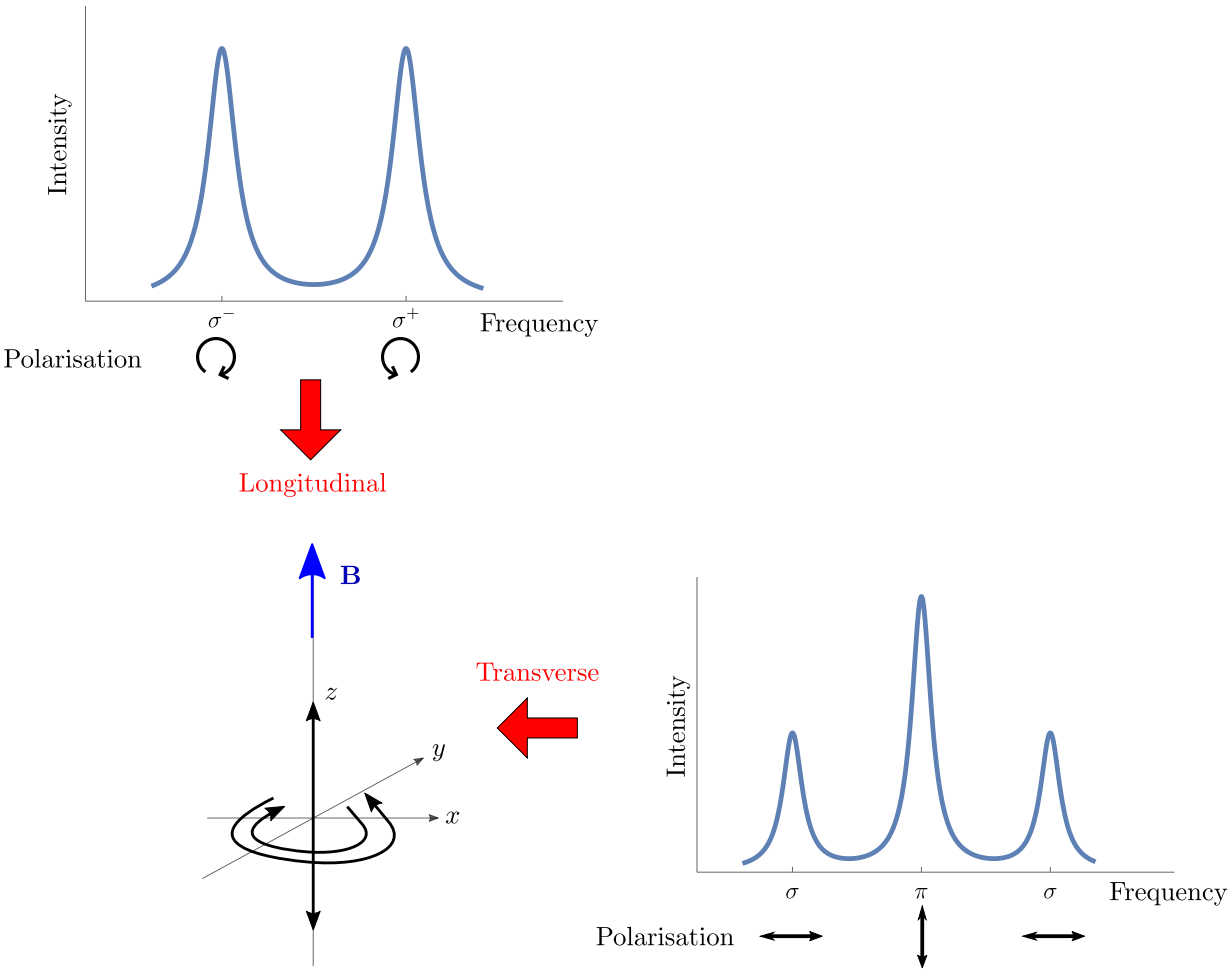

Figure 6.4 : $\Delta m \pm 1$ transitions are driven by σ polarised light. If incident along the magnetic field (longitudinal), this is *circularly* polarised, but if incident perpendicular to the field (transverse), it is *linearly* polarised. π transitions causing $\Delta m = 0$ are only feasible when light is illuminated from the side.

For reliable imaging of the atoms, we seek a closed transition in the high-field region where the atomic states are shown in figs 4.9 and 4.11. A suitable choice is the $|m_J = -1/2, m_I = 3/2\rangle \rightarrow |m_{J'} = -3/2, m_{I'} = 3/2\rangle$ transition driven by σ^- light, with a selection rule $\Delta m_J = -1$ since the nuclear spin I can only be affected by magnetic components of the radiation, which are $\propto 1/c$ reduced as per eq. 2.7. The ground state $|m_J = -1/2, m_I = 3/2\rangle$ is adiabatically connected to the low-field state $|F = 1, m_F = 1\rangle$. However, conservation of $m_F = m_J + m_I$ is also obeyed by the low-field state $|F = 2, m_F = 1\rangle$, adiabatically connected to the high-field state $|m_J = 1/2, m_I = 1/2\rangle$.

The ground state in the high-field regime is therefore:

$$|\psi\rangle_{S_{1/2}} = \sqrt{1-\epsilon^2}|m_J = -1/2, m_I = 3/2\rangle + \epsilon|m_J = 1/2, m_I = 1/2\rangle, \tag{6.12}$$

with $\epsilon \to 0$ as the magnetic field strength $|\mathbf{B}| \to \infty$.
This state is thus not pure and it prevents a fully closed transition, which undermines the accuracy of the recorded atom number.

The ^{39}K cloud also needed to be imaged from the side in order to measure its central position to extract the dipole trapping frequencies shown in fig. 5.21. This was achieved by illuminating the atoms with a linear (π) polarised imaging beam parallel to the magnetic field, with a frequency tuned to couple the $|m_J = -1/2, m_I = 3/2\rangle \to |m_{J'} = -1/2, m_{I'} = 1/2\rangle$ transition, adiabatically connected to $|F = 1, m_F = 1\rangle \to |F' = 1, m_{F'} = 0\rangle$.

6.2 Fit functions

6.2.1 Atom numbers

Condensed fraction

The spatial density for a BEC was derived in section 1.2.2 and found to be the inverted paraboloid $|\psi|^2$ of eq. 1.50.
An absorption image along the z axis records the integrated column density $n(x, y)$:

$$\begin{aligned} n(x,y) = \int_\infty^\infty |\psi|^2 \mathrm{d}z = \int_\infty^\infty n_0 \cdot \max\left[0, 1 - \frac{(x-x_0)^2}{R_x^2} - \frac{(y-y_0)^2}{R_y^2} - \frac{(z-z_0)^2}{R_z^2}\right] \mathrm{d}z = \\ \Rightarrow n(x,y) = \underbrace{\frac{4}{3}R_z}_{A_0} \cdot \max\left[1 - \frac{(x-x_0)^2}{R_x^2} - \frac{(y-y_0)^2}{R_y^2}\right]^{3/2}, \end{aligned} \tag{6.13}$$

where R_i coincide with the *Thomas-Fermi* radii only when the cloud is imaged in-situ.

The number of atoms is therefore given by:

$$\begin{aligned} N = \frac{1}{\sigma}\int n(x,y)\mathrm{d}^2\mathbf{r} = \frac{1}{\sigma}\int |\psi|^2 \mathrm{d}^3\mathbf{r} = \\ \frac{1}{\sigma}\int_\infty^\infty n_0 \max\left[0, \left(1 - \frac{(x-x_0)^2}{R_x^2} - \frac{(y-y_0)^2}{R_y^2}\right)^{3/2}\right] \mathrm{d}x\,\mathrm{d}y = \\ \Rightarrow N = \frac{A_0}{\sigma} \cdot \frac{2\pi}{5} R_x R_y. \end{aligned} \tag{6.14}$$

The BEC is a coherent state and hence not an eigenstate of the particle number operator. The image measurement projects it onto a number-specific Fock state. Hence we expect the atom number N to exhibit Poissonian fluctuations $\propto \sqrt{N}$ which are however much smaller than experimental uncertainties from other sources. Furthermore, the inverted paraboloid of eq.1.50 assumes a sharp discontinuity of the cloud density profile at the radii R_i. In reality, this would be smoothed by the healing length, ignored in the above treatment.

Deeply thermal fraction

For a fully thermal cloud $T \gg T_c$, the momentum is Boltzmann distributed according to eq. 1.10. The spatial density is then given by eq. 1.16 which, for a harmonic trapping potential, is just a Gaussian with standard deviations σ_i. The number of atoms is then given by:

$$N_{\text{ex}} = \frac{1}{\sigma}\int_{\infty}^{\infty} \mathrm{d}x \int_{\infty}^{\infty} \mathrm{d}y\, B_0 \exp\left(-\frac{(x-x_0)^2}{2\sigma_x^2} - \frac{(y-y_0)^2}{2\sigma_y^2}\right) = \frac{B_0}{\sigma}\cdot 2\pi\sigma_x\sigma_y. \tag{6.15}$$

Partially condensed fraction

For a partially condensed cloud $T \lesssim T_c$, the Bose-Einstein distribution of the excited states cannot be approximated by its classical, Boltzmann counterpart. The spatial density of the thermal fraction is then given by eq. 1.39. Because the potential $V(\mathbf{r})$ is harmonic, the argument of the polylogarithmic function g is a Gaussian with standard deviations σ_i.

The integrated density is then given by:

$$\begin{aligned} n_{\text{ex}}(x,y) &= \int_{\infty}^{\infty} |\psi|^2 \mathrm{d}z B_0\, g_{3/2}\left[\exp\left(-\frac{(x-x_0)^2}{2\sigma_x^2} - \frac{(y-y_0)^2}{2\sigma_y^2} - \frac{(z-z_0)^2}{2\sigma_z^2}\right)\right] = \\ &\Rightarrow n_{\text{ex}}(x,y) = \underbrace{B_0\cdot\sqrt{2\pi}\sigma_z}_{B_1}\, g_2\left[\exp\left(-\frac{(x-x_0)^2}{2\sigma_x^2} - \frac{(y-y_0)^2}{2\sigma_y^2}\right)\right]. \end{aligned} \tag{6.16}$$

The number of atoms is therefore:

$$N_{\text{ex}} = \frac{1}{\sigma}\int_{\infty}^{\infty} \mathrm{d}x \int_{\infty}^{\infty} \mathrm{d}y\, B_1\, g_2\left[\exp\left(-\frac{(x-x_0)^2}{2\sigma_x^2} - \frac{(y-y_0)^2}{2\sigma_y^2}\right)\right] = \frac{B_1}{\sigma}\cdot 2\pi\sigma_x\sigma_y\,\zeta(3), \tag{6.17}$$

where $\zeta(3) = 1.202$.

After time-of-flight, the same fit functions are used but with a new cloud radius $R(t_{\text{tof}}) = b(t_{\text{tof}})R_i$, as per [180].

6.2.2 Temperature

The temperature of the atomic cloud is extracted from the time-of-flight expansion of its size σ, which depends on the initial momentum distribution and hence on the temperature T according to 6.9. The cloud size after time-of-flight is the results of a convolution between the momentum $\mathbf{p}(t)$ and the initial spatial distribution $\mathbf{r}_0$.

For simplicity, the calculation is performed within the semi-classical approximation that allows expression of the thermal atoms' spatial distribution in a 3D harmonic trap with frequencies ω_i as a simple Gaussian, from eq. 1.16.

The initial phase space density of the cloud is given by:

$$\begin{aligned} \rho(\mathbf{r}_0,\mathbf{p}) &= N\cdot P(\mathbf{r}_0,\mathbf{p}) \propto \exp\left(-\frac{H_0(\mathbf{r}_0,\mathbf{p})}{k_{\text{B}}T}\right) \\ &\propto \prod_{i=x,y,z} \exp\left(-\frac{p_i^2}{2mk_{\text{B}}T}\right)\cdot\exp\left(-\frac{m\omega_i^2 r_{0i}^2}{2k_{\text{B}}T}\right), \end{aligned} \tag{6.18}$$

where the overall proportionality factor was dropped.

The spatial density at time t is then given by the convolution:

$$\begin{aligned} n_{\mathrm{ex}}(\mathbf{r},t) &= \int\int \mathrm{d}^3\mathbf{r_0}\,\mathrm{d}^3\mathbf{p}\,\rho(\mathbf{r_0},\mathbf{p})\,\delta\left(\mathbf{r}-\mathbf{r_0}-\frac{\mathbf{p}t}{m}\right) \\ &\propto \prod_{i=x,y,z}\int_{-\infty}^{\infty}\mathrm{d}p_i\,\exp\left[-\frac{p_i^2}{2mk_{\mathrm{B}}T}\right]\exp\left[-\frac{1}{2k_{\mathrm{B}}T}m\omega_i^2\left(x_i-\frac{p_i t}{m}\right)^2\right], \end{aligned} \tag{6.19}$$

which thanks to the symbolic integration performed by Mathematica can be expressed as:

$$n_{\mathrm{ex}}(\mathbf{r},t) \propto \prod_{i=x,y,z}\frac{\sqrt{2\pi}}{\sqrt{1+\dfrac{\omega_i^2 t^2}{mk_{\mathrm{B}}T}}}\exp\left[-\frac{x_i^2}{2\sigma_i(t)^2}\right]. \tag{6.20}$$

In the above,

$$\sigma_i(t)^2 = \sigma_{i0}^2 + \frac{k_{\mathrm{B}}T}{m}t_{\mathrm{tof}}^2, \quad \text{with} \quad \sigma_{i0}^2 = \frac{k_{\mathrm{B}}T}{m\omega_i^2}. \tag{6.21}$$

Hence, the temperature T is related to the standard deviation σ_i of the Gaussian:

$$T = \frac{m\sigma_i^2}{k_{\mathrm{B}}}\frac{\omega_i^2}{1+\omega_i^2 t_{\mathrm{tof}}^2} \sim \frac{m\sigma_i^2}{k_{\mathrm{B}}t_{\mathrm{tof}}^2}, \tag{6.22}$$

which agrees with an estimate from the theorem of equipartition of energy:

$$\frac{1}{2}mv_i^2 = \frac{1}{2}k_{\mathrm{B}}T \quad \xRightarrow[v_i=\sigma_i/t]{} \quad T = \frac{m\sigma_i^2}{k_{\mathrm{B}}t_{\mathrm{tof}}^2}. \tag{6.23}$$

The thermal atoms expand isotropically while the condensed fraction undergoes its characteristic aspect-ratio inversion (driven by the greater interaction energy along the compressed direction), as shown in fig. 6.5.

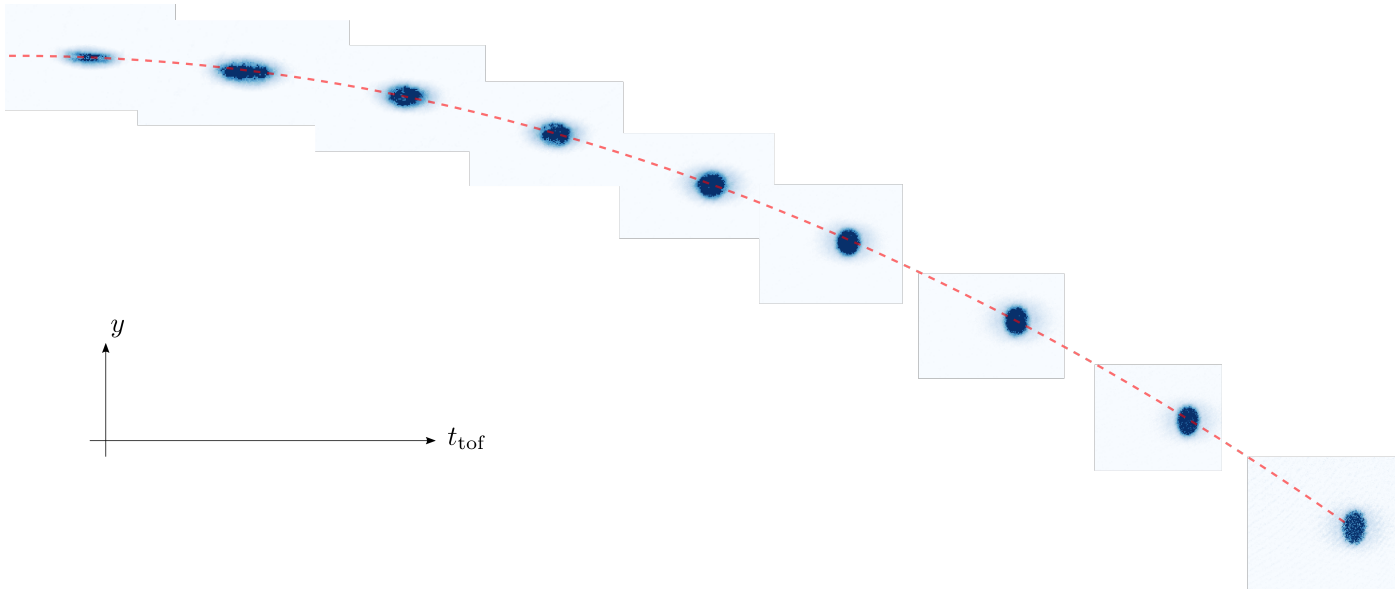

Figure 6.5 : Time-of-flight images of a ^{87}Rb BEC along the D axis, with t_{tof} ranging from 2 ms to 15 ms. The thermal fraction expands isotropically and can be used to extract the cloud's temperature. The condensed fraction starts with an asymmetric profile dictated by the dipole trap frequencies, and evolves into a profile with the inverted aspect ratio. The central position of the cloud was used in eq. 6.11 in order to extract the magnification M for this imaging axis.

Part III

Results and findings

Order is for idiots, genius can handle chaos.

Albert Einstein

Ordeeeer! Ooordeeer! ORDER!

John Bercow, Speaker of the House of Commons, 2009-present.

7

Order: sharp diffraction peaks

This chapter provides a technical description of the eightfold optical lattice apparatus, along with numerical considerations on the real space profile of the potential and its energy spectrum. Analogously to X-ray crystallography, we used matter-wave diffraction to investigate the 2D quasiperiodic optical lattice, which yielded sharp peaks and hence confirmed the long-range order of the structure. However, the seemingly pure point diffraction spectrum tends to form a dense set, uncovering a singularly continuous component which possesses a fractal dimension.

7.1 Lattice

7.1.1 Implementation

Our experiment had the objective to investigate ultracold atoms in a quasicrystalline potential, that is a lattice structure with a crystallographically forbidden rotational symmetry. The obvious choice would have then been a fivefold symmetric pattern, reminiscent of the Penrose tiling in fig. 3.6c. A minimalist implementation would have seen a Penrose-like pattern projected onto the atoms with a DMD[1], which would unfortunately have required the use of a quantum gas microscope to achieve the required resolution, and would suffer from imperfections in the potential landscape due to the presence of several spatial frequencies.

An optical lattice was then a cleaner alternative, with exactly as many spatial modes as laser beams. A set of five free running and mutually interfering beams would give rise to a fivefold symmetric structure, but would require extremely accurate stabilisation of most, if not all, of their phases in order to preserve the complex features of the interference pattern. This technical limitation may be easily overcome by retro-reflecting the beams and only allowing interference between each incident and counter-propagating pair. This

[1] Digital Mirror Device.

selective interference may be enabled by introducing a detuning between each pair of beams such that its associated frequency scale is much larger than what the atoms could respond to, and would result in an incoherent superposition of five distinct standing waves, equivalent to ten pair-wise interfering lattice beams[2].

Luckily my then colleague (and now Dr.) Konrad Viebahn realised that there is another number, less than ten, that produces a crystallographically disallowed rotational symmetry: eight. We therefore opted for the eightfold symmetric pattern created by the incoherent superposition of four standing waves shown in fig. 7.1.

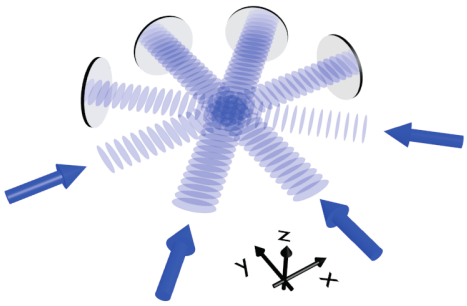

Figure 7.1 : Our eightfold symmetric optical lattice is created by incoherently superimposing four stading waves, each separated by 45°. Figure taken from [181].

The optical potential is described by:

$$V(\mathbf{r}) = V_0 \sum_{i=1}^{4} \cos^2(\mathbf{k}_i \cdot \mathbf{r} + \phi_i), \tag{7.1}$$

where $\mathbf{k}_i$ are the wavevectors of the lattice beams:

$$\mathbf{k}_1 = (1, 0), \quad \mathbf{k}_2 = (1/\sqrt{2}, 1/\sqrt{2}), \quad \mathbf{k}_3 = (0, 1), \quad \mathbf{k}_4 = (-1/\sqrt{2}, 1/\sqrt{2}). \tag{7.2}$$

The above expression assumes each beam is an ideal plane wave, though real laser beams possess a Gaussian intensity profile, as further discussed in section 9.2. The four independent phases ϕ_i, each referenced to the position of the retro-reflecting mirror, are passively stabilised by the mass of the mirror itself, and will be taken as 0 for the rest of the thesis.

The laser providing the lattice radiation can be tuned over a large range of frequencies, allowing the possibility of both a blue and a red detuned lattice (with respect to the D lines of ^{87}Rb and ^{39}K). Blue detuning with a wavelength of $\lambda = 725\,\text{nm}$ was chosen, for the following reasons:

- As further discussed in section 9.2, this option results in an overall additional anticonfining potential, which is already mitigated by the red detuned dipole trap beams. A red detuned lattice, on the other hand, would result in an overall confining potential;

[2]Three cross-interfering beams result in a global, superfluous phase factor and in two relative phases whose noise only causes translations of the lattice's centre of mass. The same happens for a square lattice created by two standing waves. However, for three standing waves or four mutually interfering beams, the number of phases exceeds the spanning set of the 2D plane. Phase noise will then not only translate the lattice but also affect its shape and geometry.

- Situated at the minima of the intensity, the atoms experience a reduced scattering rate;

- Numerical investigations on both (red and blue detuned) lattice configurations showed equally interesting and promising features.

7.1.2 Real space

Profile

The real space profile of the four-standing waves' interference pattern is shown in fig. 7.2, where it is compared to a scanning tunnelling microscope (STM) picture of an eightfold symmetric solid-state quasicrystal.

Setting the phases ϕ_i in eq. 7.1 to zero results in a global eightfold point symmetry about the centre of the lattice, as shown in fig. 7.3. A random choice of phases, on the other hand, results in a pattern with only locally eightfold symmetric regions, as shown in fig. 7.4. Ammann-Beenker tilings may be superimposed to the minima locations in both configurations. Further details on the relation between the lattice potential and the choice of phases are discussed in [94].

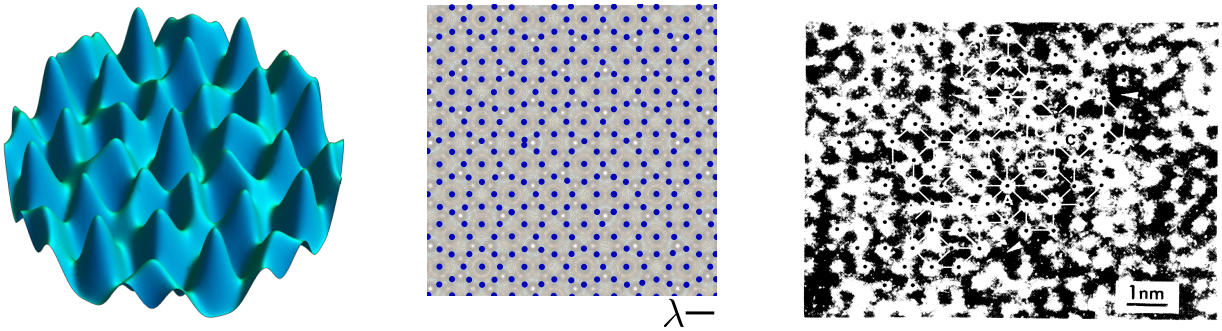

(a) in phase (b) random phases (c) STM, from [182]

Figure 7.2 : Four in-phase standing waves result in the centrally eightfold symmetric interference pattern of (a). A random choice of phases (b) results in a distribution of lattice minima locations (blue points) exhibiting the same local eightfold symmetry as (c), a high-resolution image of the octagonal phase in Cr-Ni-Si obtained with a scanning tunnelling microscope.

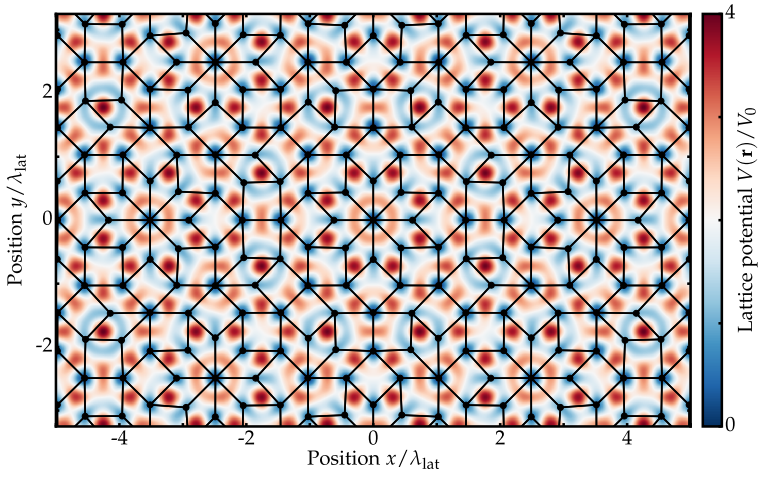

Figure 7.3 : Four in-phase standing waves result in a pattern exhibiting a global, central eightfold symmetry. The minima of the potential are superimposed with an Ammann-Beenker tiling. Figure taken from [94].

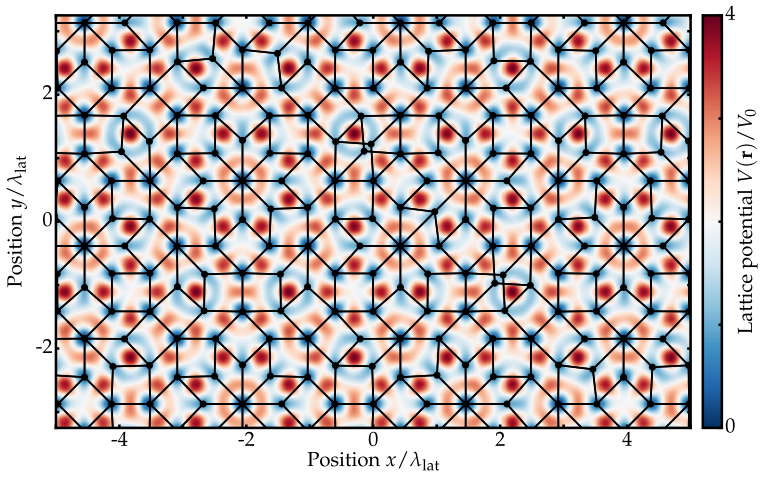

Figure 7.4 : Four standing waves with random relative phases result in a pattern which exhibits eightfold symmetry only locally. The minima of the potential can still be superimposed with an Ammann-Beenker tiling. Figure taken from [94].

Lack of band structure

Investigation of the energy spectrum of the eightfold symmetric lattice is performed in the deep lattice limit, discussed in section 2.4.2. Each potential minimum of the lattice is approximated by a harmonic oscillator in order to compute the ground state energy:

$$E_0 = E_{\mathrm{min}} + \frac{1}{2}\hbar(\omega_x + \omega_y), \tag{7.3}$$

where E_{min} is the offset and ω_i the on-site trapping frequencies, extracted according to appendix D.10.

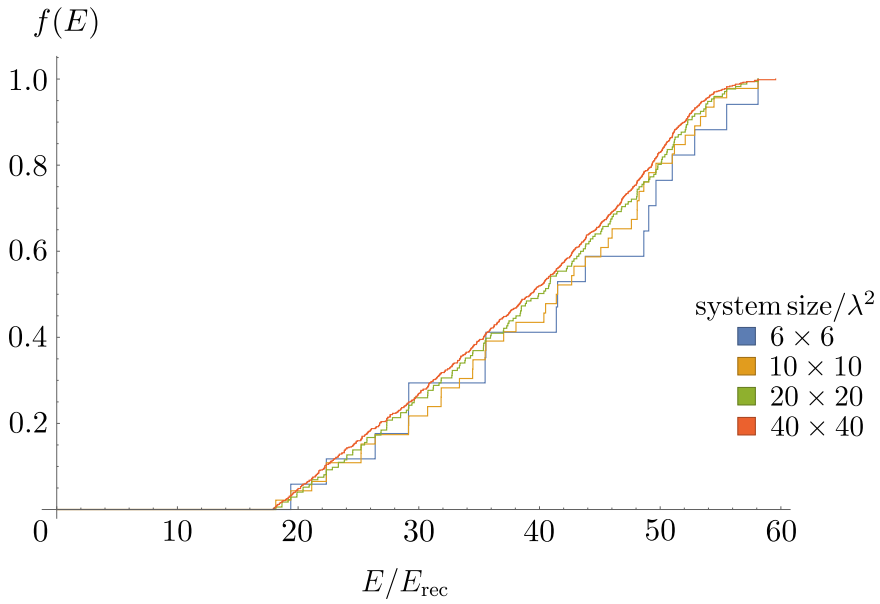

Figure 7.5: The cumulative density of states $f(E)$ defined in eq. 7.4 for different regions of the same eightfold symmetric lattice, at single-beam lattice depth $V_0 = 40\,E_{\text{rec}}$. Each curve is normalised to its maximum value. The energy spectrum is a singularly continuous function, as per the definitions in section 3.2.3.

We define the cumulative density of states $f(E)$ as:

$$f(E) = \int_0^E \mathrm{d}E'\, g(E') = \sum_i n(E_i), \tag{7.4}$$

where $g(E)$ is the density of states and $n(E)$ the number of states at energy E.

The cumulative density of states $f(E)$ is plotted in fig. 7.5 for different regions of the same quasiperiodic potential. The resemblance to the Devil's staircase of fig. 3.8 indicates the lack of robust gaps and establishes the singularly continuous nature of the energy spectrum, as per the definitions in section 3.2.3, in accordance with the results for other quasiperiodic structures [145, 146, 183]. The shrinking of the gaps stems from the presence of the irrational number $\sqrt{2}$ in the wavectors of eq. 7.2, allowing the minima of the intensity to take any value in $\mathbb{R}$.

7.1.3 Technical details

Alignment

In order for each beam to only interfere with its retro-reflected partner, their polarisation was chosen to be out-of-plane and their frequencies offset by at least 10 MHz, larger than any frequency the atoms could respond to. This frequency was also chosen so as not to allow any Zeeman-assisted transitions at high fields as per the selection rules in table 2.1.

The waists of the beams are elliptical to increase the peak intensity and to guarantee the lattice homogeneity over the atomic cloud. These are reported in table 7.1b along with the angles between the beams, measured by fitting straight lines to the diffraction patterns of 1D lattices, such as the one displayed in fig. 7.9. The maximum potential depth achieved was $40\,E_{\text{rec}}$ for each 1D lattice, for an optical power of ~ 500 mW.

axis	w_h /µm	w_v /µm
D	158	73
Y	153	71
X	161	70
T	184	91

(a) waists

axis	angle
TD	89.5°
TX	45.6°
TY	44.0°
XY	91.6°
XD	46.2°
YD	45.4°

(b) angles

Table 7.1 : The experimentally measured waists and angles of the lattice beams.

The procedure to align the lattice beams onto the atoms is detailed in [94], and summarised as follows. A Mathematica simulation[3] was used to model the beam propagation on the experiment table until the last lens f_0 before the science cell, which focusses it onto the atoms' trapped position. The pointing of each lattice beam was controlled by a piezo-actuated mirror, and was optimised via the "lattice sliding method": with the retro-beam blocked, the anticonfining effect of the blue detuned travelling wave results in a force shifting the atomic cloud sideways while at the same time broadening in, as shown in fig. 7.7a. The beam was centred onto the atoms by maximising the cloud size whilst causing minimal transverse displacement.

The retro-reflected beam was aligned by enhancing the ensuing matter-wave diffraction pattern, with the logic that perfect retro-reflection would result in maximal peak visibility. The retro-path included a lens and a mirror in the "cat's eye" configuration, illustrated in fig. 7.6, to ensure perfect beam-overlap even for Gaussian beams, and reduced sensitivity to the inclination of the mirror. Alignment of the mirror had to be performed iteratively with visual feedback from the diffraction patterns, for it to pass centrally through both lenses thus imparting no net transverse momentum onto the atoms, as shown in fig. 7.7b.

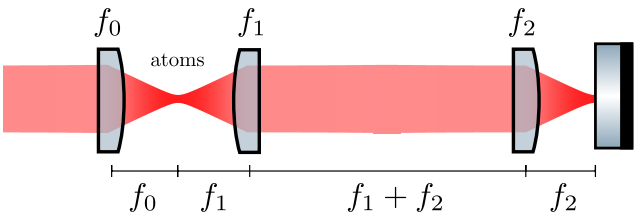

Figure 7.6 : The retro-reflection of the lattice beam is performed within a "cat's eye" apparatus. A lens (f_2) focusses the laser onto a mirror to maximise its overlap with the counter-propagating beam and to reduce sensitivity on the mirror alignment.

Two-photon processes

The interaction between the lattice beams and the atoms is described by a general time-dependent Hamiltonian H, resulting in transitions between an initial $|i\rangle$ and a final $|f\rangle$ atomic states. In the non-relativistic case, the transition rate $\Gamma_{i\to f}$ is determined by the

[3] using ABCD matrices in the paraxial approximation.

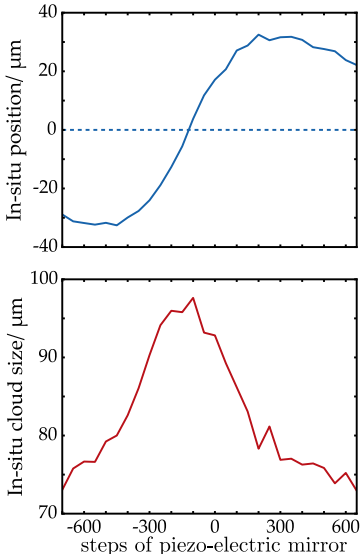

(a) "Lattice sliding method" [94]

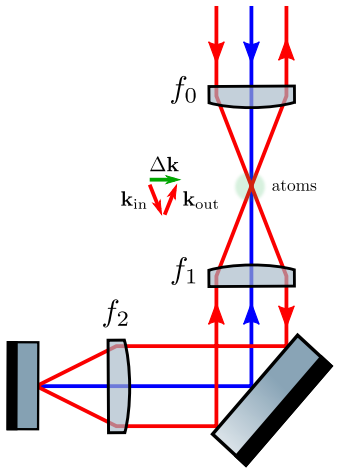

(b) Retro-beam alignment

Figure 7.7 : The forward propagating beam is centred on the atoms by maximising its anticonfining effects (a). Imperfect alignment of the retro-reflected beam results in an unwanted transverse momentum imparted onto the atoms $\Delta\mathbf{k}$.

Fermi golden rule:

$$\Gamma_{i\to f} = \frac{2\pi}{\hbar}|\langle f|H|i\rangle|^2\rho(E_f), \tag{7.5}$$

where $\rho(E_f)$ is the density of final states at energy E_f.

However, relativistic quantum mechanics provides corrections such that:

$$\Gamma_{i\to f} \propto |\langle f|H|i\rangle + \text{higher order terms}|^2 = |\langle f|S|i\rangle|^2, \tag{7.6}$$

where S is the scattering matrix.
This is defined as $S = \lim_{t\to\infty} U(t,t_0)$, where U is the *evolution* or *Dyson* operator:

$$|f\rangle = \mathcal{T}\exp\left(-\int_{t_0}^{t}\frac{\mathrm{i}}{\hbar}H(t')\mathrm{d}t'\right)|i\rangle = \underbrace{\mathcal{T}\exp\left(-\int_{t_0}^{t}\frac{\mathrm{i}}{\hbar}H_{\mathrm{I}}(t')\mathrm{d}t'\right)}_{U(t,t_0)}|i\rangle, \tag{7.7}$$

with H_{I} being the interaction component of H, as the kinetic energy is diagonal.

The transition rate is then given by $\Gamma_{i\to f} \propto |\lim_{t\to\infty}\langle f|U(t,t_0)|i\rangle|^2$ and is computed from the *Dyson series*:

$$\begin{aligned}\langle f|U(t,t_0)|i\rangle = \\ \delta_{fi} \quad - \quad \frac{\mathrm{i}}{\hbar}\int_{t_0}^{t}\mathrm{e}^{\mathrm{i}E_f(t'-t_0)/\hbar}\langle f|H_{\mathrm{I}}|i\rangle\mathrm{e}^{-\mathrm{i}E_i(t'-t_0)/\hbar}\mathrm{d}t' \quad + \\ \left(\frac{-\mathrm{i}}{\hbar}\right)^2\int_{t_0}^{t}\int_{t_0}^{t'}\sum_n \mathrm{e}^{\mathrm{i}E_f(t'-t_0)/\hbar}\langle f|H_{\mathrm{I}}|n\rangle\,\mathrm{e}^{-\mathrm{i}E_n(t'-t_0)/\hbar}\,\mathrm{e}^{\mathrm{i}E_n(t''-t_0)/\hbar}\langle n|H_{\mathrm{I}}|i\rangle\,\mathrm{e}^{-\mathrm{i}E_i(t''-t_0)/\hbar}\mathrm{d}t'\mathrm{d}t'' \ldots,\end{aligned} \tag{7.8}$$

which is derived in appendix D.7.

If H_I is time independent, the integrals can be trivially computed in the limit $t \to \infty$. The expansion can then be separated into the off-diagonal contributions to the Hamiltonian $|i\rangle \neq |f\rangle$:

$$\begin{aligned} \lim_{t\to\infty} \langle f|U(t,t_0)|i\rangle = \\ + \quad \frac{\langle f|H_\mathrm{I}|i\rangle}{E_i - E_f} \quad (i \to f \text{ direct scattering}) \\ + \quad \sum_n \frac{\langle f|H_\mathrm{I}|n\rangle\langle n|H_\mathrm{I}|i\rangle}{(E_n - E_f)(E_i - E_n)} \quad (i \to f \text{ scattering via state } n) \\ + \quad \dots, \end{aligned} \tag{7.9}$$

and the diagonal terms $|i\rangle = |f\rangle$:

$$\lim_{t\to\infty} \langle i|U(t,t_0)|i\rangle = \mathbb{1} - \frac{\mathrm{i}}{\hbar}\langle i|H_\mathrm{I}|i\rangle t - \frac{\mathrm{i}}{\hbar}\sum_{n\neq i} \frac{\langle i|H_\mathrm{I}|n\rangle\langle n|H_\mathrm{I}|i\rangle}{E_n - E_i} t^2 \dots. \tag{7.10}$$

We notice that the coefficient of the n^{th} term in eq. 7.10 is the n^{th} order perturbative correction to H_I. In the dipole approximation, the wavelength of the incident electric field $E(\mathbf{r})\hat{\mathbf{e}}$ is much larger than the size of the atom, which then only experiences a spatially homogeneous potential $H_\mathrm{I} \propto q\mathbf{r}\cdot\hat{\mathbf{e}}$. Hence the first order correction $\langle i|H_\mathrm{I}|i\rangle = 0$ because of the inversion symmetry in neutral atoms, due to the lack of a permanent electric dipole moment. As a result, the leading term is the second-order perturbative correction. This is the same conclusion drawn at the end of section 2.1.2, where the energy shift was termed *AC Stark shift*. Here we confirm that this can be interpreted as a virtual two-photon transition coupling $|i\rangle$ to itself via the excited states $|n\rangle$. For ^{87}Rb and ^{39}K, the D2 states dominate the sum over $|n\rangle$, which leads to the expression found in eq. 2.30.

With this interpretation, we turn our attention to the transition terms appearing in eq. 7.9. The first order term is just a scattering event from $|i\rangle$ to $|f\rangle$, while the second order term is again a two-photon transition coupling $|i\rangle$ and $|f\rangle$ via virtual excitations of the states $|n\rangle$. The transition rate $\Gamma_{i\to f}$ also includes the density of states $\rho(E_f)$ which enforces energy conservation. The frequency of the lattice beam ω being far detuned from any atomic transition ω_n, no direct scattering events are allowed. Only second or higher (even) order terms in the perturbative expansion are permitted, and will be referred to as *two-photon processes* in the remainder of the thesis.

The states $|i\rangle$ and $|f\rangle$ need to possess the same internal state to enforce energy conservation, but may be different motional states owing to the momentum imparted by the two-photon transition: $|i\rangle = |g\rangle \otimes |0\hbar\mathbf{k}\rangle \to |f\rangle = |g\rangle \otimes |2\hbar\mathbf{k}\rangle$, where $|g\rangle$ and $|e\rangle$ are the ground and excited internal atomic states. In this context, two-photon processes may be visualised by the physically incorrect picture of atoms absorbing one photon from the forward beam and re-emitting it into the retro beam, depicted by the Feynman diagrams of fig. 7.8.

In conclusion, the optical lattice beams result in two interactions for the atoms. Photons propagating along the same direction mediate two-photon transitions coupling the same ground state, à la Raman, and cause an AC Stark shift which for a blue detuned lattice results in an overall anticonfining potential, further discussed in section 9.2. Counter-propagating photons can impart a net $|2\hbar\mathbf{k}\rangle$ momentum onto the atoms and therefore

couple different motional states, à la Bragg. This results in the Kapitza-Dirac scattering discussed in the next section.

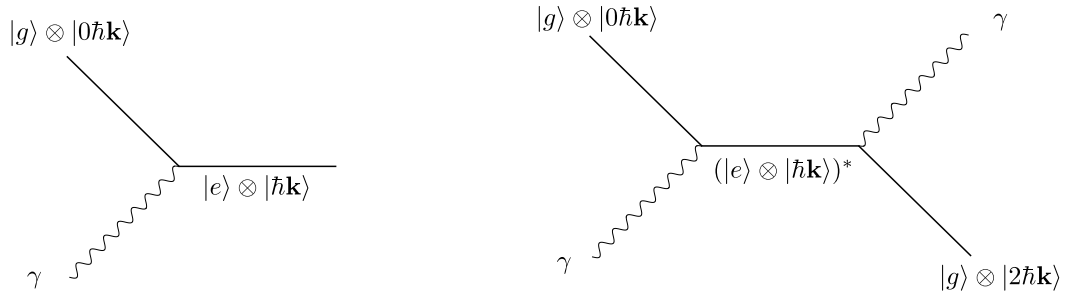

(c) (d)

Figure 7.8 : The transition terms in the perturbative Dyson expansion of eq. 7.9 can be pictorially represented by Feynman diagrams. If the lattice beam were resonant, the photon could be absorbed by an atom in the ground state $|g\rangle$ resulting in (a). For the far detuned beams used in optical lattices, however, energy conservation causes all scattering events to be mediated by "virtual states"[4](b), ensuring the final internal state is still $|g\rangle$.

Kapitza-Dirac scattering

The two-photon processes described in the previous section result in the exchange of momentum between light and atoms, which leads to the diffraction of matter-waves by the optical lattice. This is the opposite of conventional X-ray crystallography, where electromagnetic radiation is directed onto a solid-state sample and its diffraction pattern recorded. The diffraction of matter from an optical lattice, a "crystal of light", is known as Kapitza-Dirac scattering. This was predicted in 1933 [184] and first realised with electrons [185], and is quantitatively treated as follows.

A 1D optical lattice consists of two counter-propagating waves of amplitude E_0 forming a standing wave:

$$\mathbf{E} = 2E_0 \cos(kz)\hat{\mathbf{e}}. \tag{7.11}$$

The single-photon Rabi frequency introduced in section 2.1.2 is then $\Omega \propto E \propto \cos(kz)$.

For short and strong lattice pulses, the atom-light interaction energy is much larger than the atomic kinetic energy, which can then be neglected. This is the *Raman-Nath* approximation, where particles are assumed to be frozen in place and only acquire phase factors from the lattice beams.

The relationship between the single-photon Rabi frequency Ω, the detuning Δ and the lattice depth in V_0 is proved in [166] to be:

$$V_0 E_{\text{rec}} = \frac{\hbar^2 \Omega^2}{8\Delta}, \tag{7.12}$$

where E_{rec} is the recoil energy.

[4]In particle physics these would be termed "off-shell" and denoted by an asterisk.

Combining eq. 7.12 with the AC Stark shift of eq. 2.13 results in the following interaction Hamiltonian:

$$H_{\mathrm{I}}(z,t) = -\frac{V_0 E_{\mathrm{rec}}}{2}\cos(2kz). \tag{7.13}$$

Time evolution leads to:

$$|\psi_t\rangle = \mathrm{e}^{-\frac{\mathrm{i}}{\hbar}\int \mathrm{d}t' H_{\mathrm{I}}(z,t')}|\psi_0\rangle \propto \mathrm{e}^{\mathrm{i}\frac{V_0 E_{\mathrm{rec}}}{2\hbar}\cos(2kz)t}|\psi_0\rangle, \tag{7.14}$$

where the constant of proportionality is only a pure phase factor.
Using $\mathrm{e}^{\mathrm{i}\alpha\cos(\beta)} = \sum_{n=-\infty}^{\infty} \mathrm{i}^n J_n(\alpha)\mathrm{e}^{\mathrm{i}n\beta}$, where J_n is the n^{th} Bessel function of the first kind:

$$\begin{aligned} |\psi_t\rangle &\propto \sum_{n=-\infty}^{\infty} \mathrm{i}^n J_n\left(\frac{V_0 E_{\mathrm{rec}}}{2\hbar}t\right)\mathrm{e}^{\mathrm{i}2nkz}|\psi_0\rangle \\ &\propto \sum_{n=-\infty}^{\infty} \mathrm{i}^n J_n\left(\frac{V_0 E_{\mathrm{rec}}}{2\hbar}t\right)|g\rangle \otimes |2n\hbar\mathbf{k}\rangle. \end{aligned} \tag{7.15}$$

This confirms that upon interaction with the optical lattice, the atoms remain in the ground state $|g\rangle$ but may gain a momentum $2n\hbar\mathbf{k}$, n being the number of undergone two-photon events and thus referred to as the *diffraction order*. The population of the n^{th} diffraction order is given by:

$$P_n = \langle\psi_n|\psi_n\rangle = J_n^2\left(\frac{V_0}{2}\frac{t}{\tau_{\mathrm{rec}}}\right), \tag{7.16}$$

where $\tau_{\mathrm{rec}} = \hbar/E_{\mathrm{rec}}$ is the recoil time, $\sim 16\,\mu\mathrm{s}$ for $^{39}\mathrm{K}$ in a 725 nm optical lattice.

Spontaneous emission was ignored in this treatment, under the assumption that stimulated emission in the counter-propagating beam would dominate owing to bosonic enhancement.

A typical Kapitza-Dirac diffraction pattern from a 1D optical lattice is shown in fig. 7.9. Upon interaction with the lattice, the atoms gain momenta in discrete units $|2\hbar\mathbf{k}\rangle$. Imaging in time-of-flight along an axis perpendicular to the optical lattice allows the atoms to spatially separate according to their speed. The resulting atomic spatial arrangement provides a direct measurement of their momentum distribution. The n diffraction orders are then said to be the basis states in *momentum space*, where they form a *synthetic* lattice with spacing $2\hbar\mathbf{k}$. All experiments presented in this thesis are performed on this synthetic lattice.

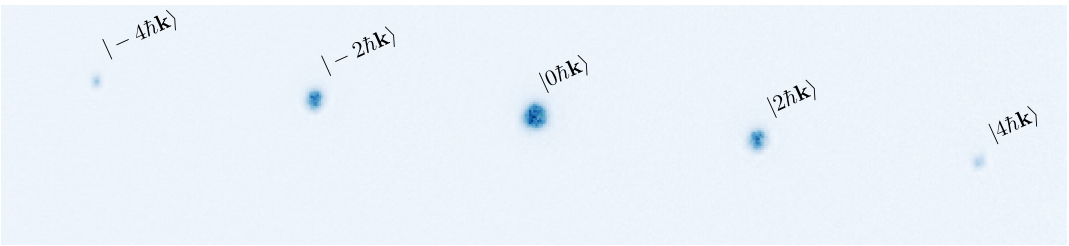

Figure 7.9 : The two-photon transitions enabled by the optical lattice impart a $2\hbar\mathbf{k}$ momentum to the atoms, which are then diffracted according to Kaptiza-Dirac scattering. The atoms separate in n diffraction orders and form a *synthetic lattice* in momentum space.

Calibration of lattice depths

The optical power in each lattice beam is set by the diffraction efficiency of an AOM, controlled by a PID loop whose inverting and non-inverting inputs are connected to a photodiode measuring the intensity close to the science cell, and to a signal generator producing arbitrary pulse shapes. A signal generator was used as it ensures better DC reproducibility, and allows simultaneous triggering of all four beams, avoiding a queue on the analogue cards and therefore achieving sub-µs pulse synchronisation. The PID loops were optimised for the specific pulse shape employed, and were made as stable as possible, e.g. by minimising cable length and other sources of noise.

Various methods were employed to calibrate the voltage generated by the signal generator to the lattice depth experienced by the atoms. Calibrations were performed for each individual 1D lattice. An initial estimate for the required (optical) power was obtained from eq. 2.30.

The first technique was lattice modulation spectroscopy.
Each 1D lattice was ramped to a depth V_0, to allow the BEC to be adiabatically loaded into its ground state, followed by an amplitude modulation about V_0 of $\delta V \sin(\omega_{\text{mod}} t)$, to drive inter-band excitations. Variation of the modulation frequency allowed observation of the first $\rightarrow$ second and first $\rightarrow$ third band transitions[5], which were quantified by measuring the "temperature" of the central $|0\hbar\mathbf{k}\rangle$ peak in fig. 7.9. This method relied on the choice of a suitable δV to cause an appreciable effect so as to be reliably captured by the fits, and needed multiple depths to be sampled to allow extrapolation. Uncertainty in the fit results was dominated by the asymmetry of the temperature profile, probably due to quantum depletion and the presence of thermal atoms.

We then opted for taking a time-series of the Kapitza-Dirac scattering pattern (fig. 7.9), and choosing the potential depth that best explained the populations of the peaks, as shown in fig. 7.10. The Raman-Nath analytical solutions of eq. 7.16 were only reliable at short pulse durations, hence the exact[6] time evolution obtained from a dynamical simulation (section 7.1.4) was used. This method allowed accurate depth calibrations to within $0.1\,E_{\text{rec}}$, and were compatible with the modulation spectroscopy estimates.

Experimental sequence

The experimental sequence used to perform lattice experiments is summarised in fig. 7.11. After creation of the BEC, the crossed dipole trap is ramped to a slightly higher power in order to reduce the evaporation rate – usually from 190 mW, $\omega_r = 2\pi \cdot 15\,\text{Hz}$ and $\omega_z = 2\pi \cdot 75\,\text{Hz}$ to 250 mW, $\omega_r = 2\pi \cdot 18\,\text{Hz}$ and $\omega_z = 2\pi \cdot 115\,\text{Hz}$.

The magnetic field is ramped from the value used during evaporative cooling to a new one determining the intra-species interaction strength during the lattice pulse – for most of the results, this was chosen to be the zero-crossing in order to investigate single-particle physics, with occasional exploration of the (repulsive) interaction regime.

The lattice is only shone when both the dipole trap and the magnetic field have reached their desired values. Concomitant with the end of the lattice pulse, the dipole confinement is turned off while the magnetic field is tuned back to its (repulsive) pre-lattice value in

[5] Parity conservation would only allow the latter [186] but dipole trap mixing also enables the former.

[6] though it still required to truncate the basis size and hence the Hamiltonian. The truncation was chosen so as for the dynamics to affect only high and non-populated diffraction orders.

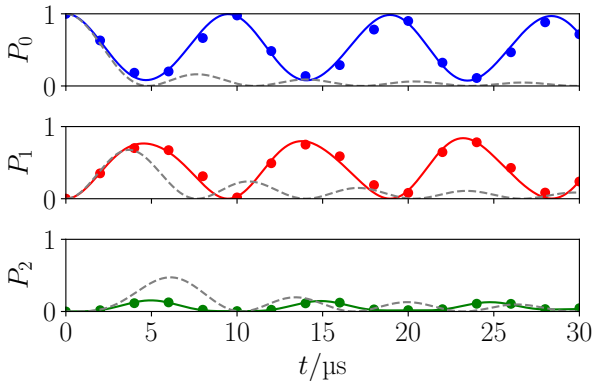

Figure 7.10 : Depth calibration for a 15.7 E_{rec} deep 1D optical lattice, such as the one resulting in fig. 7.9. A rectangular lattice pulse illuminates the atoms for a variable duration t. The numerical simulations for the time evolution (solid lines) and the Raman-Nath analytical solutions (dashed) are fitted to the first three diffraction orders.

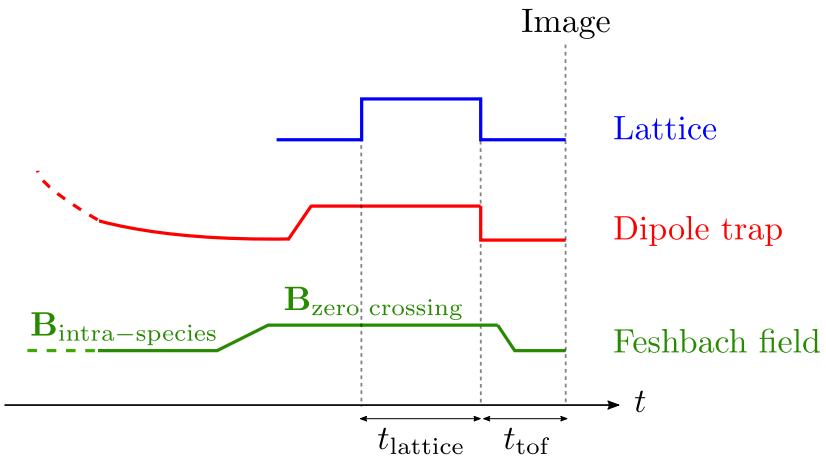

Figure 7.11 : Once a BEC is created, the lattice is shone for a time t_{lattice} when both the dipole trap and the magnetic field are tuned to the desired confining potential and interaction strength. The atoms are then released and fall under gravity for t_{tof} before being imaged.

order to "puff up" the diffraction peaks, which would otherwise be optically too dense to allow reliable extraction of the population[7]. The atoms are allowed to fall under gravity for a time-of-flight t_{tof} period of 33 ms, during which the diffraction orders caused by two-photon processes separate in space to be recorded by a camera.

7.1.4 Simulation

As shown in fig. 7.9, two-photon transitions enable the optical lattice to impart $2\hbar\mathbf{k}$ momentum to the atoms and results in a Kapitza-Dirac diffraction pattern. These points, labelled by momentum, can be thought of forming a *synthetic lattice* where two-photon transitions couple different *synthetic states*.

All experiments presented in this thesis are performed on the synthetic lattice generated by Kaptiza-Dirac scattering. This synthetic lattice also underlies the analysis of the

[7]This technique was suggested to us by the Hadzibabic-Smith group in Cambridge (2017).

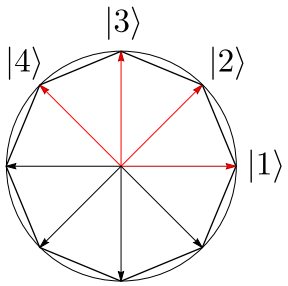

vector	4D	3D	2D
$\|1\rangle$	$(1,0,0,0)$	$(1,0,0)$	$(1,0)$
$\|2\rangle$	$(0,1,0,0)$	$(0,1,0)$	$(\cos \pi/4, \sin \pi/4)$
$\|3\rangle$	$(0,0,1,0)$	$(0,0,1)$	$(0,1)$
$\|4\rangle$	$(0,0,0,1)$		$(-\cos \pi/4, \sin \pi/4)$

Figure 7.12 : There are 4 basis states needed to span the eightfold symmetric reciprocal lattice, corresponding to a higher dimensional lattice $d = 4$. These states can be written in a 4D linearly independent basis, or in the 2D xy Cartesian representation. Any subset $d = 1, 2, 3$ can be used to describe d-beam lattice configurations.

recorded images and the numerical simulations of the results.

Momentum space basis construction

As shown in fig. 7.9, a 1D optical lattice causes atoms to scatter into n diffraction orders generating a synthetic lattice in momentum space, each labelled by $|2n\hbar\mathbf{k}\rangle$, $n \in \mathbb{Z}$. The optical lattice in our apparatus, shown schematically in fig. 7.1, consists of the superposition of four independent standing waves.

A point in the full synthetic lattice can therefore be expressed as:

$$\mathbf{b} = i|1\rangle + j|2\rangle + \ell|3\rangle + m|4\rangle \quad \text{with} \quad (i, j, \ell, m) \in \mathbb{Z}^4, \tag{7.17}$$

where the states $|2n_a\hbar\mathbf{k}_a\rangle$ were renamed to $n_a|a\rangle$ to specify the a^{th} 1D lattice causing n_a two-photon transitions. $\{|a\rangle\}$ is the basis set for the synthetic lattice, containing as many vectors as active 1D lattices, as shown in fig. 7.12.

These can be expressed in 2D as per the wavectors in eq. 7.2. The presence of the irrational number $\sqrt{2}$ is problematic for numerical simulations, as it prevents reliably accounting of duplicates. Hence, the basis is defined over a 4D regular lattice, where each vector is now linearly independent, as reported in fig. 7.12. This is also physically justified by the higher dimensional method to produce quasicrystals described in section 3.2.4.

The *generation* n of a reciprocal vector $\mathbf{b}$ is the number of two-photon scattering events it underwent from $|0\rangle$:

$$n = \sum_{j=1}^{d} \text{abs}[\mathbf{b}_j]. \tag{7.18}$$

The number of *new* states appearing in a generation n (that were not in $n-1$) is given by:

$$N(d, n) = \sum_{k=0}^{d} 2^k \binom{d}{k} \binom{n}{k}, \tag{7.19}$$

where d is the number of active lattice beams, determining the dimensionality of the higher dimensional space. This formula is derived from the field of *network theory*, where each generation of synthetic lattice states are given by the new *vertices* reached by $2d$ *edges* starting from the original point.

1D Hamiltonian

The Hamiltonian for a particle in a 1D standing wave is:

$$H(x) = \frac{\mathbf{p}^2}{2m} + V_0 \cos^2(kx), \tag{7.20}$$

where

$$V_0 \cos^2(kx) = V_0 \left(\frac{\mathrm{e}^{\mathrm{i}kx} + \mathrm{e}^{-\mathrm{i}kx}}{2} \right)^2 = \frac{V_0}{2} + \frac{V_0}{4} \left(\mathrm{e}^{\mathrm{i}2kx} + \mathrm{e}^{-\mathrm{i}2kx} \right). \tag{7.21}$$

Because of the periodicity of the lattice, Bloch's theorem can be used to write the wavefunctions of H as *Bloch waves*:

$$\phi_{n,q}(x) = u_{n,q}(x) \cdot \mathrm{e}^{\mathrm{i}qx}, \tag{7.22}$$

where q is the quasimomentum, conserved $\mod 2\hbar k$. The function u has the same periodicity as the lattice, and can therefore be expanded as a discrete Fourier series in the plane wave basis:

$$u_{n,q}(x) = \sum_{\ell=-\infty}^{+\infty} c_{n,\ell}(q)\, \mathrm{e}^{\mathrm{i}2k\ell x}. \tag{7.23}$$

Inserting this into the Schrödinger equation $H\phi_{n,q} = E_n(q)\phi_{n,q}$ results in:

$$\begin{aligned} \sum_{\ell=\infty}^{\ell=\infty} \left[\left(-\frac{\hbar^2}{2m} (2k\ell + q)^2 + \frac{V_0}{2} \right) \mathrm{e}^{\mathrm{i}2\ell k} + \frac{V_0}{4} \left(\mathrm{e}^{\mathrm{i}2(\ell+1)kx} + \mathrm{e}^{\mathrm{i}2(\ell-1)kx} \right) \right] c_{n,\ell}(q) &= E_n(q) \sum_{\ell'=-\infty}^{\infty} \mathrm{e}^{\mathrm{i}2\ell' kx} c_{n,\ell'}(q) \\ \Rightarrow \quad \sum_{\ell=-\infty}^{\infty} H_{\ell,\ell'} c_{n,\ell}(q) &= E_n(q) c_{n,\ell'}(q). \end{aligned} \tag{7.24}$$

Identifying $\mathrm{e}^{\mathrm{i}2\ell kx} = \langle x|2\ell k\rangle$, $|2\ell k\rangle$ can be used as a suitable discrete basis to construct the matrix Hamiltonian according to:

$$H_{\ell,\ell'} = \begin{cases} \frac{\hbar^2}{2m}(q + 2\ell k)^2 + V_0/2 & \text{for} \quad \ell = \ell' \\ V_0/4 & \text{for} \quad \|\ell - \ell'\| = 1 \\ 0 & \text{otherwise.} \end{cases} \tag{7.25}$$

Hamiltonian in arbitrary dimensions

We assume that the BEC, having free momentum $\mathbf{k} = 0$, has a lattice quasimomentum $q = 0$ as well. Different starting $q \neq 0$ can still be simulated and are discussed in section 8.2.5.

The kinetic energy is not just $\propto |k|^2$ like in eq. 7.25 as doing so would assume a physical three- or four-dimensional space, whereas the matter-wave diffraction and the ensuing synthetic lattice is restricted to a 2D plane. The kinetic energy associated with a $d > 2$ basis vector $\mathbf{b}_i$ is then $\propto |\mathcal{P}_d^{\parallel} \cdot \mathbf{b}_i|^2$, where $\mathcal{P}_d^{\parallel}$ is the projection operator defined in eq. 3.28. These projection operators act on the augmented 3D/4D bases and return the physical scattering vector in the 2D plane. From the bases listed in fig. 7.12, the 3D/4D projection operators are required to take the following form:

$$\mathcal{P}_3^{\parallel} = \begin{pmatrix} 1 & \cos \pi/4 & 0 \\ 0 & \sin \pi/4 & 1 \\ 0 & 0 & 0 \\ 0 & 0 & 0 \end{pmatrix} = \begin{pmatrix} 1 & \sqrt{2}/2 & 0 \\ 0 & \sqrt{2}/2 & 1 \\ 0 & 0 & 0 \\ 0 & 0 & 0 \end{pmatrix}, \tag{7.26}$$

$$\mathcal{P}_4^{\parallel} = \begin{pmatrix} 1 & \cos\pi/4 & -\cos\pi/4 & 0 \\ 0 & \sin\pi/4 & \sin\pi/4 & 1 \\ 0 & 0 & 0 & 0 \\ 0 & 0 & 0 & 0 \end{pmatrix} = \begin{pmatrix} 1 & \sqrt{2}/2 & -\sqrt{2}/2 & 0 \\ 0 & \sqrt{2}/2 & \sqrt{2}/2 & 1 \\ 0 & 0 & 0 & 0 \\ 0 & 0 & 0 & 0 \end{pmatrix}. \tag{7.27}$$

Eqs. 7.26 and 7.27 satisfy $(\mathcal{P}^{\parallel})^2 = \mathcal{P}^{\parallel}$ as expected for a projection operator.

The general d-dimensional Hamiltonian for d lattice beams is therefore:

$$H_{i,j}^{d}(t) = \begin{cases} 4E_{\text{rec}} \times |\mathcal{P}_d^{\parallel} \cdot \mathbf{b}_i|^2 + d\frac{V_0(t)}{2} & \text{for} \quad i = j \\ V_0(t)/4 & \text{for} \quad \|i-j\| = 1 \\ 0 & \text{otherwise,} \end{cases} \tag{7.28}$$

The $d\,V_0/2$ term added to the kinetic energy is a mere phase factor for time independent Hamiltonians, but its diagonal and homogeneous nature ensures it also amounts to a global phase factor for time dependent ones, as proven in appendix D.8.

An example for how the Hamiltonian looks like for a square 2D lattice is:

$$\begin{array}{cccccc} & \langle 0,0| & \langle 1,0| & \langle 0,1| & \langle \bar{1},0| & \langle 0,\bar{1}| \end{array}$$

$$H_{\text{2D}}(V_0) = \begin{pmatrix} 0+V_0 & V_0/4 & V_0/4 & V_0/4 & V_0/4 \\ V_0/4 & 8+V_0 & 0 & 0 & 0 \\ V_0/4 & 0 & 8+V_0 & 0 & 0 \\ V_0/4 & 0 & 0 & 8+V_0 & 0 \\ V_0/4 & 0 & 0 & 0 & 8+V_0 \end{pmatrix} \begin{array}{c} |0,0\rangle \\ |1,0\rangle \\ |0,1\rangle \\ |\bar{1},0\rangle \\ |0,\bar{1}\rangle \end{array}$$

which was truncated after the 1st generation, and $\bar{1} = -1$.

Time evolution

Finally, the time dynamics is computed by direct integration of the Schrödinger equation, cast for simplicity in dimensionless units:

$$H|\psi\rangle = \mathrm{i}\hbar\frac{\mathrm{d}}{\mathrm{d}t}|\psi\rangle \quad \Rightarrow \quad H'|\psi\rangle = \mathrm{i}\frac{\mathrm{d}}{\mathrm{d}\tau_{\text{rec}}}|\psi\rangle \tag{7.29}$$

where $H' = H/E_{\text{rec}}$, with $E_{\text{rec}} \approx 9.7\,\text{kHz}$ and $\tau_{\text{rec}} = \hbar/E_{\text{rec}} \approx 16\,\mu\text{s}$ for ^{39}K in a 725 nm lattice.

What underpins this elegantly simplistic treatment in the plane wave basis is the harmonic nature of the optical lattice potential, which allows its decomposition into a finite, discrete Fourier series. The above method cannot be employed to account for the effects of interactions and of additional potentials (e.g. the dipole trap), which real space methods such as the one presented later in section 8.1.3 are better suited to tackle.

7.2 Diffraction dynamics

The results in this section are contained in the publication [181], which was work primarily produced by (now Dr.) Konrad Viebahn.

7.2.1 Multiple dimensions

The synthetic lattice generated up to the fifth generation is shown in fig. 7.13, while raw images of the diffraction patterns obtained from a variable number of active lattice beams are shown in fig. 7.14.

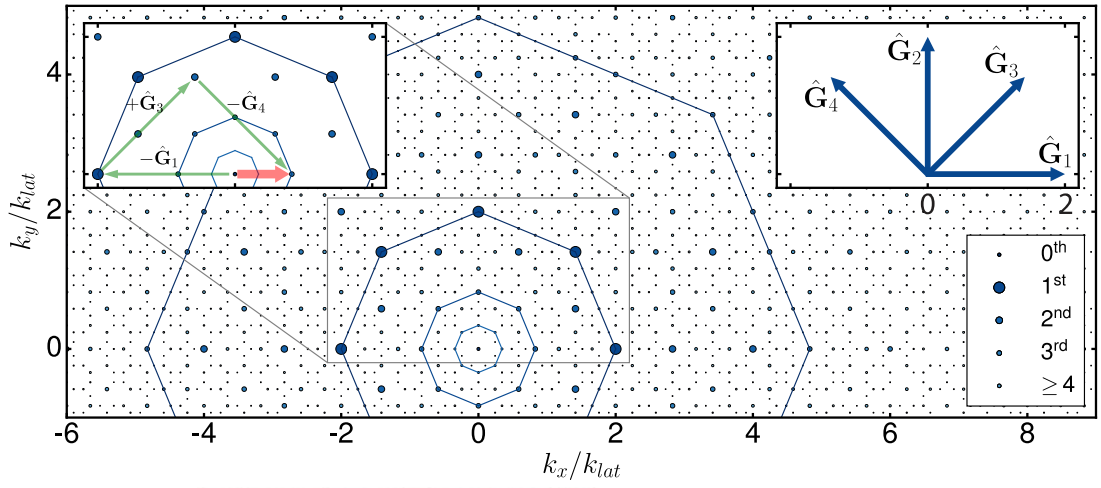

Figure 7.13 : The available synthetic lattice states reacheable by up to five two-photon processes. Here $\mathbf{G}_i = 2\hbar\mathbf{k}_i$, and the solid lines are successive inflations by the silver mean $\lambda = 1 + \sqrt{2}$, emphasising the self-similarity of the diffraction pattern. Figure taken from [181].

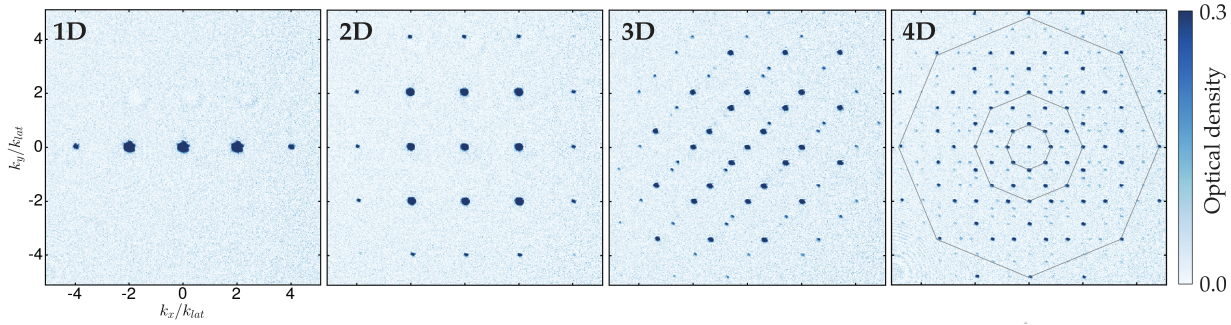

Figure 7.14 : Shining n lattice beams produces diffraction patterns compatible with projections from n-dimensional regular lattices, as explained in the text. The solid contours in the final picture correspond to successive inflations by the silver mean $\lambda = 1 + \sqrt{2}$. Figure taken from [181].

The relationship between quasicrystals and higher dimensional regular lattices discussed in section 3.2.4 is strikingly obvious in the three-beam (3D) and four-beam (4D) diffraction images of fig. 7.14, as these are exactly equal to the projections from the three- and four-dimensional hypercubes of figs. 3.11 and 3.12. These are also very similar to the electron-diffraction patterns recorded from solid-state quasicrystals with eightfold rotational symmetry, shown in fig. 7.15.

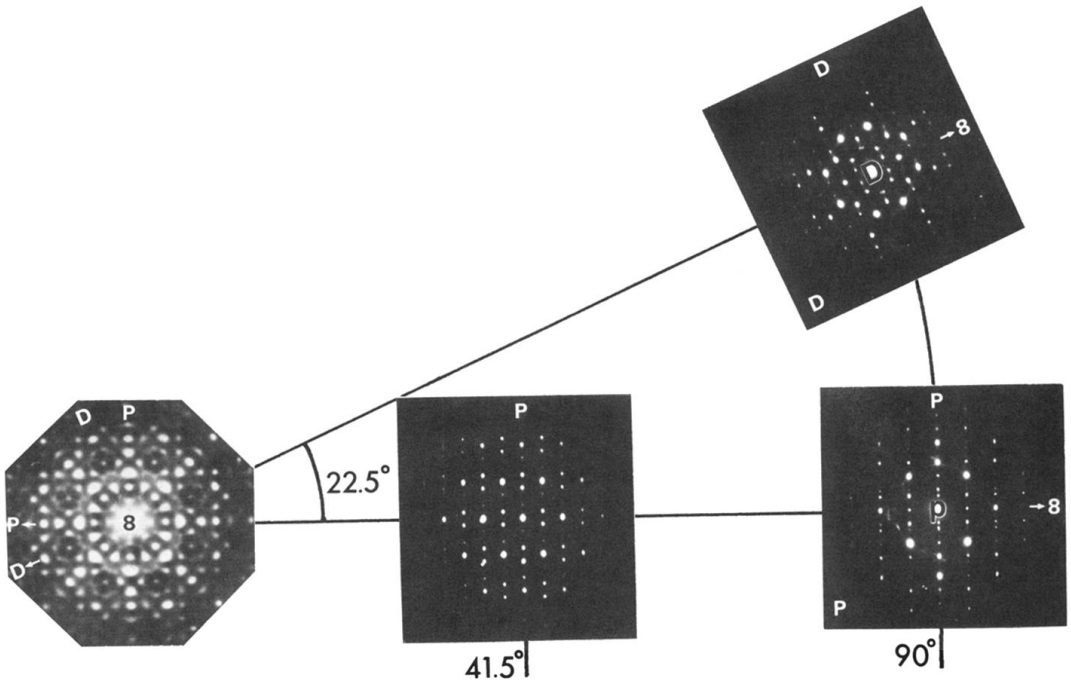

Figure 7.15 : Electron-diffraction patterns from the octagonal phase of Cr-Ni-Si, which bear outstanding resemblence to the 3D and 4D matter-wave interference patterns shown in fig. 7.14. Figure taken from [182].

In addition, fig. 7.14 also shows the different structure uncovered by high diffraction orders in the periodic (1D, 2D) and quasiperiodic (3D, 4D) lattices. For the former, high diffraction orders always possess larger momenta, and thus extend the synthetic lattice in the outward direction but does not increase its complexity owing to the periodic and thus redundant features. In the 3D and 4D configurations, on the other hand, multiple two-photon processes may culminate in high diffraction orders with a lower kinetic energy, causing a simultaneous inward and outward non-trivial and self-similar growth in the structure. As discussed later, this allows the presence of a singularly continuous component to the diffraction spectrum, which possesses a fractal dimension.

Multiple scattering vs Fourier transform

The atomic matter-wave diffraction patterns presented in fig. 7.14 are, though qualitatively similar, fundamentally different from the scattering intensity of real quasicrystals showed in fig. 7.15. Solid-state crystallographic techniques (described in chapter 3) only assume single scattering events from the complex, ionic (Coulomb) potentials constituting the crystals. Even when these potentials are periodic, they possess theoretically infinite Fourier components, which allows the *single*-scattering diffraction pattern (eq. 3.10) to result in a complex structure comprising a multitude of peaks.

Our optical lattices, on the other hand, are purely harmonic[8] and their Fourier transforms (i.e. the static structure factors, eq. 3.8) only comprise a finite set of elements. This is further quantified by the following example for 1D lattices.

[8]for ideal plane waves.

The Fourier transform $\mathcal{F}$ of a 1D optical lattice consists of a finite set in k space:

$$\mathcal{F}[-V_0\cos^2(\pi x/x_0)] = -V_0\sqrt{\frac{\pi}{2}}\left\{\frac{1}{2}\delta(k+k_0)+\delta(k)+\frac{1}{2}\delta(k-k_0)\right\}, \tag{7.30}$$

as shown in fig. 7.16a.
By contrast, the Fourier transform of an infinite ionic potential comprises an infinite series of k peaks:

$$\mathcal{F}\left[-V_0\sum_i \frac{1}{|x/x_0-i|}\right] = \frac{2\sqrt{2\pi}}{k^2}V_0\sum_{j\in\mathbb{Z}}\delta(k-jk_0), \tag{7.31}$$

as shown in fig. 7.16b.
For simplicity, in the above we took $x_0 = \lambda/2$ and $k_0 = 2\pi$. The equivalences in eqs. 7.30 and 7.31 are derived in appendix D.11.

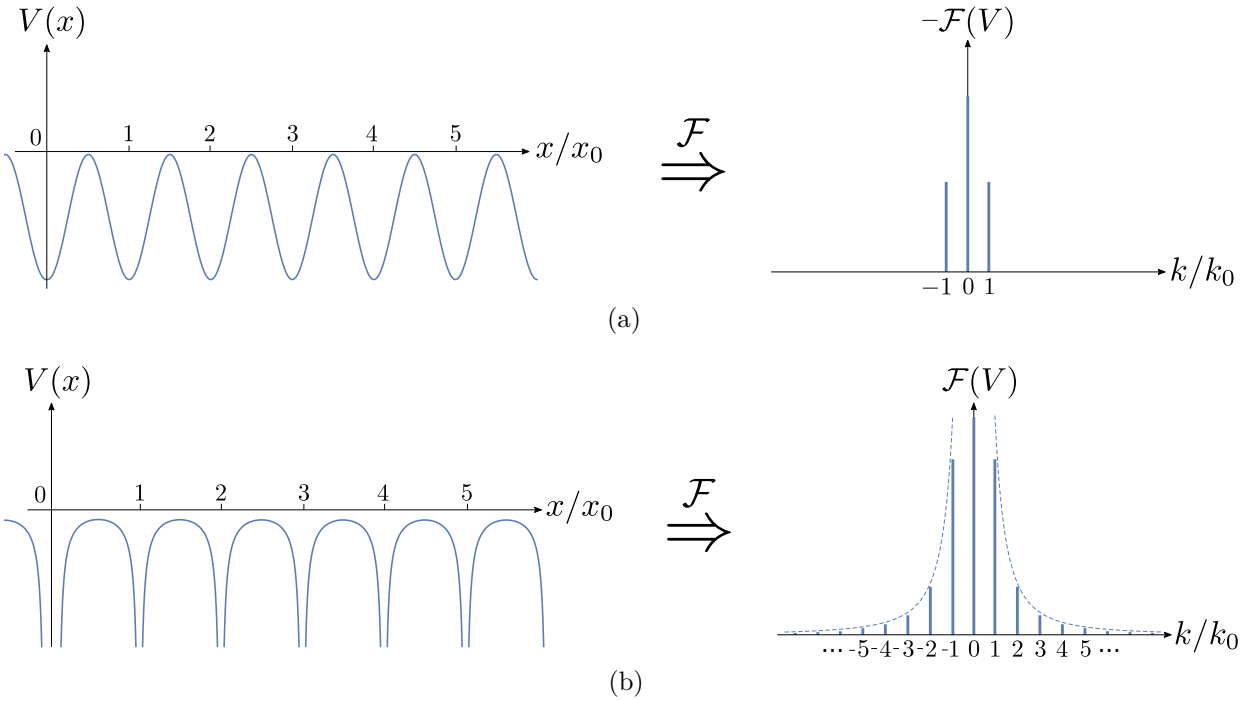

Figure 7.16 : The Fourier transform $\mathcal{F}$ of the lattice, or static structure factor, indicates the k states that can be reached via single-scattering events. While this is a finite set for a harmonic optical lattice (a), it is infinite for a solid-state ionic potential (b).

The complexity of our matter-wave interference pattern is therefore due to the presence of *multiple* scattering events, that is multiple two-photon processes. The static structure factor of our eightfold optical lattice, for instance, only comprises 9 elements ($k = |0\rangle, \pm|1\rangle, \pm|2\rangle, \pm|3\rangle, \pm|4\rangle$) and is imaged by short lattice pulses that only allow single two-photon transitions (second picture in fig. 7.17). Longer lattice pulses enable multiple two-photon transitions and uncover new and non-trivial structures, and would correspond to performing crystallography with thicker samples of real crystals.

Interestingly, however, the single scattering events from real, ionic potentials (in fig. 7.15) and the multiple scattering events from our simpler, harmonic potentials result in qualitatively similar diffraction patterns.

7.2.2 Quantum walk

In the following results, a rectangular lattice pulse is used, as shown in fig. 7.11. This has a steep rise time and short, variable duration ($\sim 0-25\,\mu s$) and fixed depth $V_0 = 14.6\,E_{rec}$.

Because of the sudden presence of the lattice, the BEC $|\mathbf{k}=0\rangle$ is not loaded into its ground state but is instead projected onto the many Bloch waves that are the eigenstates of the potential. The diffraction dynamics, shown in fig. 7.17, constitutes a continuous-time quantum walk on the synthetic lattice, where each hopping is a two-photon transition with a detuning equal to the difference in kinetic energy between the initial and final (reciprocal) states. This is quantitatively analysed in fig. 7.18, showcasing the difference between the oscillatory dynamics in 2D and the ballistic spreading of the population in 4D, where higher diffraction orders can possess lower kinetic energies and thus be energetically favoured. The Raman-Nath approximation detailed in section 7.1.3 neglects the kinetic energy and would correspond to a continuous-time quantum walk on a homogeneous (synthetic) lattice.

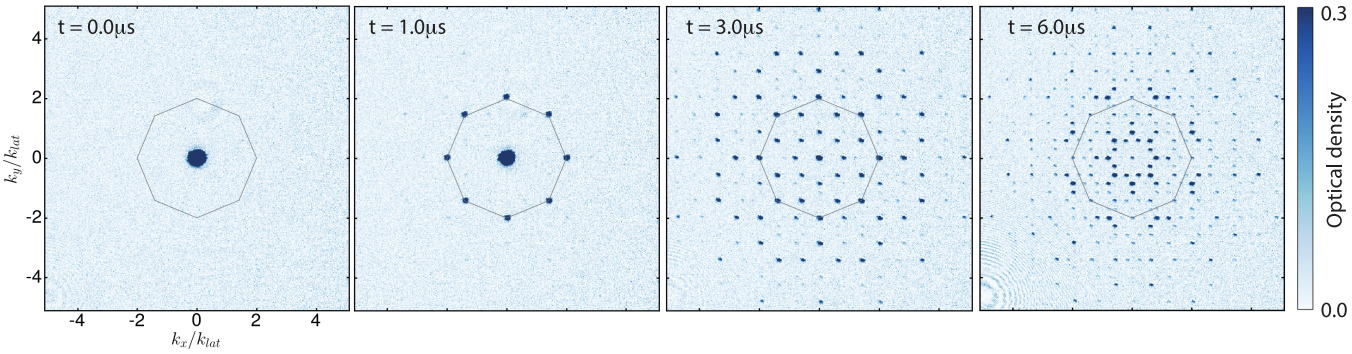

Figure 7.17 : Raw absorption images displaying the diffraction dynamics at a fixed lattice depth $14.6\,E_{rec}$ for a variable pulse duration. The octagon has circumradius $|2\hbar\mathbf{k}\rangle$. Figure taken from [181].

The transport properties on the synthetic lattice are quantified by the root-mean-square momentum:

$$\text{rms momentum} = \sqrt{\mathbf{p}^2} = \sqrt{\sum_i \frac{p_i(t)}{\sum_j p_j(t)} |\mathbf{b}_i|^2}\,, \tag{7.32}$$

where $p_i(t)$ is the population of the diffraction peak $\mathbf{b}_i$ at any given time t. This is plotted in fig. 7.19 for various lattice configurations and hence different (effective) dimensionalities D, all exhibiting a ballistic expansion for short pulse durations. The extent of the linear region depends on the lattice depth, and corresponds to the regime where the Raman-Nath approximation is valid. Intuitively, at short pulse durations Δt the Fourier broadened frequency range $\Delta\omega \sim 1/\Delta t$ is large enough not to resolve the detuning between the synthetic lattice points and hence enables a ballistic expansion[9].

[9]The linear region can be extended by means of lattice sequence composed of multiple pulses, simulated in Jonathan Mortlock's Part III report [187].

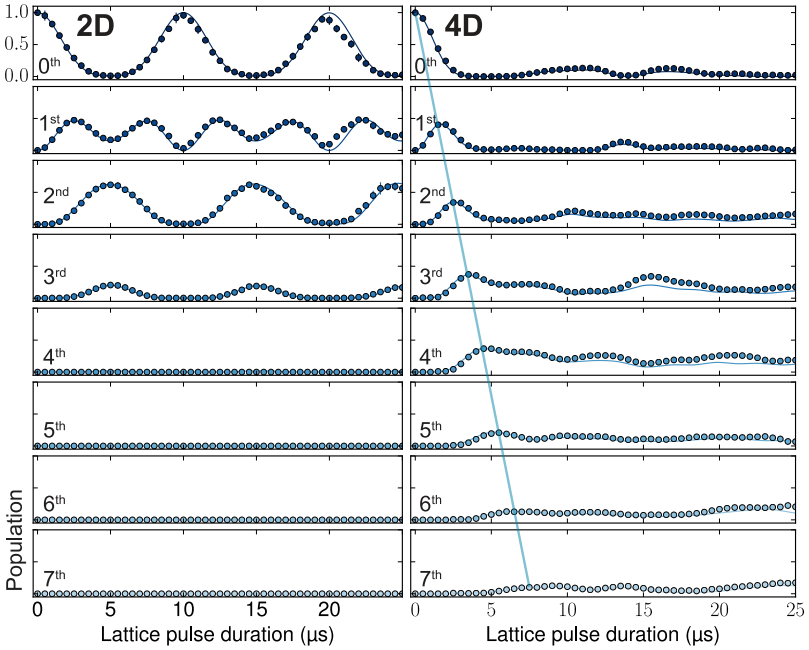

Figure 7.18 : In a regular 2D lattice (square, here) the dynamics is oscillatory. On the other hand, in the 4D quasiperiodic lattice some of the higher diffraction orders possess lower kinetic energies and are thus energetically favored, which enables a ballistic expansion shown on the right. The solid lines are obtained from simulations detailed in section 7.1.4. Figure taken from [181].

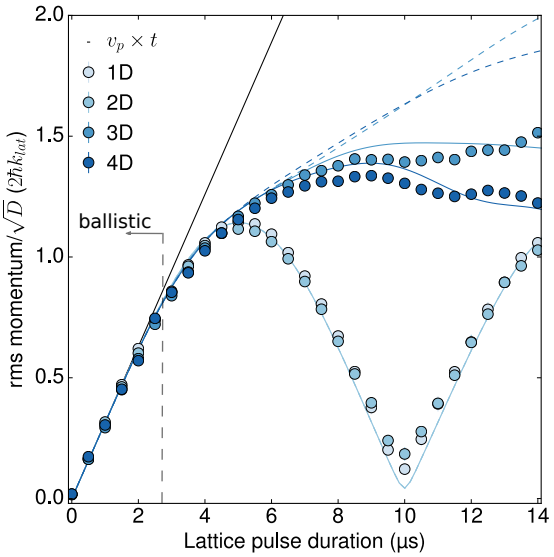

Figure 7.19 : The rms-momentum quantifies the transport of the atoms in the synthetic lattice. For short times all lattice configurations exibit ballistic expansions, while longer durations highlight the differences between the periodic and quasiperiodic ones, the former showing revivals. The solid lines are numerical simulations (section 7.1.4) for the experimental signal-to-noise ratio, while the dashed lines assume ideal detection efficiency. Figure taken from [181].

The slopes collapse to the same line when rescaled by $\sqrt{D}$, which is explained by the increased number of independent degrees of freedom contributing to the momentum $\mathbf{p}$:

$$\begin{aligned} |\mathbf{p}| &= \hbar \sqrt{\sum_{i}^{D} k_i^2} \propto \sqrt{D} \\ &= \hbar \sqrt{k_x^2 + k_y^2 + k_u^2 + k_v^2} \quad \text{for the 4D case.} \end{aligned} \tag{7.33}$$

The $\sqrt{D}$ scaling and the numerical prefactor v_p are rigorously obtained in [94] and in the supplemental material of [181].

At longer pulse durations, the distinction between periodic and quasiperiodic lattices becomes evident. Periodic 1D and 2D lattices display an oscillatory behaviour, though perfect revival (even in the simulation) is prevented from the system comprising more than two levels. This can also be understood in terms of the Poincaré recurrence theorem, which states that for a bounded phase-space and a sufficiently long time, a dynamical system will return to its original state, or at least very close to it. For two commensurate timescales n and m, the Poincaré recurrence time τ_{P} is $n \cdot m$. If m is irrational, it can be written as a rational approximant $m = p/q$, with $p, q \in \mathbb{Z}$, which only becomes exact in the limit of large $p, q \to \infty$. The Poincaré recurrence time $n \cdot q$ therefore tends to infinity $\tau_{\mathrm{P}} \to \infty$.

The quasiperiodic synthetic lattices take an infinite amount of time to return to the original state because of the infinite number of reciprocal states at smaller momenta and kinetic energies that become available at stronger and longer pulse durations. This is illustrated in fig. 7.20, where regular 2D lattices always exhibit closed contours of equal kinetic energy, thereby containing a finite number of states of the synthetic lattice. On the other hand, fig. 7.21 shows that the equal-kinetic energy contours for the 3D lattice (or equivalently a 3D hyperplane of the 4D lattice) are not bounded, but rather encompass an infinite number of synthetic states, resulting in the infinitely slow revival dynamics observed in fig. 7.19.

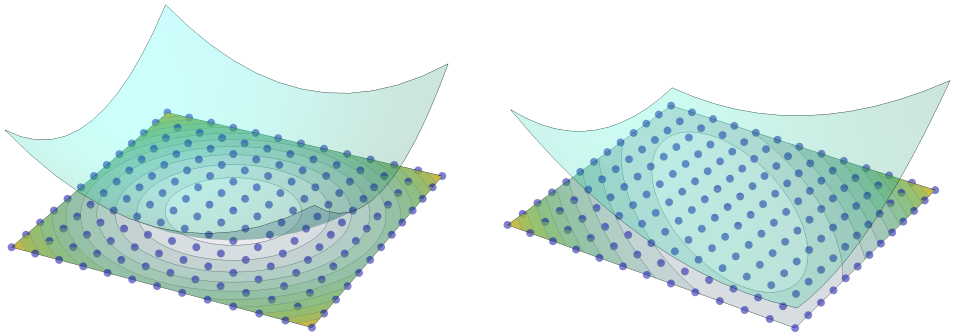

(a) Square lattice (b) “Slanted” lattice

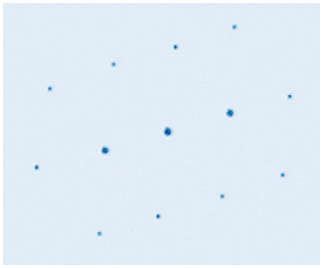

(c)

Figure 7.20 : Regular 2D (synthetic) lattices created by two standing waves at 90° (a) or 45° (b) angle between them, the latter referred to as “slanted lattice” giving rise to the diffraction pattern in (c). The kinetic energy contours (bottom) are closed and therefore contain a finite number of synthetic states.

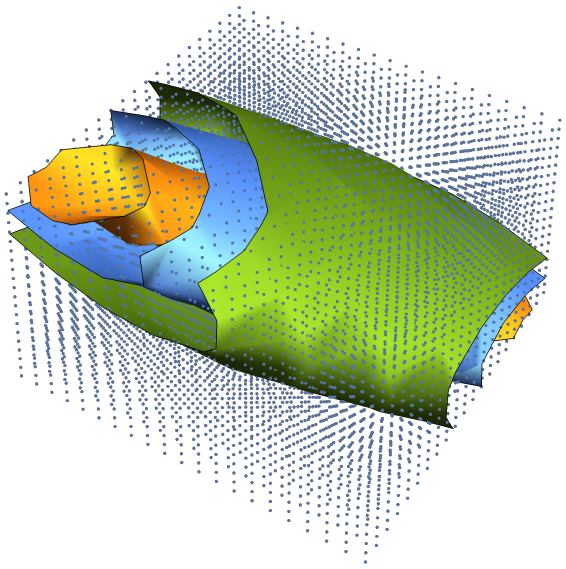

Figure 7.21 : A 3D regular lattice where the z axis corresponds to the third beam $\mathbf{k}_3 = (1/\sqrt{2}, 1/\sqrt{2})$. The contours at constant kinetic energy are not closed and thus contain an infinite number of synthetic states.

7.3 Diffraction spectrum

7.3.1 Singularly continuous component

In section 3.2.3, the scattering intensity (or diffraction spectrum) was divided into a pure point, an absolutely continuous and a singularly continuous component:

$$I(\mathbf{k})_{\text{total}} = I^{\text{pp}}(\mathbf{k}) + I^{\text{sc}}(\mathbf{k}) + I^{\text{ac}}(\mathbf{k}). \tag{7.34}$$

An image of the diffraction spectrum for the eightfold symmetric optical lattice is shown in fig. 7.22. The pure point component I^{pp} is identified as the subset of the diffraction peaks *only* caused by two-beam lattice configurations (resulting in crystallographically allowed rotational symmetries), whereas the remaining peaks belong to the singularly continuous contribution I^{sc}, as shown in fig. 7.23. The distinction between the two spectral components was based on the definitions presented in section 3.2.3. More intuitively for the examples shown here, these amount to a closure-type argument of whether or not another point belonging in the set could be found within a distance $\epsilon \to 0$ between two other points in the same set. The spectral components for a three-beam lattice pattern are shown in fig. 7.24.

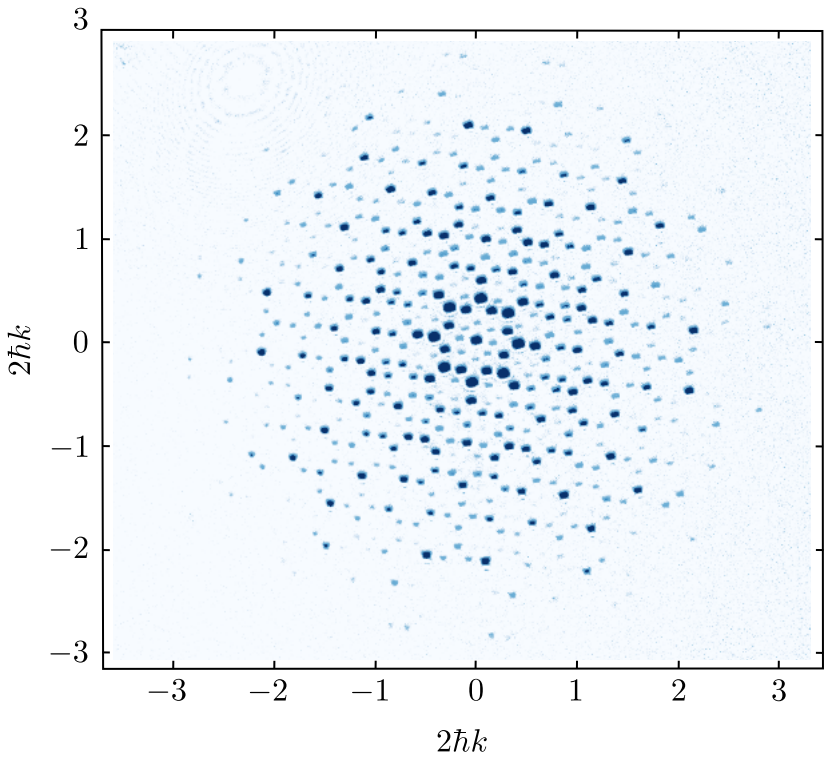

Figure 7.22 : A non-linear colour bar allowed to visually emphasise up to the 9^{th} diffraction order, the central one being the 0^{th} one.

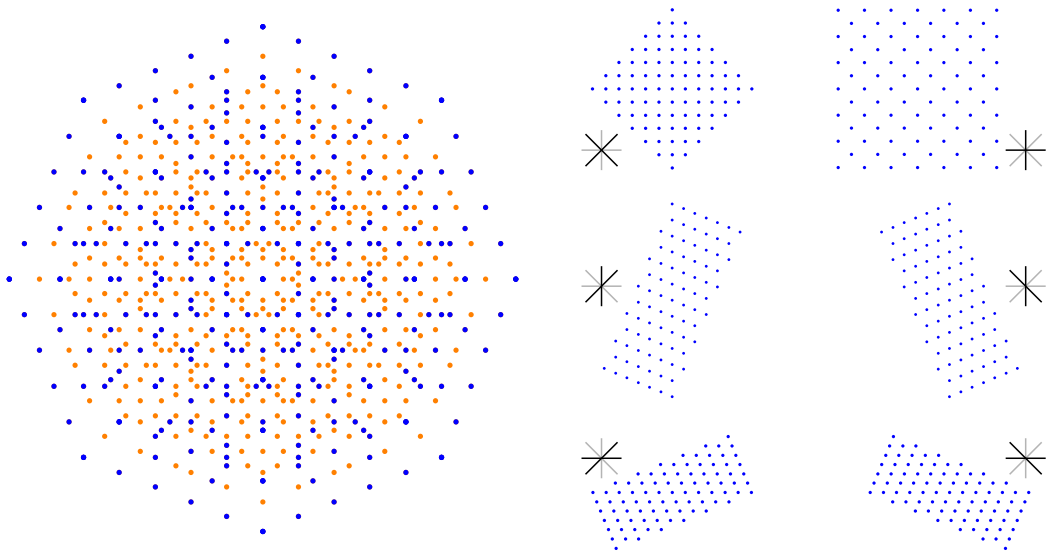

(a) Full diffraction spectrum (b) Pure point contributions

Figure 7.23 : The full diffraction spectrum for the four-beam lattice (a) with its pure point (blue) and singularly continuous (orange) contributions. The pure point component consists of the diffraction peaks caused by all two-beam sub-lattices (b), which do not violate the crystallographic restriction theorem. For the spatial extent of the spectrum shown, the pure point component is complete while the singularly continuous one was truncated.

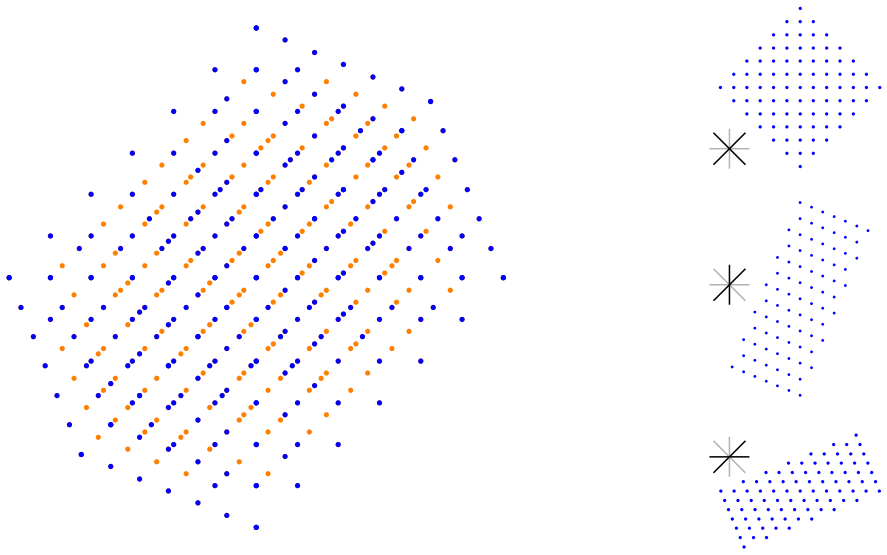

(a) Full diffraction spectrum (b) Pure point contributions

Figure 7.24 : The full diffraction spectrum for a three-beam lattice (a) with its pure point (blue) and singularly continuous (orange) contributions. The pure point component consists of the sum of the diffraction peaks caused by all two-beam sub-lattices (b). For the spatial extent of the spectrum shown, the pure point component is complete while the singularly continuous one was truncated.

The absolutely continuous I^{ac} contribution to the spectrum is not present in fig. 7.22 because the intra-species interaction strength was set to zero, preventing any scattering between atoms. Using ^{87}Rb, however, makes the scattering events noticeable as shown in fig. 7.25. Besides reducing the visibility of higher diffraction orders and increasing the peaks' size, interactions add an absolutely continuous (in the limit of infinite particle number) part to the spectrum. The *scattering spheres* are caused by the centre-of-mass collisions of atoms with the same mass while they are separating inside the BEC, resulting in the final states to lie on a sphere centred between the momentum states involved.

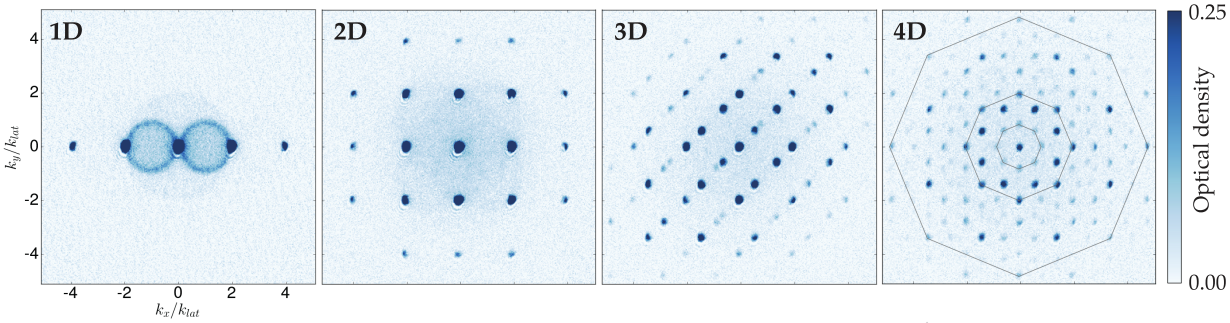

Figure 7.25 : Using ^{87}Rb with its non-zero background scattering length allows inter-atomic collisions, which result in scattering spheres, reduced visibility, increased peak size, and an absolutely continuous contribution to the diffraction spectrum. Figure taken from [94]

The size of the diffraction peaks is dominated by the near-field nature of the interference pattern and its dependence on the initial BEC size. At longer times, the peaks' size would become infinitesimally small relative to their separations. Other contributions to peak broadening are repulsive interactions (in ^{87}Rb, fig. 7.25, they also cause the crescent moon shape of the peaks[10]), and the finite size of the lattice beams and of the atomic cloud.

7.3.2 Fractal dimension

When dealing with recursive and nested geometrical patterns, it is instructive to define a measure of their space-filling capacity: if this does not scale as the dimensionality d of the embedding space, it is referred to as *fractal dimension*, introduced in section 3.2.3.

The fractal dimension for the Penrose or Ammann-Beenker tilings (figs. 3.6c and 3.6d) is trivially two, i.e. equal to the 2D plane they are drawn on, since the covering leaves no gaps [188]. For the interference patterns shown in the previous section, however, the discussion becomes more subtle since each diffraction order is a zero-dimensional point, but their collectiveness tends to form a dense set which may tile the whole 2D plane.

In order to quantify the fractal dimension of the diffraction spectrum (S), we define the box-counting dimension as the number of boxes $N(\epsilon)$ of side ϵ required to fully cover the set:

$$\dim_{\mathrm{box}}(S) = \lim_{\epsilon \to 0} \frac{\log N(\epsilon)}{\log(1/\epsilon)}. \tag{7.35}$$

[10] which are present to some extent in ^{39}K as well because of the "puff up" field in time-of-flight

For a finite set of n points, $N(\epsilon)$ eventually becomes a constant, making the box-counting dimension zero. This is the case for any pure point spectral contributions.

In general, the number of required boxes scales with the dimension of the set:

$$N(\epsilon) = k\left(\frac{1}{\epsilon}\right)^d \quad \Rightarrow \quad \log N(\epsilon) = \log(k) + d\log(1/\epsilon), \tag{7.36}$$

which can be used to extract d.

For a 2D square of normalised side 1, the above yields $k = 1$ and $N = 1/\epsilon^2$, and hence results in $d = 2$. Similarly, a cube gives $d = 3$ and a line $d = 1$, all of which are equal to the topological dimension of the set itself, hence trivial.

In order to find d for our diffraction spectra, we define ϵ as the smallest distance between the diffraction orders in a finite section of radius ℓ, and $N(\epsilon)$ as the total number of states present in the same section. This is shown in fig. 7.26, and the result of fitting eq. 7.36 is presented in fig. 7.27.

The "fractal" dimension obtained is $d = 2$, which is a trivial (non-integer) case but still of relevance given that each individual diffraction order is a zero-dimensional point. The ability of the diffraction peaks to cover the 2D plane is the result of the singularly continuous component of the diffraction spectrum. For a three-beam lattice diffraction spectrum, $d = 1$.

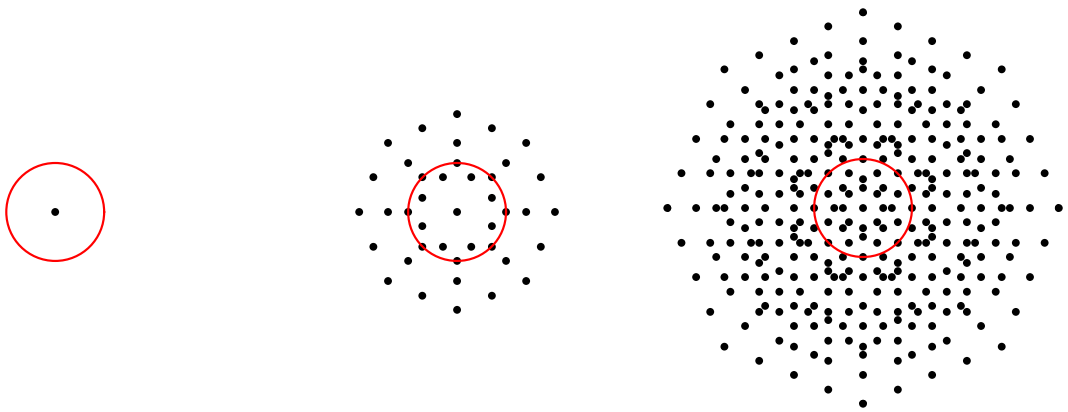

(a) $n = 1$ (b) $n = 3$ (c) $n = 5$

Figure 7.26 : Varying the number n of two-photon transitions events results in more points N in a region of radius ℓ (red contour, here $\ell = 2\hbar k$) whilst at the same time reducing the smallest separation ϵ between them.

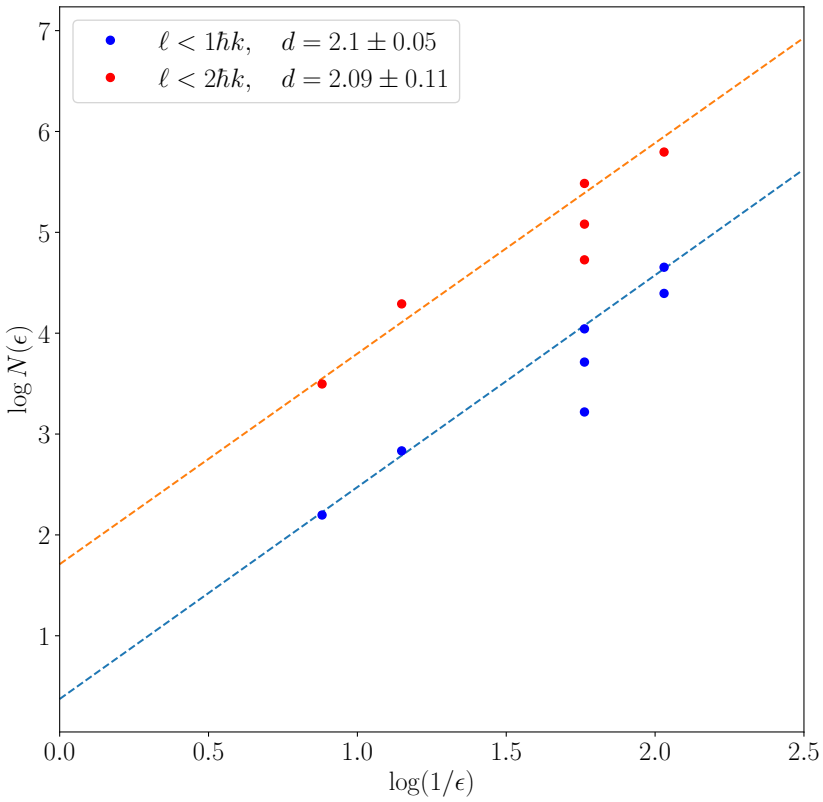

Figure 7.27: The number of boxes $N(\epsilon)$ of side ϵ required to fully account for the diffraction spectrum are related by eq. 7.36 which allows extraction of the fractal dimension d. Each datum is computed from increasing the number of two-photon transitions, as shown in fig. 7.26. The lower lying data points are caused by diffraction peaks on the rim ℓ and are excluded from the linear fit.

An interesting point that was raised in the VIVA (29$^{\text{th}}$ May 2019) was the following. A true quasicrystal results in an infinite set of diffraction peaks, that would then pave the whole 2D plane as proved in this section. Experimental images such as fig. 7.22, however, only display a *finite* number of diffraction peaks, dictated by a finite number of atoms and signal-to-noise ratio. One could then ask – what are the largest rational approximants to $\sqrt{2}$ that would explain our quasiperiodic diffraction patterns? Would they depend on the initial atom number N, and could one infer the limit for $N \to \infty$?

Chaos isn't a pit. Chaos is a ladder.

Ser Petyr Baelish (Littlefinger), from *Game of Thrones* [189]

8

Disorder: localisation transition

In the following chapter we numerically and experimentally investigate the ground state properties of bosons loaded in the 2D non-separable quasiperiodic potential. The quasi-disorder stemming from the lack of translational symmetry results in a transition from an extended ("superfluid") to a localised phase at a critical lattice depth $V_{\mathrm{loc}} \approx 1.78\, E_{\mathrm{rec}}$ in the absence of interactions, akin to the mechanism described by the Aubry-André model. The localised phase seems to be resilient against moderate repulsive interactions, which would make this the first experimental realisation of a 2D Bose glass.

8.1 Theoretical aspects of localisation

8.1.1 Context

From Anderson to Many-Body Localisation

Disorder is ubiquitous in nature, and though generally treated as a mere perturbation, often times it may lead to novel dynamics and phenomena. This was first discovered in insulating materials: band and Mott insulators were already known and understood to lack electrical and thermal conduction either due to the absence of available scattering states or due to strong repulsive interactions. In 1958 P.W. Anderson [190] realised that insulating behaviour may also stem from the presence of disorder, a phenomenon now known as *Anderson localisation*. The disorder-induced (Anderson) insulator is a *localised* phase of matter with an exponentially decaying correlation function [191] but, as opposed to the Mott insulator, it is a single-particle phenomenon. Insulating behaviour is only a mere consequence of localisation, for its defining feature is the lack of thermalisation and its inability to equilibrate, as further discussed in the next section. The localisation of the wavefunction can be understood to be a consequence of the destructive interference among the (coherent) reflections from the random features of a disordered potential, as shown in fig. 8.1. When the scattered amplitude is comparable to the incident one (quantified by

the Ioffe–Regel criterion), destructive interference and a tight confining envelope ensue.

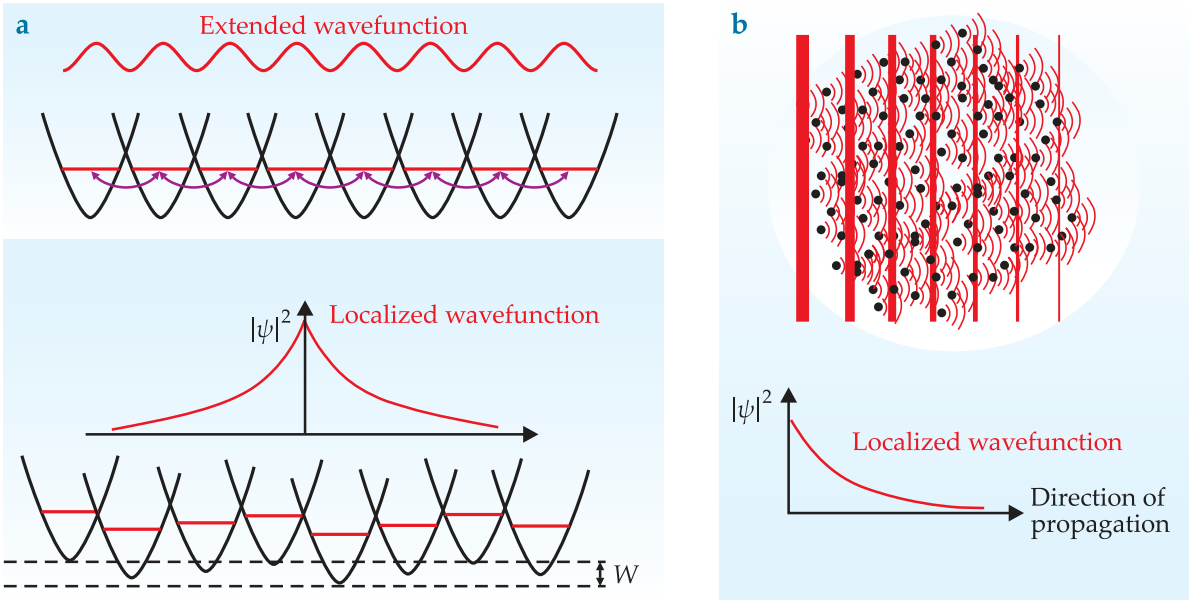

Figure 8.1 : Anderson localisation can be interpreted as the result of the destructive interference of the multiple (coherent) reflections from the random features of the disordered potential landscape. Figure taken from [30].

Anderson localisation has been experimentally observed in random [192, 193] and quasiperiodic [194] photonic lattices, in electronic systems [195–197], in optical fibres [198, 199], and in biological systems [200]. In cold atoms, this was first achieved for a BEC in a 1D optical lattice illuminated with a disordered intensity pattern generated by a laser propagating through a diffusing plate [30, 201], the results of which are shown in fig. 8.2. In order for the exponential localisation to emerge, the thermal de Broglie wavelength of the BEC needs to exceed the correlation length c of the disordered pattern, $\lambda_{\rm th} > c$, so that the atoms can react to the randomness of the potential instead of adiabatically following it. The opposite limit would correspond to classical trapping of a particle of kinetic energy lower than the potential step.

While Anderson formulated the theory for non-interacting particles, the presence of interactions, providing an additional transport and delocalisation avenue, may not, in fact, disrupt the insulating state, in what is known as *Many-Body Localisation* (MBL).

Anderson localisation in a random potential occurs for any arbitrarily small disorder[1], with stronger disorder only resulting in a tighter exponential envelope. However, when the disorder is generated by an incommensurate modulation of an underlying regular lattice, such as in the *Aubry-André* model, the localisation transition only occurs at a finite critical value, when the reflected waves reach the same amplitude of the incident one thereby resulting in destructive interference.

[1]Only in 1D and 2D. For $d \geqslant 3$, localisation only occurs above a critical disorder strength referred to as the *mobility edge*. For any strength of the disorder there is a mobility edge at finite energy.

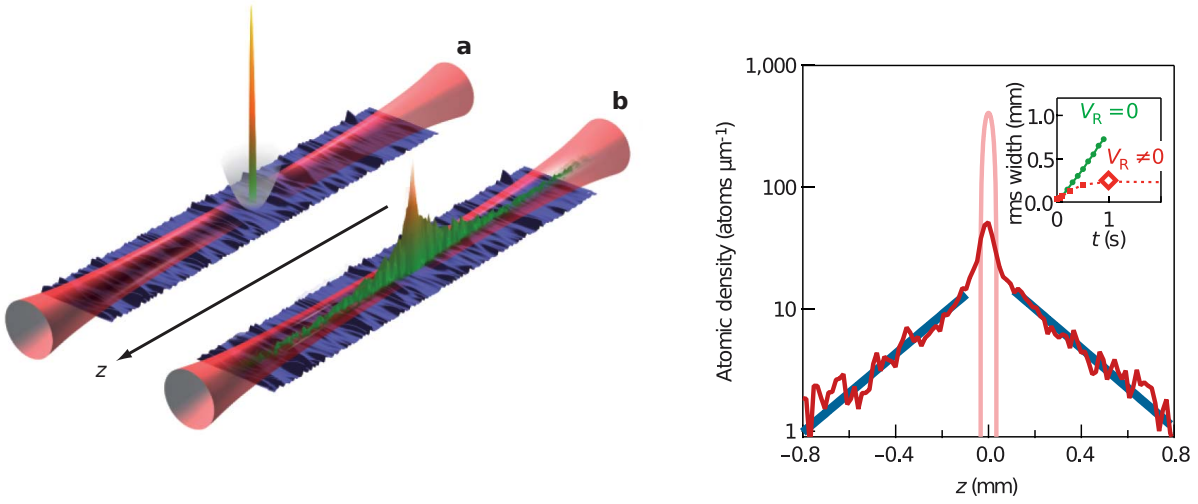

(a) (b)

Figure 8.2 : A BEC in a 1D optical lattice with random disorder introduced by a diffusive plate. In the presence of zero disorder ($V_R = 0$) the atoms expand ballistically, whereas for $V_R \neq 0$ the BEC becomes exponentially localised and shows no transport (at least on the experimental timescale). Figure taken from [201].

Importance of localised phase

A disorder-induced localised phase cannot and does not thermalise, hence it cannot be described by any thermodynamic equilibrium ensemble, rendering common techniques of statistical mechanics powerless – this is so intriguing that it deserves its own section in this thesis, largely based on the review [202]. A more mathematical treatment is presented in [203].

Classical and quantum statistical mechanics both assume that a general (non-integrable) system will, at some point, thermalise. Thermalisation cannot be dependent on the presence of an external reservoir, for an isolated quantum system would need to contain such as a reservoir itself. Hence, the system needs to act as its own reservoir, with each sub-system exchanging energy and particles with its surroundings. After thermalisation, the properties of the system are not specified by any of the (local) initial conditions, but by expectation values over the (global) thermodynamic equilibrium ensemble. If a balloon is burst in vacuum, for example, the velocity of the air molecules will eventually be described by the same Maxwell-Boltzmann distribution (eq. 1.18) no matter its initial position or size. The starting conditions of the system cannot be simply erased by the purely unitary evolution of a quantum system, however, but rather the information is distributed over the whole system, encoded in the entanglement and hence recoverable only by means of global operators.

Thermalisation may be prevented by the presence of additional conservation laws in integrable systems, though these can also be shown to thermalise in the presence of weak perturbations [204].

A disorder-induced localised state is unable to act as its own reservoir, hence thermalisation and equilibrium are prevented; the final state, no matter the elapsed time, still retains memory of the local initial details. This is a property of individual eigenstates, and it is therefore not captured by equilibrium thermodynamics whose ensembles would

average over many eigenstates. The BEC, crystals and structural glasses discussed in Part I are all equilibrium (thermal) states, identified by distinct symmetries whose breaking quantitatively characterises the phase transition. The localisation phase transition, on the other hand, can only be probed "dynamically"[2], by investigating the transport properties and the memory of the initial conditions. While DC conductivity is strictly zero for localised systems, it is not their defining feature, as there exist time-driven Floquet-engineered localised states where DC observables would be ill-defined either way [206, 207]. Interactions provide an additional avenue for particle transport and thermalisation, but MBL states are found to be resilient against small but arbitrary perturbations. MBL states are characterised by a set of localised conserved charges that are constants of motion for the system, sometimes referred to as *l-bits* [202], and are hence ("locally") integrable.

The *Eigenstate Thermalisation Hypothesis* [204] (ETH) has been found to serve as a good discriminant between thermal and localised phases, in that it only holds for the former. This essentially states that any initial wavefunction, provided the eigenstates of the Hamiltonian are thermal, will evolve into a thermal state, i.e. dephasing will eliminate the off-diagonal terms of the density matrix – this is for instance not true for the Anderson insulator discussed in the previous section. Thermal states are also *ergodic*, i.e. they explore all available phase-space so that their spatial and temporal averages look the same and are independent of the initial state (except for conserved quantities such as energy, in a closed system). Table 8.1 summarises the key differences between thermal, single-particle (Anderson) and many-body localised states.

Thermal	Single-particle localised	Many-body localised
Memory of initial conditions hidden in global operators at long times	Some memory of local initial conditions preserved in local observables at long times	
ETH true	ETH false	
DC conductivity $= 0$ or $\neq 0$	DC conductivity strictly 0	
Continuous local spectrum	Discrete local spectrum†	
Eigenstates with volume-law entanglement	Eigenstates with area-law entanglement†	
Power-law spreading of entanglement from non-entangled initial conditions	no spread of entanglement	logarithmic spreading of entanglement from non-entangled initial conditions†

Table 8.1 : Summary of the key differences between thermal and localised states. Table adapted from [202]. †: these points are qualitatively discussed in appendix D.12.

[2]Which is not the same as the dynamical phase transitions in e.g. [205], where the free energy develops a cusp as a function of time.

Localisation so far

Cold atom experiments have hitherto introduced disorder either by generating a random pattern from a diffusive plate, projecting it from a DMD, or by using bichromatic lattices with incommensurate wavelengths resulting in a quasiperiodic modulation. A DMD has recently also been used to project a 2D quasiperiodic pattern [208].

Non-localised states are usually referred to as *extended* or *superfluid* phases, the latter term often being (inappropriately) used also for a non-interacting BEC before the Anderson localisation transition – see discussion at the end of section 1.2.2.

MBL has been studied mostly in the context of fermions in highly excited states, and it has exhaustively been investigated in 1D [31, 209–212], while in 2D MBL has not always been found to be stable against interactions [213, 214]. In addition, the 2D potentials employed so far have always been separable.

The term *Bose glass* has been used for bosons in the ground state, and was theorised in [215]. Bosons in the tight-binding regime described by the Bose-Hubbard model undergo a transition from a compressible, gapless and long-range phase-ordered superfluid to a gapped, incompressible and incoherent Mott insulator driven by the competition between on-site interaction and nearest-neighbour tunnelling. In the presence of disorder, however, the Bose glass phase appears, compressible and gapless but lacking off-diagonal long-range order. Close to the transition, it is understood as an insulating phase surrounding and enclosing small pockets of superfluid, known as "rare regions" and governed by *Griffiths effects*, which grow in size and percolate at the transition. This is shown schematically in fig. 8.3.

Bose glasses have been experimentally investigated in 1D [28, 29] but not yet in 2D. A 2D boson experiment in a disordered potential exhibiting MBL was carried out in [216], but this involved quenches and therefore did not exclusively probe the ground state.

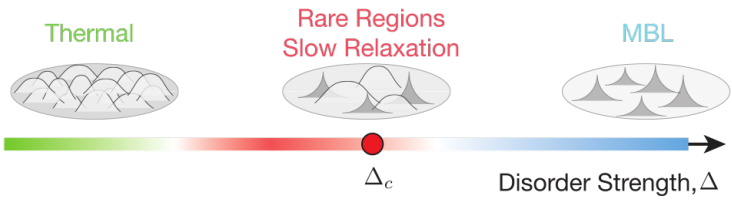

Figure 8.3 : Increasing the disorder strength Δ in an otherwise regular lattice induces a transition from a thermal (delocalised) to a localised (MBL, here) phase. The "rare regions" near the critical disorder strength Δ_c grow in size and percolate at the transition. Figure taken from [214].

Several open questions remain in the field, two of my favourite ones being:

1. Can MBL happen in translationally invariant Hamiltonians, by encoding the disorder in the initial state?
   Connections have been uncovered between the slow-relaxation mechanisms that occur in classical glasses and the non-ergodic behaviour of closed quantum systems [217]. Glasses are classical examples that break ergodicity - are they just the classical limit of MBL states, or a completely distinct phenomenon?

2. Is there a difference between pure disorder and quasiperiodicity?
   It has been argued [218] that these two systems belong to different universality classes, and that MBL not only is expected to happen in quasiperiodic systems [219], but that it would be more stable. However, other theoretical results are conflicting, claiming that interactions in 2D quasiperiodic lattices lead to thermal diffusion [220, 221]. Numerical simulations are not fully reliable because of the finite size of the analysed systems, hence experimental platforms are the most promising means to provide a definitive answer[3].

Our experiments probe a system of bosons in their ground state. In the 2D non-separable quasiperiodic potential, the observed behaviour is consistent with the bosons undergoing an extended to localised phase transition at a critical lattice strength. The localised phase seems to be resilient against moderate repulsive interactions, which would make this the first experimental realisation of a 2D Bose glass.

8.1.2 Probing localisation in real and momentum space

Disorder-induced[4] localised phases of matter have so far only been investigated in-situ, studying the atomic density distributions in real space – e.g. with single-site resolution in [216]. Typical studies usually involve imprinting a local density perturbation, either removing part of the cloud or imposing a "density wave", to determine how much of the local information of the initial state is retained in its long term evolution. Localised phases preserving local memory, they should always display traces of the original *imbalance*.

Investigations of the real space wavefunction in our experiment required construction on a novel setup, plans for which had already started and are discussed in chapter 9. However, we also wanted to test whether or not localised phases could be studied in *momentum space*, by using the time-of-flight techniques already employed in chapter 7. To our knowledge, disorder-induced localisation had never been investigated in momentum space before.

In the rest of this short section we discuss how momentum space provides a complementary framework to establish the existence of a localised phase. The next section then details numerical evidence confirming the presence of a disorder-induced phase transition in our 2D quasiperiodic lattice, quantified by the *Participation Ratio* (PR) and *Inverse Participation Ratio* (IPR).

A quantum state may be expressed in any complete orthonormal basis, for instance in the Wannier $|w_i\rangle$ or in the plane wave $|\phi_j\rangle$ bases, corresponding to the eigenstates of the (band-projected) position (x) and momentum (k) operators respectively:

$$|\Psi\rangle = \sum_i \psi_i |w_i\rangle = \sum_j \tilde{\psi}_j |\phi_j\rangle. \tag{8.1}$$

The (inverse) participation ratio PR (IPR) is defined in eq. 8.2 for both real (x) and

[3] To this date numerical simulations are limited to $\mathcal{O}(20)$ lattice sites, corresponding to at most 5×5 sites in 2D. With $\gtrsim 100\,\mu\text{m} \times 100\,\mu\text{m}$ lattice regions we can investigate regions that are $100 - 1000$ times larger.

[4] Interaction-induced localised phases such as the Mott insulator, on the other hand, were originally studied in momentum space: the absence of interference peaks after time-of-flight established the loss of phase coherence associated with the insulating phase.

momentum (k) space:

$$\begin{aligned} \mathrm{PR}_x &= \frac{1}{\sum_i |\psi_i|^4}, \qquad & \mathrm{IPR}_x &= \sum_i |\psi_i|^4, \\ \mathrm{PR}_k &= \frac{1}{\sum_j |\tilde{\psi}_j|^4}, \qquad & \mathrm{IPR}_k &= \sum_j |\tilde{\psi}_j|^4. \end{aligned} \tag{8.2}$$

Normalisation imposes $\sum_i |\psi_i|^2 = 1$, and hence $\sum_i |\psi_i|^4 \leqslant 1$, and similarly for $\tilde{\psi}_j$. The equality is only satisfied when the state is completely described by *one* basis function. Hence, the PR and IPR quantify the "purity" (not in a density matrix sense) of a quantum state in terms of its basis functions.

A fully localised state in real space (e.g. confined to one lattice site) is described by a single Wannier function, which because of its narrow features would require infinite Fourier components, meaning it would be fully *delocalised* in momentum space. From eq. 8.2, the localised phase therefore corresponds to $\mathrm{IPR}_k \to 0$ in the thermodynamic limit.

On the other hand, in the absence of a lattice the state is fully delocalised in real space and is thus described by the lowest plane wave with quasimomentum $q = 0$. As a result, it would be fully localised in momentum space, being composed of only *one* Fourier component, and corresponds to $\mathrm{IPR}_k = 1$. For shallow lattices below the localisation transition, the state is still delocalised but its composition comprises higher harmonics thus rendering $\mathrm{IPR}_k =$ finite but not infinitesimal.

Momentum space thus provides a complementary and novel framework to study disorder-induced localised phases, with the paradigm that localisation in real space corresponds to delocalisation in momentum space, and vice versa. This is summarised in table 8.2.

	definition	delocalised (extended)	localised
IPR_x	$\sum_i \lvert\psi_i\rvert^4$	$\to 0$ in thermodynamic limit	finite 1 when fully localised
IPR_k	$\sum_j \lvert\tilde{\psi}_j\rvert^4$	finite 1 for free system	$\to 0$ in thermodynamic limit

Table 8.2 : Inverse Participation Ratio (IPR) in real (x) and momentum (k) space.

8.1.3 Numerical evidence

In this section we present numerical evidence establishing the presence of a disorder-induced localised phase in our eightfold symmetric quasicrystal. The studies are performed both in momentum space (as will the experiments), and in real space for complementarity.

Momentum space

The single-particle Hamiltonian H was constructed in the plane wave basis $|\phi_j\rangle$ for various lattice configurations, but all involving beams of equal strength V_0, as detailed in section 7.1.4. The ground state of H was computed by finding its lowest eigenvalue, and the inverse participation ratio in momentum space (IPR_k) was calculated. The results for

the quasiperiodic eightfold symmetric lattice and for a regular square lattice are shown in figs. 8.4 and 8.5 for an increasing number of basis states – the n^{th} generation is reached by n two-photon scattering events.

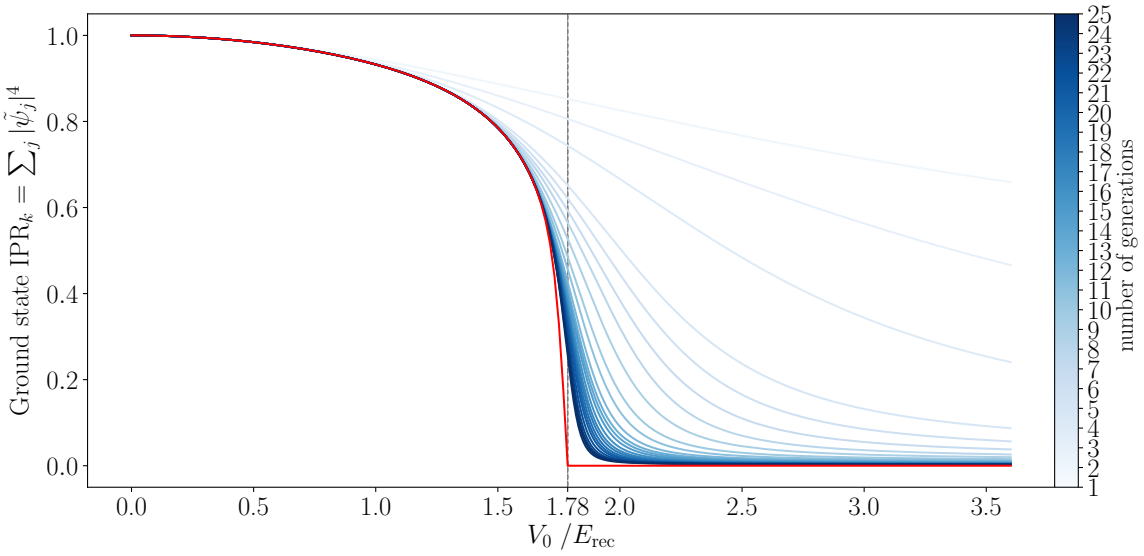

Figure 8.4 : The momentum space inverse participation ratio IPR$_k$ for the ground state of the eightfold quasiperiodic lattice shows a sharp phase transition at $V_0 \approx 1.78\, E_{\text{rec}} = V_{\text{loc}}$. The red line is the limit for the non-truncated Hamiltonian (infinite generations).

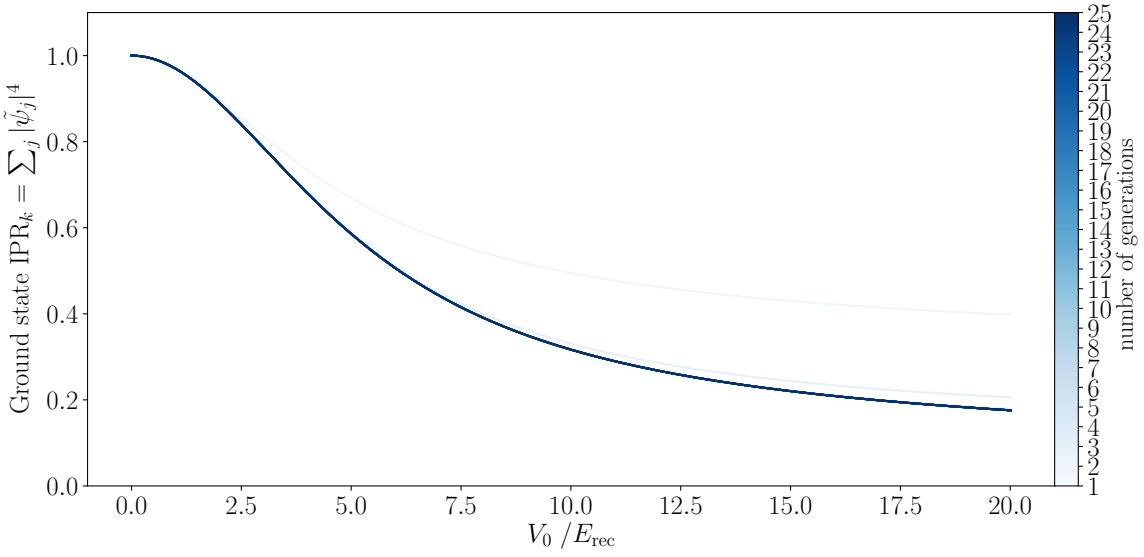

Figure 8.5 : The momentum space inverse participation ratio IPR$_k$ for the ground state of a 2D square lattice is always continuous, with no sign of any abrupt transitions. It is always finite, and only tends to zero asymptotically.

All periodic lattices exhibit the same qualitative behaviour as fig. 8.5, for which it only takes a few generations in order for the IPR$_k$ to converge to a smooth function of lattice depth V_0. By contrast, the eightfold quasicrystalline lattice exhibits a sharp transition $V_0 \approx 1.78\, E_{\text{rec}}$, hence identified as the critical strength for localisation V_{loc}. This value was

obtained by plotting the IPR_k of each lattice depth in fig. 8.4 against $1/n$, n being the number of generations. By fitting a straight line, its intercept allowed extrapolation to the real, non-truncated system ($n \to \infty$). Phase transitions for other lattice configurations are discussed in appendix C.

When $\mathrm{IPR}_k > 0$, the state is localised in momentum space, meaning only a few plane waves are occupied and hence the state is delocalised (extended) in real space – in the limit of a free system, only one plane wave is occupied and $\mathrm{IPR}_k = 1$. However, for $V_0 \gtrsim 1.78\, E_{\mathrm{rec}}$, the IPR_k drops to an infinitesimally small value, just large enough to ensure normalisation: all plane waves are occupied, which results in a localised real space wavefunction with very narrow features.

The IPR_k for the first few tens of low-lying eigenstates was also computed[5] and is shown in fig. 8.6. This was highly sensitive to both the size of the Hamiltonian and to the numerical tolerance of the eigenvalue solver algorithm (because of degeneracies in the eigenenergies), but it confirms that the first few excited states exhibit the same qualitative behaviour as the ground state, which is good news for experiments since it would be challenging to perfectly eliminate admixture from higher states.

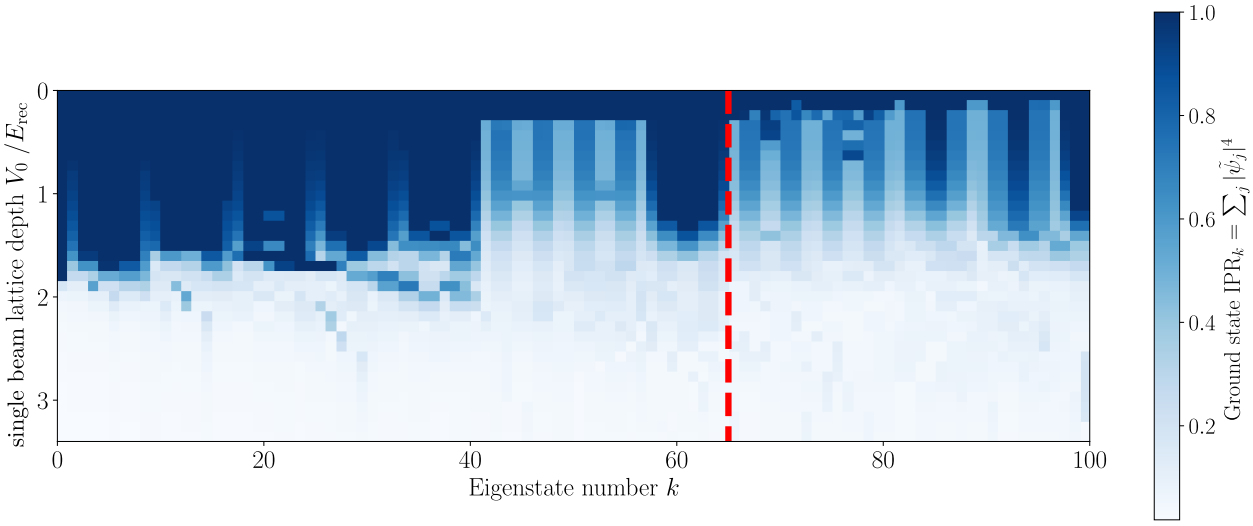

Figure 8.6: The momentum space inverse participation ratio IPR_k computed for the first few tens of excited states of the 2D quasiperiodic Hamiltonian. Features past the red dashed line had not yet converged. The calculation was performed with $n = 25$ generations.

Tight-binding

Confidence in the presence of a localisation transition had been provided by the 2016-2017 Part III student Attila Szabó. The results and conclusions discussed in this section are reproduced from his report [222], and will be the subject of a future publication.

Attila worked in the tight-binding regime modelling a 1D quasiperiodic potential as an incommensurate modulation with period $\beta = 1/\sqrt{2}$ of amplitude λ on a regular lattice,

[5] though it needed to be multiplied by 8 in order to account for the eightfold degeneracy of states with kinetic energy $\neq 0$.

a.k.a. the 1D Aubry-André model:

$$H_{1\mathrm{D}} = -J \sum_n \left(a_n^\dagger a_{n+1} + \text{c.c.} \right) - \lambda J \sum_n \cos\left(2\pi\beta n\right) a_n^\dagger a_n, \tag{8.3}$$

where $a_n^\dagger$ and a_n are the creation and annihilation operators for a lattice site n, and J is the nearest-neighbour tunnelling element.
This was further extended to 2D with a modulation Λ in order to model the eightfold quasiperiodic potential, treating two orthogonal beams as the regular (square) lattice and the remaining two diagonal ones as perturbations:

$$\begin{aligned} H_{2\mathrm{D}} = -J \sum_{nm} \left[a_{nm}^\dagger \left(a_{n+1,m} + a_{n,m+1} \right) + \text{c.c.} \right] \\ -\Lambda J \sum_{nm} \left[\cos\left(2\pi\beta(n+m)\right) + \cos\left(2\pi\beta(n-m)\right) \right] a_{nm}^\dagger a_{nm}. \end{aligned} \tag{8.4}$$

As shown in fig. 7.5, it is not possible to construct a single-band tight-binding model with four beams at equal strength, as used in the experiment. Hence the different geometry investigated here.

The ground state participation ratio PR_x[6] was computed and it yielded a sharp phase transition, as shown in fig. 8.7a. Besides the tight-binding model, Attila also constructed a model for the 2D continuum case. Choosing to replace the irrational number by a rational approximant $\sqrt{2} = N/M$ with $N, M \in \mathbb{N}$ (essentially constructing a unit cell of size $N \times M$), the momentum space basis $\{\mathrm{e}^{\mathrm{i}\mathbf{k}_i \cdot \mathbf{r}}\}$ was constructed. This method is well suited for computing the ground state but not for performing dynamical simulations that affect the excited states, for which the method outlined in the previous section is more reliable. The ground state PR_x for the 2D continuum was computed (blue curve, bottom of fig. 8.7a) and is consistent the result of the previous section.

The analysis was extended to the excited states of $H_{11\mathrm{D}}$ and $H_{2\mathrm{D}}$, highlighting the differences between the usual 1D Aubry-André model (fig. 8.7b top) and the 2D non-separable model (fig. 8.7b bottom). In the former, localisation occurs at the same $\lambda = 2$ for all states, whilst in the latter Λ alone is not sufficient to identify the phase. This is explained by the diagonal perturbative beams $\nearrow + \nwarrow = \sin\left[(x-y)/\sqrt{2}\right] + \sin\left[(x+y)/\sqrt{2}\right]$ being written as $2\sin(x/\sqrt{2})\cos(y/\sqrt{2})$, providing little to no disorder $\forall y$ at $x = 0$ even for strong Λ, and resulting in the extended states of fig. 8.8.

[6] Attila used the following convention. A delocalised wavefunction uniformly distributed over a lattice of N sites has $\mathrm{PR}_x = N$, which is then normalised to N in order to be 1 in the thermal phase.

[7] Technically what is plotted here is a rescaled PR, which Attila used in order to investigate the system-size dependence and to extract the critical exponents.

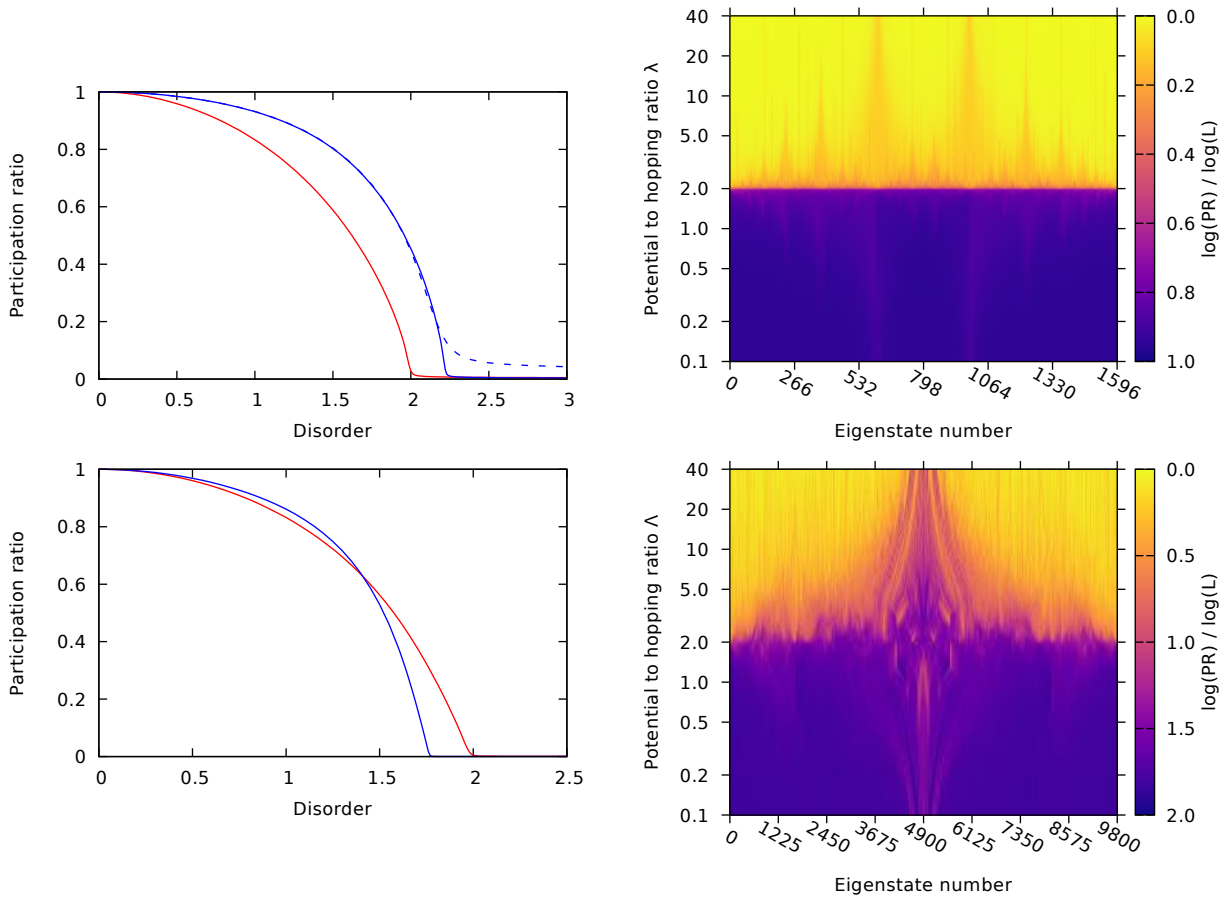

(a) (b)

Figure 8.7 : a) Ground state participation ratio (PR) of the continuum (blue) and the tight-binding (red) quasiperiodic Hamiltonians, for 1D (top) and 2D (bottom). b) The PR for the tight-binding excited states[7] indicate that in 2D (bottom), as opposed to 1D (top), the transition does not always occur at the same disorder strength. Figures from [222].

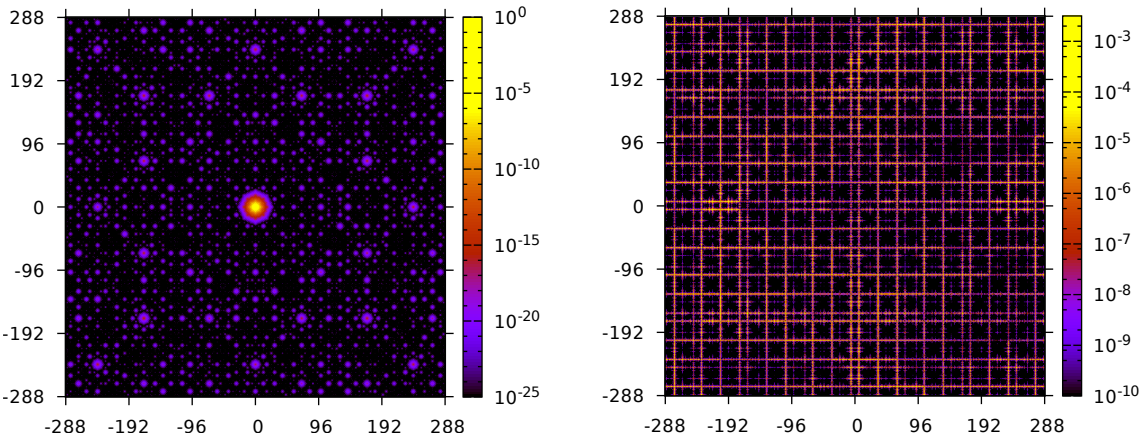

Figure 8.8 : Real space profile of eigenstates of the 2D quasiperiodic tight-binding Hamiltonian H_{2D}. A low-lying eigenstate at $\Lambda \sim 3$ (left) is localised near the origin, whilst a mid-spectrum eigenstate at $\Lambda \sim 20$ (right) can still be extended. Figures from [222].

The novel and richer phenomena that result from the non-separability of the 2D quasiperiodic potential sets our optical lattice apart from any previous experimental platform. Experiments, however, were not performed in the Aubry-André limit discussed here, but rather with all beams of equal strength. This configuration exhibits equally promising and interesting features, since Attila found the two limits to belong in the same universality class[8].

Real space

The 2D quasiperiodic potential was also numerically investigated in real space in collaboration with Dr. Alexander Gaunt from Microsoft Research.

The Gross-Pitaevskii equation (eq. 1.47) was solved using the split-step Fourier method [223] in the presence of an external potential energy term:

$$\mathrm{i}\hbar\frac{\partial\psi}{\partial t} = -\frac{\hbar^2}{2m}\nabla_x^2\psi + \alpha V(\mathbf{x})E_{\mathrm{rec}}\psi + \frac{4\pi\hbar^2 a}{m}|\psi|^2\psi, \tag{8.5}$$

where $E_{\mathrm{rec}} = \hbar^2 k_{\mathrm{lat}}^2/2m$, α is the lattice depth and a the scattering length.
Introducing the dimensionless variables $\boldsymbol{\xi} = k_{\mathrm{lat}}\mathbf{x}$, $\tau = (E_{\mathrm{rec}}/\hbar)t$, $a' = ak_{\mathrm{lat}}$ and $\psi \to \psi/k_{\mathrm{lat}}^{3/2}$, this becomes:

$$\mathrm{i}\frac{\partial\psi}{\partial\tau} = -\nabla_\xi^2\psi + \alpha V(\boldsymbol{\xi})\psi + 8\pi a'|\psi|^2\psi, \tag{8.6}$$

with $V(\boldsymbol{\xi}) = -\sum_i \cos^2(\mathbf{G}_i\cdot\boldsymbol{\xi})$, $\mathbf{G}_0 = (1,0)$, $\mathbf{G}_1 = (0,1)$, $\mathbf{G}_2 = {}^1\!/\!\sqrt{2}\,(1,1)$ and $\mathbf{G}_3 = {}^1\!/\!\sqrt{2}\,(-1,1)$.

The simulation starts with a Gaussian wavefunction $\psi(\tau=0) \propto \exp[-\xi^2/(2\sigma^2)]$, lets it propagate in the 2D quasiperiodic potential according to eq. 8.6, and measures its spatial extent $\langle\psi|\rho^2|\psi\rangle$, with $\rho^2 = \xi_x^2 + \xi_y^2$, after some time τ, as illustrated in fig. 8.9.

[8] Which might even make sense within the PV conjecture discussed at the end of section 3.2.1, according to which the irrational number $\sqrt{2}$ might be sufficient to classify and identify this type of quasicrystal.

A specific radius $\sqrt{\langle \rho_*^2 \rangle} = 35$ reached at time τ_* was chosen, so as to define a velocity $v = \sqrt{\langle \rho_*^2 \rangle}/\tau_*$ quantifying the real space transport properties in the potential. A sharp transition into an insulating state (where $\tau_* \to \infty$ and $v = 0$) is found to occur around $1.7 < \alpha < 1.8$, as shown in fig. 8.10.

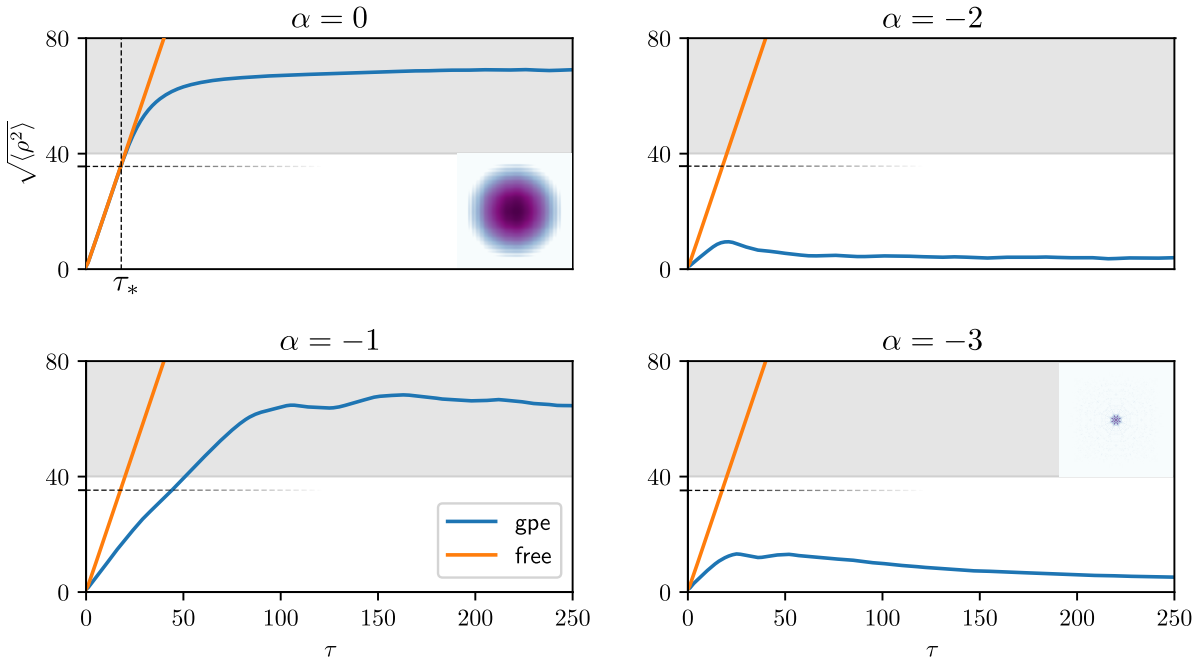

Figure 8.9 : The spatial extent of a Gaussian wavefunction propagating in the quasiperiodic lattice is measured as a function of time, for different lattice depths α. The orange line corresponds to the ballistic expansion in the absence of any potential, while the grey area indicates where finite-size effects of the simulating region start becoming noticeable. The insets show the spatial profiles of the wavefunction at $\tau = 90$. Plot produced by Dr. Alexander Gaunt.

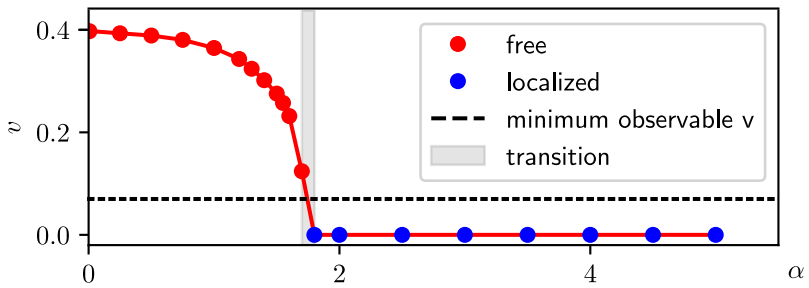

Figure 8.10 : As the lattice depth α is increased, the time τ_* required for the wavefunction to reach an arbitrarily chosen radius diverges. This results in its velocity $v \to 0$, indicating insulating behaviour and hence a transition into a localised phase, found to occur around $1.7 < \alpha < 1.8$. Plot produced by Dr. Alexander Gaunt.

The critical lattice depth was found to be insensitive to the spatial extent σ of the starting Gaussian wavefunction, and it is in agreement with the values found in both figs. 8.4 (plane wave basis) and 8.7 (tight-binding).
Unbeknownst to each other, Alex and I had been working on the same problem with two

distinct but complementary approaches, and it was not until we casually ran into each other near the Cambridge train station that we discovered our critical points agreed.

The GPE approach was used in section 8.2.4 to investigate the effects of interactions on the extended-to-localised phase transition. The GPE is only valid within mean-field theory, which is justified in our experiment because of the lack of strong confinement along the z direction. This allows the z modes to be extended and to therefore carry low kinetic energy ($\propto k^2$), hence averaging over them is unlikely to result in significant consequences. A strong confinement in z would result in Mott insulating physics, known not to be captured by mean-field theory.

By evolving the system in imaginary time from an initially (spatially) uniform state, the ground state of the 2D quasiperiodic potential was computed in real space. Lattice depths greater than the critical value result in ground states exhibiting exponential localisation akin to fig. 8.2b, as it is shown for a depth $\alpha = 2$ in fig. 8.11.

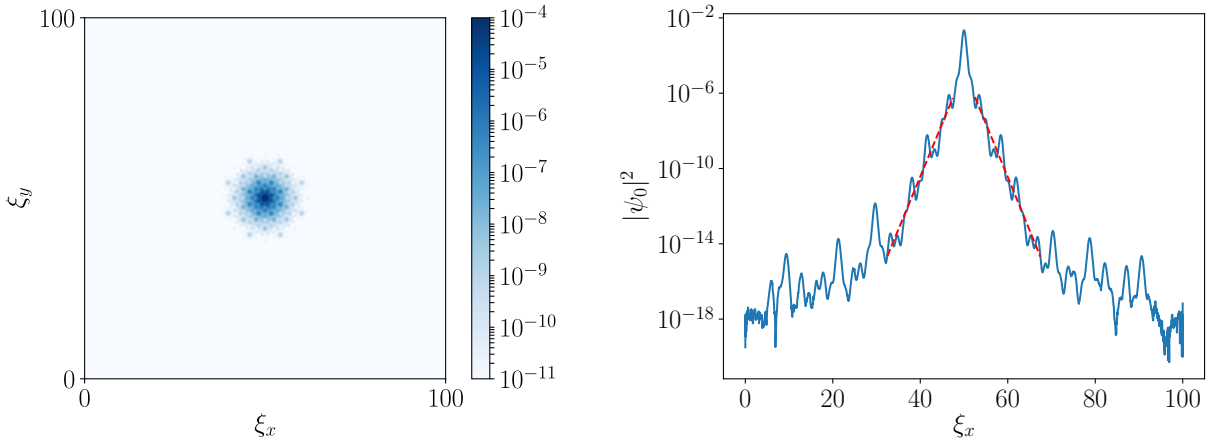

(a) (b)

Figure 8.11 : The spatial distribution of the ground state ψ_0 of the GPE of eq. 8.6, for $a = 0$ (non-interacting). A cut through $\xi_y = 0$ (b) shows exponentially decaying wings, in accordance with what is expected for a localised state. The region $|\psi_0|^2 \lesssim 10^{-13}$ is dominated by finite numerical accuracy. Plot produced from data provided by Dr. Alexander Gaunt.

8.2 Experimental investigations of localisation

8.2.1 Technical details

Scheme

Disorder-induced localised phases are not thermal and thus cannot be detected by equilibrium or steady-state analyses, but rather they need to be probed dynamically. The lattice is then programmed to produce a triangular ramp from 0, to a final depth V_0, and then back to 0 in a total time 2τ, as illustrated in fig. 8.12a. The atoms start in a BEC, hence in the zero-momentum plane wave $|0\rangle$ with amplitude $\tilde{\psi}_0 = 1$. We measure the fraction of the atoms recovered in $|0\rangle$ at the end of the ramp (after time-of-flight), as a function of the maximum depth V_0 and the total ramp duration 2τ.

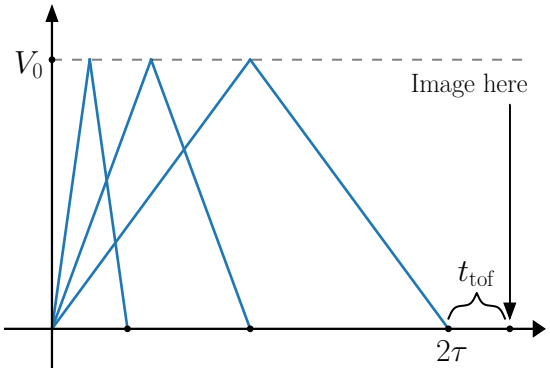

(a)

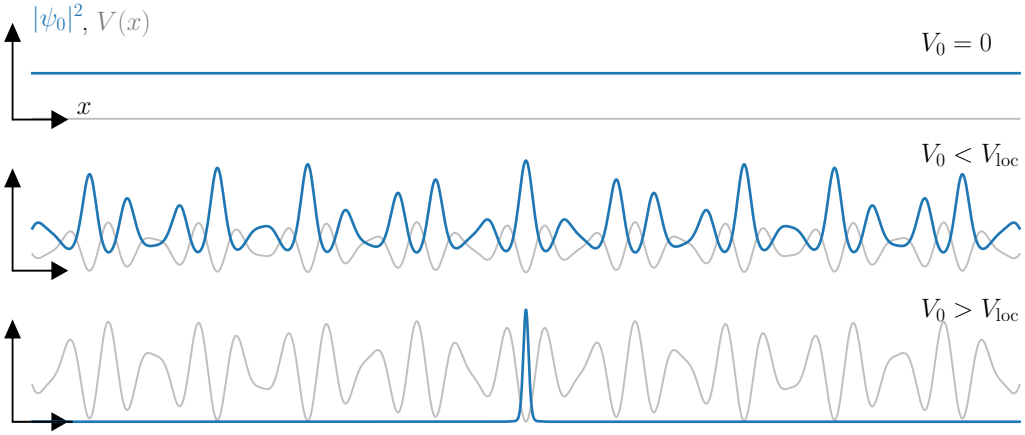

(b)

Figure 8.12 : Adiabatic following of the ground state from the extended to the localised phase would require particle transport over an infinite spatial range (b) whose timescale will therefore diverge. The divergence of said timescale provides a "dynamical" observable that can identify either phase via triangular lattice ramps (a), an idea which stemmed from [186]. In (b) the (real space) ground state wavefunctions (blue) are shown for lattice (grey) depths $V_0/E_{\text{rec}} = 0, 1$ and 2.

For small ramp durations and hence abrupt lattice changes, the BEC is projected onto the Bloch waves of the potential and the patterns of chapter 7 are recovered. When

the lattice is slowly increased over a large interval τ, however, the atoms attempt to adiabatically follow the ground state and would therefore return to the initial state at the end of the triangular ramp. Longer pulse durations had already been established to distinguish periodic from quasiperiodic lattice configurations in the synthetic lattice transport measurements of fig. 7.19, and are thus expected to play a similar role here.

If the BEC were to be adiabatically loaded into the lattice ground state for every V_0 in the ramp, then it would smoothly turn into a delocalised Bloch wave for any finite $V_0 < V_{\mathrm{loc}}$, but would become exponentially localised above a critical depth V_{loc}, as depicted in fig. 8.12b. Our quasiperiodic potential typically possesses a *single* absolute minimum, where all four standing waves interfere destructively: the absolute ground state in the localised phase would thus see all atoms tightly confined to this site, chosen to lie in the middle of the x axis in fig. 8.12b for clarity.

As the lattice depth V_0 is changed, the transition from the extended wavefunction for $V_0 < V_{\mathrm{loc}}$ to a localised state for $V_0 > V_{\mathrm{loc}}$ would require particle transport over infinite spatial separations, the time required for which diverges. In the framework of a synthetic lattice in momentum space developed in chapter 7, this transition would require an infinite number of two-photon transitions. Hence, adiabaticity is expected to break down at and above the localisation transition V_{loc}.

The (predicted) lack of recovery of the initial BEC stems from the infinite number of low-momenta states available in the quasiperiodic synthetic lattice. Instead of simply returning to the central BEC peak at the end of the ramp, atoms may undergo multiple two-photon transitions to terminate arbitrarily close it. The presence of these low-momenta states, however, is independent of the lattice strength: so why is the transition driven by a critical V_0? While high-generation states may be energetically more favourable because of their reduced kinetic energy ΔE, the ("Rabi") coupling required to reach them is governed by the lattice strength V_0. The competition between V_0 and ΔE is what results in a critical depth V_{loc}.

The fractal structure of the synthetic lattice is expected to yield non-trivial single-particle physics, hence the majority of the numerical and experimental investigations was performed in the absence of interactions.

Population extraction

The populations of the diffraction orders were extracted by fitting each peak independently. A fit was performed instead of summing the pixel counts because it allows for a reliable characterisation of the peaks even in the presence of noise and (more importantly) saturation. The 0^{th} diffraction order (the BEC) is almost always severely saturated, as shown in fig. 8.13. This is due to the high spatial density of the BEC, which causes the imaging light to be nearly completely absorbed in its central region thus not reaching the camera.

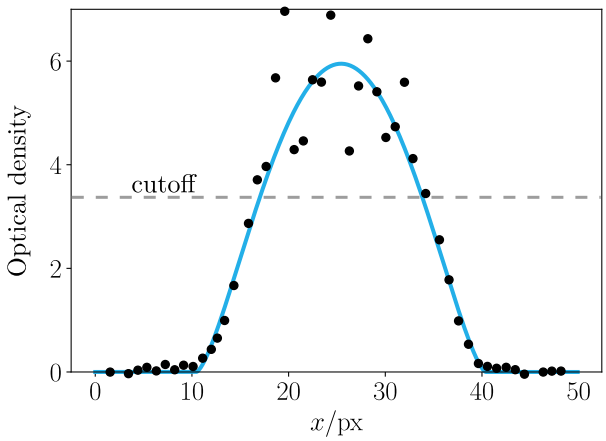

Figure 8.13 : To extract the population of the central peak (the BEC), the Thomas-Fermi profile of eq. 6.14 (blue) was fitted to it. The BEC is heavily saturated due to its high spatial density, thus all points above a certain cutoff are not considered in the fit.

According to eq. 6.6, this results in an optical density OD $\to \infty$ which is then discarded in the image processing analysis: only points below a certain "cutoff" are considered in the fit, chosen to be OD$= 3.4$. Only the wings of the atomic cloud provide data for the fitting function, which was assumed to be the inverted parabola of eq. 6.14 obtained within the weakly interacting Thomas-Fermi approximation.

As far as the other diffraction orders are concerned, the application of the fit functions is generally reliable for the square lattice (e.g. fig. 8.14a) and for the short time dynamics of the eightfold quasiperiodic one (e.g. fig. 8.19b) since the diffraction orders are well separated. On the other hand, after longer and deeper quasiperiodic lattice ramps, atoms may occupy up to the 10^{th} diffraction order[9] which renders the fitting procedure extremely challenging, aggravated by the merging of neighbouring peaks (fig. 8.14b). This results in the fit failing and the population not being recorded, causing an underestimation of the total atom number.

The presence of moderate repulsive interactions during the lattice ramp, for many-body physics investigations, causes the peaks to broaden enough to be reliably fitted even after deep and long lattice ramps (fig. 8.14c).

8.2.2 2D periodic lattice

We started our investigations by probing a regular square lattice, obtained from the superposition of two orthogonal standing waves.

Quantum adiabaticity

In the following we employ the quantum adiabatic theorem in order to estimate the timescale required to adiabatically load a BEC in a regular square lattice, to be then compared with what observed experimentally. The mathematical treatment here is based on [224].

[9] As a comparison, the number of potentially occupied diffraction peaks in each image is 25 for the 2D regular lattice, and $8,361$ for the 4D quasiperiodic one. In theory, the atoms may occupy even higher orders that are however not detected due to finite atoms numbers and signal-to-noise ratio. See fig. 8.23.

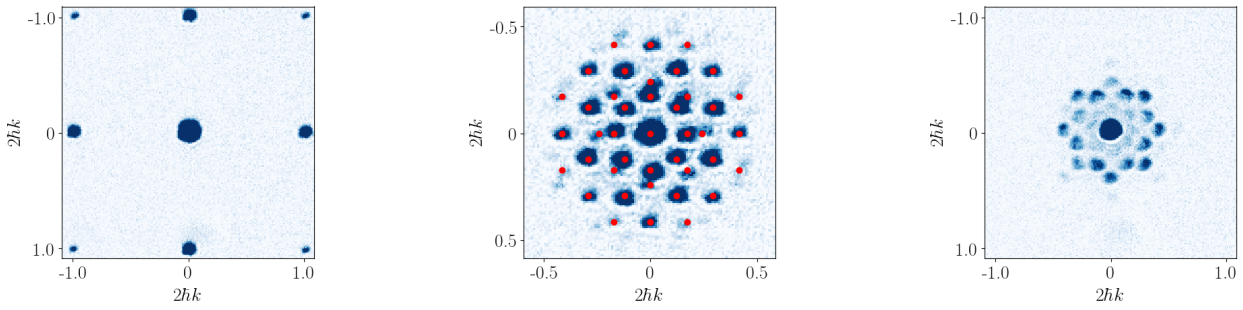

(a) (b) (c)

Figure 8.14 : In the regular square lattice (a), atoms only occupy well separated peaks which are thus easy to fit. In the deeply localised quasiperiodic lattices (b), some of the peaks appear merged causing fits to fail and resulting in an underestimated total atom number (here $V_0 = 2.4\,E_{\mathrm{rec}}, 2\tau = 500\,\mu\mathrm{s}$) – the red dots are the predicted locations of the first 10 diffraction orders. The same parameters as in (b) but with the addition of repulsive interactions ($a = 40\,a_0$) during the lattice ramp cause peak broadening and allow for reliable fits (c).

The BEC having free space momentum $\mathbf{k} = 0$, it only couples to bands at quasimomentum $q = 0$ (conserved in the lattice), and in particular will only occupy the lowest band if the ground state is to be followed adiabatically. Excitations into higher bands because of imperfect adiabaticity can be estimated as follows.

A state in a band n at quasimomentum q is an eigenstate of the (instantaneous) Schrödinger equation $H(t)|\phi_{n,q}(t)\rangle = E_n(t)|\phi_{n,q}(t)\rangle$. The time-dependent wavefunction may be expanded in the instantaneous basis: $|\psi_t\rangle = \sum_{n,q} c_{n,q}(t) \exp\left[-\frac{\mathrm{i}}{\hbar}\int_0^t E_n(t')\,\mathrm{d}t\right]|\phi_{n,q}\rangle$, which, when substituted into the Schröinger equation, results in the following time dependence for the coefficients $c_{n,q}$:

$$\dot{c}_{n,q} = -\sum_m \langle\phi_{n,q}|\dot{\phi}_{m,q}\rangle\, \mathrm{e}^{-\frac{\mathrm{i}}{\hbar}\int_0^t [E_m(t')-E_n(t')]\,\mathrm{d}t'} c_n. \tag{8.7}$$

This can be re-cast in a better form by first requiring the norm to be conserved:

$$\frac{\mathrm{d}}{\mathrm{d}t}\langle\phi_{n,q}|H(t)|\phi_{m,q}\rangle = 0 = (E_n - E_m)\,\langle\phi_n|\dot{\phi}_m\rangle + \langle\phi_n|\dot{H}|\phi_m\rangle. \tag{8.8}$$

For $m = n$, i.e. the diagonal phase, it gives rise to the pure phase factor known as the *Berry phase* γ_n. For $m \neq n$, one can write:

$$\langle\phi_n|\dot{\phi}_m\rangle = \frac{\langle\phi_n|\dot{H}|\phi_m\rangle}{(E_m - E_n)}. \tag{8.9}$$

Hence, the time evolution of the coefficients may be written as:

$$\dot{c}_{n,q} = -\mathrm{i}\gamma_n c_n - \sum_{m\neq n} \underbrace{\frac{\langle\phi_{n,q}|\dot{H}|\phi_{m,q}\rangle}{E_m - E_n}}_{\text{non-adiabatic}} \underbrace{\mathrm{e}^{-\frac{\mathrm{i}}{\hbar}\int_0^t [E_m(t')-E_n(t')]\,\mathrm{d}t'}}_{\text{free evolution}} c_n. \tag{8.10}$$

In order to adiabatically follow the ground state, the above time evolution should only amount to a phase factor. For the second term, this requires the non-adiabatic term to

contribute less strongly than the free-evolution term:

$$\begin{aligned} \frac{\partial}{\partial t}(\text{non} - \text{adiabatic}) &\ll \frac{\partial}{\partial t}(\text{free evolution}), \\ \Rightarrow \quad |\langle \phi_{n,q}|\dot{H}|\phi_{m,q}\rangle| &\ll \frac{(E_n - E_m)^2}{\hbar}, \end{aligned} \tag{8.11}$$

which is known as the *adiabaticity condition*. Technically it should really be $[\min(E_n - E_m)]^2$, since the gap may evolve in time or space as shown, for example, in fig. 2.1.

Writing $\dot{H} = \dot{V} = \Delta V_0/\tau_{\text{ramp}}$, where ΔV_0 is the change in optical lattice potential strength, and expressing the depths in terms of the recoil energy E_{rec}, eq. 8.11 results in a lower bound for the ramp duration:

$$\tau_{\text{ramp}} \gg \frac{1}{\Delta V_0}\tau_{\text{rec}}, \tag{8.12}$$

where $\tau_{\text{rec}} = \hbar/E_{\text{rec}}$ is approximately 16 µs for ^{39}K in a 725 nm lattice.
For atoms at $q = 0$ in a square lattice with the band structure of fig. 2.14, the minimum relevant ΔV_0 that may cause inter-band excitations is from the bottom of the first band to the top of the second band, $\Delta V_0 = 4\,E_{\text{rec}}$. This would require $\tau_{\text{ramp}} \gg 4$ µs to ensure the BEC is adiabatically loaded into the ground state of the square lattice.

Other time evolution contributions that were ignored here include interactions and the dipole-trap harmonic confinement, though we work primarily in the non-interacting regime which thus results in an infinitely slow interacting timescale. Our lattice ramps are adiabatic with respect to the internal dynamics, as quantitatively discussed in this section, but not with respect to the dipole trap. In fact, the harmonic confinement has a maximum trapping frequency of ~ 100 Hz (in z) and results in a timescale $T/4 \sim 2.5$ ms, much larger than the ~ 100 µs lattice ramp durations employed in the experiment. The ramps are fast (non-adiabatic) in order for the dipole trap not to affect the cloud density and position. With respect to the dipole trap, the lattice ramp can be regarded as instantaneous ($^{\partial}/_{\partial t}\,\text{dipole} - \text{trap} = 0$).

Experiment

The square lattice was ramped to depths V_0 ranging from 0.6 to 4.6 E_{rec} and then back to 0 in durations $2\tau = 1 \rightarrow 200$ µs. The population of the 0^{th} plane wave ($|\tilde{\psi}_0|^2$, the initial BEC) was recorded as shown in fig. 8.15. Typical images are presented in fig. 8.16.

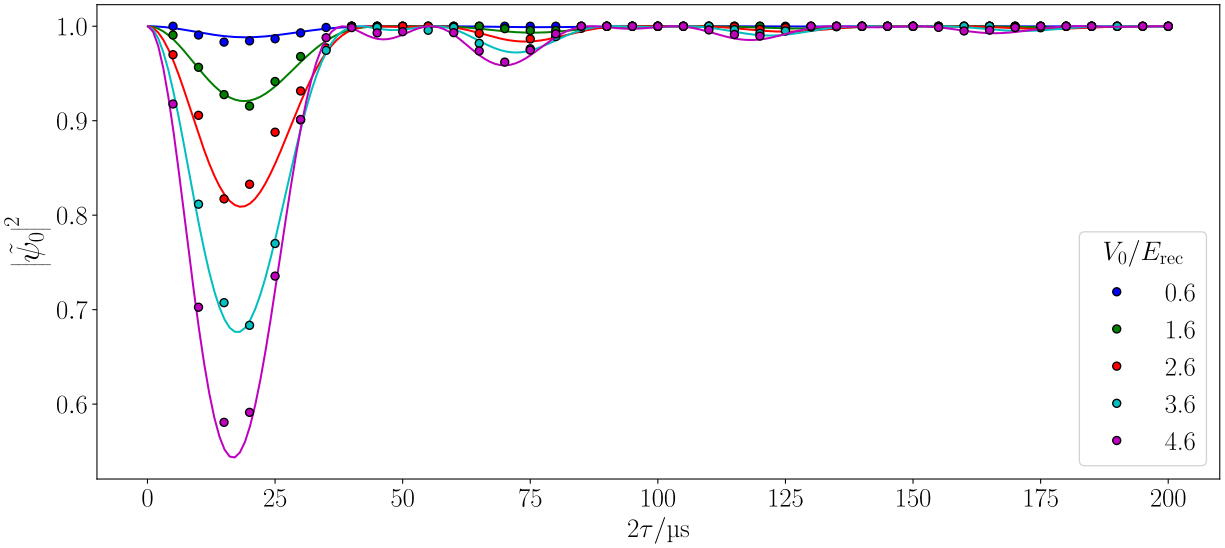

Figure 8.15 : The recovery of the population of the initial BEC ($|\tilde{\psi}_0|^2$) as a function of the total ramp duration 2τ. For long enough ramps, the atoms are adiabatically loaded into the ground state of the square lattice for any depth V_0, and they hence return to the BEC at the conclusion of the ramp. The solid line is the numerical simulation described in section 7.1.4.

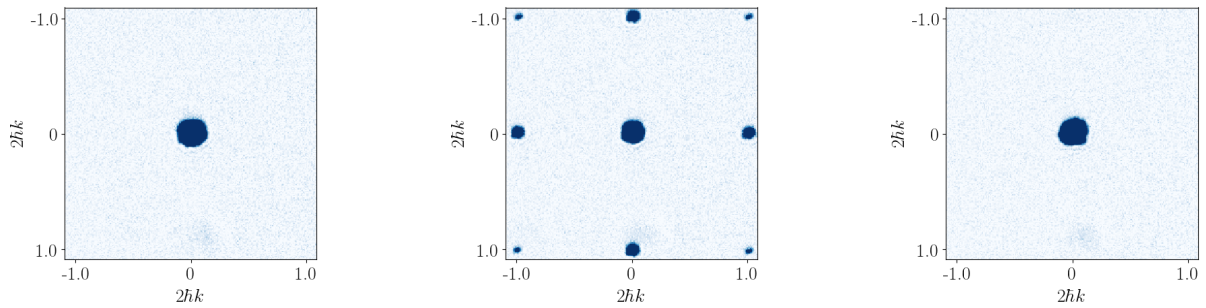

(a) $2\tau = 0\,\mu s$ (b) $2\tau = 20\,\mu s$ (c) $2\tau = 200\,\mu s$

Figure 8.16 : Typical images taken at the end of the triangular ramps (and after time-of-flight), for the $V_0 = 4.6\,E_{rec}$ curve in fig. 8.15. The colour bar has been adjusted to emphasise the higher orders.

The BEC population was always recovered with a slow enough ramp, in this case $2\tau \gtrsim 40\,\mu s$, which is compatible with the estimate $\gg 4\,\mu s$ from the previous section, and agrees with the numerical simulation described in section 7.1.4.

For short pulse durations, the lattice is abruptly increased and the BEC is hence projected onto many Bloch waves, akin to the rectangular pulses of section 7.2.2. Multiple, smaller dips in the BEC population are present even for $2\tau > 40\,\mu s$, and are probably the result of interference effects between the ramp time and the finite discrete set of frequencies in the Hamiltonian.

The non-adiabaticity does not depend on the lattice depth V_0 reached so much as it does on the slope of the ramp, for the losses are always primarily caused by the same excitation

from the bottom of the first to the top of the second band discussed earlier. Hence, all the depths in fig. 8.15 exhibit the same qualitative behaviour at equal ramp times. This is further confirmed by the numerical simulation on the "slanted" lattice shown in fig. 8.17. This lattice consists of two standing waves at 45° separation, where the difference between the bottom of the first to the top of the second band is roughly half than for a regular square lattice: this was observed to result in a doubled adiabatic recovery timescale, as expected from eq. 8.12.

In addition, the fact that nearly total BEC population recovery is possible for up to $2\tau = 200\,\mu s$ sets a lower bound on the heating rates and hence on the lifetime of the atoms in the square lattice. This is compatible with other groups routinely performing experiments with lattice durations of up to $\sim 500\,ms$.

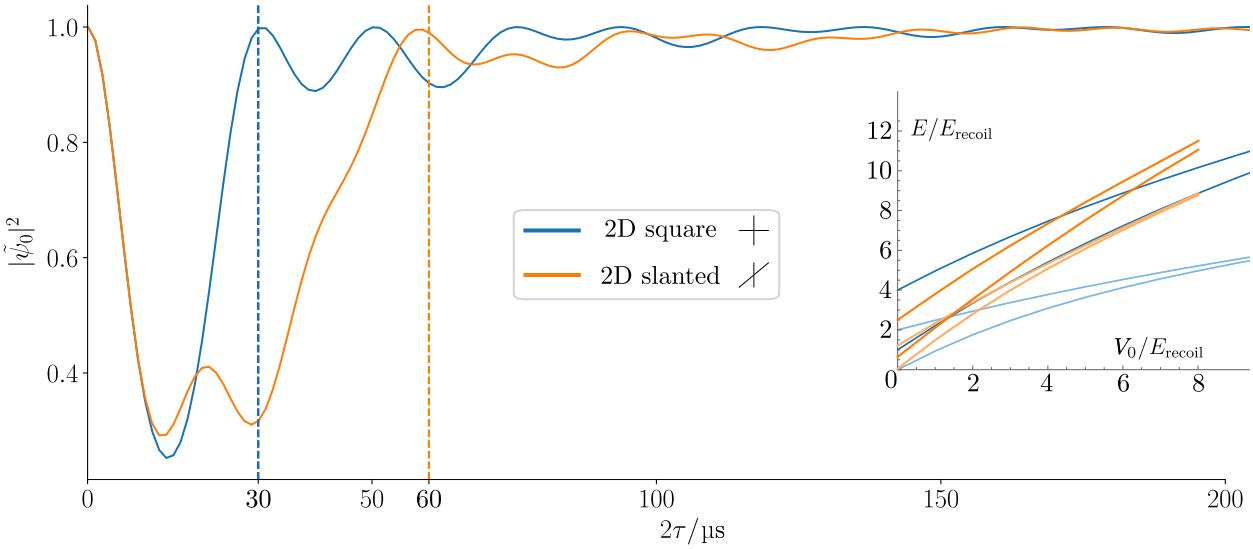

Figure 8.17 : The recovery of the BEC population is simulated for the regular square lattice (blue) and for the slanted lattice (orange), with $V_0 = 7.5\,E_{rec}$. The inset shows the width of the first two bands for both configurations. The minimum energy inter-band excitation for atoms in $q = 0$ is $4\,E_{rec}$ for the square and $\sim 2\,E_{rec}$ for the slanted lattice. The slanted lattice therefore exhibits an adiabatic recovery at a timescale roughly $\sim 4/2 = 2$ times slower than for its square counterpart.

8.2.3 2D quasiperiodic lattice

Experiment

In the periodic lattices of the previous section it was always possible to fully recover the BEC population, given slow enough ramps, even for peak depths $V_0 \gg V_{loc} \approx 1.78\,E_{rec}$. This is very different from what observed in the 2D quasiperiodic lattice, shown in fig. 8.18 along with typical images presented in fig. 8.19. Two regimes are observed depending on the lattice depth V_0: some recovery curves seem to return to unity whilst others exhibit the opposite behaviour and seem to tend to zero.

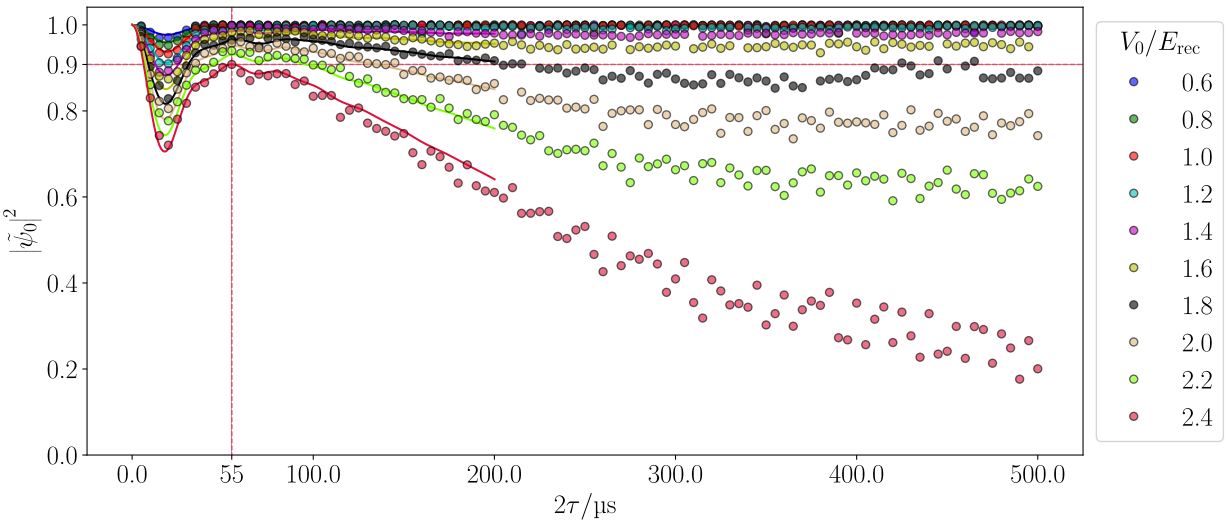

Figure 8.18 : For the 2D quasiperiodic lattice, the recovery of the population of the initial BEC ($|\tilde{\psi}_0|^2$) at large ramp durations 2τ is only observed for $V_0 \leqslant 1.2$. The other depths exhibit a gradually more significant negative slope (shown in fig. 8.20). The solid line is the numerical simulation described in section 7.1.4. The dashed crimson line denotes the maximum recovery of the population in the $V_0 = 2.4\,E_{rec}$ curve.

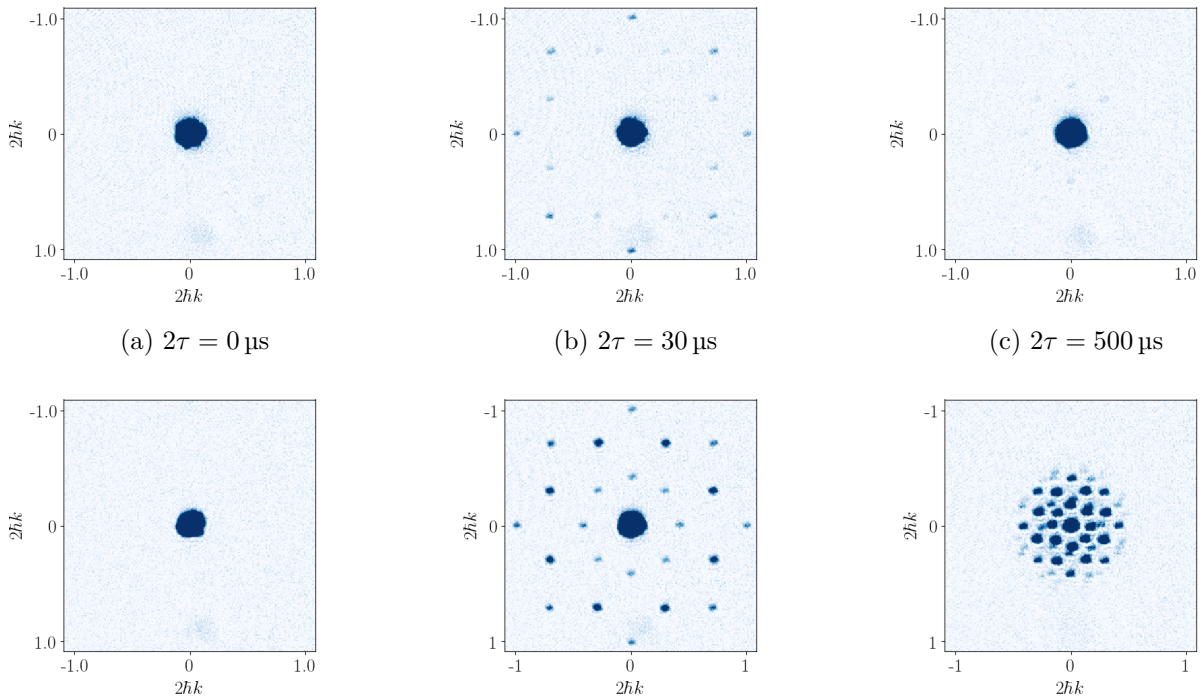

(a) $2\tau = 0\,\mu s$ (b) $2\tau = 30\,\mu s$ (c) $2\tau = 500\,\mu s$

(d) $2\tau = 0\,\mu s$ (e) $2\tau = 30\,\mu s$ (f) $2\tau = 500\,\mu s$

Figure 8.19 : Typical images taken at the end of the triangular lattice ramps (and after time-of-flight), for the $V_0 = 1.2\,E_{rec}$ (top, a→c) and $V_0 = 2.4\,E_{rec}$ (bottom, d→f) curves in fig. 8.18. The colour bar has been adjusted to emphasise the higher orders.

The BEC population is observed to be recovered for $V_0 \leqslant 1.2\,E_{rec}$. The other curves

display a negative slope, which increases in magnitude with lattice depth V_0, and are further discussed in the following section in order to pinpoint the critical strength V_{loc} triggering the localisation transition.

The apparent maximum reached by all curves around $2\tau \sim 50\,\mu\text{s}$ is qualitatively similar to what observed for the 2D regular lattice in fig. 8.15. At these short ramp durations, in fact, the atoms have not yet had the time to explore enough phase space to display the features that are unique to the quasiperiodic configuration. For the $V_0 = 2.4\,E_{\text{rec}}$ curve, a maximum recovery $|\tilde{\psi}_0|^2 = 0.9$ is reached at $2\tau = 55\,\mu\text{s}$, used later to discuss the effect of interactions during the lattice ramp.

It is important to note that, in the localised regime $V_0 > V_{\text{loc}} \approx 1.78\,E_{\text{rec}}$, the recovery of the initial population becomes worse as slower ramps are employed. This may be counter-intuitive at first, as it is the opposite of what would be expected from the Kibble-Zurek mechanism[10]. However, this is explained by the many synthetic lattice points with lower kinetic energies that become accessible at larger V_0 and longer 2τ. The complexity offered by the quasiperiodic lattice potential is what allows the atoms to populate an increasing number of synthetic states via Kapitza-Dirac scattering, thus further depleting the zero-momentum plane wave $|0\rangle$ (the initial BEC).

Since our investigation is limited to the 500 µs duration of the experimental run, we in principle cannot exclude a BEC recovery occurring over much longer scales. The observed behaviour is however consistent with the theoretical expectations from fig. 8.21a, discussed later. For long and deep ramp durations, such as $V_0/E_{\text{rec}} = 2.0 \to 2.4$ and $2\tau \gtrsim 250\,\mu\text{s}$, the BEC is not saturated and a pixel sum of the picture may be performed. This yielded a qualitatively similar result to the fit analysis shown in fig. 8.18, though significantly noisier.

Even in the localised phase (e.g. fig. 8.19f), the images still exhibit sharp and distinct diffraction peaks, suggesting the atoms did not have enough time to lose phase coherence. The timescale for this to happen is expected to be larger than what probed thus far, but could be easily investigated by ramping and subsequently holding the lattice at $V_0 > V_{\text{loc}}$ for a variable interval of time.

Critical strength for the localisation transition

The following describes the extraction of the critical lattice strength V_{loc} from the experimental data, and its comparison to the theoretical expectation $V_{\text{loc}} \approx 1.78\,E_{\text{rec}}$ obtained from the numerical simulation of fig. 8.4.

A straight line was fitted to the $100\,\mu\text{s} \leqslant 2\tau \leqslant 200\,\mu\text{s}$ region of fig. 8.18. This region was chosen because, from the 2D regular lattice results of the previous section (fig. 8.15), other sources of atomic loss were established to be negligible[11]. These are plotted in fig. 8.20, and show that both theory and experiment already exhibit a negative slope for $V_0 < V_{\text{loc}}$. While this establishes that unit recovery is precluded on the $2\tau = 500\,\mu\text{s}$ timescale probed in the experiment, it does not exclude that the $V_0 < V_{\text{loc}}$ curves may fully recover over slower ramp durations. A simulation is then considered to explore longer dynamics.

The numerical simulation shown in fig. 8.18 is performed in the plane wave basis, as

[10] where essentially the slower the ramp, the more adiabatic the following.

[11] for the square lattice. For the 2D quasiperiodic, this is not necessarily also the case and would require careful measurements.

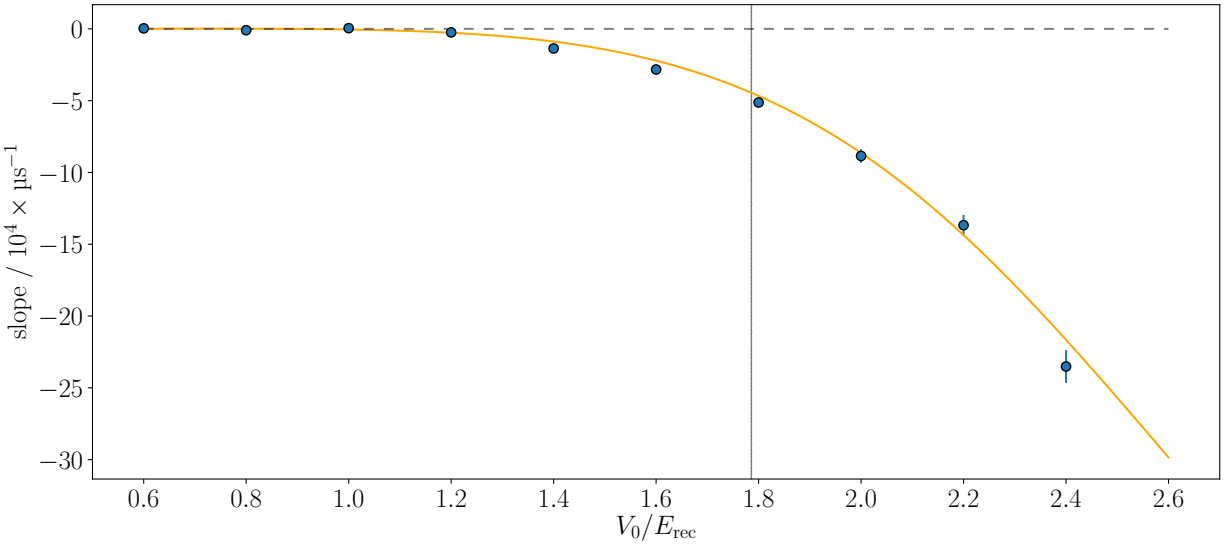

Figure 8.20 : The downward slopes of the straight lines fitted to the population recovery curves in fig. 8.18, along with the theoretical prediction (orange solid line). The predicted critical localisation strength $V_{loc} \approx 1.78\, E_{rec}$ (grey solid line) is obtained from fig. 8.4.

described in section 7.1.4. The momentum space basis is computationally intensive for long ramp durations as the time dynamics involves multiplications of large[12] Hamiltonian matrices for each time step.

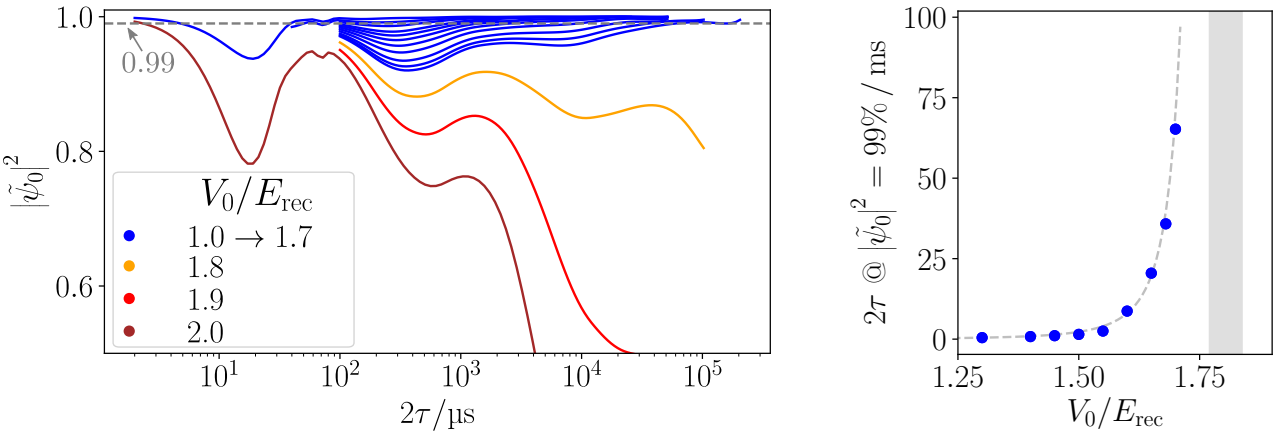

(a) (b)

Figure 8.21 : The real space simulation outlined in the last part of section 8.1.3 enables numerical investigation of the BEC recovery fraction for much longer ramp durations (a), establishing the different behaviour exhibited for lattices below and above the expected critical lattice strength $V_{loc} \approx 1.78\, E_{rec}$. The adiabatic timescale is also computed and is seen to diverge around the same lattice depth (b). Plots produced from data provided by Dr. Alexander Gaunt.

Luckily, our collaborator Dr. Alexander Gaunt performed the same simulation in real

[12]For $n = 25$ generations, these are $283,401 \times 283,401$ sparse matrices.

space (last part of section 8.1.3) and with more computing power, which enabled probing much longer ramp durations, as shown in fig. 8.21a. The distinct recovery behaviour exhibited by lattices above and below the expected localisation transition $V_0 \approx 1.78\,E_{\text{rec}}$ is then very clear. Gentle downward slopes in the $100\,\mu\text{s} \leqslant 2\tau \leqslant 200\,\mu\text{s}$ region, displayed for $V_0 \leqslant 1.6\,E_{\text{rec}}$ in the experiment, lead to a full recovery over much longer timescales. On the other hand, the stronger negative slopes of $V_0 \geqslant 1.8\,E_{\text{rec}}$ are seen to result in a BEC recovery tending to zero (at least until the maximum simulated $2\tau = 100\,\text{ms}$).

Hence, the experimental data presented in figs. 8.18 and 8.20 are consistent with the localisation transition occurring between $1.7\,E_{\text{rec}}$ and $1.8\,E_{\text{rec}}$, that is the blue and orange curves in fig. 8.21a. A strong negative slope is thus taken to be a good indicator of localisation, and will be further employed in the investigations involving interactions presented in section 8.2.4.

It is also possible to quantitatively measure the breakdown of the adiabatic timescale, predicted in section 8.2.1, by computing the minimum ramp duration required for all subsequent points to exhibit a BEC recovery of $\geqslant 99\%$ (grey dashed line in fig. 8.21a). This is shown in fig. 8.21b and is observed to diverge for a critical lattice depth $V_{\text{loc}}/E_{\text{rec}} = 1.80 \pm 0.03$, consistent with the prediction $V_{\text{loc}} \approx 1.78\,E_{\text{rec}}$ from fig. 8.4.

The data in fig. 8.21b was fitted with:

$$y = \frac{a}{(V_{\text{loc}} - V_0)^b}, \quad \text{with} \tag{8.13}$$

	value	error
a	0.05	0.04
V_{loc}	1.80	0.03
b	3.15	0.80

which provided an estimate for $V_{\text{loc}}/E_{\text{rec}} = 1.80 \pm 0.03$, shown as the grey error bar.

Technical comments

We consider here a few technical aspects that may have affected the data.

The total atomic population in each image for the 2D quasiperiodic lattice experiments is found to be roughly consistent, as shown in fig. 8.22a. This suggests that the fit analysis to extract the peaks' populations, discussed in section 8.2.1, is reliable. Deep and long lattice ramps enable the atoms to occupy high diffraction orders and result in some of the peaks to merge (fig. 8.14b). This causes fits to either be highly distorted or to fail, resulting in increased noise or in an underestimation of the total population, respectively. The lower recorded total populations for the $2.0 \to 2.4\,E_{\text{rec}}$ curves at $2\tau \gtrsim 300\,\mu\text{s}$ in fig. 8.22 establish that the respective BEC recovery curves in fig. 8.18 should not be plateauing but rather exhibit a stronger negative slope. For completeness, the total populations of the 2D square lattice discussed in section 8.2.2 are shown in fig. 8.22b.

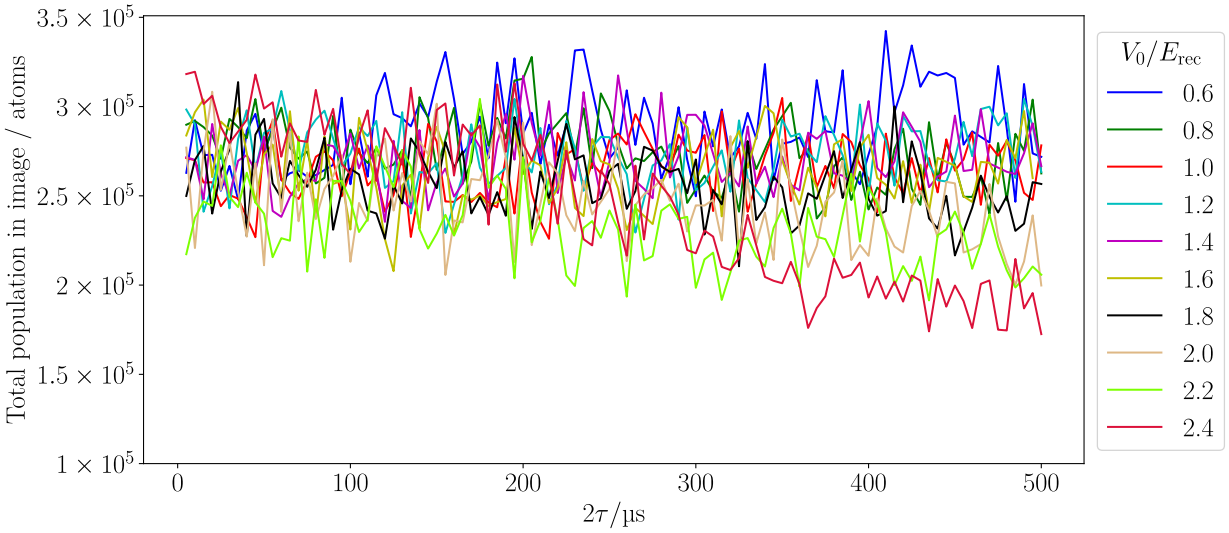

(a) 2D quasiperiodic

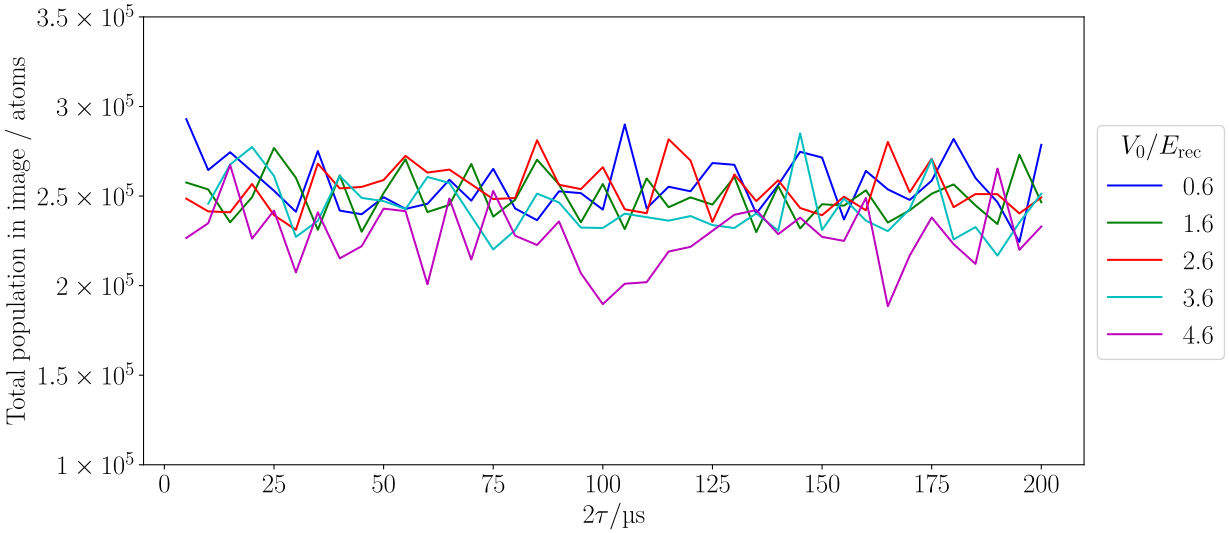

(b) 2D square

Figure 8.22 : The fit analysis employed to extract the peaks' populations is observed to result in consistent total atom numbers. For the deeply localised regions of the 2D quasiperiodic lattice (large V_0 and 2τ in a), however, some of the diffraction peaks merge causing fits to fail and the total population to be underestimated.

As explained at the end of section 7.1.3, repulsive interactions ($a = 280\,a_0$) are re-introduced 2 ms into the $t_{tof} = 33$ ms time-of-flight fall. This is done in order to broaden ("puff up") the diffraction peaks and allow the fits to reliably characterise them. The 2 ms time separation was intended to prevent scattering between particles of different momenta which would otherwise lead to the scattering spheres of fig. 7.25. Although for the arbitrarily closely spaced peaks in the 2D quasiperiodic lattice this might not be long enough, the lack of scattering spheres in the images shown in fig. 8.19 suggests the "puff up" does not cause any significant effects.

The experimental images for the 2D quasiperiodic lattice were observed to display up to

the 10^{th} diffraction order. In order to verify that higher diffraction orders were indeed expected not to be significantly populated, the image at $V_0 = 2.4\,E_{\text{rec}}$ and $2\tau = 200\,\mu\text{s}$ was compared to its simulated counterpart. This is shown in fig. 8.23, where orders $> 10^{\text{th}}$ (red) are seen to account for extremely low populations, easily falling below the detectable threshold of the experiment.

The peaks' positions in the $x - y$ plane of the camera are given by:

$$r/\mu\text{m} = 22 \cdot (p/2\hbar k) \cdot (t_{\text{tof}}/\text{ms}), \tag{8.14}$$

so after $t_{\text{tof}} = 33\,\text{ms}$ the $2\hbar k$ peaks have covered a distance of $727\,\mu\text{m}$.

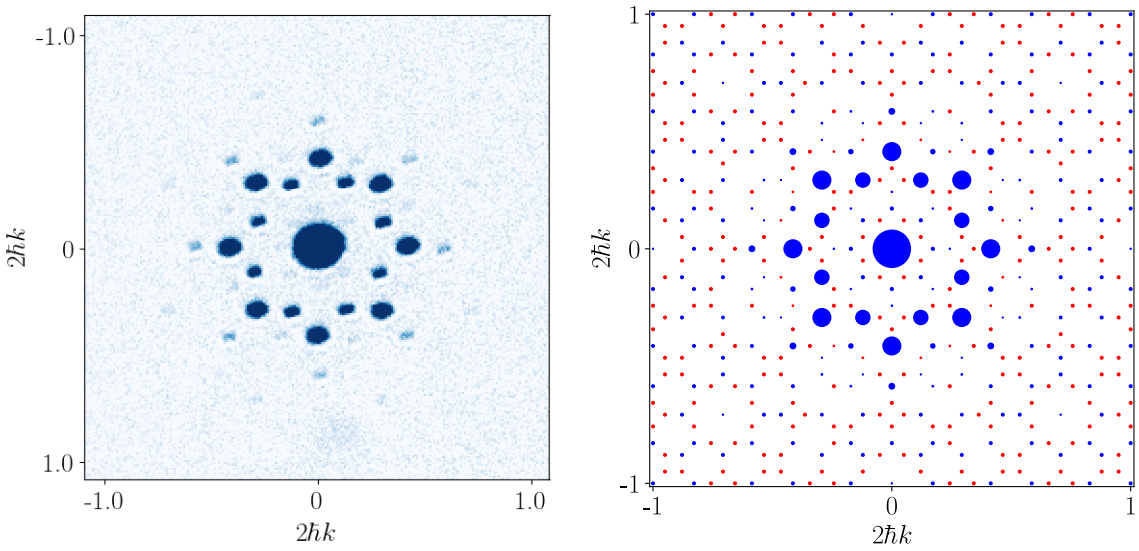

(a) (b)

Figure 8.23 : Comparison of the observed (a) and simulated (b) image for $V_0 = 2.4\,E_{\text{rec}}$, $2\tau = 200\,\mu\text{s}$ and $t_{\text{tof}} = 33\,\text{ms}$. The size of the simulated peaks are proportional to their population. The $> 10^{\text{th}}$ diffraction orders (red) are not observed in the experiment but contribute an insignificant fraction to the total population.

8.2.4 Interactions

2D Bose glass?

The lattice ramps were so far conducted at a magnetic field as close as possible to the zero-crossing of the scattering length, in order to eliminate interactions and probe single-particle physics.

In order to quantitatively investigate the effect of (repulsive) interactions on the extended-to-localised transition in the 2D quasicrystalline lattice, the magnetic field during the lattice ramp was varied to sample scattering lengths of up to $200\,a_0$.
A priori, the effect of interactions could have been:

- non-existent;
- to fully destroy localisation for any $a \neq 0$, however small;
- to allow persistence of the localised phase, at least for moderate a.

The result is shown in fig. 8.24, where the very low BEC recovery in a deeply localised region ($2\tau = 500\,\mu s$ and $V_0 = 2.4\,E_{rec}$) was observed to increase from ~ 0.2 almost back to unity with growing interaction strength. Typical images are shown in fig. 8.25.

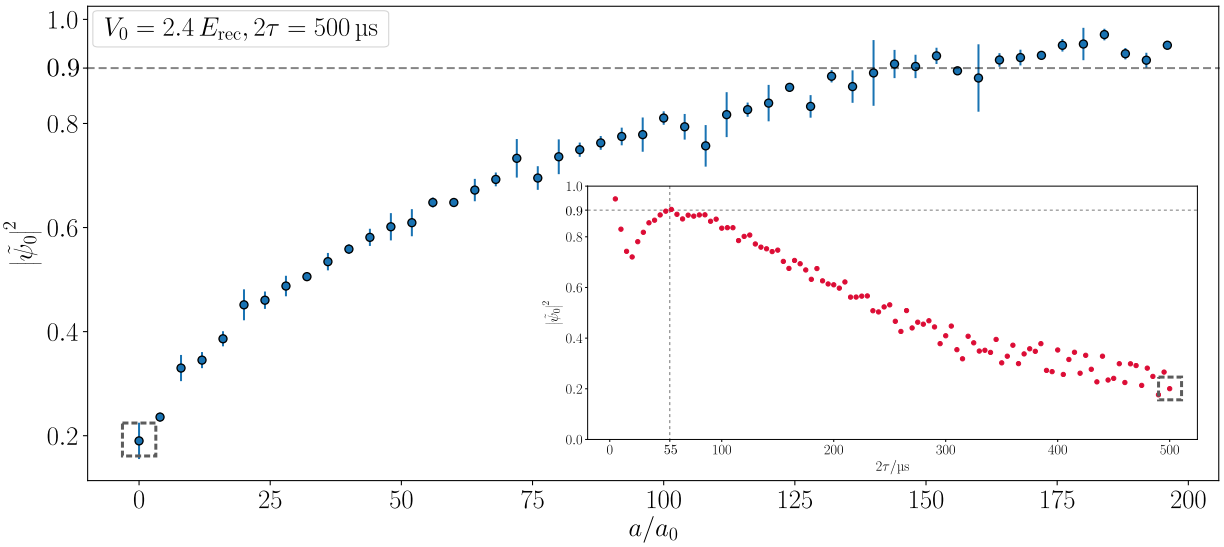

Figure 8.24 : The BEC population in the 2D quasiperiodic potential at $2\tau = 500\,\mu s$ and $V_0 = 2.4\,E_{rec}$ is very low as it is deep in the localised phase. However, this is shown to increase for a growing inter-species scattering length. The dashed line at $|\tilde{\psi}_0|^2 = 0.9$ is the maximum recovery experienced by the non-interacting $2.4\,E_{rec}$ curve (inset). The error bar corresponds to three repetitions of each datum.

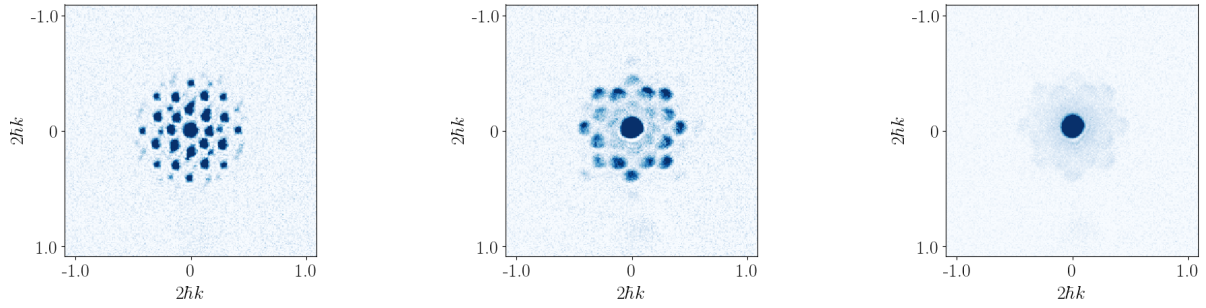

(a) $a = 0\,a_0$ (b) $a = 40\,a_0$ (c) $a = 200\,a_0$

Figure 8.25 : Typical images taken at the end of the triangular ramps (and after time-of-flight) for the $V_0 = 2.4\,E_{rec}$ and $2\tau = 500\,\mu s$ curves in fig. 8.24. The colour bar has been adjusted to emphasise the higher orders.

The increasing final BEC population at larger interaction strengths suggests the downward slopes of the recovery curves (inset in fig. 8.24) decrease in magnitude and eventually become positive for $|\tilde{\psi}_0|^2 > 0.9$ (grey dashed line). 0.9 is the maximum recovered population occurring at $2\tau = 55\,\mu s$, which is expected to be unaffected by the interaction strengths probed here, as justified in the next section.

This establishes that interactions significantly affect the system's dynamics, and suggests that the localised phase may persist for $a \neq 0$, which is compatible with the theoretical

prediction of fig. 8.28 showing stronger interactions shift the transition to higher lattice depths.

The interaction energy of the atomic cloud is quantified by the chemical potential $\mu \propto a^{2/5}$. When plotted against μ, the data asymptotically tends to a straight line, as shown in fig. 8.26. It would be interesting to perform further investigations to establish whether the slope of this line depends on the specific ramp duration 2τ and lattice strength V_0.

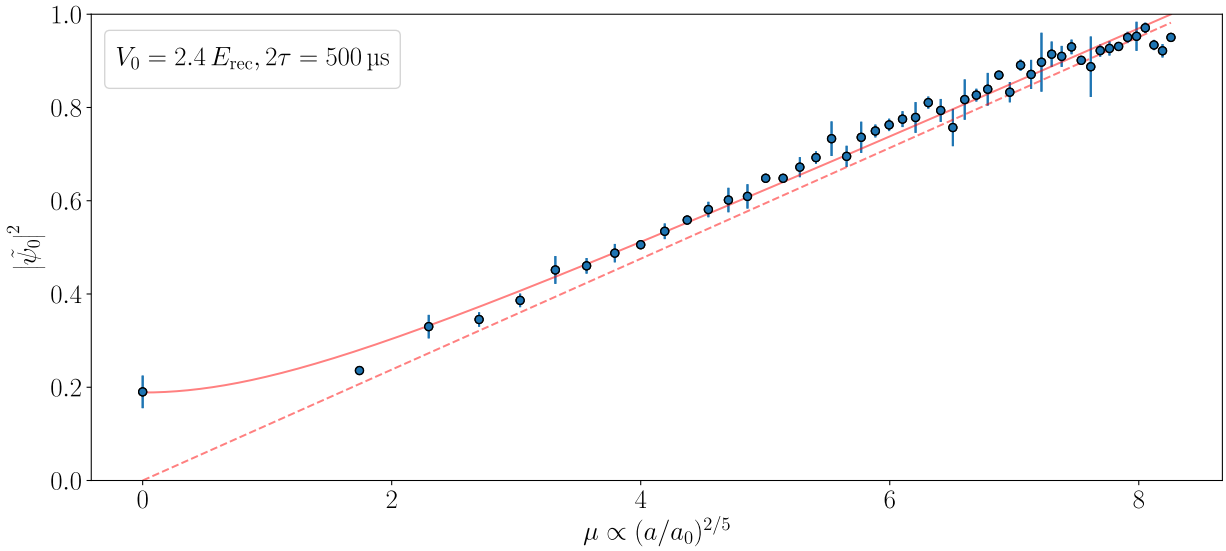

Figure 8.26 : The data in fig. 8.24, when plotted against the chemical potential $\mu \propto a^{2/5}$ (quantifying the interaction energy), tends to a straight line (dashed) for large scattering lengths a. The solid curve is a fit using eq. 8.15.

The fit function used in fig. 8.26 is:

$$y = \sqrt{b^2 + c^2 \cdot x^2}, \quad \text{with} \quad \begin{array}{lll} & \text{value} & \text{error} \\ b & 0.19 & 0.08 \\ c & 0.12 & 0.01 \end{array}, \tag{8.15}$$

and the asymptotic straight line is given by $y = cx$.

In conclusion, figs. 8.24 and 8.26 show that the BEC population from a deeply localised region may be (almost completely) recovered by increasing the interaction strength. This suggests the localised phase may be resilient against moderate (repulsive) interactions, potentially establishing this as a many-body localised phase. This would be the first experimental realisation of a 2D Bose glass.

Negative slopes and interactions

The interpretation of fig. 8.24 heavily relies on the BEC recovery curves for $V_0 \geqslant V_{\mathrm{loc}}$ to exhibit a downward trend also in the presence of interactions. That is because a strong negative slope had been established as a good indicator of localisation.

Here, we provide an argument for why the the maximum recovery $|\tilde{\psi}_0|^2 = 0.9$ at $2\tau = 55\,\mu\mathrm{s}$ displayed by the $V_0 = 2.4\,E_{\mathrm{rec}}$ curve (inset of fig. 8.24) should remain constant for the

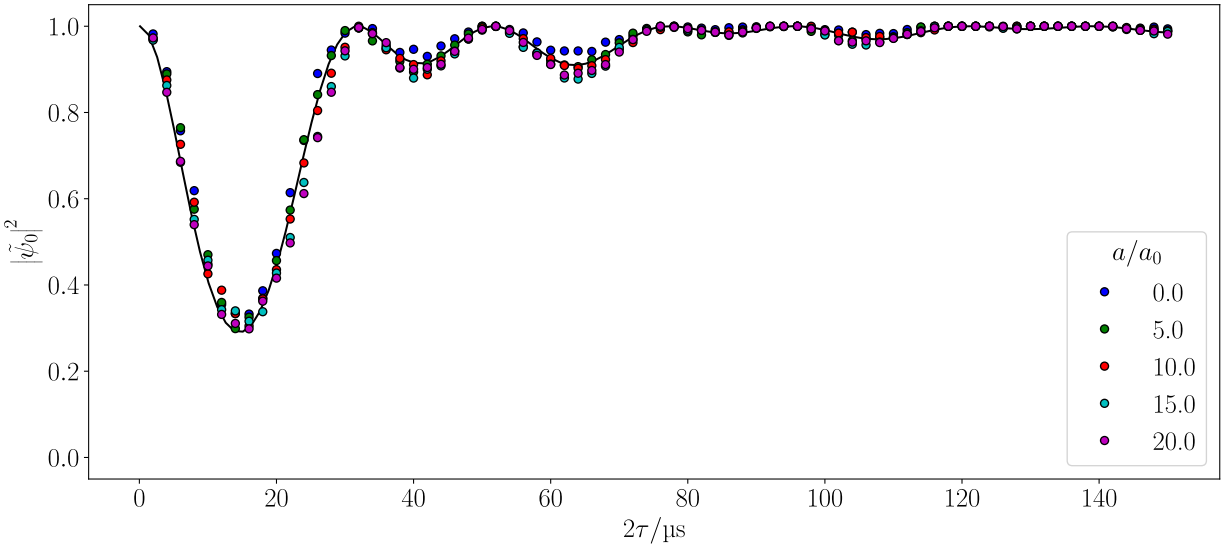

Figure 8.27 : The recovery of the BEC population in the 2D square lattice (here at $V_0 = 7\,E_{\rm rec}$) shows no change for weak interactions, at least until $2\tau = 150\,\mu s$. The solid line is the (non-interacting) numerical simulation of section 7.1.4.

interaction strengths investigated here. The recovered populations at $2\tau = 500\,\mu s$ shown in fig. 8.24 would then be enough to determine the slope of the whole curve[13].

For small interactions (up to $a = 20\,a_0$), the BEC recovery in the 2D square lattice showed no change around $2\tau \sim 55\,\mu s$, as illustrated in fig. 8.27. To extend the argument for up to $a = 200\,a_0$, we consider the relevant timescale associated with the interactions, related to the chemical potential μ.

The chemical potential μ of an atomic cloud in a harmonic trap is given by [54]:

$$\mu = \frac{\hbar\bar{\omega}}{2}\left(\frac{15Na}{\bar{a}_{\rm ho}}\right)^{2/5}, \tag{8.16}$$

where a is the scattering length, $\bar{\omega}$ the geometric mean of the trap frequencies, N the atom number and $\bar{a}_{\rm ho}$ the mean harmonic oscillator length, given by:

$$\bar{a}_{\rm ho} = \sqrt{\frac{\hbar}{m\bar{\omega}}}\,. \tag{8.17}$$

During the lattice pulse, $(\omega_x, \omega_y, \omega_z) = 2\pi\cdot(19.1, 17.5, 115.3)$ Hz and hence $\bar{\omega} = 2\pi\cdot 33.8$ Hz. For our ^{39}K BEC, $\bar{a}_{\rm ho} \approx 2.8\,\mu m$. With typical atom numbers of $1.5 - 3.0 \times 10^5$, the chemical potential of the cloud at the strongest interaction strength ($a = 200\,a_0$) is $\mu/h \approx 742 \pm 84$ Hz.

The (shortest) timescale $\tau_{\rm int}$ associated with the interactions is then $\tau_{\rm int} \sim h/\mu \sim 1.5\,ms \gg 55\,\mu s$. It was argued in section 8.2.3 that the short-time ($2\tau \lesssim 55\,\mu s$) dynamics is approximately the same for both the square the quasiperiodic lattices. Hence, we claim interactions are unlikely to affect the $V_0 = 2.4\,E_{\rm rec}$ BEC recovery curves around $2\tau \sim 55\,\mu s$ in

[13]The experimental apparatus has undergone a catastrophic failure in November 2018, from which it has yet not recovered at the time of the final version of this thesis (7$^{\rm th}$ October 2019). Hence the unavailability of additional data, and the need to justify the negative slopes' argument indirectly.

fig. 8.24. This would guarantee that the recovered population at $2\tau \sim 55\,\mu s$ is constant for the interaction strengths probed in the experiment, making the measured $2\tau = 500\,\mu s$ points enough to determine the slope of the recovery curves.

Theoretical model

A real space simulation performed by Dr. Alexander Gaunt is shown in fig. 8.28. It establishes that interactions require a larger critical lattice depth V_{loc} for localisation to occur. Interactions thus shift the transition to higher lattice depths.

The simulation solved for the ground state of the lattice (eq. 8.6) subject to "twisted boundary conditons" (based on [225]), whereby the phase of the wavefunction is required to differ by a small angle θ between two boundaries of the simulation region. A wavefunction localised at the origin is unaffected by such twist, because of its vanishing magnitude at the boundary: the ground state of the localised phase is hence the same in both twisted and untwisted system. On the other hand, a delocalised wavefunction displays a phase difference θ over the system size L, corresponding to a drift velocity $v \propto \theta/L$. This provides the extended wavefunction in the twisted system with an additional kinetic energy contribution, associated with the drift.

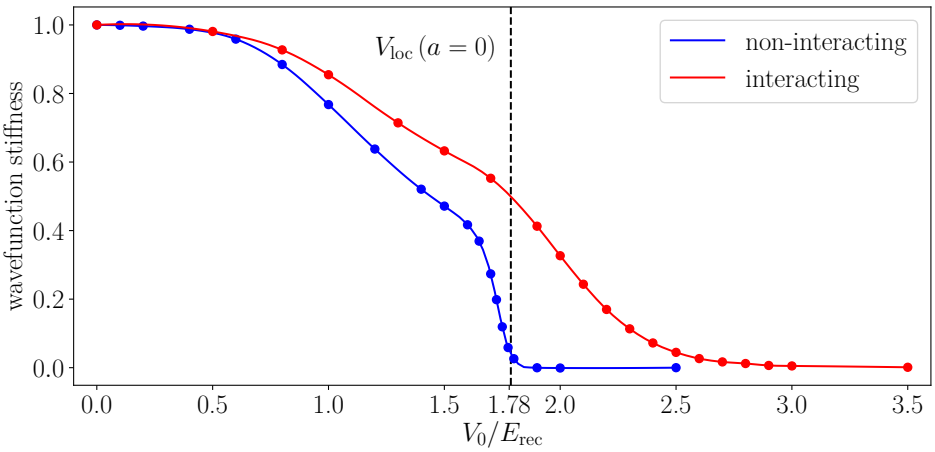

Figure 8.28 : Numerical simulations of interacting atoms in a 2D quasiperiodic potential show that the critical point is shifted to larger depths[14]. The wavefunction stiffness is related to the superfluid fraction and hence vanishes in the localised phase. Plot produced with data provided by Dr. Alexander Gaunt.

In the simulation, the observable to distinguish between the localised and the extended ("superfluid") phase is the difference of the ground state energy between the untwisted and twisted systems, related to the superfluid fraction and referred to as "wavefunction stiffness". This is plotted in fig. 8.28 against lattice depth: no energy difference in the localised phase results in zero superfluid fraction ($V_0 > V_{loc}$), while the entire wavefunction moving at the drift velocity gives unit superfluid fraction ($V_0 = 0$).

[14]The interaction strength is quantified by the $8\pi a'|\psi|^2$ term in eq. 8.6, where $|\psi|^2$ (in dimensionful units) is the atom number N. For the interacting (red) curve, a value $8\pi a' N = 345.2$ was used.

8.2.5 Limitations of simulation

The simulations discussed in this chapter (unless when otherwise specified) are performed by me in the plane wave basis, as detailed in section 7.1.4.

Because of the finite RAM of the computers used (usually 8 GB), only a finite Hamiltonian matrix could be loaded. Exact diagonalisation was numerically not allowed for $\gtrsim 12$ generations, requiring the use of sparse matrices that allowed computing the ground state for up to 25 generations used in the IPR_k plot of fig. 8.4. The finite number of CPUs (usually 4 logical cores) does not allow efficient parallelisation and hence results in long computing times when simulating the time evolution of the state.

Hence, only relatively short 2τ ramp durations were simulated, and the plane wave basis was truncated at some maximum generation $n_{\max}$. The finite number of simulated diffraction peaks then results in a finite number of basis states composing the synthetic lattice. For the 2D quasiperiodic potential, the synthetic lattice is then a finite four-dimensional hypercube. Long enough ramp durations therefore allow the population to reach its boundaries and to be reflected from them, as shown in fig. 8.29.

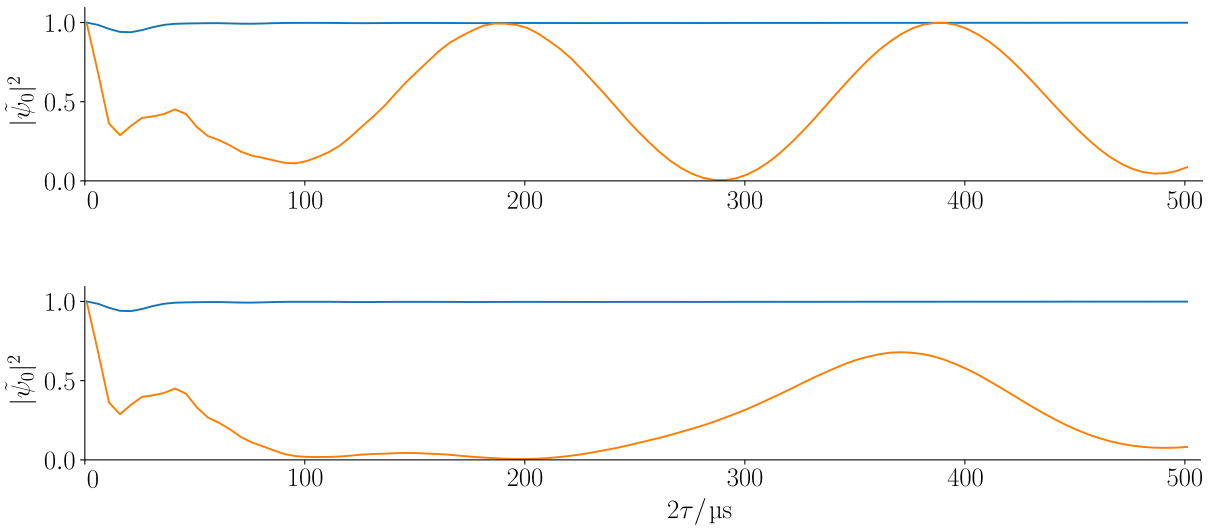

Figure 8.29 : Simulated BEC recovery in the 2D quasiperiodic lattice, for depths $V_0 = 1\,E_{\mathrm{rec}}$ (blue) and $V_0 = 5\,E_{\mathrm{rec}}$ (orange) and maximum generation $n_{\max} = 5$ (top) and $n_{\max} = 15$ (bottom). The finite size of the synthetic lattice allows for reflections from its boundaries, whose effects is relegated to longer ramp durations 2τ for larger $n_{\max}$.

All simulations presented so far used a Hamiltonian with quasimomentum $q = 0$, justified by the BEC possessing free momentum $\mathbf{k} = 0$. Experimentally, the BEC is not fully in $\mathbf{k} = 0$ because of quantum depletion and the finite size of the trap. In order to quantitatively account for this, the Hamiltonian was computed for different quasimomenta $q \neq 0$ and the BEC recovery simulations were performed. These are shown in figs. 8.30a and 8.30b for the regular square and the 2D quasiperiodic lattices, respectively.

In both configurations, a higher q results in a less-adiabatic evolution, with the initial population dip extending farther down and the population recovery occurring at larger ramp durations 2τ. These may be simply explained by the higher initial kinetic energy $\propto q^2$ enabling to reach higher states and therefore further depopulating the initial BEC.

As a complementary explanation, a higher q reduces the energy gap to the next band, thus increasing its coupling strength.

The slopes of the initial depopulation region are observed to be the same for all q, as they are probably set by the quantum speed limit related to the "Rabi" coupling $\Omega \propto V_0$. In the square lattice case, the time dynamics for particles at the edge of the Brillouin zones ($q \in \mathbb{Z}$) exhibits periodicity and revival, justified by these points being degenerate with points at $-q$. Because of this degeneracy, the band gap never vanishes and no dynamics can ever be adiabatic with respect to it.

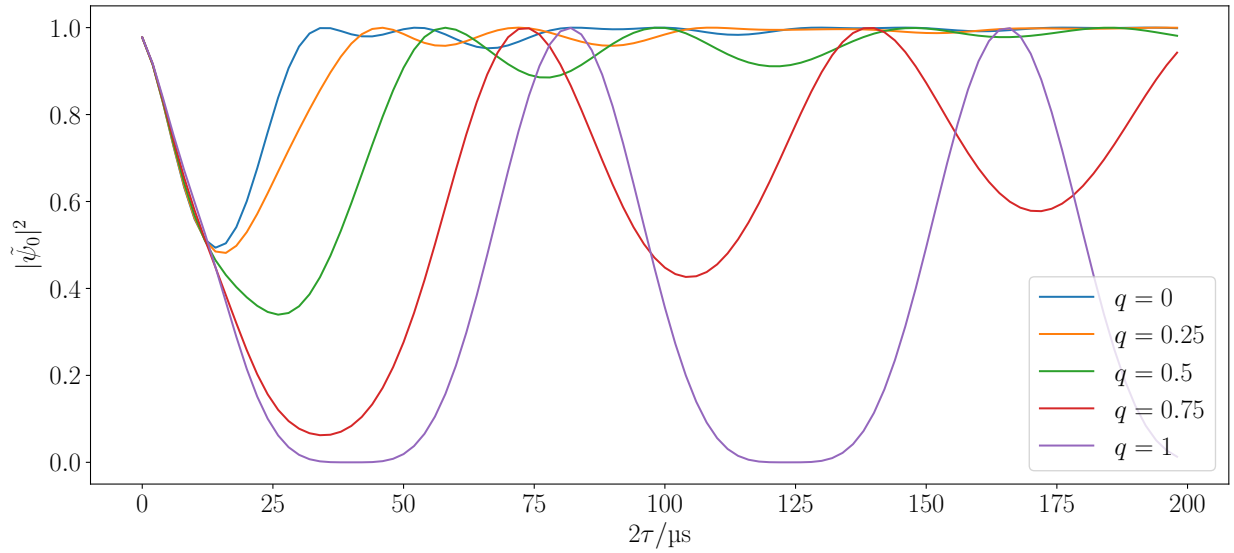

(a) 2D square

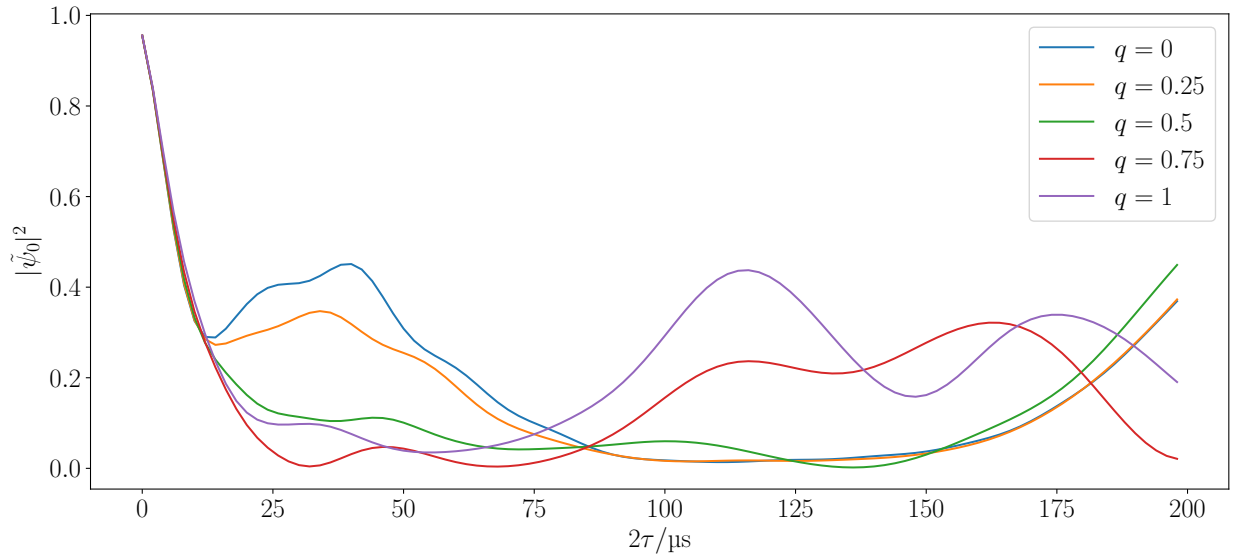

(b) 2D quasiperiodic

Figure 8.30 : The Hamiltonian was computed for different quasimomenta $q \neq 0$ and the BEC recovery simulations performed for the square (a) and quasiperiodic (b) lattices. The lattice depth was set to $V_0 = 5\,E_{\text{rec}}$ for all simulations.

Das ist nicht nur nicht richtig; es ist nicht einmal falsch.

Wolfgang Pauli

9

Plans for Z experiments

This chapter summarises miscellaneous results obtained while planning the next upgrade to the experiment, a vertical (Z) apparatus enabling 2D confinement, strong interactions and access to real space observables. A scheme to compensate the anticonfining effects of the blue detuned quasiperiodic lattice beams was devised, and the diffraction pattern of an axicon was numerically and experimentally investigated.

9.1 Z setup

Originally, the localisation transition was going to be experimentally investigated in real space and not in momentum space as presented in chapter 8.
Steps had already been taken to plan, design and characterise the apparatus required to probe the atomic cloud in-situ. These were supposed to combine upgrades, diagnostics and tools to perform a number of experiments from localisation transitions to topological effects. This apparatus is code-named "Z setup" and is schematically shown in fig. 9.1.

Its components and the experiments they will allow to perform are described in the following.

1. A novel imaging optical path including a high-magnification ($\times 30$) objective mounted on a 5-axis stage to compensate for aberrations and misalignments. This will allow high-resolution in-situ images of the atomic cloud;

2. A vertical optical lattice: "Z lattice".
   In the experiments described in chapters 7 and 8, the minima of the 2D quasiperiodic optical lattice are actually 1D tubes, elongated along the vertical direction due to the weak confinement of the optical trap[1]. The lack of confinement prevents strong correlations and thus enables a mean-field treatment and use of the Gross-Pitaevskii

[1] The trapping frequency of the dipole trap along z for $\sim 0.25\,\mathrm{W}$ is about $\omega_z \sim 120\,\mathrm{Hz}$, much lower than the on-site trapping frequencies of the lattice minima $\sim 10\,\mathrm{kHz}$.

equation. A vertical lattice will break the 1D tubes, thus enhancing correlations and granting access to strongly interacting physics. This would allow production of a Mott insulator in regular lattices, and the investigation of Mott physics in the quasiperiodic ones;

3. A vertical attractive beam: "Z dipole".
   The in-plane blue detuned optical lattice beams result in an overall anticonfining effect in the xy plane, which will be compensated by a vertical attractive beam thus guaranteeing the dynamics of the atoms are controlled solely by the quasiperiodic landscape. This is essential for the real space transport experiments that will be conducted to probe the localisation transition by recording the expansion of the atomic cloud in the 2D quasiperiodic lattice, akin to fig. 8.10. The anticonfining potential and the Z dipole beam are numerically investigated in section 9.2;

4. A DMD will be used to superimpose arbitrary potential landscapes to the 2D quasiperiodic lattice, as shown in fig. 9.2. On the one hand, this will allow to include transient local perturbations to the existing potential and probe their survival in the long-term dynamics of the spatial density of the cloud, distinguishing thermal from localised phases. On the other hand, the DMD will enable to create a sharp, repulsive circular barrier around the quasiperiodic potential, in order to investigate the topology of the edge states. To reduce the power loss in the generation of the circular ring, an axicon will be employed to result in a more suitable beam profile. This is numerically and experimentally studied in section 9.3.

5. To guarantee a large numerical aperture for the incoming DMD beam, the Stern-Gerlach coils placed around the science cell had to be re-arranged. Their presence is still essential as a diagnostic tool, and may be employed in future experiments to provide transient gradients to the atoms, e.g. for quasiperiodic Bloch oscillations.

9.2 Anticonfining potential

In section 2.2.2 it was shown how a travelling wave with Gaussian intensity generates an attractive or repulsive potential. The same effect is present for standing waves generated by Gaussian beams, and results in an additional overall confining or anti-confining potential, for red or blue detuned lattices.

9.2.1 On-site trapping frequencies

A travelling wave $\mathbf{E}_1 = \sqrt{I_0}\sin kz$ is retro-reflected to create a standing wave:

$$\mathbf{E}_{\text{tot}} = \mathbf{E}_1 + \mathbf{E}_2 = \sqrt{I_0}\sin(kz) - \sqrt{I_0}\sin(-kz) = 2\sqrt{I_0}\sin(kz). \tag{9.1}$$

The intensity I and the potential V experienced by the atoms are then:

$$I = 4I_0\sin^2(kz), \quad V = \underbrace{4\alpha I_0}_{V_0}\sin^2(kz), \tag{9.2}$$

where α is the atomic polarisability.
The central intensity of a Gaussian beam is:

$$I_0 = \frac{2P}{\pi w_{\text{h}} w_{\text{v}}}, \tag{9.3}$$

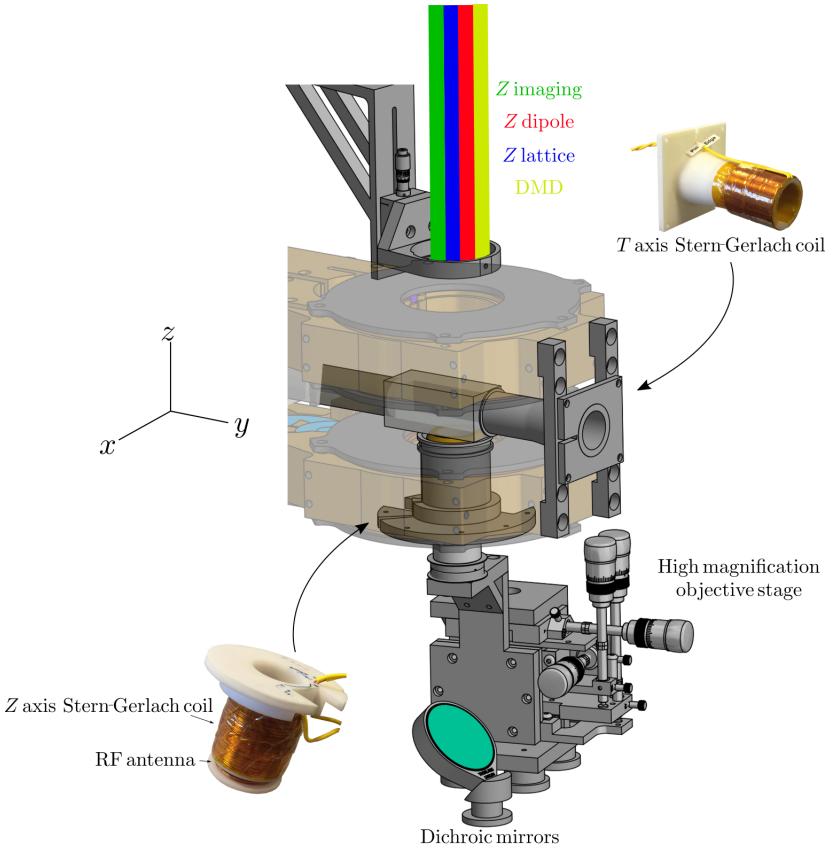

Figure 9.1 : The plan for the Z setup. This will include a high-magnification objective to perform high-resolution in-situ imaging, a vertical lattice to enhance correlations, a vertical attractive beam to compensate the anticonfining effects of the blue detuned optical lattice beams, and a DMD to project arbitrary potential landscapes onto the atoms.

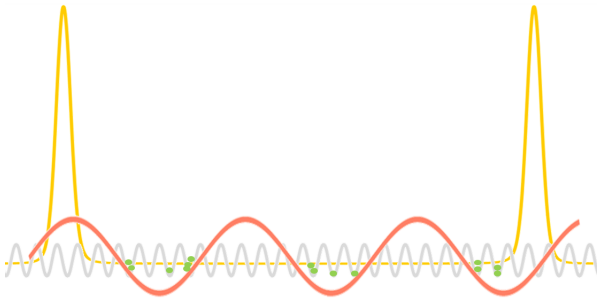

Figure 9.2 : With a DMD, the atoms (green) will not only be made to experimence the 2D quasiperiodic potential (grey), but also sharp repulsive walls (yellow) and local perturbations (red). Figure taken from [177].

and hence the central potential depth is:

$$V_0 = 4\alpha I_0 = 4\alpha \frac{2P}{\pi w_\mathrm{h} w_\mathrm{v}}, \tag{9.4}$$

where w_v and w_h are the vertical and horizontal waists of the Gaussian beam.

In the deep lattice limit, the minima of the optical lattice potential can be approximated as harmonic oscillators, as was shown in fig. 2.12c. Near each minimum, a Taylor expansion can be performed:

$$V(z) = V_0 \sin^2(kz) \approx V_0\, k^2 z^2, \tag{9.5}$$

which can be then treated as a harmonic oscillator:

$$V_0\, k^2 z^2 \ = \frac{1}{2} m \omega_{\mathrm{on-site}}^2 z^2 \Rightarrow \omega_{\mathrm{on-site}} = \sqrt{\frac{2V_0 k^2}{m}}, \tag{9.6}$$

where $\omega_{\mathrm{on-site}}$ is the on-site trapping frequency.

In higher dimensions, the on-site trapping frequencies are obtained by:

$$\begin{aligned} &V(x, y \dots)|_{\min} \approx V_0 + \frac{1}{2} m (\omega_x x^2 + \omega_y y^2 \dots) \\ \Rightarrow \quad &\omega_x = \sqrt{\frac{1}{m}\frac{\partial^2 V}{\partial x^2}}, \quad \omega_y = \sqrt{\frac{1}{m}\frac{\partial^2 V}{\partial y^2}}, \dots \end{aligned} \tag{9.7}$$

The ground state energy is then given as:

$$E_0 = V_0 + \frac{1}{2}\hbar \left(\omega_x + \omega_y + \dots\right), \tag{9.8}$$

and depends both on the amplitude of the intensity $V_0 \propto I_0$, and on its curvature $\omega \propto \sqrt{\partial^2 I}$.

9.2.2 1D lattice

For red detuned beams, the polarisability is negative $\alpha < 0$ and the atoms are attracted to the maxima of the intensity pattern, which results in two effects:

1. an overall *confining* effect because of the Gaussian profile of the beam, with a maximum intensity in the middle and hence the largest potential depth and offset V_0.

2. an overall *anti-confining* effect due to the decaying intensity profile reducing the trapping frequency $\omega \propto \sqrt{\partial^2 I}$ and hence the ground state energy away from the centre of the beam. This is shown in fig. 9.3.

Both effects can also be characterised by a harmonic oscillator, by re-introducing the

Gaussian envelope of the optical lattice beam $V(z) = V_0 \sin^2(kz)\, \mathrm{e}^{-\frac{2x^2}{w_0^2}}$:

$$\begin{aligned} E_g &= -V_0 + \frac{1}{2}\hbar\omega_{\text{on site}}, \\ &= -V_0 \mathrm{e}^{\frac{2x^2}{w_0^2}} + \frac{1}{2}\hbar\sqrt{\frac{V_0 k^2}{2m}}\, \mathrm{e}^{-\frac{x^2}{w_0^2}} \\ &\approx -V_0\left(1 - \frac{2x^2}{w_0^2}\right) + \frac{1}{2}\hbar\sqrt{\frac{V_0 k^2}{2m}}\left(1 - \frac{x^2}{w_0^2}\right)\ldots \\ &= -V_0 + \frac{1}{2}\hbar\sqrt{\frac{V_0 k^2}{2m}} + \frac{1}{2}m\omega_{\text{conf}}^2 x^2 - \frac{1}{2}m\omega_{\text{ac}}^2 x^2 \\ &\propto \frac{1}{2}m\omega_{\text{total}} x^2, \end{aligned} \tag{9.9}$$

where

$$\omega_{\text{total}}^2 = \omega_{\text{conf}}^2 - \omega_{\text{ac}}^2 = \frac{4V_0}{mw_0^2} - \left(\frac{h}{mw_0\lambda}\right)\sqrt{\frac{V_0}{E_{\text{rec}}}}. \tag{9.10}$$

Note that the waist of the anticonfining potential (w_{ac}) is a factor of $\sqrt{2}$ larger than that of the lattice beam itself, $w_{\text{ac}} = \sqrt{2}\, w_0$.

In a blue detuned optical lattice, the polarisability is positive $\alpha > 0$ and the atoms are placed at the intensity minima. The same derivation performed before applies, but the offset V_0 is negligible and only the anticonfining contribution prevails.

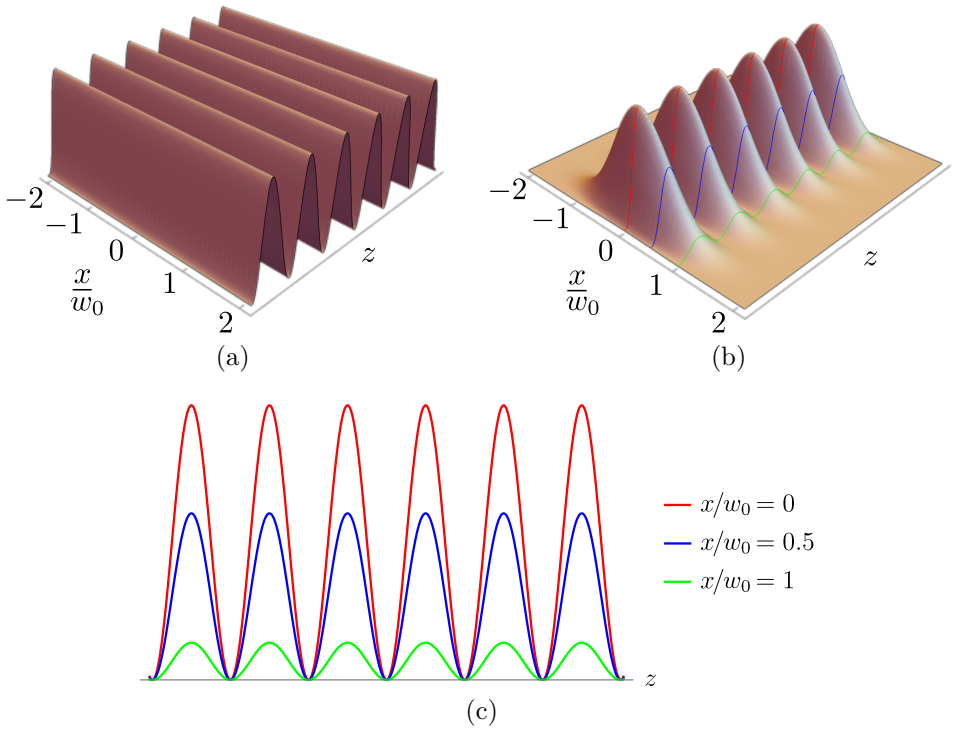

Figure 9.3 : An optical lattice created by plane waves (a) does not result in additional potentials. In optical lattices created by Gaussian beams (b), the intensity decrease in the transverse direction (along the waist w_0) reduces the trapping frequency (c) and thus the ground state energy, resulting in an anticonfining effect.

Fig. 9.4 shows the numerical result for a 1D blue detuned optical lattice created by a Gaussian beam. The anticonfining potential in this case is also exactly a Gaussian, with a $\sqrt{2}$ larger waist, because of the separability between the propagation and transverse direction enabled only in 1D.

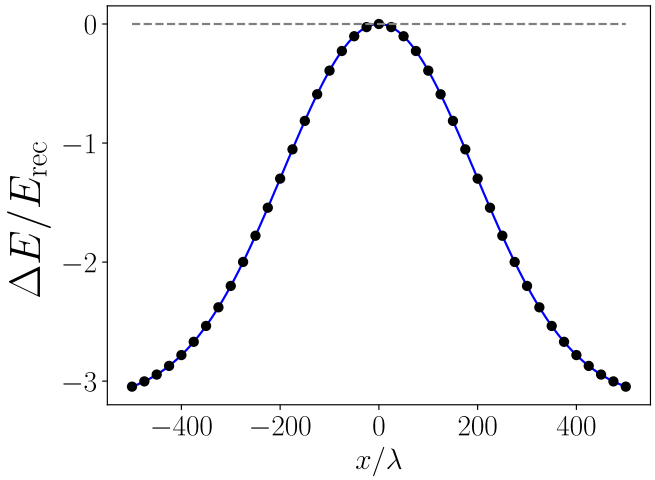

Figure 9.4 : Difference in the on-site ground state energies between an optical lattice created by plane waves and one created by Gaussian beams with waist w_0 (black points). Because of the separability of the problem in 1D, the anticonfining potential is analytically a Gaussian (solid blue line), with waist $w_{\mathrm{ac}} = \sqrt{2}\,w_0$. Here, $w_0/\lambda = 275$ and $w_{\mathrm{ac}}/\lambda = 389$.

9.2.3 2D lattice

Method

2D optical lattices created by Gaussian beams are not separable in their variables, and therefore require a fully numerical treatment. Blue detuned lattices are assumed in the following, since they are used in the experiment.

The 2D quasiperiodic optical lattice potential generated by the four standing waves described in section 7.1.1 is:

$$V(\mathbf{r}) = V_0 \left[\sin^2(kx) + \sin^2(ky) + \sin^2\left(\frac{k}{\sqrt{2}}(x+y)\right) + \sin^2\left(\frac{k}{\sqrt{2}}(x-y)\right)\right], \tag{9.11}$$

where ideal plane wave were assumed.
With Gaussian beams, this becomes:

$$\begin{aligned} V(x,y) = V_0 \sin^2(kx)\, \mathrm{e}^{-\frac{2y^2}{w_0^2}} + V_0 \sin^2(ky)\, \mathrm{e}^{-\frac{2x^2}{w_0^2}} + \\ + V_0 \sin^2\left(\frac{k}{\sqrt{2}}(x+y)\right) \mathrm{e}^{-\frac{(x-y)^2}{w_0^2}} + V_0 \sin^2\left(\frac{k}{\sqrt{2}}(x-y)\right) \mathrm{e}^{-\frac{(x+y)^2}{w_0^2}}. \end{aligned} \tag{9.12}$$

In order to approximate each potential minimum as a harmonic oscillator:

$$V(x,y) = \frac{1}{2} m\omega_x^2 x^2 + \frac{1}{2} m\omega_y^2 y^2, \tag{9.13}$$

we define the Hessian matrix $H(x, y)$:

$$H(x,y) = \begin{pmatrix} \partial_{x,x}V(x,y) & \partial_{x,y}V(x,y) \\ \partial_{y,x}V(x,y) & \partial_{y,y}V(x,y) \end{pmatrix}, \tag{9.14}$$

and diagonalise it to yield:

$$\begin{pmatrix} m\omega_x^2 & 0 \\ 0 & m\omega_y^2 \end{pmatrix} = \begin{pmatrix} \lambda_1 & 0 \\ 0 & \lambda_2 \end{pmatrix}. \tag{9.15}$$

The on-site ground state energies are then given by:

$$E_0 = \frac{1}{2}\hbar(\omega_x + \omega_y) = \frac{1}{2}\hbar\left(\sqrt{\frac{\lambda_1}{m}} + \sqrt{\frac{\lambda_2}{m}}\right). \tag{9.16}$$

The calculation was performed in dimensionless units as outlined in appendix D.10, and was based on the method developed in [75].

Square lattice

We first consider a regular square lattice created by two orthogonal standing waves, with a Gaussian intensity profile of waist w_0:

$$V(x,y) = V_0 \sin^2(kx)\, \mathrm{e}^{-\frac{2y^2}{w_0^2}} + V_0 \sin^2(ky)\, \mathrm{e}^{-\frac{2x^2}{w_0^2}}. \tag{9.17}$$

The on-site ground state energies are computed both for the potential of eq. 9.17 and for its ideal, plane wave counterpart, their difference plotted in fig. 9.5. As for the 1D case, lower energies are available away from the centre of the lattice, which results in an anticonfining potential. This may be quantified by fitting a 2D Gaussian with waist w_{ac}:

$$V_{\mathrm{ac}}(x,y) = \sqrt{V_0}\left(\mathrm{e}^{-2\frac{x^2+y^2}{w_{\mathrm{ac}}^2}} - 1\right). \tag{9.18}$$

However, the non-separability of the potential in eq. 9.17 forbids an analytical solution for the anticonfining potential, rendering 2D Gaussians only an approximation. In fact, different system sizes result in different anticonfining waists w_{ac}, as shown in fig. 9.6a. This dependence can be reduced and eliminated by less stringent requirements on the fitting function, for instance using a (truncated) power series:

$$V'_{\mathrm{ac}}(x,y) = \sqrt{V_0}\left(-2\frac{x^2+y^2}{w_{\mathrm{ac}}^2} + 12\frac{x^2y^2}{w_{\mathrm{ac}}^2}\right). \tag{9.19}$$

This establishes that in 2D, the anticonfining potential is not described by an analytic function, and can only be approximately compensated for a given system size. As in 1D, fig. 9.6a shows that the waist of the anticonfining potential w_{ac} is larger that the waist of each Gaussian lattice beam w_0.

The potential being anticonfining for blue detuned lattices, the compensation is to be performed by attractive (red detuned) beams. Experimentally, these could be the same beams creating the optical crossed-beam dipole trap (section 5.3.3) which lie in the same

plane as the optical lattice. Alternatively, an ad-hoc vertical attractive beam can be superimposed to the atoms, with waist and optical power optimised to provide the compensation.

In order to quantify the effect of these two solutions, the quantity χ^2 is defined as follows:

$$\chi^2 = \frac{1}{N} \sum_j \left(\frac{\Delta E_j}{E_j^{\text{ideal}}} \right), \tag{9.20}$$

where E^{ideal} is the on-site ground state energy in the lattice generated by plane waves, ΔE the difference between the E^{ideal} and the energy resulting from Gaussian beam lattices and compensating potentials, and N the number of lattice sites the sum runs over. The results for χ^2 are plotted as a function of system size in fig. 9.6b, and show that a vertical attractive beam, such as the Z dipole planned for in fig. 9.1, is the best option.

Quasicrystalline lattice

The on-site ground state energies of the 2D quasiperiodic lattice described by eq. 9.12 are computed, and their deviation from the ideal ones given by plane waves is shown in fig. 9.7. As opposed to the regular lattices presented thus far, the lattice sites energies of the quasicrystal are quasi-random due to the non-periodic geometry, so a fit can only extract the overall trend. The results of the fit are shown in fig. 9.8a, and are performed in the same way as previously described for the square lattice. In this case, however, the waist w_{ac} of the anticonfining potential is smaller than the waist of each Gaussian lattice beam w_0. The compensation provided by the in-plane crossed dipole trap beams and by a vertical beam is again quantified by χ^2 and shown in fig. 9.8b.

Due to the scattered nature of fig. 9.7, the Gaussian fits quantifying the anticonfining potential only provide an estimate for the average of all the lattice sites minima. The fit is then performed on the ground state energies above or below a certain threshold, to quantify their individual contribution to the anticonfining potential, as shown in fig. 9.9.

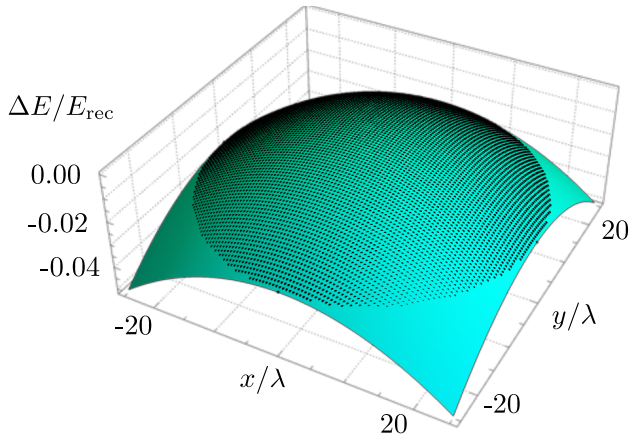

Figure 9.5 : Difference between on-site ground state energies for the ideal (plane wave) and real (Gaussian beams) square lattice. A Gaussian fit is performed in order to extract the waist w_{ac} of the anticonfining potential.

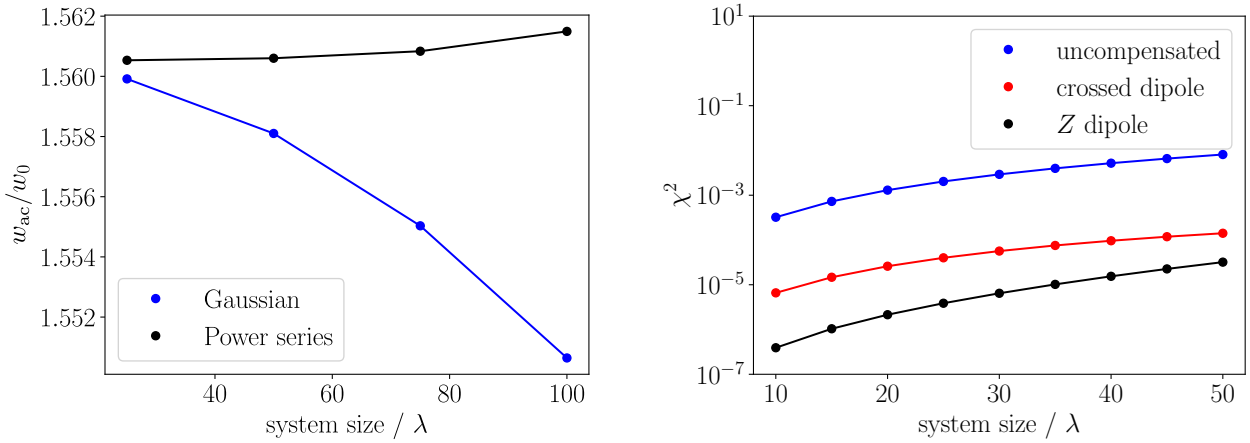

Figure 9.6 : a) The Gaussian fit of fig. 9.5 is performed for different system sizes $2\lambda \times 2\lambda$, resulting in a variation of the extracted waist w_{ac} (blue points). This correlation is explained by a Gaussian not being the analytical solution, and can be reduced by performing the fit with a simple (truncated) power series (black points). b) The quantity χ^2 quantifies the deviation of the on-site ground state energies from their ideal value in a lattice generated by plane waves. Both the in-plane crossed dipole trap beams and a vertical beam reduce the anticonfining potential in the optical lattice, the latter providing a better performance.

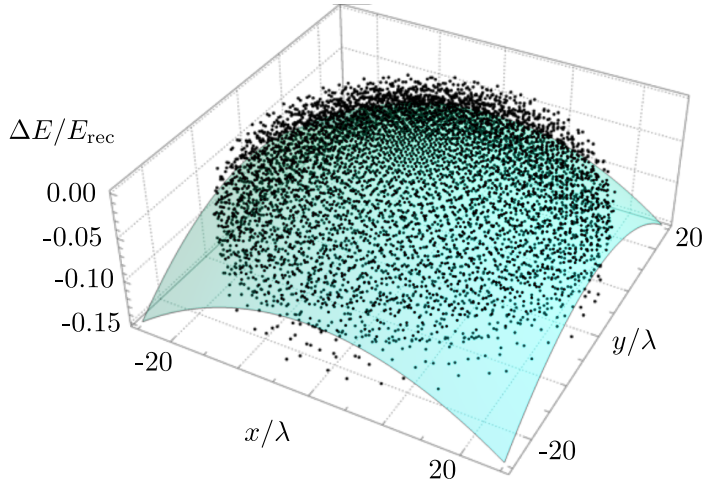

Figure 9.7 : Difference between on-site ground state energies for the ideal (plane wave) and real (Gaussian beams) quasicrystalline lattice. A Gaussian fit is performed in order to extract the waist w_{ac} of the anticonfining potential.

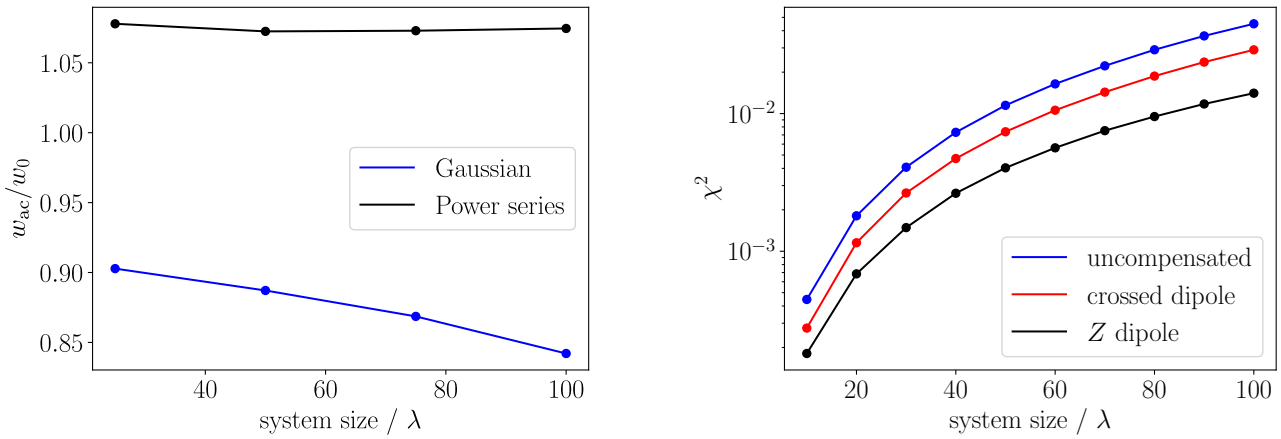

Figure 9.8 : a) The Gaussian fit of fig. 9.7 is performed for different system sizes $2\lambda \times 2\lambda$, resulting in a variation of the waist w_{ac} (blue points). This correlation is explained by a Gaussian not being the analytical solution, and can be reduced by performing the fit with a simple (truncated) power series (black points). b) The quantity χ^2 quantifies the deviation of the on-site ground state energies from their ideal value in a lattice generated by plane waves. Both the in-plane crossed dipole trap beams and a vertical beam reduce the anticonfining potential in the optical lattice, the latter providing a better performance.

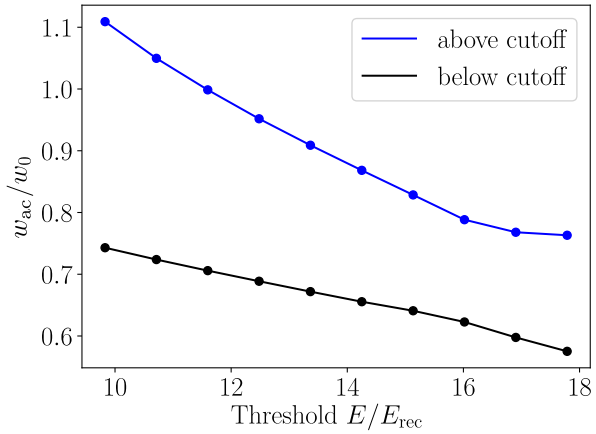

Figure 9.9 : The Gaussian fit of fig. 9.7 is performed for ground state energies above (below) a certain threshold, given by the x coordinates, to quantify their contribution to the overall anticonfining potential. This seems to suggest that the lowest energies contribute the most to the anticonfining effect.

9.3 Axicon

The DMD will allow projection of a circular ring of blue detuned light, to provide sharp repulsive boundaries to the quasiperiodic potential. Creation of a ring from an incident Gaussian beam, however, requires the diversion of most of the incident power and hence a dramatically low efficiency. To guarantee a higher efficiency, it would be beneficial to illuminate the DMD with an intensity profile that already approximates a circular ring. This is provided by the diffraction pattern of a system comprising an axicon and a converging lens, shown in fig. 9.10 and investigated in the following section.

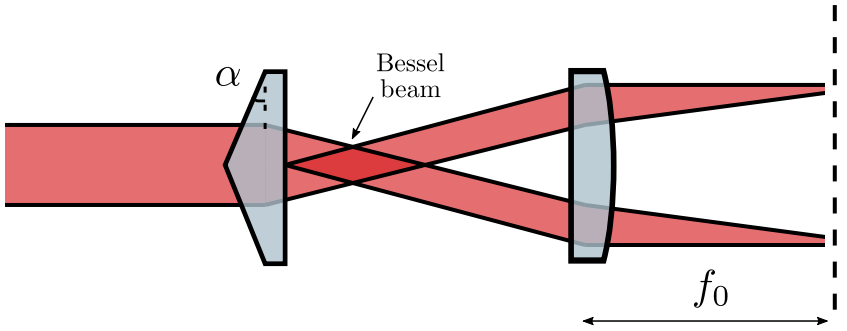

Figure 9.10 : The optical apparatus comprising an axicon (conical angle α) and a converging lens (focal length f_0) can be used to produce a circular ring as their diffraction pattern (dashed line). The near-diffraction of the axicon itself results in a Bessel beam, discussed later.

9.3.1 Mathematical derivations

The mathematical derivation reported here builds on the work presented in [226].

Incident Gaussian beam

Under the Helmholtz and paraxial approximations, a solution to Maxwell's equations in vacuo is a Gaussian beam propagating in z of the form:

$$E_{\text{in}}(\rho, z) = \frac{w_0}{w(z)} \exp\left[-\frac{\rho^2}{w^2(z)}\right] \exp\left[\mathrm{i}\left(kz - \theta(z) + \frac{k\rho^2}{2R_{\text{c}}(z)}\right)\right]. \tag{9.21}$$

The waist w, radius of curvature R_{c}, and Gouy shift θ are given by:

$$\begin{aligned} w^2(z) &= w_0^2\left[1 + \left(\frac{z}{z_{\text{R}}}\right)^2\right], \\ R_{\text{c}}(z) &= z\left[1 + \left(\frac{z_{\text{R}}}{z}\right)^2\right], \\ \theta(z) &= \arctan\left(\frac{z}{z_{\text{R}}}\right), \end{aligned} \tag{9.22}$$

where z_{R} is the Rayleigh range of the beam.

The above will be used as the incident beam onto the axicon in fig. 9.10.

Thin lens and axicon

Within the *thin* lens approximation, the interaction between incident radiation and an optical element only amounts to a phase correction to the wavefront, caused by the refractive index affecting the propagation of the wave. Further interaction between the dielectric material and the incoming electric field is neglected.

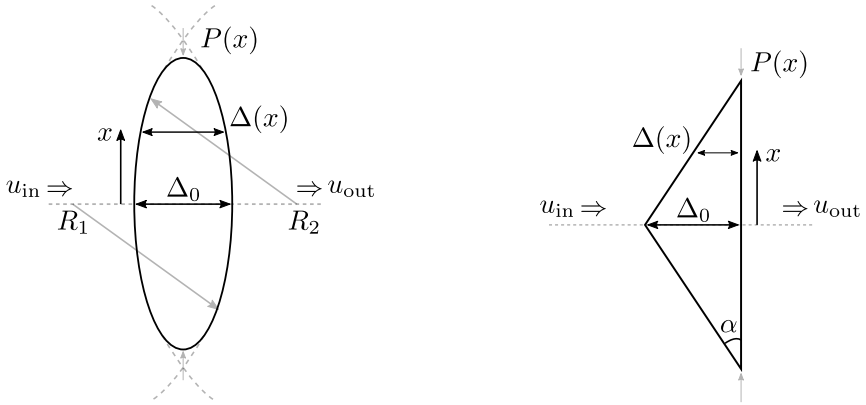

(a) Converging lens (b) Axicon

Figure 9.11 : The refractive index n of the optical element affects the propagation of an incident EM wave, resulting in a phase correction dependent on the width of the material. $P(x)$ is the pupil function, limiting the $(-\infty, \infty)$ integrations (discussed later) only to the area covered by the aperture (the optical component).

An optical component with index of refraction n and central thickness Δ_0 causes a ray propagating through it to acquire a phase factor $\phi(x)$, depending on its transverse position x, as shown in fig. 9.11:

$$\phi(x) = kn\Delta(x) + k[\Delta_0 - \Delta(x)]. \tag{9.23}$$

For the converging lens in fig. 9.11a, the path length depends on the radii of curvature R of the front (R_1) and back (R_2) surfaces:

$$\Delta(x) = \Delta_1 + \Delta_2 = \Delta_0 - R_1\left(1 - \sqrt{1 - \frac{x^2}{R_1^2}}\right) + R_2\left(1 - \sqrt{1 - \frac{x^2}{R_2^2}}\right). \tag{9.24}$$

Using the paraxial approximation such that $x \ll R$ and $\sqrt{1 - \frac{x^2}{R^2}} \sim 1 - \frac{x^2}{2R^2}$, this can be expressed as:

$$\Delta(x) = \Delta_0 - \frac{1}{2}\left(\frac{1}{R_1} - \frac{1}{R_2}\right), \tag{9.25}$$

where the focal length f_0 is defined as

$$\frac{1}{f_0} = (n-1)\left(\frac{1}{R_1} - \frac{1}{R_2}\right), \tag{9.26}$$

leading to the a total phase factor:

$$\phi(x) = kn\Delta(x) + k[\Delta_0 - \Delta(x)] = kn\Delta_0 - \frac{k}{2f_0}x^2. \tag{9.27}$$

The non-trivial (only spatially dependent) correction to the wavefront of the propagating wave by a thin lens is therefore:

$$\tau_{\mathrm{L}}(\rho) = \mathrm{e}^{-\mathrm{i}\frac{k}{2f_0}\rho^2}, \tag{9.28}$$

while a similar calculation for the axicon in fig. 9.11b results in:

$$\tau_{\mathrm{A}}(\rho) = \mathrm{e}^{-\mathrm{i}b\rho}, \quad \text{with} \quad b = \frac{2\pi(n-1)}{\lambda}\tan\alpha, \tag{9.29}$$

where α is the conical angle of the axicon.

Diffraction

The lens and the axicon are also finite apertures which will cause diffraction of the beam, irregardless of the refractive index.

The resulting electric field distribution emerging from an aperture such as in fig. 9.12 is given by the Fresnel-Kirchhoff diffraction formula [227]:

$$E(x,y,z) = \frac{-\mathrm{i}}{\lambda}\int\int_{\text{aperture}} E_{\text{in}}(x',y',0)\,\frac{\mathrm{e}^{\mathrm{i}\mathbf{k}\cdot\mathbf{R}}}{R}\left(\frac{1+\cos(\mathbf{R}\angle\hat{\mathbf{z}})}{2}\right)\mathrm{d}x'\,\mathrm{d}y'. \tag{9.30}$$

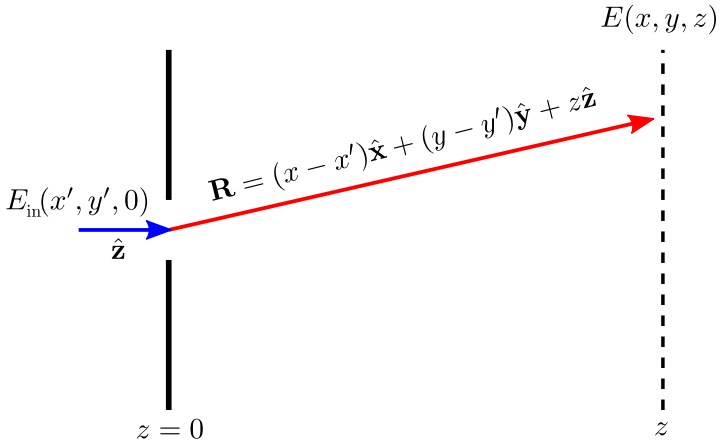

Figure 9.12 : The electric field resulting from the diffraction through an aperture is controlled by the incident radiation and by the distance to the screen. It is given by the Fresnel-Kirchhoff diffraction formula in eq. 9.30.

Using the paraxial approximation, $\cos \sim 1$ and $\frac{1}{R} \sim \frac{1}{z}$, and focussing on the far-field pattern where $z^2 \gg (x-x')^2 + (y-y')^2$, results in:

$$R = z\sqrt{1 + \frac{(x-x')^2+(y-y')^2}{z^2}} \sim z\left(1 + \frac{(x-x')^2+(y-y')^2)}{2z^2}\right), \tag{9.31}$$

and hence:

$$E(x,y,z) \approx \frac{-\mathrm{i}\mathrm{e}^{\mathrm{i}kz}\mathrm{e}^{\mathrm{i}\frac{k}{2z}(x^2+y^2)}}{\lambda z}\int\int_{\text{aperture}} E_{\text{in}}(x',y',0)\,\mathrm{e}^{\mathrm{i}\frac{k}{2z}(x'^2+y'^2)}\mathrm{e}^{-\mathrm{i}\frac{k}{z}(xx'+yy')}\mathrm{d}x'\,\mathrm{d}y'. \tag{9.32}$$

In a system with cylindrical symmetry, where $E(x', y', z = 0) \rightarrow E(\rho', z = 0)$, $x = \rho\cos\phi$ and $y = \rho\sin\phi$, the integral can be written as:

$$E(\rho, z) = \frac{-\mathrm{i}\mathrm{e}^{\mathrm{i}kz}\mathrm{e}^{\mathrm{i}\frac{k}{2z}\rho^2}}{\lambda z}\int \mathrm{d}\phi' \int_{\text{aperture}} \mathrm{d}\rho'\rho' E_{\text{in}}(\rho', 0)\,\mathrm{e}^{\mathrm{i}\frac{k}{2z}\rho'^2}\mathrm{e}^{-\mathrm{i}\frac{k}{z}(\rho\rho'\cos\phi\cos\phi' + \rho\rho'\sin\phi\sin\phi')},$$
$$E(\rho, z) = \frac{-\mathrm{i}\mathrm{e}^{\mathrm{i}kz}\mathrm{e}^{\mathrm{i}\frac{k}{2z}\rho^2}}{\lambda z}\int \mathrm{d}\phi' \int_{\text{aperture}} \mathrm{d}\rho'\rho' E_{\text{in}}(\rho', 0)\,\mathrm{e}^{\mathrm{i}\frac{k}{2z}\rho'^2}\mathrm{e}^{-\mathrm{i}\frac{k}{z}(\rho\rho'\cos(\phi - \phi')}. \tag{9.33}$$

The following identity involving the 0^{th} Bessel function of the first kind J_0:

$$\int_0^{2\pi} \mathrm{e}^{-\mathrm{i}\frac{k}{z}(\rho\rho'\cos(\phi-\phi')}\mathrm{d}\phi' = 2\pi J_0\left(\frac{k\ \rho\rho'}{z}\right) \tag{9.34}$$

can be used to provide in the final expression for the far-field diffraction pattern in cylindrical coordinates:

$$E(\rho, z) = \frac{2\pi\mathrm{e}^{\mathrm{i}kz}\mathrm{e}^{\mathrm{i}\frac{k}{2z}\rho^2}}{\mathrm{i}\lambda z}\int_{\text{aperture}} \mathrm{d}\rho'\rho' E_{\text{in}}(\rho', 0)\,\mathrm{e}^{\mathrm{i}\frac{k}{2z}\rho'^2} J_0\left(\frac{2\pi}{\lambda z'}\rho'\rho\right), \tag{9.35}$$

where the integral is known as the *Hankel* transform of the incident field $E_{\text{in}}(\rho', 0)$.

In the apparatus shown in fig. 9.11, the resulting field distribution is given by the diffraction through both the lens and the axicon, weighted by the wavefront corrections they impose on the propagating radiation:

$$E(\rho, z) = \frac{2\pi\mathrm{e}^{\mathrm{i}kz}}{\mathrm{i}\lambda z}\mathrm{e}^{\frac{\mathrm{i}\pi\rho^2}{\lambda z}}\int_{\text{aperture}} \tau_{\text{A}}(\rho')\,\tau_{\text{L}}(\rho') E_{in}(\rho', 0)\,\mathrm{e}^{\frac{\mathrm{i}k}{2z'}\rho'^2} J_0\left(\frac{2\pi}{\lambda z'}\rho'\rho\right)\rho'\mathrm{d}\rho'. \tag{9.36}$$

For simplicity, the axicon and the lens are assumed to be at the same position, thereby only requiring one integration over the element with the smallest diameter. All pure phase factors in the integral can be discarded as the measured intensity only depends on the squared modulus of the electric field.

9.3.2 Results

The near-field diffraction pattern of the axicon is known to be a Bessel beam, as shown in fig. 9.13. This comprises a narrow region of high intensity which is exploited, for instance, in laser drilling applications.

The far-field diffraction pattern of the axicon-lens compound of fig. 9.10 is shown in fig. 9.14. The incident Gaussian beam is transformed into a circular ring, which could then be shone onto the DMD in order to provide a sharp boundary with far less incident optical power. The simulated intensity pattern from eq. 9.36 is shown in fig. 9.14a, and the recorded pattern in fig. 9.14b. The discrepancy between theory and experiment may be explained by the finite distance between the axicon and the lens, which were assumed to be at the same position when deriving eq. 9.36. This could easily be computed numerically by allowing a region of free propagation of the beam between the two optical components. Irregardless of these discrepancies, the measurement shows the intensity of the ring is enhanced by a factor of ~ 5 over the Gaussian amplitude. This confirms that the axicon can be used in order for the DMD to generate a circular ring trap with far less optical powers than if incident with a Gaussian beam.

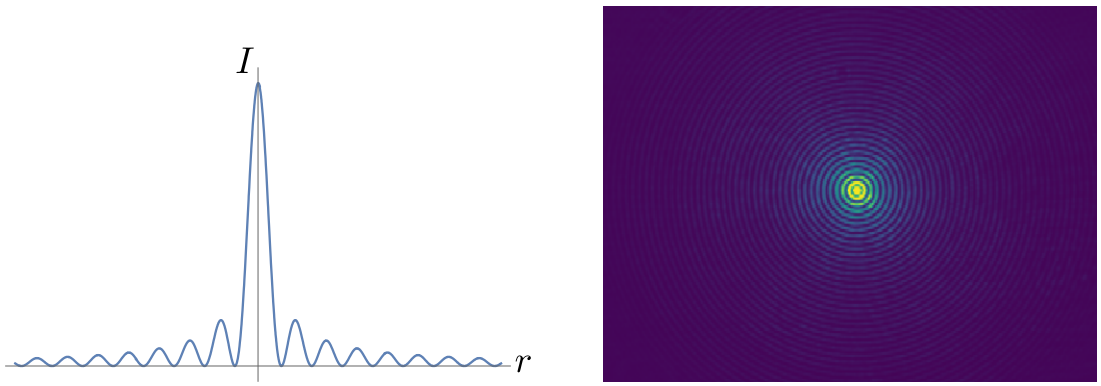

(a) (b)

Figure 9.13 : The near-field diffraction pattern of an axicon results in a Bessel beam with intensity $I \propto J_0(r)^2$. A numerical simulation is shown in (a), while the measured intensity pattern is recorded in (b).

Further numerical simulations are shown in figs. 9.16, in order to gain a qualitative understanding on the effects of different parameters on the ring-shaped intensity pattern. These were performed for an axicon of $\alpha = 2°$ and $n = 1.5$, a lens with $f_0 = 125\,\text{mm}$, an incident Gaussian beam with single-waist $w_0 = 1.85\,\text{mm}$ and wavelength $\lambda = 532\,\text{nm}$.

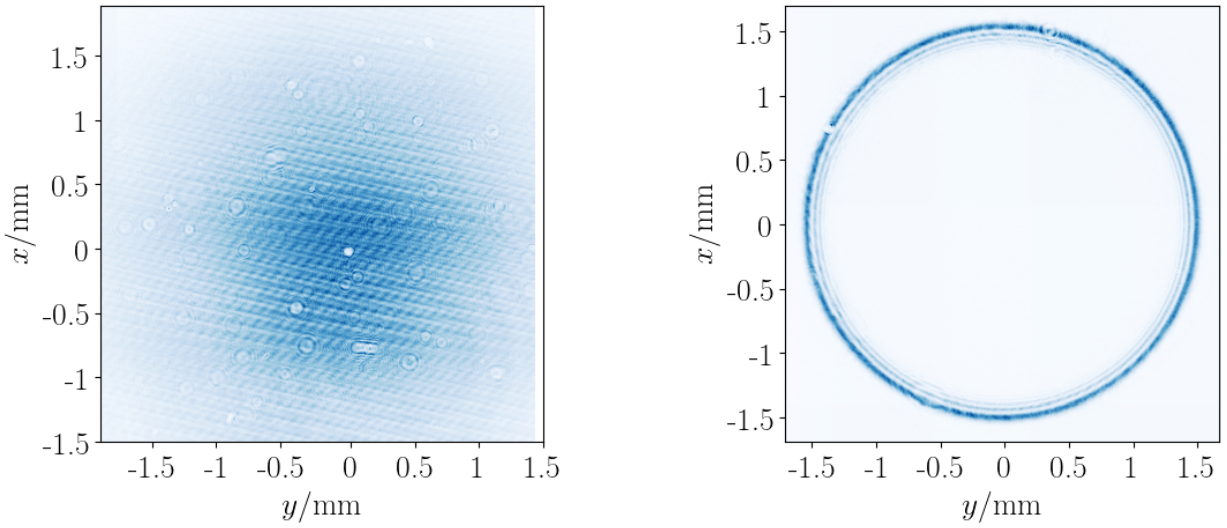

(a) (b)

Figure 9.14 : A Gaussian beam (a) propagates through the axicon-lens compound shown in fig. 9.11 and results in a ring-shaped intensity pattern (b).

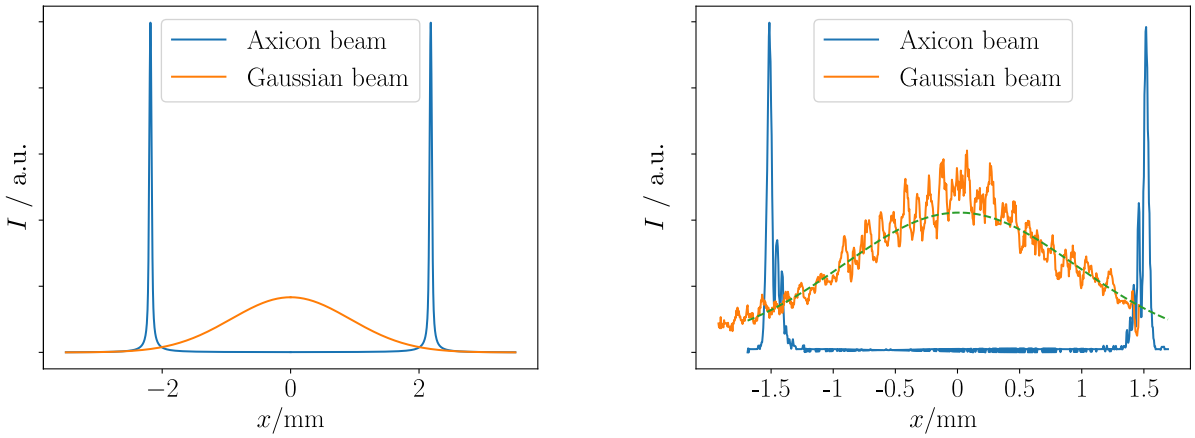

(a) theory (b) experiment

Figure 9.15 : The simulated intensity profile of the axicon-lens apparatus (a) is in qualitative agreement with the recorded intensity pattern (b), for an axicon of $\alpha = 2°$ and $n = 1.5$, a lens with $f_0 = 125\,\text{mm}$, an incident Gaussian beam with single-waist $w_0 = 1.85\,\text{mm}$ and wavelength $\lambda = 767\,\text{nm}$.

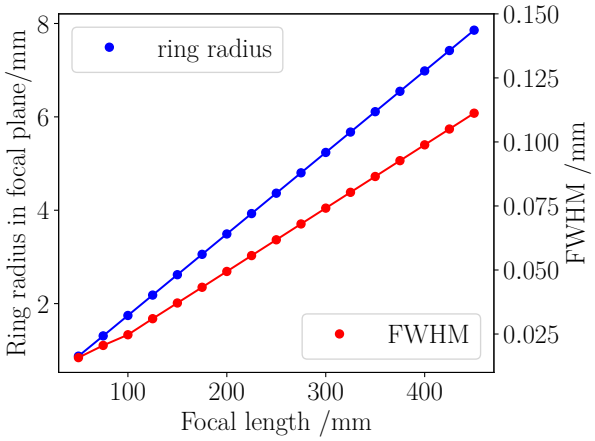

(a)

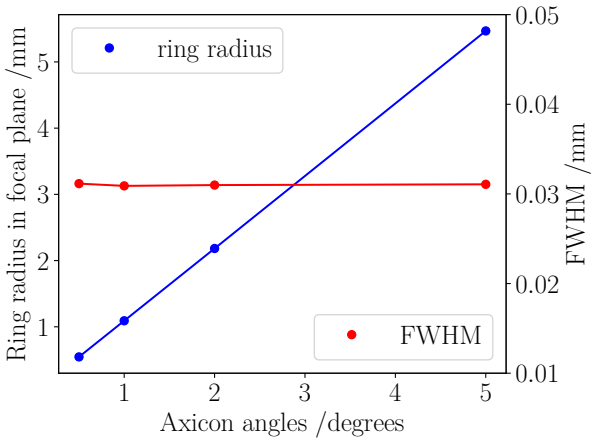

(b)

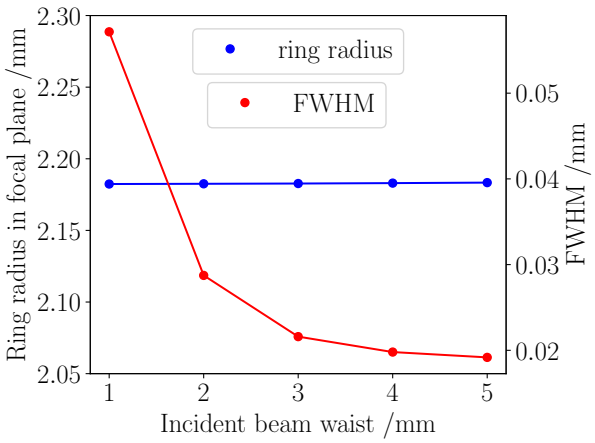

(c)

Figure 9.16 : Further numerical simulations using eq. 9.36 were performed in order to quantify the dependence of ring diameter and width on the lens' focal length (a), the axicon's conical angle (b) and the incident beam waist (c).

Quaerite et invenietis; Seek and you will find.

Matthew 7:7

Conclusions and Outlook

In the 1980s, quasicrystals emerged as a class of materials that stands in an interesting middle ground between order and disorder. While they lack translational invariance and periodicity, they possess long-range order and display crystallographically forbidden rotational symmetries. This distinguishes them from both crystalline and amorphous solids, and sparked great interest in metallurgy and condensed matter physics. The intrigue in quasiperiodic structures quickly spread to other fields of science, from search algorithms and the Riemann hypothesis, to fractals and tilings. Computational models are limited by the numerical intractability of large aperiodic systems, while the artificial methods to synthesise real quasicrystals introduce unwanted impurities and defects.

Quantum simulation of quasicrystals with cold atoms in optical lattice provides a solution to all the limitations encountered thus far. It combines the flexible, versatile and defect-free potential landscape resulting from the interference of light, with the highly controllable parameters offered by cold atoms. The experiments presented in this thesis are the first experimental realisation of degenerate quantum gases in a 2D, non-separable quasiperiodic potential.

Short lattice pulses where first employed to study the synthetic lattice created in momentum space by the Kapitza-Dirac scattering of matter-waves from the optical quasicrystal. This unveiled a singularly continuous diffraction spectrum, composed of a dense set of sharp Bragg peaks displaying fractal-like self-similarity upon rescaling by the silver mean $\lambda = 1 + \sqrt{2}$. The measured diffraction spectra are compatible with projections from higher dimensional regular crystals, which establishes the presence of long-range order in the structure and enables ballistic transport on the synthetic lattice for short pulse durations.

Longer, triangular lattice ramps were used to adiabatically load the BEC into the ground state of the quasiperiodic lattice in order to probe its properties. The adiabatic timescale was found to be finite for regular lattices, irregardless of their geometry and strength, but was observed to diverge for quasiperiodic lattices above a critical lattice strength. This is compatible with multiple distinct numerical simulations predicting a phase transition to a disorder-induced localised state at a critical lattice depth $V_{\mathrm{loc}} \approx 1.78\, E_{\mathrm{rec}}$. The localised phase of matter seems to be resilient against moderate interactions, which would make this the first experimental realisation of a 2D Bose glass.

These first two experiments showcased the presence of both ordered and disordered features in our system, and pave the way for many more future investigations.
The short term plans have already been briefly outlined in section 9.1. An in-situ imaging apparatus is going to probe the real space transport properties of the quasiperiodic optical lattice. A DMD will also result in the addition of sharp walls to probe topological edge states, and the imprinting of local perturbations in the initial atomic density to further quantify the onset of localisation. In addition, a vertical optical lattice will grant access to

strongly interacting physics, enabling investigation of the Bose glass and Mott insulator phases, and of their phase diagrams. The 2D disordered Bose-Hubbard model is predicted to exhibit a re-entrant phase [228], so far only experimentally reproduced in a 1D Bose glass [29].

A number of experiments for the long-term run of the machine are proposed as follows.

- The synthetic lattices in momentum space of chapter 7 may be revisited and probed with pulsed sequences. These have been predicted [187] to enhance the effects of Fourier broadening and therefore extend the linear region in fig. 7.19.
- The recovery curves of chapter 8 could be investigated further, theoretically and experimentally, in the presence of interactions in order to map the V_0-a phase diagram of the (potential) 2D Bose glass.
- A constant force may be exerted on the atoms in the optical lattice, which would result in quasiperiodic Bloch oscillations.
- The retro-reflected mirrors could be controlled by a piezo-electric transducer in order to enable dynamical control of the phase of each lattice beam. This can be used to drive phasonic strain and shake the lattice to perform Hamiltonian engineering, study Floquet physics and topological pumps such as in [229].
- The optics around the science cell is placed on a breadboard. This can be removed and replaced with one enabling generation a fivefold optical lattice, to experimentally prove the proposals in [230].
- The machine enables experiments on three distinct species, ^{87}Rb, ^{39}K and ^{40}K, along with Bose-Bose (^{87}Rb-^{39}K) and Bose-Fermi (^{40}K-^{87}Rb) mixtures. Mixtures would allow experiments in self-generated disorder, where the lattice is deeper for one species than for the other. They could allow experimental realisations of proposals such as [46], where bosonic gauge fields are coupled to cold fermionic matter. In addition, the 2D optical lattice proposed in [231] was shown to correspond to a non-Abelian gauge theory, namely $SU(2)$. Could the 4D (inherited) character of our quasiperiodic optical lattice be a gateway to new non-Abelian gauge theories such as $SU(4)$[1] ?

[1] This is particularly interesting in the context of AdS/CFT correspondance. There is a duality between Type IIB string theory on an $AdS_5 \times S^5$ space and an $N = 4$ (super) Yang–Mills theory on the 4D boundary of AdS_5, as first discussed in [232–234]. This is just to emphasise the potentially interesting physics that can *only* be investigated with our experiment, beyond MBL and other disorder-related topics that have already been studied on other platforms. Together with the connections to cosmology and high-energy physics discussed in the introduction, this shows how the field of cold atoms may rise to be a cross-disciplinary, multi-purpose, cheap and compact experimental platform, which might one day replace large and expensive structures such as telescopes, particle accelerators and (some) laser interferometers.

Everybody brings joy to this office, some when they enter, most when they leave.
Ominous sign in the office of Gary Large, mechanical workshop manager

Acknowledgements

I finished a theoretical physics degree in 2015 from Imperial College London, with a final year project on data analysis from the LHCb experiment at CERN[1], which left me with no hardware skills, no experimental intuition and no knowledge of what it really means to carry out scientific research (best exemplified in the picture below).

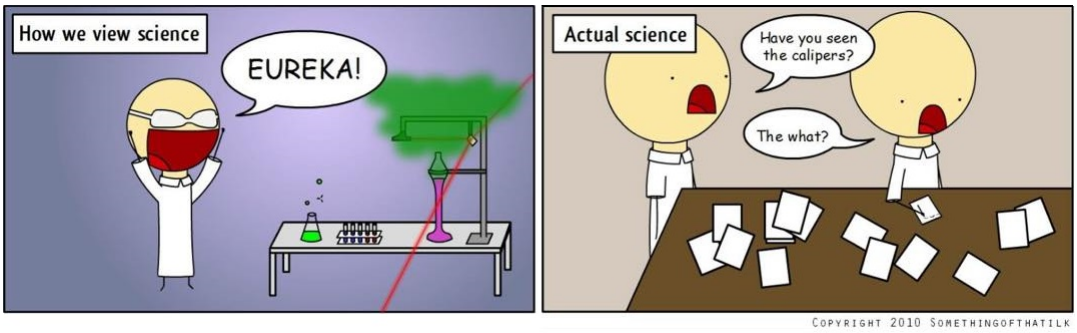

Scientific research in films and outreach talks (left) vs day-to-day lab work (right).
Story of my life.

Multiple people have been directly or indirectly responsible for this masterpiece in prose, and for the environment (physical and social) that enabled the research presented herein. Convention dictates I now have to thank these people, or at least my favourite ones. This is not a work of fiction. Names, characters, businesses, places, events, locales, and incidents are neither the products of the author's imagination nor used in a fictitious manner. Any resemblance to actual persons, living or dead, or actual events is not coincidental.

I thank my supervisor Dr. Ulrich Schneider[2] for recruiting an inexperienced theoretical physicist in an initially (October 2015) fully German team[3]: Oliver Brix, Konrad Viebahn, and Hendrik von Raven. Funnily enough now, at the end of my PhD, I am the most German in #TeamQuasicrystal thanks to my maternal grandmother (...from germany to gerfew?). Thank you Ulrich, for giving me the chance of building a lab and learning so much. I appreciated, especially in the later years of my PhD, useful and insightful discussions about experiments and theory, whence I greatly benefitted from your vast, deep and intuitive understanding of the field.

(Dr.) Konrad Gilbert Heinrich Viebahn[4], like all (future) PIs working on cold atoms in optical lattices, came from the Bloch group at LMU München, where he had already done plenty of lasers, optics and theory - which made one of us, at least. Luckily for me,

[1]together with my valued undergraduate lab partner Hlynur Sveinbjörnsson.
[2]Memorable quote: "Glimmer!".
[3]Maybe he had not realised I was from the *wrong side* of the Südtirol border.
[4]Memorable quote: "You're not helping".

he was not just a skilled source of knowledge and experience, but a respected leader, a great mentor, and a clever guy, and I will forever be in his debt for the patient, diligent, tenacious and never arrogant way he trained me. Luckily for both us, we shared the same mentality and views on work ethics and lab routines: from the search for perfection, elegance, simplicity and minimalism, to the efficient and effective use of time. Our PhD was not done 9 to 5, Monday to Friday: I am most grateful for his presence and company on the innumerable week-ends and late nights spent in the lab, and the constant exchange of ideas via texts, emails, and audio messages. There are too many anecdotes to recite, which I shall leave to my biographer and just mention here that one could tell who between us left the lab last from the way the spanners had been put back in the drawer[5]. And indeed his presence is something that I missed after he left: it was a funny feeling not seeing him behind my computer screen, his presence reduced to a mere voice on the phone, text, or email. American poet Maya Angelou said: "...people will forget what you said, people will forget what you did, but people will never forget how you made them feel". And indeed, I will never forget.
Whilst I was not a fan of him never being hungry for lunch on time, having eaten a full English breakfast beforehand, I am most grateful to the many formal dinners, breakfasts, and feasts I got to enjoy at Trinity College[6], and all the times Konrad took me out to dinner and talked to me in my depressed moments. I learnt from the best, and I look forward to a lifetime of friendship with my cherished colleague.

I also thank the rest of the quasi-scientists that joined #TeamQuasicrystal from our second year onwards: Edward Carter, Jr-Chiun Yu and Shaurya Bhave - especially Ed for his role of walking English dictionary and thesaurus, being the first and only fully British member of the team. Thanks for helping running the lab, eventually taking over and allowing us to remain in the office being useless doing theory and data analysis. I also thank the Master's students that joined our quest during my time here, first and foremost Hendrik von Raven. Leaving aside the fact that for months he had a PCB with bare 230 V worryingly within my arms' reach, he installed, developed and served as tech support for QControl, monitoring software and DDS. I congratulate Hendrik, along with Konrad, for their (continued) patience dealing with my catastrophic ineptitude with computing, software and coding. Oliver Brix was in charge of the magnetic transport and experiment coils, and had the herculean task of designing and oversee the manufacturing of the cooling block. Michael Höse finalised the design of our reliable and cheap shutters and worked with Konrad on the image analysis software. Max Melchner von Didiowa designed and assembled the dipole trap, and I am especially grateful for his continued help with Mathematica, and his Oreos.

Max enjoyed Cambridge so much that he joined the newly created (Summer 2017) Kagome group, #TeamKagome, which soon after also recruited Daniel Reed, Dr. Tiffany Harte, and Florian Störtz as a one-year Master's student. Apologies (but not sorry) for my *occasional* rants about borrowing and not returning components, for not replenishing stock and for not maintaining tidiness and order in the quasicrystal lab. Let me also mention the temporary, Summer and Part III students who worked with us during my time here: Gregory Chant, Robin Croft, Elvinas Ribinskas, Luca Donini, Joannis Koepsell, Callum Stevens, Attila Szabó, Shreya Arya, Marius Weber, Péter Juhász, Jonathan Mortlock, and Jared Jeyaretnam.

[5]Konrad aligning them one by one next to each other, which I found to be an utter and complete waste of time.

[6]Along with a roofs tour of questionable legality.

I am grateful to Max, Dan and Emily (Dan's fiancée) for our fortnightly breakfast at Wetherspoons, for random meals here and there, and for our escapades using Dan's car around Cambridge and beyond (Heathrow airport). Max and I shared a tent both in Snowdonia and on the top of Mt Kilimanjaro, during which I can barely imagine Max's pain in having to deal with the loquacious and talkative fellow that I am. Dan's epic improvement at table tennis is literally the most fascinating thing I have witnessed during my PhD.

Special thanks to the Hadzibabic-Smith[7] group at Cambridge, for constant collaboration, lending of components, technical advice, and also social activities, sports, occasional office meals and barbecues. I thank Zoran for his advice on Serbian tourist spots, careers and physics questions, and I apologise for the time I stole from his PostDocs due to the lack of such in my group. Indeed, I cannot thank enough the BEC I, II and III PostDocs that I have bothered, hunted down, shadowed, interrupted, stalked and tormented on innumerable occasions: Dr. Raphael Lopes, Dr. Nir Navon[8], and Dr. Julian Schmitt. Raphael and Nir were there from day 1, and they spared neither mercy nor political correctness in their opinions of my late-night questions on theory, experiment and software – I was forged in fire. Thanks also to Dr. Richard Fletcher, Dr. Alexander Gaunt (especially for the on-going collaboration, plots and support for chapter 8), Dr. Timon Hilker and Dr. Jinyi Zhang, and the PhD/Master's students Christoph Eigen, Jake Glidden, Jay Man, Panos Christodoulou, Maciej Galka, Lena Bartha, Milan Krstajic, Maximilian Sohmen, and Nathaniel Vilas.

I also thank other groups at the Cavendish for lending equipment and providing guidance, such as Mete Atatüre's group (especially Alejandro Rodríguez-Pardo Montblanch, Lucio Stefan and Dr. Matteo Barbone), experimental Astrophysics, SMF (especially Dr. David Ward, Dr. Nadav Avidor and Fulden Eratam), TFM (especially Dr. Adrian Ionescu) and SP (especially Dr. Joanna Waldie), along with Stephen Spurrier and Attila Szabó from TCM for useful discussions.
Cambridge would not be able to maintain its worldwide academic reputation were it not for its technical and administrative staff[9]. Peter Norman, and the maintenance team headed by Alan Turner, whom I thank for providing assistance and intervention in tasks outside their jurisdiction (e.g. bringing back the air-conditioning on more than one occasion). The mechanical workshop, headed by Gary Large and before him Chris Summerfield[10], and the many times I liaised with Tom, Ollie, Matt, Jim, Kevin, Ashley and Scott. The Cryogenics Facility Manager Dan Cross, the Electronics workshop and the IT team, especially Alex Crook and Andrew Alderwick for the many questions they had the patience to answer. The Rutherford hub but before them Pam Smith for her outstanding efficiency in administrating AMOP. Marzena and the cleaning crew, stores, and the kitchen staff, whose Thursdays' curry will always have a place in my heart.

A special thank you goes to the AMOP's electronic engineer Dr. Stephen Topliss, for building, testing and closely working with students on several projects, especially the H-bridge, the MOSFET boxes, and the DDS.
I also thank people from external companies who provided continued support throughout my PhD, Jonathan Ramwell and Dariusz Swierad (Toptica), Jürgen Borchers (Lens Op-

[7]Robert Smith moved to Oxford as an Associate Professor in the Summer of 2018
[8]Memorable quotes "It's crazy", "Spin-pol is a no-brainer".
[9]Even though I *may* have unsubscribed from all HR-related mailing lists.
[10]Memorable quote: "Come back at 4".

tics), and Radu and Ben from Thorlabs whom I called with the weirdest questions about their parts and from whom I appreciate the honesty, sometimes against their commercial interest.

I thank my college, Churchill, mainly for offering a free meal every once in a while. My involvement in college was only through Dr. Lisa Jardine-Wright, IA & IB Physics DoS, who gave me the opportunity to teach first year physics students. I particularly enjoyed teaching and I thank Lisa and all of my students for the good questions that made me grow personally and professionally.

Before starting my PhD, I spent two weeks in the Fermi-I group at LMU München, under the supervision of Henrik Lüschen and Pranjal Bordia whom I thank for their patience, and for Pranjal's advice not to do a PhD, which I sometimes wished I had followed. I also thank the Fermi-II crew, i.e. the machine our lab is based on, for enduring my (our) calls, emails and personal visits: Lucia Duca, Tracy Li, Martin Reitter and Jacob Näger.

Finally, let me thank my housemates Jasleen[11], Brian, Nick, Priscilla, Sho and Hannah, along with all other friends and treasured acquaintances with whom I shared film nights, lab breakfasts, formal dinners, travels, sports, and BBQs. Special mention to Alison Tully, whom I met in my first year tutorial group at Imperial College, for our muffin tradition, bouldering sessions, and for an exclusive CERN tour. I am also grateful to the Astronomy boardgames crew who constituted the bulk of my social activities, the usual suspects being Jasleen, Nick, Adam, Scottish Douglas, Shorts Douglas, Laura, Lukas, Rob, Sid, and Sophie. The Madingley road Kebab van, for the occasional free drinks and desserts, and for memorising my order. The Internet community of StackOverflow and Physics StackExchange[12]. My one true love Aldi, and my newly found religion Mathematica. The Cold Atom Laboratory group at JPL for making me press the button to make a BEC on the International Space Station, which was quite cool. I am also grateful to EPSRC for providing a stipend and the academic enrichment grant. Thanks to J.K. Rowling for writing the Harry Potter series, which prompted me to learn English and led to me enrolling at Imperial College. I tried to find suitable Harry Potter quotes to include in the chapters, but unfortunately Hogwarts did not offer curricular activities on cold atoms, quantum gases or quasicrystals. So I am going for "It is our choices, Harry, that show what we truly are, far more than our abilities" [235], such as the choice of devoting four years of my life to an underpaid PhD.

Last but not least, I thank my Mum Gabriella who, despite challenges of her own, always found the time to listen, console, encourage, and comfort me.

[11] Memorable quotes: "Wonky", "Innit bruv", "Allow it", "Bo'le of wa'er".

[12] Few people know my username and please do keep it to yourself otherwise Imperial might ask for the degree back, after seeing the sort of questions I asked...

(a) cold

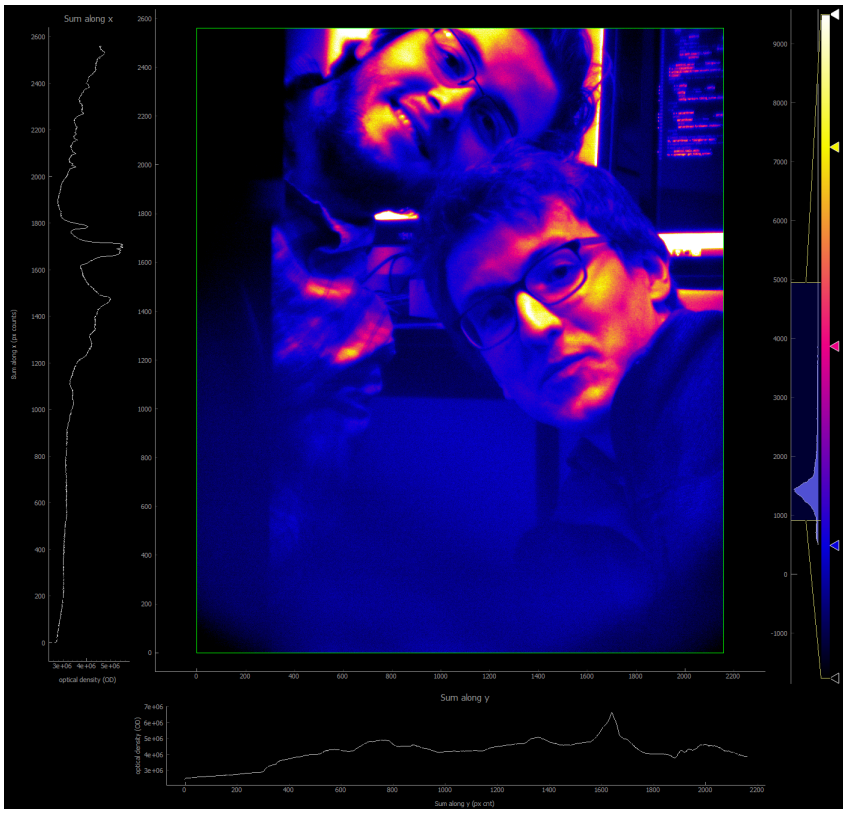

(b) ultracold

Boson 1 and boson 2 (note the label swapping) at different cooling stages.

Bibliography

[1] M. H. Anderson, J. R. Ensher, M. R. Matthews, C. E. Wieman and E. A. Cornell, "Observation of Bose-Einstein Condensation in a Dilute Atomic Vapor", Science **269**, 198–201 (1995) (cited on page 1).

[2] K. B. Davis, M. O. Mewes, M. R. Andrews, N. J. van Druten, D. S. Durfee, D. M. Kurn and W. Ketterle, "Bose-Einstein Condensation in a Gas of Sodium Atoms", Phys. Rev. Lett. **75**, 3969–3973 (1995) (cited on page 1).

[3] D. Stamper-Kurn, "Atoms interacting in interesting optical lattices", Colloquium at the "Advances in Quantum Simulation with Ultracold Atoms" workshop, Natal (2018) (cited on page 1).

[4] J. Hu, A. Urvoy, Z. Vendeiro, V. Crépel, W. Chen and V. Vuletić, "Creation of a Bose-condensed gas of ^{87}Rb by laser cooling", Science **358**, 1078–1080 (2017) (cited on page 1).

[5] P. W. Anderson, "More Is Different", Science **177**, 393–396 (1972) (cited on page 1).

[6] I. Ferrier-Barbut, H. Kadau, M. Schmitt, M. Wenzel and T. Pfau, "Observation of Quantum Droplets in a Strongly Dipolar Bose Gas", Phys. Rev. Lett. **116**, 215301 (2016) (cited on page 1).

[7] C. R. Cabrera, L. Tanzi, J. Sanz, B. Naylor, P. Thomas, P. Cheiney and L. Tarruell, "Quantum liquid droplets in a mixture of Bose-Einstein condensates", Science **359**, 301–304 (2018) (cited on page 1).

[8] W. Zwerger, *The BCS-BEC crossover and the unitary Fermi gas*, Vol. 836, Lecture Notes in Physics (Springer, Heidelberg, 2012) (cited on page 1).

[9] R. J. Fletcher, R. Lopes, J. Man, N. Navon, R. P. Smith, M. W. Zwierlein and Z. Hadzibabic, "Two- and three-body contacts in the unitary Bose gas", Science **355**, 377–380 (2017) (cited on pages 1, 21–22).

[10] C. E. Klauss, X. Xie, C. Lopez-Abadia, J. P. D'Incao, Z. Hadzibabic, D. S. Jin and E. A. Cornell, "Observation of Efimov Molecules Created from a Resonantly Interacting Bose Gas", Phys. Rev. Lett. **119**, 143401 (2017) (cited on page 1).

[11] B. DeMarco, "Onset of Fermi Degeneracy in a Trapped Atomic Gas", Science **285**, 1703–1706 (1999) (cited on page 1).

[12] C. Regal and D. Jin, "Experimental Realization of the BCS-BEC Crossover with a Fermi Gas of Atoms", in *Advances In Atomic, Molecular, and Optical Physics*, Vol. 54 (Elsevier, 2007), pages 1–79 (cited on page 1).

[13] R. Wynar, "Molecules in a Bose-Einstein Condensate", Science **287**, 1016–1019 (2000) (cited on page 1).

[14] C. A. Regal, C. Ticknor, J. L. Bohn and D. S. Jin, "Creation of ultracold molecules from a Fermi gas of atoms", Nature **424**, 47 (2003) (cited on page 1).

[15] Z. Hadzibabic, P. Krüger, M. Cheneau, B. Battelier and J. Dalibard, "Berezinskii–Kosterlitz–Thouless crossover in a trapped atomic gas", Nature **441**, 1118 (2006) (cited on page 1).

[16] Z. Zheng, M. Gong, Y. Zhang, X. Zou, C. Zhang and G. Guo, "FFLO Superfluids in 2d Spin-Orbit Coupled Fermi Gases", Scientific Reports **4**, 6535 (2014) (cited on page 1).

[17] N. Navon, A. L. Gaunt, R. P. Smith and Z. Hadzibabic, "Emergence of a turbulent cascade in a quantum gas", Nature **539**, 72 (2016) (cited on page 1).

[18] J. Beugnon and N. Navon, "Exploring the Kibble–Zurek mechanism with homogeneous Bose gases", Journal of Physics B: Atomic, Molecular and Optical Physics **50**, 022002 (2017) (cited on page 1).

[19] C.-L. Hung, V. Gurarie and C. Chin, "From Cosmology to Cold Atoms: Observation of Sakharov Oscillations in a Quenched Atomic Superfluid", Science **341**, 1213–1215 (2013) (cited on page 1).

[20] J.-C. Jaskula, G. B. Partridge, M. Bonneau, R. Lopes, J. Ruaudel, D. Boiron and C. I. Westbrook, "Acoustic Analog to the Dynamical Casimir Effect in a Bose-Einstein Condensate", Phys. Rev. Lett. **109**, 220401 (2012) (cited on page 1).

[21] J. Steinhauer, "Observation of quantum Hawking radiation and its entanglement in an analogue black hole", Nature Physics **12**, 959 (2016) (cited on page 1).

[22] J. Rodríguez-Laguna, L. Tarruell, M. Lewenstein and A. Celi, "Synthetic Unruh effect in cold atoms", Phys. Rev. A **95**, 013627 (2017) (cited on page 1).

[23] R. P. Feynman, "Simulating Physics with Computers", International Journal of Theoretical Physics **21**, 467–488 (1982) (cited on pages 1, 43).

[24] J. I. Cirac and P. Zoller, "Goals and opportunities in quantum simulation", Nature Physics **8**, 264 (2012) (cited on page 1).

[25] M. Greiner, O. Mandel, T. Esslinger, T. W. Hänsch and I. Bloch, "Quantum phase transition from a superfluid to a Mott insulator in a gas of ultracold atoms", Nature **415**, 39 (2002) (cited on page 2).

[26] J.-R. Li, J. Lee, W. Huang, S. Burchesky, B. Shteynas, F. Top, A. O. Jamison and W. Ketterle, "A stripe phase with supersolid properties in spin–orbit-coupled Bose–Einstein condensates", Nature **543**, 91 (2017) (cited on page 2).

[27] J. Léonard, A. Morales, P. Zupancic, T. Esslinger and T. Donner, "Supersolid formation in a quantum gas breaking a continuous translational symmetry", Nature **543**, 87 (2017) (cited on page 2).

[28] L. Fallani, J. E. Lye, V. Guarrera, C. Fort and M. Inguscio, "Ultracold Atoms in a Disordered Crystal of Light: Towards a Bose Glass", Phys. Rev. Lett. **98**, 130404 (2007) (cited on pages 2, 165).

[29] C. D'Errico, E. Lucioni, L. Tanzi, L. Gori, G. Roux, I. P. McCulloch, T. Giamarchi, M. Inguscio and G. Modugno, "Observation of a Disordered Bosonic Insulator from Weak to Strong Interactions", Phys. Rev. Lett. **113**, 095301 (2014) (cited on pages 2, 165, 214).

[30] A. Aspect and M. Inguscio, "Anderson localization of ultracold atoms", Physics Today **62**, 30–35 (2009) (cited on pages 2, 162).

[31] M. Schreiber, S. S. Hodgman, P. Bordia, H. P. Luschen, M. H. Fischer, R. Vosk, E. Altman, U. Schneider and I. Bloch, "Observation of many-body localization of interacting fermions in a quasirandom optical lattice", Science **349**, 842–845 (2015) (cited on pages 2, 165).

[32] M. White, M. Pasienski, D. McKay, S. Q. Zhou, D. Ceperley and B. DeMarco, "Strongly Interacting Bosons in a Disordered Optical Lattice", Phys. Rev. Lett. **102**, 055301 (2009) (cited on page 2).

[33] W. S. Bakr, J. I. Gillen, A. Peng, S. Fölling and M. Greiner, "A quantum gas microscope for detecting single atoms in a Hubbard-regime optical lattice", Nature **462**, 74 (2009) (cited on page 2).

[34] J. F. Sherson, C. Weitenberg, M. Endres, M. Cheneau, I. Bloch and S. Kuhr, "Single-atom-resolved fluorescence imaging of an atomic Mott insulator", Nature **467**, 68 (2010) (cited on page 2).

[35] G. Jotzu, M. Messer, R. Desbuquois, M. Lebrat, T. Uehlinger, D. Greif and T. Esslinger, "Experimental realization of the topological Haldane model with ultracold fermions", Nature **515**, 237 (2014) (cited on page 2).

[36] M. Aidelsburger, M. Atala, M. Lohse, J. T. Barreiro, B. Paredes and I. Bloch, "Realization of the Hofstadter Hamiltonian with Ultracold Atoms in Optical Lattices", Phys. Rev. Lett. **111**, 185301 (2013) (cited on page 2).

[37] A. Celi, P. Massignan, J. Ruseckas, N. Goldman, I. B. Spielman, G. Juzeliunas and M. Lewenstein, "Synthetic Gauge Fields in Synthetic Dimensions", Phys. Rev. Lett. **112**, 043001 (2014) (cited on pages 2, 57).

[38] M. Mancini, G. Pagano, G. Cappellini, L. Livi, M. Rider, J. Catani, C. Sias, P. Zoller, M. Inguscio, M. Dalmonte and L. Fallani, "Observation of chiral edge states with neutral fermions in synthetic Hall ribbons", Science **349**, 1510–1513 (2015) (cited on pages 2, 57).

[39] M. Messer, K. Sandholzer, F. Görg, J. Minguzzi, R. Desbuquois and T. Esslinger, "Floquet Dynamics in Driven Fermi-Hubbard Systems", Phys. Rev. Lett. **121**, 233603 (2018) (cited on page 2).

[40] J. Klinder, H. Keßler, M. Wolke, L. Mathey and A. Hemmerich, "Dynamical phase transition in the open Dicke model", Proceedings of the National Academy of Sciences **112**, 3290–3295 (2015) (cited on page 2).

[41] A. Derevianko and H. Katori, "Colloquium: Physics of optical lattice clocks", Rev. Mod. Phys. **83**, 331–347 (2011) (cited on page 2).

[42] J. G. Bohnet, B. C. Sawyer, J. W. Britton, M. L. Wall, A. M. Rey, M. Foss-Feig and J. J. Bollinger, "Quantum spin dynamics and entanglement generation with hundreds of trapped ions", Science **352**, 1297–1301 (2016) (cited on page 2).

[43] J. Klaers, J. Schmitt, F. Vewinger and M. Weitz, "Bose–Einstein condensation of photons in an optical microcavity", Nature **468**, 545 (2010) (cited on page 2).

[44] D. Dung, C. Kurtscheid, T. Damm, J. Schmitt, F. Vewinger, M. Weitz and J. Klaers, "Variable potentials for thermalized light and coupled condensates", Nature Photonics **11**, 565 (2017) (cited on page 2).

[45] W. B. Cairncross, D. N. Gresh, M. Grau, K. C. Cossel, T. S. Roussy, Y. Ni, Y. Zhou, J. Ye and E. A. Cornell, "Precision Measurement of the Electron's Electric Dipole Moment Using Trapped Molecular Ions", Phys. Rev. Lett. **119**, 153001 (2017) (cited on page 2).

[46] L. Barbiero, C. Schweizer, M. Aidelsburger, E. Demler, N. Goldman and F. Grusdt, "Coupling ultracold matter to dynamical gauge fields in optical lattices: From flux-attachment to Z2 lattice gauge theories", arXiv:1810.02777 (2018) (cited on pages 2, 214).

[47] D. T. Son, "Toward an AdS/cold atoms correspondence: A geometric realization of the Schrödinger symmetry", Phys. Rev. D **78**, 046003 (2008) (cited on page 2).

[48] K. Balasubramanian and J. McGreevy, "Gravity Duals for Nonrelativistic Conformal Field Theories", Phys. Rev. Lett. **101**, 061601 (2008) (cited on page 2).

[49] P. W. Graham, J. M. Hogan, M. A. Kasevich and S. Rajendran, "New Method for Gravitational Wave Detection with Atomic Sensors", Phys. Rev. Lett. **110**, 171102 (2013) (cited on page 2).

[50] Z. Weinersmith, *Science: Abridged Beyond the Point of Usefulness*, 1st edition, eBook (2017) (cited on page 5).

[51] Peyton Reed, *Ant-Man and the Wasp*, distributed by Marvel Studios, written by Chris McKenna, Erik Sommers, Paul Rudd, Andrew Barrer, Gabriel Ferrari, 2018 (cited on page 7).

[52] B. Simon, "Holonomy, the Quantum Adiabatic Theorem, and Berry's Phase", Phys. Rev. Lett. **51**, 2167–2170 (1983) (cited on page 8).

[53] S. Weinberg, *The quantum theory of fields* (Cambridge University Press, Cambridge, 1995) (cited on pages 15, 263–264).

[54] L. P. Pitaevskiĭ, S. Stringari, *Bose-Einstein condensation and superfluidity* (Oxford University Press, Oxford, 2016) (cited on pages 15, 20, 190).

[55] C. J. Pethick and H. Smith, *Bose–Einstein Condensation in Dilute Gases*, 2nd edition (Cambridge University Press, Cambridge, 2008) (cited on pages 15, 41).

[56] N. Tammuz, R. P. Smith, R. L. D. Campbell, S. Beattie, S. Moulder, J. Dalibard and Z. Hadzibabic, "Can a Bose Gas Be Saturated?", Phys. Rev. Lett. **106**, 230401 (2011) (cited on page 16).

[57] I. Bloch, T. W. Hänsch and T. Esslinger, "Measurement of the spatial coherence of a trapped Bose gas at the phase transition", Nature **403**, 166 (2000) (cited on page 16).

[58] P. C. Hohenberg, "Existence of Long-Range Order in One and Two Dimensions", Phys. Rev. **158**, 383–386 (1967) (cited on page 16).

[59] N. D. Mermin and H. Wagner, "Absence of Ferromagnetism or Antiferromagnetism in One- or Two-Dimensional Isotropic Heisenberg Models", Phys. Rev. Lett. **17**, 1133–1136 (1966) (cited on page 16).

[60] S. Coleman, "There are no Goldstone bosons in two dimensions", Communications in Mathematical Physics **31**, 259–264 (1973) (cited on page 16).

[61] T. Lancaster and S. J. Blundell, *Quantum field theory for the gifted amateur* (Oxford University Press, Oxford, 2014) (cited on page 17).

[62] A. J. Leggett, *Quantum liquids : Bose condensation and Cooper pairing in condensed-matter systems* (Oxford University Press, Oxford, 2006) (cited on pages 17, 19).

[63] R. Smith and Z. Hadzibabic, "Effects of Interactions on Bose-Einstein Condensation of an Atomic Gas", Physics of Quantum Fluids, Springer Series in Solid-State Sciences **177**, Springer, Berlin, Heidelberg (2013) (cited on pages 19, 22).

[64] A. Griffin, D. W. Snoke and S. Stringari, *Bose-Einstein condensation* (Cambridge University Press, Cambridge, 1995) (cited on page 19).

[65] M. Mantina, A. C. Chamberlin, R. Valero, C. J. Cramer and D. G. Truhlar, "Consistent van der Waals Radii for the Whole Main Group", The Journal of Physical Chemistry A **113**, 5806–5812 (2009) (cited on page 20).

[66] C. Chin, R. Grimm, P. Julienne and E. Tiesinga, "Feshbach resonances in ultracold gases", Rev. Mod. Phys. **82**, 1225–1286 (2010) (cited on pages 21–22).

[67] P. O. Fedichev, M. W. Reynolds and G. V. Shlyapnikov, "Three-Body Recombination of Ultracold Atoms to a Weakly Bound s Level", Phys. Rev. Lett. **77**, 2921–2924 (1996) (cited on page 22).

[68] D. Sesko, T. Walker, C. Monroe, A. Gallagher and C. Wieman, "Collisional losses from a light-force atom trap", Physical Review Letters **63**, 961–964 (1989) (cited on page 22).

[69] W. Durant, *The Life of Greece: The Story of Civilization*, The Story of Civilization (Simon & Schuster, 2011) (cited on page 25).

[70] J. J. Sakurai, *Modern quantum mechanics* (Cambridge University Press, Cambridge, United Kingdom, 2017) (cited on page 26).

[71] A. C. Vutha, "A simple approach to the Landau–Zener formula", European Journal of Physics **31**, 389–392 (2010) (cited on page 29).

[72] E. Majorana, "Atomi orientati in campo magnetico variabile", Il Nuovo Cimento (1924-1942) **9**, 43–50 (1932) (cited on page 32).

[73] D. E. Pritchard, "Cooling Neutral Atoms in a Magnetic Trap for Precision Spectroscopy", Phys. Rev. Lett. **51**, 1336–1339 (1983) (cited on page 32).

[74] T. Esslinger, I. Bloch and T. W. Hänsch, "Bose-Einstein condensation in a quadrupole-Ioffe-configuration trap", Phys. Rev. A **58**, R2664–R2667 (1998) (cited on page 32).

[75] M. Melchner, *An optical dipole trap for ultracold atomic gases*, Master's thesis (ETH Zürich, Apr. 2017) (cited on pages 33, 201).

[76] R. Grimm, M. Weidemüller and Y. B. Ovchinnikov, "Optical Dipole Traps for Neutral Atoms", in *Advances In Atomic, Molecular, and Optical Physics*, Vol. 42 (Elsevier, 2000), pages 95–170 (cited on page 33).

[77] B. Arora and B. K. Sahoo, "State-insensitive trapping of Rb atoms: Linearly versus circularly polarized light", Physical Review A **86** (2012) (cited on page 33).

[78] C. Foot, *Atomic Physics*, Oxford Master Series in Physics (OUP Oxford, 2004) (cited on pages 39, 95).

[79] H. J. Metcalf and P. van der Straten, *Laser Cooling and Trapping*, edited by R. S. Berry, J. L. Birman, J. W. Lynn, M. P. Silverman, H. E. Stanley and M. Voloshin, Graduate Texts in Contemporary Physics (Springer, New York, 1999) (cited on pages 40, 42).

[80] J. Dalibard and C. Cohen-Tannoudji, "Laser cooling below the Doppler limit by polarization gradients: simple theoretical models", Journal of the Optical Society of America B **6**, 2023 (1989) (cited on page 40).

[81] L. D. Landau, *Mechanics* (Pergamon Press, Oxford New York, 1976) (cited on page 41).

[82] H. F. Hess, "Evaporative cooling of magnetically trapped and compressed spin-polarized hydrogen", Phys. Rev. B **34**, 3476–3479 (1986) (cited on page 41).

[83] M. F. Kling and M. J. Vrakking, "Attosecond Electron Dynamics", Annual Review of Physical Chemistry **59**, 463–492 (2008) (cited on page 44).

[84] Hubbard, J., "Electron correlations in narrow energy bands", Proceedings of the Royal Society of London. Series A. Mathematical and Physical Sciences **276**, 238–257 (1963) (cited on page 44).

[85] A. Mazurenko, C. S. Chiu, G. Ji, M. F. Parsons, M. Kanász-Nagy, R. Schmidt, F. Grusdt, E. Demler, D. Greif and M. Greiner, "A cold-atom Fermi–Hubbard antiferromagnet", Nature **545**, 462 (2017) (cited on page 44).

[86] T. A. Hilker, G. Salomon, F. Grusdt, A. Omran, M. Boll, E. Demler, I. Bloch and C. Gross, "Revealing hidden antiferromagnetic correlations in doped Hubbard chains via string correlators", Science **357**, 484–487 (2017) (cited on page 44).

[87] C.-C. Chien, S. Peotta and M. Di Ventra, "Quantum transport in ultracold atoms", Nature Physics **11**, 998 (2015) (cited on page 45).

[88] I. Calvino, *The complete Cosmicomics* (Penguin Classics, London, 2009) (cited on page 49).

[89] T. Janssen, G. Chapuis and M. d. Boissieu, *Aperiodic Crystals: From Modulated Phases to Quasicrystals: Structure and Properties* (Oxford University Press, June 2018) (cited on page 49).

[90] P. J. Steinhardt and S Ostlund, *The Physics of Quasicrystals* (World Scientific, Dec. 1987) (cited on pages 49, 54).

[91] S. Walter and S. Deloudi, *Crystallography of Quasicrystals: Concepts, Methods and Structures* (Springer Science & Business Media, Aug. 2009) (cited on pages 49, 70).

[92] J. Kepler, *The six-cornered snowflake* (Oxford University Press, Oxford, 2014) (cited on page 49).

[93] R. Haüy, *Traité de minéralogie*, Traité de minéralogie v. 1 (Bachelier et Huzard, 1822) (cited on page 49).

[94] K. G. H. Viebahn, "Quasicrystalline optical lattices for ultracold atoms", Apollo - University of Cambridge Repository, PhD thesis (2019) (cited on pages 52, 76, 93, 106, 108, 113, 118, 135–136, 138–139, 153, 157).

[95] W C. Koehler, J W. Cable, E O. Wollan and M K. Wilkinson, "Neutron Diffraction Study of Magnetic Ordering in Thulium", Journal of Applied Physics **33**, 1124–1125 (1962) (cited on page 52).

[96] Vera Daniel, Henry Solomon Lipson and William Lawrence Bragg, "An X-ray study of the dissociation of an alloy of copper, iron and nickel", Proceedings of the Royal Society of London. Series A. Mathematical and Physical Sciences **181**, 368–378 (1943) (cited on page 52).

[97] P. M. de Wolff, "The Pseudo-Symmetry of Modulated Crystal Structures", Acta Crystallographica Section A **30**, 777–785 (1974) (cited on page 53).

[98] T. Janssen, A. Janner and E. Ascher, "Crystallographic groups in space and time: I. General definitions and basic properties", Physica **41**, 541 –565 (1969) (cited on page 53).

[99] D. Shechtman, I. Blech, D. Gratias and J. W. Cahn, "Metallic Phase with Long-Range Orientational Order and No Translational Symmetry", Phys. Rev. Lett. **53**, 1951–1953 (1984) (cited on pages 53, 56).

[100] D. Levine and P. J. Steinhardt, "Quasicrystals: A New Class of Ordered Structures", Phys. Rev. Lett. **53**, 2477–2480 (1984) (cited on page 53).

[101] W. Steurer, "Quasicrystals: What do we know? What do we want to know? What can we know?", Acta Crystallographica Section A Foundations and Advances **74**, 1–11 (2018) (cited on page 55).

[102] *Quasicrystal - Online Dictionary of Crystallography*, last accessed on 12/06/2019 and available at http://reference.iucr.org/dictionary/Quasicrystal (cited on page 55).

[103] P. Steinhardt, *The second kind of impossible : the extraordinary quest for a new form of matter* (Simon & Schuster, New York, 2019) (cited on page 56).

[104] L. Bindi, P. J. Steinhardt, N. Yao and P. J. Lu, "Natural Quasicrystals", Science **324**, 1306–1309 (2009) (cited on page 56).

[105] J. A. Kromer, M. Schmiedeberg, J. Roth and H. Stark, "What Phasons Look Like: Particle Trajectories in a Quasicrystalline Potential", Phys. Rev. Lett. **108**, 218301 (2012) (cited on pages 56, 70).

[106] K. Edagawa, K. Suzuki and S. Takeuchi, "High Resolution Transmission Electron Microscopy Observation of Thermally Fluctuating Phasons in Decagonal Al-Cu-Co", Phys. Rev. Lett. **85**, 1674–1677 (2000) (cited on pages 56, 71).

[107] K. Barkan, M. Engel and R. Lifshitz, "Controlled Self-Assembly of Periodic and Aperiodic Cluster Crystals", Phys. Rev. Lett. **113**, 098304 (2014) (cited on page 56).

[108] S. Gopalakrishnan, I. Martin and E. A. Demler, "Quantum Quasicrystals of Spin-Orbit-Coupled Dipolar Bosons", Phys. Rev. Lett. **111**, 185304 (2013) (cited on page 56).

[109] J. Hou, H. Hu, K. Sun and C. Zhang, "Superfluid-quasicrystal in a Bose-Einstein condensate", Physical review letters **120**, 060407 (2018) (cited on page 56).

[110] K. Giergiel, A. Miroszewski and K. Sacha, "Time Crystal Platform: From Quasicrystal Structures in Time to Systems with Exotic Interactions", Phys. Rev. Lett. **120**, 140401 (2018) (cited on page 56).

[111] P. A. Thiel and J.-M. Dubois, "Quasicrystals. Reaching maturity for technological applications", Materials Today **2**, 3–7 (1999) (cited on page 56).

[112] J. Dolinšek, "Electrical and thermal transport properties of icosahedral and decagonal quasicrystals", Chemical Society Reviews **41**, 6730 (2012) (cited on page 56).

[113] M. Bobnar, P. Jeglič, M. Klanjšek, Z. Jagličić, M. Wencka, P. Popčević, J. Ivkov, D. Stanić, A. Smontara, P. Gille and J. Dolinšek, "Intrinsic anisotropic magnetic, electrical, and thermal transport properties of d-Al-Co-Ni decagonal quasicrystals", Phys. Rev. B **85**, 024205 (2012) (cited on page 56).

[114] K. Kamiya, T. Takeuchi, N. Kabeya, N. Wada, T. Ishimasa, A. Ochiai, K. Deguchi, K. Imura and N. K. Sato, "Discovery of superconductivity in quasicrystal", Nature Communications **9**, 154 (2018) (cited on page 56).

[115] R. Merlin, K. Bajema, R. Clarke, F. Y. Juang and P. K. Bhattacharya, "Quasiperiodic GaAs-AlAs Heterostructures", Phys. Rev. Lett. **55**, 1768–1770 (1985) (cited on page 57).

[116] X. Zeng, G. Ungar, Y. Liu, V. Percec, A. E. Dulcey and J. K. Hobbs, "Supramolecular dendritic liquid quasicrystals", Nature **428**, 157–160 (2004) (cited on page 57).

[117] K. Hayashida, T. Dotera, A. Takano and Y. Matsushita, "Polymeric Quasicrystal: Mesoscopic Quasicrystalline Tiling in ABC Star Polymers", Phys. Rev. Lett. **98**, 195502 (2007) (cited on page 57).

[118] S. Fischer, A. Exner, K. Zielske, J. Perlich, S. Deloudi, W. Steurer, P. Lindner and S. Förster, "Colloidal quasicrystals with 12-fold and 18-fold diffraction symmetry", Proceedings of the National Academy of Sciences **108**, 1810–1814 (2011) (cited on page 57).

[119] J. Mikhael, J. Roth, L. Helden and C. Bechinger, "Archimedean-like tiling on decagonal quasicrystalline surfaces", Nature **454**, 501 (2008) (cited on page 57).

[120] D. V. Talapin, E. V. Shevchenko, M. I. Bodnarchuk, X. Ye, J. Chen and C. B. Murray, "Quasicrystalline order in self-assembled binary nanoparticle superlattices", Nature **461**, 964 (2009) (cited on page 57).

[121] S. J. Ahn, P. Moon, T.-H. Kim, H.-W. Kim, H.-C. Shin, E. H. Kim, H. W. Cha, S.-J. Kahng, P. Kim, M. Koshino, Y.-W. Son, C.-W. Yang and J. R. Ahn, "Dirac electrons in a dodecagonal graphene quasicrystal", Science **361**, 782–786 (2018) (cited on page 57).

[122] Z. V. Vardeny, A. Nahata and A. Agrawal, "Optics of photonic quasicrystals", Nature Photonics **7**, 177 (2013) (cited on page 57).

[123] A. L. Mackay, "Crystallography and the penrose pattern", Physica A: Statistical Mechanics and its Applications **114**, 609–613 (1982) (cited on page 57).

[124] A. Dareau, E. Levy, M. B. Aguilera, R. Bouganne, E. Akkermans, F. Gerbier and J. Beugnon, "Revealing the Topology of Quasicrystals with a Diffraction Experiment", Phys. Rev. Lett. **119**, 215304 (2017) (cited on page 57).

[125] L. Guidoni, C. Triché, P. Verkerk and G. Grynberg, "Quasiperiodic Optical Lattices", Phys. Rev. Lett. **79**, 3363–3366 (1997) (cited on page 57).

[126] L. Guidoni, B. Dépret, A. di Stefano and P. Verkerk, "Atomic diffusion in an optical quasicrystal with five-fold symmetry", Phys. Rev. A **60**, R4233–R4236 (1999) (cited on page 57).

[127] L. Sanchez-Palencia and L. Santos, "Bose-Einstein condensates in optical quasicrystal lattices", Phys. Rev. A **72**, 053607 (2005) (cited on page 57).

[128] S. Wessel, A. Jagannathan and S. Haas, "Quantum Antiferromagnetism in Quasicrystals", Phys. Rev. Lett. **90**, 177205 (2003) (cited on page 57).

[129] A. Szallas, A. Jagannathan and S. Wessel, "Phason-disordered two-dimensional quantum antiferromagnets", Phys. Rev. B **79**, 172406 (2009) (cited on page 57).

[130] E. Agliari, A. Blumen and O. Mülken, "Quantum-walk approach to searching on fractal structures", Phys. Rev. A **82**, 012305 (2010) (cited on page 57).

[131] A. Patel and K. S. Raghunathan, "Search on a fractal lattice using a quantum random walk", Phys. Rev. A **86**, 012332 (2012) (cited on page 57).

[132] T. S. Cubitt, D. Perez-Garcia and M. M. Wolf, "Undecidability of the spectral gap", Nature **528**, 207 (2015) (cited on page 57).

[133] F. J. Dyson, *Birds and Frogs: Selected Papers of Freeman Dyson, 1990–2014* (World Scientific, May 2015) (cited on page 59).

[134] Kepler, J., *Harmonices Mundi*, available online by Carnegie-Mellon University (1619) (cited on pages 59, 61).

[135] R. Lück, "Dürer–Kepler–Penrose, the development of pentagon tilings", Materials Science and Engineering: A **294-296**, 263–267 (2000) (cited on page 59).

[136] R Penrose, "The role of aesthetic in pure and applied mathematical research", Bull Inst Math Appl **10** (1974) (cited on page 59).

[137] M. Baake and U. Grimm, *Aperiodic Order* (Cambridge University Press, Cambridge, Aug. 2013) (cited on page 62).

[138] G. Goodson, *Chaotic Dynamics* (Cambridge University Press, Cambridge, 2017) (cited on page 62).

[139] Clark A., Bruin H. and Fokkink R., "The Pisot Substituion Conjecture", Topology and its Applications **205**, 1–138 (2016) (cited on page 63).

[140] E. Schrödinger, *What is Life?: With Mind and Matter and Autobiographical Sketches* (Cambridge University Press, Jan. 1992) (cited on page 63).

[141] P. Ball, "Schrödinger's cat among biology's pigeons: 75 years of What Is Life?", Nature **560**, 548–550 (2018) (cited on page 63).

[142] O. Nielsen, *An introduction to integration and measure theory* (Wiley, New York, 1997) (cited on page 63).

[143] M. Baake and U. Grimm, "Kinematic diffraction is insufficient to distinguish order from disorder", Phys. Rev. B **79**, 020203 (2009) (cited on page 64).

[144] J. Puig, "Cantor Spectrum for Quasi-Periodic Schrödinger Operators", in *Mathematical Physics of Quantum Mechanics*, Vol. 690, edited by J. Asch and A. Joye (Springer Berlin Heidelberg, 2006), pages 79–91 (cited on page 64).

[145] A. Sütő, "Singular continuous spectrum on a cantor set of zero Lebesgue measure for the Fibonacci Hamiltonian", Journal of Statistical Physics **56**, 525–531 (1989) (cited on pages 64, 137).

[146] J. M. Luck, "Cantor spectra and scaling of gap widths in deterministic aperiodic systems", Physical Review B **39**, 5834–5849 (1989) (cited on pages 64, 137).

[147] M. Baake and U. Grimm, "Mathematical diffraction of aperiodic structures", Chemical Society Reviews **41**, 6821 (2012) (cited on page 64).

[148] N. Lo Gullo, C. V. Ambarish, T. Busch, L. Dell'Anna and C. M. Chandrashekar, "Dynamics and energy spectra of aperiodic discrete-time quantum walks", Physical Review E **96** (2017) (cited on page 64).

[149] K. J. Vinoy, K. A. Jose and V. K. Varadan, "Multi-band characteristics and fractal dimension of dipole antennas with Koch curve geometry", in IEEE Antennas and Propagation Society International Symposium, Vol. 4 (June 2002), 106–109 vol.4 (cited on page 65).

[150] *Benoît Mandelbrot: Fractals and the art of roughness | TED Talk* (cited on page 65).

[151] S. N. Kempkes, M. R. Slot, S. E. Freeney, S. J. M. Zevenhuizen, D. Vanmaekelbergh, I. Swart and C. M. Smith, "Design and characterization of electrons in a fractal geometry", Nature Physics **15**, 127–131 (2019) (cited on page 65).

[152] S. Ostlund and D. C. Wright, "Scale Invariance and the Group Structure of Quasicrystals", Phys. Rev. Lett. **56**, 2068–2071 (1986) (cited on page 67).

[153] H. Hiller, "The crystallographic restriction in higher dimensions", Acta Crystallographica Section A Foundations of Crystallography **41**, 541–544 (1985) (cited on pages 67, 69).

[154] N. Mailer, *Of a Fire on the Moon* (Random House Publishing Group, 2014) (cited on page 73).

[155] D. C. McKay, D. Jervis, D. J. Fine, J. W. Simpson-Porco, G. J. A. Edge and J. H. Thywissen, "Low-temperature high-density magneto-optical trapping of potassium using the open 4 S $\rightarrow$ 5 P transition at 405 nm", Physical Review A **84**, 063420 (2011) (cited on page 78).

[156] W. Süptitz, G. Wokurka, F. Strauch, P. Kohns and W. Ertmer, "Simultaneous cooling and trapping of ^{85}Rb and ^{87}Rb in a magneto-optical trap", Optics Letters **19**, 1571 (1994) (cited on page 78).

[157] M. Landini, S. Roy, G. Roati, A. Simoni, M. Inguscio, G. Modugno and M. Fattori, "Direct evaporative cooling of ^{39}K atoms to Bose-Einstein condensation", Phys. Rev. A **86**, 033421 (2012) (cited on page 78).

[158] G. Salomon, L. Fouché, S. Lepoutre, A. Aspect and T. Bourdel, "All-optical cooling of ^{39}K to Bose-Einstein condensation", Phys. Rev. A **90**, 033405 (2014) (cited on page 78).

[159] L. Duca, *Probing topological properties of Bloch bands with ultracold atoms in a honeycomb optical lattice*, PhD thesis (Ludwig-Maximilians-Universität München, Sept. 2015) (cited on page 78).

[160] T. Li, *Probing Bloch band geometry with ultracold atoms in optical lattices*, PhD thesis (Ludwig-Maximilians-Universität München, July 2016) (cited on page 78).

[161] M. Reitter, *Scattering processes in interacting Floquet systems*, PhD thesis (Ludwig-Maximilians-Universität München, Dec. 2017) (cited on page 78).

[162] T. Li, *An Apparatus for Probing Fermions in a Quasi-Two-Dimensional Geometry*, Masters' thesis (Ludwig-Maximilians-Universität München, Oct. 2011) (cited on page 78).

[163] M. Reitter, *Ultracold Fermions in a novel 2d setup*, Masters' thesis (Ludwig-Maximilians-Universität München, Sept. 2012) (cited on page 78).

[164] Bills, DG and Arnold, PC, "Vacuum gauge", US Patent 4307323 (1981) (cited on page 81).

[165] C. B. Alcock, V. P. Itkin and M. K. Horrigan, "Vapour Pressure Equations for the Metallic Elements: 298–2500k", Canadian Metallurgical Quarterly **23**, 309–313 (1984) (cited on page 82).

[166] D. A. Steck, *Quantum chaos, transport, and decoherence in atom optics*, PhD thesis (University of Texas at Austin, 2001) (cited on pages 84, 141).

[167] T. G. Tiecke, "Properties of Potassium", 2011 (cited on pages 84, 241, 245).

[168] T. W. Hänsch, M. D. Levenson and A. L. Schawlow, "Complete Hyperfine Structure of a Molecular Iodine Line", Phys. Rev. Lett. **26**, 946–949 (1971) (cited on page 91).

[169] P. W. Smith and R. Hänsch, "Cross-Relaxation Effects in the Saturation of the 6328-å Neon-Laser Line", Phys. Rev. Lett. **26**, 740–743 (1971) (cited on page 91).

[170] R. W. P. Drever, J. L. Hall, F. V. Kowalski, J. Hough, G. M. Ford, A. J. Munley and H. Ward, "Laser phase and frequency stabilization using an optical resonator", Applied Physics B Photophysics and Laser Chemistry **31**, 97–105 (1983) (cited on page 94).

[171] E. D. Black, "An introduction to Pound–Drever–Hall laser frequency stabilization", American Journal of Physics **69**, 79–87 (2001) (cited on page 94).

[172] H. von Raven, *Direct digital synthesis and integrated experiment control for a novel lattice setup*, Masters' thesis (Ludwig-Maximilians-Universität München, Oct. 2016) (cited on pages 95–96).

[173] R. Croft, "Optimisation of a Cold Atom Experiment using an Evolutionary Algorithm", Vacation Project report (University of Cambridge) (2017) (cited on pages 96, 111).

[174] D. W. Sesko, T. G. Walker and C. E. Wieman, "Behavior of neutral atoms in a spontaneous force trap", Journal of the Optical Society of America B **8**, 946 (1991) (cited on page 104).

[175] T. Walker, D. Sesko and C. Wieman, "Collective behavior of optically trapped neutral atoms", Phys. Rev. Lett. **64**, 408–411 (1990) (cited on page 104).

[176] Plato, *Plato's The Republic* (New York : Books, Inc., 1943) (cited on page 121).

[177] J.-C. Yu, "Ultracold Atoms in Quasicrystalline Optical Lattices", First year report (University of Cambridge) (2018) (cited on pages 122, 197).

[178] A. M. Steane, M. Chowdhury and C. J. Foot, "Radiation force in the magneto-optical trap", Journal of the Optical Society of America B **9**, 2142 (1992) (cited on page 122).

[179] N. Tammuz, *Thermodynamics of ultracold 39k atomic Bose gases with tuneable interactions*, PhD thesis (University of Cambridge, Nov. 2011) (cited on page 123).

[180] Y. Castin and R. Dum, "Bose-Einstein Condensates in Time Dependent Traps", Phys. Rev. Lett. **77**, 5315–5319 (1996) (cited on page 128).

[181] K. Viebahn, M. Sbroscia, E. Carter, J.-C. Yu and U. Schneider, "Matter-Wave Diffraction from a Quasicrystalline Optical Lattice", Phys. Rev. Lett. **122**, 110404 (2019) (cited on pages 134, 147–148, 151–153).

[182] N. Wang, H. Chen and K. H. Kuo, "Two-dimensional quasicrystal with eightfold rotational symmetry", Phys. Rev. Lett. **59**, 1010–1013 (1987) (cited on pages 135, 149).

[183] H. Q. Yuan, U. Grimm, P. Repetowicz and M. Schreiber, "Energy spectra, wave functions, and quantum diffusion for quasiperiodic systems", Phys. Rev. B **62**, 15569–15578 (2000) (cited on page 137).

[184] P. L. Kapitza and P. A. M. Dirac, "The reflection of electrons from standing light waves", Mathematical Proceedings of the Cambridge Philosophical Society **29**, 297–300 (1933) (cited on page 141).

[185] D. L. Freimund, K. Aflatooni and H. Batelaan, "Observation of the Kapitza–Dirac effect", Nature **413**, 142–143 (2001) (cited on page 141).

[186] J. H. Denschlag, J. E. Simsarian, H. Häffner, C. McKenzie, A. Browaeys, D. Cho, K. Helmerson, S. L. Rolston and W. D. Phillips, "A Bose-Einstein condensate in an optical lattice", Journal of Physics B: Atomic, Molecular and Optical Physics **35**, 3095–3110 (2002) (cited on pages 143, 175).

[187] J. Mortlock, "Pulsed optical lattices", Part III report (University of Cambridge) (2019) (cited on pages 151, 214).

[188] P Ramachandrarao, A. Sinha and D Sanyal, "On the fractal nature of Penrose tiling", Current Science **79** (2000) (cited on page 157).

[189] Alik Sakharov, *Game of Thrones, season 3 episode 6*, distributed by HBO, written by David Benioff and D.B. Weiss, 2013 (cited on page 161).

[190] P. W. Anderson, "Absence of Diffusion in Certain Random Lattices", Phys. Rev. **109**, 1492–1505 (1958) (cited on page 161).

[191] L. Sanchez-Palencia, D. Clément, P. Lugan, P. Bouyer, G. V. Shlyapnikov and A. Aspect, "Anderson Localization of Expanding Bose-Einstein Condensates in Random Potentials", Phys. Rev. Lett. **98**, 210401 (2007) (cited on page 161).

[192] S. John, "Localization of Light", Physics Today **44**, 32–40 (1991) (cited on page 162).

[193] D. S. Wiersma, P. Bartolini, A. Lagendijk and R. Righini, "Localization of light in a disordered medium", Nature **390**, 671 (1997) (cited on page 162).

[194] Y. Lahini, R. Pugatch, F. Pozzi, M. Sorel, R. Morandotti, N. Davidson and Y. Silberberg, "Observation of a Localization Transition in Quasiperiodic Photonic Lattices", Phys. Rev. Lett. **103**, 013901 (2009) (cited on page 162).

[195] J. I. Pascual, J. Mendez, J. Gomez-Herrero, A. M. Baro, N. Garcia, U. Landman, W. D. Luedtke, E. N. Bogachek and H. P. Cheng, "Properties of Metallic Nanowires: From Conductance Quantization to Localization", Science **267**, 1793–1795 (1995) (cited on page 162).

[196] C. Gómez-Navarro, P. J. D. Pablo, J. Gómez-Herrero, B. Biel, F. J. Garcia-Vidal, A. Rubio and F. Flores, "Tuning the conductance of single-walled carbon nanotubes by ion irradiation in the Anderson localization regime", Nature Materials **4**, 534–539 (2005) (cited on page 162).

[197] T. Ying, Y. Gu, X. Chen, X. Wang, S. Jin, L. Zhao, W. Zhang and X. Chen, "Anderson localization of electrons in single crystals: Li $_x$ Fe $_7$ Se $_8$", Science Advances **2**, e1501283 (2016) (cited on page 162).

[198] S. Karbasi, C. R. Mirr, P. G. Yarandi, R. J. Frazier, K. W. Koch and A. Mafi, "Observation of transverse Anderson localization in an optical fiber", Optics Letters **37**, 2304 (2012) (cited on page 162).

[199] S. Karbasi, R. J. Frazier, K. W. Koch, T. Hawkins, J. Ballato and A. Mafi, "Image transport through a disordered optical fibre mediated by transverse Anderson localization", Nature Communications **5**, 3362 (2014) (cited on page 162).

[200] S. H. Choi, S.-W. Kim, Z. Ku, M. A. Visbal-Onufrak, S.-R. Kim, K.-H. Choi, H. Ko, W. Choi, A. M. Urbas, T.-W. Goo and Y. L. Kim, "Anderson light localization in biological nanostructures of native silk", Nature Communications **9**, 452 (2018) (cited on page 162).

[201] J. Billy, V. Josse, Z. Zuo, A. Bernard, B. Hambrecht, P. Lugan, D. Clément, L. Sanchez-Palencia, P. Bouyer and A. Aspect, "Direct observation of Anderson localization of matter waves in a controlled disorder", Nature **453**, 891 (2008) (cited on pages 162–163).

[202] R. Nandkishore and D. A. Huse, "Many-Body Localization and Thermalization in Quantum Statistical Mechanics", Annual Review of Condensed Matter Physics **6**, 15–38 (2015) (cited on pages 163–164).

[203] D. Basko, I. Aleiner and B. Altshuler, "Metal–insulator transition in a weakly interacting many-electron system with localized single-particle states", Annals of Physics **321**, 1126–1205 (2006) (cited on page 163).

[204] M. Rigol, V. Dunjko and M. Olshanii, "Thermalization and its mechanism for generic isolated quantum systems", Nature **452**, 854 (2008) (cited on pages 163–164).

[205] A. A. Zvyagin, "Dynamical quantum phase transitions", Low Temperature Physics **42**, 1240–1267 (2016) (cited on page 164).

[206] L. D'Alessio and A. Polkovnikov, "Many-body energy localization transition in periodically driven systems", Annals of Physics **333**, 19–33 (2013) (cited on page 164).

[207] P. Ponte, A. Chandran, Z. Papić and D. A. Abanin, "Periodically driven ergodic and many-body localized quantum systems", Annals of Physics **353**, 196–204 (2015) (cited on page 164).

[208] T. A. Corcovilos and J. Mittal, "Two-dimensional optical quasicrystal potentials for ultracold atom experiments", Applied Optics **58**, 2256 (2019) (cited on page 165).

[209] P. Bordia, H. Lüschen, U. Schneider, M. Knap and I. Bloch, "Periodically driving a many-body localized quantum system", Nature Physics **13**, 460 (2017) (cited on page 165).

[210] H. P. Lüschen, P. Bordia, S. Scherg, F. Alet, E. Altman, U. Schneider and I. Bloch, "Observation of Slow Dynamics near the Many-Body Localization Transition in One-Dimensional Quasiperiodic Systems", Phys. Rev. Lett. **119**, 260401 (2017) (cited on page 165).

[211] H. P. Lüschen, P. Bordia, S. S. Hodgman, M. Schreiber, S. Sarkar, A. J. Daley, M. H. Fischer, E. Altman, I. Bloch and U. Schneider, "Signatures of Many-Body Localization in a Controlled Open Quantum System", Phys. Rev. X **7**, 011034 (2017) (cited on page 165).

[212] H. P. Lüschen, S. Scherg, T. Kohlert, M. Schreiber, P. Bordia, X. Li, S. Das Sarma and I. Bloch, "Single-Particle Mobility Edge in a One-Dimensional Quasiperiodic Optical Lattice", Phys. Rev. Lett. **120**, 160404 (2018) (cited on page 165).

[213] P. Bordia, H. P. Lüschen, S. S. Hodgman, M. Schreiber, I. Bloch and U. Schneider, "Coupling Identical one-dimensional Many-Body Localized Systems", Phys. Rev. Lett. **116**, 140401 (2016) (cited on page 165).

[214] P. Bordia, H. Lüschen, S. Scherg, S. Gopalakrishnan, M. Knap, U. Schneider and I. Bloch, "Probing Slow Relaxation and Many-Body Localization in Two-Dimensional Quasiperiodic Systems", Phys. Rev. X **7**, 041047 (2017) (cited on page 165).

[215] M. P. A. Fisher, P. B. Weichman, G. Grinstein and D. S. Fisher, "Boson localization and the superfluid-insulator transition", Phys. Rev. B **40**, 546–570 (1989) (cited on page 165).

[216] J.-y. Choi, S. Hild, J. Zeiher, P. Schauss, A. Rubio-Abadal, T. Yefsah, V. Khemani, D. A. Huse, I. Bloch and C. Gross, "Exploring the many-body localization transition in two dimensions", Science **352**, 1547–1552 (2016) (cited on pages 165–166).

[217] J. M. Hickey, S. Genway and J. P. Garrahan, "Signatures of many-body localisation in a system without disorder and the relation to a glass transition", Journal of Statistical Mechanics: Theory and Experiment **2016**, 054047 (2016) (cited on page 165).

[218] V. Khemani, D. N. Sheng and D. A. Huse, "Two Universality Classes for the Many-Body Localization Transition", Phys. Rev. Lett. **119**, 075702 (2017) (cited on page 166).

[219] S. Iyer, V. Oganesyan, G. Refael and D. A. Huse, "Many-body localization in a quasiperiodic system", Phys. Rev. B **87**, 134202 (2013) (cited on page 166).

[220] W. De Roeck and F. Huveneers, "Stability and instability towards delocalization in many-body localization systems", Phys. Rev. B **95**, 155129 (2017) (cited on page 166).

[221] M. Žnidarič and M. Ljubotina, "Interaction instability of localization in quasiperiodic systems", Proceedings of the National Academy of Sciences **115**, 4595–4600 (2018) (cited on page 166).

[222] A. Szabó, "Electronics states of quasicrystals in one and two dimenions", Part III report (University of Cambridge), May 2016 (cited on pages 169, 171–172).

[223] A. Gaunt, *Degenerate Bose Gases: Tuning Interactions & Geometry*, PhD thesis (University of Cambridge, 2015) (cited on page 172).

[224] F. Gerbier, "Quantum gases in optical lattices", Lecture notes (2017) (cited on page 177).

[225] E. H. Lieb, R. Seiringer and J. Yngvason, "Superfluidity in dilute trapped Bose gases", Physical Review B **66** (2002) (cited on page 191).

[226] K. Aït-Ameur and F. Sanchez, "Gaussian beam conversion using an axicon", Journal of Modern Optics **46**, 1537–1548 (1999) (cited on page 206).

[227] J. Jackson, *Classical electrodynamics* (Wiley, New York, 1999) (cited on page 208).

[228] S Söyler, M. Kiselev, N. V. Prokofev and B. V. Svistunov, "Phase Diagram of the Commensurate Two-Dimensional Disordered Bose-Hubbard Model", Phys. Rev. Lett. **107**, 185301 (2011) (cited on page 214).

[229] Y. E. Kraus and O. Zilberberg, "Topological Equivalence between the Fibonacci Quasicrystal and the Harper Model", Phys. Rev. Lett. **109**, 116404 (2012) (cited on page 214).

[230] S. Spurrier and N. R. Cooper, "Semiclassical dynamics, Berry curvature, and spiral holonomy in optical quasicrystals", Phys. Rev. A **97**, 043603 (2018) (cited on page 214).

[231] K. Osterloh, M. Baig, L. Santos, P. Zoller and M. Lewenstein, "Cold Atoms in Non-Abelian Gauge Potentials: From the Hofstadter "Moth" to Lattice Gauge Theory", Phys. Rev. Lett. **95**, 010403 (2005) (cited on page 214).

[232] S. Gubser, I. Klebanov and A. Polyakov, "Gauge theory correlators from non-critical string theory", Physics Letters B **428**, 105–114 (1998) (cited on page 214).

[233] E. Witten, "Anti de Sitter space and holography", Advances in Theoretical and Mathematical Physics **2**, 253–291 (1998) (cited on page 214).

[234] J. Maldacena, "The Large-N Limit of Superconformal Field Theories and Supergravity", International Journal of Theoretical Physics **38**, 1113–1133 (1999) (cited on page 214).

[235] J. K. Rowling, *Harry Potter and the chamber of secrets* (Bloomsbury Pub, London, 1998) (cited on page 218).

[236] D. A. Steck, "Rubidium 87 D Line Data", (2003) (cited on pages 241, 245).

[237] E. Arimondo, M. Inguscio and P. Violino, "Experimental determinations of the hyperfine structure in the alkali atoms", Rev. Mod. Phys. **49**, 31–75 (1977) (cited on page 242).

[238] M. Roberts, P. Taylor, G. P. Barwood, P. Gill, H. A. Klein and W. R. C. Rowley, "Observation of an Electric Octupole Transition in a Single Ion", Phys. Rev. Lett. **78**, 1876–1879 (1997) (cited on page 242).

[239] N. Ramsey, *Nuclear moments.* (Wiley, New York, 1953) (cited on pages 242, 244).

[240] M. Sbroscia, "Towards optical quasicrystals with ultracold atoms", First year report (University of Cambridge) (2016) (cited on pages 247, 250, 255).

[241] S. V. Kagwade, C. R. Clayton, D. Chidambaram and G. P. Halada, "Photochemical breakdown of acetone on copper", Electrochimica Acta **46**, 2337–2342 (2001) (cited on page 249).

[242] J. Senior, *Optical fiber communications : principles and practice* (Pearson, New Delhi, 2009) (cited on page 251).

[243] A. Briguet and J. Chankji, "On the magnetic field of rectangular coils", Review of Scientific Instruments **56**, 1626–1631 (1985) (cited on page 254).

[244] Simpson, James C., Lane, John E., Immer, Christopher D., Youngquist, Robert C. and Steinrock, Todd, "Simple Analytic Expression for the Magnetic Field of a Circular Current Loop", NASA Technical Report (2001) (cited on page 254).

[245] K. A. Madsen, E. J. Bergholtz and P. W. Brouwer, "Topological equivalence of crystal and quasicrystal band structures", Phys. Rev. B **88**, 125118 (2013) (cited on page 260).

[246] M. Scully and M. Suhail Zubairy, *Quantum optics* (Cambridge University Press, Cambridge, 1997) (cited on page 265).

Appendices

A

Hyperfine structure

A.1 Hamiltonian

The quantum numbers L, S, J, I and F are introduced in section 2.1.1.

The full Hamiltonian for an electron bound to an atom by the Coulomb interaction $V(\mathbf{r})$ and subject to an external electromagnetic field $A^\mu = (\phi, \mathbf{A})$ is:

$$H = \frac{(\mathbf{p} + q\mathbf{A})^2}{2m} - q\phi + V(\mathbf{r}) + H_{\text{fine}} + H_{\text{hyp}} + H_{\text{Lamb}}, \tag{A.1}$$

where $H_{\text{fine}} \propto \mathbf{L} \cdot \mathbf{S} \propto \mathbf{J}^2$ is the *fine structure* and $H_{\text{hyp}} \propto \mathbf{I} \cdot \mathbf{J} \propto \mathbf{F}^2$ is the *hyperfine structure*. H_{Lamb} is the Lamb shift due to QED corrections and is ignored here. The energy scales of these contributions are summarised in table A.1.

contribution	energy scale
gross structure	$\sim \alpha^2 mc^2$
fine structure	$\sim \alpha^4 mc^2$
hyperfine structure	$\sim \alpha^4 m/m_p$
Lamb shift	$\sim \alpha^5 \ln(\alpha) mc^2$

Table A.1 : Energy scales, m is the mass of the electron, m_p of the proton, α the fine-structure constant that sets the scale.

The total electronic $\mathbf{J}$ and atomic $\mathbf{F}$ angular momenta are defined as:

$$\mathbf{J} = \mathbf{L} + \mathbf{S}, \quad \mathbf{F} = \mathbf{J} + \mathbf{I}. \tag{A.2}$$

For a uniform magnetic field $\mathbf{B}$ in the Coulomb gauge $\nabla \cdot \mathbf{A} = 0$, we can write $\mathbf{A} = \frac{1}{2}\mathbf{B} \times \mathbf{r}$, hence $\mathbf{A} \cdot \mathbf{p} = \frac{1}{2}\mathbf{B} \cdot \mathbf{L}$ and $\mathbf{A}^2 = \frac{1}{2}\mathbf{B}^2(x^2 + y^2)$.

The Hamiltonian can therefore be expressed as:

$$H = \frac{\mathbf{p}^2}{2m} + V(\mathbf{r}) + H_{\text{fine}} + H_{\text{hyp}} - \underbrace{\frac{q}{2m}(\mathbf{L}\cdot\mathbf{B})}_{\text{Linear Zeeman effect}} + \underbrace{\frac{q^2\mathbf{B}^2}{8m}(x^2+y^2)}_{\text{Quadratic Zeeman effect}} . \tag{A.3}$$

At zero external field, the Coulomb and the fine structure contributions are dominant and provide the basis to be used in the perturbative treatment of the hyperfine component H_{hyp}.

The hyperfine structure takes into account all the aspects of the interaction between the electron and nucleus that go beyond the simple point-charge treatment contained in the gross structure $V_0 \propto q_e Q_{\text{nucleus}}$. Analogously to eq. 2.7 , the full expression for the Hamiltonian H_{hyp} can be broken into electric and magnetic multipole contributions:

$$H_{\text{hyp}} = \underbrace{A_{\text{hfs}}\mathbf{I}\cdot\mathbf{J}}_{\text{magnetic dipole}} + \underbrace{B_{\text{hfs}}\frac{3(\mathbf{I}\cdot\mathbf{J})^2 + \frac{3}{2}(\mathbf{I}\cdot\mathbf{J}) - \mathbf{I}^2\mathbf{J}^2}{2I(2I-1)J(2J-1))}}_{\text{electric quadrupole}} + \underbrace{C_{\text{hfs}}}_{\text{magnetic octupole}} + \dots \tag{A.4}$$

The constants are experimentally determined and are reported in table A.2, while the vectors $\mathbf{I}$ and $\mathbf{J}$ are dimensionless and constructed as detailed below. The absence of some terms in the multipole expansion is discussed later.

Construction of angular momentum matrices

For a generic angular momentum with associated quantum numbers s, m_s, the $(2s+1)\cdot(2s+1)$ matrices are constructed in the $|m_s\rangle$ basis according to:

$$s_x = \frac{1}{2}(s_+ + s_-), \quad s_y = \frac{1}{2\mathrm{i}}(s_+ - s_-), \quad s_z = \text{diag}(s), \tag{A.5}$$

with the following rules:

$$\begin{aligned} \langle m_s'|s_+|m_s\rangle &= \delta_{m_s',m_s+1}\sqrt{s(s+1) - m_s(m_s+1)}, \\ \langle m_s'|s_-|m_s\rangle &= \delta_{m_s',m_s+1}\sqrt{s(s+1) - m_s(m_s+1)}, \\ \langle m_s'|s_z|m_s\rangle &= \delta_{m_s',m_s}\, m_s. \end{aligned} \tag{A.6}$$

s_+ and s_- are the raising and lowering ladder operators.

For the atomic species used in this thesis, ^{87}Rb and ^{39}K, the matrices for the states involved in the D2 transition were constructed in the $|m_I, m_J\rangle$ basis, where $I = 3/2$ and $J = 3/2$:

$$\begin{aligned} I_x &= s_x(I)\otimes\mathbb{1}(J) = s_x(3/2)\otimes\mathbb{1}(3/2) \\ &\dots \\ \mathbf{I} &= (I_x, I_y, I_z). \end{aligned} \tag{A.7}$$

Similarly for $\mathbf{J}$, so as to define the total angular momentum $\mathbf{F}$ as:

$$\mathbf{F} = \mathbf{I}\otimes\mathbb{1}_{\mathbf{J}} + \mathbb{1}_{\mathbf{I}}\otimes\mathbf{J}. \tag{A.8}$$

One could also employ the $|m_S, m_L, m_I\rangle$ basis, which would result in both D1 and D2 states because of the different $J = |L-S|\dots L+S$, though an appropriate $\mathbf{L}\cdot\mathbf{S}$ term

needs to be added to the Hamiltonian in order to obtain the correct fine structure energy splitting.

order	term	symbol	^{87}Rb	^{39}K
Magnetic dipole	$^2S_{1/2}$	A_{hfs}	$h \cdot 3.417\,\mathrm{GHz}$	$h \cdot 230.86\,\mathrm{MHz}$
	$^2P_{1/2}$	A_{hfs}	$h \cdot 408.328\,\mathrm{MHz}$	$h \cdot 27.77\,\mathrm{MHz}$
	$^2P_{3/2}$	A_{hfs}	$h \cdot 84.72\,\mathrm{MHz}$	$h \cdot 6.093\,\mathrm{MHz}$
Electric quadrupole	$^2P_{3/2}$	B_{hfs}	$h \cdot 12.496\,\mathrm{MHz}$	$h \cdot 2.786\,\mathrm{MHz}$

Table A.2 : Experimentally measured pre-factors for the multipole expansion of eq. A.4, from [167, 236].

A.2 Higher multipole moments

The gross structure considers the nucleus and the electron as point charges, which is essentially only taking the monopole moment in the multipole expansion of the electrostatic interaction.

The full electrostatic Hamiltonian H is:

$$H = \frac{1}{4\pi\epsilon_0}\int_{\mathbf{r}_e}\int_{\mathbf{r}_n}\frac{\rho_e(\mathbf{r}_e)\rho_n(\mathbf{r}_n)}{|\mathbf{r}_e-\mathbf{r}_n|}\,\mathrm{d}^3\mathbf{r}_e\,\mathrm{d}^3\mathbf{r}_n, \tag{A.9}$$

where r is the distance from the origin for both the electron (e) and the nucleus (n). Assuming $\mathbf{r}_e > \mathbf{r}_n$, one can perform the usual multipole expansion:

$$\begin{aligned}\frac{1}{|\mathbf{r}_e-\mathbf{r}_n|} &= \frac{1}{\sqrt{r_e^2-2\mathbf{r}_e\cdot\mathbf{r}_n+r_n^2}} = \\ \frac{1}{r_e}P_0(\cos\theta_{en}) &+ \frac{r_n}{r_e^2}P_1(\cos\theta_{en}) + \frac{r_n^2}{r_e^3}P_2(\cos\theta_{en}) + \cdots + \frac{r_n^\ell}{r_e^{\ell+1}}P_\ell(\cos\theta_{en}),\end{aligned} \tag{A.10}$$

where the Legendre polynomial is given by:

$$P_\ell(\cos\theta_{en}) = \frac{4\pi}{2\ell+1}\sum_{m=-\ell}^{\ell}(-1)^m Y_\ell^{-m}(\theta_n,\phi_n)\,Y_\ell^m(\theta_e,\phi_e) \tag{A.11}$$

with $Y_\ell^m(\theta,\phi) = \langle\theta,\phi|\ell,m\rangle$ being the spherical harmonics. These satisfy $(Y_\ell^m)^*(\theta,\phi) = (-1)^m\,Y_\ell^{-m}(\theta,\phi)$, $L^2Y_\ell^m = L^2Y_\ell^m = \ell(\ell+1)Y_\ell^m$ and $L_zY_\ell^m = m_\ell Y_\ell^m$. In general, L^2, L_z and ℓ can be any angular momentum quantum number among L, S, J, I and F.

The Hamiltonian can be therefore expressed as:

$$H = \sum_\ell H_\ell = \sum_\ell \frac{1}{4\pi\epsilon_0}\int_{\mathbf{r}_e}\int_{\mathbf{r}_n}\frac{\rho_e(\mathbf{r}_e)\rho_n(\mathbf{r}_n)}{r_e}\left(\frac{r_n}{r_e}\right)^\ell P_\ell(\cos\theta_{en})\,\mathrm{d}^3\mathbf{r}_e\,\mathrm{d}^3\mathbf{r}_n. \tag{A.12}$$

With $P_0 = 1$, $P_1 = x$ and $P_2 = {}^1\!/_2\,(3x^2-1)$, this becomes:

$$H \propto \int\rho(\mathbf{r_n})\,\rho(\mathbf{r_e})\left(\underbrace{\frac{1}{r_e}}_{\text{monopole}} - \underbrace{\frac{\hat{\mathbf{r}}\cdot\mathbf{r}_n}{r_e^2}}_{\text{dipole}} + \underbrace{\frac{1}{2r_e^3}(3(\hat{\mathbf{r}}\cdot\mathbf{r}_n)-r_n^2)}_{\text{quadrupole}} + \ldots\right). \tag{A.13}$$

In general, the 2^ℓ-pole correction to the Hamiltonian is given by:

$$H_\ell = \mathbf{Q}_\ell \cdot (\nabla \mathbf{E})_\ell = \sum_{m=-\ell}^{\ell} (-1)^m Q_\ell^m (\nabla \mathbf{E})_\ell^m, \tag{A.14}$$

where we have separated the nuclear and electronic coordinates into Q and $\nabla\mathbf{E}$, as outlined in [237]:

$$\begin{aligned} Q_\ell^m &= \left(\frac{4\pi}{2\ell+1}\right)^{1/2} \int_{\mathbf{r}_n} \rho(\mathbf{r}_n) r_n^\ell Y_\ell^{-m}(\theta_n, \phi_n) \mathrm{d}^3\mathbf{r}_n, \\ (\nabla \mathbf{E})_\ell^m &= \frac{1}{4\pi\epsilon_0} \left(\frac{4\pi}{2\ell+1}\right)^{1/2} \int_{\mathbf{r}_e} \rho(\mathbf{r}_e) r_e^{-(\ell+1)} Y_\ell^m(\theta_e, \phi_e) \mathrm{d}^3\mathbf{r}_e. \end{aligned} \tag{A.15}$$

It is worthy of notice that $\nabla\mathbf{E} = \nabla \otimes \mathbf{E} = \partial^2 V/(\partial x_i \partial x_j)$ quantifies the interaction dependence on the electric field gradient rather than on its strength (captured by the electric dipole term).

The $\ell = 0$ term is the monopole term included in the gross strcture of the Hamiltonian. Neutral atoms do not have a permanent electric dipole moment, and therefore display an inversion symmetry $\mathbf{r}_e \to -\mathbf{r}_e$ which results in the contribution of odd powers r^ℓ to vanish. The leading correction is therefore the electric quadrupole moment ($\ell = 2$), detailed below. Note that these restrictions only apply to the diagonal corrections, i.e. energy shifts, of the Hamiltonian, but not to off-diagonal elements corresponding to transitions: for example, electric octupole transitions have been measured in trapped ions [238].

The above treatment only considered the electrostatic interaction. The magnetic interaction can also be divided into a multipole expansion, though each therm possesses opposite parity than its electric counterpart. Hence, the $\ell = 1$ contribution is non-zero and is the magnetic dipole term resulting in the $\mathbf{I}\cdot\mathbf{J}$ interaction of eq. A.4. The next magnetic term would be the magnetic octupole $\ell = 3$ contribution, which has not yet been measured for ^{87}Rb and ^{39}K. There is no $\ell = 0$ magnetic contribution as magnetic monopoles have not yet been discovered at the time of writing this thesis.

Electric quadrupole

The following provides a derivation for the electric quadrupole contribution to eq. A.4.

Noting that $\mathbf{r}_e \cdot \mathbf{r}_n = r_e r_n \cos\theta_{en}$ can be expressed as $\sum_i x_{ni} x_{ei}$, the algebra detailed in [239] shows that the electric quadrupole $\ell = 2$ term can be cast in tensor notation:

$$\begin{aligned} H_{\ell=2} &= \frac{1}{4\pi\epsilon_0} \int_{\mathbf{r}_e} \int_{\mathbf{r}_n} r_n^2 \rho_n(\mathbf{r}_n) \frac{1}{2}(3\cos^2\theta_{en} - 1) \frac{\rho_e(\mathbf{r}_e)}{r_e^3} \,\mathrm{d}^3\mathbf{r}_e \,\mathrm{d}^3\mathbf{r}_n \\ &= \frac{1}{4\pi\epsilon_0} \int_{\mathbf{r}_e} \int_{\mathbf{r}_n} \rho_n(\mathbf{r}_n) \left(\frac{3}{2}\sum_{ij} x_{ni} x_{nj} x_{ei} x_{ej} - \frac{1}{2} r_n^2 r_e^2\right) \frac{\rho_e(\mathbf{r}_e)}{r_5^5} \,\mathrm{d}^3\mathbf{r}_e \,\mathrm{d}^3\mathbf{r}_n \\ &\Rightarrow H_{\ell=2} = -\frac{1}{6}\sum_{ij} Q_{ij} (\nabla\mathbf{E})_{ij}, \end{aligned} \tag{A.16}$$

where

$$\begin{aligned} Q_{ij} &= \int_{\mathbf{r}_n} \rho_n(\mathbf{r}_n) \left(3\frac{x_{ni}x_{nj} + x_{nj}x_{ni}}{2} - \delta_{ij} r_n^2\right) \mathrm{d}^3\mathbf{r}_n, \\ (\nabla\mathbf{E})_{ij} &= -\frac{1}{4\pi\epsilon_0} \int_{\mathbf{r}_e} \frac{\rho_e(\mathbf{r}_e)}{r_e^5} \left(3\frac{x_{ei}x_{ej} + x_{ej}x_{ei}}{2} - \delta_{ij} r_e^2\right) \mathrm{d}^3\mathbf{r}_e, \end{aligned} \tag{A.17}$$

where the doubling in the x sum only serves to emphasise the symmetric nature of the tensor, and normalisation constants have been dropped as they will be summarised in an overall constant at the end of the calculation.

We now invoke the Wigner-Eckardt theorem, which essentially states that matrix elements of tensor operators with respect to angular momentum eigenstates can be split into:

- a Clebsch-Gordan coefficient: this depends purely on geometry and is determined by the orientation of the system with respect to the choice of the z axis, hence it is only an angular contribution;
- a reduced matrix element: this summarises all non-angular contributions.

According to the above, a generic tensor operator V_i acting on a basis $|\alpha, \ell, m\rangle$, where ℓ, m are angular momenta and α is a non-angular variable, can be decomposed as:

$$\langle \alpha, \ell, m|V_i|\alpha, \ell, m\rangle \propto \langle \alpha, \ell, m|\mathbf{L}\cdot\mathbf{V}|\alpha, \ell, m\rangle \cdot \langle \ell, m|L_i|\ell, m\rangle. \tag{A.18}$$

In our specific case concerning the D2 line of ^{87}Rb and ^{39}K, the nuclear component Q_{ij} is computed in the basis $|I, m\rangle$:

$$\langle \alpha, I, m_I|Q_{ij}|\alpha, I, m_I\rangle \propto \langle \alpha, I, m_I|\mathbf{I}_i\cdot\mathbf{Q}\cdot\mathbf{I}_j|\alpha, I, m_I\rangle \cdot \langle I, m_I|\mathbf{I}_i\,\mathbf{I}_j|I, m_I\rangle, \tag{A.19}$$

resulting in the simpler form:

$$Q_{ij} = B_1\left(3\frac{\mathbf{I}_i\mathbf{I}_j + \mathbf{I}_i\mathbf{I}_j}{2} - \delta_{ij}\mathbf{I}^2\right), \tag{A.20}$$

where B_1 contains all non-angular dependencies.

Similarly, the electronic part with tensor operator $\nabla\mathbf{E}_{ij}$ is computed in the basis $|J, m_J\rangle$:

$$(\nabla\mathbf{E})_{ij} = B_2\left(3\frac{\mathbf{J}_i\mathbf{J}_j + \mathbf{J}_i\mathbf{J}_j}{2} - \delta_{ij}\mathbf{J}^2\right). \tag{A.21}$$

If the nuclear charge density is cylindrically symmetric about z, i.e. it is "squashed" along z, then the dominant term is Q_{zz}. The pre-factors B can be obtained from an integral in the $|I, m_I\rangle$ basis:

$$\begin{gathered} Q = 2\langle I, m_I|Q_{zz}|I, m_I\rangle = 2\int_{\mathbf{r}_n}\rho_n\left(3z_n^2 - r_n^2\right)\mathrm{d}^3\mathbf{r}_n = \\ = 2B_1\,\langle I, m_I|3\mathbf{I}_z^2 - \mathbf{I}^2|I, m_I\rangle = 2B_1\,(3I^2 - I(I+1)) = 2B_1\,I(2I-1) \\ \Rightarrow B_1 = \frac{Q}{2I(2I-1)}, \end{gathered} \tag{A.22}$$

and similarly for the electronic component (the factor of 2 here is conventional) resulting in:

$$\begin{aligned} Q_{ij} &= \frac{Q}{2I(2I-1)}\left(3\frac{\mathbf{I}_i\mathbf{I}_j + \mathbf{I}_i\mathbf{I}_j}{2} - \delta_{ij}\mathbf{I}^2\right), \\ (\nabla\mathbf{E})_{ij} &= \frac{q_J}{J(2J-1)}\left(3\frac{\mathbf{J}_i\mathbf{J}_j + \mathbf{J}_i\mathbf{J}_j}{2} - \delta_{ij}\mathbf{J}^2\right), \end{aligned} \tag{A.23}$$

where

$$q_J \propto \int_{\mathbf{r}_e}\rho(\mathbf{r}_e)\,\frac{3z_e^2 - r_e^2}{r_e^5}\,\mathrm{d}^3\mathbf{r}_e. \tag{A.24}$$

Note that for I or $J = 1/2$ the quadrupole correction vanishes, and thus does not affect the S and $P_{1/2}$ states. Intuitively, in the $J = 1/2$ state there is no orbital angular momentum which prevents the electron from sampling the anisotropy of the electric field gradient.

Finally, tedious algebra covered in [239] leads to the final form the electric quadrupole contribution to the Hamiltonian in eq. A.4:

$$H_{\ell=2} = \frac{B_{\text{hfs}}}{2I(2I-1)J(2J-1)} \left(3(\mathbf{I}\cdot\mathbf{J})^2 + \frac{3}{2}(\mathbf{I}\cdot\mathbf{J}) - \mathbf{I}^2\mathbf{J}^2\right), \tag{A.25}$$

where B_{hfs} includes all other constants, and is experimentally measured as reported in table A.2.

A.3 Magnetic fields

In the presence of magnetic fields, two more terms are to be included in the electronic Hamiltonian of eq. A.3:

$$H = \ \ldots \ \underbrace{\frac{q}{2m}(\mathbf{L}\cdot\mathbf{B})}_{\text{Linear Zeeman effect}} + \underbrace{\frac{q^2\mathbf{B}^2}{8m}(x^2+y^2)}_{\text{Quadratic Zeeman effect}} . \tag{A.26}$$

The quadratic Zeeman effect is usually ignored in our applications, as it only results in sizeable contributions for very large fields ($\propto \mu_{\text{B}} B^2(1-m_F^2)$).

The linear effect, however, is the bread and butter of cold atoms experiments as it underlies magnetic trapping and laser cooling schemes. It is the result of the interaction between the external magnetic field and the magnetic dipole terms of the electron caused by its angular momenta. These do not only include the orbital one $\mathbf{L}$ present in eq. A.26, but also the spin $\mathbf{S}$ and the nuclear $\mathbf{I}$ contributions.

Depending on the basis used to construct the Hamiltonian, the linear Zeeman contribution is given by:

$$\begin{aligned} H_{\text{Zeeman}} &= \mu_{\text{B}}(g_S\mathbf{S} + g_L\mathbf{L} + g_I\mathbf{I})\cdot\mathbf{B}, \\ H_{\text{Zeeman}} &= \mu_{\text{B}}(g_J\mathbf{J} + g_I\mathbf{I})\cdot\mathbf{B}, \\ H_{\text{Zeeman}} &= \mu_{\text{B}} g_F \mathbf{F}\cdot\mathbf{B}, \end{aligned} \tag{A.27}$$

where all angular momenta are dimensionless. Usually, for a homogeneous field $\mathbf{B} = B_z\hat{\mathbf{z}}$, the z axis is chosen as the axis of quantisation, simplifying the above expression to:

$$\begin{aligned} H_{\text{Zeeman}} &= \mu_{\text{B}}(g_S m_S + g_L m_L + g_I m_I)B_z, \\ H_{\text{Zeeman}} &= \mu_{\text{B}}(g_J m_J + g_I m_I)B_z, \\ H_{\text{Zeeman}} &= \mu_{\text{B}} g_F m_F B_z. \end{aligned} \tag{A.28}$$

The Landé factors are reported in table A.3.

Parameter	$S_{1/2}$	$P_{1/2}$	$P_{3/2}$
g_S	2.002		
g_L	0.999		
g_J	2.002	2/3	4/3
g_I	^{87}Rb : −0.000995, ^{39}K: −0.000142		
g_F	−1/2 for $F = 1$ 1/2 for $F = 2$	−1/6 for $F = 1$ 1/6 for $F = 2$	2/3

Table A.3 : Values from [167, 236].

The strength of the interaction with the external magnetic field determines the perturbative treatment of the atomic Hamiltonian. Namely, it determines which quantum numbers and hence which basis is suitable for use. The different regimes are summarised in table A.4. The plots in section 4.3.1 are computed from diagonalising the full Hamiltonian, therefore not performing a perturbative expansion.

At strong enough fields, the coupling between **I** and **J** to form **F** fails, as they individually precess about the magnetic field axis and the states are labelled by $|m_I, m_J\rangle$. This is the Paschen-Back regime for IJ coupling.
The fine structure can also be included by adding an $\mathbf{L} \cdot \mathbf{S}$ term in the Hamiltonian. When the energy from the interaction with the field is comparable to the fine structure, LS coupling also fails and the states are labelled by $|m_L\rangle$ and $|m_S\rangle$. This is the Paschen-Back regime for the LS coupling.

	strength	region	comments	
B ↑				Landau limit
	$H_{\text{Zeeman}} \gg H_0$	Landau tubes		
	$H_{\text{Zeeman}} \approx H_0$	n-mixing	n not good	
		L-mixing	L not good	
	$H_{\text{Zeeman}} \ll H_0$	Paschen-Back (LS)	L and S good, J not good	
		Paschen-Back (IJ)	I and J good, F not good	
		Zeeman effect	F good	
B = 0				Coulomb limit

Table A.4 : The relative strength of the Coulomb H_0 and magnetic field interaction H_{Zeeman} determines the regime governing the system.

B

More Experimental details

B.1 Vacuum

Differential pumping

A comprehensive treatment of the differential pumping formulae and vacuum calculus behind the circuit in fig. 4.3 is presented here, based on the appendix of my first year report [240] but with more revisions and fewer mistakes.

Conductances are in units of pumping speed, L s^{-1}, and obey the following addition rules:

$$\text{series:} \quad \frac{1}{C_{\text{tot}}} = \sum_i \frac{1}{C_i}\,, \quad \text{parallel:} \quad C_{\text{tot}} = \sum_i C_i \tag{B.1}$$

and for two components connected in parallel,

$$C_{\text{tot}} = \sum_i C_i\,. \tag{B.2}$$

The effective speed of a pump (S^*) is computed by combining its nominal pumping speed (S) with the conductance of its connection to the system (C_P):

$$\frac{1}{S^*} = \frac{1}{C_P} + \frac{1}{S}\,. \tag{B.3}$$

The equations for the conductances of apertures and pipes are derived from statistical physics, and are therefore only valid within the molecular flow regime where Knudsen number $\text{Kn} \gg 1$.

The conductance of a circular aperture of area A is:

$$C_{\text{ap}} = \frac{v}{4}A \quad [\text{L}\,\text{s}^{-1}]. \tag{B.4}$$

This result can be derived from the flux of particles crossing a small patch of area $\mathrm{d}A$ at an angle θ, in a cloud of density ρ:

$$\text{flux} = \frac{\text{number of particles}}{\mathrm{d}A\,\mathrm{d}t} = \frac{\rho\, v\cos\theta\,\mathrm{d}A\,\mathrm{d}t}{\mathrm{d}A\,\mathrm{d}t} = \rho\, v\cos\theta \to \rho\cos\theta\, v f(v)\,\mathrm{d}v, \tag{B.5}$$

where the last step generalised the expression to a a (classical) statistical ensemble via $v \to v f(v)\,\mathrm{d}v$, where

$$f(v)\,\mathrm{d}v = 4\pi\left(\frac{m}{2\pi k_{\mathrm{B}}T}\right)^{3/2} \mathrm{e}^{-\frac{mv^2}{k_{\mathrm{B}}T}}\, v^2\,\mathrm{d}v\sin\theta\,\mathrm{d}\phi\,\mathrm{d}\theta \tag{B.6}$$

is the Maxwell-Boltzmann distribution.

Integrating over the forward direction and defining the mean thermal velocity $\bar{v} = \left(\frac{8k_{\mathrm{B}}T}{\pi m}\right)^{1/2}$, the total flux J reads

$$J = \int \rho\cos\theta\, v\, f(v)\,\mathrm{d}v = 4\pi\left(\frac{m}{2\pi k_{\mathrm{B}}T}\right)^{3/2} \int_0^\infty v^3\,\mathrm{e}^{-\frac{mv^2}{k_{\mathrm{B}}T}}\mathrm{d}v \int_0^{\frac{\pi}{2}} \cos\theta\sin\theta\,\mathrm{d}\theta \int_0^{2\pi}\mathrm{d}\phi \tag{B.7}$$

$$\Rightarrow \quad J\cdot A = \frac{\bar{v}A}{4} \qquad [\mathrm{L\,s^{-1}}]$$

Similarly, the conductance of a pipe of diameter d and length ℓ can be found to be:

$$C_{\text{pipe}} = \frac{\pi\, v\, d^3}{12\ell}. \tag{B.8}$$

The total conductance C_{T} of the circuit shown in fig.4.3 is:

$$C_{\mathrm{T}} = \left(\frac{1}{S_1^* + \dfrac{C_2 S_2^*}{C_2 + S_2^*}} + \frac{1}{C_1}\right)^{-1} = C_{\mathrm{T}} = \frac{C_1\left(\dfrac{C_2 S_2^*}{C_2 + S_2^*} + S_1^*\right)}{C_1 + S_1^* + \dfrac{C_2 S_2^*}{C_2 + S_2^*}}. \tag{B.9}$$

The total "currents" (throughputs) flowing in the circuit are therefore

$$I_0 = P_0\, C_{\mathrm{T}}\,, \quad I_1 = P_1\, S_1^*, \quad \text{and} \quad I_2 = P_1 \frac{S_2^* C_2}{S_2^* + C_2}. \tag{B.10}$$

Kirchhoff's law requires:

$$I_0 = I_1 + I_2. \tag{B.11}$$

So:

$$P_0\, C_T = P_1\left(S_1^* + \frac{S_2^* C_2}{S_2^* + C_2}\right) \Rightarrow \frac{P_1}{P_0} = \frac{C_1}{C_1 + S_1^* + \dfrac{C_2 S_2^*}{C_2 + S_2^*}}. \tag{B.12}$$

Similarly,

$$\frac{P_2}{P_0} = \frac{C_2}{C_2 + S_2^*}\cdot\frac{C_1}{C_1 + S_1^* + \dfrac{C_2 S_2^*}{C_2 + S_2^*}}. \tag{B.13}$$

All conductances above combine that of a pipe and of the aperture:

$$C_{\text{ap+pipe}} = \left(\frac{1}{C_{\text{ap}}} + \frac{1}{C_{\text{pipe}}}\right)^{-1} = \frac{\pi v d^3}{4(4d + 3\ell)}. \tag{B.14}$$

The TSP is modelled as a horizontal tube, ignoring its vertical dimension.

Part	Symbol	Length mm	Diameter mm	Aperture diameter mm	Conductance L s^{-1}
2D MOT differential pumping section	C_1	54	1.5	1.5	4.6
3D MOT differential pumping section	C_2	198	10	16	367
Science cell tube	C_3	120	20	20	not needed
TSP MOT	C_{P_1}	258	100	40	112
TSP Knee	C_{P_2}	285	100	100	294
Ion pump MOT	S_1				75
Ion pump Knee	S_2				150
Effective Ion pump MOT	S_1^*				45
Effective Ion pump Knee	S_2^*				100

Table B.1 : Technical details of the vacuum components in fig. 4.3. All conductances combine the contributions of the aperture and of the pipe For pumps, the effective pumping speed S^* combines the connection conductance (C_P) with the nominal pumping speed (S).

Cleaning procedure

Our vacuum components were ordered from specialised companies and were therefore delivered clean, in sealed bags filled with inert gases (nitrogen or argon). Nonetheless, as problems arose for some components, we cleaned them ourselves as well. Key protagonist in the cleaning procedure was an ultrasonic bath, which shook all surfaces at high frequency causing dust and impurities to be detached.

The following steps were taken in cleaning vacuum equipment:

- ultrasonic bath in cleaning solution diluted in de-mineralised, warm, clean water for ~ 40 minutes;
- ultrasonic bath in clean water for ~ 20 minutes to remove the residual detergent from the previous step;
- once dry, and immediately before placing the component under vacuum, they were dusted with a pressurised-air container, and rinsed first with acetone and then with IPA (Isopropyl alcohol) in order to remove all specs of dust.

Gaskets are made of copper, and I learnt the hard way that copper and acetone react to form a blue-ish compound [241]. This caused the failure of the scroll pump, which had to be disassembled and thoroughly cleaned to remove the blue residue which was preventing it from descending below ~ 12.5 mbar.

Bake-out

As discussed in the main text of section 4.2, the ultimate pressure in the system is determined by the degassing rate of the internal surfaces. In order to speed this process and attain low pressures faster, the apparatus was heated to high temperatures – it was "baked".

Two bakes were performed. The first one ("Pre-bake") at maximum $\sim 400°C$, and only included the differential pumping section, the knee and the science cell TSP (see fig. 4.1). This was done to increase the diffusion of the hydrogen that accumulates in the steel components during manufacturing.

Stage	Turbo	MOT	Science	
Pre-bake	1×10^{-7} mbar			start
	6×10^{-7} mbar			day 15 (at 350 °C)
	1×10^{-9} mbar			day 16 (at room temperature)
			6×10^{-11} mbar	overnight, ion pump only
Main-bake	2.5×10^{-7} mbar	2×10^{-5} mbar	3×10^{-5} mbar	start
		$\sim 8 \times 10^{-7}$ mbar	$\sim 8 \times 10^{-7}$ mbar	day 11 (at 130 °C)
		$\sim 3 \times 10^{-9}$ mbar	$\sim 5 \times 10^{-9}$ mbar	day 13 (at room temperature)
	2.5×10^{-9} mbar	4×10^{-11} mbar	2.7×10^{-11} mbar	couple of days, ion pumps only
Atoms		7.92×10^{-11} mbar	2.15×10^{-11} mbar	atomic sources open, sealed system

Table B.2 : Summary of the pressures reached in different parts of the apparatus.

The second bake ("Main bake") was performed on the whole system, including the glass parts, and was around $130°C$ to allow evaporation of water vapour. The science cell was heated via irradiation from a cylindrical aluminium case placed around it.

The bake procedure is detailed in the appendix of my first year report [240]. The temperatures were increased very slowly ($\sim$ few degrees per hour) to allow all parts to expand at the same rate, especially the metal to glass transitions.

Silver plated copper gaskets were used for the pre-bake components as they would not oxidise, making it easier to remove them when assembling the rest of the apparatus. Annealed copper gaskets were employed for viewport connections as they are more ductile and less pressure was needed to tighten them.

A summary of the pressures reached during the bakes is reported in table B.2.

B.2 Laser tables

Lasers

The lasers are divided into two optical tables. The "Red" table, preparing the radiation used for laser cooling and imaging, and the "High Power" (or "Harry Potter") table with the optical dipole trap and the lattice lasers. These are shown in figs B.2, B.3, and B.4.

All lasers use frequency selective components to tune the output frequency from the broadband emission spectrum of the diode to a monochromatic radiation with linewidth ~ 100 kHz, as shown in fig. B.1.

The lasers on the "Red" table are manufactured by Toptica, and use a piezo-actuated grating in the Littrow configuration and a controllable pump current for the diode to change the effective length of the cavity and hence the frequency output. These are controlled by a PID loop that stabilises the output frequency based on the error signal generated from Doppler-free saturation spectroscopy, discussed in section 4.3.2.
The lattice laser (Matisse) uses several frequency selective components such as a birefringent filter, thin and thick etalons, and is locked to an external cavity (ECDL).

The laser for the optical dipole trap (Mephisto) is only passively stabilised by a sturdy and rigid internal cavity, and is not locked.

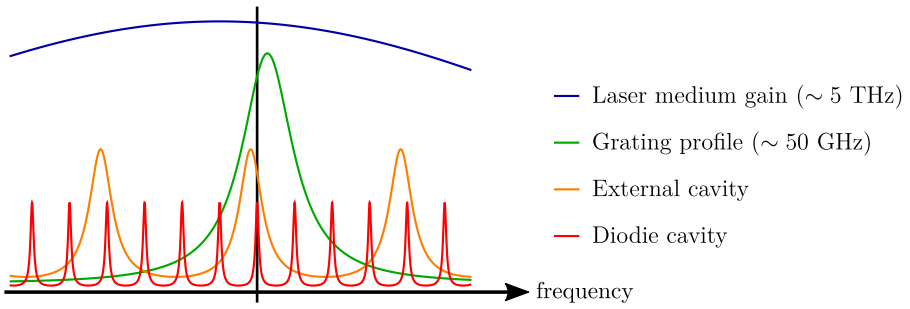

Figure B.1 : Frequency selective components in the Toptica lasers on the "Red" table. The black line is the emission frequency, corresponding to the maximum gain of the cavity.

Fibres and couplers

The 1064 nm light from the Mephisto is divided into ∼ 10 W per optical fibre, to be transported to the experimental chambers. This is too much power for usual glass-based optical fibres, hence large-mode photonic crystal fibres are used instead.

All other radiation, however, is coupled in glass-based optical fibres. In order to maximise transmission, a collimated laser beam with diameter d_1 is focussed onto the fibre core with diameter d_2 (also known as Mode Field Diameter, MFD) by a fibre coupler with a lens f:

$$d_1 = \frac{4f\lambda}{\pi d_2}. \tag{B.15}$$

The MFD of the fibre is provided on the datasheet of the Thorlabs fibre used: P3-630PM_FC with core diameter $d = 3.64\,\mu\text{m}$ at $\lambda = 630\,\text{nm}$, NA = 0.12 and cutoff wavelength $\lambda_c = 570\,\text{nm}$. The 630 nm fibre was chosen as it had a lower cutoff wavelength so as to guarantee single-mode transmission of both 780 (Rb) and 767 nm (K) light.

To calculate the dependence of the MFD on the laser frequency, the following formulae from [242] were used:

$$\begin{aligned} \text{core} &= 2\frac{2.405}{2\pi}\cdot\frac{\lambda_c}{\text{NA}}, \qquad V = \frac{\pi}{\lambda}\cdot\text{core}\cdot\text{NA}, \\ \text{MFD} &= \text{core}\cdot\left(0.65 + \frac{1.619}{V^{3/2}} + \frac{2.879}{V^6}\right), \end{aligned} \tag{B.16}$$

resulting in the values reported in table B.3.

Wavelength λ nm	V-number V	Mode field diameter MFD µm
630	2.18	4.30
780	1.76	5.25
767	1.79	5.15

Table B.3 : Mode Field Diameter calculated for different frequencies coupled into a P3-630PM_FC Thorlabs optical fibre.

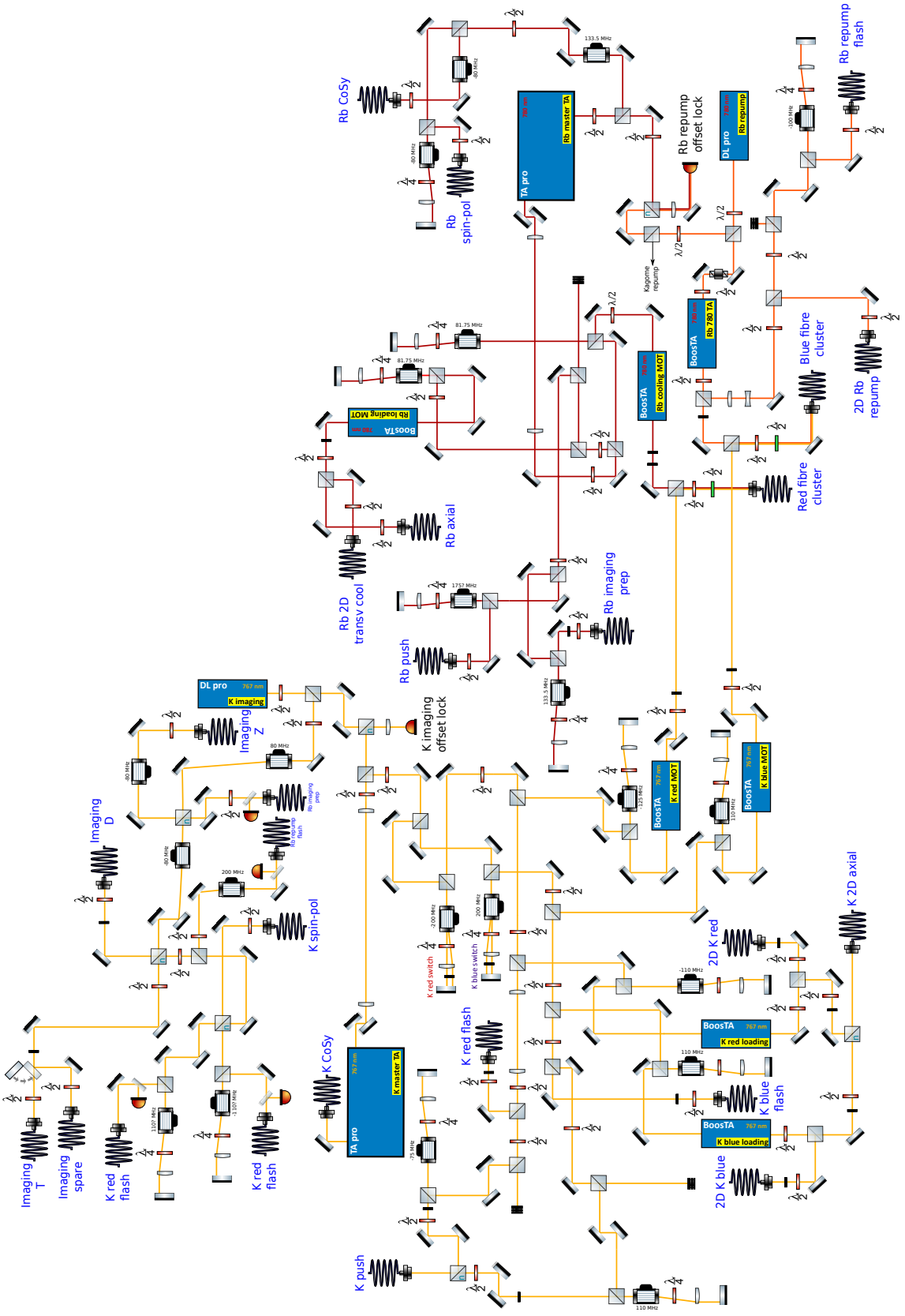

Figure B.2 : The "Red" table prepares the light for laser cooling and imaging. The "CoSy" is the device performing the Doppler-free saturation spectroscopy in section 4.3.2.

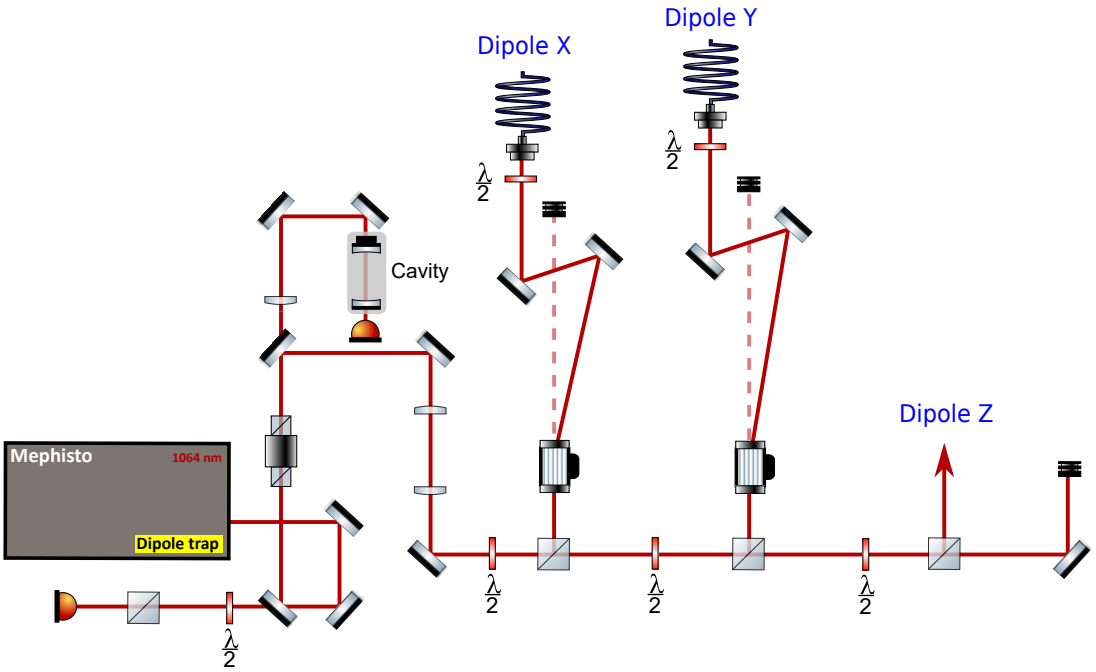

Figure B.3 : The first half of the "High Power" ("Harry Potter") table is dedicated to preparing the optical dipole trap.

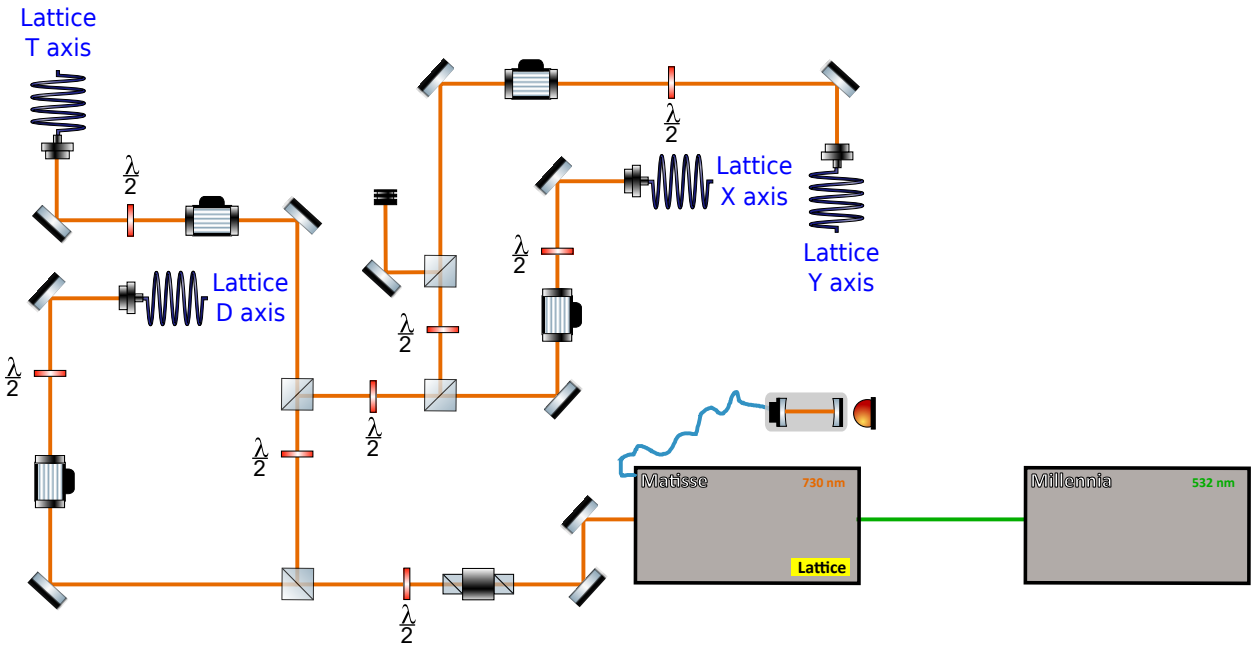

Figure B.4 : The second half of the "High Power" ("Harry Potter") table is dedicated to preparing the lattice light.

Magnetic fields

Rectangular coils

Analytical expressions for the magnetic field generated by the rectangular coil shown in fig. B.5 are derived in [243] and reported as follows.

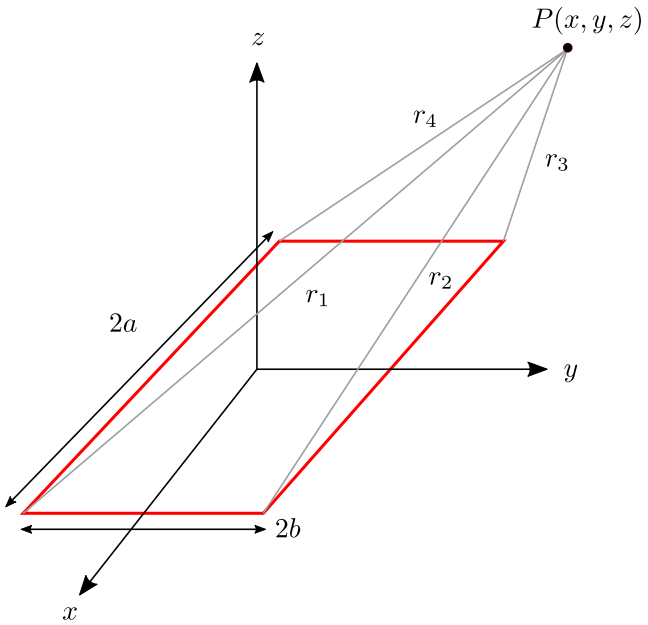

Figure B.5 : The rectangular coil used in the magnetic field formulae reported in this section.

$$
\begin{aligned}
B_z &= \frac{\mu_0 I}{4\pi}\sum_{a=1}^{4}\left[\frac{(-1)^{\alpha}d_{\alpha}}{r_{\alpha}(r_{\alpha}+(-1)^{\alpha+1}C_{\alpha})}-\frac{C_{\alpha}}{r_{\alpha}(r_{\alpha}+d_{\alpha})}\right],\\
B_x &= \frac{\mu_0 I}{4\pi}\sum_{a=1}^{4}\frac{(-1)^{\alpha+1}z}{r_{\alpha}(r_{\alpha}+d_{\alpha})},\\
B_y &= \frac{\mu_0 I}{4\pi}\sum_{a=1}^{4}\frac{(-1)^{\alpha+1}z}{r_{\alpha}(r_{\alpha}+(-1)^{\alpha+1}C_{\alpha})}
\end{aligned}
\tag{B.17}
$$

with

$$
\begin{aligned}
C_1 = -C_4 = a+x, \quad C_2 = -C_3 = a-x,\\
d_1 = d_2 = y+b, \quad d_3 = d_4 = y_b,\\
r_1 = \sqrt{(a+x)^2+(y+b)^2+z^2}, \quad r_2 = \sqrt{(a-x)^2+(y+b)^2+z^2},\\
r_3 = \sqrt{(a-x)^2+(y-b)^2+z^2}, \quad r_4 = \sqrt{(a+x)^2+(y-b)^2+z^2}.
\end{aligned}
\tag{B.18}
$$

Circular coils

The derivation of the field from a current loop is detailed in [244], and quoted as follows.

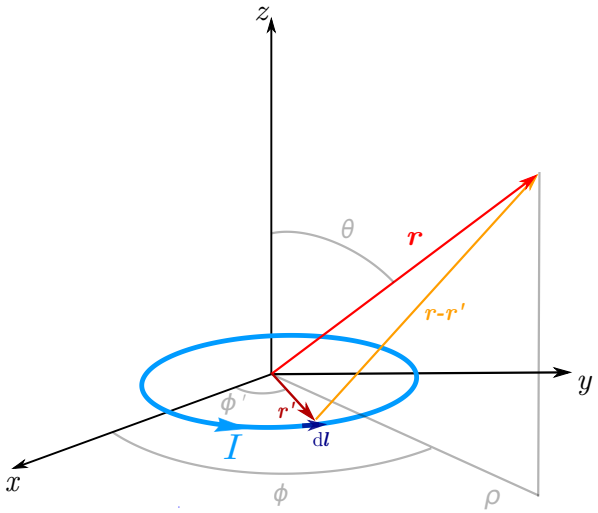

Figure B.6: Diagram for field generated from a current loop.

$$B_\rho(\rho,z) = \frac{\mu_0 I}{2\pi}\frac{z}{\rho\sqrt{(\rho+a)^2+z^2}}\left[\frac{a^2+\rho^2+z^2}{(a-\rho)^2+z^2}E(k)-K(k)\right], \tag{B.19}$$

$$B_\phi(\rho,z) = \frac{\mu_0 I}{2\pi}\frac{1}{\sqrt{(\rho+a)^2+z^2}}\left[\frac{a^2-\rho^2-z^2}{(a-\rho)^2+z^2}E(k)+K(k)\right]. \tag{B.20}$$

These expressions can be shifted by replacing $z \to (z-L)$, so as to calculate the fields from coils pairs in the Helmholtz and anti-Helmholtz configurations.

On the axis $\rho = 0$, the elliptical integrals are trivially equal to $\pi/2$ and hence:

$$B_\rho(\rho,z) = 0, \quad \text{and} \quad B_z(0,z) = \frac{\mu_0 I}{2\pi}\frac{a^2}{(z^2+a^2)^{3/2}}, \tag{B.21}$$

which is the known result for the field along the axis of a loop.

B.3 Plumbing

Calculation of the losses in the pressure and flow of the cooling water was performed in order to determine the required specifications of the water supply. Suitable chillers were purchased providing enough pressure to guarantee sufficient water flow to cope with the thermal dissipation of the electromagnets. The calculation is detailed in the appendix of my first year report [240] and reproduced here.

Coils producing the magnetic fields for 2D-MOTs and for the magnetic transport (and Feshbach) generate a large quantity of dissipated heat. They therefore require to water-cool the brass heat sinks which the coils are wound around.

The 'cooling block' (transport and experiment coils) and the 2D MOTs coils are connected in parallel, as shown in fig. B.7. Considering this as an electronic circuit, parallel loads need lower pressure, hence a cheaper chiller and a lower consumption.

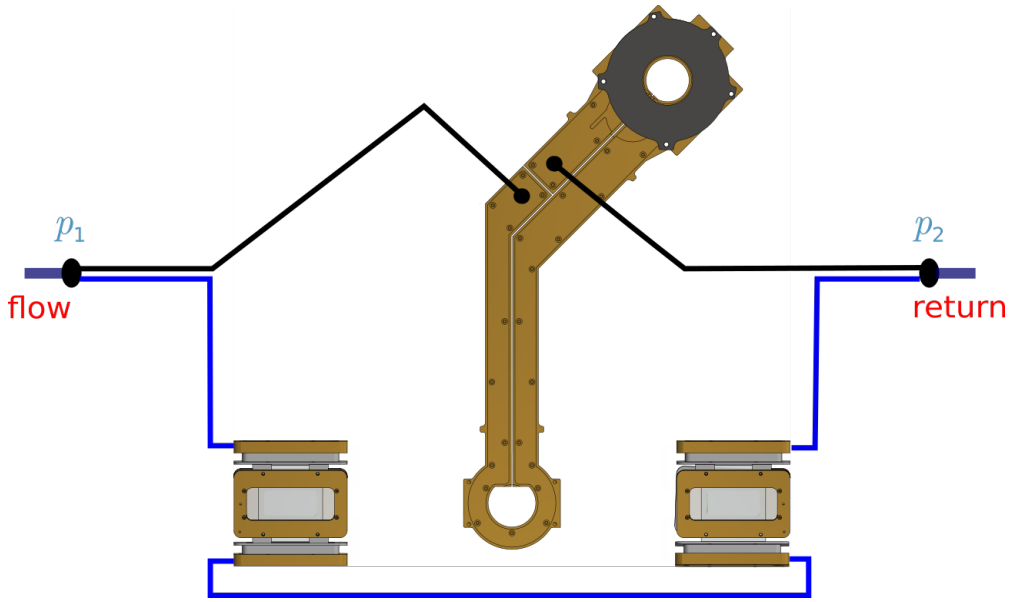

Figure B.7 : 2D MOT coils and magnetic transport coils are connected in parallel.

Oliver Brix, the Master's student that designed the magnetic transport system derived the required chiller and derived that the pressure available at the connection $(p_2 - p_1)$ is 0.18 mbar.

The continuity equation for an incompressible liquid requires the volumetric flow Q to be constant throughout the circuit, so:

$$Q = uA = \text{constant}, \tag{B.22}$$

where u is speed of fluid and A the cross section of the pipe.

The volumetric flow is fixed by the power dissipated ($P_{\text{dissipated}}$) by our electrical system and by the desired temperature increase of the cooling liquid ΔT:

$$Q_{\text{required}} = \frac{P_{\text{dissipated}}}{\Delta T\, \rho\, C}, \tag{B.23}$$

ρ and C being the density and specific heat capacity of the cooling liquid.

A certain pressure is required to maintain a certain flow, due to the 'ideality' of the incompressible fluid being spoiled by the viscous forces with the pipe walls. Pressure losses arising from the circuit are quantified with a *head loss*, which relates the kinetic energy of an incompressible fluid to the potential energy stored static column of equivalent volume, an analogy allowed by Bernouilli's principle.

A hydraulic head is given by the *elevation* and the *pressure* heads. The elevation pressure is required to pump the fluid from the ground to the level of the heat sinks ($\sim$ 1 m). Pressure heads are given by the pressure loss in pipes, due to friction, and in corners due to direction change.

The friction in the pipe causes a pressure head give by the Darcy-Weisbach equation:

$$\Delta h = \frac{f_D}{2g}\frac{u^2 L}{d}, \tag{B.24}$$

L and d being the length and diameter of the pipe, and f_D the coefficient of friction given by:

$$f_D = \frac{0.079}{\mathrm{Re}^{1/4}} = 0.079\left(\frac{\mu}{\rho}\right)^{1/4}\frac{1}{u^{1/4}d^{1/4}}, \tag{B.25}$$

Re being the Reynolds number. This is an empirical expression that is valid for high Reynolds numbers such as the ones encountered in a liquid.

The head loss associated with bends is given by:

$$\Delta h = k\frac{u^2}{2g}, \tag{B.26}$$

k being a coefficient associated with the type of bend, e.g. for a square bend 90 degrees is given by $k_1 = 1.3$.

Sudden contraction and expansion also cause pressure loss, and have same expression as above, with coefficients $k_2 = 0.44$ and $k_3 = \left(1 - \frac{A_1}{A_2}\right)^2$ respectively. The flow being from A_1 to A_2.

The pressure is derived from the head loss via

$$\Delta p = \rho\, g\, \Delta h. \tag{B.27}$$

The chiller must then be able to supply a pressure p_{chiller}:

$$\underbrace{p_{\text{chiller}}}_{\text{pressure required}} = \underbrace{\Delta p_{\text{MOTs}}}_{\substack{\text{2D MOTs}\\ \text{heat sink}}} + \underbrace{\Delta p_{\text{pipe}}}_{\substack{\text{pipe between}\\ \text{two 2D MOTs}}} + \underbrace{\Delta p_{\text{bends}}}_{\substack{\text{bends and}\\ \text{corners}}} + \underbrace{\Delta p_{\text{sudden}}}_{\substack{\text{sudden expansions}\\ \text{and/or contractions}}}, \tag{B.28}$$

$$\underbrace{p_{\text{chiller}}}_{\substack{\text{pressure}\\ \text{required}}} = \underbrace{f_D\frac{\rho u^2 L}{2d}}_{\substack{\text{2D MOTs}\\ \text{heat sink}}} + \underbrace{N_1 k_1\frac{\rho u^2}{2}}_{\substack{\text{pipe between}\\ \text{two 2D MOTs}}} + \underbrace{f'_D\frac{\rho u_p^2 L_p}{2d_p}}_{\substack{\text{bends and}\\ \text{corners}}} + \underbrace{N_2 k_2\frac{\rho u^2}{2}}_{\substack{\text{sudden}\\ \text{expansions}}} + \underbrace{N_3 k_3\frac{\rho u^2}{2}}_{\substack{\text{sudden}\\ \text{contractions}}}, \tag{B.29}$$

where the speed in the pipe u_p, from B.22:

$$u_p = u\left(\frac{d}{d_p}\right)^2. \tag{B.30}$$

So:

$$\frac{1}{2}\rho u^2\left[f_D\frac{L}{d} + f'_D\frac{L_p}{d_p}\left(\frac{d}{d_p}\right)^4 + N_1 k_1 + N_2 k_2 + N_3 k_3\right], \tag{B.31}$$

$$f_D = 0.079\left(\frac{\mu}{\rho}\right)^{1/4}\frac{1}{u^{1/4}d^{1/4}}, \tag{B.32}$$

$$f'_D = 0.079 \left(\frac{\mu}{\rho}\right)^{1/4} \frac{1}{u_p^{1/4} d_p^{1/4}} = 0.079 \left(\frac{\mu}{\rho}\right)^{1/4} \frac{d_p^{1/4}}{u^{1/4} d^{1/4}}, \tag{B.33}$$

$$k_3 = \left(1 - \frac{A_1}{A_2}\right)^2 = \left(1 - \frac{d_1^2}{d_2^2}\right)^2. \tag{B.34}$$

Combining B.22 with B.23 allows extraction of the necessary fluid speed u:

$$u = \frac{4P_{\text{dissipated}}}{\pi \rho C \Delta T d^2}, \tag{B.35}$$

and hence the expression for the pressure:

$$\begin{aligned} p_{\text{chiller}} = \frac{8P_{\text{dissipated}}^2}{\pi^2 \rho \Delta T^2 C^2 d^4} \left[0.079 \left(\frac{\mu}{\rho}\right)^{0.25} \left(\frac{\pi \rho \Delta T C}{4P_{\text{dissipated}}}\right)^{0.25} \left(\frac{L}{d^{3/4}} + L_p \frac{d^4}{d_p^{19/4}}\right) \right] \\ + \frac{8P_{\text{dissipated}}^2}{\pi^2 \rho \Delta T^2 C^2 d^4} \left[N_1 k_1 + N_2 k_2 + N_3 k_3 \left(1 - \frac{d_1^2}{d_2^2}\right)^2 \right]. \end{aligned} \tag{B.36}$$

With p_{chiller} equal to the pressure available between points 1 and 2 in fig. B.7, 0.18 mbar, and the following data: $L_p = 3\,\text{m}$, $d_p = 8\,\text{m}$, $N_1 = 27$, $N_2 = 2$, $N_3 = 2$, we only need the power dissipated by the coils to calculate the temperature increase of the coolant liquid to make sure it is reasonable.

The power dissipated P by a current I in a conductor of electrical resistivity ρ_e, length L and cross-sectional area A_0 is:

$$P = I^2 \rho_e \frac{L}{A_0}. \tag{B.37}$$

A single rectangular 2D-MOT coil, with maximum 10 A delivered from the power supplies and 1.25 mm diameter coil, with $L = 0.420\,\text{m}$ of wire per turn with 70 turns in total ($L \sim 30\,\text{m}$) dissipates $\sim 47\,\text{W}$. For eight coils, the total dissipated power is $P_{\text{dissipated}} \sim 380\,\text{W}$.

From this data, the temperature increase of the cooling liquid is $\Delta T = 2.7\,^\circ\text{C}$, and the water flow is $Q \sim 2\,\text{L}\,\text{s}^{-1}$. This is the worst case scenario, with the coils assumed to be always on and with maximum current. Radiative heating from the black-anodised coil holder reduces the dissipated power the water needs to cool.

Compensation coils were not included in this calculation.

C

More localisation transitions

The same code used to produce the momentum space Inverse Participation Ratio (IPR_k) plots in section 8.1.3 was used to numerically probe localisation transitions in other lattice configurations. As before, the size of the Hamiltonian was limited by the RAM of the computers that performed the calculation.

Three beam case

The interference pattern for the three-beam lattice configuration is shown in fig. 7.14, labelled as "3D". This results in a regularly spaced array of 1D quasiperiodic systems.

The ground state IPR in momentum space for the three-beam lattice is shown in fig. C.1 and exhibits a transition between $2 < V_0/E_{\mathrm{rec}} < 3$, most likely around $2.75\, E_{\mathrm{rec}}$.

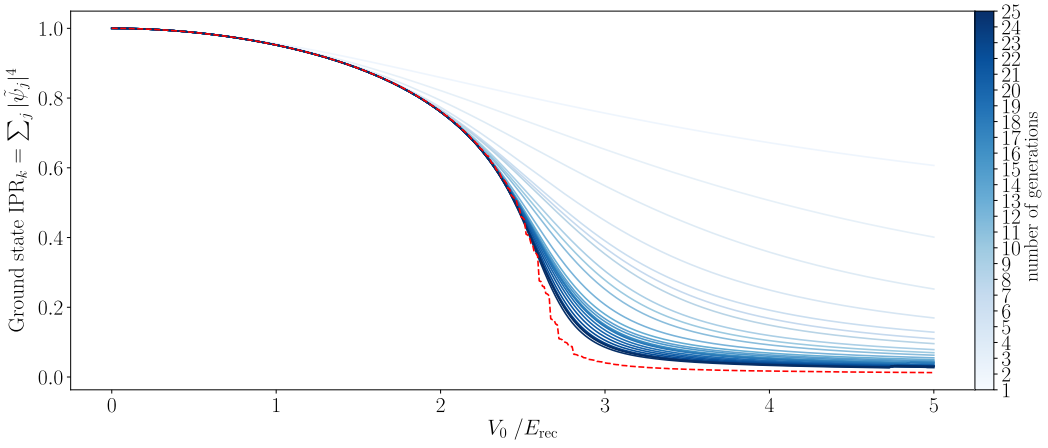

Figure C.1 : The momentum space inverse participation ratio IPR_k for the ground state of a three-beam lattice, which consists of regularly spaced 1D quasiperiodic systems. The red dashed line is computed for 50 generations.

Other four-dimensional cases

According to table 3.1, a four-dimensional regular lattice is not only compatible with eightfold rotational symmetry, but also five-, ten- and twelvefold. The physical question here is: can we probe the 4D Chern number in, for instance, a fivefold symmetric lattice? While there is literature that claims no novel topological features are guaranteed by the higher dimensional inheritance of quasicrystals [245], a quick investigation into other 4D compatible rotational symmetries was performed.

In the following I quote the bases in 4D and 2D corresponding to the relevant n-fold rotational symmetry, along with the projection matrices $\mathcal{P}^{\parallel}$ to obtain the latter from the former. These are used to compute the kinetic energy contribution to the Hamiltonian in eq. 7.28 while employing the same off-diagonal lattice ($\propto V_0$) terms computed for the eightfold case. The IPR_k plots were all computed up to 25 generations, and essentially all looked like fig. 8.4 and are hence are not shown.

The relation between the 4D hyperspace and the 2D bases reported below is justified as the matrix representations of both obey the same groups operations. However, these representations are not faithful, since the bases in 4D are not linearly independent. This means that a particular point in momentum space cannot be uniquely identified by its *generation*, as it was done for the eightfold case in section 7.1.4, which undermines the confidence in the IPR_k plots and in any dynamical simulation performed in this basis. This is further confirmed by the projection matrices all giving $(\mathcal{P}^{\parallel})^2 \neq \mathcal{P}^{\parallel}$, as opposed to what found for eqs. 7.26 and 7.27.

In conclusion, I think that a reliable simulation for fivefold symmetry would require a 5D parent regular lattice, where the 5 roots of unity can be mapped onto a set of 5 linearly independent vectors. Similarly for the other rotational symmetries. Unfortunately this would require even more RAM and CPUs than available at the time of these investigations.

Fivefold

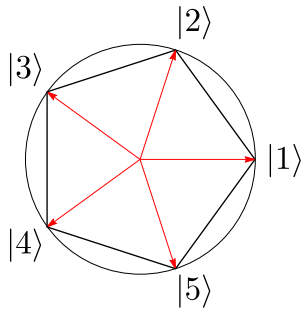

vector	4D	2D
$\|1\rangle$	$(1,0,0,0)$	$(1,0)$
$\|2\rangle$	$(0,1,0,0)$	$(\cos(2\pi/5), \sin(2\pi/5))$
$\|3\rangle$	$(0,0,1,0)$	$(-\cos(\pi/5), \sin(\pi/5))$
$\|4\rangle$	$(0,0,0,1)$	$(-\cos(\pi/5), -\sin(\pi/5))$
$\|5\rangle$	$(-1,-1,-1,-1)$	$(\cos(2\pi/5), -\sin(2\pi/5))$

$$\mathcal{P}_5^{\parallel} = \begin{pmatrix} 1 & \cos(2\pi/5) & -\cos(\pi/5) & -\cos(\pi/5) \\ 0 & \sin(2\pi/5) & \sin(\pi/5) & -\sin(\pi/5) \\ 0 & 0 & 0 & 0 \\ 0 & 0 & 0 & 0 \end{pmatrix}. \tag{C.1}$$

Notice how $\sum_i |G\rangle_i = 0$, so that we can always express one of the vectors as the sum over the others: $|5\rangle = |1\rangle + |2\rangle + |3\rangle + |4\rangle$. This intuitively justifies why the four-dimensional space still provides a representation for the fivefold rotational symmetry.

The ground state IPR in momentum space for the 4D basis showed a transition around $1.75 < V_0/E_{\text{rec}} < 1.80$.

The Hamiltonian in the 5D basis was also computed, though only up to 20 generations due to RAM limitations, showing a transition around $1.25 < V_0/E_{\text{rec}} < 1.35$.

Tenfold

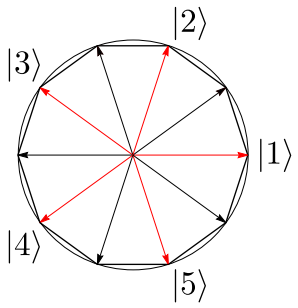

vector	4D	2D
$\|1\rangle$	$(1,0,0,0)$	$(1,0)$
$\|2\rangle$	$(0,1,0,0)$	$(\cos(2\pi/5), \sin(2\pi/5))$
$\|3\rangle$	$(0,0,1,0)$	$(-\cos(\pi/5), \sin(\pi/5))$
$\|4\rangle$	$(0,0,0,1)$	$(-\cos(\pi/5), -\sin(\pi/5))$
$\|5\rangle$	$(-1,-1,-1,-1)$	$(\cos(2\pi/5), -\sin(2\pi/5))$

$$\mathcal{P}_{10}^{\parallel} = \begin{pmatrix} 1 & \cos(2\pi/5) & -\cos(\pi/5) & -\cos(\pi/5) \\ 0 & \sin(2\pi/5) & \sin(\pi/5) & -\sin(\pi/5) \\ 0 & 0 & 0 & 0 \\ 0 & 0 & 0 & 0 \end{pmatrix}. \tag{C.2}$$

The ground state IPR in momentum space for the 4D basis showed a transition around $1.75 < V_0/E_{\text{rec}} < 1.80$. This is the same as for the fivefold symmetric case, as expected because reflection symmetry makes the two synthetic lattice configurations equivalent.

Twelvefold

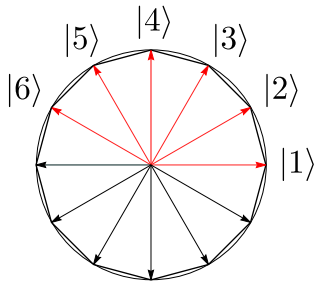

vector	4D	2D
$\|1\rangle$	$(1,0,0,0)$	$(1,0)$
$\|2\rangle$	$(0,1,0,0)$	$(\cos(\pi/6),\sin(\pi/6))$
$\|3\rangle$	$(0,0,1,0)$	$(\cos(\pi/3),\sin(\pi/3))$
$\|4\rangle$	$(0,0,0,1)$	$(0,1)$
$\|5\rangle$	$(-1,0,1,0)$	$(-\cos(\pi/3),\sin(\pi/3))$
$\|6\rangle$	$(0,-1,0,1)$	$(-\cos(\pi/6),\sin(\pi/6))$

$$\mathcal{P}_{12}^{\parallel} = \begin{pmatrix} 1 & \cos(\pi/6) & \cos(\pi/3) & 0 \\ 0 & \sin(\pi/6) & \sin(\pi/3) & 1 \\ 0 & 0 & 0 & 0 \\ 0 & 0 & 0 & 0 \end{pmatrix}. \tag{C.3}$$

The ground state IPR in momentum space for the 4D basis showed a transition around $1.65 < V_0/E_{\mathrm{rec}} < 1.75$.

D

Miscellaneous

D.1 Spin-statistics theorem

The foundation of the proof leading to eq. 1.28 lies in the commutator $[\phi_A, \phi_B]$, where ϕ is defined in eq. 1.27. The full, rigorous and index-full proof is given in [53] in the section about *General causal fields*. I am just going to sketch the proof here, as a guide for the argument presented in the reference.

The commutator $[\phi_A, \phi_B]$ depends on the commutators $[f_A, f_B]$ and $[h_A, h_B]$ of the functions that define the field operator in eq. 1.27. Hence we will turn our attention to the coefficients f and h.

The function $f(\mathbf{p})$ for a generic momentum $\mathbf{p}$ can be generated from one at rest $f(\mathbf{0})$ by a Lorentz boost Λ: $f(\mathbf{p}) = D(\Lambda)f(\mathbf{0})$, with D being some irreducible representation of the Lorentz group. The latter affects both space and time, and therefore obeys $SO(4)$ algebra – technically $SO(1,3)$ – which is isomorphic to $SO(3) \times SO(3)$. This can be easily understood by considering the same isomorphism in one fewer dimension: $SO(3)$ is isomorphic to $SO(2) \times SO(2)$, because any position on a 3D sphere can be written as a linear superposition of two orthogonal 2D circles. Hence, we can replace the four-dimensional vector $\mathcal{J} \in SO(4)$ by two three-dimensional vectors $\mathbf{J}, \mathbf{K} \in SO(3)$, with quantum numbers j and k obeying the usual angular momentum algebra and hence $2j + 1, 2k + 1 \in \mathbb{N}$.

Luckily we already know that the spherical harmonics Y_ℓ^m are the basis functions of the irreducible $2\ell + 1$ space, and they transform according to $Y_\ell^m(-\mathbf{r}) = (-1)^\ell Y_\ell^m(\mathbf{r})$. Extending this to the generic representation $D(\Lambda)$, we expect a transformation $D(\Lambda) \to (-1)^j(-1)^k = (-1)^{j+k}$.

Identical particles transform according to the same irreducible representation of the Poincaré group, uniquely labelled by their mass $m = \sqrt{{}^1\!/_{c^2}\, p^\mu p_\mu}$ and spin. If A and B are

identical, that is with equal mass and spin, then:

$$[f_A, f_B] \propto D(\Lambda)D(\Lambda) \propto (-1)^{j+k}(-1)^{j+k} = (-1)^{2(j+k)}. \tag{D.1}$$

Hence, the total angular momentum $j+k$ determines the sign of the commutator and the statistics obeyed by the particles, resulting in the expressions in eq. 1.28.

The treatment in this section was simplified by only considering real scalar fields, though it can be easily extended to complex fields representing charged particles. More importantly, the fields were assumed to be non-interacting and hence expressed in terms of single mode $\mathbf{p}$ creation and annihilation operators. Proofs of the spin-statistics theorem for interacting fields are much harder, and to be quite frank I did not understand them. However, it is argued in [53] that the *cluster decomposition theorem* ensures interacting fields can always be constructed from the non-interacting components considered here.

D.2 Derivation of transition matrix element

Here I report the tedious maths needed to result in the transition matrix element of eq. 2.7.

First of all, the $\mathbf{d}$ operator is defined as:

$$\mathbf{d} = \frac{-\mathrm{i}}{m\omega}\langle f|\mathrm{e}^{\mathrm{i}\mathbf{k}\cdot\mathbf{r}}\mathbf{p}|i\rangle, \tag{D.2}$$

and the complex exponential is expanded as:

$$\mathrm{e}^{\mathrm{i}\mathbf{k}\cdot\mathbf{r}} = 1 + \mathrm{i}\mathbf{k}\cdot\mathbf{r} + \dots. \tag{D.3}$$

The *dipole approximation* assumes the electron's orbit is much smaller than the wavelength of the incoming radiation, $\mathbf{k}\cdot\mathbf{r} \sim 0$, resulting in the atom experiencing only a DC field. Retaining only the first term of the expansion (1) and using:

$$[\mathbf{r}, H_0] = \frac{\mathrm{i}\hbar\mathbf{p}}{m}, \tag{D.4}$$

where $H_0 = \mathbf{p}^2/2m + V(\mathbf{r})$, results in:

$$\hat{\mathbf{e}}\cdot\mathbf{d} = \frac{-\mathrm{i}}{m\omega}\hat{\mathbf{e}}\cdot\langle f|\mathrm{e}^{\mathrm{i}\mathbf{k}\cdot\mathbf{r}}\mathbf{p}|i\rangle \approx \langle f|\hat{\mathbf{e}}\cdot\mathbf{r}|i\rangle, \tag{D.5}$$

which we identify as the electric dipole contribution to the transition element.

We now turn our attention to the leading correction in the above power expansion, $\mathrm{i}\mathbf{k}\cdot\mathbf{r}$. The transition matrix element is given by:

$$\hat{\mathbf{e}}\cdot\mathbf{d} = \frac{1}{m\omega}\langle f|(\mathbf{k}\cdot\mathbf{r})(\hat{\mathbf{e}}\cdot\mathbf{p})|i\rangle = \frac{1}{mc}\langle f|(\hat{\mathbf{k}}\cdot\mathbf{r})(\hat{\mathbf{e}}\cdot\mathbf{p})|i\rangle. \tag{D.6}$$

The rest of the section details suitable substitutions to bring the above expression to one of greater physical interpretation.
First, we notice that defining $\hat{\mathbf{n}} = \hat{\mathbf{k}}\times\hat{\mathbf{e}}$ enables writing:

$$\hat{\mathbf{n}}\cdot\mathbf{L} = (\hat{\mathbf{k}}\times\hat{\mathbf{e}})\cdot(\mathbf{r}\times\mathbf{p}) = (\hat{\mathbf{k}}\cdot\mathbf{r})(\hat{\mathbf{e}}\cdot\mathbf{p}) - (\hat{\mathbf{e}}\cdot\mathbf{r})(\hat{\mathbf{k}}\cdot\mathbf{p}), \tag{D.7}$$

which is half of the expression in eq. D.6. We also take the liberty of adding $2\mathbf{S}$ to $\mathbf{L}$, where $\mathbf{S}$ is the spin of the electron and 2 its (approximate) gyromagnetic ratio, motivated by the experimental evidence that the two can be treated on equal footing.

The other half of eq. D.7 can be derived if we define a well-crafted concoction C:

$$C = \frac{\mathrm{i}m}{\hbar}[H_0, (\hat{\mathbf{e}}\cdot\mathbf{r})(\hat{\mathbf{k}}\cdot\mathbf{p})], \tag{D.8}$$

which can be expanded as:

$$C = \frac{\mathrm{i}m}{\hbar}\hat{e}_j\hat{k}_k[H, r_j, r_k] = \frac{\mathrm{i}m}{\hbar}e_j\hat{k}_k(r_j[H, r_k] + [H, r_j]r_k) \tag{D.9}$$

Using the commutator of eq. D.4, this results in:

$$\begin{aligned} S = \hat{e}_j\hat{k}_k(r_jp_k + p_jr_k) = \hat{e}_j\hat{k}_k(r_jp_k + r_kp_j - \mathrm{i}\hbar\delta_{jk}) \\ \Rightarrow S = (\hat{\mathbf{e}}\cdot\mathbf{r})(\hat{\mathbf{k}}\cdot\mathbf{p}) + (\hat{\mathbf{k}}\cdot\mathbf{r})(\hat{\mathbf{e}}\cdot\mathbf{p}), \end{aligned} \tag{D.10}$$

where $\hat{\mathbf{e}}\cdot\hat{\mathbf{k}} = 0$ was assumed because we are considering a plane wave.

Eq. D.9 can also be used to directly compute the matrix element:

$$\langle f|C|i\rangle = \frac{\mathrm{i}m}{\hbar}\hat{e}_j\hat{k}_k\langle f|(r_jHr_k - r_jr_kH + Hr_jr_k - r_jHr_k)\,|i\rangle = \frac{\mathrm{i}m}{\hbar}\hat{e}_j\hat{k}_k\langle f|r_jr_k|i\rangle, \tag{D.11}$$

from which we define the electric quadrupole tensor as

$$Q_{jk} = \langle f|r_jr_k - r^2\delta_{jk}/3|i\rangle, \tag{D.12}$$

made traceless to guarantee the plane wave condition $\hat{\mathbf{e}}\cdot\hat{\mathbf{k}} = 0$.

Combination of all of the above results in:

$$\hat{\mathbf{e}}\cdot\mathbf{d} \quad = \quad \underbrace{\langle f|\hat{\mathbf{e}}\cdot\mathbf{r}|i\rangle}_{\text{electric dipole}} \quad + \quad \underbrace{\frac{1}{2mc}(\hat{\mathbf{k}}\times\hat{\mathbf{e}})\cdot\langle f|\mathbf{L} + 2\mathbf{S}|i\rangle}_{\text{magnetic dipole}} \quad + \quad \underbrace{\frac{\mathrm{i}\omega}{2c}\hat{\mathbf{e}}\cdot\mathbf{Q}\cdot\hat{\mathbf{k}}}_{\text{electric quadrupole}} \quad \ldots \tag{D.13}$$

D.3 Spontaneous decay rate

The spontaneous decay rate used in table 2.1 was estimated as follows. A hydrogen atom was used, but the procedure can be extended to hydrogenic atoms by including Z, thereby being applicable to the ^{87}Rb and ^{39}K atoms treated in this thesis.

From [246], the spontaneous decay rate w^{sp} between a state $|f\rangle$ and $|i\rangle$ is given by:

$$w^{\mathrm{sp}}_{f\to i} = \frac{4\alpha\omega^3}{3c^2}\,|\langle f|\mathbf{d}|i\rangle|^2, \tag{D.14}$$

where $\mathbf{d}$ is the transition operator and $\hbar\omega$ the energy gap between the two states, α the fine-structure constant and c the speed of light. In a hydrogen atom, we can take $\hbar\omega \sim \alpha^2mc^2$ as per the gross structure, with m being the (reduced) mass of the electron.

For electric dipole transitions, $\mathbf{d}$ is the electric dipole operator and can be approximated as ea_0, where e is the charge of the electron and $a_0 = \hbar/(mc\alpha)$ is the Bohr radius. These results allow for expressing the spontaneous decay rate for electric dipole transitions as:

$$w^{\mathrm{sp}}_{\text{electric dipole}} \sim \alpha^5\,\frac{mc^2}{\hbar}. \tag{D.15}$$

For the magnetic dipole transitions, we need to identify a suitable $\mathbf{d}$ which from eq. D.13 may be taken as $\sim {}^{1}\!/_{mc}\,(\mathbf{L}+2\mathbf{S})$. Estimating the angular momentum to be of order $\hbar$, and the ω between fine structure levels in the same n manifold (for parity rules in table 2.1) $\hbar\omega \sim \alpha^4 mc^2$ (as per table A.1), we get:

$$w^{\text{sp}}_{\text{magnetic dipole}} \sim \alpha^{13}\,\frac{mc^2}{\hbar}. \tag{D.16}$$

For electric quadrupole transitions, we take $\mathbf{d} \sim {}^{\omega}\!/_{c}\,\mathbf{Q}$, and we estimate $\hbar\omega \sim \alpha^2 mc^2$ as for the electric dipole, and $|\mathbf{Q}| \sim a_0^2$ from eq. D.12. Leading to:

$$w^{\text{sp}}_{\text{electric quadrupole}} \sim \alpha^{7}\,\frac{mc^2}{\hbar}. \tag{D.17}$$

D.4 Proof of reciprocal space

I here provide a proof for eq. 3.6:

$$\rho(\mathbf{r}) = \rho(R\mathbf{r}+\mathbf{t}) \quad \Leftrightarrow \quad \hat{\rho}(\mathbf{k}) = \mathrm{e}^{\mathrm{i}(R\mathbf{k}\cdot\mathbf{t})}\,\hat{\rho}(R\mathbf{k}). \tag{D.18}$$

where $\hat{\rho}(\mathbf{k})$ is the Fourier transform (structure factor) of the density distribution $\rho(\mathbf{r})$, defined as:

$$\hat{\rho}(\mathbf{k}) = \int \rho(\mathbf{r})\mathrm{e}^{-\mathrm{i}\mathbf{k}\cdot\mathbf{r}}\,\mathrm{d}^3\mathbf{r}. \tag{D.19}$$

Under a plane group symmetry operation, can combine a translation $\mathbf{t}$ and a rotation R to result in $\mathbf{r}' = R\mathbf{r}+\mathbf{t}$, which upon being inverted yields $\mathbf{r} = R^{-1}\mathbf{r}' - R^{-1}\mathbf{t}$. Because $R^{-1} = R^T$, then $\mathbf{k}R^{-1}\mathbf{r} \Rightarrow (R\mathbf{k})\mathbf{r}$, which in the exponent results in $-\mathbf{k}\cdot\mathbf{r} = -(R\mathbf{k})\cdot\mathbf{r}' + (R\mathbf{k})\cdot\mathbf{t}$.

Hence:

$$\hat{\rho}(\mathbf{k}) = \int \rho(\mathbf{r})\,\mathrm{e}^{-\mathrm{i}\mathbf{k}\cdot\mathbf{r}}\,\mathrm{d}^3\mathbf{r} = \int \rho(\mathbf{r})\,\mathrm{e}^{-\mathrm{i}(R\mathbf{k})\cdot\mathbf{r}'+(R\mathbf{k})\cdot\mathbf{t}}\,\mathrm{d}^3\mathbf{r} = \mathrm{e}^{\mathrm{i}(R\mathbf{k}\cdot\mathbf{t})}\,\hat{\rho}(R\mathbf{k}), \tag{D.20}$$

as quoted in in eq. 3.6.

D.5 Groups and field extensions

Groups are the best way to mathematically classify and quantify symmetries. Based on the relation between n-fold symmetry and m-dimensional regular lattices outlined in section 3.2.4, one could speculate that if a point group possesses more than d d-dimensional irreducible representations, it is not a crystallographic point group and it violates eq. 3.5.

The symmetry of regular n polygons is described by the dihedral group D_n. The number of irreducible representations of D_n is $(n-1)/2$ for odd n, and $(n-2)/2$ for even n. For $d = 2$, dihedral groups with $n > 6$ are then not crystallographic, with 5 and 6 being undecided as the number of representations is exactly equal to $d = 2$.

We then look at the smallest *splitting field* for different D_n, listed in table D.1. This can be thought of as the smallest extension to $\mathbb{Z}$ that contains all the coefficients of the characteristic polynomial of the n-fold rotation matrix.

Table D.1 then confirms what already discussed about eq. 3.5. One-, two-, three-, four- and sixfold symmetries are crystallographic because $2\cos(2\pi/n) \in \mathbb{N}$, while fivefold and eightfold symmetries require a field extension by an irrational number.

Degree n	Order $2n$	Dihedral group D_n	Number and dimensions of irreducible representations	Smallest splitting field
1	2	D_1 or $\mathbb{Z}_2$	1, 1	$\mathbb{Q}$
2	4	D_2 or V_4 (Klein)	1,1,1,1	$\mathbb{Q}$
3	6	D_3 or S_3	1,1,2	$\mathbb{Q}$
4	8	D_4	1,1,1,1,2	$\mathbb{Q}$
5	10	D_5	1,1,2,2	$\mathbb{Q}(\sqrt{5})$
6	12	D_6	1,1,1,1,2,2	$\mathbb{Q}$
7	14	D_7	1,1,2,2,2	$\mathbb{Q}(\cos 2\pi/7)$
8	16	D_8	1,1,1,1,2,2,2	$\mathbb{Q}(\sqrt{2})$

Table D.1 : Summary of the properties of dihedral groups D_n.

Notice that threefold symmetry involves the angle $\phi = 2\pi/3$, such that $\cos(2\pi/3) = 1/2 \in \mathbb{Q}$ but $\sin(2\pi/3) = \sqrt{3}/2 \notin \mathbb{Q}$. But threefold symmetry is still crystallographic because $\mathbb{Q}(\cos 2\pi/3) = \mathbb{Q}$. Put simply, the n-fold symmetry will be non-crystallographic only if $\cos(2\pi/n) \notin \mathbb{N}$. This is justified by the argument leading to eq. 3.5, and also by quoting a general non-orthogonal rotation matrix:

$$\mathcal{R} = \begin{pmatrix} 0 & -1 \\ 1 & 2\cos(2\pi k/n) \end{pmatrix}, \tag{D.21}$$

with $n, k \in \mathbb{N}$. This matrix is constructed with a non-orthogonal basis[1] such as the unit vectors in the directions of the vertices of an n polygon, and it still satisfies eq. 3.5.

D.6 Free energy minimisation

In thermodynamics, the equilibrium state is usually found by minimising the (Helmholtz) free energy $F = U - TS$. But why?

An equilibrium macroscopic state, from the second law of thermodynamics, corresponds to a state of maximal entropy S. The entropy is related to the statistical weight W by Boltzmann's relation $S = k_\text{B} \ln \Omega$ and therefore to the total *number of microscopic states* N ($\Omega \propto N$). Equilibrium dictates maximising the entropy S, thus the number of microstates states N.

In a closed system (the *microcanonical ensemble*), the number of microstates N at a fixed energy U is obtained from the entropy:

$$S(U) \propto \ln N(U) \quad \Rightarrow \quad N \propto \mathrm{e}^{S(U)}, \tag{D.22}$$

hence equilibrium is simply when the entropy is maximised.

If our system is put into contact with a reservoir at temperature T (the *canonical ensemble*), equilibrium is attained when the *total* (reservoir+system) number of states N_tot is maximised:

$$N_\text{tot} \propto \mathrm{e}^{S(U)} \cdot \mathrm{e}^{S_\text{res}(U_\text{tot}-U)} = \mathrm{e}^{S(U)+S_\text{res}(U_\text{tot}-U)}. \tag{D.23}$$

[1] For the rotation matrix M in Cartesian coordinates of eq. 3.4, with $\phi = 2\pi/n$ for an n-sided regular polygon, the characteristic equation is $M^2 - \mathrm{tr}(M)M + \det(M) = 0$. Applying to v_1, with $v_2 = Mv_1$, one gets $Mv_2 = -v_1 + 2\cos(2\pi k/n)\, v_2$.

The entropy of the reservoir can be expanded as:

$$S_{\text{res}}(U_{\text{tot}} - U) \approx S_{\text{res}}(U_{\text{tot}}) - U\frac{\partial S}{\partial U} = S_{\text{res}}(U_{\text{tot}}) - \frac{U}{T}, \tag{D.24}$$

where we have used the thermodynamic relation $\partial U/\partial S = T$.

Hence the total number of microstates is given by:

$$N_{\text{tot}} \propto \mathrm{e}^{S} \cdot \mathrm{e}^{-U/T} = \mathrm{e}^{(TS-U)/T} = \mathrm{e}^{-F/T}, \tag{D.25}$$

where the (Helmholtz) free energy F was defined as $F = U - TS$.

Maximising the number of states corresponds to minimising the free energy F.

D.7 Derivation of Dyson expansion

This section provides a proof for the Dyson series of eq. 7.8.

In the Schödinger picture, the time-evolution is carried by the states while the operators are time-independent:

$$|\psi_t\rangle = U(t, t_0)|\psi_0\rangle. \tag{D.26}$$

In the *interaction* picture[2], the time depence in encoded in the operators themselves, requiring a shift $U \to U^{(\text{int})}$. In this picture, $U^{(\text{int})}$ obeys the Schrödinger equation:

$$\mathrm{i}\hbar\frac{\mathrm{d}U^{(\text{int})}}{\mathrm{d}t} = H_{\text{I}}^{(\text{int})}U^{(\text{int})}, \tag{D.27}$$

where H_I is the interaction contribution to the Hamiltonian, which provides a non-trivial evolution dynamics.

The equation may be solved iteratively with a boundary condition $U^{(\text{int})}(t = t_0) = 1$ to give:

$$U^{(\text{int})}(t, t_0) = 1 - \frac{\mathrm{i}}{\hbar}\int_{t_0}^{t} H_{\text{I}}^{(\text{int})}(t') \underbrace{U^{(\text{int})}(t')}_{\left(1-\frac{\mathrm{i}}{\hbar}\int_{t_0}^{t'} H_{\text{I}}^{(\text{int})}(t'')\underbrace{U^{(\text{int})}(t'')}_{\dots}\,\mathrm{d}t''\right)} \mathrm{d}t' \tag{D.28}$$

which results in the expression:

$$U^{(\text{int})}(t, t_0) = 1 - \frac{\mathrm{i}}{\hbar}\int_{t^0}^{t}\mathrm{d}t' H_{\text{I}}^{(\text{int})}(t') + \left(\frac{-\mathrm{i}}{\hbar}\right)^2\int_{t_0}^{t}\mathrm{d}t'\int_{t_0}^{t'}\mathrm{d}t'' H_{\text{I}}^{(\text{int})}(t')H_{\text{I}}^{(\text{int})}(t'')\dots \tag{D.29}$$

Finally, we return to the Schrödinger picture:

$$U^{(\text{int})} = \mathrm{e}^{\mathrm{i}H_0 t/\hbar}U\mathrm{e}^{-\mathrm{i}H_0 t/\hbar}, \quad H_I^{(\text{int})} = \mathrm{e}^{\mathrm{i}H_0 t/\hbar}H_{\text{I}}\mathrm{e}^{-\mathrm{i}H_0 t/\hbar}, \tag{D.30}$$

where H_0 is the free (non-interacting) component of the Hamiltonian.

Using the energy eigenbasis, $\mathrm{e}^{\mathrm{i}H_0 t/\hbar}|i\rangle = \mathrm{e}^{\mathrm{i}E_i t/\hbar}$, we obtain the expression quoted in eq. 7.8.

Finally, for the integration:

[2]There are technical differences between the *Heisenberg* and *interaction* pictures that I will ignore.

- Off-diagonal terms:

$$\int \mathrm{d}t' \; \mathrm{e}^{\mathrm{i}(E_f - E_i)(t'-t0)} \sim \frac{1}{E_f - E_i} \mathrm{e}^{\mathrm{i}(E_f - E_i)(t'-t0)}. \tag{D.31}$$

  The largest contribution form the pre-factor is when $E_f \approx E_i$, and in the limit of $t \to \infty$, $t_0 \to -\infty$ the phase factor becomes large and common to all perturbative terms, and can hence be dropped.

- Diagonal terms: $E_f = E_i$ hence the phase factor in the above integral is trivially 1, and all remaining phase factors are common to each perturbative terms and can hence be dropped.

D.8 Time-varying constant in the Hamiltonian

Construction of the Hamiltonian detailed in 7.1.4 included diagonal terms $d\,V_0/2$, where d is the dimensionality of the simulated system and V_0 the single-beam lattice depth. While these terms only amount to phase factors for the time-independent lattices used in chapter 7, it is not immediately obvious whether or not they can also be neglected for the time-dependent $V_0(t)$ ramps presented in chapter 8. This is what I mean by the oxymoron "time-varying constant": a purely diagonal contribution to the Hamiltonian, whose entries are all the same, but which happens to be time dependent.

In this case, the Schrödiner equation can be written as:

$$\mathrm{i}\frac{\mathrm{d}|\psi\rangle}{\mathrm{d}t} = (H'(t) + \Phi(t))\,|\psi\rangle, \tag{D.32}$$

with solution:

$$|\psi_t\rangle = \mathcal{T} \exp\left[-\frac{\mathrm{i}}{\hbar}\int_0^t (H'(t) + \Phi(t))\,\mathrm{d}t\right]|\psi_0\rangle, \tag{D.33}$$

where $\Phi(t) = \mathrm{diag}\,[f(t)]$ is the purely diagonal time dependent contribution to the Hamiltonian, and $\mathcal{T}$ the time-ordering operator.

Using $[H', \Phi] = 0$, we obtain:

$$|\psi_t\rangle = \mathcal{T}\left[\exp -\left(\frac{\mathrm{i}}{\hbar}\int_0^t H'(t)\mathrm{d}t\right)\exp\left(-\frac{\mathrm{i}}{\hbar}\int_0^t \Phi(t)\mathrm{d}t\right)\right]|\psi_0\rangle. \tag{D.34}$$

Because Φ is diagonal,

$$\exp\left(-\frac{\mathrm{i}}{\hbar}\int_0^t \Phi(t)\mathrm{d}t\right) = \mathbb{1}\exp\left(-\frac{\mathrm{i}}{\hbar}\int_0^t f(t)\mathrm{d}t\right). \tag{D.35}$$

Also, since $\mathcal{T}(a\cdot b) = \theta(t_1 - t_2)(a\cdot b) + \theta(t_2 - t_1)(a\cdot b) = \mathcal{T}(a)\cdot\mathcal{T}(b)$, where θ is the Heaviside step function:

$$\mathcal{T}\left[\mathbb{1}\exp\left(-\frac{\mathrm{i}}{\hbar}\int_0^t f(t)\mathrm{d}t\right)\right] = \exp\left(-\frac{\mathrm{i}}{\hbar}\int_0^t f(t)\mathrm{d}t\right), \tag{D.36}$$

because the entries $f(t)$ commute at unequal times $\forall t$.

Hence, the dynamical evolution of the state is given by:

$$|\psi_t\rangle = \exp\left(-\frac{\mathrm{i}}{\hbar}\int_0^t f(t)\mathrm{d}t\right)\mathcal{T}\left[\exp\left(-\frac{\mathrm{i}}{\hbar}\int_0^t H'(t)\mathrm{d}t\right)\right]|\psi_0\rangle. \tag{D.37}$$

This proves that the time-dependence of a homogeneous and diagonal contribution to the Hamiltonian only amounts to a phase factor.

D.9 ARB documentation

This section provides a short documentation for the class and methods used to generate the ARBitrary lattice pulses of chapters 7 and 8. The signal generators used are the Keysight 33500 B series, with option 33512B. They have 16 MSa memory, and a maximum sample rate of 250 MSa/s = 30 MHz.

A library was written to interface them with our timing software `QControl`, which is in `qcontrol\qcontrol\server\drivers\VisaDriver\CamWavGen.py`. The main method added to the signal generator class `K33500B` is:

```
self.addChannels(VisaChannel('Arbitrary', None,
 ('arbname', '0, .1, .2, .3, .4, .5, .6, .7, .8, .9',
 'arbname', '2.0', '5e 3'),
 description = 'Send arbitrary waveform',
 hw_hint = 'FUNC ARB; DATA:ARB %s, %s ; :FUNC:ARB %s;
 :VOLT %s ; :VOLT:OFFS: 0;
 :FUNC:ARB:FILTER OFF; :FUNC:ARB:PER %s' ))
```

where `VisaChannel` is the `QControl` class for all VISA (*Virtual instrument software architecture*) devices. Its non-keyword arguments are the name and units (if any) of the command, and a string with the details of the pulse sequence. The string in the example above is the default value of the method, and will be replaced by a user-defined argument. Each element in the string replaces the `%s` in the *hardware hint* `hw_hint`, which is the actual string sent to the device. This employs the SCPI language, where commands are separated by a semicolon (equivalent to a line break) and a colon specifies a sub-system. `FUNC ARB` selects the arbitrary waveform functionality, `DATA:ARB` specifies that this will be generated from a list of user-provided points, `VOLT` determines the maximum voltage and the offset which all other points in the waveform are referenced to, and `PER` is the duration of the waveform.

The methods defined above are then used in sequences such as in `sequence\client\latticepulse.py`:

```
if self.P['do_lattice_ramp_hold']:
  arb = CamWavGen.Arb(self.P['lattice_resolution'])
  data = arb.compile('RAMPHOLD',
      arb.LinearRamp(0*V, voltage, self.P['lattice_ramp_dur']),
      arb.Hold(voltage, self.P['lattice_hold_dur'] + 10*ms)
      arb.ReturnZero(1*ms)
```

where `Arb` is the class defining how to generate the points in the waveform. The output `data` is an array of numbers (the steps in the output voltage), which the method `compile` converts into strings with a waveform name that appears on the screen (in this case `RAMPHOLD`), ready to be sent to the signal generator. Finally, `lattice resolution` is in units of time, controls how many points the generator is going to output. We cannot directly control the duration of the waveform, only the sample rate of the device. The number of points in the waveform and the sample rate then determine the duration. Understanding and implementing this is essential to guarantee the independent duration of each separate part of the arbitrary waveform, and not cause an overall scaling. The

resolution needs to be increased for short pulses, and reduced for long ones in order not to run out of memory.

Extensions

While I stood on the shoulders of giants when writing the above methods, I am not a giant myself – literally and figuratively.
Hence my solution is certainly not definitive. Extensions and modifications that I would have implemented with more time are reported below.

- Loading the arbitrary waveform to the signal generator during the upload phase of the sequence, and not when the subclass is called. This would speed up the process and prevents the GUI from freezing.
- Use the `DATA:SEQ` subsystem together with `repeat mode`. This allows to only specify *one* voltage value that is repeated multiple times as opposed to waste memory on generating a string of numbers with equal value.

D.10 Dimensionless units for lattice potential

Eq. 7.3 describes the ground state energy for atoms localised on each minimum of the optical lattice potential. This assumes the deep lattice limit discussed in section 2.4.2, where the minima are approximated as harmonic oscillators to result in a ground state energy E_0:

$$E_0 = E_{\text{min}} + \frac{\hbar\omega_x + \hbar\omega_y}{2}, \tag{D.38}$$

where E_{min} is the offset.
It is beneficial to compute this in dimensionless units, detailed as follows.

All the energies are defined in units of the *recoil energy* $E_{\text{rec}} = \frac{\hbar k^2}{2m}$, so the potential V is expressed in terms of a dimensionless parameter $\widetilde{V}$: $V = \widetilde{V} E_{\text{rec}}$. Likewise, positions are in units of the wavelength λ: $x = \tilde{x}\lambda$ and $k = \tilde{k}\lambda$, so that $\tilde{k} = 2\pi$.

The angular frequency ω is obtained via:

$$\omega^2 = \frac{1}{m}\frac{\partial^2 V}{\partial x^2}\bigg|_{\text{min}} = \frac{1}{m\lambda^2}\frac{\partial^2 V}{\partial \tilde{x}^2}\bigg|_{\text{min}} = \frac{E_r}{m\lambda^2}\frac{\partial^2 \widetilde{V}}{\partial \tilde{x}^2}\bigg|_{\text{min}} = \frac{E_r k^2}{4\pi^2 m}\frac{\partial^2 \widetilde{V}}{\partial \tilde{x}^2}\bigg|_{\text{min}} = \frac{E_r^2}{2\pi^2\hbar^2}\frac{\partial^2 \widetilde{V}}{\partial \tilde{x}^2}\bigg|_{\text{min}}. \tag{D.39}$$

Now we define $\widetilde{V} = \alpha I$ where $I = \sum \cos^2$ is the functional dependence of the intensity of the optical lattice, and α essentially the atomic polarisability (section 2.2.2).

Hence:

$$\omega^2 = \frac{\alpha E_{\text{rec}}^2}{2\pi^2\hbar^2}\frac{\partial^2 I}{\partial \tilde{x}^2}\bigg|_{\text{min}}, \quad \omega = \sqrt{\frac{\alpha E_{\text{rec}}^2}{2\pi^2\hbar^2}\frac{\partial^2 I}{\partial \tilde{x}^2}\bigg|_{\text{min}}},$$

$$\hbar\omega = \underbrace{\sqrt{\frac{\alpha}{2\pi^2}\frac{\partial^2 I}{\partial \tilde{x}^2}\bigg|_{\text{min}}}}_{\text{Calculated from code, in units of } E_{\text{rec}}.} E_{\text{rec}}, \tag{D.40}$$

$$E_0 = \alpha I E_{\text{rec}} + \frac{1}{2}\left(\sqrt{\frac{\alpha}{2\pi^2}\frac{\partial^2 I}{\partial \tilde{x}^2}\bigg|_{\text{min}}} + \sqrt{\frac{\alpha}{2\pi^2}\frac{\partial^2 I}{\partial \tilde{y}^2}\bigg|_{\text{min}}}\right) E_{\text{rec}}.$$

So, the energy E_0 in units of E_{rec} is:

$$E_0/E_{\text{rec}} = \alpha I + \frac{1}{2}\left(\sqrt{\frac{\alpha}{2\pi^2}\left.\frac{\partial^2 I}{\partial \widetilde{x}^2}\right|_{\text{min}}} + \sqrt{\frac{\alpha}{2\pi^2}\left.\frac{\partial^2 I}{\partial \widetilde{y}^2}\right|_{\text{min}}}\right). \tag{D.41}$$

D.11 Fourier transforms

The derivations of the equations quoted in section 7.2.1 are presented here.

A 1D harmonic optical lattice results in the following potential:

$$V(x) = -V_0 \cos^2(\pi x/x_0), \tag{D.42}$$

where x_0 can be taken as $\lambda/2$ in order for the lattice sites to occur $\forall i \in \mathbb{Z}$. Its Fourier transform is a finite set, as the potential can be expressed as a Fourier series:

$$\mathcal{F}[V] = \mathcal{F}[-V_0 \cos^2(\pi x/x_0)] = -V_0\sqrt{\frac{\pi}{2}}\left\{\frac{1}{2}\delta(k+k_0) + \delta(k) + \frac{1}{2}\delta(k-k_0)\right\}, \tag{D.43}$$

where $k_0 = 2\pi$.

For a real ionic crystal, the potentials are given by the Coulomb interaction:

$$V = -V_0 \sum_{i\in\mathbb{Z}} \frac{1}{|x/x_0 - i|}, \tag{D.44}$$

which can be also written as a convolution ($*$):

$$V = -V_0\left(\sum_{i\in\mathbb{Z}} \delta(x/x_0 - i) * \frac{-1}{|x/x_0|}\right) \tag{D.45}$$

so that its Fourier transform may be analytically obtained by means of the convolution theorem:

$$\begin{aligned}\mathcal{F}[V] &= \mathcal{F}\left[-V_0\left(\sum_{i\in\mathbb{Z}} \delta(x/x_0 - i) * \frac{-1}{|x/x_0|}\right)\right] \\ &= \mathcal{F}\left[-V_0 \sum_{i\in\mathbb{Z}} \delta(x/x_0 - i)\right] \cdot \mathcal{F}\left[\frac{-1}{|x/x_0|}\right].\end{aligned} \tag{D.46}$$

The Fourier transform of the Coulomb potential is known to be:

$$\mathcal{F}\left[\frac{-1}{|x/x_0|}\right] = \frac{4\pi}{k^2}, \tag{D.47}$$

and that of an infinite Dirac comb is just another infinite Dirac comb:

$$\mathcal{F}\left[\sum_{i\in\mathbb{Z}} \delta(x/x_0 - i)\right] = \frac{1}{\sqrt{2\pi}} \sum_{j\in\mathbb{Z}} \delta(k - jk_0). \tag{D.48}$$

Hence:

$$\mathcal{F}\left[-V_0 \sum_i \frac{1}{|x/x_0 - i|}\right] = \frac{2\sqrt{2\pi}}{k^2} V_0 \sum_{j\in\mathbb{Z}} \delta(k - jk_0), \tag{D.49}$$

i.e. an infinite series of Dirac peaks with an decaying envelope.

D.12 Properties of localised states

In this section we qualitatively discuss the last three points of table 8.1.

D.12.1 Local discrete spectrum

Imagine locally exciting a system, for example by kicking it at a fixed position x. The response of the wavefunction can be inferred from the response of the eigenstates composing it. A 1D optical lattice exhibits Bloch waves (given by eq. 2.65), which are an example of delocalised, thermal states. As shown in fig. D.1a, there are infinitely many Bloch waves (the first three of which are plotted) and hence a *continuum* of states affected by the local excitation. On the other hand, the eigenstates of a disorder-induced localised state are exponentially decaying wavefunctions centred on each lattice site; hence, as shown in fig. D.1b, a local excitation only affects a finite number of them.

The local spectrum in the (disorder-induced) localised phase is hence discrete, as opposed to a continuum spectrum for a thermal, delocalised phase.

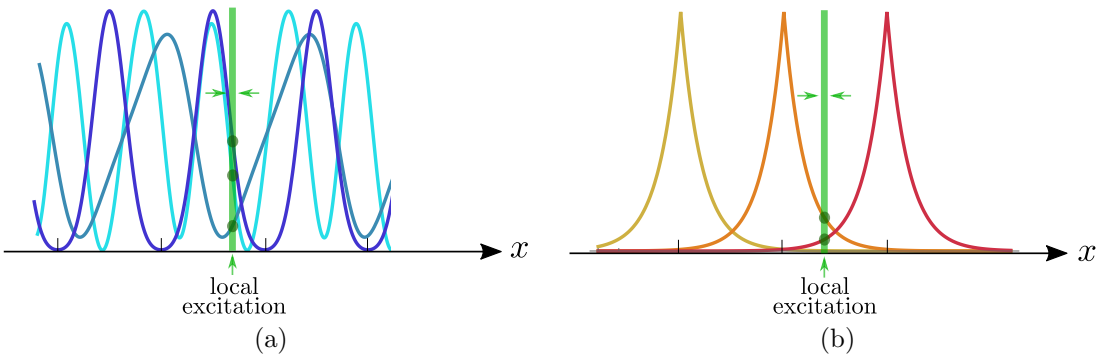

Figure D.1 : A local excitation (green bar) affects infinitely many Bloch waves in the thermal phase (a) and hence results in a continuous local spectrum. On the other hand, a local excitation of the localised phase (b) only affects a finite number of eigenstates and thus results in a discrete local spectrum.

D.12.2 Volume- and area-law entanglement

As for the previous section, the wavefunction in a thermal, delocalised phase is composed of thermal, delocalised eigenstates such as, for instance, the Bloch waves (eq. 2.65). The wavefunction in the disorder-induced localised phase can be decomposed into exponentially decaying functions centred on each lattice site. In a given "volume" of the system, each eigenstate ψ (thermal or localised) contributes a weight $\propto |\psi|^2$.

While thermal states are delocalised and thus contribute more $|\psi|^2$ for larger "volumes", localised states only contribute their $|\psi|^2$ when the boundary ("area") delimiting the "volume" includes them, as shown schematically in fig. D.2. This qualitatively justifies the volume-law growth of the entanglement in thermal states, and the area-law growth in single-particle or many-body localised states.

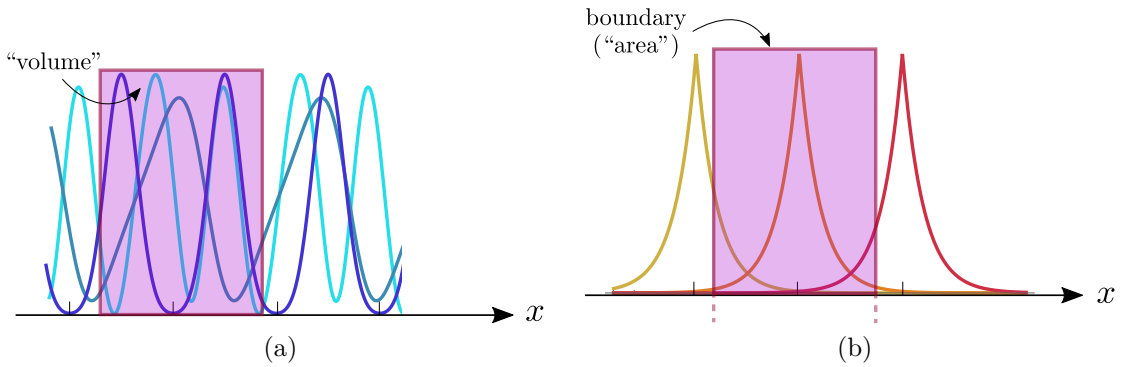

Figure D.2 : Thermal states (Bloch waves, here) are delocalised and their $|\psi|^2$ weight thus increases with an increasing "volume" of interest (a). Localised states (b) are tightly confined on single lattice sites, and thus only contribute their weight when the boundary ("area") includes them.

D.12.3 Logarithmic spreading of the entanglement

In the delocalised phase, the spread of the entanglement is related to the transport properties of the material, which are characterised by a a power-law and thus categorised as diffusive, sub-diffusive, ballistic etc.

In the localised phase, particle transport is prevented by the insulating nature of the state. In the Anderson phase, the absence of interactions precludes the spreading of entanglement over any distance L, or the change of its value should there be any to begin with. On the other hand, in the many-body localised (MBL) phase, interactions allow for a dynamic change of the entanglement.

Given the exponential confinement of the localised wavefunction, it is natural to assume a similar expression for the tunnelling element J as a function of distance L:

$$J \propto J_0 \, \mathrm{e}^{-\frac{L}{\xi}}, \tag{D.50}$$

where ξ is the localisation length.

In the tight-binding model, the Hamiltonian H is directly proportional to the tunnelling element J, $H \propto J$. The Hamiltonian also controls time evolution by $|\psi_t\rangle = \mathrm{e}^{\mathrm{i}Ht/\hbar}|\psi_0\rangle$. For entanglement to spread over a region L, we define a time t such that $Jt \geqslant 1$. Re-arranging, this results in $L \sim \xi \ln(J_0 t)$ and hence in a logarithmic spread of the entanglement.

D.13 Comic relief

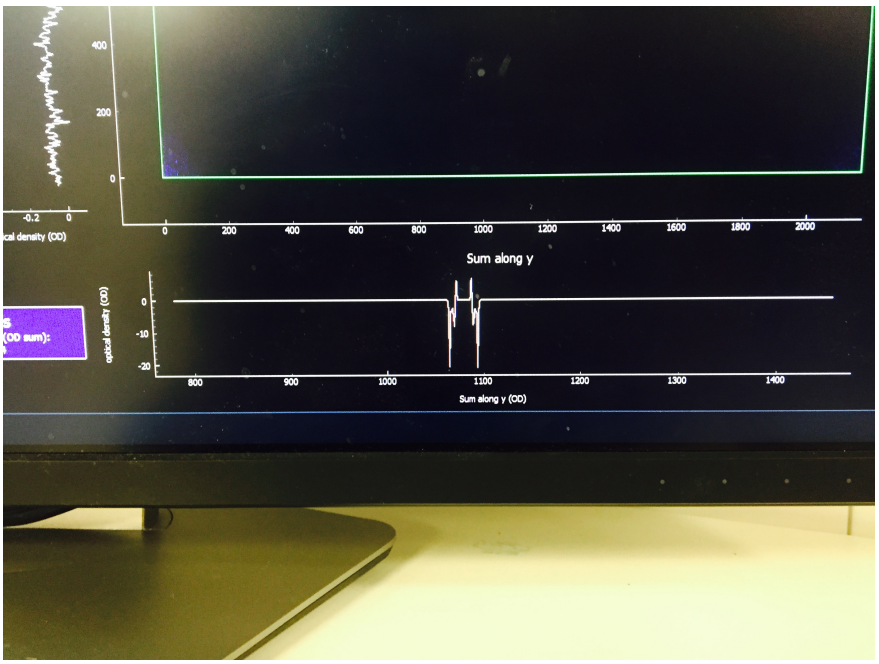

Not the absorption image we deserve, but the one we need right now. A silent guardian, a watchful protector. A dark knight.

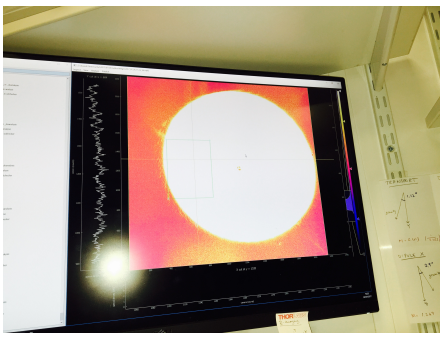

(a) The Sun

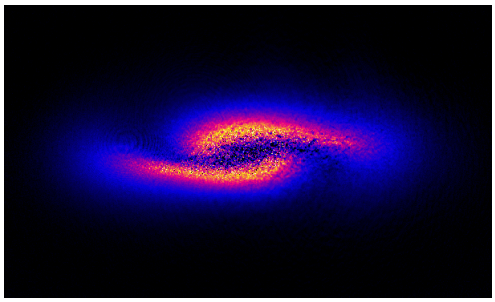

(b) A spiral galaxy

The camera needs to be focussed at infinity, so we used astrophysical objects.

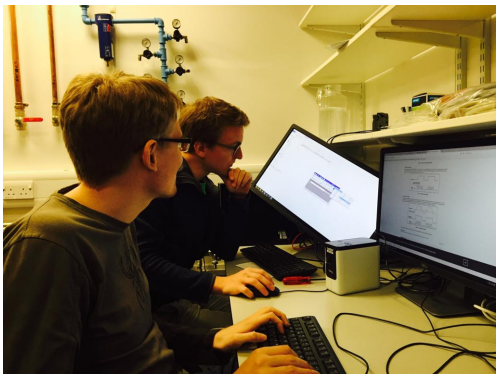

(a)

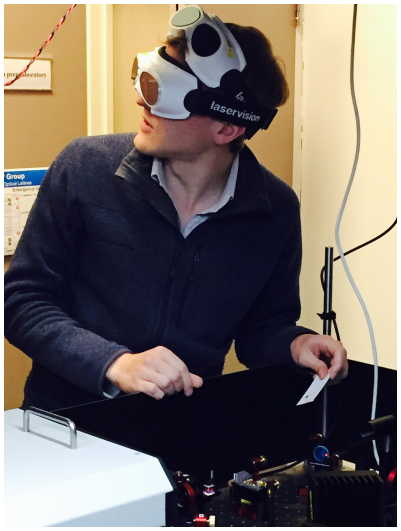

(b)

Konrad testing alternative ways to visualise projections from higher dimensional spaces. Tilting the screen by 45 degrees (a) to serve as $V^{\perp}$ in fig. 3.13, and using two sets of 3D glasses (b) to probe $SO(4) \cong SO(3) \times SO(3)$.

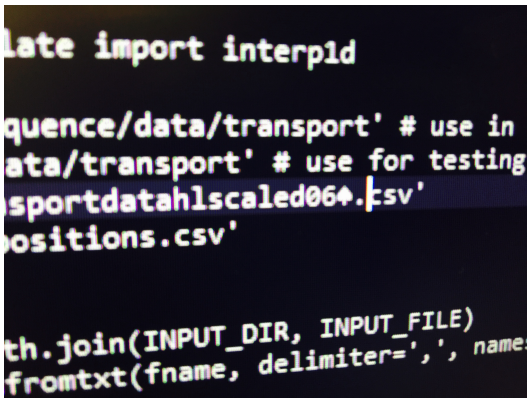

(a) ♠

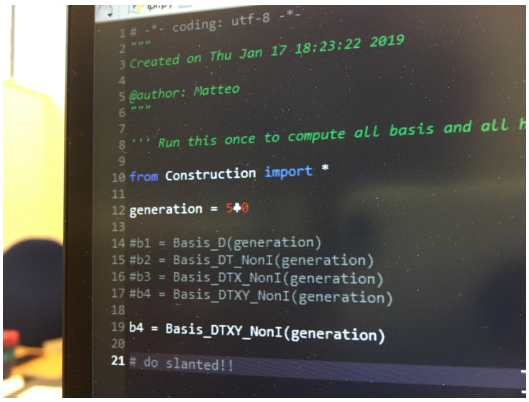

(b) ♣

Typical inexplicable bugs which would cripple our python code and make us reconsider our life choices.

The search for truth is more valuable than its possession.

Gotthold Ephraim Lessing